OCS Study
BOEM 2015-046

Use of Morphological Models to Predict Physical Processes and Assess Impacts in Support of Dredging Operations on the U.S. Outer Continental Shelf

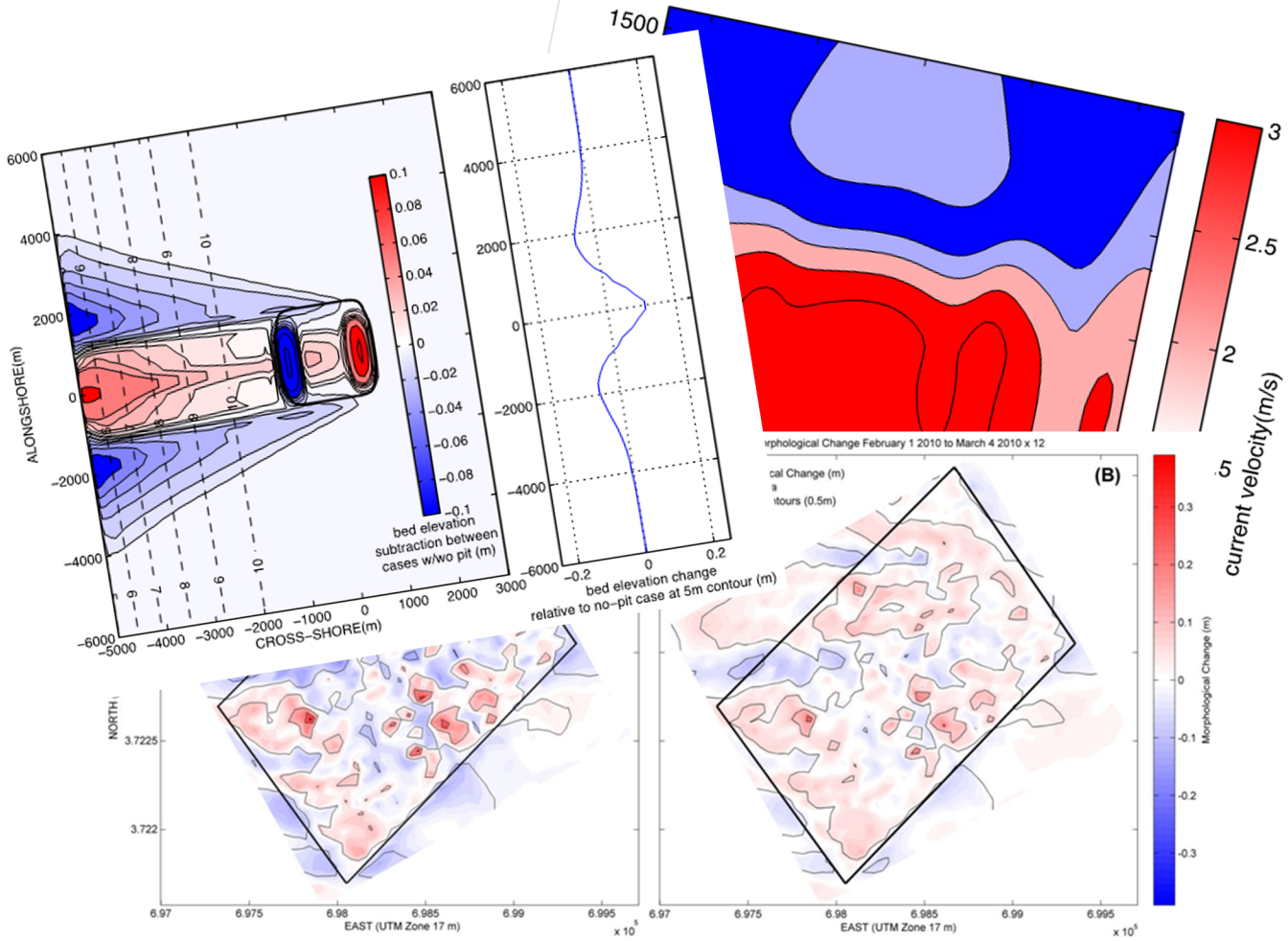

US Department of the Interior
Bureau of Ocean Energy Management
Headquarters

BOEM
Bureau of Ocean Energy Management

OCS Study
BOEM 2015-046

Use of Morphological Models to Predict Physical Processes and Assess Impacts in Support of Dredging Operations on the U.S. Outer Continental Shelf

Prepared under BOEM Contract Number M10PC00118 by:

John Ramsey, P.E.
Gwen Simmons
Rebecca Quan

Applied Coastal Research and Engineering, Inc.
766 Falmouth Road, Suite A-1
Mashpee, MA 02649

Fengyan Shi, Ph.D.
James T. Kirby, Ph.D.

Center for Applied Coastal Research
University of Delaware
Newark. DE 19716

Giovanni Vittori, Ph.D.

UNIVERSITÀ DEGLI STUDI DI GENOVA,
16145 GENOVA - Via Montallegro

Julio Zyserman, Ph.D.

DHI Water & Environment, Inc.
100 Second Avenue South
Suite 302 North
St. Petersburg, FL 33701

Prepared for:

U.S. Department of the Interior
Bureau of Ocean Energy Management
Headquarters
September 8, 2015

OCS Study
BOEM 2015-046

DISCLAIMER

Study concept, oversight, and funding were provided by the US Department of the Interior, Bureau of Ocean Energy Management, Environmental Studies Program, Washington, DC, under Contract Number M10PC00118. This report has been technically reviewed by BOEM and it has been approved for publication. The views and conclusions contained in this document are those of the authors and should not be interpreted as representing the opinions or policies of the US Government, nor does mention of trade names or commercial products constitute endorsement or recommendation for use.

REPORT AVAILABILITY

To download a PDF file of this Environmental Studies Program report, go to the US Department of the Interior, Bureau of Ocean Energy Management, Environmental Studies Program Information System website and search on OCS Study BOEM 2015-046.

CITATION

Ramsey, J.S., G. Simmons, R. Quan, F. Shi, G. Vittori, J. Zyserman, J. Kirby, 2014. Best Practices for Physical Process and Impact Assessment in Support of Dredging Operations on the U.S. Outer Continental Shelf. U.S. Department of the Interior, Bureau of Ocean Energy Management, Herndon, VA. OCS Study BOEM 2015-046, 262 pp. + 13 pp. appendices.

TABLE OF CONTENTS

LIST OF FIGURES

LIST OF TABLES

ABBREVIATIONS AND ACRONYMS

2D	Two-Dimensional
ADCIRC	Advanced Circulation Model
ADCP	Acoustic Doppler Current Profilers
BOEM	Bureau of Ocean Energy Management
CIRP	Coastal Inlets Research Program
CMS	Coastal Modeling System
COAWST	Coupled-Ocean-Atmosphere-Wave-Sediment-Transport
CPU	Central Processing Unit
CRM	Coastal Relief Model
CSTMS	Community Sediment Transport Modeling System
DHI	Danish Hydraulic Institute
GIS	Geographic Information System
GT	Georgia Institute of Technology
JONSWAP	Joint North Sea Wave Project
MCF	Model Calibration Factor
MCM	Million Cubic Meters
MLLW	Mean Lower Low Water
MMS	Minerals Management Service
MPI	Message Passing Interface
NAD	North American Datum
NAVD	North American Vertical Datum
NDBC	National Data Buoy Center
NearCoM	Nearshore Community Model
NGDC	National Geophysical Data Center
NOAA	National Oceanic and Atmospheric Administration
NOPP	National Oceanography Partnership Program
NOS	National Ocean Service
OCM	Online Correction Method
OCS	Outer Continental Shelf
Q3D	Quasi Three-Dimensional
RANS	Reynolds Averaged Navier Stokes
ROMS	Regional Ocean Modeling System
SEDMOC	Sediment Transport Modeling in Marine Coastal Environments
SHORECIRC	Nearshore Circulation Model
SMS	Surface-water Modeling System
STP	Sediment Transport Program
STWAVE	Steady-State Spectral Wave
SWAN	Simulating Waves Nearshore
TIN	Triangulated Irregular Network

Abbreviations and Acronyms Continued

TVD	Total Variation Diminishing
USACE	United States Army Corps of Engineers
USC	University of South Carolina
USGS	United States Geological Survey
UTM	Universal Transverse Mercator
WGS	World Geodetic System
WIS	Wave Information Studies
WP	Work Product
WRF	Weather Research and Forecasting

I. INTRODUCTION

The Bureau of Ocean Energy Management (BOEM; previously Minerals Management Service (MMS)) Marine Minerals Program is responsible for the environmentally responsible management of Outer Continental Shelf (OCS) sand and gravel resources. The importance of the OCS sand resources will increase as the demand for sand supply for coastal restoration and protection projects grow. Some OCS sand resources will likely need to be long-term sources of borrow material for coastal restoration and protection, especially in the face of sea level rise. The need for access to large sand inventories for immediate/emergency repair of beaches and barrier islands will also potentially increase due to the increasing intensity and frequency of episodic extreme events such as storms and hurricanes. BOEM must continue to ensure that any use of OCS sand resources will not adversely affect the physical and biological environments, both in the near-field of the borrow area, as well as in the far-field near the coast (Giordano et al., 1999; Drucker, 2004). In addition to immediate and short-term impacts, repeated use of OCS sites raises questions about potential long-term cumulative near-field and far-field impacts that need to be addressed (Michel, 2004).

Past studies funded by the BOEM have primarily been directed at quantifying far-field shoreline impacts, focusing on wave transformation over the borrow area and induced gradients in longshore sediment transport potential (Kelley et al. 2001; Kelley et al., 2004; Byrnes et al. 2004; Hayes and Nairn, 2004), although recent efforts have considered longer-term morphological evolution at the borrow area. Near-field and far-field effects depend on many factors, including but not limited to borrow area location (water depth, distance from shore, proximity to ridges), borrow area geometry (length, width, depth, side slopes), orientation relative to tidal and nearshore currents, dominant wave directions etc., and variations in the complexity of adjacent bathymetry and sediment characteristics. Morphological evolution of borrow sites following dredging events is important for BOEM management of nearshore resources as these processes can impact adjacent (potentially sensitive) seafloor habitat, influence bedform recovery with respect to pre-dredging morphology and the associated impacts to shelf geomorphic processes, and possible migration of borrow site into archaeological buffers. Previous studies related to sand extraction in offshore areas have often focused on the simplifying analogue of trench morphology. Trenches and navigation channels are characterized by a length that is much larger than their width, justifying the assumption of spatial uniformity along the longitudinal axis and thereby allowing for the idealized application of two-dimensional vertical models such as SUTRENCH (Van Rijn and Tan, 1985) or LITTREN (DHI, 2009). This simplified approach, owing to the efficiency of analytical, semi-empirical and two-dimensional vertical numerical modeling tools, can be very useful for preliminary studies and rapid assessment of trench evolution.

However, the geometry of a sand borrow area is in practice constrained in both horizontal directions. Sandpits experience flow contraction, which is enhanced by friction-topography interactions and Coriolis effects (Roos et al., 2008). The flow contraction in turn can cause instabilities leading to the gradual deformation of the borrow area itself, including migration and formation of adjacent humps as well as large-scale features such as tidal sand banks (Ribberink,

2004). The borrow area may act as a sink for sediments, potentially including sediment from the nearshore system (Walstra et al., 2002). The area of influence of the borrow area may extend over tens of kilometers outside the original mining area when considering time scales from decades to centuries. The interaction between a sand borrow area and existing large-scale bed forms (ridges, sand banks etc.) is important with regard to optimization of extraction locations as well as long-term impact assessment (De Swart and Calvete, 2003; Roos and Hulscher, 2007).

The fundamental challenges of morphological modeling is the requirement to describe complicated interconnected physical mechanisms (waves, flow, sediment), over long time periods. As CPU requirements for long-term simulations using comprehensive process-based models are prohibitive for practical applications, simplifications are required. These simplifications take the form of "process filtering" and "input filtering" approaches. Process filtering implies the simplification or omission of processes. Examples are neglecting 3D effects, applying a simplified wave model, providing only intermittent morphological feedback to the bathymetry, or applying "speed-up" factors to accelerate the morphological change. "Input filtering" simplifies the forcing mechanisms input to the model. Examples are describing a uniform representative "morphological tide" rather than a continuously varying one, or simulating a limited number of wave conditions rather than a full climate, or considering sediment to be a single uniform grain size. Whether filtering processes or inputs, these simplifications need to be carefully chosen and defended, lest the morphological projections be unreliable. Morphological projections generated within the Sediment Transport and Morphology of Offshore Sand Mining Pits/Area (SANDPIT) project were shown to vary widely, depending upon the details of the filtering methodology implemented in various models.

The objective of this project is to test, tailor and apply existing numerical morphological modeling tools and methods in order to provide robust and defensible predictions of morphological behavior in OCS sand extraction pits/areas, as well as the associated near-field and far-field impacts. Although much progress has been made through previous studies (including those funded by BOEM within the U.S., as well as European efforts such as SANDPIT, SEDMOC, and others), the current state-of-the-art regarding morphological behavior or borrow areas remains limited. Multiple tools at various levels of complexities must thus be brought to bear (Hommes et al. 2007) to provide the *practical* guidance regarding OCS sand extraction sought by BOEM. The primary questions which are of direct relevance to BOEM's mandate are:

- What are the infilling rates of extraction pits/areas after completion?
- What are the deformation/migration rates and directions for the extraction pits/areas on longer time scales (decades to centuries)?
- What impact does the geometry and location of the offshore sand extraction pit/areas have on the far-field, including coastline evolution?
- What are the optimum dimensions of the sand extraction pits/areas with regard to minimizing near-field and far-field impacts?

The above questions must be addressed by numerical models, or by guidance derived in large part from numerical models. Some of the main questions that are targeted as part of this research include:

- How do predictions from process-based modeling tools compare to observed morphology?
- Which model "sensitivity" parameters cause the largest changes in the predicted response in the near-field and far-field?
- What are the relative strengths and weakness in the predictive capabilities for various process-based modeling tools, including both established commercial packages and recently developed community models?
- What combination of model system(s), model options and environmental forcing scenarios can be considered best practice for impact assessments supporting OCS sand extraction?

Through this evaluation approach, the performance of several process-based morphodynamic modeling packages that describe sediment transport and morphological changes under the combined action of waves and currents will be assessed. The candidate models include the public domain Nearshore Community Model (NearCoM) developed by various researchers in the United States, as well as commercial models from DHI Water and Environment, Inc. and the United States Army Corps of Engineers (USACE), the latter being available through Aquaveo (http://www.aquaveo.com/) as the Coastal Modeling System (CMS). Each of these model systems are:

- State-of-the art
- Extensively tested, validated, and quantified with regard to skill assessed in different applications and environments
- Widely accepted and used by the research community for their stated purpose as evidenced in peer-reviewed literature, and
- Well described in model documentation and user manuals

Prior to implementing the series of near-field morphological models, long-term boundary conditions for the selected site offshore of the South Carolina coast were required to parameterize the models. The calibrated Coupled-Ocean-Atmosphere-Wave-Sediment Transport (COAWST) model developed for another application in the Long Bay region offshore South Carolina (Warner, et al, 2012) provided the required input for the site-specific simulations required for this study. The COAWST modeling suite links four (4) separate modeling tools: the Weather Research and Forecasting (WRF) large-scale atmospheric model, the Regional Ocean Modeling System (ROMS) as the hydrostatic free surface oceanographic circulation module, the Simulating Waves Nearshore (SWAN) as the full plane spectral wave action model that simulates shoaling, refraction, diffraction, and reflection, and the generalized Community Sediment Transport Modeling System (CSTMS) to simulate different forms of sediment transport leading to overall morphological bed changes. CSTMS can incorporate various sediment transport modeling tools to provide maximum functionality, depending on the application.

The fundamental challenge of morphological modeling is the requirement to describe complicated interconnected physical mechanisms (waves, flow, sediment) over long time periods. Simplifications are required in both physical formulations, referred to as process filtering, and input parameters, referred to as input filtering.

Overall, the model's ability for predicting morphological changes was quantified using bathymetric data sets from the pre- and post-dredge surveys of borrow sites. Since the goal of the overall project was to evaluate morphological response of sand and gravel shoal dredging along the Atlantic coast of the U.S., a series of well-documented dredging projects were evaluated along the shoreline including sites from Virginia to southern Florida (see Figure I-1).

In addition to evaluating available data sets from each of these offshore borrow sites (e.g. concurrent wave and current data sets, as well as post-dredging bathymetric change information available for the same time period), it was critical that the site selected represented "typical" oceanographic and morphologic shoals that are dredged along the U.S. East Coast. While it is understood that each potential offshore borrow site is unique, the goal of this evaluation was aimed at identifying a site that could be considered typical for the purposes of developing "best practice" guidelines for the use of morphological change models to assist BOEM in the overall management of these resources.

Specifically for the U.S. Atlantic OCS, potential offshore borrow areas in federal waters tend to be in water depths between 40 feet (~12 meters) and 100 feet (~30 meters). Due to generally 'weak' tidal currents and modest wave climate, measurable sediment transport of sand-sized material only occurs during high energy events. Sediment movement and the associated morphological change during these high energy storm events tends to be dominated by waves, where tidal currents typically play a secondary role to sediment movement. Due to the storm-induced nature of sediment transport within the typical regional offshore borrow areas, utilization of the various available sediment transport formulations also becomes an important consideration that strongly influences the modeled morphological change.

Since the overall purpose of this assessment focuses on management of OCS sand resources, previous studies may have limited applicability to the low-relief shoals characteristic of the U.S. Atlantic OCS dredging sites. For this reason, sensitivity analyses were performed for various key model input decisions such as model-specific settings, spatial resolution, simplified parameterization and/or compression of environmental forcing, and application of "speed up factors" to improve model efficiency and the associated forecasting ability. Within this context, similar efforts to provide guidance for offshore sand mining practices (e.g. Dibajnia and Nairn, 2010) can be evaluated relative to specific modeling considerations.

Figure I-1. Sand and gravel shoal mining sites evaluated for the morphological modeling analysis including Sandbridge Shoals (Virginia), Long Bay (South Carolina), Canaveral Shoals (Florida), and Jupiter Island (Florida).

II. REVIEW OF PREVIOUS STUDIES AND AVAILABLE GUIDANCE

The quantification of local sand transport rates in the marine environment has been studied by numerous academic and industry research groups over the past few decades. More recently, offshore sand mining studies have focused on the prediction of shoreline evolution, as well as morphological changes, that potentially impact the coastal system. A review of existing literature, data and relevant information from previous studies within the United States (focusing on the Atlantic coast) and abroad (notably SANDPIT and SEDMOC) was performed to provide context for use of numerical techniques, specifically morphological models, to assess anthropogenic impacts associated with offshore borrow areas (e.g. Walstra et al., 2002; Roos et al., 2007; Roos et al., 2008; and Dibajnia and Nairn, 2010).

While the overall goals of the various research projects differed, each study provided valuable information regarding the state-of-the-science of numerical modeling associated with sediment transport within the vicinity of potential sand mining sites. In several cases, inter-comparisons of available modeling tools were performed to determine relative strengths and weaknesses of different approaches. In addition to the evaluation of numerical sediment transport methodologies, other studies recommended "best practices" guidance to ensure that offshore sand mining is performed in a manner that protects the integrity of the nearshore and coastal environment. Some of the more practical "best guidance" studies also provided suggested numerical limits to constrain potential adverse impacts associated with sand mining.

The review of past studies revealed that detailed understanding of sediment transport and the associated morphological change processes is limited, where general trends (e.g. direction of transport and overall areas of accretion/erosion) are often predictable; however, actual magnitudes for different modeling approaches can vary widely. Previous studies using numerical morphologic change models have indicated the following:

- No single numerical modeling tool or set of tools yields consistent agreement with field and/or laboratory measurements for a broad range of geomorphic and oceanographic conditions
- Numerical modeling tools generally perform better in plan-bed (flat bottom) cases than cases involving rippled beds (i.e. sand waves)
- Numerical modeling tools generally perform better under conditions of larger waves and stronger bottom currents
- Based on the models evaluated to date, some field measurements are required to provide reasonably accurate predictions of sediment transport processes

Although previous studies have indicated that general use of either research or practical models in an un-tuned manner to make real-world predictions likely will not yield useful results, modeling tools that are 'calibrated' with site-specific field data greatly reduce uncertainty.

II.A. Previous Studies of Morphological Change Caused by Offshore Sand Mining

Numerous applied research efforts have focused on the prediction of morphological change in the nearshore region, including several studies that addressed issues related to offshore sand mining. Starting in 1998, European researchers embarked on a series of model evaluations that attempted to address the predictive capability of these advanced tools relative to hydrodynamics, sediment transport, and the related morphological change. In general, researchers surmised that if local bed level elevations are lowered substantially via dredging of a borrow area (or channel), the local flow and wave fields could be influenced and modify the associated sand transport rates due to modification of wave shoaling, refraction, and reflection patterns. In addition, there were concerns that the borrow area (slopes) may migrate towards the shore over time and/or potentially act as sink (trap) for sediments from the nearshore system.

Initial efforts for evaluating numerical morphological models focused on relatively simple test cases based upon laboratory experiments. In addition, European researchers compared results from a large-scale field experiment with numerous numerical morphological models in an attempt to validate the models to a 'real-world' application. Between October 1999 and March 2000, an extensive monitoring effort was undertaken to evaluate hydrodynamics, water quality, and morphological evolution in the vicinity of a large sand borrow area in the North Sea, approximately 10 km off the Dutch Coast near Hoek van Holland (Walstra, et al., 2002), which is referred to in literature as the PUTMOR dataset. The dimensions of the borrow area were 1,300 meters in length, 500 meters in width, and a depth of 10 meters, where the ambient seabed depth was approximately 24 meters. The total borrow area excavation volume was approximately 6,500,000 cubic meters. Detailed measurements consisted of bathymetry, flow velocities, water levels, water temperature, conductivity, turbidity, dissolved oxygen, and bottom grain size.

As part of the model comparison effort, an in-depth study termed SANDPIT (Sand Transport and Morphology of Offshore Sand Mining Pits/Areas) was performed between 2002 and 2005 (Ribberink, 2004). As part of the project a number of benchmark tests were developed to establish the efficacy of morphodynamic models in predicting the behavior of large-scale sand mining borrow areas. These tests consisted of both small-scale laboratory experiments and field experiments, with the PUTMOR dataset providing the primary source for model comparisons. In general, model comparison showed satisfactory predictions of the depth-averaged velocities inside and outside the borrow area. Although depth-averaged velocities were comparable to datasets, the ultimate morphological predictions showed significant differences that were primarily ascribed to complex three-dimensional effects of in the near-bed velocity field. Specifically, near-bed currents were determined to be the primary driving force governing sediment movement and uncertainties related to the near-bed velocity profile prevented accurate representations of bed change by the models.

The applied validation methodology utilized for SANDPIT enabled objective comparison of the models for a series of benchmark cases. However, despite the scaling of the sediment transport and the application of common boundary conditions/model parameter settings, the differences between the model predictions were relatively large. More in-depth analyses of

model results as part of the SANDPIT project indicated that subtle differences in the morphological model calibration process can yield a relatively large range of predictions, even if the underlying hydrodynamics were nearly identical. In general, models that had delayed settling of suspended sediment included through an advection-diffusion equation yielded the best agreement with the observed values. The applied factors to scale sediment transport rates to the measured observed values were in the range of 0.2 to 5 (Walstra, et al., 2002), indicating that scaling beyond typical variation of model parameters within the sediment transport formulas was required to match observed transport rates. Therefore, it was determined that uncertainties in morphological modeling were primarily a result of the various sediment transport formulations. For this reason, some researchers working on SANDPIT made minor modifications to the most commonly utilized sediment transport formulation; the Soulsby-Van Rijn 1997 (Soulsby, 1997) formulation.

Due to the complexity of the field site (PUTMOR) evaluated for the SANDPIT analysis, the overall modeling approach varied for the various researchers involved in the project. For example, development of wave conditions incorporated into the morphological modeling approach ranged from varying wave conditions throughout the simulation period (both temporally and spatially) to a single representative wave condition across the model domain for the full duration of the simulation. In addition to the comparison of morphological change results to evaluate the performance of individual models, the SANDPIT comparison of morphological models showed that standardization of model schematizations and calibration methods was critical to understand the meaning of the term ‘calibration’. Researchers involved with SANDPIT utilized various model calibration techniques ranging from direct scaling of the sediment transports to modified transport specific parameters and/or bottom roughness. This variety on scaling methods resulted in substantially different model results even with the same input wave, flow, and transport formulations. Instead, it was recommended that scaling factors should be applied on the sediment transport rates determined by the original formulations. This enabled a direct comparison between models and also standardizes the model calibration process.

The results suggest that, at the stage of model development available to the SANDPIT researchers, “considerable uncertainty should be expected if un-tuned models are used to make absolute predictions for field conditions” (Davies, et al., 2002). The availability of some *in situ* measurements is necessary for high-accuracy sand transport predictions. Since many of the present models exhibit agreement in their relative behavior over wide ranges of wave and current conditions, available models provided a solid hydrodynamic baseline for supporting morphodynamic predictions. Ongoing research continues to improve sediment transport formulations and the associated morphologic predictions; however, accurate modeling warrants data-driven site-specific model validation and/or tuning. Overall, model estimates of the measured longshore component of suspended sand transport yielded agreement to within a factor of 2 in 22% to 66% of cases tested in SANDPIT (Davies, et al., 2002).

Efforts in the U.S. have been less extensive, with limited morphological model evaluations performed within the context of a USGS led effort (Community Model for Coastal Sediment Transport), as well as modeling work for the Minerals Management Service that focused on the evaluation of offshore shoal stability (Dibajnia and Nairn, 2010). The USGS-led effort consists of ongoing work associated with the development of a three-dimensional model that includes

sediment transport and morphologic evolution utilizing the Regional Ocean Modeling System (ROMS) for hydrodynamics linked to the SWAN wave model. Model development is described in Warner, et al. (2008), where initial comparisons were made for the Massachusetts Bay region. No field verification related to morphologic change predicted by the Community Model was performed; rather, the bottom shear stress predicted by the model was compared to Bay-wide grain size distribution.

In an attempt to formulate and recommend guidelines for offshore sand mining of shoals along the U.S. Atlantic OCS, Dibajnia and Nairn (2010) utilized numerical hydrodynamic, wave, and sediment transport models to predict the effects of dredging on shoal morphology. The modeling effort focused on the Isle of Wight Shoal offshore of the Maryland coast. Earlier work by Hayes and Nairn (2004) surmised that the well-developed shoal systems characteristic of the Mid-Atlantic Bight (Figure II-1) were maintained off of the coast of Maryland and Delaware as a result waves refracting and shoaling on the shoals causing a convergence of sand transport over the shoal crest. The prediction of morphological change incorporated a full-plane spectral wave model (SWAN), a simple depth-averaged hydrodynamic module, and a sheet flow transport formulation developed by Dibajnia and Watanabe (1992). It was anticipated that the shallow depths of the shoal system modeled would have sediment transport dominated by storm wave energy; therefore, sheet flow estimates would be accurate.

Utilizing the example of the Isle of Wight Shoal, which was oriented in the prescribed NE-SW direction, a modeling evaluation of various shoal dredging alternatives was performed. The initial model assessments included comparisons to regional hydrodynamic and wave data; however, the model calibration appeared to be primarily derived from visual comparisons with the data. Similarly, the comparison of morphologic change to the available data was also visual, with the model consistently over-predicting accretion along the crest of the shoal feature. Due to the sheet flow sediment transport formulation selected, it is possible that the wave-induced component of transport over-predicted sediment movement during periods of high wave energy (storms). Regardless, the model was utilized to predict the influence of shoal excavation on long-term morphology of the overall shoal system. The general conclusions of this study indicated that shoals that are dredged in water depths exceeding 10 meters will only reform to a smaller shoal once dredged. In addition, the greater volume removed, the smaller the resulting reformed shoal volume. Specifically, numerical modeling results indicated that there is a limit to shoal height recovery if material is taken directly from the crest of the shoal, where the Relative Shoal Height was utilized as the basis for recommended dredging guidelines. Dibajnia and Nairn (2010) concluded with recommendations regarding appropriate dredging practices for shoal fields; however, these conclusions were largely driven by the selection of sediment transport formulation (i.e. sheet flow) and may not be universally appropriate for shoal fields throughout the U.S. Atlantic OCS.

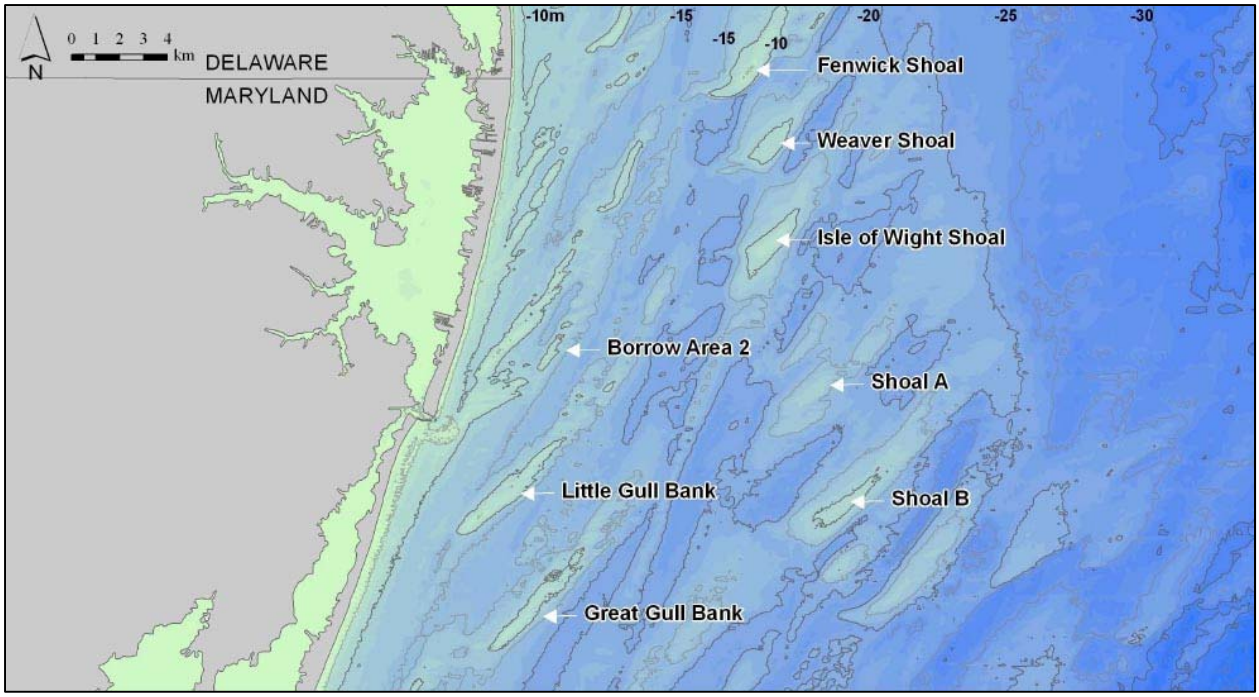

Figure II-1. Bathymetry offshore of Delaware and Maryland illustrating the typical shoal and swale topography of the Mid-Atlantic Bight (from Dibajnia and Nairn, 2010).

II.B. Overall Status of Morphological Modeling of Offshore Borrow Areas

While significant progress has been made over the past two decades relative to the development of numerical methods that can predict morphological evolution under the action of currents and wave forcing, our ability to accurately predict migration of shoal features, as well as the evolution of shoals following dredging, is somewhat limited. Although inter-comparison of models have typically yielded substantial differences in the absolute prediction of sediment transport quantities, the relative behavior of the models relative to observations is equally important. As described in Davies, et al., 2002, it is critical that model predictions describe the proper relative behavior (a) as a function of the various input parameters (waves, currents, and bottom grain size) and (b) over the observable range of conditions that may involve several orders of magnitude in the sediment transport rate. From a resource management perspective, it is critical that geomorphic modeling is performed in a manner that allows accurate prediction of sediment transport dynamics to support management decisions.

Due to the inherent complexities associated with sediment movement on the Outer Continental Shelf, absolute predictions are difficult to obtain with existing models. The results from European researchers suggest that, at the stage of model development available to the SANDPIT project, "considerable uncertainty should be expected if un-tuned models are used to make absolute predictions for field conditions" (Davies, et al., 2002). Therefore, *in situ* measurement continue to be necessary to develop predicative modeling tools for assessment of sediment transport and the associated geomorphic change. Since many of the present models exhibit agreement in their relative behavior over wide ranges of wave and current conditions,

available models can provide a solid hydrodynamic baseline for supporting morphodynamic predictions. Ongoing research continues to improve sediment transport formulations and the associated morphologic predictions; however, accurate modeling warrants data-driven site-specific model validation and/or tuning.

To date, research efforts in Europe relative to nearshore sediment transport processes associated with borrow areas have been more extensive than those performed in the United States. Regardless, the tools developed through the extensive European researchers combined with site-specific information and updated numerical modeling tools allow for continued advancement for morphodynamic predictions, specifically for the U.S. Atlantic OCS.

III. REVIEW AND COLLATION OF DATASETS

A review of available data sources has been performed to evaluate information that can be used in the development of the process-based morphodynamic models. Required data include bathymetric data, meteorological records, wave and sediment data which will be used to parameterize, calibrate and validate the models. Specifically, sites along the U.S. Atlantic OCS were targeted for this study. The initial step in this evaluation was to pick the most appropriate previously dredged offshore borrow area where high-quality data exists to parameterize the morphodynamic models. In addition, it was critical to select a site representative of 'typical' offshore conditions along the U.S. Atlantic OCS, where depths at the borrow area are between 10 and 25 meters, the tidal currents are relatively weak, and sediment transport is dominated by the local wave climate.

Bathymetric datasets that were in the possession of the project team at the initiation of the study included pre- and post-dredge surveys of borrow areas offshore of Jupiter Island, Florida and Sandbridge, Virginia. The Jupiter Island dataset included bathymetry surveys of eight borrow areas from three separate time periods (1982, 1994, and 2005). All borrow areas for Jupiter Island lie approximately 1 km offshore of the island. A cumulative total of 6.3 million cubic meters (MCM) were extracted from these sites and placed along a 9.6 km reach of the island shoreline starting in the early 1970s. Most sites were located in water depths of 9 m, and the deepest excavations had total depth of more than 18 m. In addition to the offshore data, shoreline surveys have been performed, and detailed records of beach nourishment volumes have been maintained for the more than 30-year span of the ongoing shoreline maintenance program of the Town of Jupiter Island. These data offer a great long-term, detailed dataset that includes measured borrow area evolution and resulting shoreline impacts based on the response to the development of erosional "hot spots" along the shoreline. The "hot-spots" have been directly linked to the wave refraction effects of the borrow areas (Kelley and Ramsey, 2006). Members of the research team also have experience working with BOEM in the analysis of borrow area impacts from sand mining at Sandbridge Shoal, Virginia (Kelley, et al., 2001 and Kelley and Ramsey, 2001). Data from these sites are potentially useful in the development and evaluation of morphological modeling tools for the proposed study.

Other possible study sites and sources of data were added to the two sites listed above. In total, evaluation of four (4) potential offshore sites has been undertaken to determine which area would provide the best overall dataset to support accurate morphological change modeling of a borrow area representative of the U.S. East Coast. The four sites considered in this review include: Sandbridge Shoal in Virginia, Long Bay in South Carolina, Cape Canaveral Shoals in Florida, and Jupiter Island also in Florida (Figure III-1). The comparison and ultimate ranking of these sites was based on whether the site represented 'typical' morphological and oceanographic conditions along the U.S. Atlantic OCS, the availability and breadth of historic data, as well as the existence of previously developed numerical hydrodynamic, wave, and sediment transport models.

Figure III-1. Sand and gravel shoal mining sites evaluated for the morphological modeling analysis including Sandbridge Shoal (Virginia), Long Bay (South Carolina), Canaveral Shoals (Florida), and Jupiter Island (Florida).

The quality and coverage of available data directly impact the accuracy of any model and also its effectiveness as a planning or engineering tool. Data required for the development of a morphological model include bathymetry, waves, currents, winds, and sediment characteristics. In addition to considering the different types of available data that would be used to parameterize a model, it is also important to consider the temporal coverage of the datasets. Ideally, available wave, wind and current velocity datasets would overlap in time and be available for multiple years. It is important also to have a series of bathymetric surveys of the study area that show borrow area conditions immediately post-dredging as well as other surveys that document the morphological evolution of the dredged borrow area through time.

III.A. Review of DataSets

A review of available data sources was performed in order to locate information that could be used in the development of the process-based morphodynamic models. For this project four potential east U.S. Atlantic Coast borrow sites (Figure III-1) were chosen to review the available the data in order to determine which site would provide the great advantage to this study. The four preliminary sites were Sandbridge Shoals in Virginia (Figure III-2), three shoals in Long Bay which is in South Carolina (Figure III-3), Cape Canaveral Shoals in Florida, and the shoals near Jupiter Island which is also in Florida (Figure III-4). The comparison and ultimate ranking of these sites was based on the availability and breadth of historic data and also on the existence of previously developed computer models.

Sandbridge Shoal has been dredged six times (1996, 1998, 2002, 2003, 2007, and 2014) to nourish Virginia Beach from Dam Neck to Sandbridge Beach. The sand to nourish these projects came from two offshore borrow areas, Area A and B (Figure III-2). Apart of Area B has been dredged for all five nourishments, while part of Area A has only been dredged for the 1998 and 2007 projects. These borrow areas are a part of a large sand shoal approximately 3 to 5 miles from the project area and in water depths of -36.0 to -60.0 NOS MLLW. In the 2007 nourishment project (the period of time when detailed bathymetric and oceanographic data was available) a total of 2,395,473 yd^3 of sand was taken from the borrow areas, 2,229,723 yd^3 from Area A and 165,750 yd^3 from Area B.

The Long Bay site has three different offshore borrow shoals, Little River, Cane South, and Surfside (Figure III-3). All three borrow areas have been dredged twice for the 1996 to 1998 nourishment project and the 2007 to 2009 nourishment project. Each borrow area was used for a different part of the nourishment project; Little River was dredged for North Myrtle Beach, Cane South nourished Myrtle Beach and Surfside shoal was used for Garden City-Surfside Beach. In total approximately 26 miles of shoreline was nourished in the 2007-2009 project. Little River shoal is 1.3 mi^2 and prior to the 2007-2009 nourishment had an average depth of -36.3 ft. During the 2007-2009 nourishment approximately 1,069,390 yd^3 of sediment was removed from Little River making the average depth of the shoal after dredging -36.6 ft. Cane South is 0.85 mi^2 with an average depth of -34.9 ft prior to the 2007-2009 nourishment. During the 2007-2009 project an estimated 1,580,740 yd^3 was removed from Cane South making the new average depth -35.7 ft. The third offshore borrow area, Surfside, is 0.64 mi^2 and before the 2007-2009 project it had an average depth of -32.3 ft. An estimated 838,350 yd^3 was removed from Surfside shoal to make the average depth of the shoal -32.6 ft.

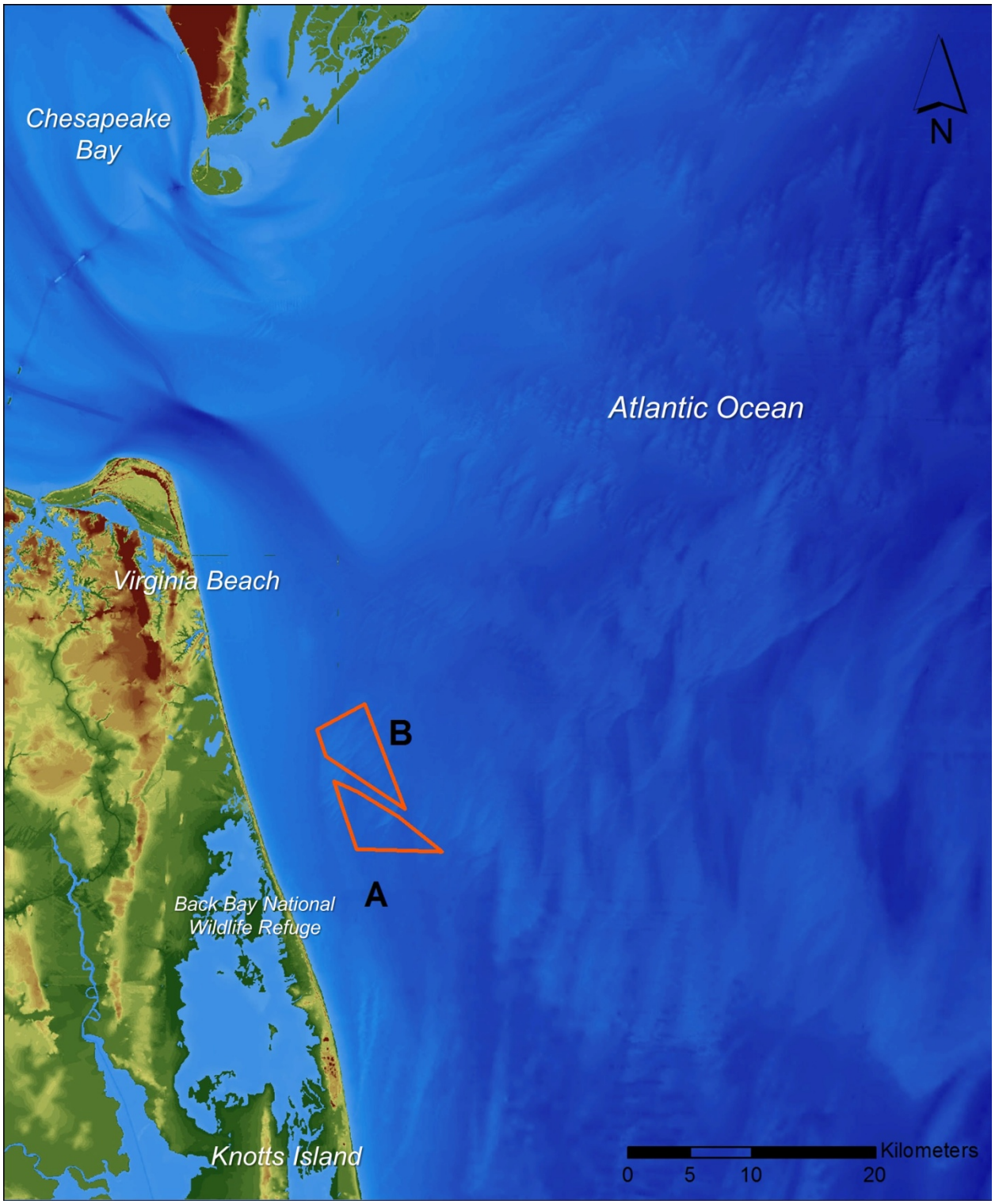

Figure III-2. Sand and gravel shoal mining sites evaluated for the morphological modeling analysis including Sandbridge Shoal (Virginia),

Three offshore borrow areas were identified offshore Brevard County, Florida, Canaveral Shoal I and II and Space Coast Shoal II. Of these three sites Canaveral Shoal II has been dredged for four projects (2000/2001, 2002/2003, 2005, and 2010) while Canaveral Shoal I has never been dredged. The Space Coast Shoal II has been dredged once for the 2002/2003 nourishment project. Canaveral Shoal II is approximately 5 miles offshore of Cape Canaveral Air Force Station and covers 1,200 acres of seabed. The depth of Canaveral Shoal II ranges from -10 to -46 ft MLW. From these four projects a total of approximately 7.58 million cubic yards of sand has been dredged from Canaveral Shoal II.

From 1973 until 1987 eight different offshore borrow areas were used for beach nourishment of Jupiter Island Beach. All of the borrow areas lie approximately 1 km offshore of the island and have a mean depth of -9 m (Figure III-4). Once these borrow areas were dredged the deepest excavation locations had a total depth of approximately -18 m. A cumulative total of 6.3 million cubic meters was extracted from these offshore borrow areas.

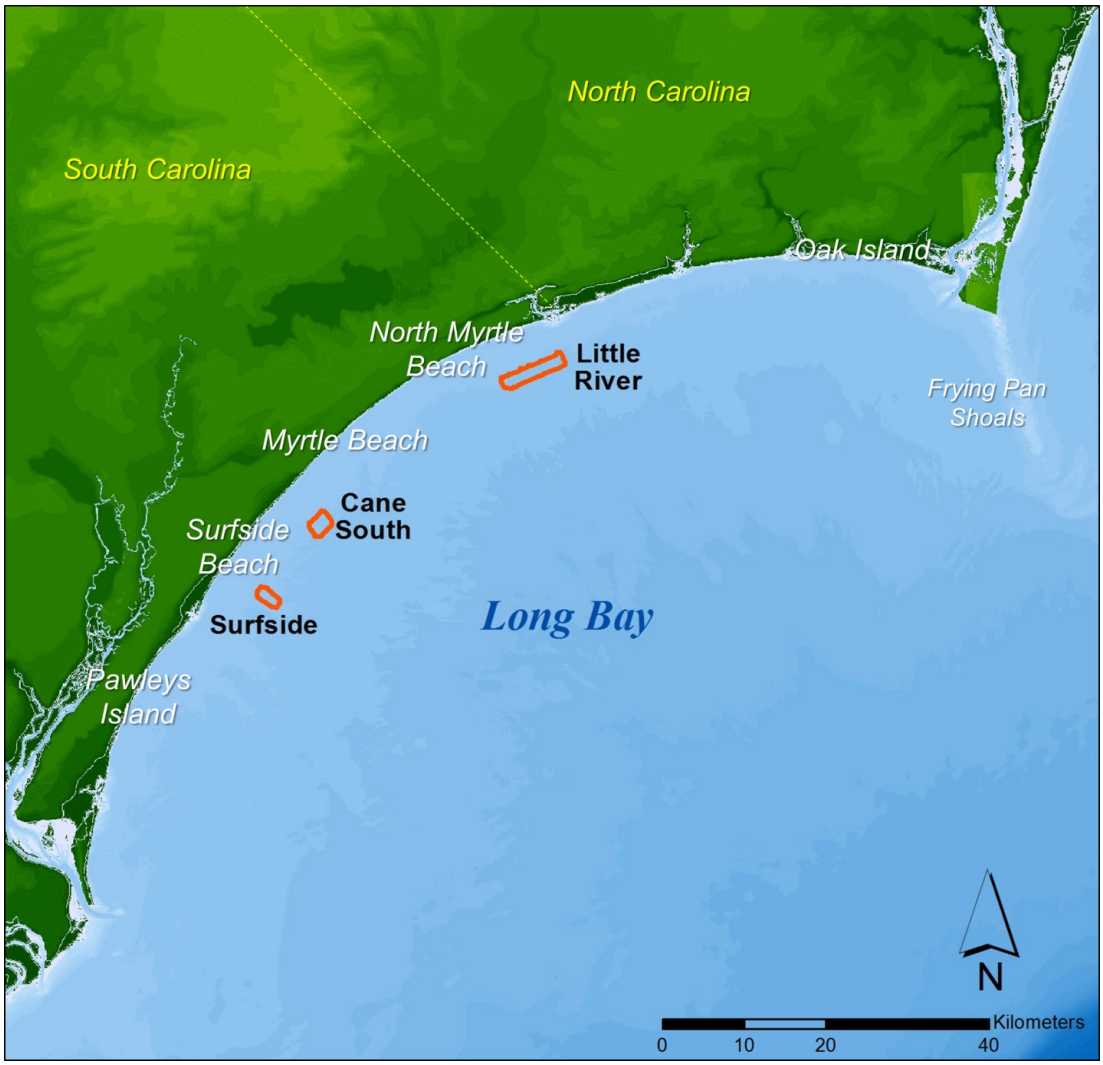

Figure III-3. Sand shoal mining sites evaluated for the morphological modeling analysis including Long Bay (South Carolina)

Figure III-4. Sand and gravel shoal mining sites evaluated for the morphological modeling analysis including Canaveral Shoals (Florida), and Jupiter Island (Florida).

III.A.1 Bathymetry Data

As previously mentioned, it is important to have bathymetric surveys for the dredged location prior to and directly after dredging as well as long term bathymetric monitoring of the site to document the morphological change. The four east coast offshore borrow locations all have bathymetric surveys available that document dredging conditions (Table III-1).

In total 10 bathymetric surveys have been done of Sandbridge Shoal area A (2 surveys) and B (8 surveys) to monitor the material taken from Sandbridge Shoal from the five dredge events. For the 1996 dredge event there was a pre- and post-dredge bathymetric survey of area B done by Weeks Marine Inc. There were no offshore bathymetric surveys done for the 1998 dredging of Sandbridge Shoal. The only bathymetric survey for the 2002 dredging event is a pre-dredge survey that occurred in July 2001 by the U.S. Army Corps of Engineers. For both the 2003 and 2007 offshore dredging events there are bathymetric surveys for pre- and post-dredge. These bathymetric surveys were done by Waterway Surveys & Engineering, Ltd. for the 2007 event pre- and post-dredging bathymetric surveys were done for both area A and B. In October 2003, five months after the 2003 dredging project was completed there was another survey done of area B. Overall, for Sandbridge Shoal there has been relatively good bathymetric monitoring of the offshore borrow area pre and post dredging. However, there has not been 1 year post-dredging bathymetric monitoring of the shoal, making morphologic modeling comparisons over a 1 year (or less) duration problematic.

For the three (3) Long Bay offshore borrow areas, a total of 9 bathymetric surveys exist; three for each borrow area. All of these bathymetric surveys were undertaken to monitor the 2007 to 2009 nourishment project, no bathymetric surveys exist for the 1996 to 1998 project. There is a pre-, post-, and 1 year post-dredging survey for Cane South and Surfside, that were all done by the U.S. Army Corps of Engineers Charleston District. For Little River the bathymetric surveys are for pre-, post- and 2 months post-dredging which occurred in June 2008, December 2008, and January 2009, respectively. The Little River surveys were also done by the U.S. Army Corps of Engineers Charleston District. Long Bay is the most recent nourishment project to have pre-, post-, and 1 year post-dredging bathymetric surveys available.

Canaveral Shoal II has had 12 bathymetric surveys to monitor the removal of sediment for the beach nourishment projects in Brevard County, Florida. For the October 2000 to April 2001 nourishment project a bathymetric survey was taken pre-, post-, and 9 months post- dredging. In addition there was an interim survey taken during this project in December 2000. All four of these surveys were done by Great Lakes Dredge and Dock Company. The long term post-dredging survey was done prior to a year after because Canaveral Shoal II was to be dredged again for the second project that started in January 2002. For this second project a pre-, post-, and 1 year post-dredging bathymetric surveys were done in January 2002, May 2003, and August 2004, respectively. The 2005 nourishment project was divided into two parts, the dredging of Canaveral Shoal II for the Patrick Air Force Base (PAFB) and for the North and South Reaches of Brevard County Florida. Pre- and post-dredging bathymetric surveys for the PAFB 2005 nourishment project were done by Weeks Marine on March 3, 2005 and March 18, 2005, respectively. The post-dredging survey for the PAFB nourishment was also used as the

Table III-1. Bathymetric survey data available for Sandbridge Shoal, Long Bay, Cape Canaveral, and Jupiter Island					
Proposed Site	Dredging Project Year	Pre-Dredge Survey	Post-Dredge Survey	1 Year Post-Dredge Survey	Additional Information
Sandbridge Shoal (SS)	1996	Yes July 1996	Yes Nov. 1996	No	Area B Horizontal projection: Virginia State Plane South NAD83 ft Soundings in ft Survey lines spaced 100 ft
SS	1998	No	No	No	NA
SS	2002	Yes July 2001	No	No	Area B Horizontal projection: Virginia State Plane South NAD83 ft Soundings in NGVB29 ft Survey lines spaced 500 ft
SS	Jan. – May 2003	Yes	Yes May 2003	No	Area B Horizontal projection: Virginia State Plane South NAD83 ft Soundings in ft Dredge survey lines spaced 200 ft
SS	June – Sept. 2007	Yes	Yes	No	Area A and B Horizontal projection: Virginia State Plane South NAD83 ft Soundings in ft Pre- dredge survey points spaced every 25 ft Post- dredge survey lines spaced 500 ft
Long Bay (LB)	1996-1998	No	No	No	NA
LB	Nov. 2007 - Jan. 2009	Yes June 2008[$] Feb. 2008[^] Oct. 2007[#]	Yes Dec. 2008[$] April 2009[^] May 2008[#]	Yes March 2010[^] June 2009[#]	Horizontal Projection: South Carolina State Plane NAD83 ft Soundings in NAVD88 ft Survey lines spaced 246 ft × 492 ft
Cape Canaveral (CC)	Oct. 2000 –April 2001	Yes Sept. 2000	Yes April 2001	Yes Jan. 2002	Shoal II Horizontal projection: Florida State Plane East NAD27 ft Soundings in MLW ft Survey lines spaced 250 ft
CC	Jan. 2002 – April 2003	Yes Jan. 2002	Yes May 2003	Yes Aug. 2004	Shoal II Horizontal projection: Florida State Plane East NAD27 ft Soundings in MLW ft Survey lines spaced 250 ft
CC	Jan. – May 2005	Yes Aug. 2004 March 2005	Yes May 2005	No	Shoal II Horizontal projection: Florida State Plane East NAD27 ft Soundings in MLW ft Survey lines spaced 250 ft
CC	Feb. – April 2010	Yes Dec. 2009	Yes May 2010	No	Shoal II Horizontal projection: Florida State Plane East NAD83 ft Soundings in NAVD88 ft Survey lines spaced 150 ft
Jupiter Island	1973-1987	No	Yes 1982	No	Horizontal Projection: Florida State Plane NAD27 m Soundings in MLW m Survey line spacing 400 ft to 800 ft

[$]Little River Borrow Area [^]Cane South Borrow Area [#]Surfside Borrow Area

pre-dredging survey for the North and South Reaches nourishment project. The post-dredging survey for the North and South Reaches was done again by Weeks Marine in May 2005. No one year post-dredging bathymetric surveys exist for the 2005 nourishment project; however, there is a three year post-dredge survey that occurred in June of 2008. The last nourishment project for this location occurred in 2010. The Army Corps of Engineers did a pre- and post-bathymetric survey for the 2010 project.

As mentioned above, several borrow areas approximately 1 km offshore of Jupiter Island were actively dredged between 1973 and 1987. Three bathymetric surveys of these offshore borrow areas have been done in 1982, 1994, and 2005. The 1982 survey is helpful in telling the condition of the borrow areas before the sites were dredged in 1983 to 1987. The 1994 and 2005 surveys are helpful with long term borrow area recovery, however, the condition of the borrow area prior to dredging in 1973 is unknown.

Additional bathymetric data are available for all four locations from NOAA National Ocean Service (NOS). For Sandbridge Shoal NOS has two surveys that cover the borrow areas. One survey is from 1922 (Survey ID: H04286) and the other survey is from 1981 (Survey ID: H09948). Long Bay's borrow areas are covered by three NOS surveys all from 1972 (Survey IDs: H09229, H09230, H09289). Canaveral Shoal II has NOS surveys from 1956 (Survey IDs: H08343 and H08344) and 2006/2007 (Survey ID: H11590). The H11590 survey could be used as the 1 year post bathymetric survey. The one NOS survey that covers the Jupiter Island borrow areas was done in 1967 (Survey ID: H08955). An additional bathymetric dataset is available for Long Bay, SC from the USGS. This bathymetric data was collected from 1999-2003 for the South Carolina Coastal Erosion Study. The survey covers approximately 700 km^2 from Little River Inlet to North Inlet and extends from seaward of breaking waves (< 1 km) to approximately 10 km offshore with 100 m grid spacing.

III.A.2 Meteorological, Wave, and Hydrodynamic Data

Meteorological, wave and current data are important to sediment transport and morphology modeling because these processes force the sediment to move and alter the seafloor. The National Data Buoy Center (NDBC) maintains a network of stations that collect continuous oceanographic data throughout the world. Every potential site, excluding Jupiter Island has at least one NDBC station in the general vicinity of the borrow area.

The NDBC station, 44014, is roughly 64 nautical miles from the Sandbridge Shoal borrow area. This station has archived wave data from October 1990 to the present, including spectral density; however there are only directional spectral data from 1998 to present. This station also has archived current data for the month of March in 2007, as well as archived current data from March 1, 2010 to the present.

The Long Bay site has NDBC station 41013, roughly 55 nautical miles from the borrow area. This station has archived wave data from 2003 to the present, which includes spectral wave direction and density. There are no tidal current data available from the NDBC for this site.

Cape Canaveral has two NDBC stations nearby, station 41009 (roughly 20 nautical miles from the borrow area) and station 41010 (roughly 120 nautical miles from the site). Station 41009 has archived wave data from 1996, including spectral density; however, there is only directional spectral wave data for 1996. There is no current data available from this station. Station 41010 also has archived wave data from 1996, including spectral density; however, there is no directional spectral wave data available for this site. There is ocean current data available from Station 41010 for 2010 for this borrow area.

Although some nearshore wave buoys exist in the vicinity of Jupiter Island (i.e. NDBC station 41114 at Fort Pierce, approximately 33 miles north of Jupiter Island), there is no NDBC dataset available to serve as boundary conditions for wave modeling at this site. Due to natural protection of this shoreline by the Bahama Banks, as well as the lack of available long-term offshore wave data, it is not possible to utilize NDBC data for wave modeling.

A summary of the NDBC data is provided in Table III-2. In addition, Figure III-5 shows the location of the relevant NDBC stations for the borrow areas evaluated.

Wave hindcast data is also available from the U.S. Army Corps of Engineers through the Wave Information Studies (WIS) website. These hindcast data are output from regional wave models; therefore, they would be considered a secondary source of wave data. All of the WIS stations have data from 1980 to 1999. Station 63201 (located at longitude -75.75 and latitude 36.75 in a depth of 59 feet) is the closest station to Sandbridge Shoal (roughly 11.0 miles offshore). Station 63325 (located at longitude -78.67 and latitude 33.50 at a depth of 52 feet) is the closest station to Long Bay (roughly 17.3 miles offshore). Station 63439 (located at longitude -80.42 and latitude 28.33 at a depth of 56 feet) is the closest station to Cape Canaveral (roughly 10.5 miles offshore). Station 63455 (located at longitude -79.92 and latitude 27.08 at a depth of 560 feet) is the closest station to Jupiter Island (roughly 12.3 miles offshore). Figure III-6 shows the location of the U.S. Army Corps of Engineers WIS stations relative to each borrow area evaluated, and Figures III-7 through III-10 show the wave rose for each of these WIS stations.

Additional wave data is available for two of the four sites. Cape Canaveral has wave data available through a Scripps Institution of Oceanography nearshore station CDIP143 (NDBC station 41113), located immediately offshore of Cape Canaveral. This data ranges from 2006 to present and could possibly serve as a data source for wave model calibration, especially if the 2010 dredging efforts were utilized for further morphological change modeling.

As part of ongoing evaluations of offshore sand deposits in South Carolina, oceanographic observations made at eight locations in Long Bay, from October 2003 through April 2004 (shown in Figure III-11). These locations were offshore of Myrtle Beach, South Carolina, and centered on a shore-oblique sand deposit that is approximately 6 miles in length, 1 mile in width, and approximately 10 feet thick (Sullivan, et al., 2006). The observations were collected through a collaborative effort with the U.S. Geological Survey (USGS), the University of South Carolina (USC), and Georgia Institute of Technology (GT) as part of a larger study to understand the physical processes that control the transport of sediments in Long Bay. Tripod mounted acoustic Doppler current profilers (ADCPs) were deployed at each of these sites and provided wave spectral properties.

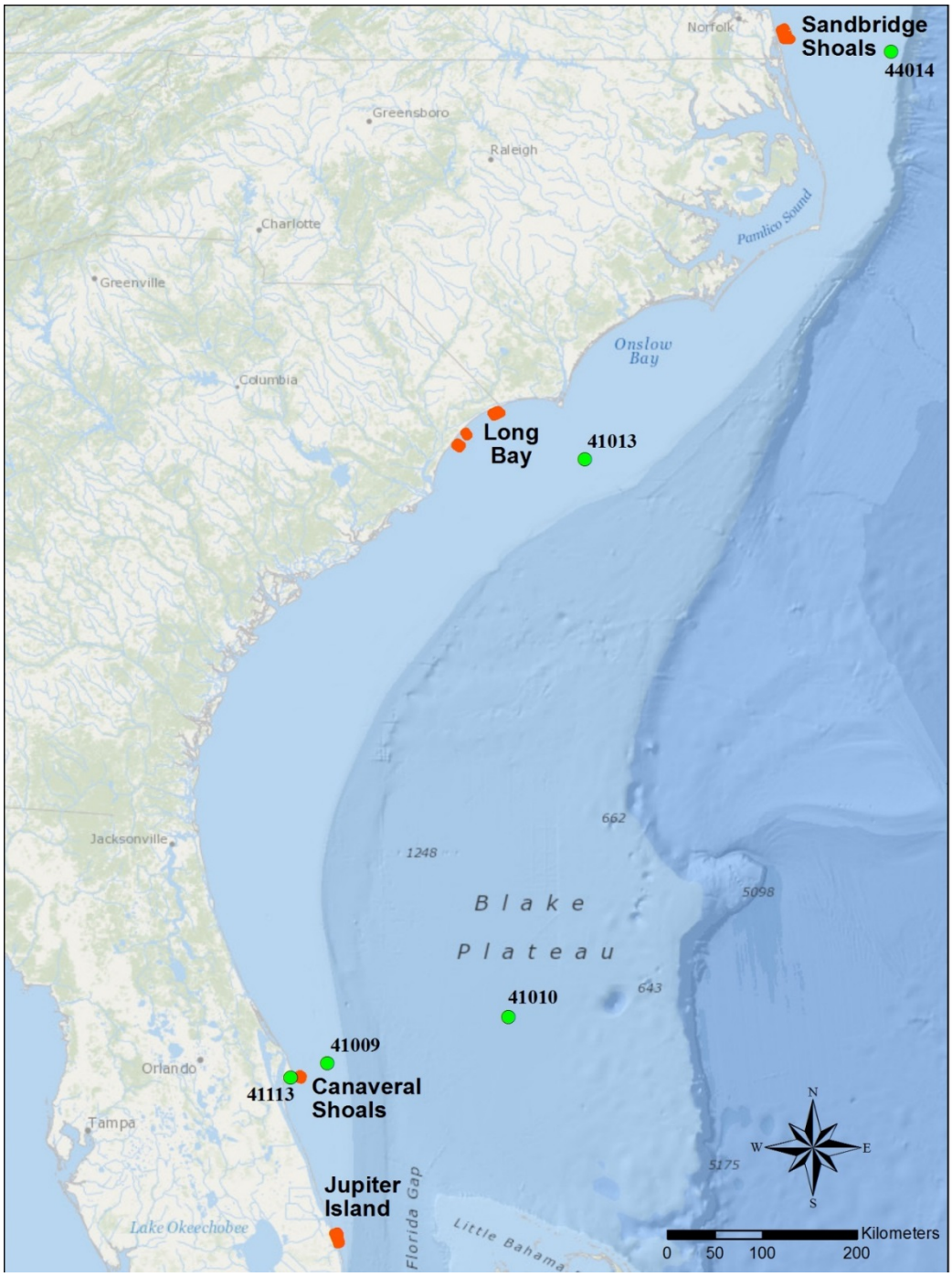

Figure III-5. Sand and gravel shoal mining sites evaluated for the morphological modeling analysis including Sandbridge Shoal (Virginia), Long Bay (South Carolina), Canaveral Shoals (Florida), and Jupiter Island (Florida) including appropriate NDBC wave monitoring stations.

Table III-2. NDBC data availability for Sandbridge Shoal, Long Bay, Cape Canaveral, and Jupiter Island							
Proposed Site	Buoy Number(s)	Wave and Wind Data	Years Spanned	Directional Spectral Data	Years Spanned	Current Data	Years Spanned
Sandbridge Shoal	44014	Yes	1990-present	Yes	1998 - present	Yes	2007, 2010-present
Long Bay	41013	Yes	2003-present	Yes	2003 - present	No	
Cape Canaveral	41009 and 41010	Yes	1996-present	Yes	1996 (Station 41009)	Yes	2010 (Station 41010)
Jupiter Island	NA	NA	NA	NA	NA	NA	NA

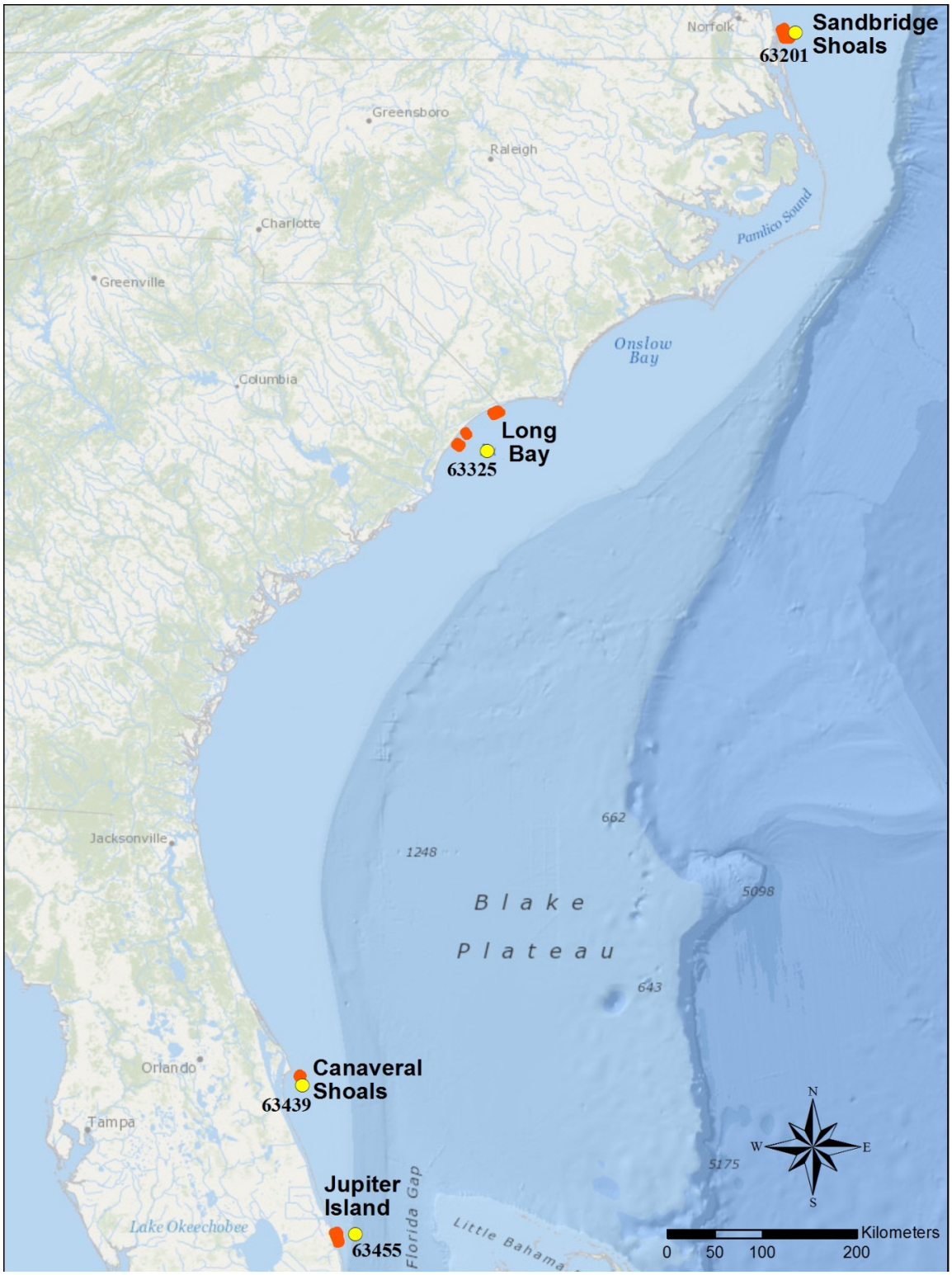

Figure III-6. Sand and gravel shoal mining sites evaluated for the morphological modeling analysis including Sandbridge Shoal (Virginia), Long Bay (South Carolina), Canaveral Shoals (Florida), and Jupiter Island (Florida) including appropriate WIS wave hindcast stations.

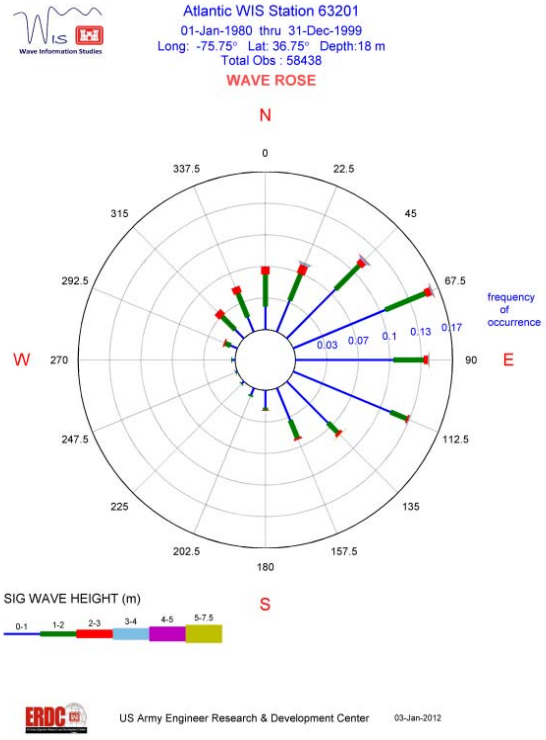

Figure III-7. Wave Rose for WIS Station 63201 (Sandbridge Shoal) in meteorological convention.

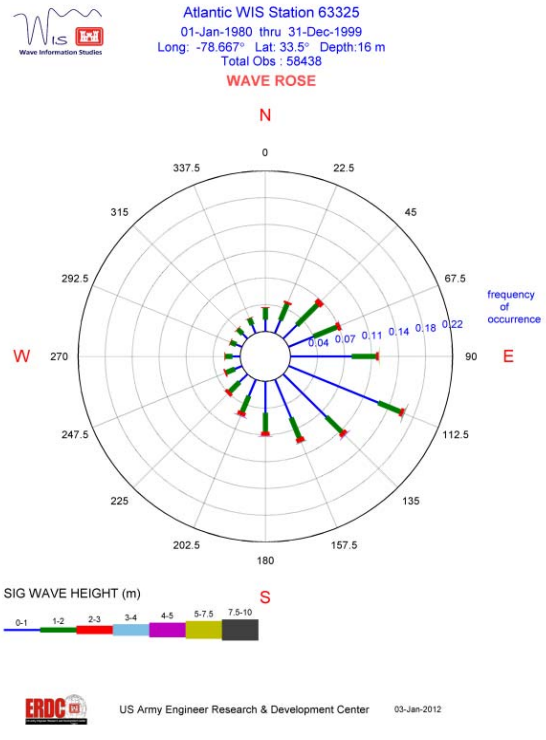

Figure III-8. Wave Rose for WIS Station 63325 (Long Bay) in meteorological convention.

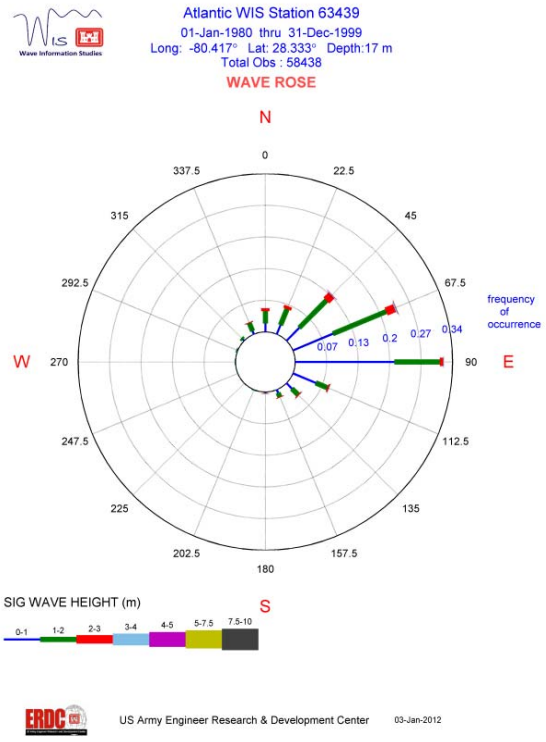

Figure III-9. Wave Rose for WIS Station 63439 (Cape Canaveral) in meteorological convention.

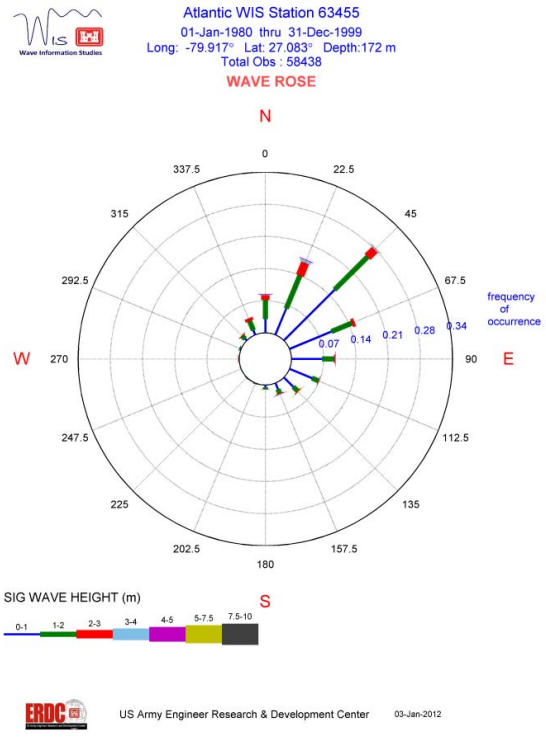

Figure III-10. Wave Rose for WIS Station 63455 (Jupiter Island) in meteorological convention.

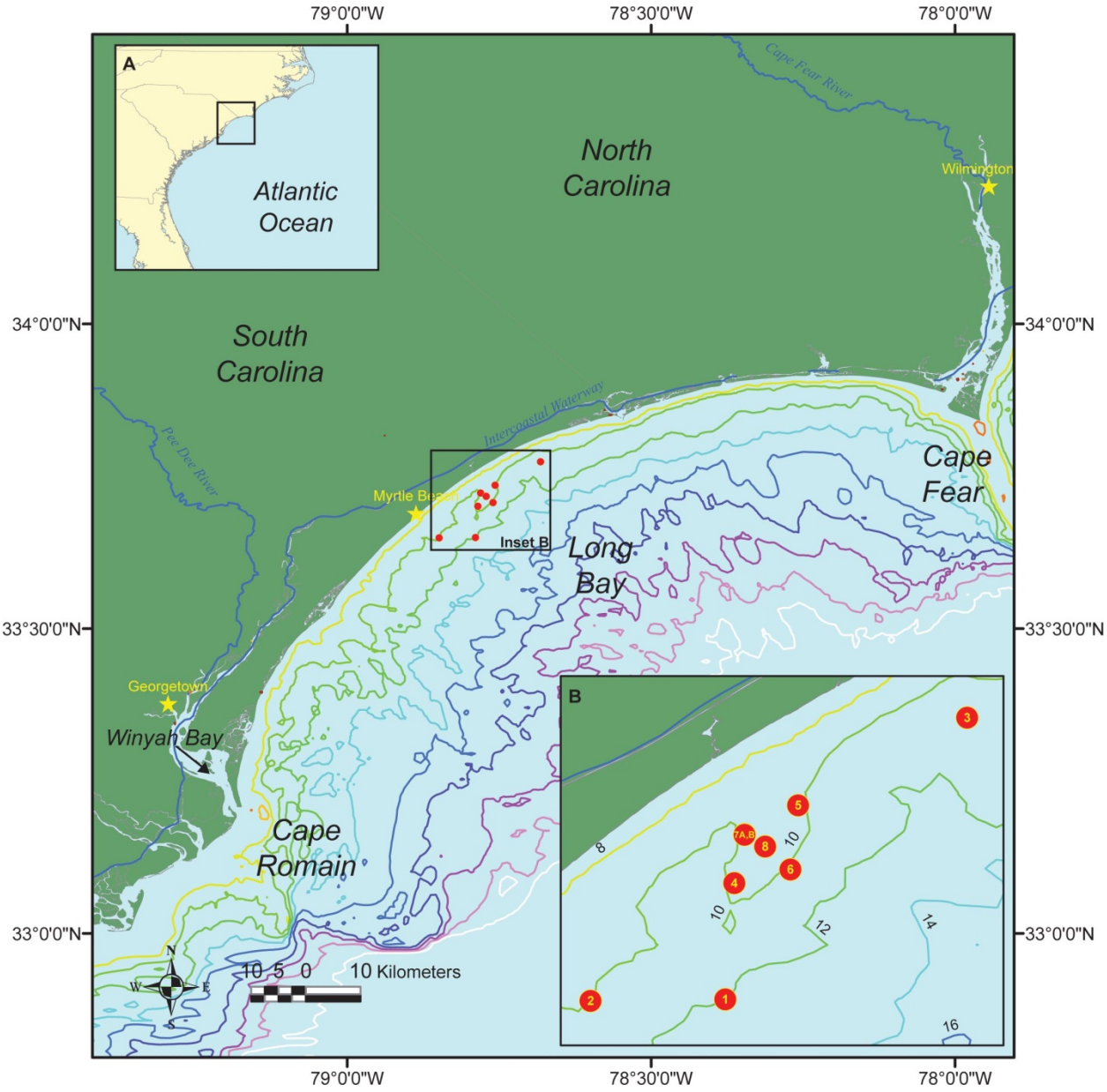

Figure III-11. Location Map for Long Bay, South Carolina (SC) illustrating USGS observations at eight sites (Inset B) offshore of Myrtle Beach, SC from October 2003 through April 2004.

III.B. Initial Site Assessment and Review of Previous Regional Modeling Efforts

After initial evaluation of the hydrodynamic and bathymetric datasets from each of the offshore borrow areas (e.g. concurrent wave and current datasets, as well as post-dredging bathymetric change information available for the same time period), an initial assessment of the various potential model domains was performed. While the initial focus for the borrow area evaluation was simply to determine what data were available to drive and calibrate/verify future morphodynamic modeling efforts, it was critical that the site selected represented "typical" oceanographic and morphologic shoals for sand borrow areas dredged along the U.S. Atlantic

OCS. In addition, the availability of existing calibrated and/or validated numerical hydrodynamic models is critical to ensure that the site-specific evaluation can be performed with in an efficient manner that represents site conditions over the time period of borrow area recovery. While it is understood that each potential offshore borrow area is unique, the goal of this evaluation was aimed at identifying a site that could be considered typical for the purposes of developing "best practice" guidelines for the use of morphological change models to assist BOEM in the overall management of these resources.

III.B.1 Initial Site Assessment

Specifically for the U.S. Atlantic OCS, potential offshore borrow areas in federal waters tend to be in water depths in excess of 40 feet (~12 meters). Due to generally 'weak' tidal currents and modest wave climate, measurable sediment transport of sand-sized material only occurs during high energy events (Byrnes et al., 2000). Sediment movement and the associated morphological change during these high energy storm events tend to be dominated by waves, where tidal currents typically play a secondary role to sediment movement (Byrnes et al., 2000).

In general, the four selected sites all consisted of appropriate offshore water depths, general shoal features where sand was mined, and bottom sediment transport dominated by wave and/or storm action. On closer evaluation of available information, concerns regarding two of the sites (Sandbridge Shoal and Canaveral Shoals) resulted from potential complexities associated either with geomorphic or oceanographic processes as described below:

Sandbridge Shoal – The Sandbridge Shoal borrow areas are approximately 12 miles south of the Chesapeake Bay entrance. The continental shelf bathymetry is dominated by the ridge and swale features that are typical of the U.S. Atlantic inner shelf. Horseshoe-shaped Sandbridge Shoal was identified by the U.S. Army Corps of Engineers (2009) as a high-quality source of primarily medium to coarse-grained sand for beach nourishment. From a geologic perspective alone, the Sandbridge Shoal represent a viable site for morphodynamic assessment; however, complications with regional oceanographic processes associated with regional estuarine circulation patterns alter typical wave-dominated sediment transport. As described in Valle-Levinson, *et al*. (1998), the influence of the freshwater plume exiting Chesapeake Bay is significant and alters regional oceanographic processes. For example, measured offshore currents in 1996 within the plume reached nearly 0.6 m/s (2 feet per second) and were significantly different from flows measured at greater depths. During high freshwater inflow periods, the surface estuarine water deflects anti-cyclonically in the Northern Hemisphere. Therefore, the buoyant plume exiting Chesapeake Bay tends to form a boundary current with the coastline on its right-hand side or to the south, along the beach towards Sandbridge Shoals. As shown in Figure III-12, the plume can extend more than 6 miles offshore in the vicinity of Sandbridge. Due to the influence of this freshwater circulation on regional hydrodynamics, it is anticipated that morphologic evolution of the Sandbridge Shoal would be markedly influenced by these nearshore currents alterations. While modeling of this buoyant plume effect is possible and the total influence on long-term shoal morphology may be limited, it likely is inappropriate to characterize the oceanographic conditions at Sandbridge Shoal as 'typical' for the U.S. Atlantic OCS.

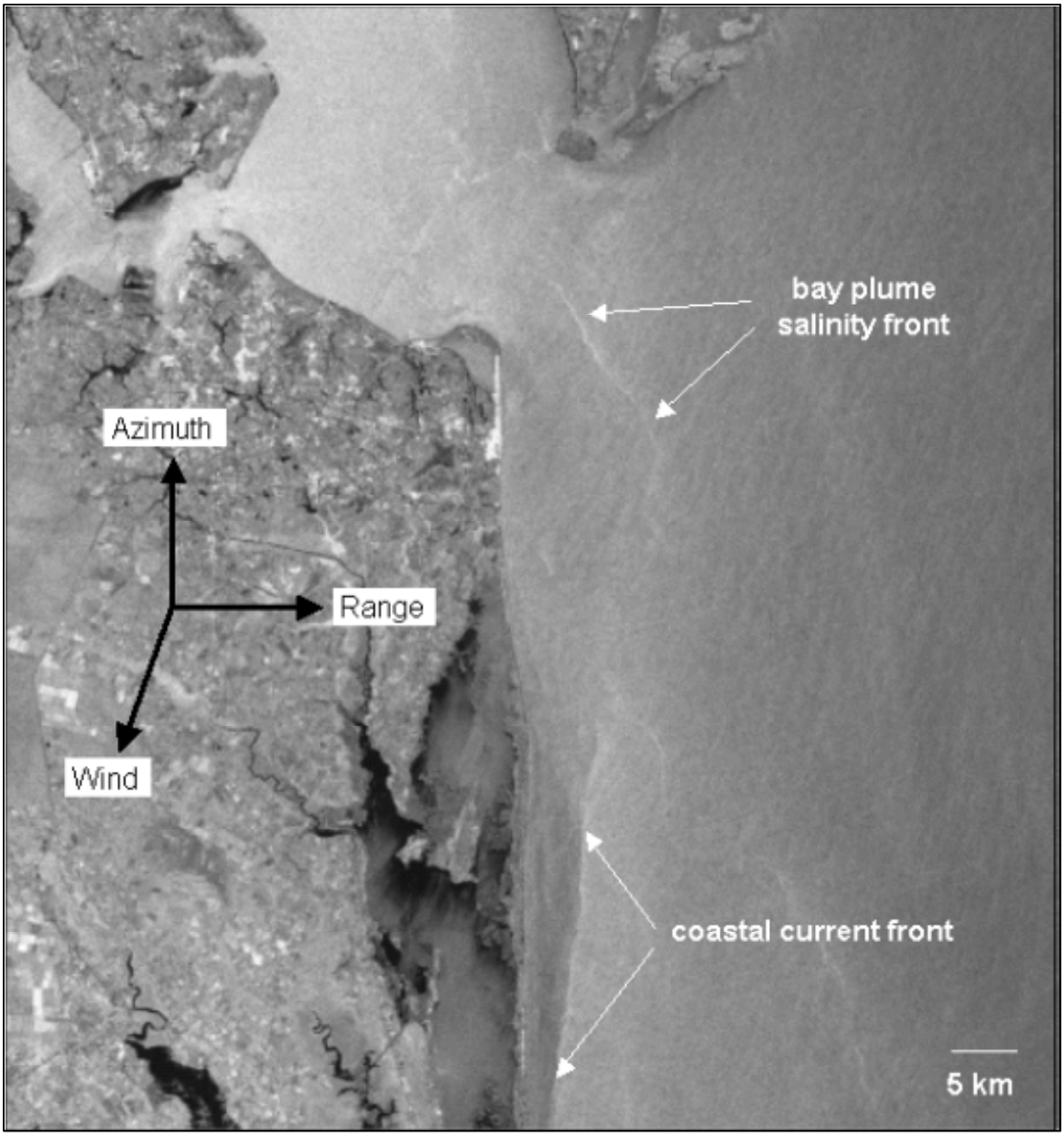

Figure III-12. Image of the buoyant Chesapeake Bay plume along the coast on September 24, 1996. The freshwater plume forces the coastal current more than 6 miles offshore in the vicinity of Sandbridge (Fewings, et al., 2013).

Canaveral Shoals – The borrow area is located on "Southeast Shoals", a large contiguous sand deposit that extends approximately seven (7) miles from the shoreline of Cape Canaveral. This deposit, along with the cuspate shape of the Cape Canaveral shoreline, was formed from geologically recent littoral processes, dominated by southerly directed transport (Byrnes et al., 2003). This southerly directed drift results in a southerly migration of the shoal and ridge system inclusive of the Cape Canaveral and False Cape system. The nearshore region consists of medium sands overlying marine clays, where the shoals are actively changing in configuration, as evidenced by bathymetric survey data dating to 1878 (USACE, 1998). Over this time period

(1878 to present), the shoal deposits have generally broadened and increased in overall sediment thickness. As a result of the observed large-scale migration of this feature, as well as the direct influence of sub-aerial Cape Canaveral, it was determined that the shoal feature was not in equilibrium, indicating that the overall shoal feature exhibited significant migration. Therefore, morphodynamic modeling of the Canaveral Shoals would be complex, as influence of nearshore features on shoal migration need to be considered in the analysis. While modeling of these shoreline/nearshore processes in conjunction with shoal morphology may be possible, this site would not be considered 'typical' for the U.S. Atlantic OCS.

The concerns regarding the two potential borrow areas for further assessment, Sandbridge Shoals and Canaveral Shoals, represent structural issues related to modeling that force these sites to be considered "secondary". These structural issues relate to both large-scale hydrodynamic (in the case of Sandbridge Shoal) and geologic (in the case of Canaveral Shoals) complexities that are not characteristic of typical shoal systems along the U.S. East Coast. As such, these sites would be eliminated from further consideration for the morphodynamic modeling analysis, if one of the remaining sites was found to have equivalent data and previous hydrodynamic/wave modeling information.

III.B.2 Review of Previous Hydrodynamic and Sediment Transport Models

Previous numerical hydrodynamic and sediment transport modeling to provide the baseline for potential morphological modeling of a borrow area are relatively limited for most of the four sites evaluated. Substantial efforts have been made to evaluate wave-induced sediment transport at the shoreline, as well as influence of bathymetric changes associated with borrow area dredging on the local wave-induced sediment transport regime in the surf zone. While evaluation of wave climate alone is certainly valuable, these types of modeling efforts are not directly relevant.

For the entire Gulf and Atlantic coasts of the U.S., the U.S. Army Corps of Engineers developed a large-scale ocean circulation model, driven by global tidal constituents. The hydrodynamic model is an unstructured version of the ADCIRC model that can be combined with a full range of atmospheric forcing and wave action models (Massey, 2013). To utilize this suite of models to provide boundary conditions for the site-specific morphodynamic models would require substantial region-specific forcing input, as well as calibration and verification datasets. While the overall unstructured model grid is available, a calibrated regional model for any of the four borrow areas under investigation does not exist.

Site-specific modeling for each of the sites is listed below:

Sandbridge Shoal – The shoal system has been a long-term source of beach nourishment material for Sandbridge Beach. A series of numerical wave and sediment transport modeling efforts were carried out between 1993 and 2001. Initial numerical modeling of waves and sediment transport potential was performed by Maa (1995). Basco (1999) performed a study utilizing the MIKE21 wave model to assess the impact of sand mining on nearshore wave climate, where the site at Sandbridge Shoal provided the field information for the study. More recently, Kelley, et al. (2001) performed a study for the Minerals Management Service to address

the need for physical environmental information to support potential lease decisions offshore the east coast of the U.S. from southern New Jersey to Cape Canaveral, Florida. While the study examined several offshore borrow areas, Sandbridge Shoal was one of the four sites selected for detailed analysis. The U.S. Army Corps of Engineers' STeady-state spectral WAVE model (STWAVE) was utilized in this study to assess nearshore wave transformation. Second, a standard method was developed to qualify the significance of changes associated with borrow area excavation to determine the influence of borrow area geometry on local wave refraction and sediment transport patterns. The model grids for this study are shown in Figure III-13.

Long Bay – Substantial geological and oceanographic analysis efforts were attempted to understand physical processes along the coast of Long Bay, South Carolina as part of the offshore sand mining and beach nourishment program along the Myrtle Beach coastline. Numerical hydrodynamic and wave modeling efforts were led by USGS (Warner, et al. 2010) using the Coupled Ocean Atmospheric-Wave-Sediment Transport Modeling System (COAWST). This regional-scale model was used to perform a detailed study of the Long Bay region and was validated by field data (see Figure III-11). In addition, the model was used to simulate the complex coupling of an atmospheric and ocean circulation model for Hurricane Isabel in September 2003. Datasets for the large-scale model are readily available from USGS and the model is maintained in a manner that allows near real time predictions of regional oceanographic properties. This allows COAWST to be an ideal basis for boundary conditions needed to parameterize near-field morphodynamic models.

Canaveral Shoals – In the same analysis utilized for Sandbridge Shoal, Kelley, et al. (2001) performed a study for the Minerals Management Service to address the need for physical environmental information to support potential lease decisions offshore the east coast of the U.S. from southern New Jersey to Cape Canaveral, Florida. While the study examined several offshore borrow areas, Canaveral Shoals was one of the four sites selected for detailed analysis. STWAVE was utilized in this study to assess nearshore wave transformation and a new methodology was developed to quantify the "allowable" influence of borrow area dredging on local wave refraction and sediment transport patterns. The model grids for this study are shown in Figure III-14.

Jupiter Island – The most recent numerical wave and sediment transport modeling effort in the Jupiter Island, Florida was performed by Kelley and Ramsey (2006). The purpose of this numerical modeling effort was to quantify the impacts associated with past nearshore dredging efforts. Local erosion "hot-spots" in the proximity of the nearshore borrow areas used as the source of sand for the Island until 1987 were found to be caused by wave focusing associated with the borrow areas. The sites were all located 1 km offshore the beach, and in approximate 9-meter water depths. In the application of the "spatial and temporal" method to the Jupiter Island shoreline, the mean annual transport potential was computed first for each of the 20 years in the WIS hindcast (1980 to 1999) record from offshore the island. Waves were refracted from the offshore WIS station to the shoreline using the STWAVE wave model. The model grid utilized a 20-meter node spacing in the nearshore region (to 1.6 km offshore), and extended along a 16 km stretch of beach adjacent to the offshore borrow areas.

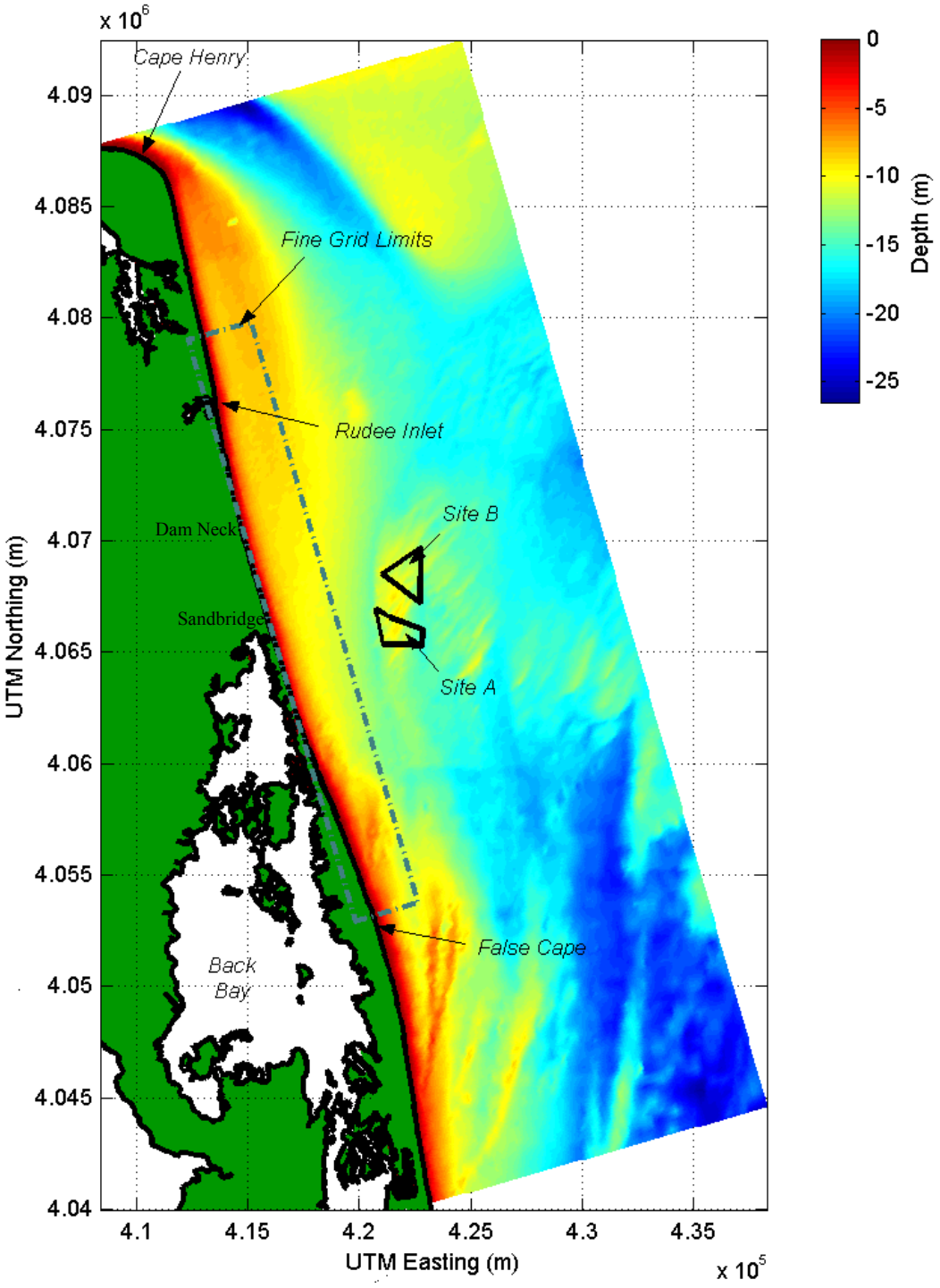

Figure III-13. Color contour plot of coarse model grid (200 m × 200 m grid spacing) of offshore southeastern Virginia including the Sandbridge Shoal borrow areas. Depths are relative to NAVD. Borrow area locations are indicated by solid black lines, and fine grid limits are indicated by a dashed line.

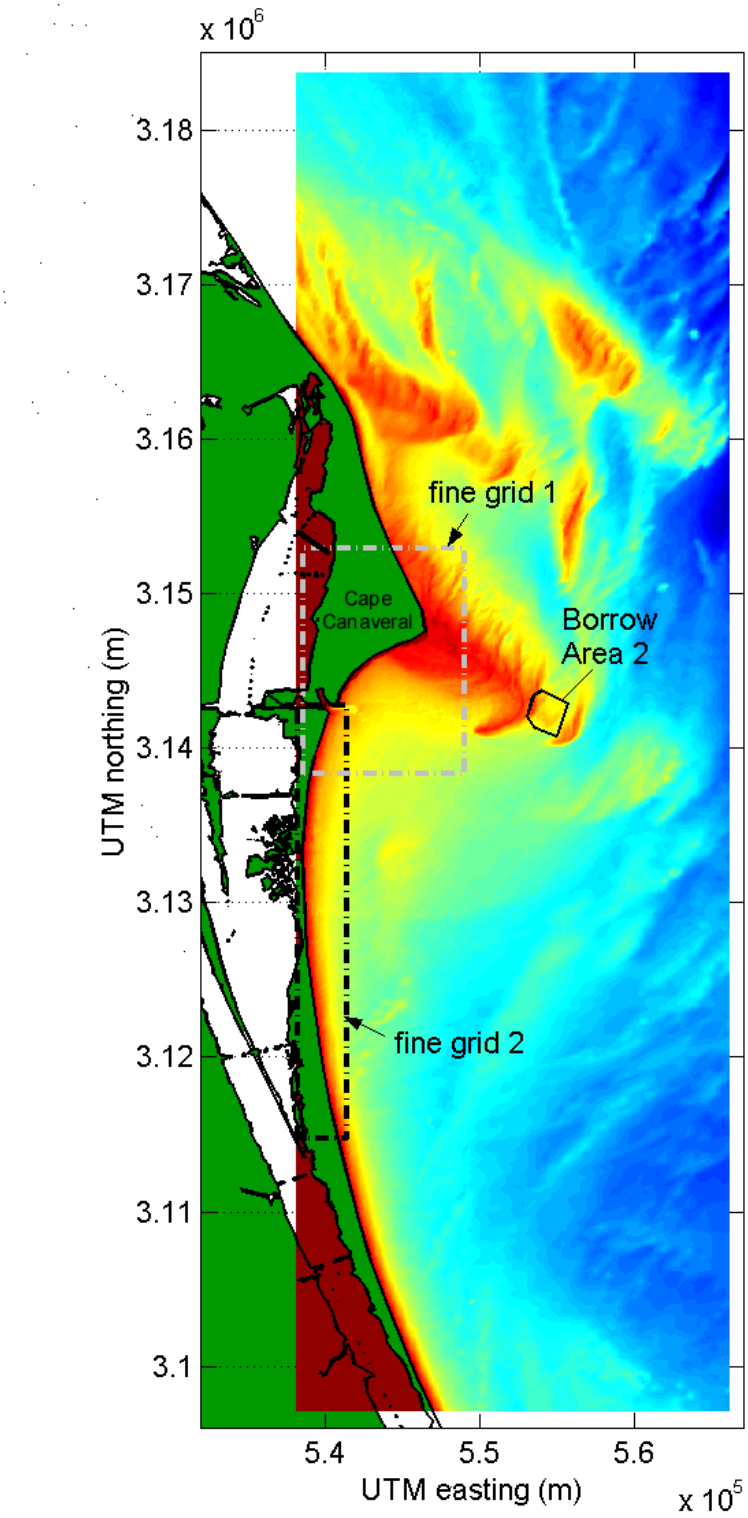

Figure III-14. Color contour plot of coarse model grid (200 m × 200 m grid spacing) for offshore Cape Canaveral, FL. Depths are relative to NAVD. Borrow area locations are indicated by solid black lines, and fine grid limits are indicated by a dashed line.

III.B.3 Selection of the Long Bay, South Carolina Site

Criteria for selecting the appropriate site for more detailed analysis by morphodynamic modeling depended on a variety of parameters including:

- Regional recent bathymetry data with sufficient detail to describe morphology of the local shoal field.
- Availability of borrow area bathymetry and geotechnical data that included (a) before dredging surveys to determine shoal morphology prior to dredging, (b) immediate post-dredging surveys to evaluate maximum alteration to the shoal system, (c) post-dredging surveys within one year of the dredging event to assess borrow area recovery, and (d) native grain size distribution within the borrow area. This data would provide the basis for calibrating morphologic change predicted by the model.
- Local wave data that could be utilized to drive the numerical wave model with information appropriate for the time period extending from pre-dredging to post-dredging surveys that showed borrow area recovery. These data are critical for ensuring that the waves utilized to drive the model represent actual conditions influencing the site.
- A regional hydrodynamic model that had preferably been calibrated/validated utilizing field data for the area of interest, including the influence of large-scale atmospheric and oceanographic forcing parameters. Similar to the wave data described above, detailed hydrodynamic information for the time period of interest is critical to predicting morphologic evolution of the seabed.
- The morphology and governing oceanographic conditions of the nearshore shoal system should be representative of borrow areas along the U.S. Atlantic OCS, where no aberrant site conditions can be tolerated that might cause the site to be considered 'atypical'.

As the Long Bay, South Carolina borrow areas were found to be the only borrow areas to meet all of the above criteria, these sites were selected for further analysis utilizing the morphodynamic modeling tools. The regional hydrodynamic, wave, and sediment transport model (COAWST) was utilized by USGS for a Long Bay specific assessment of localized sediment transport patterns. The more detailed model grid for this assessment did not include all borrow areas dredged offshore of the Myrtle Beach area (Figure III-3). The only borrow area included within the USGS near-field grid was Cane South; therefore, this borrow area was selected for the detailed analysis described in this report.

A more detailed description of the datasets available for Long Bay is described below:

Additional Bathymetric Survey Information – In addition to the bathymetry associated with the borrow area dredging operations, a coastal relief model of Myrtle Beach containing spatially coincident bathymetry and topography data of the area was developed by the National Geophysical Data Center (NGDC) for use in a tsunami inundation model of the area (Taylor, et al., 2008). Bathymetry data within the model were compiled from several NOAA National Ocean Service (NOS) datasets, USGS data, and NOAA Nautical Chart #11534. The bulk of this data was from the 1972 NOS survey and the 1999-2002 USGS survey. An image of the area covered by this coastal relief model may be seen within the red box in Figure III-15, where the parameters for this model grid are provided in Table III-3. This elevation model covers an area

larger than necessary for this study and it may sufficiently represent the pre-dredging far-field area of interest as it precedes the 2008-2009 dredging events in the area.

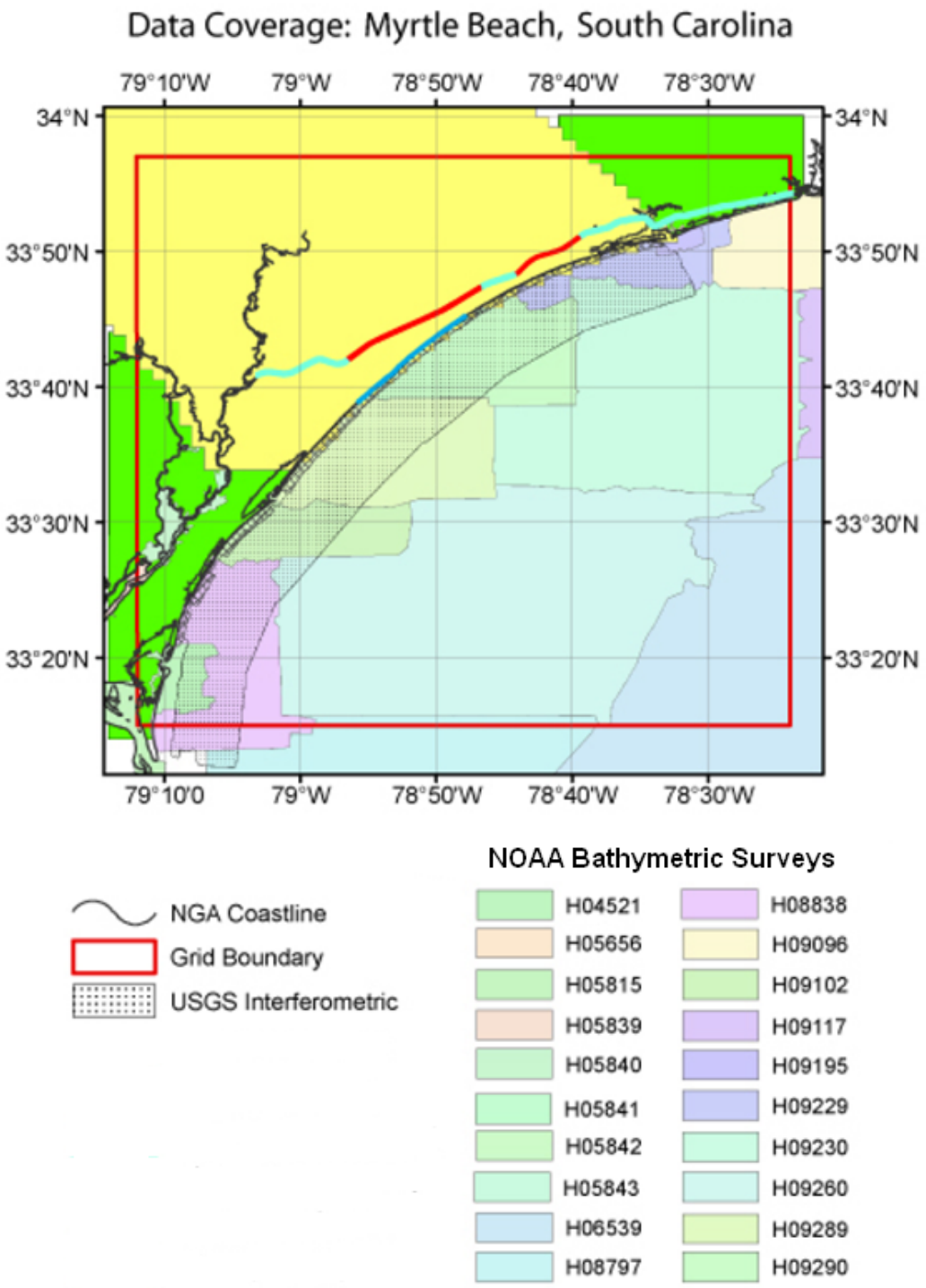

Figure III-15. Coverage of data sources used to compile the 1 arc-second and 1/3 arc-second Myrtle Beach, South Carolina grids (Taylor, et al., 2008).

A USGS grid containing swath bathymetric data of the inner shelf of Long Bay, South Carolina was collected using acoustic surveys between 1999 and 2002. Digital gridded data are available from USGS, as shown in Table III-3, which was utilized in conjunction with the coastal relief model existing bathymetric conditions for the far-field. There are several small gaps within this dataset that were resolved using the other bathymetric grids acquired. To supplement this information, a total of 20 NOAA National Ocean Service hydrographic surveys were conducted between 1925 and 1972 covering the northern South Carolina and Long Bay region; however, the primary source for the Long Bay region was the 1972 survey. Bathymetric data from the most recent of these surveys was used to augment the available data sources. Data tide-corrected to ensure a common elevation datum was used for each dataset and more information on these surveys is shown in Figure III-15 and Table III-3.

Table III-3. Regional bathymetric datasets available for numerical morphodynamic modeling of the Long Bay, SC littoral system.

Grid Name	*Grid Spacing*	*Vertical Datum*	*Vertical Resolution*	*Horizontal Datum*
NOS Coastal Relief Model	1/3 arc second (~10 meters) Or 1 arc second (~90 meters)	Mean High Water (meters)	0.1 meters to 5% of the water depth	WGS 84 (Geographic Decimal Degrees)
USGS Grand Strand Bathymetry	100 meter	Mean Lower Low Water (meters)	1 meter	Universal Transverse Mercator
NOS Hydrographic Surveys	200-400 meters	Mean Low Water (feet)	N/A	NAD 83 (feet)

Geological Information – Regionally, geological work of the nearshore system has included extensive efforts by USGS to identify Holocene sediment deposits on the inner continental shelf, where the thickest deposits are generally located offshore of modern tidal inlets (Denny et al., 2013). Grab samples of surface sediments of the inner shelf within Long Bay primarily consist of poorly sorted sands very coarse sand (-1 phi or 2 mm) to a coarse silt (6 phi or 0.016 mm), with a mean grain size of medium sand (1.6 phi or 0.33 mm). The northeast-to-southwest trending shore-oblique shoal system offshore of Myrtle Beach is characterized by up to 3 meters of well-sorted, medium sand (Denny et al., 2007). Due to the presence of modern swash systems on the adjacent upland, younger channels inshore of the shoal system, and the Holocene age of the shoal deposit, Denny et al. (2013) interpreted this feature to represent the remnants of an ebb-tidal delta complex produced by an inlet system that did not survive the most recent marine transgression.

While a substantial amount of geophysical work was performed, parameters critical to the morphodynamic modeling of the borrow area are strictly related to sediment grain size, as long as no hard-bottom is located within the site that could prevent erosion of the seafloor. As part of the environmental regulatory process, areas of hard-bottom were avoided for the borrow area

selection process; therefore, the Cane South was characterized by sandy sediments that could be mobilized by tidal and/or wave-induced currents. The U.S. Army Corps of Engineers took 27 vibracores in the vicinity of the Cane South borrow area, where 11 were located within the 'footprint' dredged in 2008-2009 (Figure III-16). Based on the information provided, the size of the site was approximately 0.85 square miles, where 1,581,000 cubic yards were dredged and placed on the beach. This beach fill was completed on January 9, 2009. Based on grain size analysis derived from the core data, the composite mean grain size (D_{50}) was determined to be 0.27 mm. For the various sediment transport formulations, different grain size statistics could be readily computed for the composite information generated for samples in Cores 17-27 (shown in Figure III-16).

Wave Data – As described previously, NDBC station 41013 (Frying Pan Shoals, NC), roughly 55 nautical miles from the Cane South borrow area, had data available for the entire 2009-2010 time period that extended from post-dredging to one year post-dredging bathymetric surveys. A wave rose for the approximate one-year period subsequent to the post-dredging survey for Cane South is shown in Figure III-17. This wave data source was located far offshore from the actual borrow area; therefore, numerical modeling techniques would be required to refract the waves observed at NDBC station 41013 and the offshore limit of the model grids utilized for this study. As an example of this influence, wave height data for the November 2003 to April 2004 time period for sites 1 and 2 (shown on Figure III-11) is compared to offshore wave data from NDBC station 41013 on Figure III-18. While lower energy wave events exhibit similar wave heights at all sites, high energy events exhibit significantly larger waves at the NDBC buoy site.

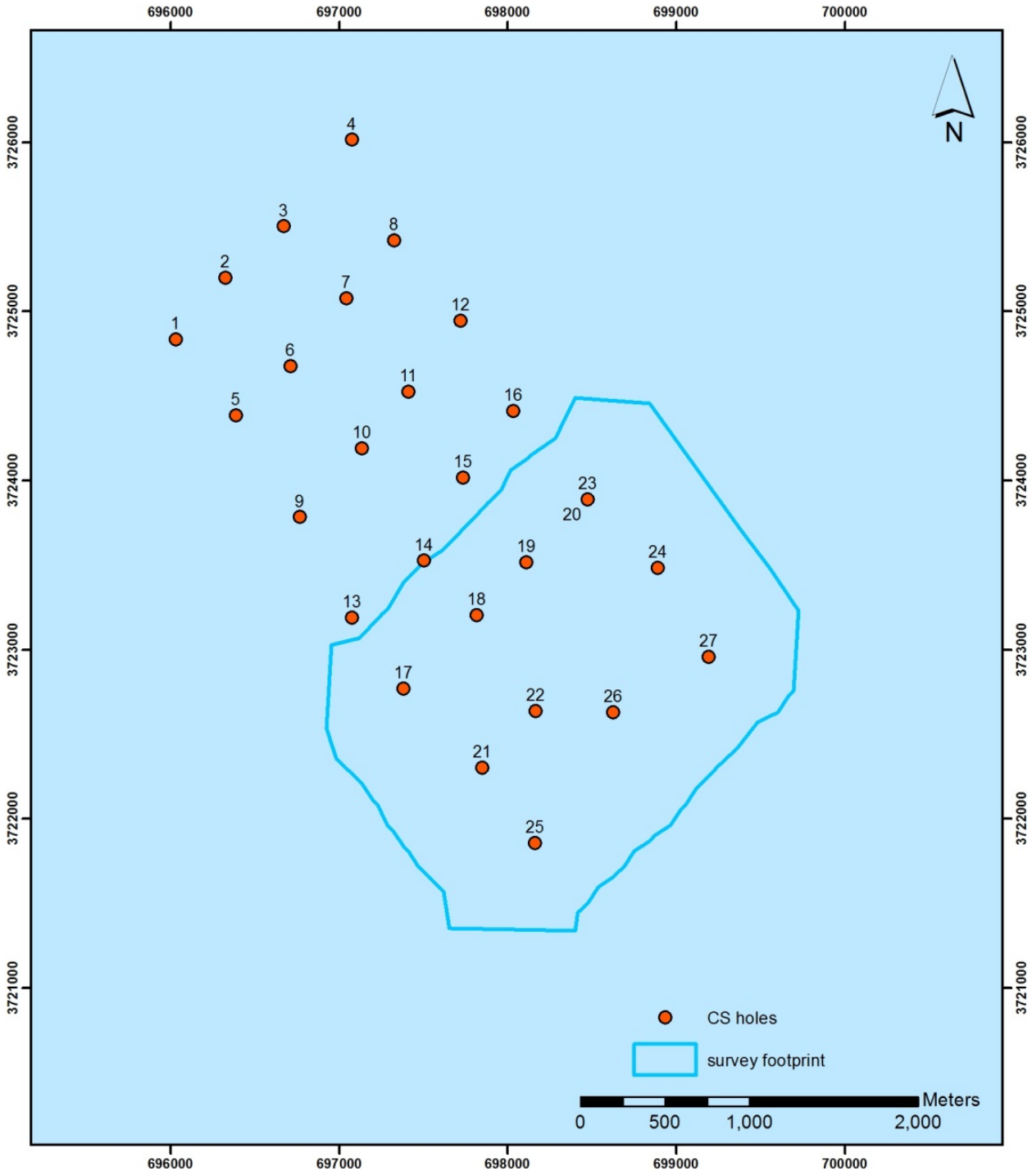

Figure III-16. Vibracore locations in the vicinity of the Cane South borrow area, where the area outlined in blue generally represents the dredging 'footprint' for the 2008-2009 project.

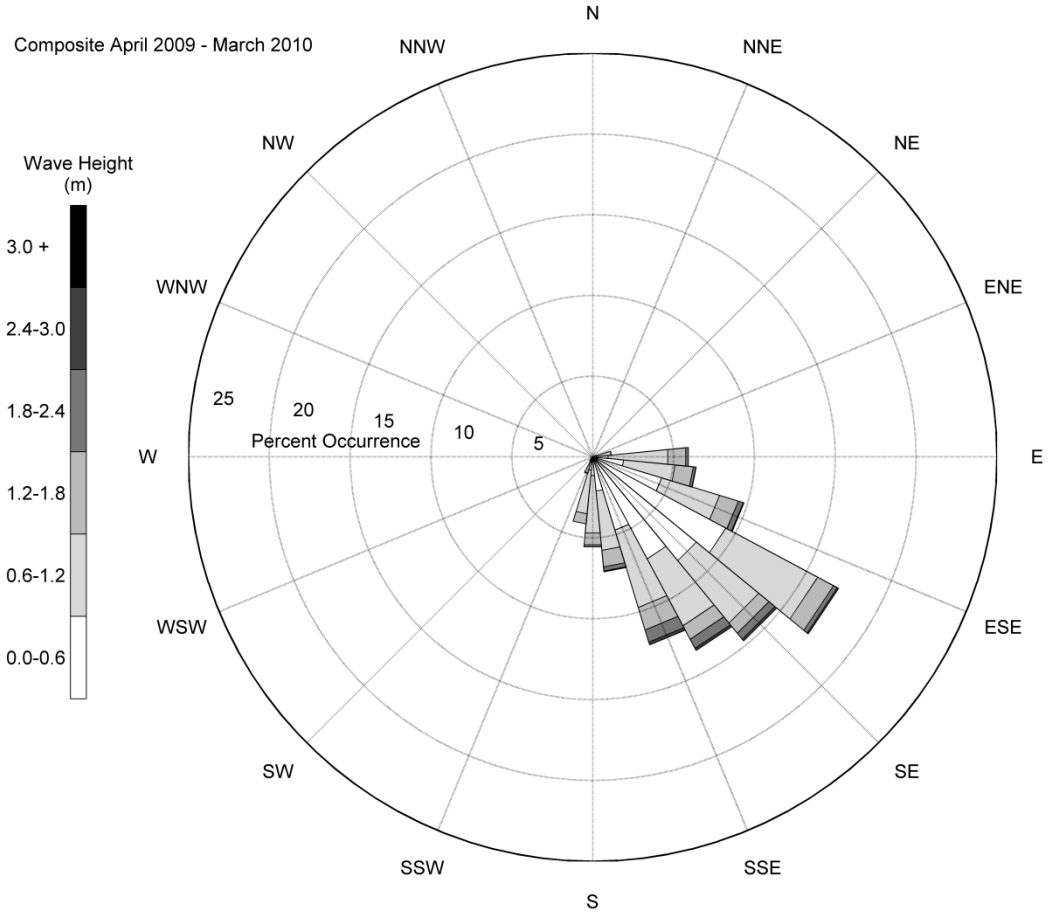

Figure III-17. Wave rose for April 2009 to March 2010 at Cane South, where waves from NDBC Buoy #41013 (Frying Pan Shoal, NC) served as the source for incoming wave energy to the morphodynamic model grids. Wave directions are in metrological convention.

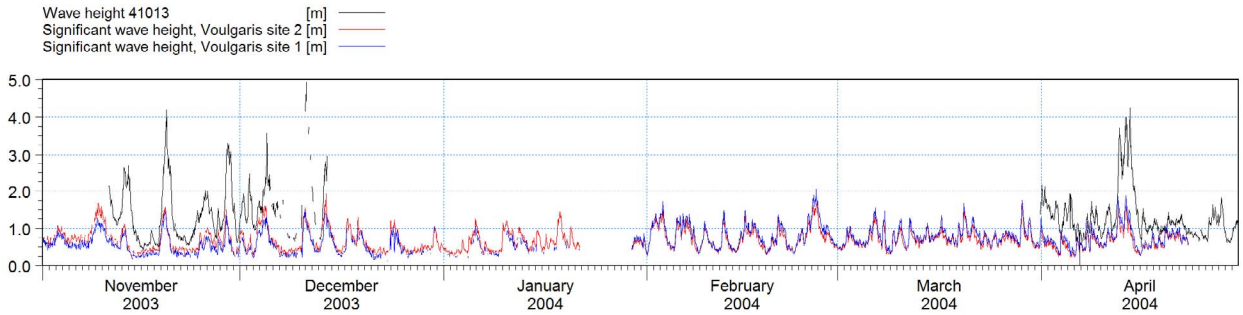

Figure III-18. Comparison of measured wave heights for November 2003 to April 2004: NDBC Buoy #41013 (Frying Pan Shoal, NC), Voulgaris 1, and Voulgaris 2. For information related to nearshore wave data, see Sullivan, et al., 2006.

IV. MODEL TO MODEL COMPARISON

IV.A. SELECTED MODELS

The initial stages of the project focused on comparing the performance of several process-based morphodynamic modeling packages that describe sediment transport and morphological changes under the combined action of waves and currents. The candidate models include the public domain Nearshore Community Model (NearCoM) and Community Sediment Transport Modeling System (CSTMS) developed by various researchers in the United States, as well as commercial models from DHI Water and Environment, Inc. and the United States Army Corps of Engineers (USACE), the latter being available through Aquaveo (http://www.aquaveo.com/) as the Coastal Modeling System (CMS). Each of these model systems are:

- State-of-the art
- Extensively tested, validated, and quantified with regard to skill assessed in different applications and environments
- Widely accepted and used by the research community for their stated purpose as evidenced in peer-reviewed literature, and
- Well described in model documentation and user manuals

Specifically, the project team focused on implementation of the NearCoM package as the core modeling suite of this proposed study. Recent improvements in the model with regard to increased computational efficiency make it a particularly attractive choice for practical applications in large spatial domains (Shi et al., 2007). As it is a public domain and freely available package, it has a clear cost advantage when compared to other commercial packages such as Delft3D, MIKE21 and CMS. In addition, NearCoM does not have the proprietary computer code restrictions associated with commercial software.

Models were initially applied to assess their predictive ability in quantifying morphological changes for the Cane South borrow area. Comparisons were made documenting model skill in terms of simulated wave, flow and morphology, to the degree supported by the measured dataset. As part of this effort, sensitivity tests were performed for all candidate models (as relevant) to assess the influence of key input decisions made in the application of the candidate model systems, such as:

- *Model formulation* – the refractive/scattering response of the wave field as it interacts with dredged slopes will be highly dependent on the choice of wave model (Misra et al., 2008). Similarly, the morphological development of the borrow area will be very sensitive to the sediment transport formulation.
- *Model-specific settings* – choices such as the directional spectral parameters of the incident wave field, the turbulence closure and bed roughness of the flow model, and a host of user-defined inputs to sediment transport models will have the potential to significantly influence morphological development.
- *Spatial resolution* – due to its extreme effect on CPU time, it is always desirable to apply the coarsest grid resolution possible without omitting the dominant physical processes.

- *Input filtering* – considerable CPU time can be saved by either a) omitting simulations during periods of negligible morphology ("time series compression" for environmental forcing) or by simulating environmental conditions which are arguably representative of longer historical periods in terms of the induced morphological response, ("flow and wave schematization").
- *"Speed-up factors"* – a form of process filtering, speed-up factors are used to enhance the morphological response, such that the simulation results are taken as being representative of a longer time period than actually simulated. This can be applied in terms of a static factor for all ongoing morphology, or can be applied at discrete periods such as once per tidal cycle or once per tidal fortnight. Such a method requires that the time scale of significant morphological changes are long compared to the period of time for which average bed level change rates are calculated, and must be used with great care.

The following subsections provide a description of the regional model used for boundary conditions for the candidate morphodynamic models, as well as the different modeling packages utilized for this study.

IV.A.1. Regional Model, COAWST

The Coupled Ocean Atmospheric-Wave-Sediment Transport Modeling System (COAWST), which was used to determine the long term boundary conditions to parameterize the morphology models, integrates several model components that include models for the ocean, atmosphere, surface waves, sediment transport and modeling utilities for exchanging data fields and re-gridding (Warner et al., 2010).

The ocean model used in COAWST is the Regional Ocean Modeling System (ROMS) which solves the three dimensional Reynolds-averaged Navier-Stokes equations using the hydrostatic and Boussinesq approximations (Shchepetkin and McWilliams, 2005, 2009, Haidvogel *et a*l., 2008). ROMS uses finite-difference approximations on a horizontal curvilinear grid and on a vertical stretched terrain-following coordinate. Momentum, scalar advection, and diffusive processes are solved using transport equations. An equation of state computes the density field that accounts for temperature, salinity, and suspended-sediment contributions.

The atmospheric model used in COAWST is the Advanced Research Weather Research and Forecasting (WRF) Model (Skamarock *et al*., 2005). It is a non-hydrostatic, quasi-compressible atmospheric model with boundary layer physics schemes and a variety of physical parameterizations of sub-grid scale processes for predicting meso- and micro-scales of motion. The model predicts three-dimensional wind momentum components, surface pressure, dew point, precipitation, surface sensible and latent heat fluxes, longwave and shortwave radiative fluxes, relative humidity, and air temperature on a sigma-pressure vertical coordinate grid.

The wave model component in the coupled system is Simulating Waves Nearshore (SWAN). SWAN is a spectral wave model specifically designed for shallow water. It solves the wave action balance equation in generalized curvilinear coordinates (Booij et al., 1997). SWAN simulates wind wave generation and propagation and includes the physical processes of wave

refraction, diffraction (de-coupled), shoaling, nonlinear wave-wave interactions, and dissipation due to white capping, depth-limited wave breaking, and bottom friction.

Detailed documentation of COAWST can be found in Warner *et al*. (2010).

IV.A.2. Morphological Models

IV.A.2. NearCoM

The Nearshore Community Model (NearCoM) was developed during the National Oceanography Partnership Program (NOPP)-funded project – Development and Verification of a Comprehensive Community Model for Physical Processes in the Nearshore Ocean. NearCoM is an open-source model that can be used to predict nearshore hydrodynamics, sediment transport, and seabed morphology changes given offshore wave conditions and initial bathymetry. It integrates a wave module, a circulation module and a seabed module, which can be selected from a group of candidate models with standardized interaction threads, inputs and outputs. Recently, NearCoM has been extended by Shi et al. (2013) and Chen et al. (2014) to integrate the wave module SWAN and the Quasi-3D circulation model SHORECIRC with TVD schemes and several sediment transport models. The newly developed NearCoM system is named as NearCoM-TVD (Chen *et al*., 2014).

The wave module SWAN used in the NearCoM package is based on the structured grid Version 40.51AB which is the last stable version before the release of the unstructured grid version UnSWAN. The non-stationary mode of SWAN is coupled with the circulation module in a two-way coupling manner. This coupling scheme enables wave simulations with wave-current fully interacted in the time domain.

The circulation model SHORECIRC is a quasi-3D nearshore circulation model. It is a 2D horizontal model which incorporates the effect of the vertical structure of horizontal flows (Putrevu and Svendsen, 1999). The original version of SHORECIRC is based on governing equations in Cartesian coordinates and implemented by using finite difference schemes. The latest version of SHORECIRC (used in the present project) uses the contravariant form of the mass conservation and momentum equations in generalized curvilinear coordinates. A TVD-type hybrid numerical scheme combining the finite volume and the finite difference methods was implemented in the model. The latest version also takes into account large-scale forcing, such as tidal forcing, Coriolis forcing, wind stress and atmospheric pressure, for applications of both wave- and tide- dominant processes.

NearCoM originally includes two sediment transport models: Soulsby-Van Rijn model (Soulsby, 1997) and Kobayashi model (Kobayashi et al., 2008). Because Kobayashi model was developed for surfzone applications, Soulsby-Van Rijn model was initially applied in model testing. Soulsby-Van Rijn (1997) formula calculates the total load (bed load plus suspended load) transport induced by currents and waves and applies to total load sediment transport in combined waves and currents on horizontal and sloping beds. It is intended for conditions in which the bed is rippled. Additionally, although this Soulsby-Van Rijn formula takes into account wave-induced sediment transport, it still favors current-dominant conditions as described in Soulsby

(1997). The effect of waves is simply to enhance the amount of mobilized sediment without considering sediment transport induced by wave asymmetry. Moreover the direction of sediment transport is determined by current direction only. During this project, a new sediment transport model was implemented based on Van Rijn's (1991) formulas for applications of wave-dominant sediment transport. A detailed description of the Soulsby-Van Rijn 1997 and Van Rijn 1991 sediment transport formulas related to this project can be found in Chapter V.C.4.

The morphology module in NearCoM includes a morphology factor following van der Wegen and Roelvink (2008) in order to accelerate morphology evolution relative to modeled hydrodynamic time scales. This approach has been used by van der Wegen and Roelvink (2008) and van der Wegen et al. (2008) to obtain simulations of tidal embayment evolution over millennial time scales. In addition, following Roelvink (2006), a so-called "parallel online" scheme has been developed as part of this project (Shi et al., 2010) to allow use of a large morphology factor for long-term simulations of morphological evolution.

For this project NearCoM-TVD was fully parallelized using the Message Passing Interface (MPI) with non-blocking communication. The parallelized codes of SHORECIRC and the morphological model use a 2D domain decomposition technique to subdivide the problem into multiple regions and assign each subdomain to a separate processor core. For the SWAN code, the existing 1D domain decomposition scheme was incorporated into an equal-CPU load parallelization scheme based on a two-step mapping method.

IV.A.2.b MIKE 21

DHI utilized the MIKE 21 Coupled Model FM to simulate hydrodynamics, sediment transport and bathymetry changes over selected periods of time within the area of interest for this project. It consists of several modules, each of them tailored to the description and simulation of specific physical process(es). In the present case, the following modules were used: spectral wave module (SW), hydrodynamic module (HD), non-cohesive sediment transport (ST), and morphology module (Morph). The selected approach allows full feedback of the calculated bed level changes on the waves and hydrodynamics, as well as dynamic coupling of waves and currents.

The MIKE 21 Coupled Model FM can be used for investigating the morphological evolution of the nearshore bathymetry in response to coastal structure, dredging works, etc. Coastal structures include submerged or surface-piercing breakwaters, groins, harbors, etc.; also soft interventions such as shore face nourishments can be investigated. The coupled model is mostly suitable for medium-term morphological simulations (weeks to months) over a limited coastal area, typical dimensions being ~6 miles in longshore direction and ~1.5 mile in cross-shore extent. A brief description of the capabilities of the different MIKE 21 modules is provided below.

The Spectral Wave Module MIKE 21 SW simulates the growth, decay and transformation of wind-waves and swell in offshore and coastal areas. The wave model accounts for the following physical phenomena: wave growth by wind action, non-linear wave-wave interaction, dissipation of wave energy due to white capping, dissipation of wave energy due to bottom friction,

dissipation of wave energy due to depth-limited breaking, refraction and shoaling due to variations in water depth, wave-current interaction, diffraction, time-varying water depth, eventually combined with flooding and drying. MIKE 21 SW includes two different numerical formulations: fully spectral formulation and directionally decoupled parametric formulation.

The fully spectral formulation is based on the wave action conservation equation, as described in Komen et al. (1994) and Young (1999), where the direction-frequency wave action spectrum is the dependent variable. Significant reduction in computational time can be achieved in some cases by adopting the directionally decoupled parametric formulation, which is based on a parameterization of the wave action conservation equation. This parameterization occurs in the frequency domain by introducing the zero-th and first moments of the wave action spectrum as dependent variable, following Holthuijsen (1989).

The Hydrodynamic Module MIKE 21 HD FM simulates the time variation of water levels and depth-averaged flows in response to a variety of forcing functions in coastal regions, lakes, estuaries and rivers. The model is based on the numerical solution of the shallow water equations, also known as the depth-integrated incompressible Reynolds Averaged Navier-Stokes (RANS) equations. The hydrodynamic model accounts for the following physical phenomena: flooding and drying, momentum dispersion due to turbulent fluctuations, bottom friction, Coriolis forcing, surface wind shear stress, barometric pressure gradients, precipitation and evaporation, wave radiation stresses, sources and sinks.

The Non-cohesive Sediment Transport Module MIKE 21 ST FM simulates the transport, deposition and erosion of sand under the combined actions of waves and current. MIKE 21 ST FM utilizes DHI's deterministic intra-wave sediment transport program STP to calculate the total load (bed load + suspended load) transport rates of non-cohesive sediment (sand). STP is an advanced sediment transport model that accounts for the effects of waves propagating at an arbitrary angle to the current, breaking/unbroken waves, uniform/graded bed sediment, plane/ripple covered bed when calculating the local rates of total load transport. The current may be tidal, wave-driven, wind-driven or a combination of two or more sources.

STP uses the boundary layer model developed by Fredsøe (1984) to compute the time-varying hydrodynamics in combined waves plus current situations within the wave period, both inside and above the wave boundary layer. The boundary layer model also computes the instantaneous bed shear stress, which is then used to calculate the instantaneous bed load transport rate (using the theory of Engelund and Fredsøe, 1976) and the near-bed concentration of suspended sediment (Zyserman and Fredsøe, 1994).

The instantaneous concentration profile is obtained from the numerical solution of the diffusion equation for suspended sediment, as described in Fredsøe et al. (1985). For surf zone conditions, the additional turbulence associated with the breaking waves is accounted for as described in Deigaard et al. (1986a, b). Instantaneous suspended load transport is calculated by integration over the water depth of the product of instantaneous velocity (from the wave boundary layer model) times instantaneous concentration of suspended sediment (from the solution of the diffusion equation). The bed load and suspended load transport rates are time

averaged (over the wave period) and added to obtain the total load transport rates of non-cohesive sediment.

The original version of STP uses a two dimensional (2D) approach to calculate the sediment transport rates, meaning that sediment transport is calculated exclusively in the direction of the mean current, even within the surf zone and/or when waves and current aren't aligned. The effect of breaking waves is simply included as enhanced turbulence close to the free surface, which results in larger amounts of sediment in suspension and transport rates compared to the situation with unbroken waves (Deigaard et al., 1986a). No net sediment transport rates are calculated in the direction of wave propagation.

The 2D sediment transport model was later extended to include a quasi-three-dimensional (Q3D) description of the flow and the sediment transport, see Elfrink et al. (1996, 1999) for examples of application of the Q3D approach. In the Q3D version of STP, the time-averaged (over a wave period) velocity profiles are calculated by integration of the three-dimensional shear stress distribution derived by Deigaard (1993). Use of this approach allows calculation of velocity profiles and net sediment transport rates both in the direction of wave propagation and in the direction of the mean current. For example, for surf zone applications, the model will calculate a logarithmic velocity profile in longshore direction and the typical undertow profile in cross-shore direction, each of these with its associated longshore and offshore sediment transport rates, respectively.

The morphological evolution of the seabed is included by updating the model bathymetry at every time step on the basis of the gradients in the calculated sediment transport field, i.e. the continuity equation for bed sediment. The porosity of the bed material is accounted for when translating gradients in sediment transport to bed level changes.

IV.A.2.c CMS

Applied Coastal used the Coastal Modeling System (CMS) which is an integrated suite of numerical models to model the hydrodynamics, waves, sediment transport, and morphological changes for the Cane South borrow area over the selected time periods for this project. The US Army Corps of Engineers (USACE) has been developing and refining the CMS for more than a decade to be used as a research and engineering tool in coastal areas. It was designed to be used on desk-top computers for practical applications in sediment management for coastal inlets and beaches and for navigation channel performance. CMS utilizes the Surface-water Modeling System (SMS) interface for grid generation, model setup, and post-processing the results. The two principal components of CMS are CMS-Flow and CMS-Wave, which can be coupled or run individually. A brief description of the capabilities of the CMS is provided below.

CMS-Flow is a coupled hydrodynamic and sediment transport model that applies the finite volume method on a non-uniform Cartesian grid. Together the two models of CMS-flow can simulate the depth-averaged circulation, salinity and sediment transport forced by tides, wind, atmospheric pressure gradient, river inflow and waves. In addition, CMS-flow is capable of estimating the morphological bed change from the bedload and suspended load sediment transport. The hydrodynamic model solves the conservative shallow water equations which

includes terms for the Coriolis force, wind stress, wave stress, bottom stress, vegetation flow drag, bottom friction, and turbulent diffusion. Within the sediment transport model there are three formulations available, a sediment mass balance, an equilibrium advection-diffusion method, and a non-equilibrium advection-diffusion transport method. In addition, depending on the chosen formulation different transport formulations are available. The three transport formulations are Lund-CIRP (Camenen and Larson, 2008), Van Rijn (2007), and Wantanabe (1987).

The Lund-CIRP formulation is a wave and current induced sediment transport formula for bed and suspended loads developed by Camenen and Larson (2005, 2007, 2008). This formula was designed for both symmetric and asymmetric waves, but for simplicity the CMS model assumes the waves to be symmetric. According to the CMS user manual the Lund-CIRP formulation does well predicting the sediment transport within the surf zone. However, this formula tends to overestimate the amount of transport in deep water (>10 m) and in the wetting and drying limit.

The Van Rijn formulation included in CMS is composed of the 1984 transport equations for bed load and suspended load with recalibrated coefficients from 2007. According to Van Rijn (2007) if the velocities are higher than 0.6 m/s then this formulation used in CMS predicts the bed transport rates within a factor of 2. However, if the velocities are close to initiation of motion the transport predicted by this formulation under-predicts by a factor of 2- 3.

The last transport formulation included in CMS is the 1987 Watanabe total-load transport formulation. Unlike the two previous formulations, this transport equation calculates the total load compared to the suspended and bed loads. According to the CMS User Manual the Watanabe formulation tends to underestimate the transport in deep water (<10 m).

CMS-Wave is a finite difference, phased-averaged spectral wave model that solves the steady-state wave-action balance equation on a non-uniform Cartesian grid, similar to CMS-Flow (Mase, 2001). CMS-Wave can represent important physical phenomena including wind wave generation and growth, diffraction, reflection, dissipation due to bottom friction, white capping and breaking, wave-wave and wave-current interactions, wave runup, wave setup, and wave transmission through structures (Lin *et al*. 2008, 2011).

IV.B. SELECTION OF SIMULATION PERIOD

The boundary conditions for the morphology models would need to span the time period between the post-dredging and one year post-dredging bathymetric surveys. It was determined that a year-long COAWST simulation would take approximately 100 days to complete using 44 processors. Instead, a representative month-long time period during 2009-2010 was selected to allow efficient computation of appropriate boundary conditions. A month-long COAWST simulation took approximately 10 days.

In order to determine a representative month based on wave climatology between the post-dredging and the one year post-dredging bathymetric surveys detailed analysis of the wave data recorded by NOAA's Buoy 41043 was completed. This buoy is located at the Frying Pan Shoals,

NC, approximately 55 nautical miles from the Cane South borrow area. The spectra wave data was refracted using CMS to the Cane South borrow area (Figure IV-1). The monthly spectra wave data was downloaded from http://www.nodc.noaa.gov/BUOY/41013.html#netcdftable for April 2009 to March 2010. The bed elevations were interpolated to the model bathymetry from the COAWST grids described in section IV.C.

Upon refracting the wave data using CMS the wave height and wave direction were extracted from the middle of the borrow area every hour. This data was compiled into directional frequency figures for the year (Figure IV-2) and monthly (e.g. Figure IV-3), see Appendix A for all of the monthly wave rose figures. In addition, the wave energy for each month and the annual average wave energy were determined, along with the monthly R^2 values for each month relative to the annual average (Figure IV-4). From these results, February 2010 was selected as the representative month, as it was shown to have the highest R^2 value. Figure IV-5 displays the annual average and February's wave energy.

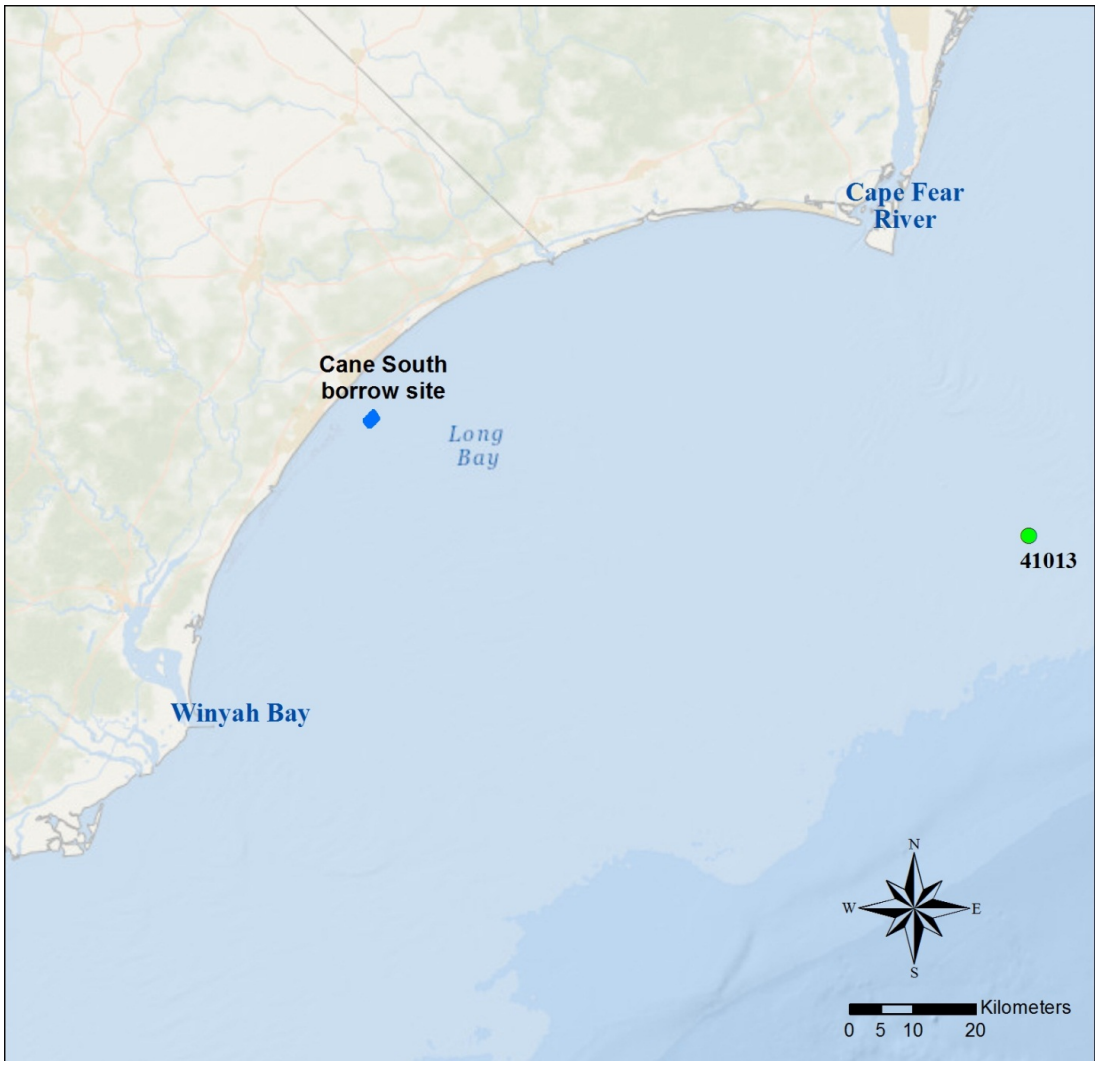

Figure IV-1. Map showing NBDC 41013 and the Cane South borrow area locations. The NDBC 41013 wave data was refracted to borrow area to determine the representative month.

IV.C. REGIONAL SCALE MODEL

COAWST was used to conduct the month-long simulation, from February 1, 2010 00:00 to March 4, 2010 00:00, using the U.S. East Coast domain, which was previously calibrated for Long Bay for another application (Warner *et al*., 2012), in order to provide boundary conditions for near-field grid in vicinity of Cane South borrow area. The existing COAWST model set up was utilized which included three-nested grids, the U.S. East Coast grid (Figure IV-6), the North and South Carolina grid (Figure IV-7) and Long Bay grid (Figure IV-8) for the existing COAWST model for Long Bay, SC was used. Table IV-1 includes a detailed list of the model parameters included in this COAWST model.

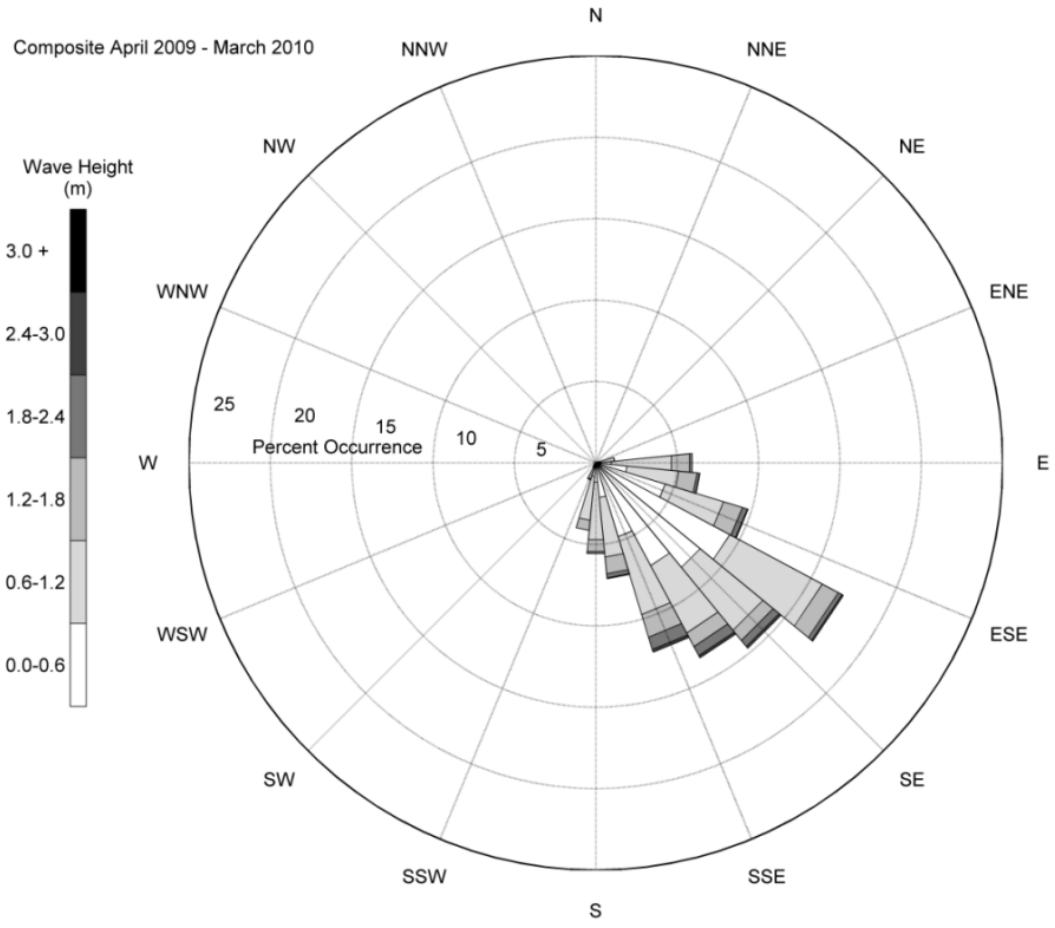

Figure IV-2. Wave rose for April 2009 to March 2010 at Cane South, where waves from NDBC Buoy #41013 (Frying Pan Shoal, NC) were refracted to the Cane South borrow area. Wave directions are in meteorological convention.

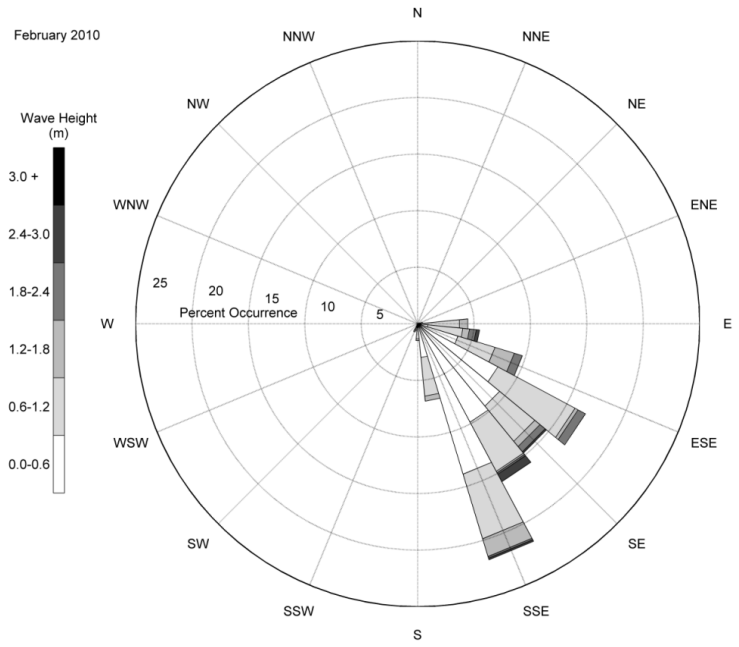

Figure IV-3. Wave rose for February 2010 at Cane South, where waves from NDBC Buoy #41013 (Frying Pan Shoal, NC) were refracted to the Cane South borrow area. Wave directions are in meteorological convention.

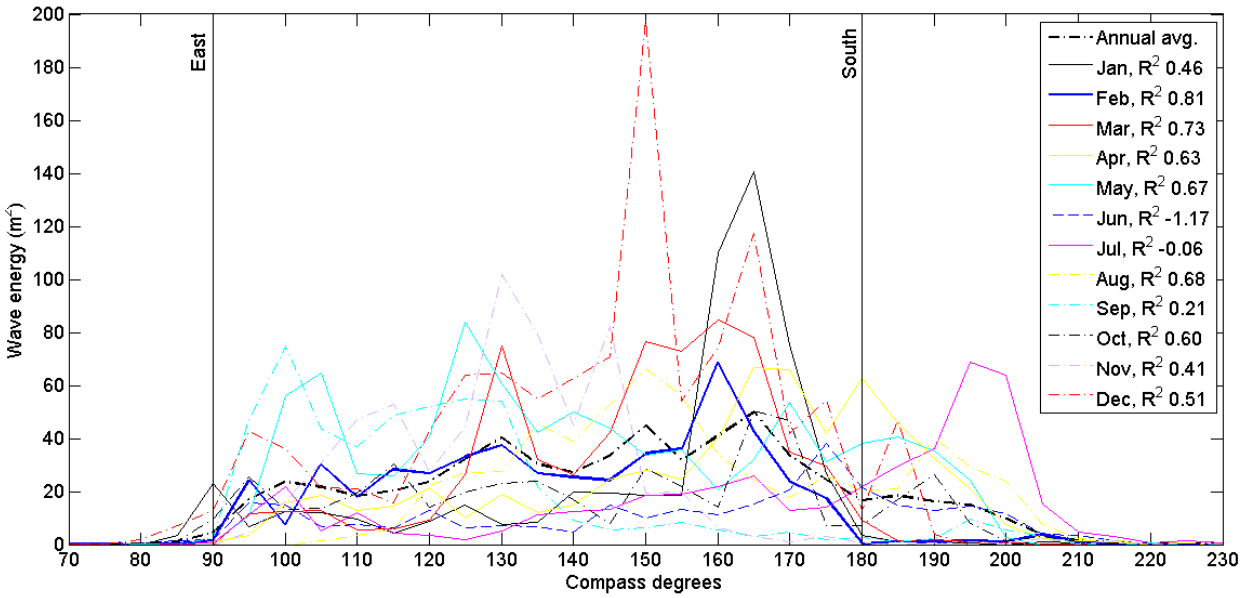

Figure IV-4. Year average and monthly wave energy by direction (meteorological convention). R-squared correlations are shown in the legend for each month.

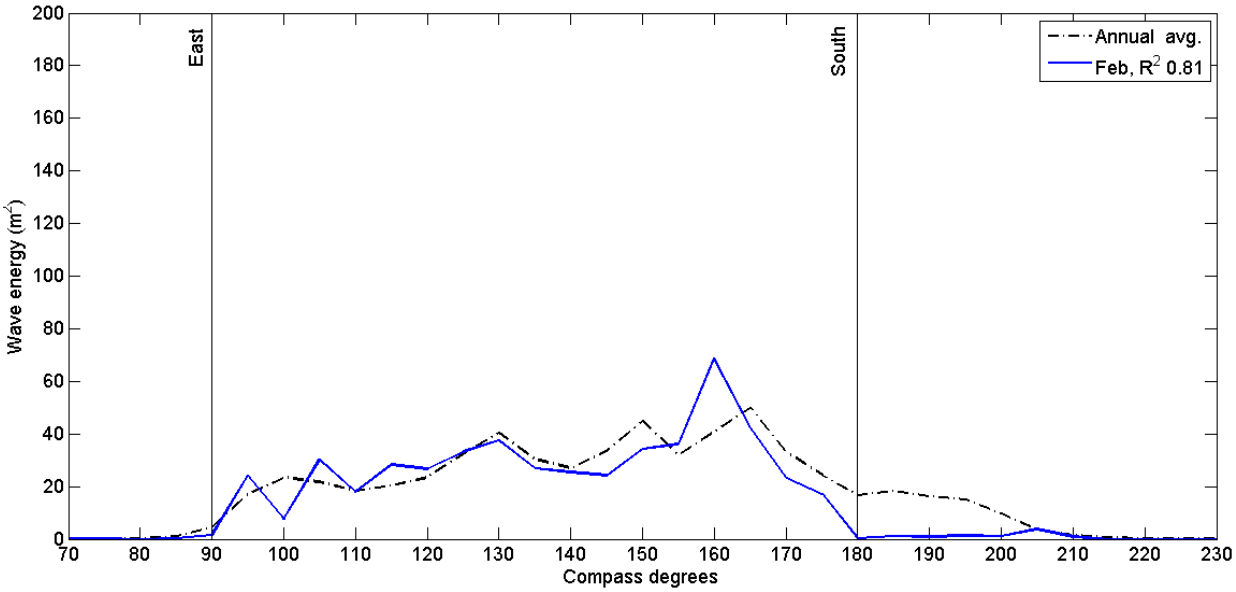

Figure IV-5. Year average and February 2010 wave energy by direction (meteorological convention). R-squared correlation is shown in the legend for February.

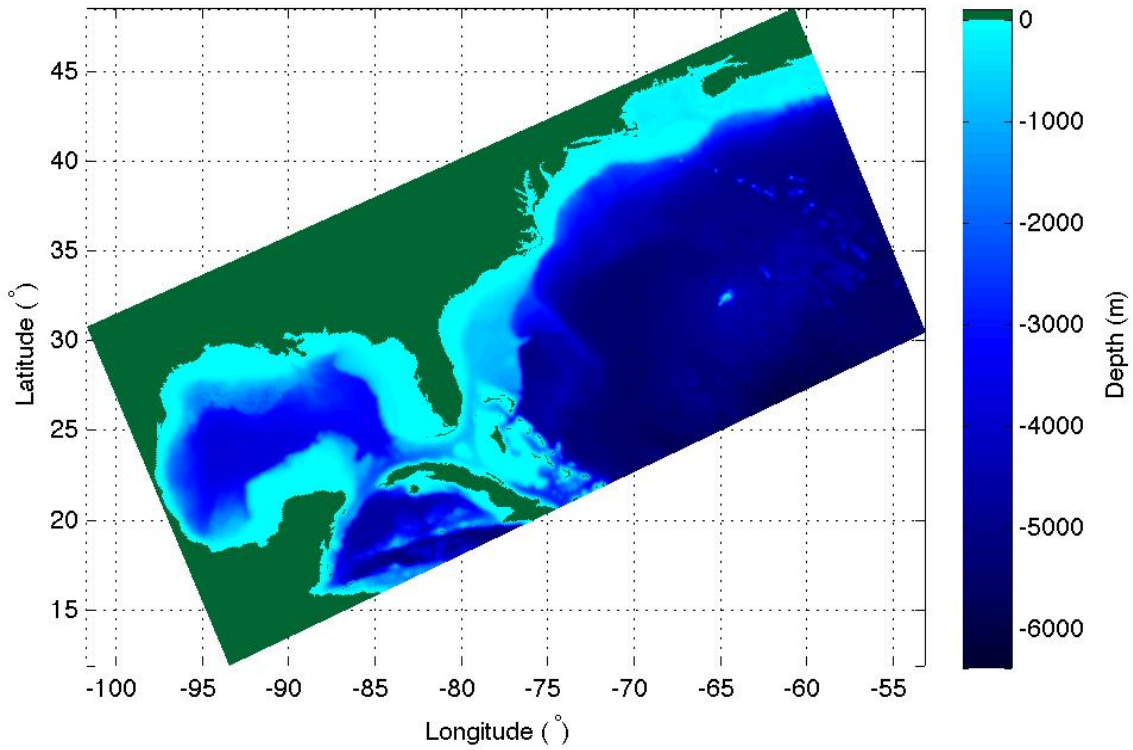

Figure IV-6. U.S. East Coast domain in COAWST.

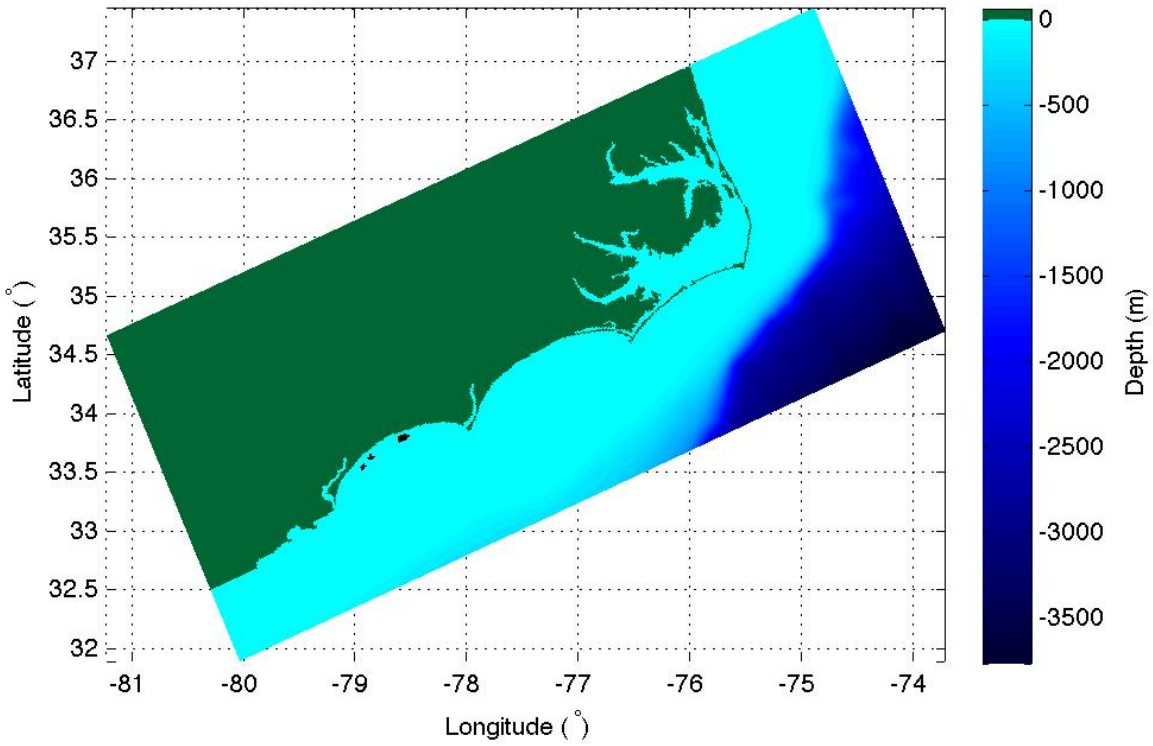

Figure IV-7. North and South Carolina domain in COAWST.

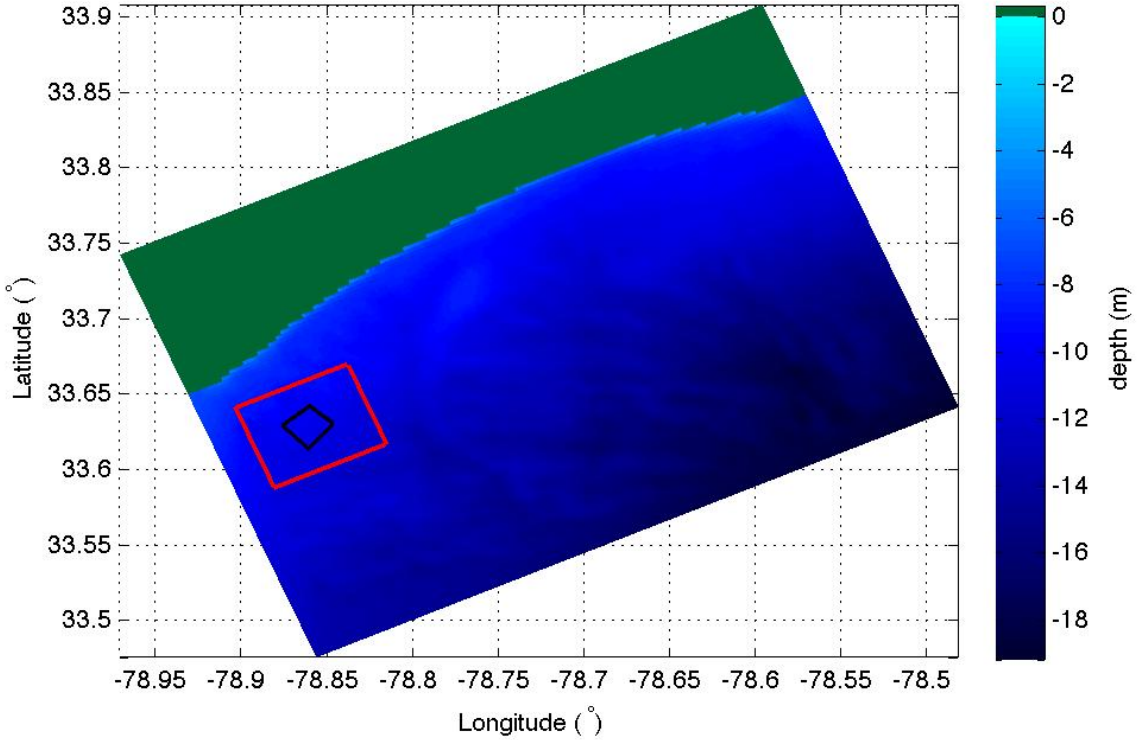

Figure IV-8. Long Bay domain in COAWST. The black quadrilateral represents Cane South borrow area and red quadrilateral is the boundaries of near-field grid used by NearCoM, MIKE 21 and CMS.

Table IV-1. COAWST model parameters.		
COAWST Wave Model		
Parameter/Process	**Value**	**Comments**
Spectral formulation	JONSWAP Gamma=3.3	Spectral shape is not resolved through a finite number of frequencies; a spectral shape (JONSWAP) is assumed instead, directional spectrum D(θ) resolved with 16 bins
Time formulation	Nonstationary	
Wave-current interaction	Included	
Wind generation of waves	Included	
Wave diffraction	Included	SWAN's de-couple technique
Wave breaking	White-capping Battjes and Janssen alpha=1.0 Gamma=0.73	Gamma is breaking parameter due to limited depth, alpha is a proportionality factor relating dissipation in the wave bore to dissipation in a hydraulic jump
Bottom friction	Madsen, $C_f = 0.05$	C_f = friction coefficient Effect of bottom friction on mean wave period included
Boundary conditions	H_{mo} (significant wave height), T_p (peak wave period), PWD (peak wave direction), JONSWAP at open boundaries of U.S. east coast grid	Parameters vary in time and along boundaries, see Figure IV-6 for U.S. east coast grid
Time step	600 seconds	Quasi stationary wave field
Instantaneous free surface elevation	From Circulation module ROMS	
Output	H_{mo}, T_p, PWD	Saved at 1 hour intervals
COAWST Hydrodynamic Model		
Time step	240.0s/ 48.0s/ 24.0s	Respectively for three nest grids from largest to smallest grid
Density	Baroclinic	
Horizontal eddy viscosity	Turbulence closure	
Bed resistance	$C_d = 0.003$	Quadratic bottom drag coefficient
Coriolis forcing	Included	
Wind forcing (surge)	Included	
Precipitation/evaporation	Excluded	
Radiation stresses	From wave module SWAN	VF formula
Sources/sinks	Excluded	
Structures	Not Available	
Initial conditions	From HYCOM results	
Boundary conditions	Tidal boundary conditions at U.S. east coast grid	See Figure IV-6 for U.S. east coast grid.
Output	Elevation, current velocity, salinity, temperature	Saved at 1 hour intervals

The tidal current magnitude, direction and surface elevation results from the COAWST month-long simulation are shown in Figure IV-11, IV-12 and IV-13, respectively, at Point 1 – Point 5 specified in Figure IV-9. As shown in Figure IV-9 the tidal currents are generally weak with a magnitude of less than 0.2 m/s. The primary current directions are towards the west, west-northwest, southeast, and east-southeast as shown in Figure IV-10. The tidal range is approximately 1.5 m for all five points.

Significant wave height, peak wave direction, and peak wave period are shown in Figure IV-14, IV-15 and IV-16, respectively, at Point 1 – Point 5. There are several high energy wave events in February as shown in Figure IV-14. The biggest wave event occurred around February 6th when the wave height reached approximately 3 meters. During the majority of the other high energy wave events (where wave periods were greater than 7 seconds and wave heights exceeded 1 meter) the wave heights were approximately 1.5 to 2 meters. During these wave events, the wave direction was generally from SE and SSE and had peak periods of approximately 10 seconds. The wave height slightly decayed from the southern grid boundary to the northern boundary.

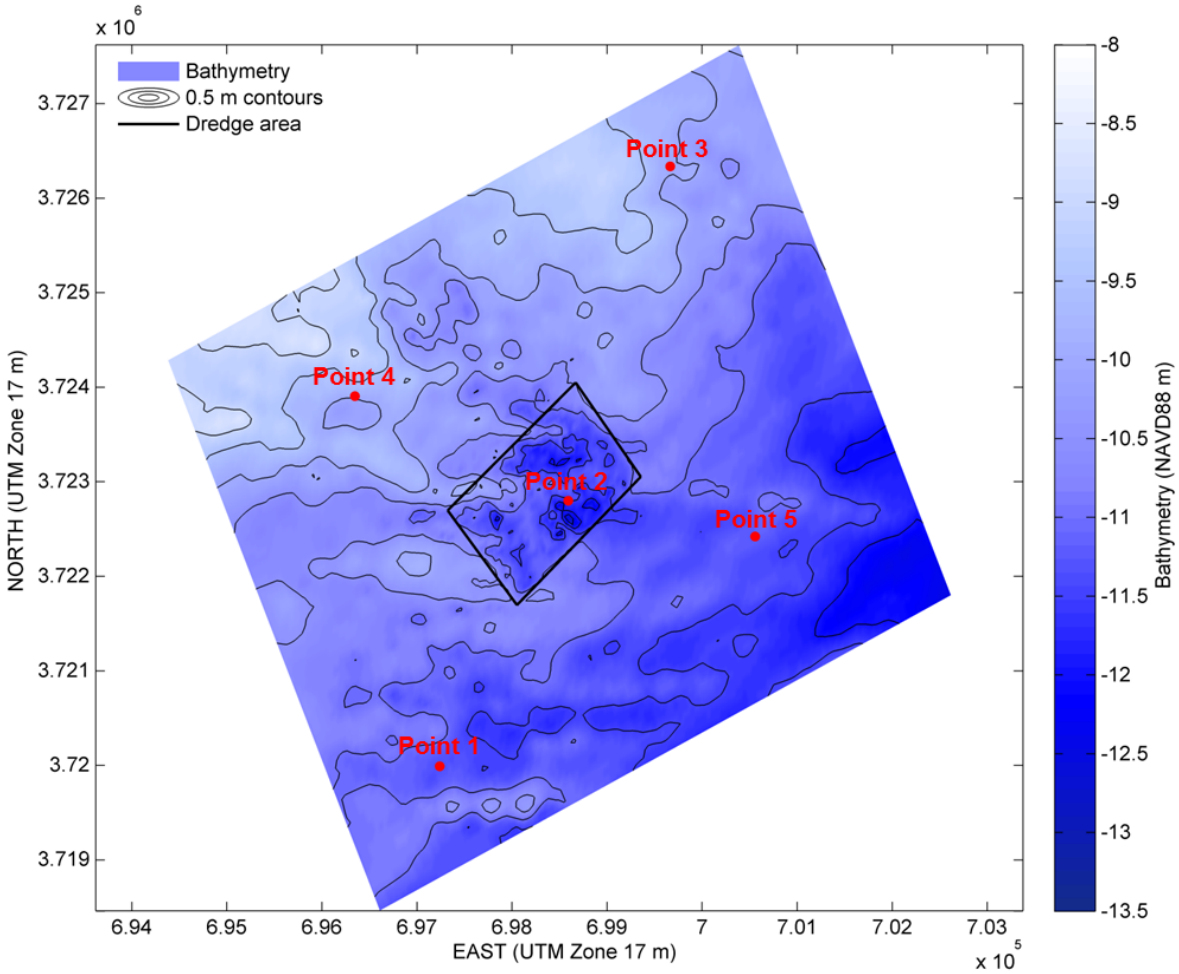

Figure IV-9. Locations of Point 1 – 5 used to show COAWST results in Figures IV-11 through IV-16.

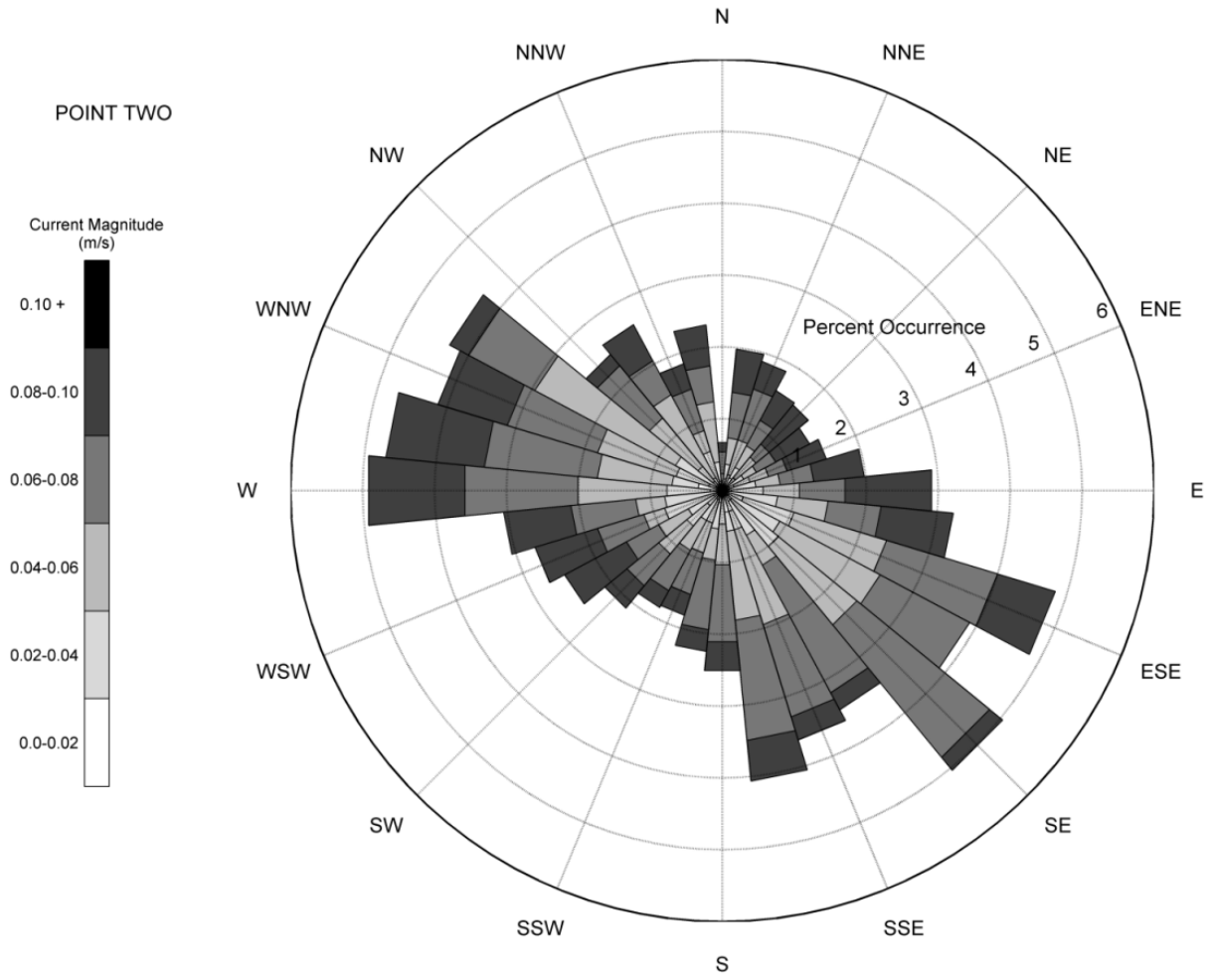

Figure IV-10. Current rose for point two of the comparison points. The current directions are in oceanographic convention, direction towards.

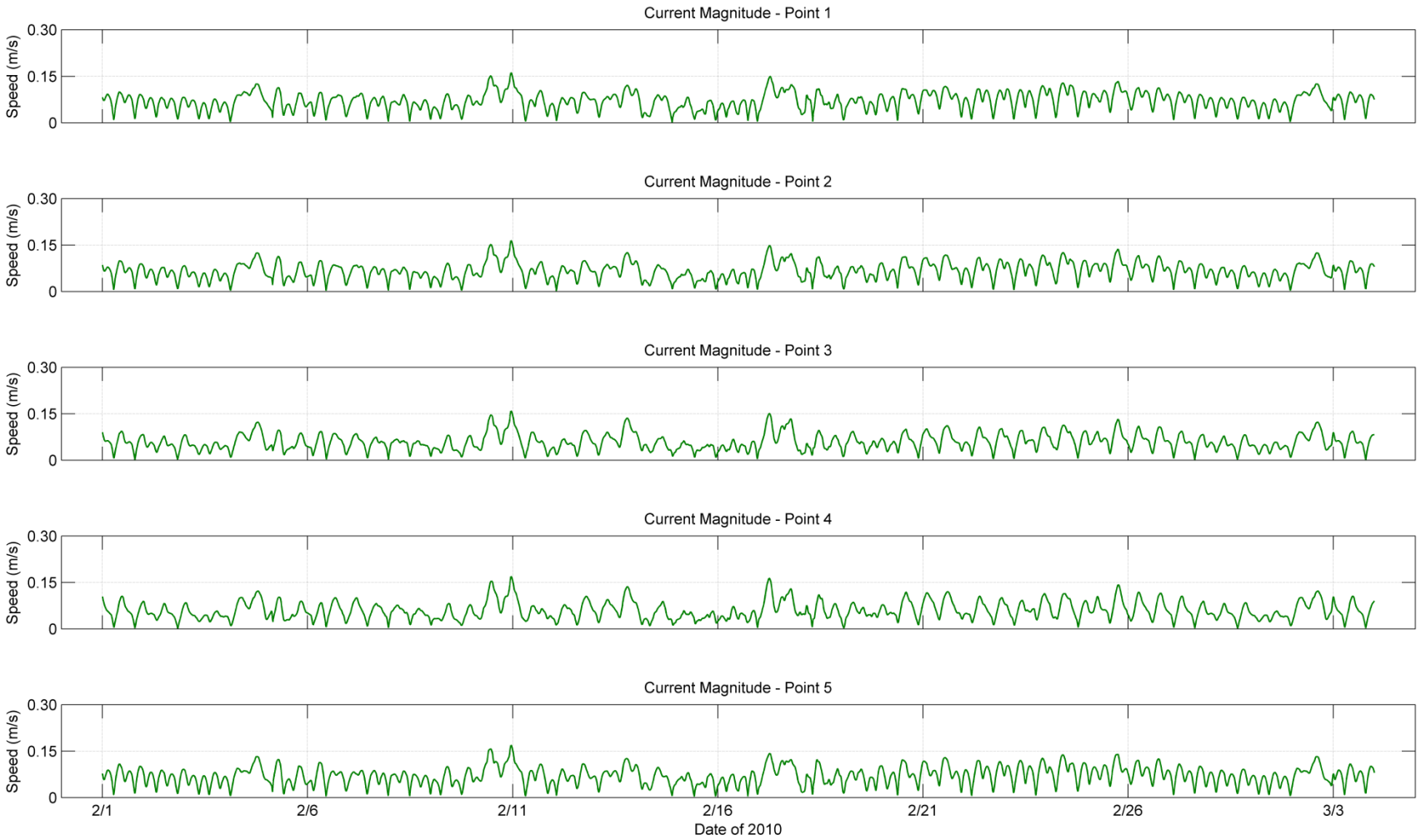

Figure IV-11. COAWST results of tidal current magnitude at Point 1 – Point 5.

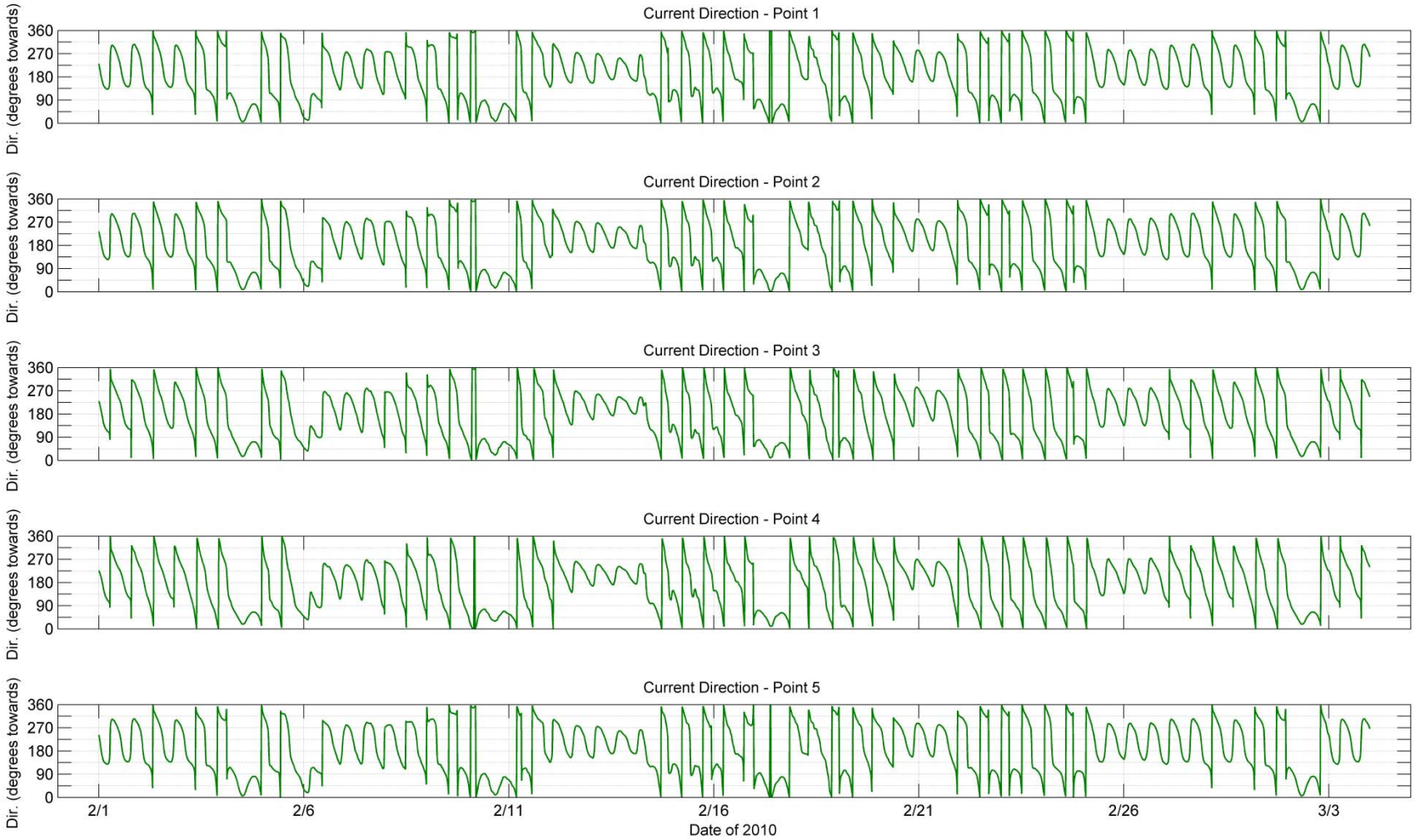

Figure IV-12. COAWST results of tidal current direction (oceanographic convention) at Point 1 – Point 5.

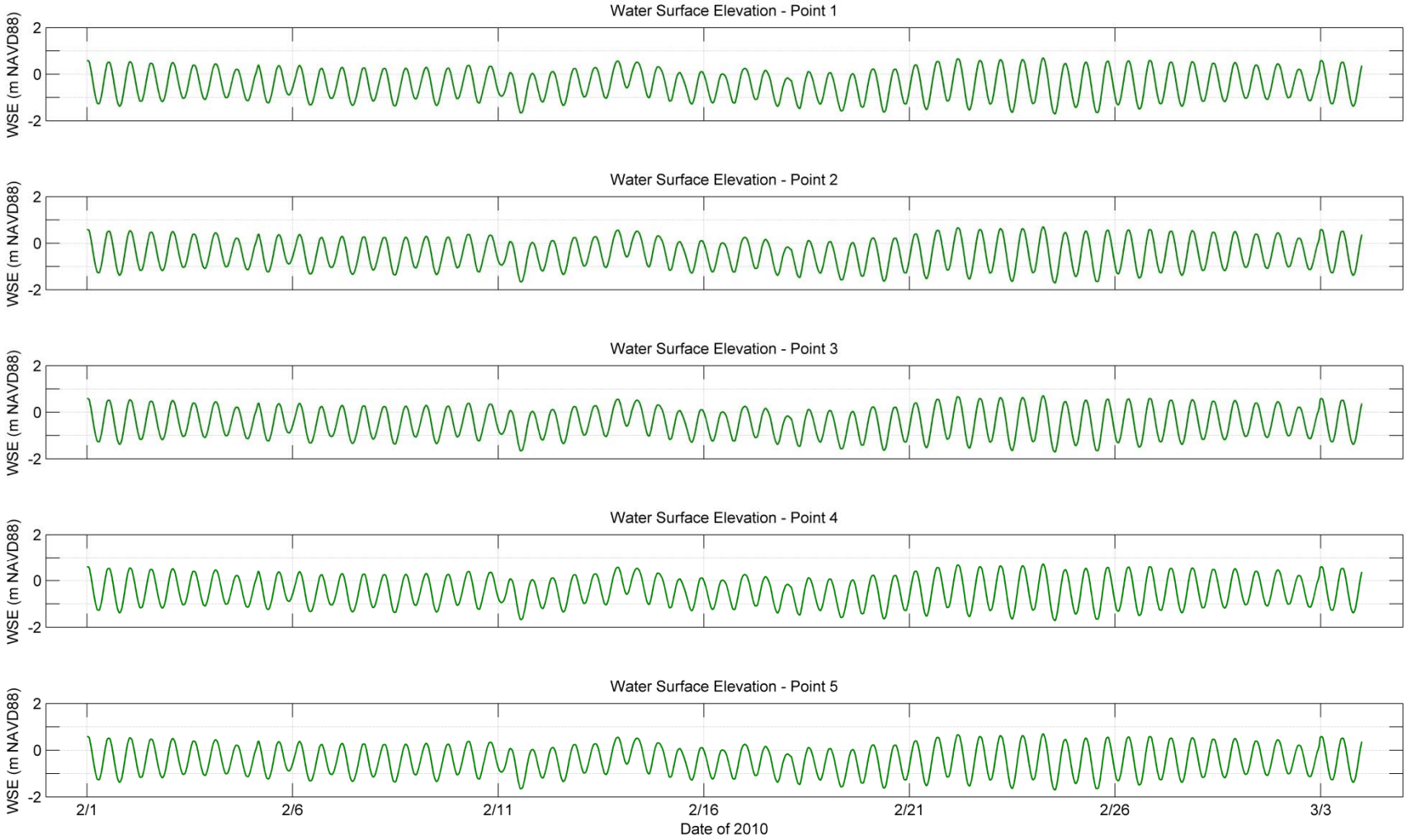

Figure IV-13. COAWST results of water surface elevation at Point 1 – Point 5.

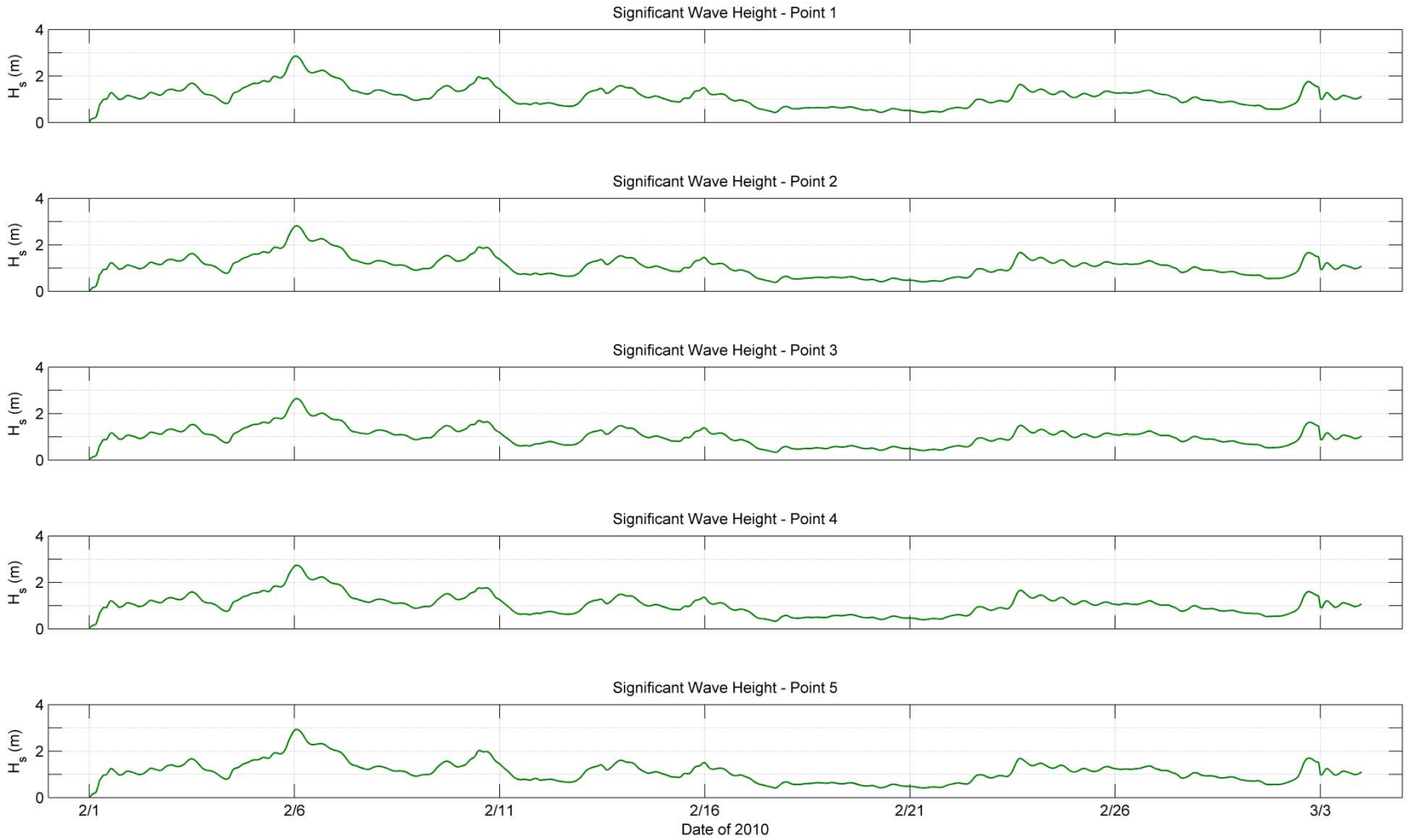

Figure IV-14. COAWST results of significant wave height at Point 1 – Point 5.

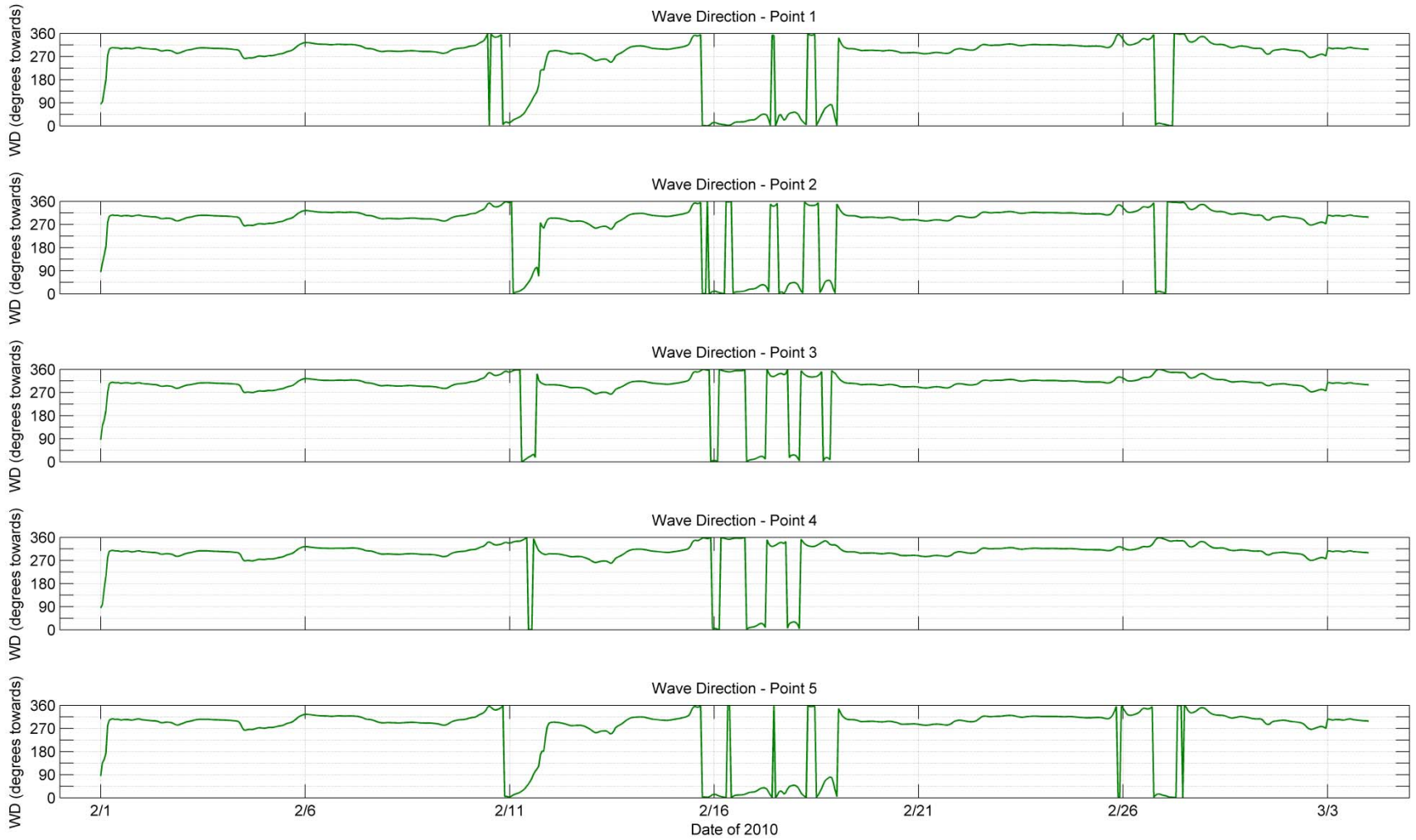

Figure IV-15. COAWST results of peak wave direction (oceanographic convention) at Point 1 – Point 5.

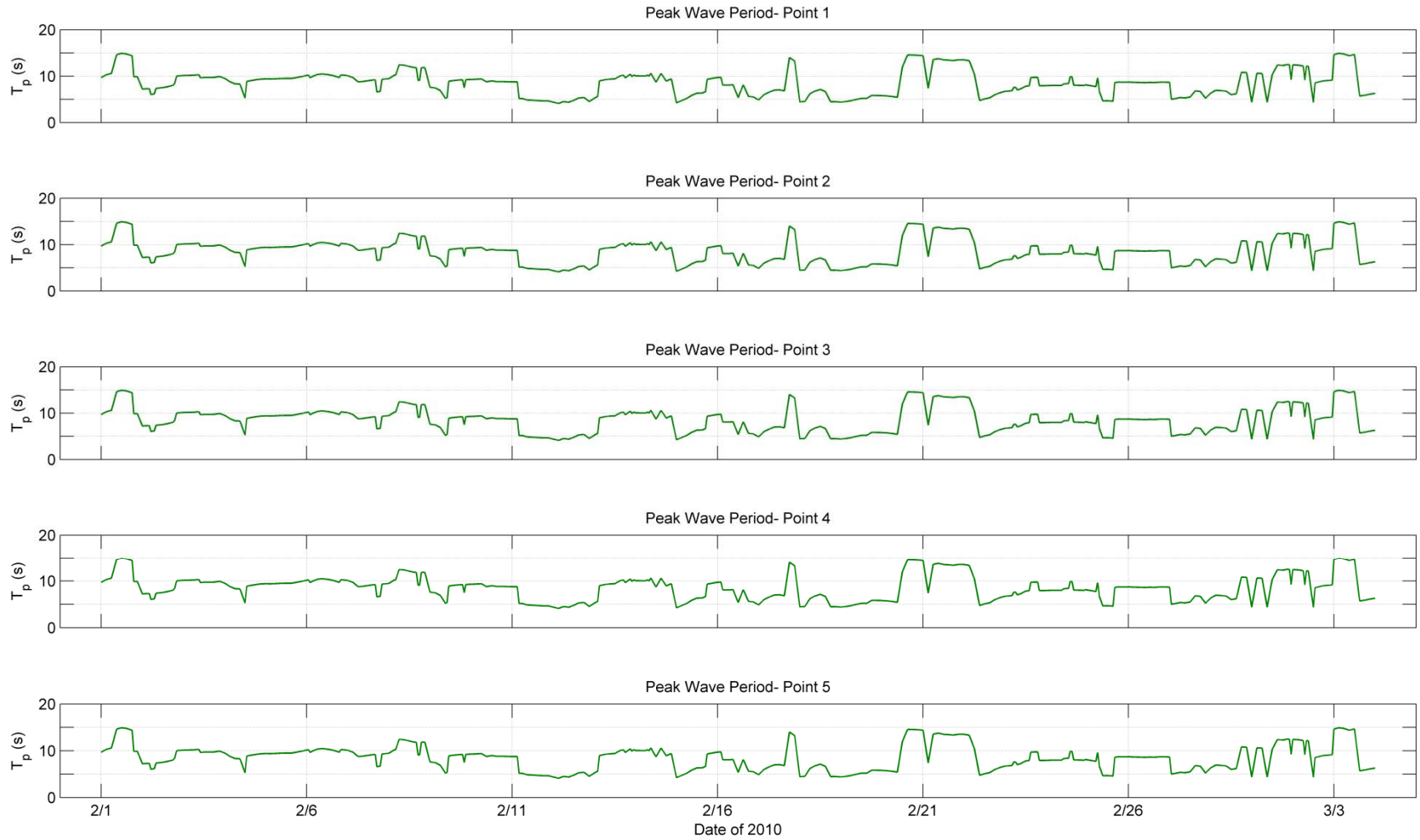

Figure IV-16. COAWST results of peak wave period at Point 1 – Point 5.

IV.D. LOCAL SCALE MODELS

The three morphodynamic models, NearCoM, MIKE 21, and CMS, were setup to run for the representative month, February 2010, and for the year between the post-dredging and one year post-dredging bathymetric survey. This section focuses on the model setup for the month-long simulation; the setup for the year simulation is discussed in section IV.G.3. The month-long simulation started on February 1, 2010 at 00:00 and went to March 4, 2010 00:00, i.e. a total of 744 hourly time steps.

The starting bathymetry for the three morphodynamic models is from a combination of a portion of the 1/3 arc-second grid from the coastal relief model of Myrtle Beach, South Carolina and the post-dredge bathymetric survey of the Cane South borrow area, Figure IV-17. The coastal relief model covered a larger area than the morphodynamic model' grids; therefore, only a portion of this data was used (Figure IV-18). In addition, the coastal relief model bathymetry data covering the post-dredge bathymetric survey area was removed for accuracy in the dredged area. The boundary and initial conditions for the different models were extracted from the COAWST model simulation (explained in section IV.C) which was run for the same period as the month-long simulation.

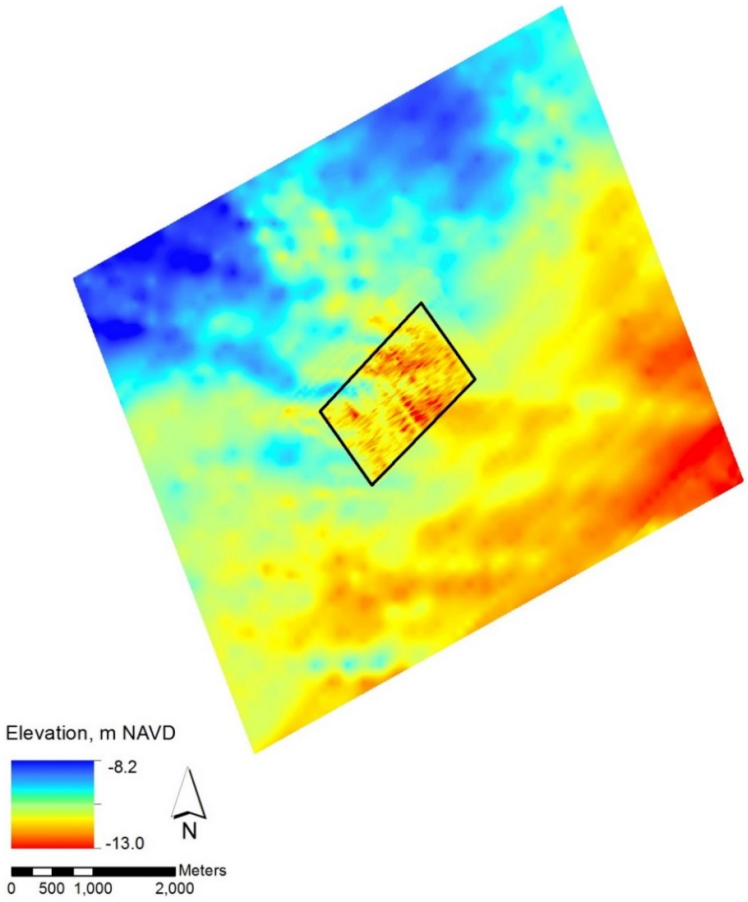

Figure IV-17. Starting bathymetry for the morphology models, which is a combination of 1/3 arc-second DEM grid for Myrtle Beach, SC and the post-dredge bathymetric survey for cane south. The black rectangle outlines the extent of the post-dredge survey.

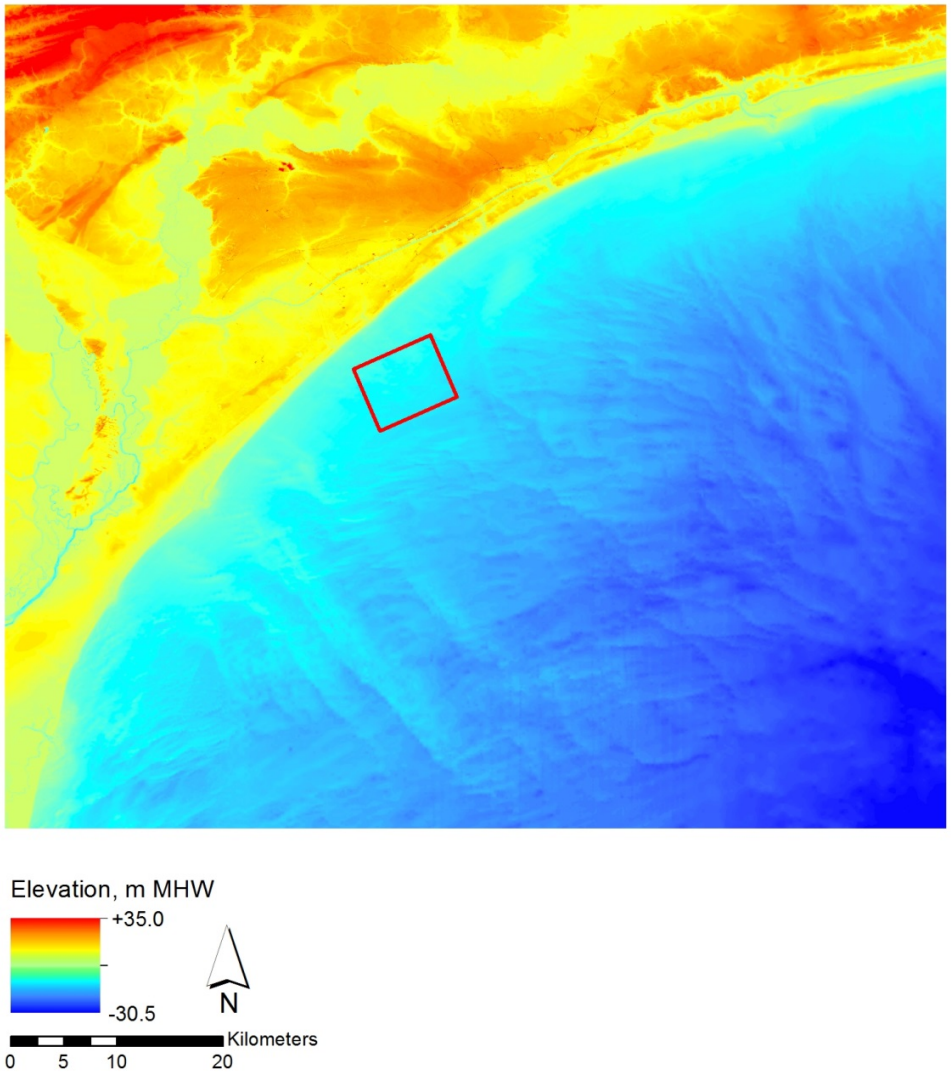

Figure IV-18. Coverage of the 1/3 arc-second grid of the Myrtle Beach, SC DEM. The red rectangle outlines the portion of the grid that was used for this project.

IV.D.1. NearCoM

To simulate wave propagation, hydrodynamics, and sediment transport, a coupled NearCoM model was setup for the month-long simulation. A schematic diagram of this coupled NearCoM model is shown in Figure IV-19. The NearCoM model was initially setup on a curvilinear grid with approximately 50 m resolution, Figure IV-20. The starting bathymetry for the NearCoM model, Figure IV-21, was interpolated to this curvilinear grid from the bathymetric survey explained above. The bathymetry in this figure is in meters NAVD88. The circulation model, SHORECIRC, is forced by the COAWST hydrodynamic boundary conditions which came from the COAWST results. These results included depth-averaged current velocity and surface elevation at 15 minute intervals. The wave model, SWAN, was forced by the JONSWAP spectra calculated from COAWST model every hour at the four NearCoM grid boundaries. Local wind forcing was not taken into account in NearCoM. However, it was taken into account in the COAWST model and therefore the impact of the wind on the waves was included. A more detailed list of the model parameters used in NearCoM are listed in Table IV-2.

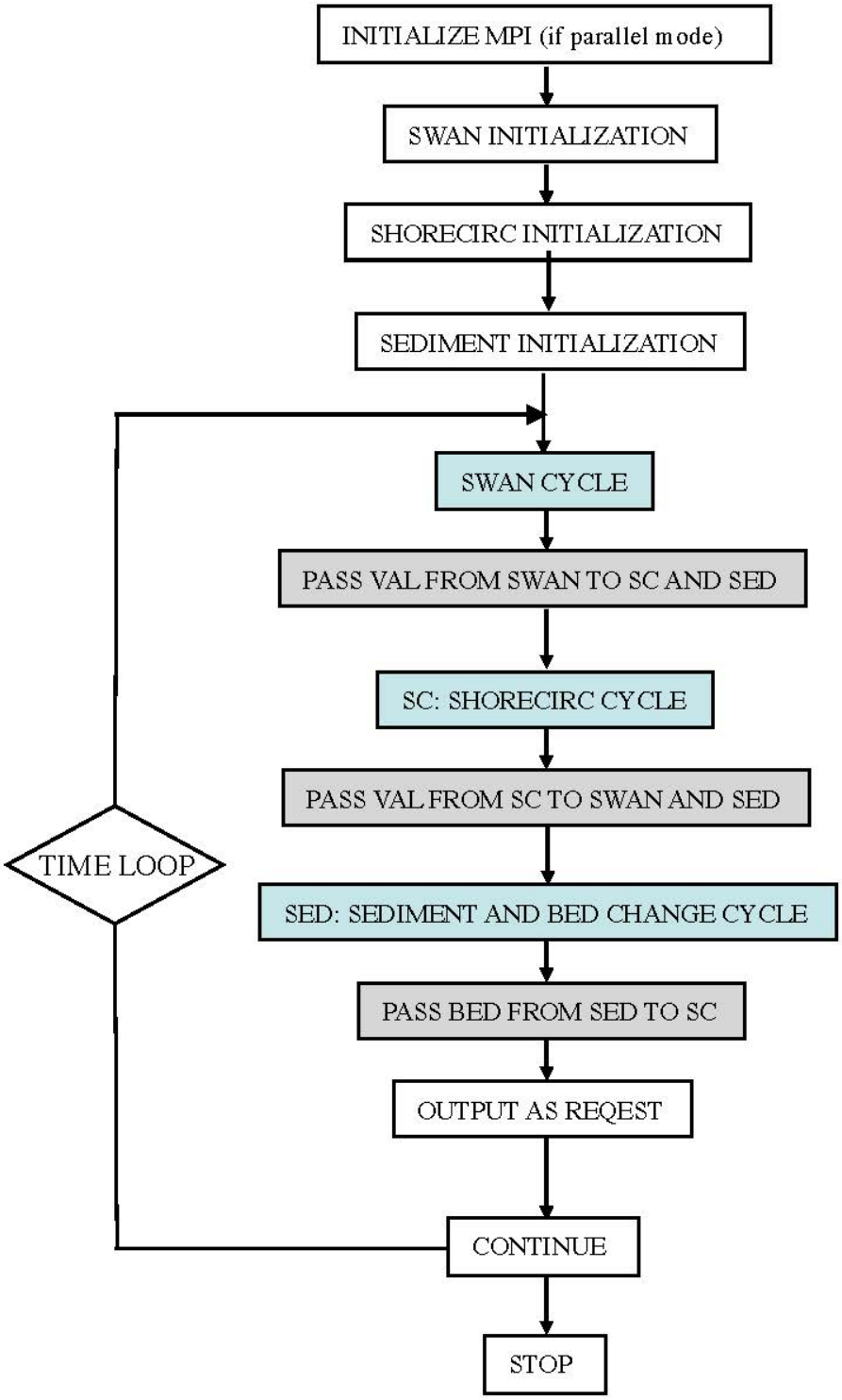

Figure IV-19. Schematic diagram of NearCoM.

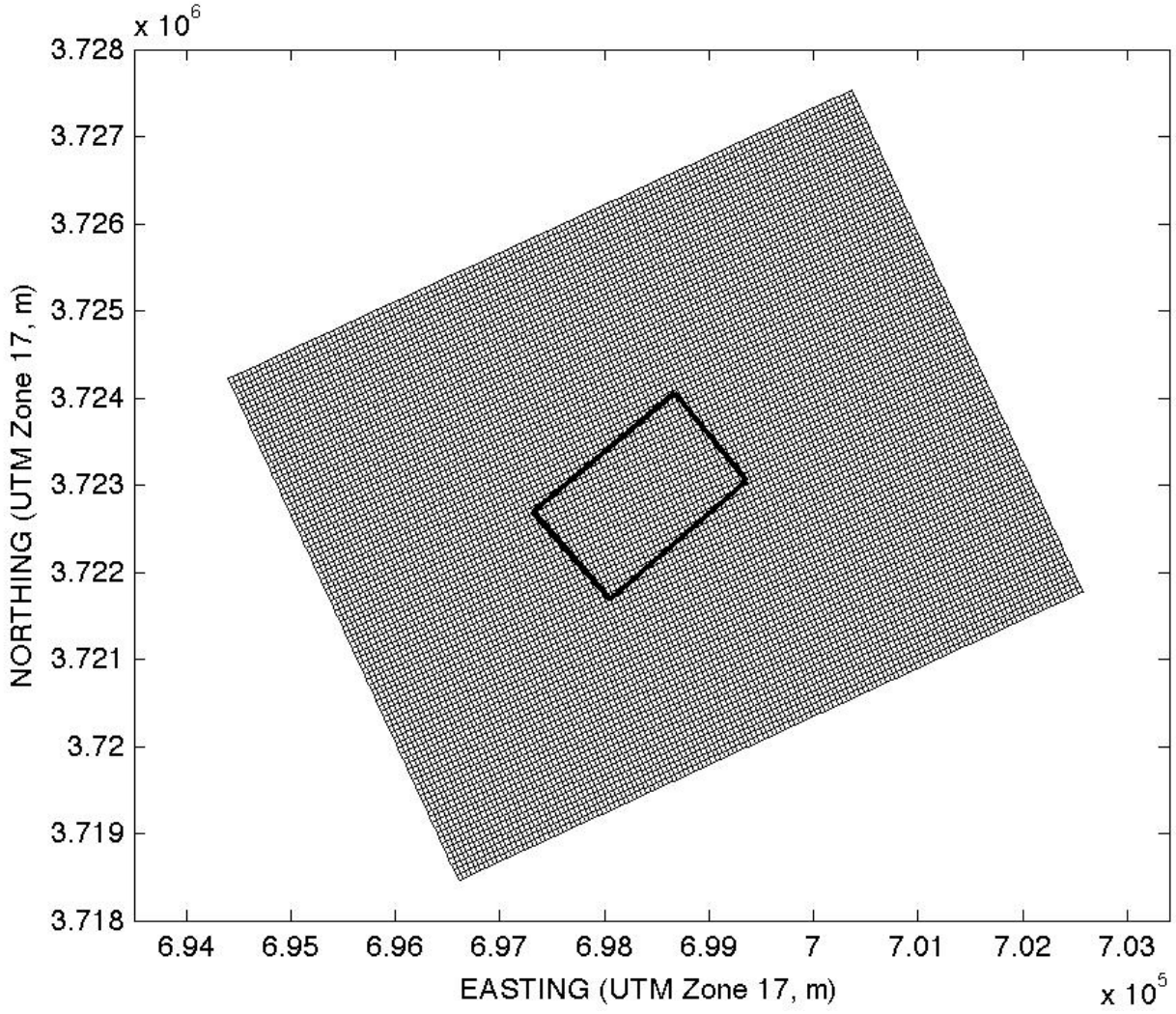

Figure IV-20. Local NearCoM curvilinear grid with approximately 50 m resolution. Horizontal coordinates are in meters in the UTM-17 system. Bed levels are in m NAVD88. The inner rectangle identifies the dredged area.

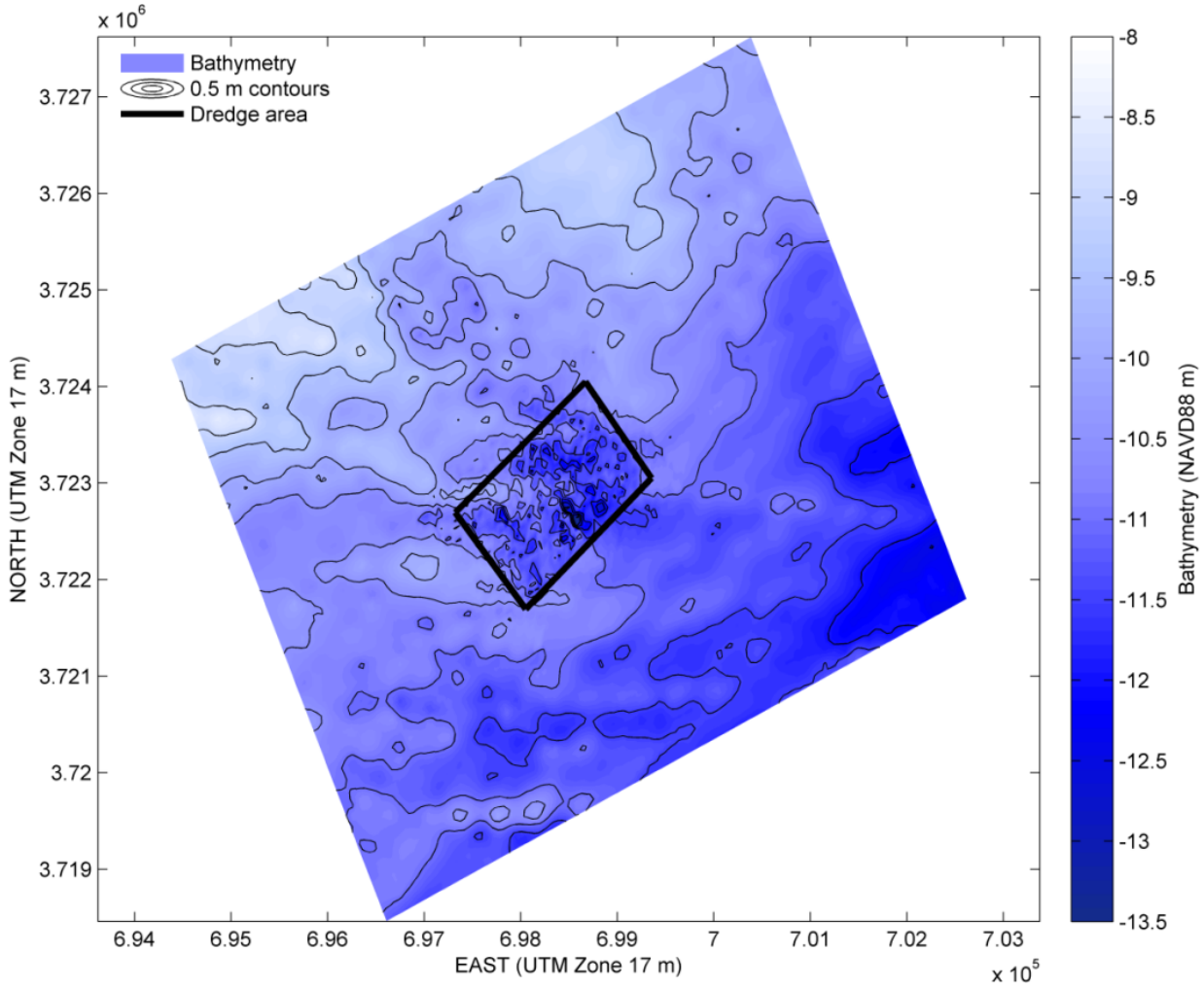

Figure IV-21. Local NearCoM model post-dredge bathymetry. Horizontal coordinates are in meters in the UTM-17 system. Bed levels are in m NAVD88. The inner rectangle identifies the dredged area.

Table IV-2. NearCoM model parameters.		
NearCoM Wave Model		
Parameter/Process	**Value**	**Comments**
Spectral formulation	JONSWAP Gamma=3.3	Spectral shape is not resolved through a finite number of frequencies; a spectral shape (JONSWAP) is assumed instead, directional spectrum D(θ) resolved with 16 bins
Time formulation	Nonstationary	
Wave-current interaction	Included	Current and surface elevation are from SHORECIRC
Wind generation of waves	Excluded	
Wave diffraction	Swan's de-coupled scheme	
Wave breaking	White-capping, Battjes and Janssen alpha=1.0 Gamma=0.73	Gamma is a parameter for depth-limited breaking. Alpha is a proportionality factor relating dissipation in the wave bore to dissipation in a hydraulic jump
Bottom friction	JONSWAP Default, C_f=0.067	Effect of bottom friction on mean wave period included
Boundary conditions	H_{mo}, T_p, PWD, JONSWAP at four open BND	Hourly at four open boundaries, the wave bulk parameters are from COAWST results
Time step	1 hour	
Instantaneous free surface elevation	From Circulation module, SHORECIRC	
Output	H_{mo}, T_p, WD	Saved at 15 minute intervals
NearCoM Hydrodynamic Model		
Time step	Adaptive based on CFL	
Density	Constant	
Horizontal eddy viscosity	3D mixing	Putrevu and Svendsen
Bed resistance	Manning =0.02	
Coriolis forcing	Included	
Wind forcing (surge)	Excluded	
Precipitation/evaporation	Excluded	
Radiation stresses	From wave module	
Sources/sinks	Excluded	
Structures	None	
Initial conditions	Zero	
Boundary conditions	Full nesting boundary conditions from COAWST	Every 15 minutes at the four open boundaries
Output	Elevation, velocity at 15 minute intervals	
NearCoM Sediment Transport/Morphology Model		
Start simulation at time step	Zero	Corresponds to February 1, 2010 00:00
Sediment properties	D_{50}=0.27mm D_{90}=0.74mm Porosity=0.40	
Hydrodynamic parameters	From circulation module	
Wave parameters	From wave module	
Bed level update	Included	
Start simulation at time step	Zero	Corresponds to February 1, 2010 00:00
Output	Bed level, sediment transport rate	Saved at 15 minute intervals

IV.D.2. MIKE21

The MIKE 21 SW spectral wave module, the MIKE 21 HD FM hydrodynamic module and the MIKE 21 ST FM non-cohesive sediment transport module of MIKE 21 were adopted for the month-long simulation of wave propagation and transformation, water levels and currents and sediment transport and morphological changes, respectively. All modules were executed in coupled fashion (i.e. simultaneously), meaning that calculated model results were shared among the three modules as required as the solution advanced in time, a schematic diagram of the modules is shown in Figure IV-22. For example, waves are propagated in MIKE 21 SW on the instantaneous water level calculated by MIKE 21 HD FM. Sediment transport rates are calculated by MIKE 21 ST FM using as input the total water depth and current speed and direction calculated by MIKE 21 HD FM, together with the wave parameters (height, period and direction) calculated by MIKE 21 SW.

The model mesh for the local scale MIKE 21 model is shown in Figure IV-23, the open boundaries of the mesh are highlighted in color. Most of MIKE 21's mesh is quadrangular elements of approximately 50 m × 50 m in size. However, coarser triangular elements were used to transition towards lower resolution along the mesh boundaries. The starting bathymetry for this model is shown in Figure IV-24. Bed levels in the figure are in meters (relative to the NAVD88 vertical datum) and were interpolated to the mesh from the bathymetric dataset explained above. In both figures, the inner rectangle identifies the extent of the dredged area. The model parameters for the three MIKE 21 modules have been listed in Table IV-3.

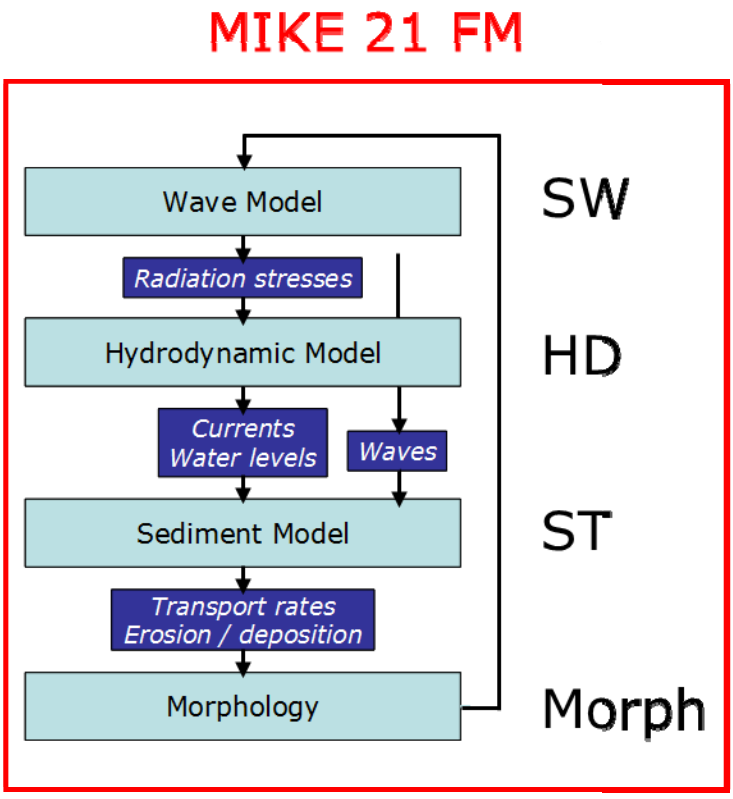

Figure IV-22. Schematic diagram of MIKE 21.

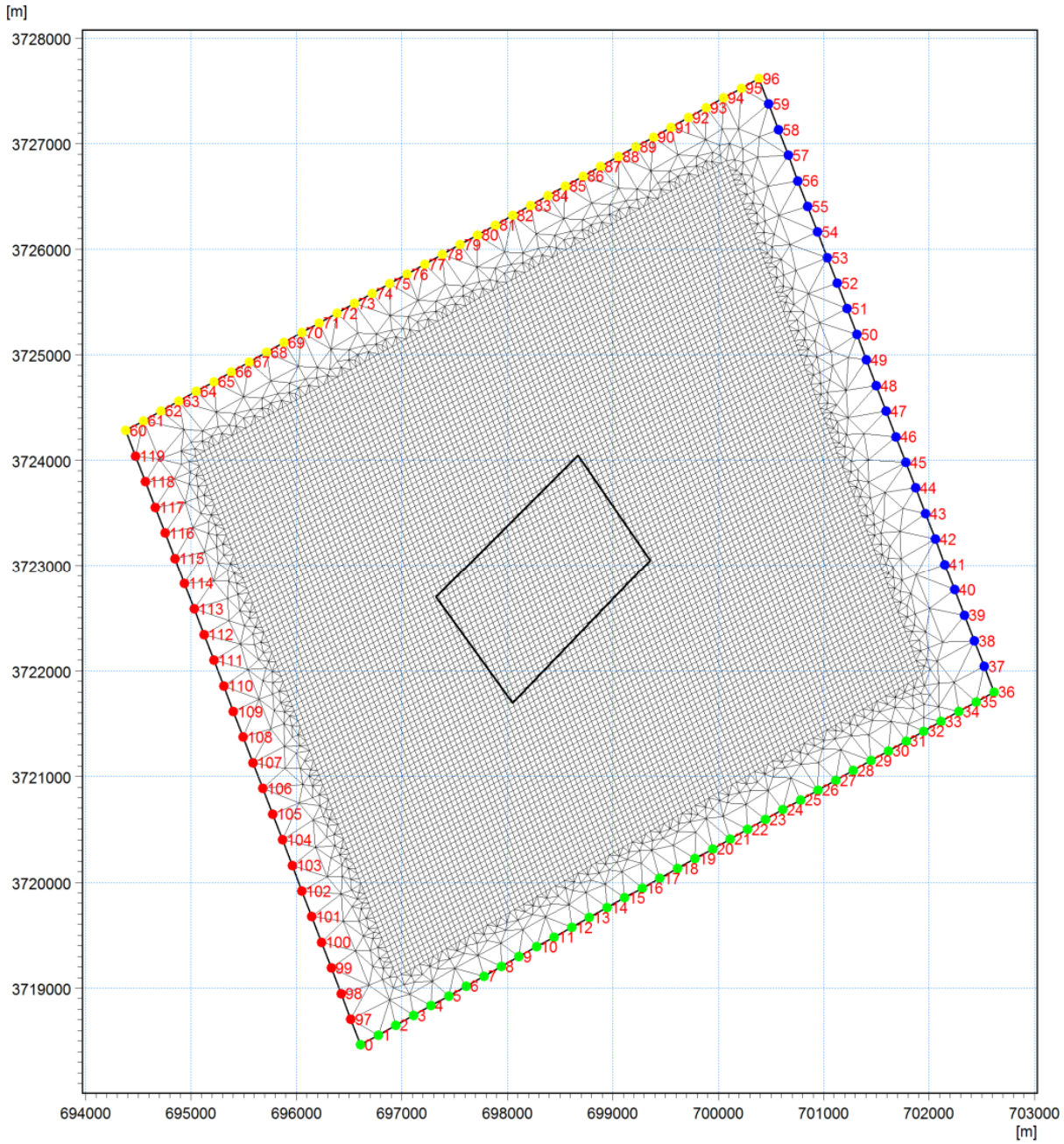

Figure IV-23. Local MIKE 21 model mesh. Horizontal coordinates are in meters in the UTM-17 system. Bed levels are in m NAVD88. The inner rectangle identifies the dredged area.

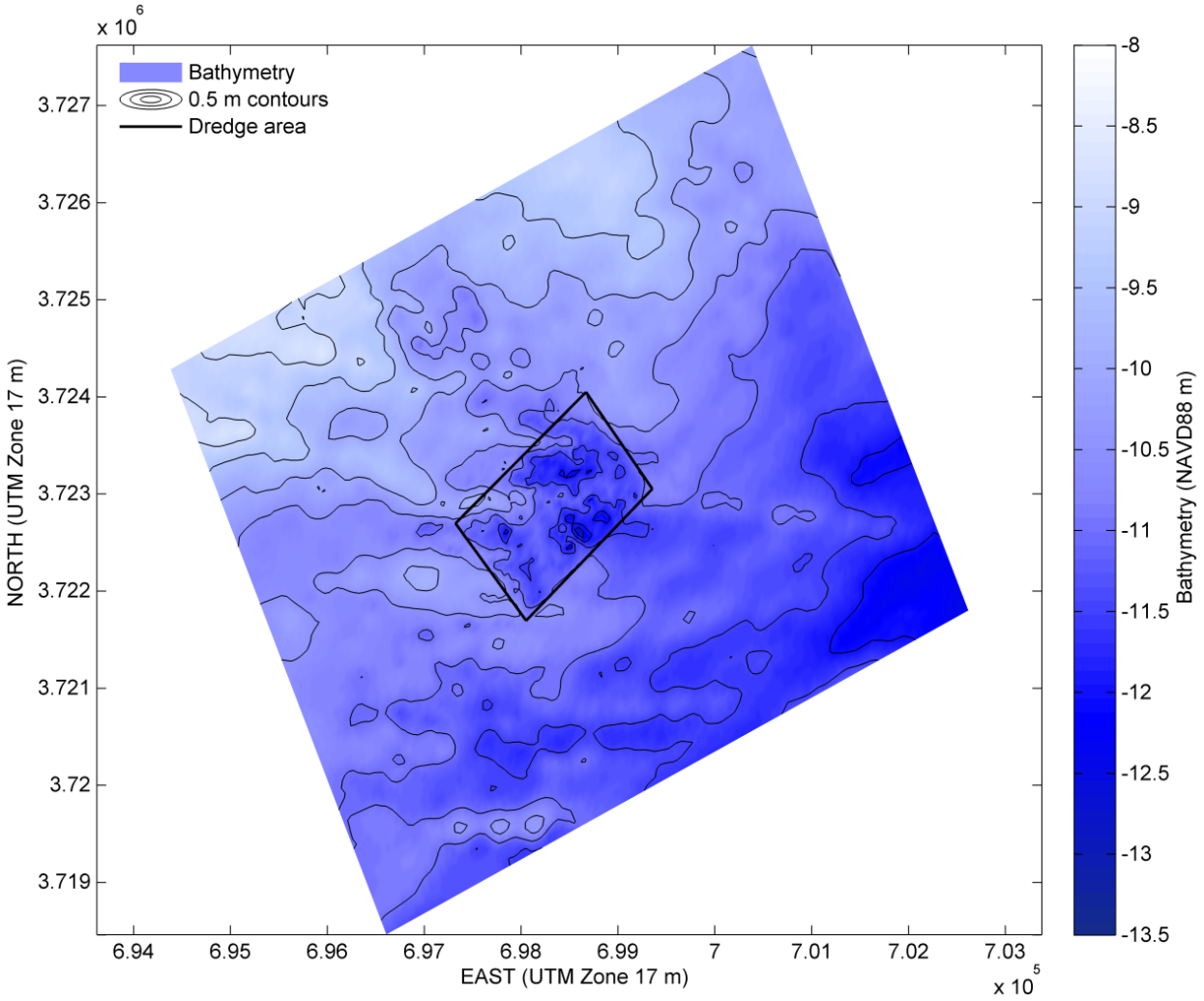

Figure IV-24. Local MIKE 21 model post-dredge bathymetry. Horizontal coordinates are in meters in the UTM-17 system. Bed levels are in m NAVD88. The inner rectangle identifies the dredged area.

Table IV-3. MIKE 21 model parameters.		
MIKE 21 SW FM		
Parameter/Process	**Value**	**Comments**
Spectral formulation	Directionally decoupled parametric	A spectral shape (JONSWAP) is assumed, directional spectrum resolved with 16 bins
Time formulation	Quasi stationary	Wave field at a given time step is independent of conditions at previous steps
Wave-current interaction	Excluded	
Wind generation of waves	Excluded	
Wave diffraction	Excluded	
Wave breaking	Battjes & Janssen with $\gamma_1 = 4$ $\gamma_2 = 0.73$ $\alpha = 1$	γ_1 and γ_2 are breaking parameters; α is a proportionality factor relating dissipation in the wave bore to dissipation in a hydraulic jump; effect of breaking on wave period excluded
Bottom friction	Constant, $k_N = 0.004$ m	Nikuradze's roughness, effect of bottom friction on mean wave period included
Boundary conditions	H_{mo}, T_p, PWD n (in $\cos^n$ directional distribution), specified hourly	Wave parameters from COWAST results at all four open boundaries; n = 12 (assumed), parameters vary in time and along boundaries
Time step	1 hour	Wave field re-calculated every time step
Instantaneous free surface elevation	From HD simulation	All three modules run in coupled mode
Output	H_{mo}, T_p, MWD, PWD saved at 1 hr. intervals	Output written to 2D maps and as time series at selected extraction points
MIKE 21 HD FM		
Time step	Adaptive based on CFL	Max. = 1 hour
Density	Barotropic (constant)	
Horizontal eddy viscosity	$\varepsilon = 1$ m^2/s	Constant in space and time
Bed resistance	Constant in space and time; $M = 50$ m$^{1/3}$/s	Manning number M is the inverse of Manning's coefficient n
Coriolis forcing	Included	Spatially varying throughout domain as function
Wind forcing (surge)	Excluded	
Precipitation/evaporation	Excluded	
Radiation stresses	From SW simulation	All three modules run in coupled mode
Sources/sinks	Excluded	
Structures	None	
Initial conditions	Initial water level	Level from COWAST results
Boundary conditions	Water level and velocity components	Parameters specified every 15 mins. from COWAST results, vary in time and space
Output	Surface elevation and velocity components	Saved hourly, output written to 2D maps and as time series at selected extraction points
MIKE 21 ST FM		
Model definition	Waves and current	Pure current is another option
Start simulation at time step	Zero	Corresponds to February 1, 2010 00:00
Sediment properties	$d_{50} = 0.27$ mm; $d_{16} = 0.17$ mm; $d_{84} = 0.54$ mm $d_{90} = 0.74$ mm; $\sigma_g = (d_{84}/d_{16})^{0.5} = 1.78$ porosity = 0.40	
Hydrodynamic parameters	From HD simulation	
Wave parameters	From SW simulation	
Bed level update	Included	
Output	Total load transport, rate of bed level change, bed level change and bed level	Save at hourly intervals, output written to 2D maps and as time series at selected extraction points

IV.D.3. CMS

CMS Flow and CMS Wave were coupled for the month-long simulation to simultaneously calculate the hydrodynamics, wave propagation and transformation, sediment transport, and morphological changes. A schematic diagram of the coupled CMS model is shown in Figure IV-25. Similar to MIKE 21 the waves are propagated in CMS Wave on the bed and water levels and tidal currents calculated by CMS Flow and then the wave and hydrodynamic data is used to calculate the sediment transport and morphological change which is then used to calculate the next time step for the hydrodynamic and wave parameters.

The Cartesian grid for the coupled CMS model had a grid spacing of 50 m and is shown in Figure IV-26, the open boundaries of the grid are highlighted in red. The starting bathymetry for this model, Figure IV-27, was interpolated to this grid from the bathymetric dataset explained above and shown in Figure IV-24. The bathymetry in this figure is in meters NAVD88. The model parameters for the coupled CMS model have been listed in Table IV-4.

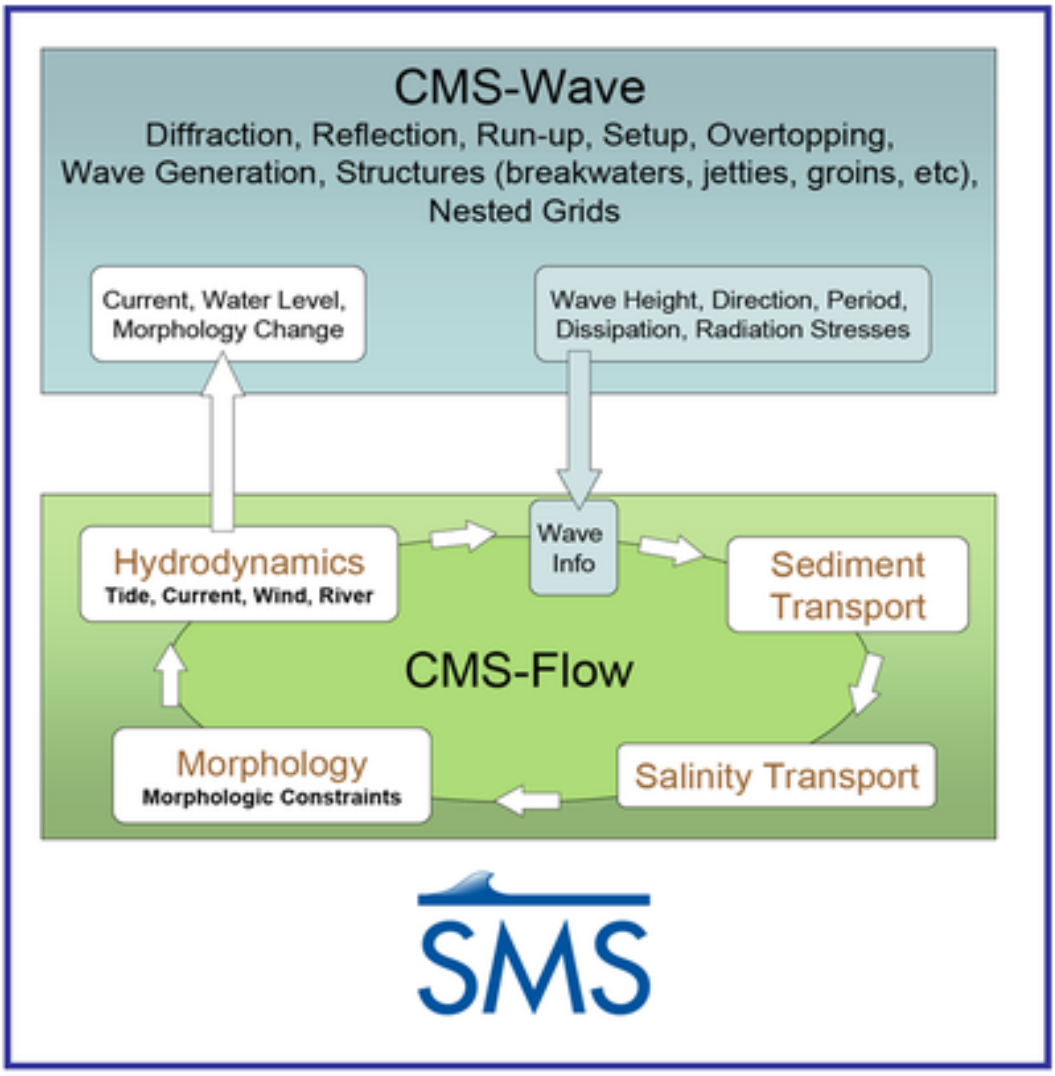

Figure IV-25. Schematic diagram of CMS. (*http://cirpwiki.info/wiki/CMS*)

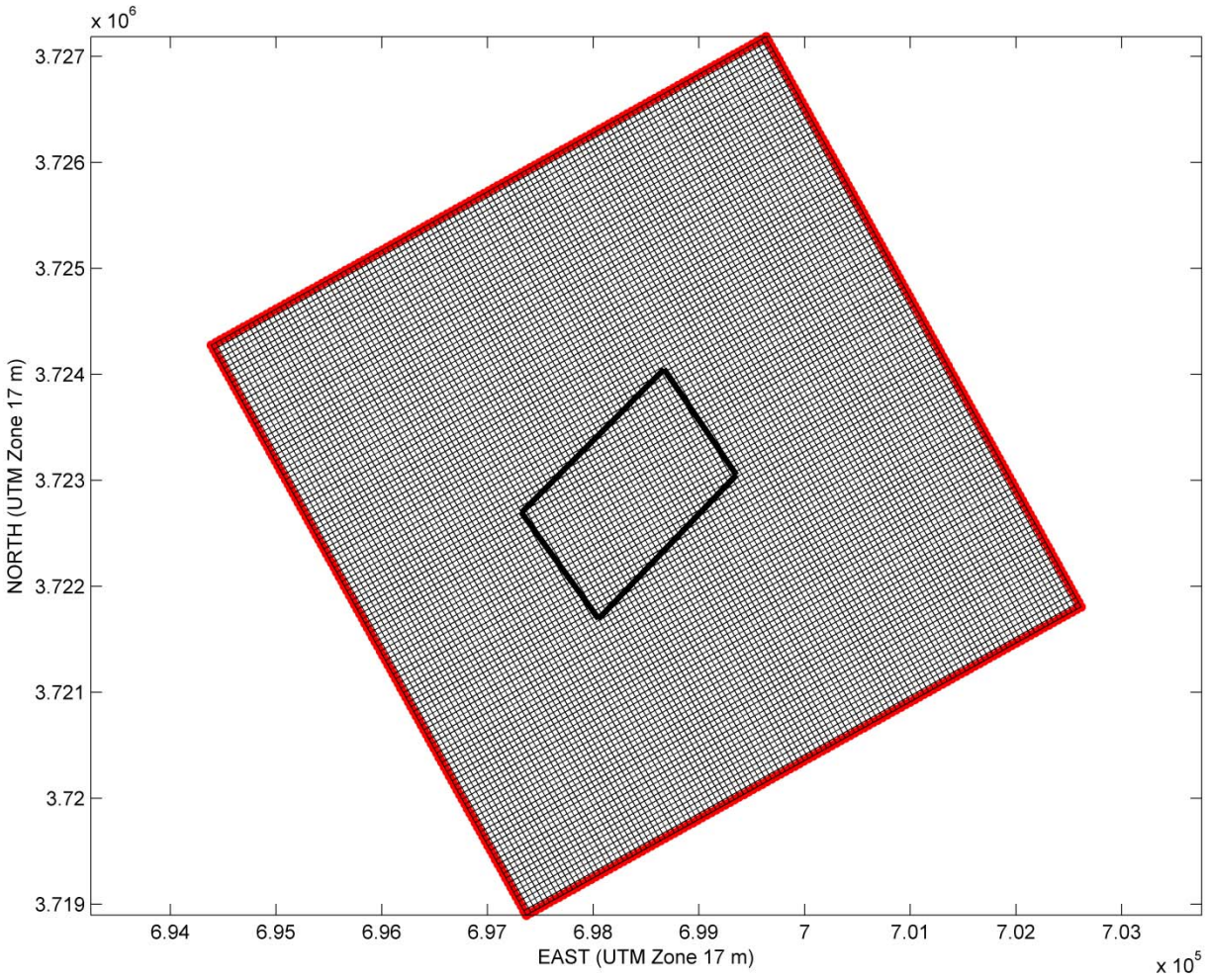

Figure IV-26. Local CMS 50 m spacing model grid. Horizontal coordinates are in meters in the UTM-17 system. Bed levels are in m NAVD88. The inner rectangle identifies the dredged area.

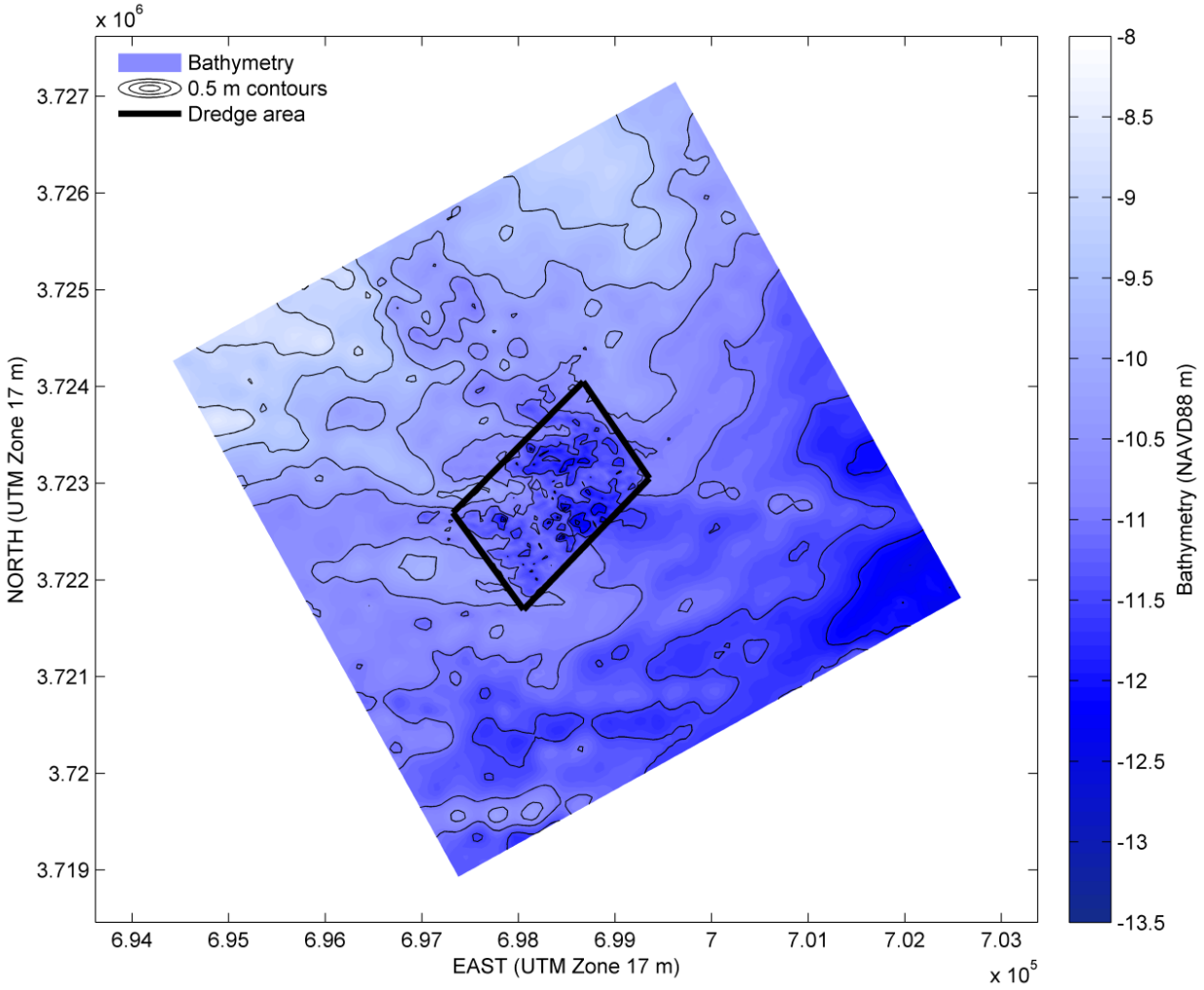

Figure IV-27. Local CMS model post-dredge bathymetry. Horizontal coordinates are in meters in the UTM-17 system. Bed levels are in m NAVD88. The inner rectangle identifies the dredged area.

Table IV-4. CMS model parameters		
CMS Wave		
Parameter/Process	**Value**	**Comments**
Spectral formulation	JONSWAP	Gamma=3.3, Directional Spreading distribution: cosine power
Time formulation	Quasi stationary	Wave field is independent of conditions at previous steps
Wave-current interaction	Included	
Wind generation of waves	Excluded	
Wave diffraction	Included	
Wave breaking	Battjes & Janssen	Energy dissipation
Bottom friction	Manning friction coefficient = 0.02	
Boundary conditions	H_{mo}, T_p, PWD, gamma = 3.3, nn = 4, and depth = 11.5625 m specified hourly at the southern open boundary	Wave parameters varied hourly from an average of the southern boundary COWAST model results; gamma is the spectral peak dispersion factor, nn is the peak dispersion factor, and the depth is the average depth of the southern boundary
Time step	1 hour	
Instantaneous free surface elevation	Average of the southern grid boundary from COAWST results	
Output	H_{mo}, T_p, and MWD saved at 1 hour intervals	Output written to as time series at selected extraction points
CMS Flow		
Time step	15 minutes	
Density	Barotropic (constant)	
Horizontal eddy viscosity	Varied, using default parameters	
Bed resistance	Manning's coefficient = 0.02	
Coriolis forcing	Included	Constant value
Wind forcing (surge)	Excluded	
Precipitation/evaporation	Excluded	
Radiation stresses	From CMS-Wave	
Sources/sinks	Excluded	
Structures	None	
Sediment formulation	Non-equilibrium, Advection-diffusion	
Transport formulation	Lund-Cirp 2006	Also tested Van Rijn (1998)
Sediment properties	d_{50} = 0.27 mm, porosity = 0.40	
Initial conditions	Initial water level from COWAST results	
Boundary conditions	Water level and velocity components specified every 15-min at all four open boundaries	Hydrodynamic parameters taken from COWAST model result s and vary in time and along the boundaries
Output	Water surface elevation, velocity components and speed, wave height, period and direction, components of total sediment transport, and morphological change saved at 1 hr. intervals	Output written as time series at selected extraction points and grid nodes

IV.E. MONTH-LONG SIMULATIONS - INITIAL RESULTS

Each of the three models were run for the month-long simulation under the parameters listed in Tables IV-5, IV-6, and IV-7, respectively. The computational time to complete these month-long simulations was 12 hours using 32 processors for NearCoM, 10 hours using an 8 core processor PC for MIKE 21, and 2.5 hours using an 8 core processor PC for CMS. Before comparing the models' predicted sediment transport and morphological change the hydrodynamics and wave parameters were inter-model compared at five points (Figure IV-28) to ensure that the sediment transport forcing was similar between the models. The three hydrodynamic parameters, current magnitude and direction, and water surface elevation, were similar when compared at the five points, Figures IV-29, IV-30, and IV-31, respectively. Wave height, direction, and period were compared at the five points to show that the three models had similar wave parameters, Figure IV-32, IV-33, and IV-34, respectively. NearCoM's peak current magnitudes (Figure IV-29) were slightly higher than other two models. However, NearCoM's current magnitudes still showed similar values and trends as the COAWST results, refer to the mean root mean square error (RMSE) values in Table IV-5. Additionally, Table IV-5 includes the mean RMSE for significant wave height and water surface elevation for the five comparison points for the three morphological models. As displayed by Table IV-5 the error for all three parameters and all three models are negligible.

Table IV-5. Mean root mean squared error for the five comparison points for each model for significant wave height, current speed, and water surface elevation.

Model	**Mean Root Mean Squared Error Compared With COAWST Results**		
	Significant Wave Height (m)	**Current Speed (m/s)**	**Water Surface Elevation (NAVD m)**
NEARCOM	0.17	0.02	0.03
MIKE 21	0.08	0.01	0.00
CMS	0.08	0.01	0.09

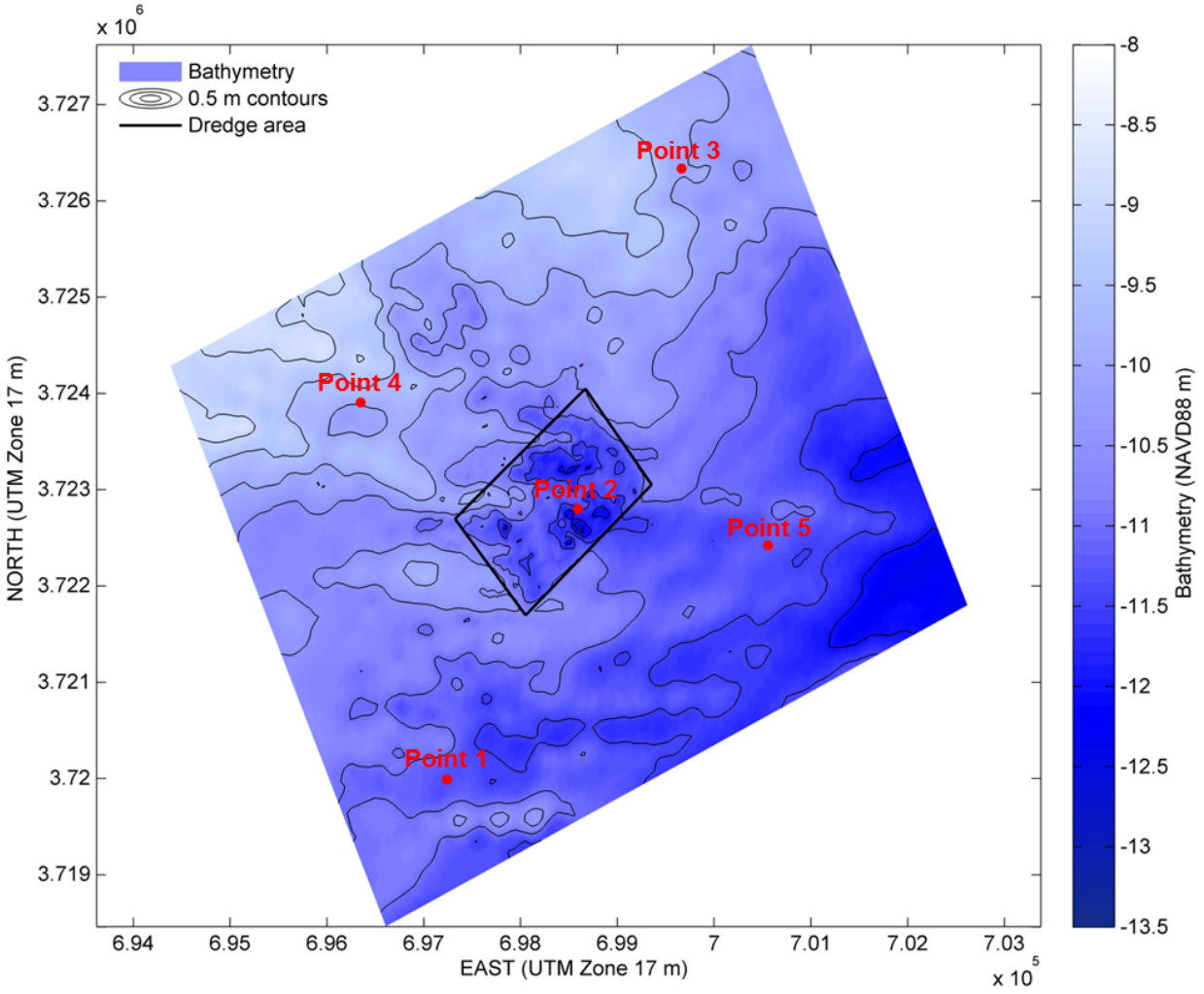

Figure IV-28. Intra-model comparison point locations. The point locations are shown on the MIKE21 post-dredge bathymetry in meters NAVD88. The inner rectangle identifies the dredged area.

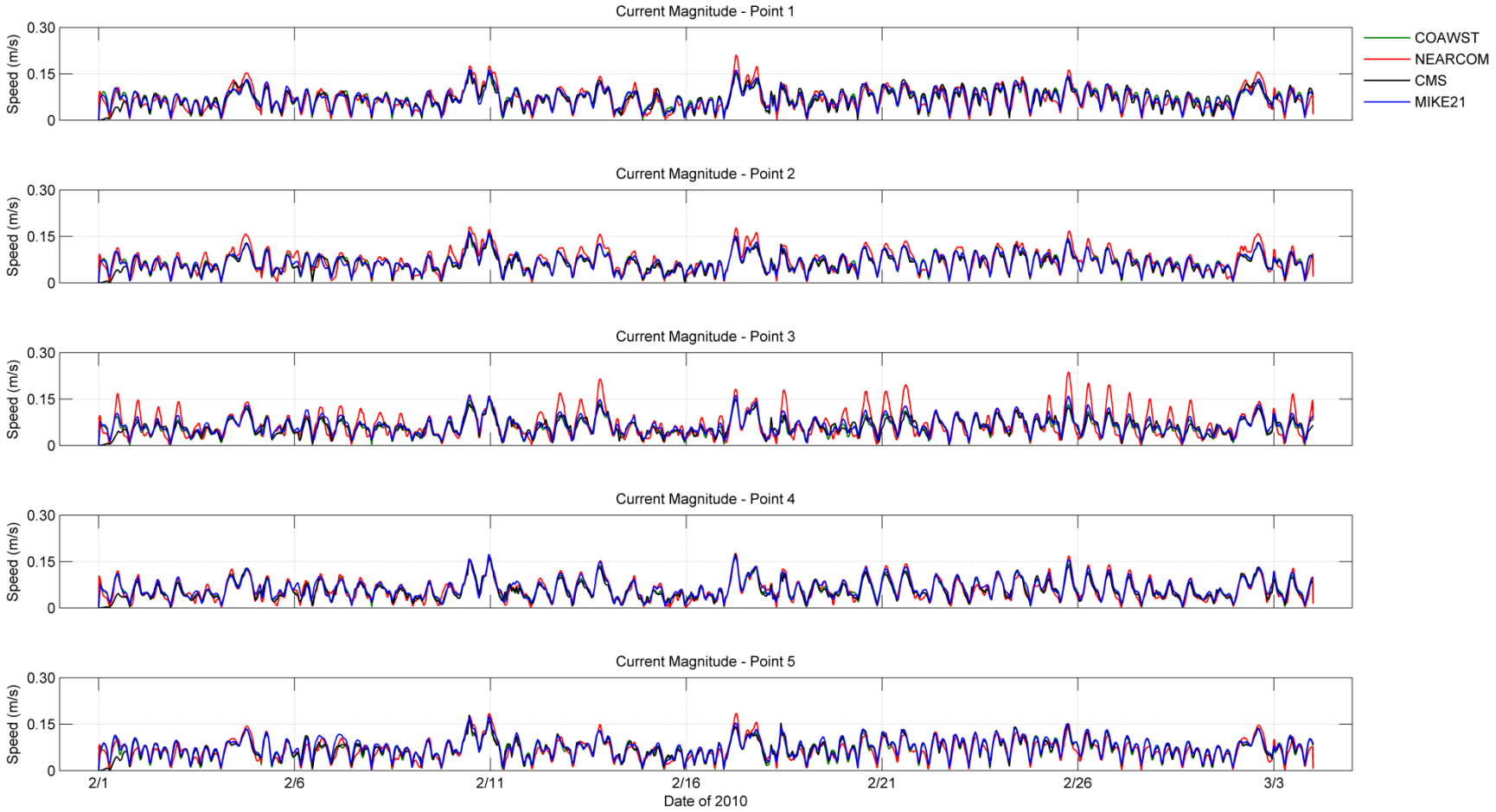

Figure IV-29. Current magnitude (m/s) for the four models at the five comparison points.

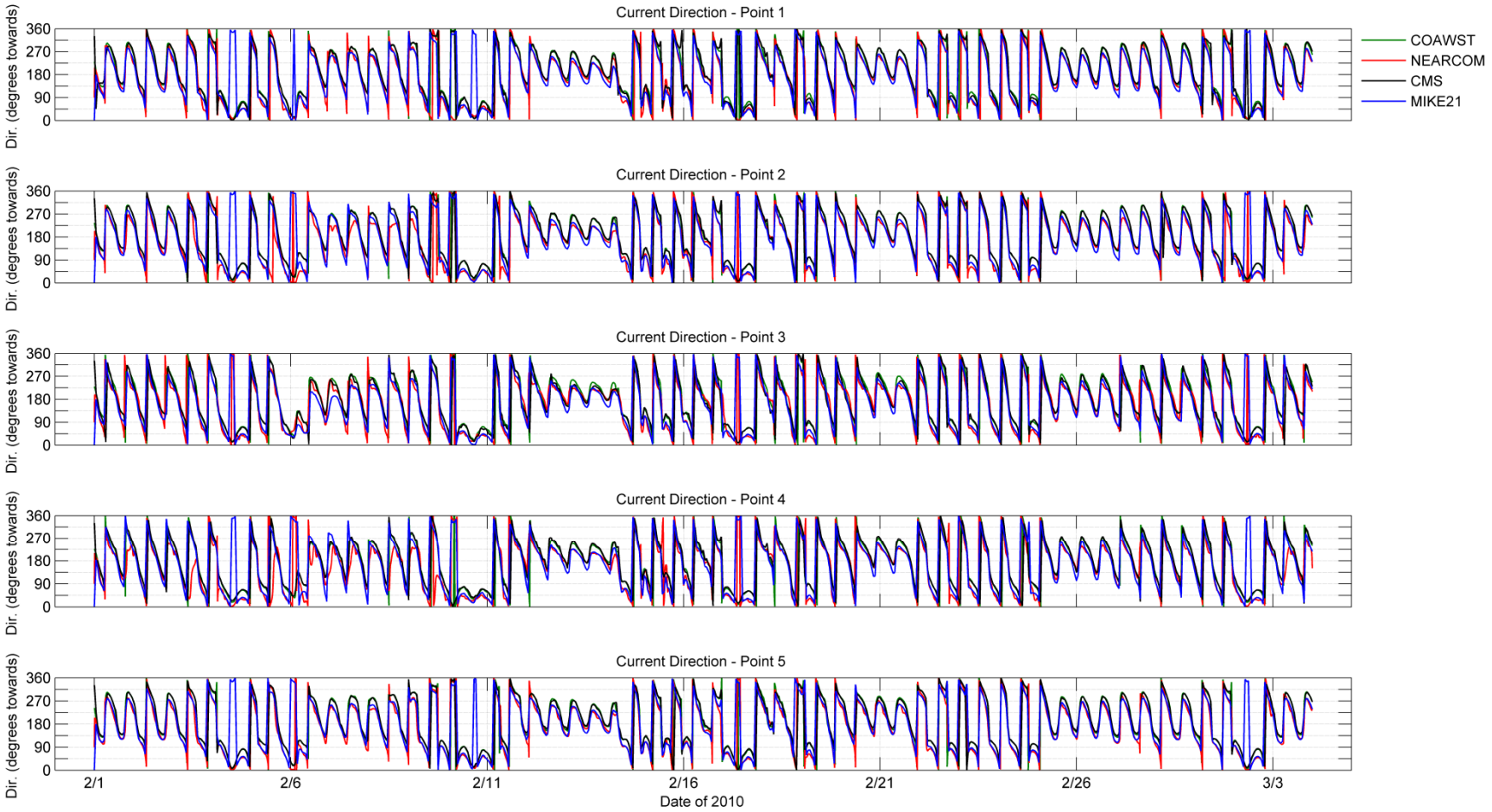

Figure IV-30. Current direction (oceanographic convention) for the four models at the five comparison points.

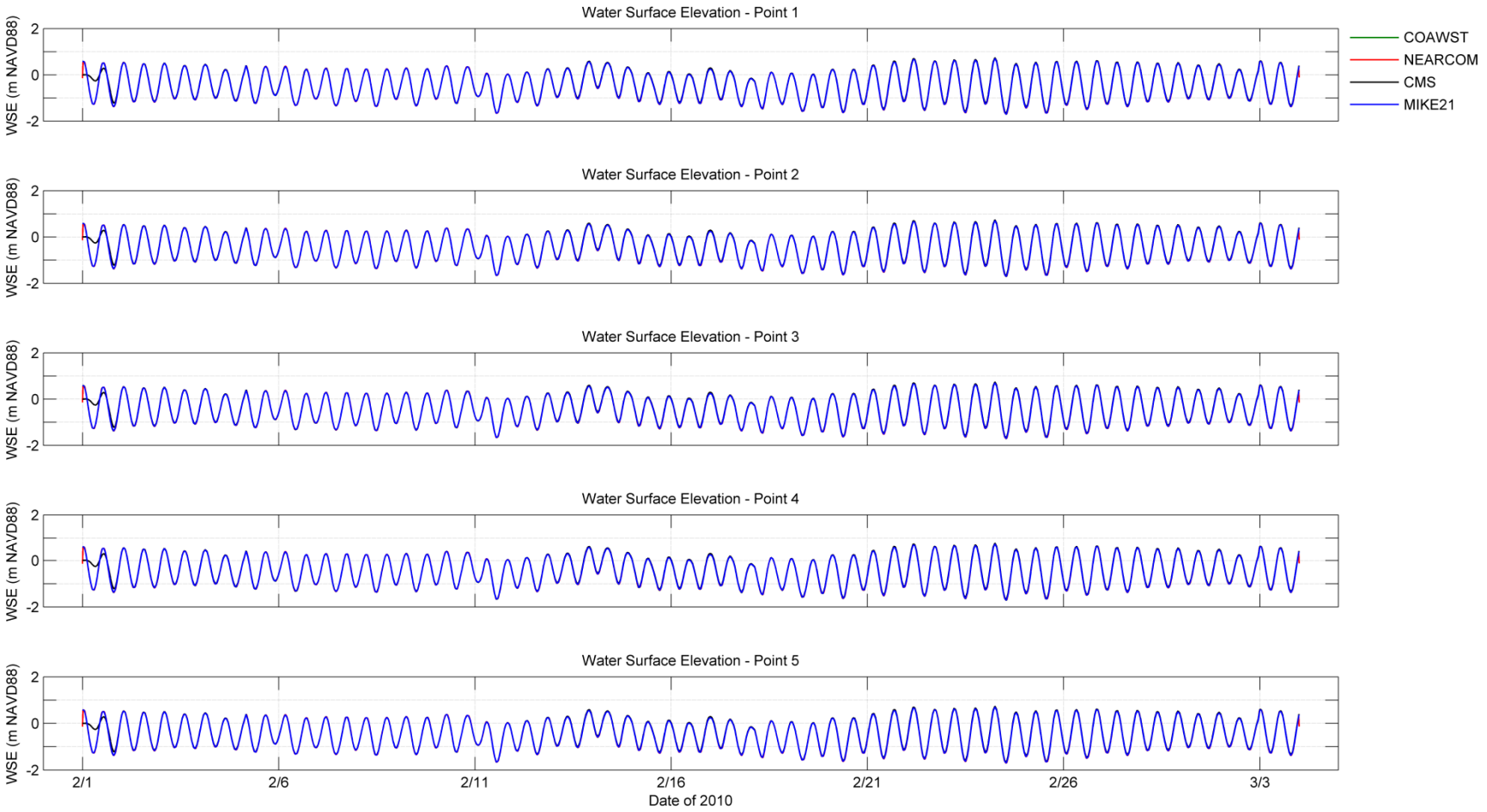

Figure IV-31. Water surface elevation (m NAVD88) for the four models at the five comparison points.

Figure IV-32. Significant wave height (m) for the four models at the five comparison points.

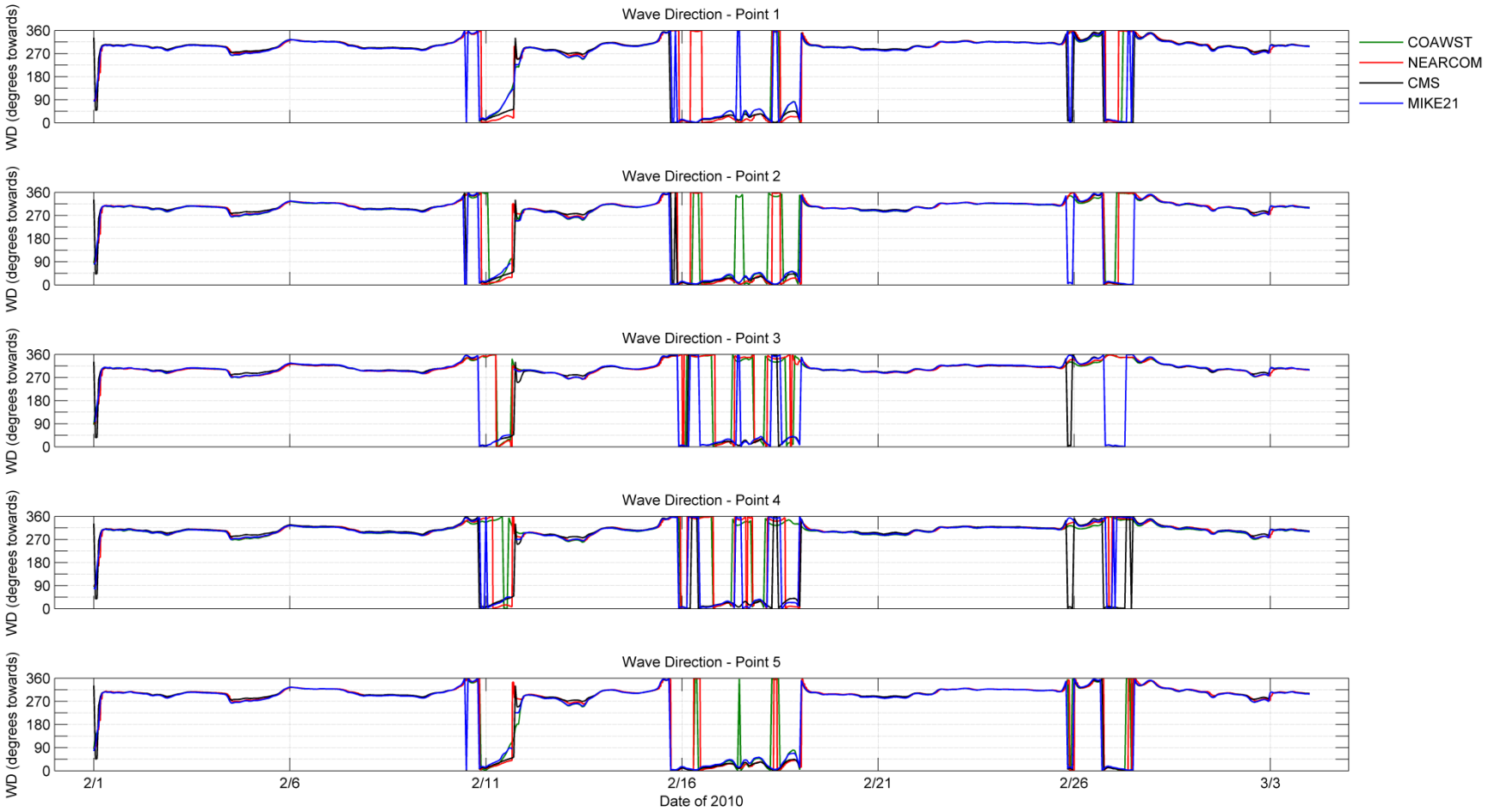

Figure IV-33. Wave direction (oceanographic convention) for the four models at the five comparison points.

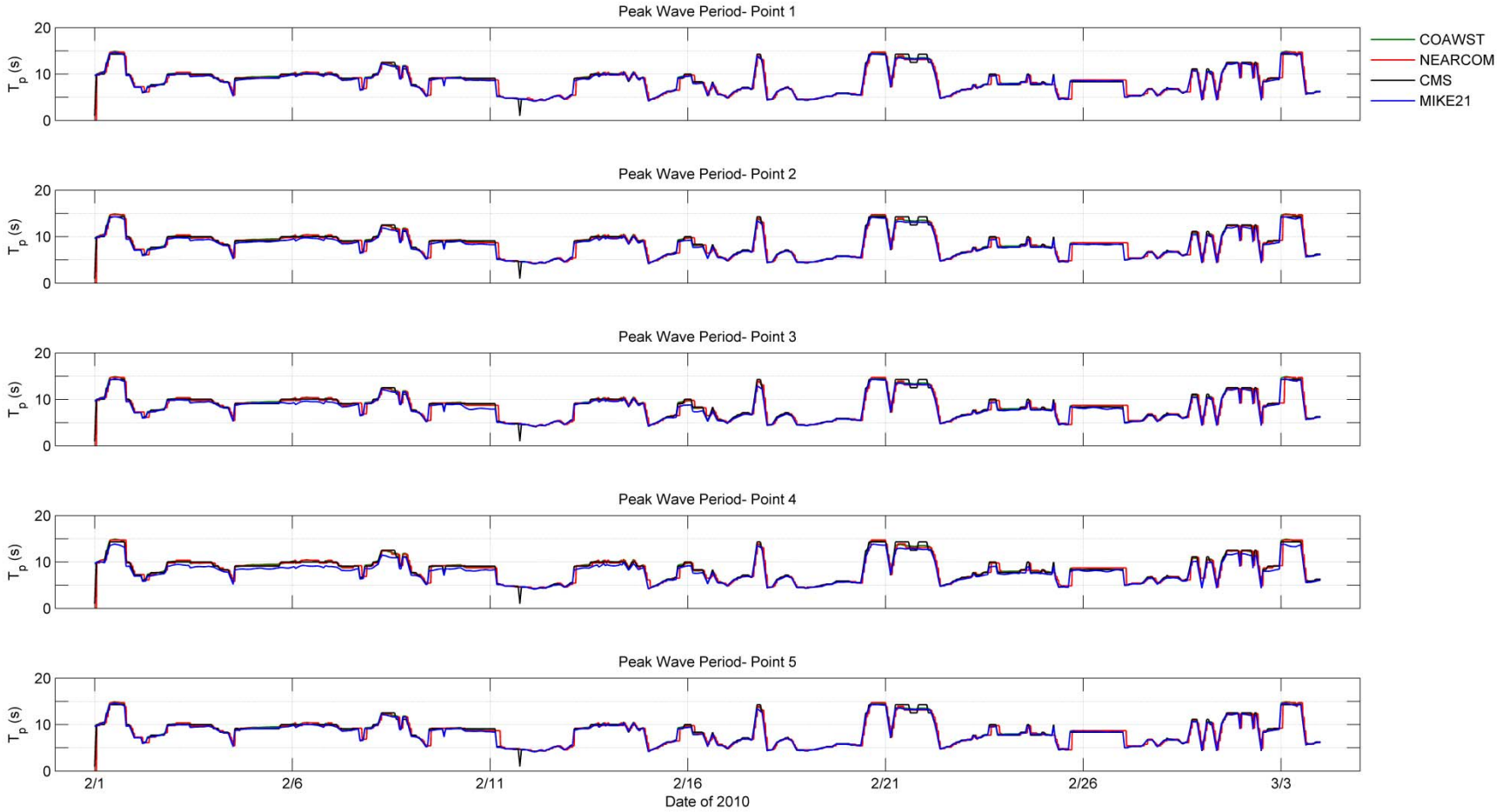

Figure IV-34. Peak wave period (s) for the four models at the five comparison points.

IV.F. INITIAL MODELED MORPHOLOGICAL CHANGE

From the month-long simulations, the initial morphological change, Figure IV-35, was determined for each model and its respective sediment transport formulations. This morphological change figure shows the results in the same scale from NearCoM using the Soulsby-Van Rijn 1997 sediment transport formulation; MIKE 21 using the 2D and Q3D approaches; and CMS using the Lund-CIRP and Van Rijn sediment transport formulations. As shown there is significant variability in the models' initial change results. The net volume changes and the max erosional and accretional values within the dredge area for the three models and their respective sediment transport formulations are listed in Table IV-6. The change results from NearCoM and CMS using the Lund-CIRP formulation have similar magnitude. In a similar fashion, the change results from MIKE 21 using both the 2D and Q3D approach and CMS using the Van Rijn formulation generally have the same magnitude of change. NearCoM and MIKE 21 using the Q3D approach show overall accretion, while CMS using both formulations and MIKE 21 using the 2D approach show net erosion.

Table IV-6. Initial net volume changes and max erosion and accretion values within the dredge area for each numerical model. A negative value indicates erosion.

Model	Net Erosion (m^3)	Net Deposition (m^3)	Net Total (m^3)	Morphological Change (m)	
				Max Erosion	Max Accretion
NearCoM Soulsby-Van Rijn 1997	-12,556	13497	941	-0.045	0.046
MIKE 21 Q3D	-1,783	1349	-434	-0.0027	0.0031
MIKE 21 2D	-549	567	18	-0.0009	0.0021
CMS Lund-CIRP 2006	-24,142	2394	-21,748	-0.016	0.023
CMS Van Rijn 1998	-1,206	934	-272	-0.016	0.0038

To better understand the patterns of morphological change from each model the bed change was plotted individually in Figures IV-36 to IV-42 with varying scales depending on the model and sediment transport formulation. Figure IV-36 displays the initial morphological change for NearCoM using the Soulsby-Van Rijn 1997 sediment transport formula. Overall, the NearCoM results are showing an alternating pattern of accretion and erosion with the orientation of the bed forms being NNW/SSE. In addition when comparing the eastern and western halves of the dredge area it appears that there is slightly more erosion occurring in the eastern half and slightly more accretion in the western half. Figure IV-37 shows a time series at point two of the COAWST's results of the significant wave height and current magnitude, and NearCoM's results of sediment transport magnitude using the Soulsby-Van Rijn 1997 formulation. The sediment transport magnitude with this formulation appears to be dominated by the wave energy. The

model predicts sediment transport magnitudes close to zero when the wave energy is low, but the magnitudes increase given an increase in wave energy. In addition, these wave induced peaks in sediment transport have a tidal influence by the short time scale peaks and troughs.

The initial MIKE 21 morphological change results using the Q3D and 2D approach are shown in Figure IV-38 and IV-39, respectively. These two figures are on the same scale; however, the scale differs from the previous figures in this section. The morphological change with the Q3D approach shows a lateral elongated E/W pattern in the bed form orientation. The bed forms with the 2D approach displays a NNW/SSE orientation, with a few oriented ENE/WSW. The magnitude of the morphological change from the Q3D approach is larger than the modeled change from the 2D approach.

To further compare the two approaches Figure IV-40 shows a time series at point two of the significant wave height, wave direction, current magnitude, and current direction, and MIKE 21's results of sediment transport magnitude for both approaches. As previously stated, the Q3D approach includes a wave-related transport component and calculates the net sediment transport rates both in the direction of wave propagation and in the direction of the mean current. The 2D approach only includes the effect of the wave boundary layer to enhance the bed shear stresses and the turbulence close to the seabed; still it calculates the transport in the mean current direction. As a result, from Figure IV-40 it appears that most of the time the wave-related transport component in the Q3D approach increases the total transport magnitude as calculated by the 2D model. However, there are time periods when the 2D model predicts transport magnitudes close to zero (for example, February 19 to 21, 2010) while the Q3D model predicts very large transport rates. This situation is a result of the wave related sediment transport component under weak current conditions being of similar order of magnitude as the current related sediment transport component under small wave conditions and/or combined waves and current. Since the direction of the wave related transport component under high waves and weak current is significantly different from the direction of the current related transport, use of the Q3D approach significantly changes the morphological response calculated by the MIKE 21 model.

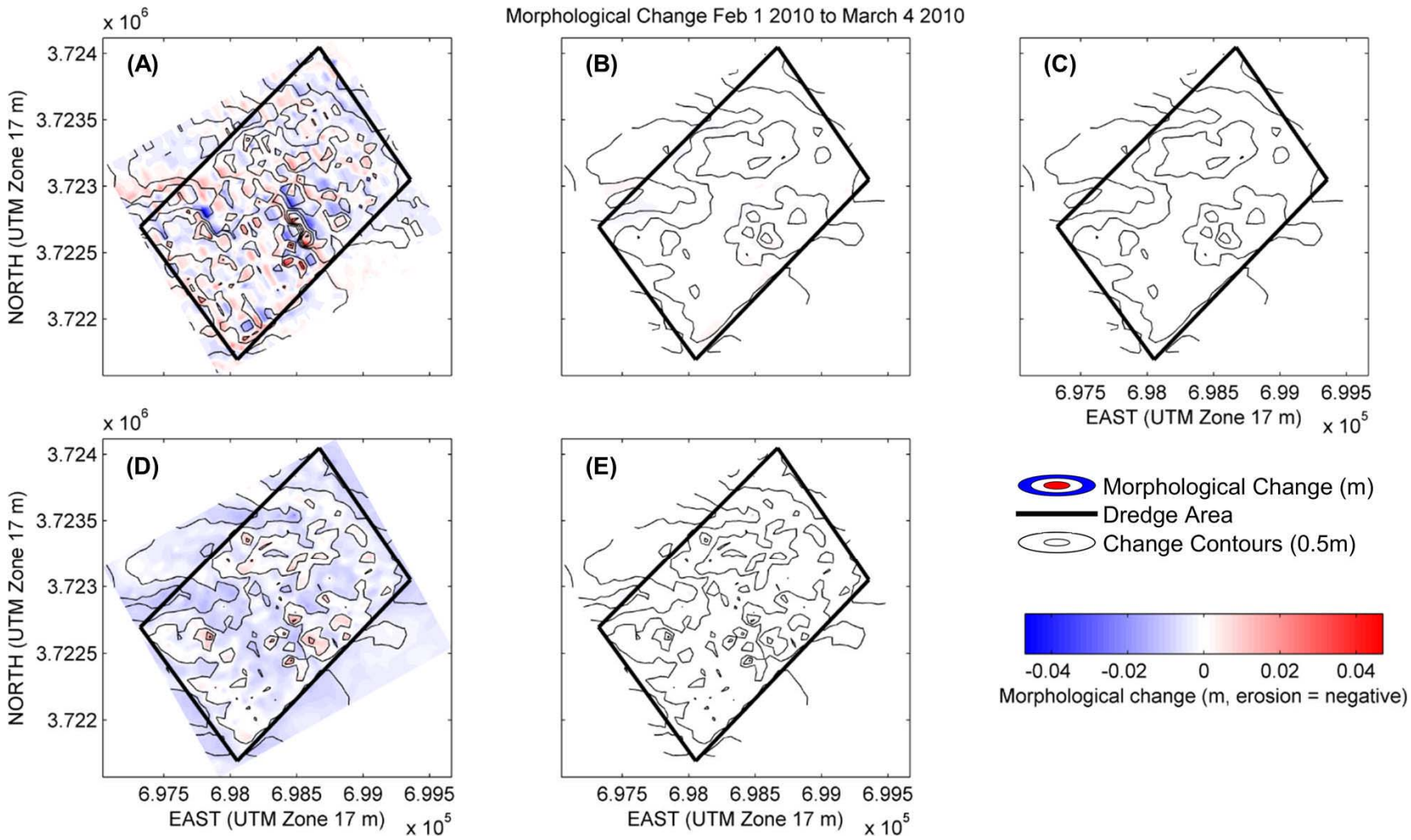

Figure IV-35. Initial morphological change for **(A)** NearCoM using the Soulsby-Van Rijn 1997 formulation **(B)** MIKE21 using the Q3D approach **(C)** MIKE21 using the 2D approach **(D)** CMS using the Lund-CIRP 1997 formula **(E)** CMS using the Van Rijn 1998 formula.

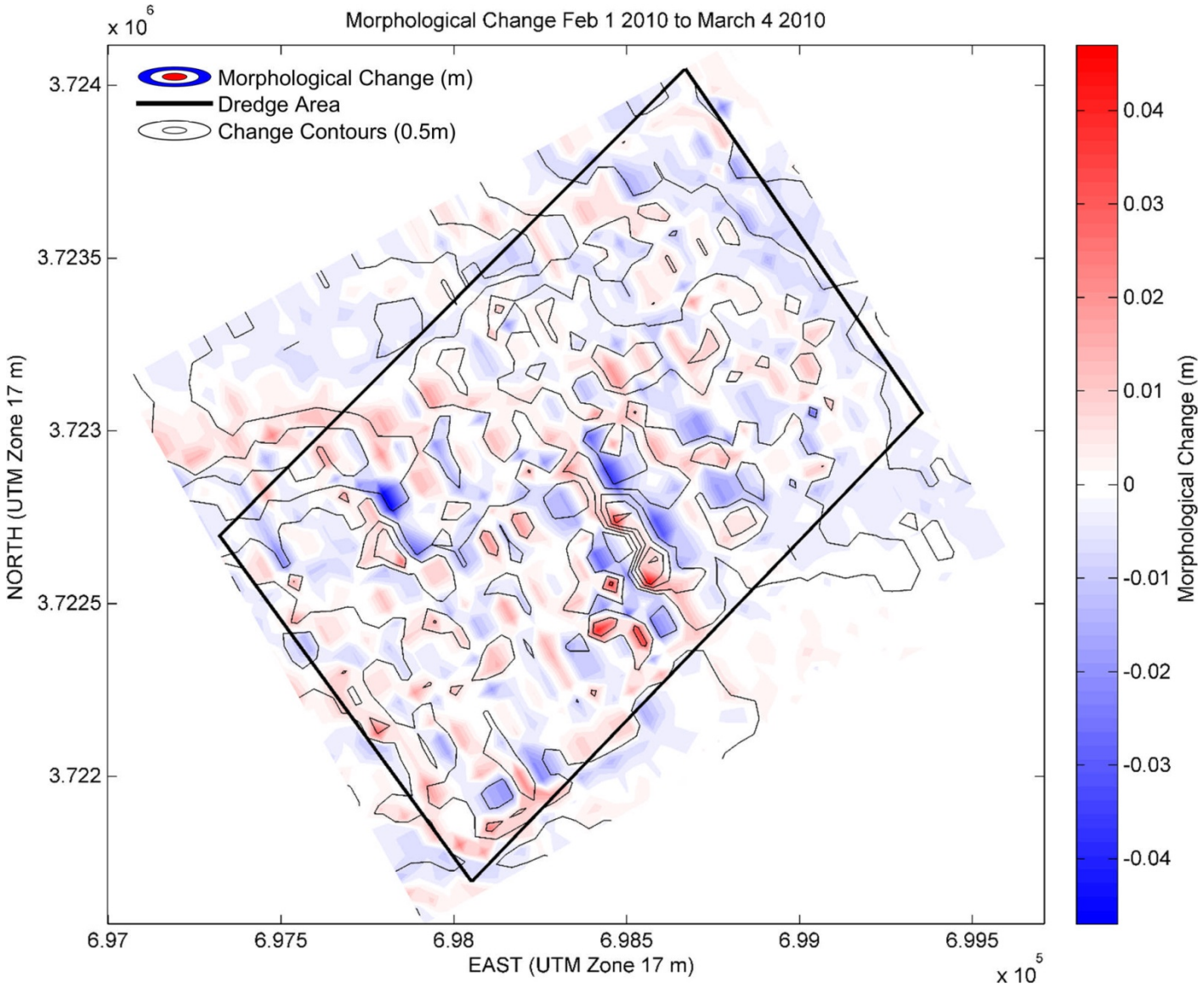

Figure IV-36. Morphological change for NearCoM using the Soulsby-Van Rijn 1997 formulation.

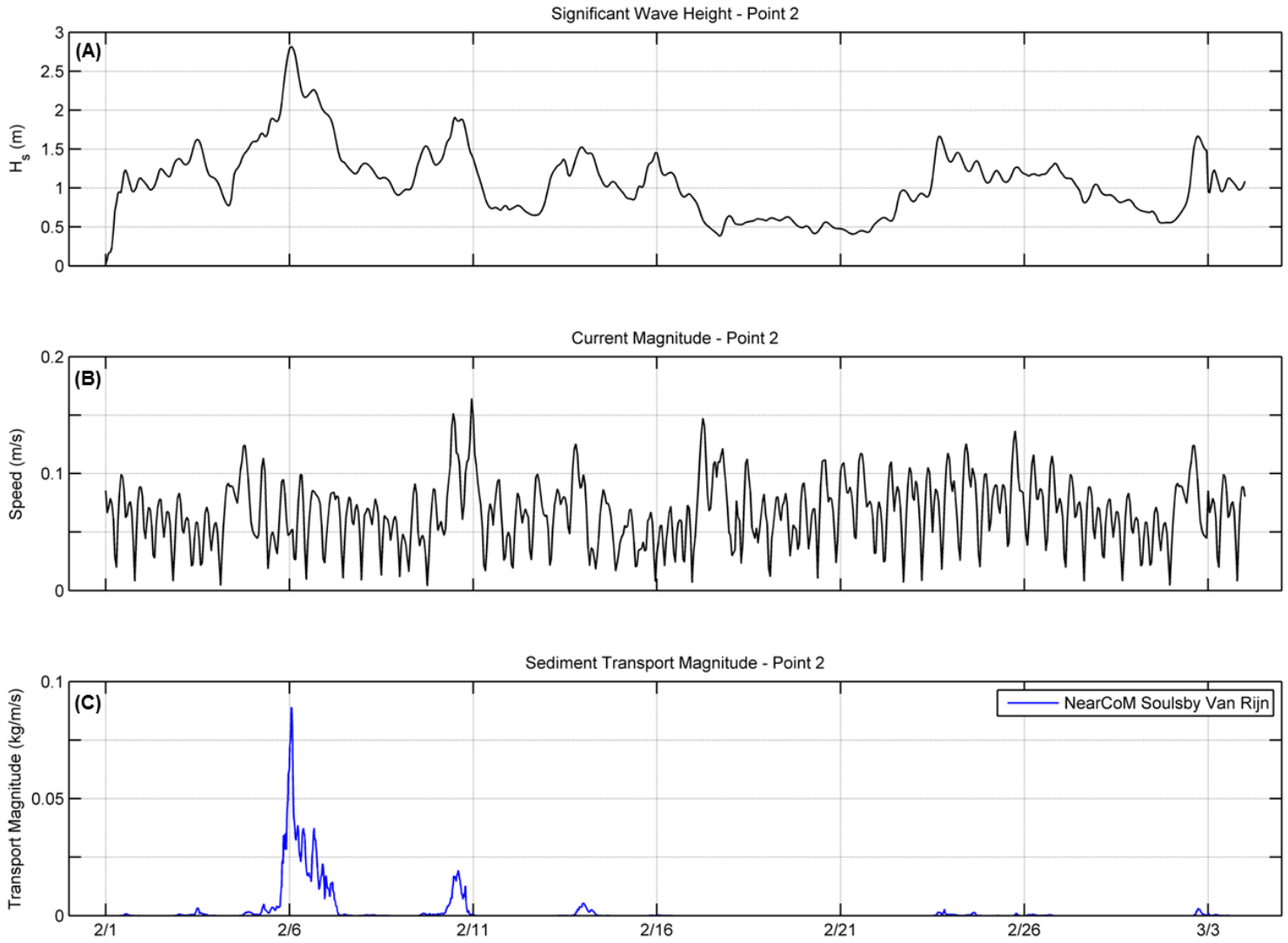

Figure IV-37. Times series of (A) COAWST significant wave height (B) COAWST current magnitude (C) NearCoM Soulsby-Van Rijn sediment transport magnitude.

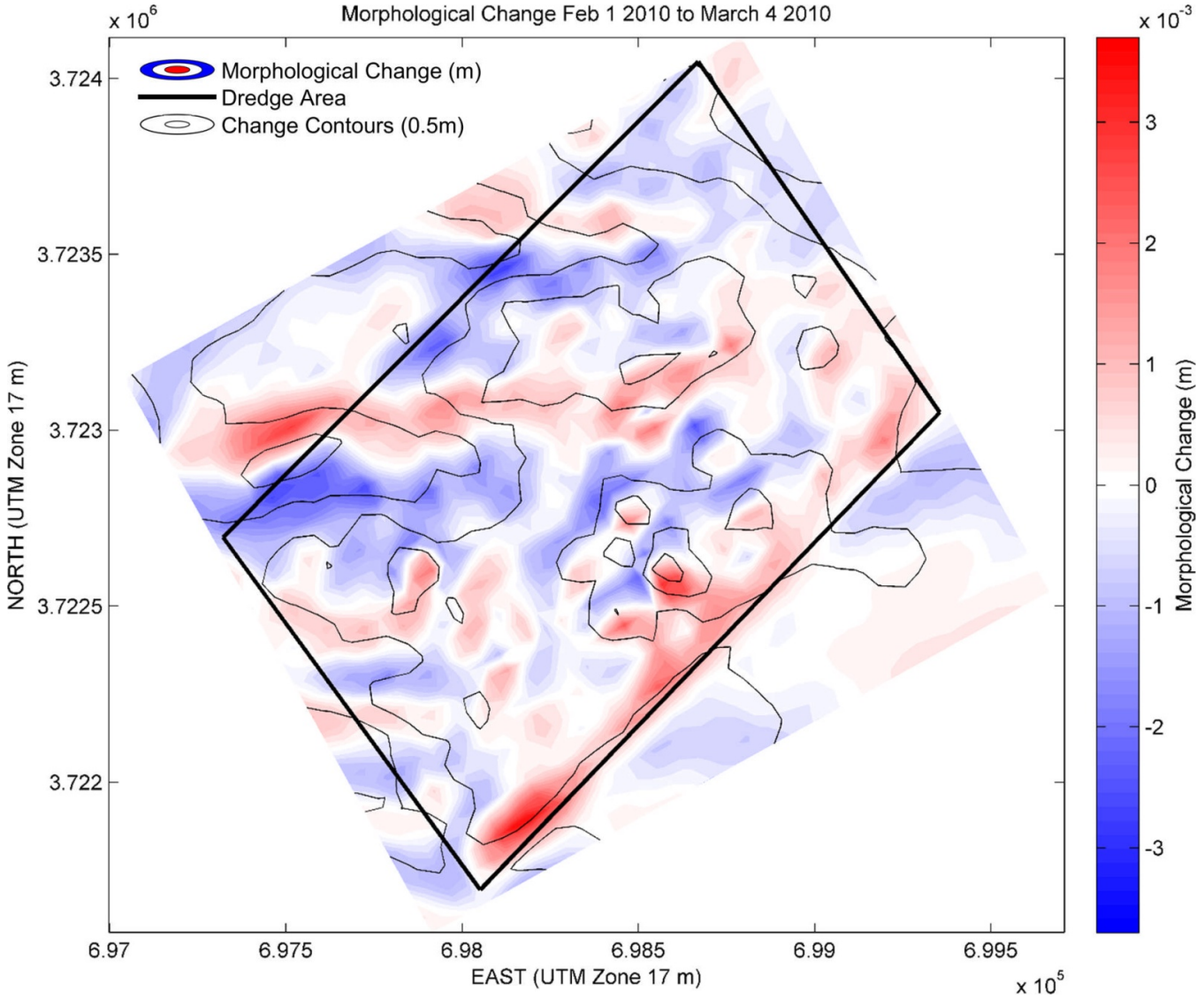

Figure IV-38. Morphological change for MIKE 21 using the Q3D approach.

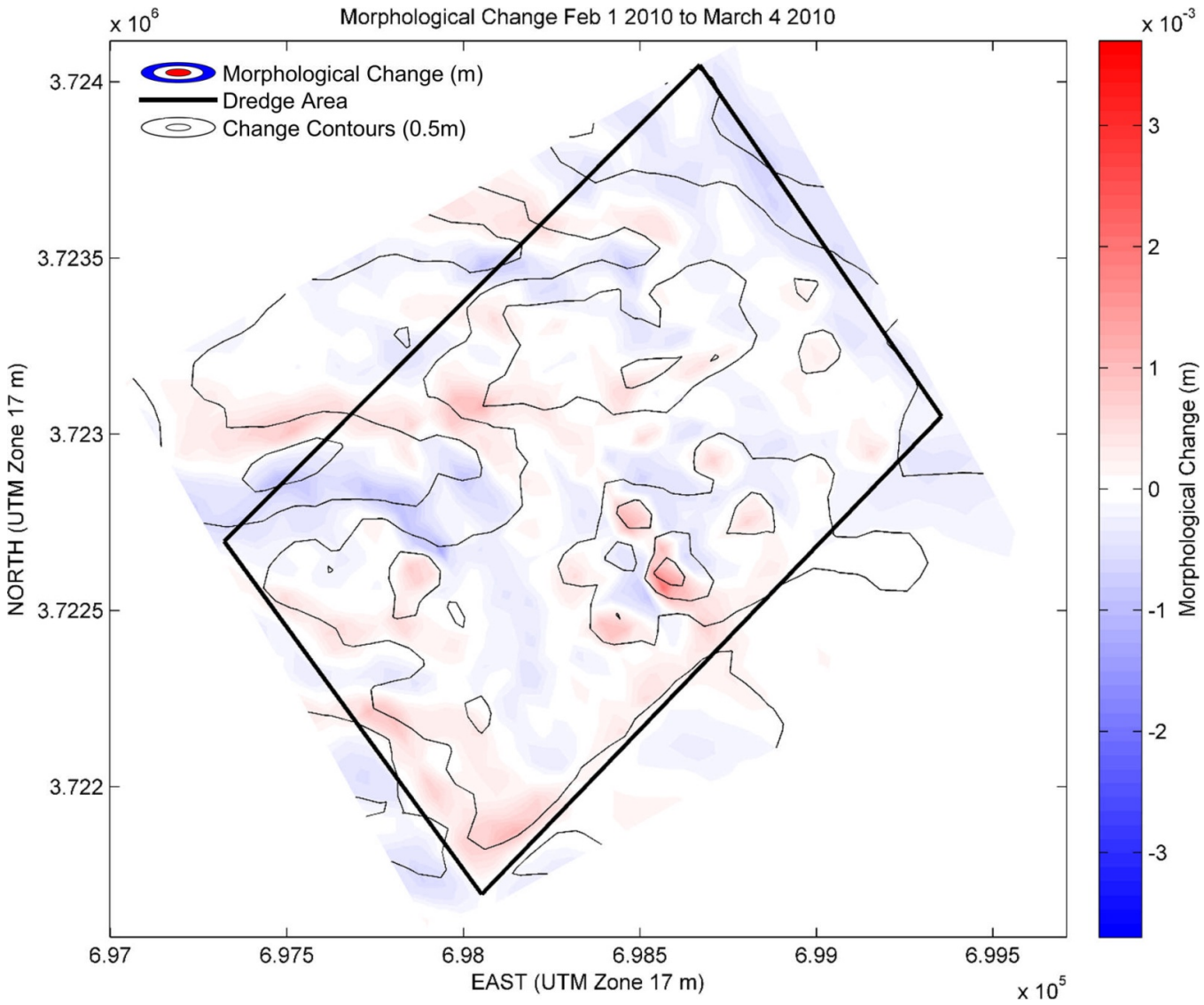

Figure IV-39. Morphological change for MIKE 21 using the 2D approach.

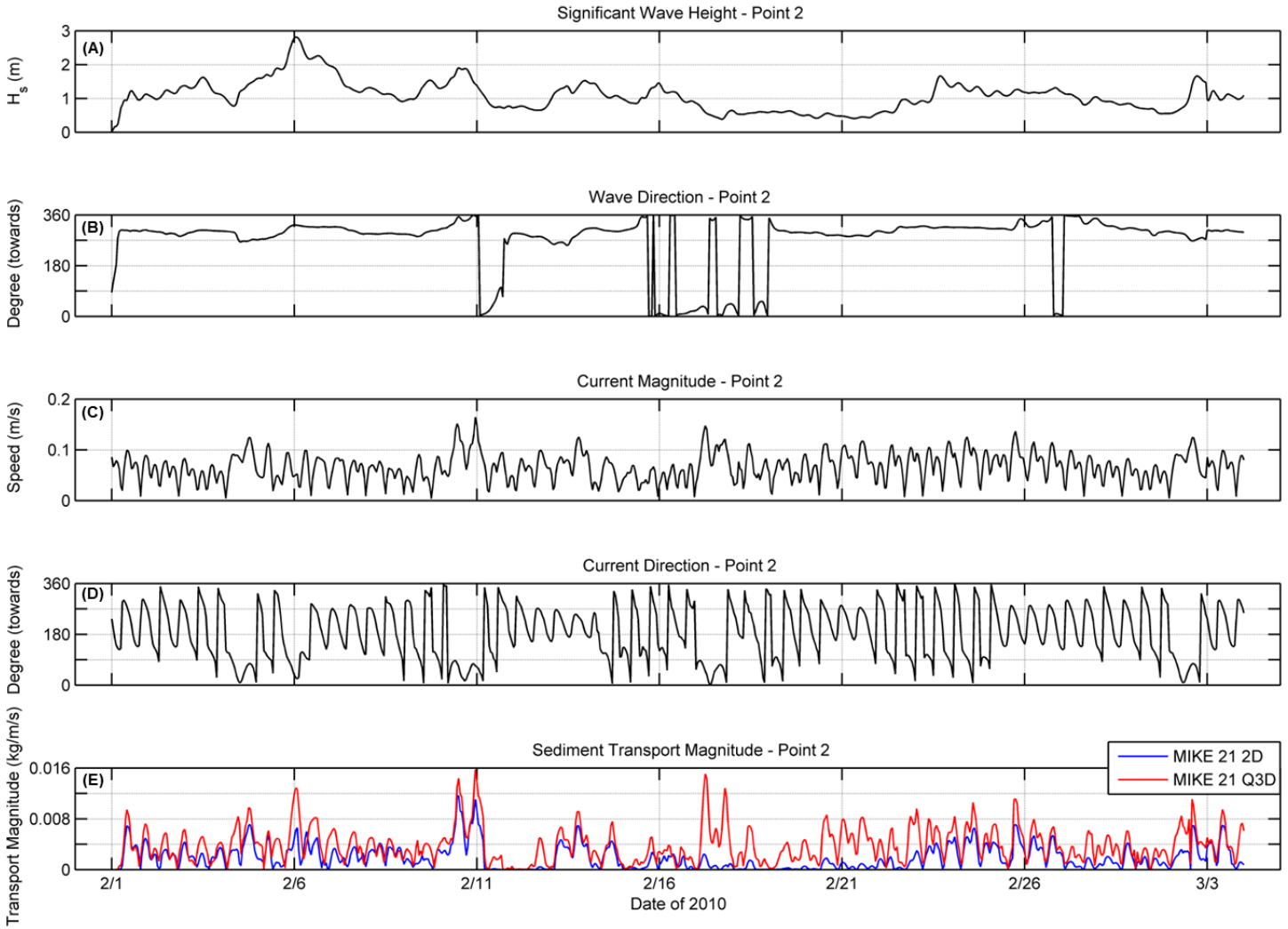

Figure IV-40. Times series of (A) COAWST significant wave height (B) COAWST wave direction (C) COAWST current magnitude (D) COAWST current direction (E) MIKE 21 2D (blue) and Q3D (red) sediment transport magnitude.

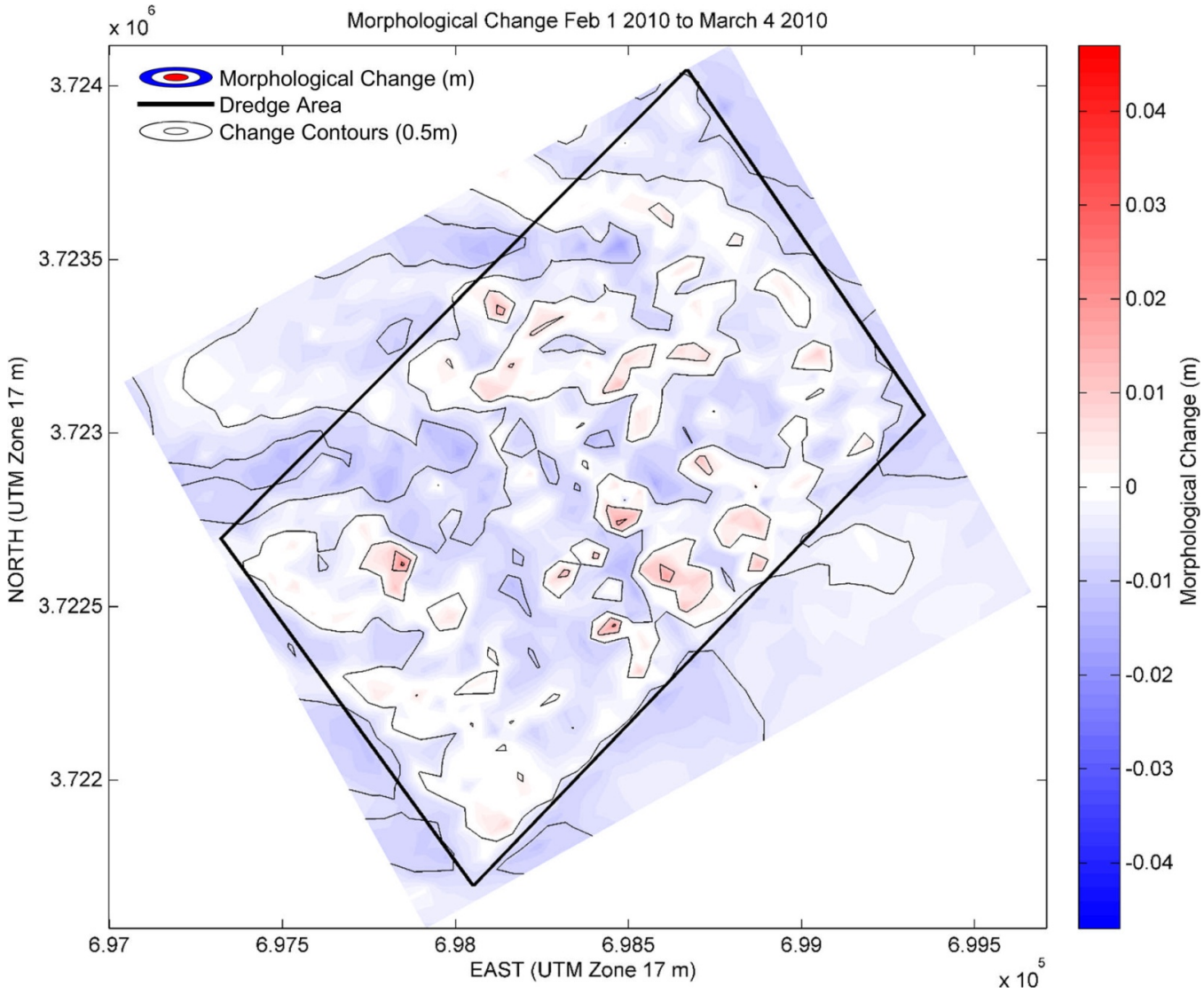

Figure IV-41. Morphological change for CMS using the Lund-CIRP 2006 formulation.

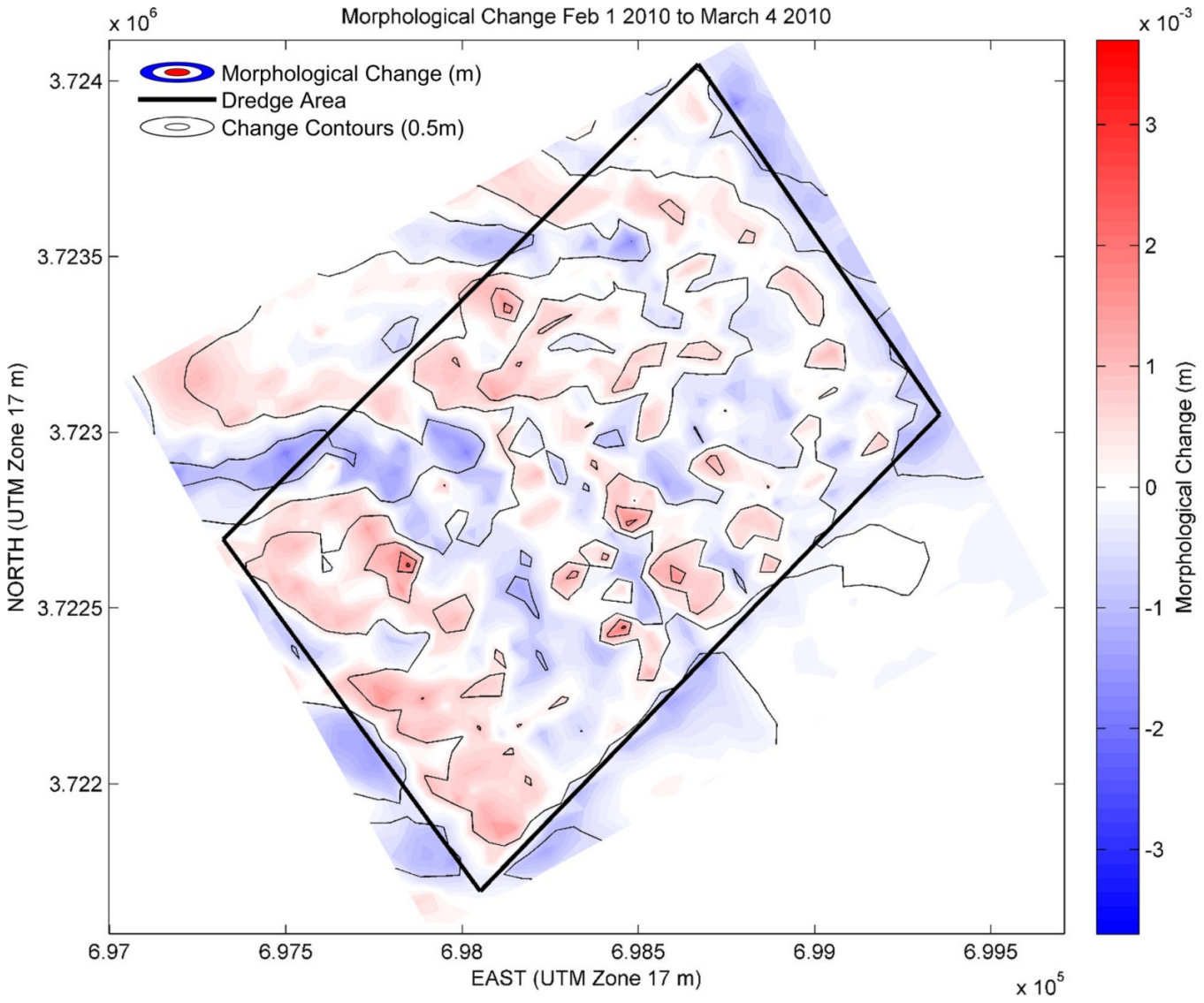

Figure IV-42. Morphological change for CMS using the Van Rijn 1998 formulation.

The initial morphological change results from CMS using the Lund-CIRP 2006 and Van Rijn 2007 sediment transport formulations are shown with different scales in Figure IV-42 and IV-43, respectively. When the Lund-CIRP sediment transport formula is used, erosion occurs throughout the majority of the dredge area while only a small fraction of the model domain shows accretion. When the Van Rijn formulation was used, qualitatively it appears that more locations are undergoing accretion, even though quantitatively the dredge area experiences overall erosional. The general orientation of the bed forms for both formulations are NNW/SSE. The magnitude of morphological change from the Lund-CIRP formulation is an order of magnitude greater than the change from the Van Rijn formula.

To further compare the two formulations used in CMS Figure IV-43 shows a time series at point two of the significant wave height and current magnitude, and CMS's results of sediment transport magnitude for both formulas. From Figure IV-43 the sediment transport magnitude with the Van Rijn 1998 formula appears to be predicting magnitudes close to zero when the wave energy is low. However, when the wave energy is high there is a corresponding increase in the transport magnitudes. Additionally, these wave induced peaks of the sediment transport still appear to have a tidal influence by the short time scale peaks and troughs. The sediment transport magnitude with the Lund-CIRP formula is an order of a magnitude greater than the Van Rijn transport magnitudes. The transport magnitude from the Lund-CIRP formula appears to be primarily tidal dominated by the transport peaks and troughs, closely following the current magnitude and no visible peak during periods of high wave energy.

IV.G DEVELOPMENT OF ANNUAL HYDRODYNAMICS AND WAVE CONDITIONS

IV.G.1. Hydrodynamic Conditions

The hydrodynamic data for the one-year model simulation were extrapolated from repeating the month-long COAWST results as measured data was not available in the vicinity of the borrow area between the post-dredging and one year post-dredging surveys. Based upon the agreement in water surface elevation of the COAWST results and ensuring a complete tidal lunar cycle was included the portion of the data that was repeated was from February 1, 2010 00:00 to March 2, 2010 23:45. The data was repeated to create a year-long time series spanning between April 2, 2009 17:00 and March 31, 2010 20:00. The water surface elevation and U and V current components for the year-long simulation are shown in Figure IV-44.

IV.G.2. Wave Conditions

For the wave conditions for the year-long simulation a year of wave parameters recorded by NOAA's Buoy 41013, located at Frying Pan Shoals, NC (33°26'11" N 77°44'35" W) were downloaded from NDBC's Web site (http://www.ndbc.noaa.gov/station_page.php?station=41013). The hourly data covers the period from April 1, 2009 through March 31, 2010 and includes significant wave height, dominant and average peak periods, and mean wave direction, apart from wind speed and direction, gust speed, atmospheric pressure, air and water temperature. Time series of hourly wave parameters are shown in Figure IV-45 for the time period of interest.

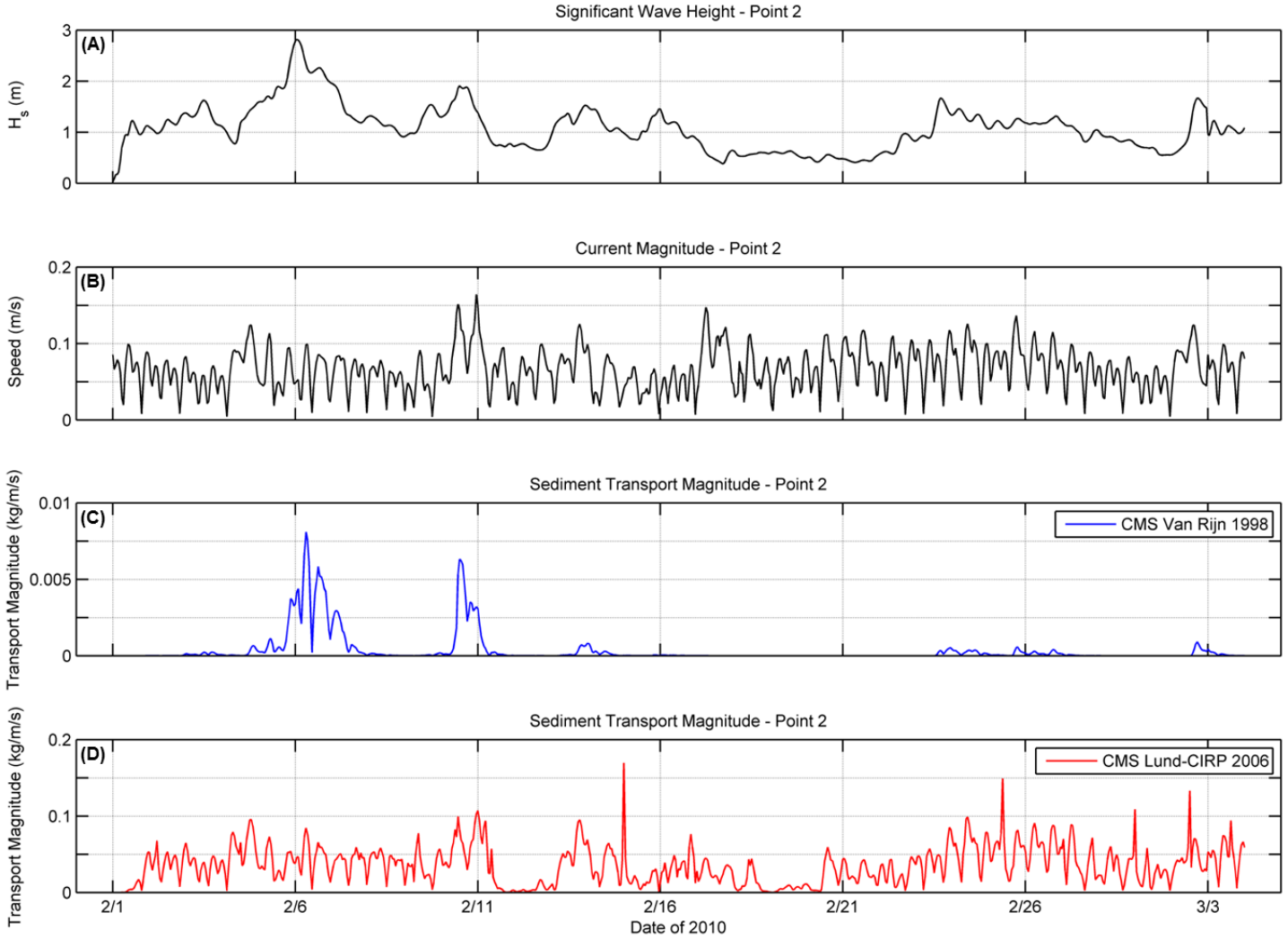

Figure IV-43. Times series of (A) COAWST significant wave height (B) COAWST current magnitude (C) CMS Van Rijn sediment transport magnitude (D) CMS Lund-CIRP sediment transport magnitude.

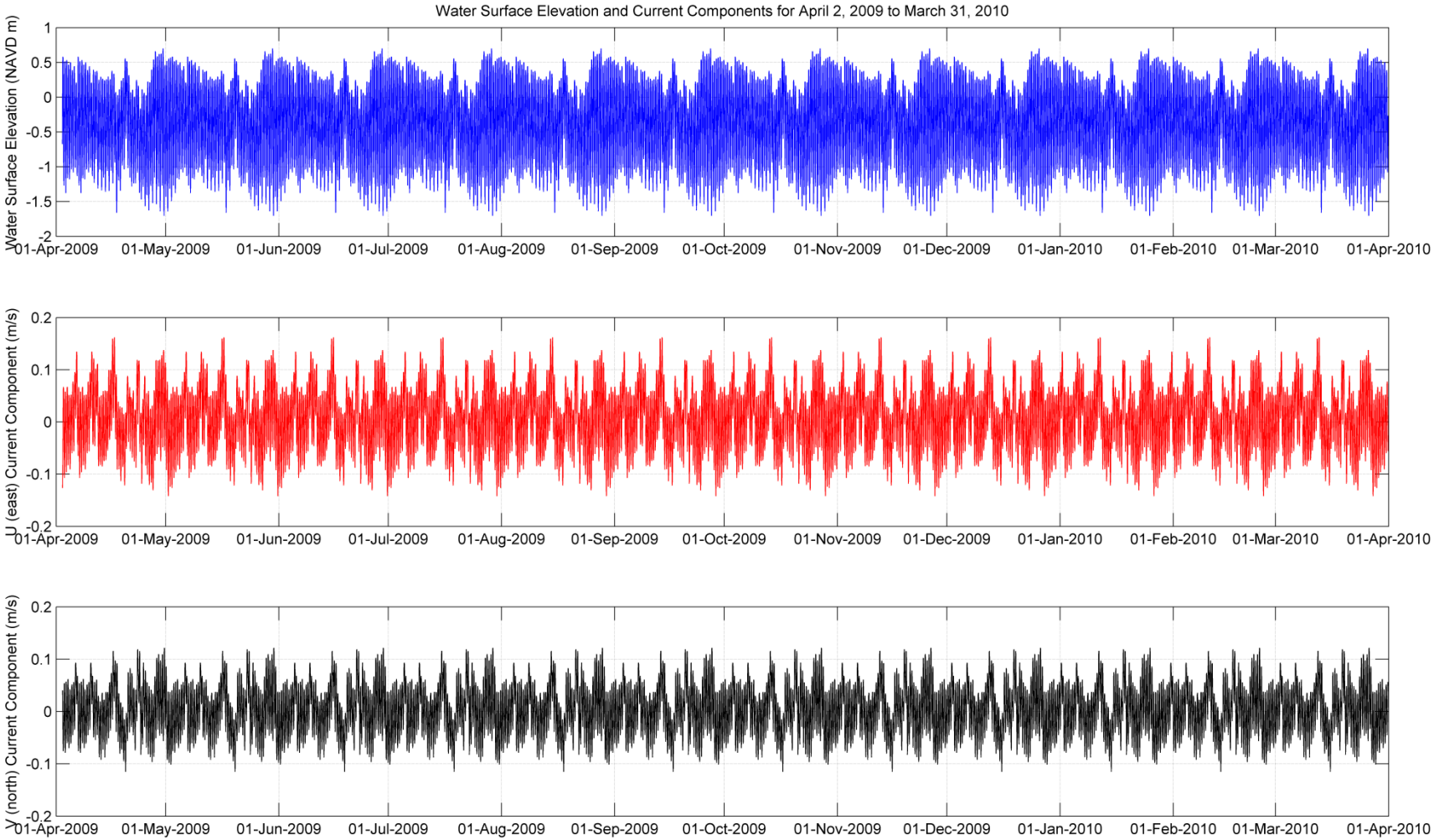

Figure IV-44. Hydrodynamic conditions, water surface elevation (blue), U current component (red), V current component (black), for the year-long simulation.

Waves derived from NOAA Buoy 41013 were propagated to the study site on the model bathymetry shown in Figure IV-46 using DHI's spectral wave model MIKE 21 SW. Bed elevations were interpolated to the model bathymetry from NGDC's 3 arc-second U.S. Coastal Relief Model (CRM).

The most relevant features of the model setup used to propagate the waves from the offshore measurement location to the study site are summarized in the list below:

- Directionally decoupled parametric formulation
- Directional discretization: 360° rose, 16 directions
- Waves propagated on time-varying water levels in agreement with records from NOAA station 8661070 Springmaid Pier, SC
- Wind generation of waves included according to the formulation in Shore Protection Manual (1984); wind speed and direction from NDBC Buoy 41013's records
- Wave diffraction not included
- Wave breaking included (Battjes and Janssen's model, $\alpha = 1.0$, $\gamma_1 = 4.0$, $\gamma_2 = 0.8$)
- Bottom friction included, Nikuradze's roughness coefficient $k_N = 0.01$ m (related to D_{50} as described in Soulsby, 1997); effect of bed friction on mean frequency disregarded
- Wave boundary data consisted of significant wave height, peak wave period and mean wave direction taken directly from NDBC Buoy 41013's records; a directional spreading factor n = 8 was assumed

It should be mentioned that model parameters were selected based on the results from a few sensitivity tests and on DHI's experience from similar applications of the MIKE 21 SW model. An attempt to use the wave data collected as a part of the South Carolina Coastal Erosion Study from October 2003 – April 2004 at Site 2 (Figure IV-47), Deployments 1 and 2, for model calibration/validation was initially carried out. The recorded wave heights were rather low, and using them as guidance to define the wave model parameters resulted in too low waves being calculated at the study site compared to the COAWST results. As issues of bio-fouling were known to cause problems with the instrument deployments at this location (Sullivan, *et al*., 2006), the lower measured wave heights in Long Bay could be anticipated. Therefore, it was decided not to make use of the Voulgaris wave data and to base the selection of the MIKE 21 SW model parameters on experience and results from sensitivity tests.

Time series of hourly model results, consisting of wave height, period and direction, were extracted at the 120 points located around the local MIKE 21 model mesh (see Figure IV-23). These model results were used as the wave parameters for the year-long simulations. Figure IV-48 shows a comparison between the time series of significant wave height recorded at the buoy and the corresponding time series extracted at the center point (point 18) of the southern boundary of the study area in Figure IV-46.

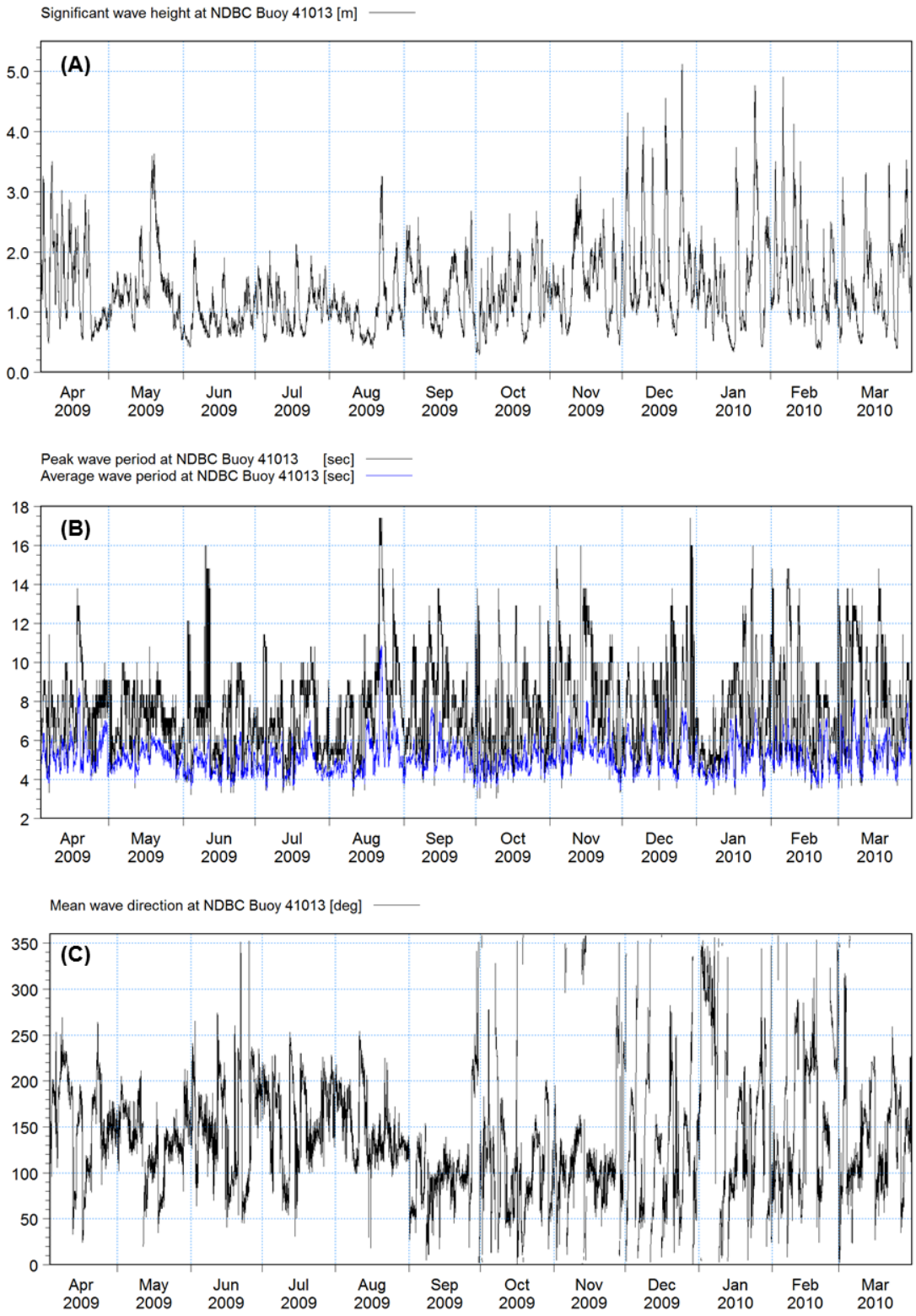

Figure IV-45. Time series of wave parameters recorded by NDBC Buoy 41013 during the period of April 2009 through March 2010. (A) Significant wave height, (B) peak and average periods, and (C) mean wave direction.

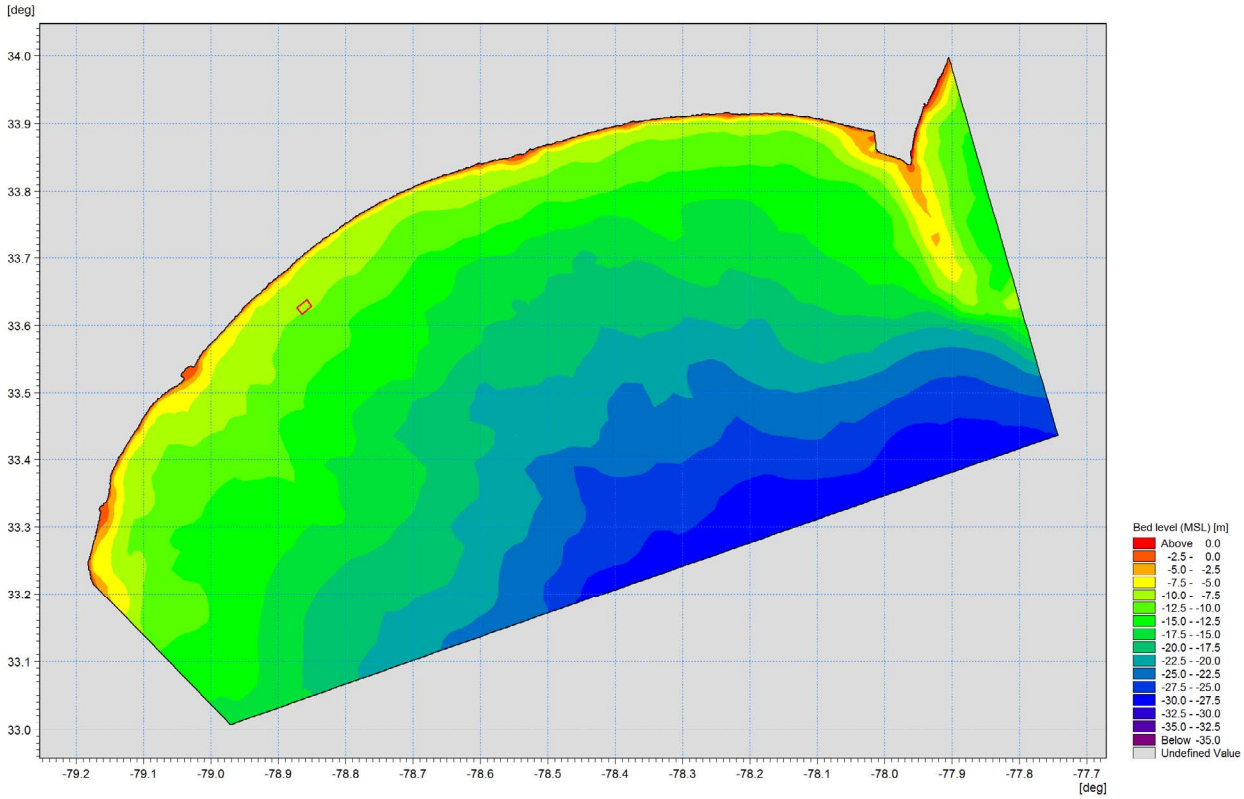

Figure IV-46. MIKE 21 SW model bathymetry, bed levels are in m and relative to MSL. Horizontal coordinates are longitude and latitude in degrees. The location of the study site is shown as a red rectangle. The position of NDBC Buoy 41013 (33.436°N, 77.743°W) is coincident with the bottom-right corner of the model domain.

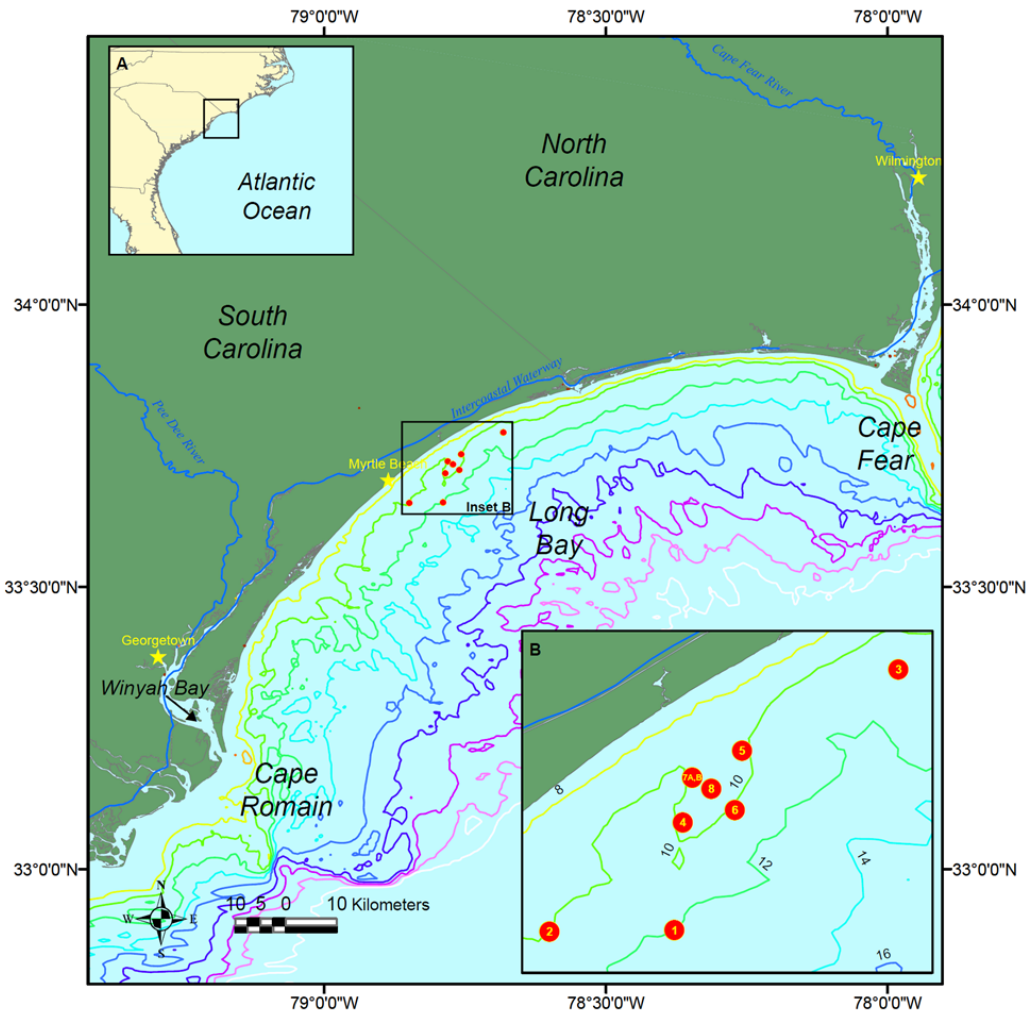

Figure IV-47. Location map for the data collected as a part of the South Carolina Coastal Erosion Study from October 2003 – April 2004 (http://woodshole.er.usgs.gov/pubs/of2005-1429/start.html).

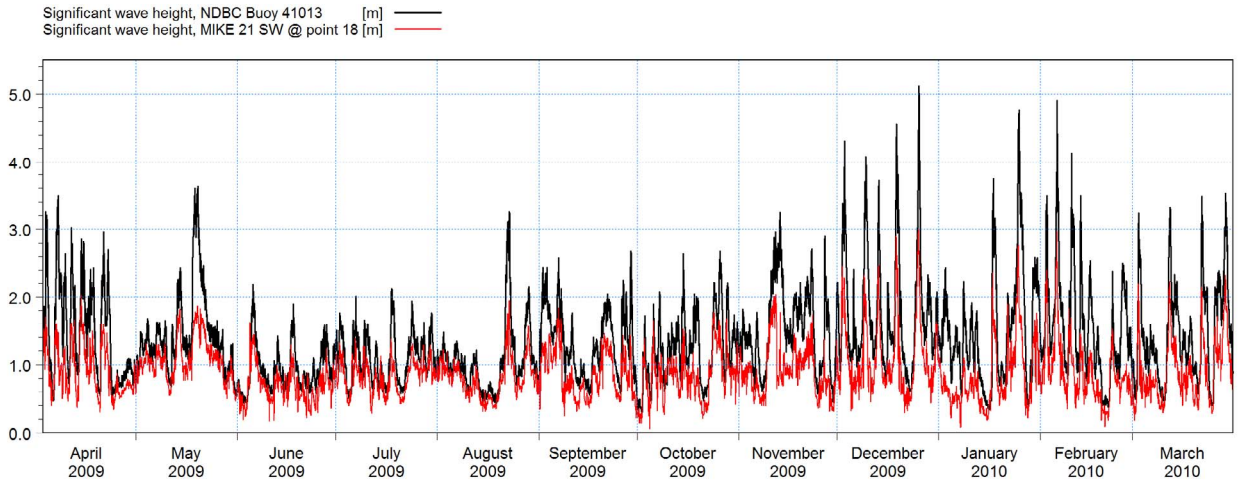

Figure IV-48. Time series of significant wave height measured (black line) and propagated by the MIKE 21 SW model to the southern boundary of the study area (red line)

IV.G.3 One-Year Simulation

A one-year simulation was conducted for each morphodynamic model using the same parameters, starting bathymetry, and grids/meshes as the month-long simulations, with the only differences being the time period of the simulation and the forcing wave and hydrodynamic conditions, which are described in section IV.G. The one-year simulation started on April 2, 2009 at 17:00 and went to March 31, 2010 20:00, i.e. a total of 8715 hourly time steps. The computational time to complete these year-long simulations was approximately 4.5 days using 16 processors for NearCoM, 5 days using an 8 core processor PC for MIKE 21, and 1.3 days using an 8 core processor PC for CMS. The year-long NearCoM, MIKE 21, and CMS models used the Soulsby-Van Rijn 1997 sediment transport formula, the 2D approach, and the Lund-CIRP formula, respectively. The morphological change from these three model simulations are shown in Figure IV-49 on the same color scale. The net erosion, deposition and total volumes along with the maximum erosion and accretion values within the dredge area are displayed in Table IV-7. In comparing the three plots, the bed change from the CMS simulation is significantly greater than the change from NearCoM and MIKE 21. The maximum morphological change values for NearCoM and MIKE 21 are an order of magnitude less than the values for CMS.

Table IV-7. One-year net volume changes and max erosion and accretion values within the dredge area for each numerical mode simulation. A negative value indicates erosion.

Model	**Net Erosion (m^3)**	**Net Deposition (m^3)**	**Net Total (m^3)**	**Morphological Change (m)**	
				Max Erosion	**Max Accretion**
NearCoM Soulsby-Van Rijn 1997	-18,719	20,226	1,507	-0.071	0.061
MIKE 21 2D	-2,883	2,307	-576	-0.018	0.018
CMS Lund-CIRP 2006	-120,514	114,061	-6,453	-0.182	0.388

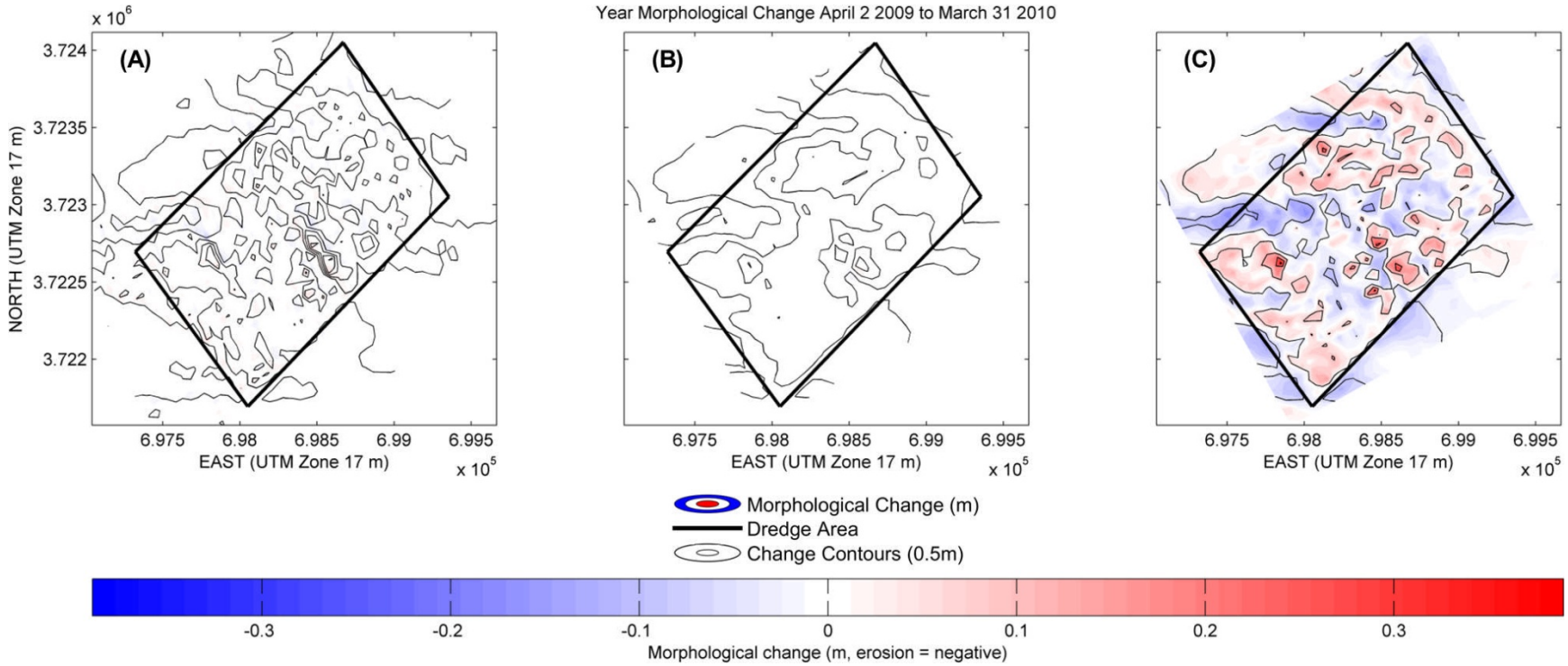

Figure IV-49. Year-long simulation morphological change for (A) NearCoM using the Soulsby-Van Rijn 1997 formulation (B) MIKE 21 using the 2D approach (C) CMS using the Lund-CIRP 2006 formulation.

IV.G.4. One-Year Simulations versus "Typical" Month × 12

Instead of running the one-year simulation which took approximately double the computational time of the month-long simulation, the month-long simulation results were multiplied by twelve as a "speed up factor" to increase the effective forecasting period of the models. Overall, this "speed up factor" is advantageous in reducing your model computational time specifically when trying to calibrate the numerical models which have numerous parameters that need to altered throughout the calibration process. For each model the morphological change results for the year-long and month-long multiple by twelve are shown in Figure IV-50 to IV-52. It should be noted that the month-long results that were multiplied by twelve came from extracting the data from the year-long simulation and not the month-long simulations discussed in Section IV.E which were forced with different boundary conditions. The patterns of the year-long results compared to the month-long results multiplied by twelve are similar for each model. The amount of volume change within the dredge area for the year-long simulation and the month simulation multiplied by twelve are listed in Table IV-8. The net erosion and net deposition for NearCoM and MIKE 21 for the month simulations multiplied by twelve is slightly greater than its respective one-year simulation. The net total change for MIKE 21's one-year simulation is approximately 100 m^3 more than the "speed up factor" month-long simulation, while the difference between the NearCoM's simulations is 300 m^3 with the month-long simulation having greater change. The difference between the year-long and "speed up factor" month-long simulations for CMS is greater than the other two models with the one-year simulation, showing significantly more erosion and accretion than the month-long simulation. This significant difference was accounted for when determining what model to simulate the idealized cases for Chapter VI.

Table IV-8. Net volume change results from the year-long and month-long multiplied by twelve within the dredge area for each numerical model. A negative value indicates erosion.

Model	**NearCoM Soulsby-Van Rijn 1997**		**MIKE 21 2D**		**CMS Lund-CIRP 2006**	
	Year	**Month × 12**	**Year**	**Month × 12**	**Year**	**Month × 12**
Net Erosion (m^3)	-18,719	-22,170	-2,883	-3,706	-120,514	-56,372
Net Deposition (m^3)	20,226	24,058	2,307	3,246	114,061	105,852
Net Total (m^3)	1,507	1,888	-576	-460	-6,453	49,480

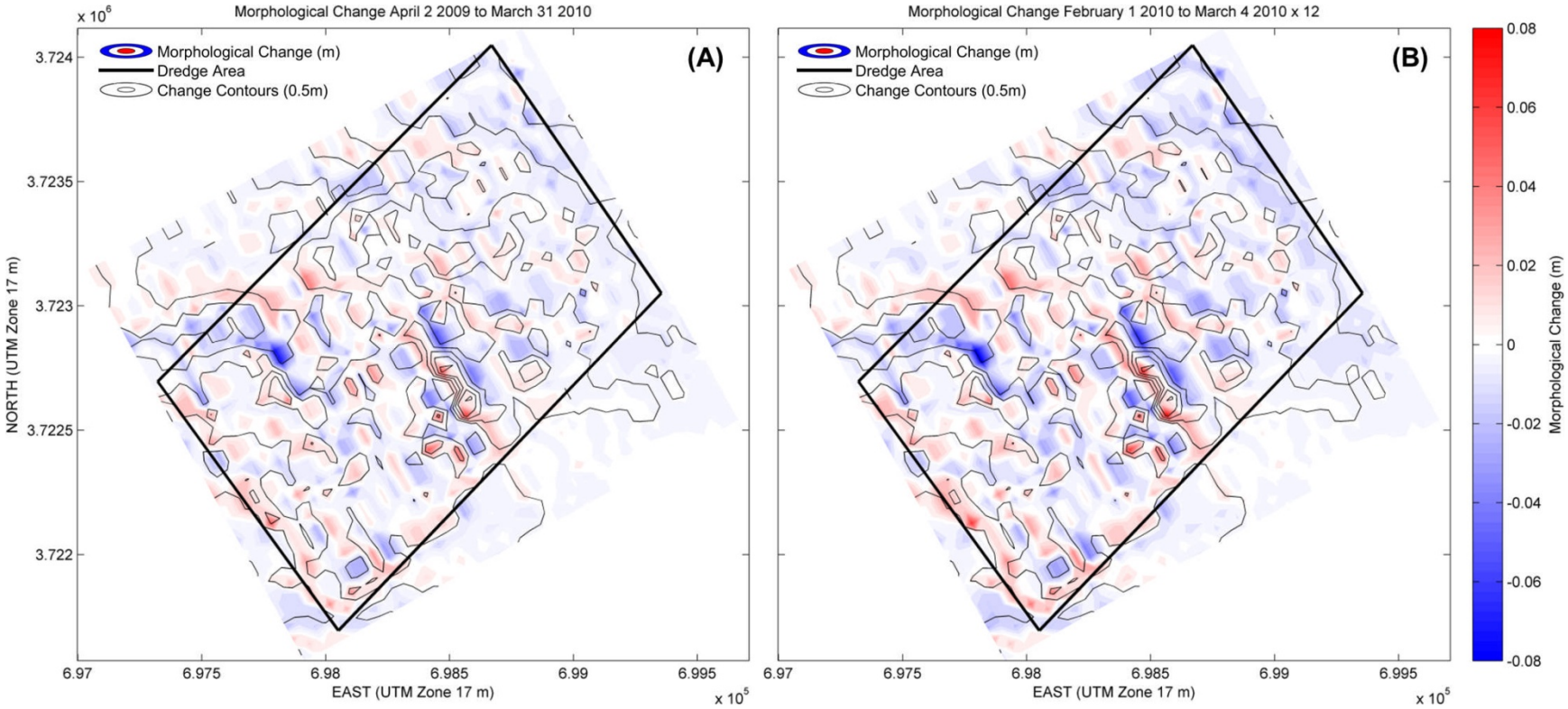

Figure IV-50. NearCoM Soulsby-Van Rijn 1997 (A) year-long simulation (B) month-long simulation × 12.

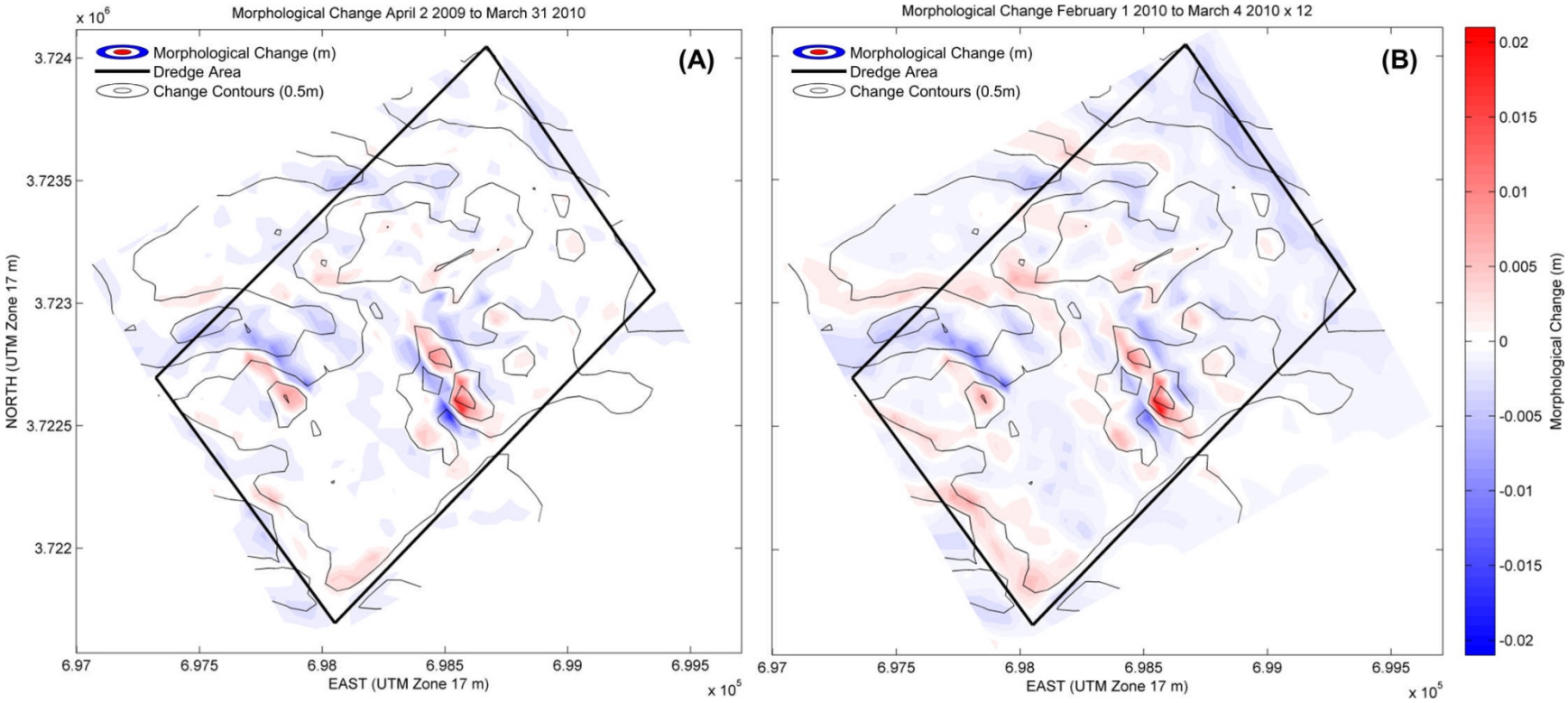

Figure IV-51. MIKE 21 2D (A) year-long simulation (B) month-long simulation × 12.

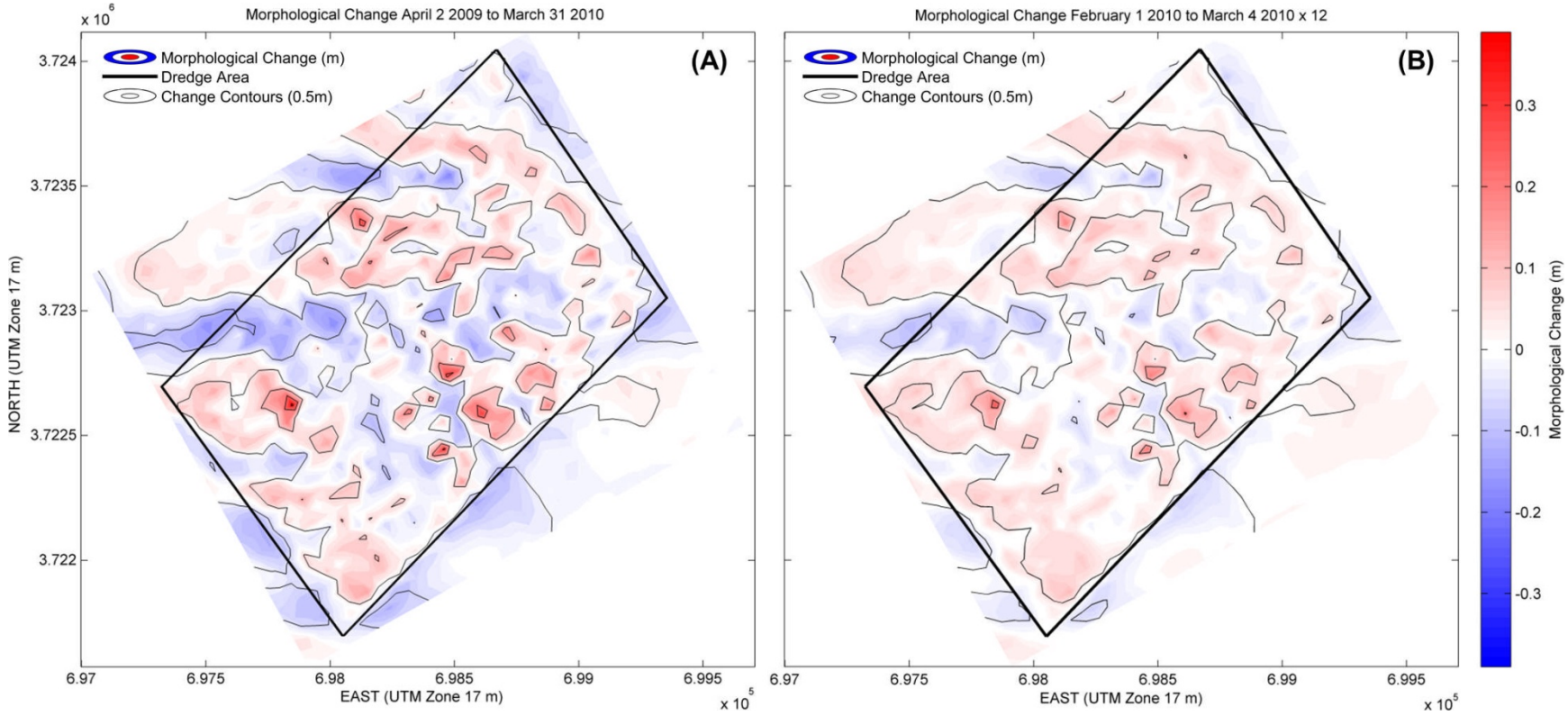

Figure IV-52. CMS Lund CIRP 2006 (A) year-long simulation (B) month-long simulation × 12.

V. MODEL TO MEASURED DATA CALIBRATION

All three modeling packages were applied to assess their predictive ability in quantifying morphological changes for the Cane South borrow area. This effort required a high level of data analysis, both for the bathymetric data sets and analyzing the model results. Comparisons documenting model skill in terms of morphologic change were the ultimate goal of the assessment; however, the influence of key input decisions for each of the candidate models remained critical. Key decisions regarding the application of the candidate model systems for assessing morphological change included:

- *Spatial resolution* – due to its extreme effect on CPU time, it is always desirable to apply the coarsest grid resolution possible without omitting the dominant physical processes; however, it was found that increasing grid resolution from 50 m to 25 m (both for the bathymetric data sets and the candidate models) greatly improved the model-to-data comparisons.
- *Sediment transport model formulation* – With weak observed tidal currents the current-induced bottom stress rarely reached the threshold value able to move the sediment at the borrow area depth. As a result it was determined that the sediment transport at Cane South was strongly wave-dominated. The only available model that incorporated an appropriate sediment transport formulation for cases of this nature was NearCoM, which can incorporate the formulation developed by Van Rijn (1991).
- *"Speed-up factors"* – a form of process filtering, speed-up factors are used to enhance the morphological response, such that the simulation results are taken as being representative of a longer time period than actually simulated. Due to the shortcoming associated with most of the sediment transport formulations applied, speed-up factors were necessary to "match" the magnitude of morphological change observed at Cane South for the one-year period subsequent to dredging.
- *Online correction and slope factor* – To refine the final model results for NearCoM, minor additional modifications to the final sediment transport results were added to ensure appropriate physical representation of site-specific issues. A slope factor was added as an acknowledgement that the bathymetry at Cane South is not flat. In addition, a technique called the "online correction method" was implemented to ensure that the influence of slope equilibration was not influencing modeled bathymetric change at the Cane South borrow area. This additional factor was necessary as relatively steep slopes shown in the bathymetry dataset could adjust over time even without oceanographic forcing.

The following sections detail the morphological modeling calibration procedures for the three models. A description of the bathymetric data sources and surface modeling are also provided, as this procedure can strongly influence the model-to-data comparisons.

V.A MEASURED MORPHOLOGICAL CHANGE

Three bathymetric surveys (pre-, post-, and one year post-dredge) were conducted as a part of the Grand Strand Renourishment Project, as previously explained in Section III.B.3. The morphological change between these three surveys is shown in Figure V-1, V-2 and V-3. The largest elevation change from the pre- to post-dredge surveys occurred in the center section of the borrow area where there was approximately a meter or more of bed elevation change, presumably as a result of dredging. Between the post- and one year post-dredging surveys, the sections with the largest elevation change experienced infilling, while adjacent sections to these borrow areas experienced erosion. This infilling can be seen additionally in the pre- to one year post-dredge change plot where the magnitude of the change was less than the amount of change indicated between the pre- to post-dredge survey. Throughout these three change figures high backscatter lineations were exhibited by the sharp boundaries of change as a result of dredging the borrow area (i.e. steep side slopes created by the dragheads of the dredge).

The focus of this study was to evaluate the ability of the morphological models, NearCoM, MIKE 21 and CMS to reproduce the bed changes seen between the post- and one year post-dredge surveys. Ideally, the three models would predict the same magnitude of change as the measured data, which ranged from approximately -1 to 1 m, and duplicate the same patterns of where erosion and accretion occurred throughout the dredge area. Generally, between the post- and one year post-dredge surveys the right side of the dredge area underwent accretion while the left side of the domain primarily experienced erosion, with the maximum accretion occurring where the borrow area was excavated to the greatest extent.

V.B. INITIAL MODEL TO MEASURED MORPHOLOGICAL CHANGE COMPARISON PLOTS

As discussed throughout Chapter II numerous simulations were run for model to model comparison. When it came to comparing and calibrating the models to the measured data it was decided that the characteristic month-long model simulation multiplied by twelve would be used instead of the year-long simulation. This decision was based on (1) the month-long simulations computational time being approximately 50% of the year-long simulations and (2) the results between the month-long times 12 and year-long simulations were similar. It was advantageous to reduce the model computational time especially to calibrate the numerous parameters of the models to the measured data. The primary trade-off with this approach is the use of the one-month wave record to characterize annual conditions; however, this simplification was necessary to allow accurate model calibration in a reasonable time horizon. The initial model morphological change plots compared to the measured plot are shown in Figure V-4 through V-8. It should be noted that these figures have different scales due to the difference in magnitude of the results. The net volume changes and the max erosion and accretion values within the dredge area for the measured data and the three models and their respective sediment transport formulations are listed in Table V-1.

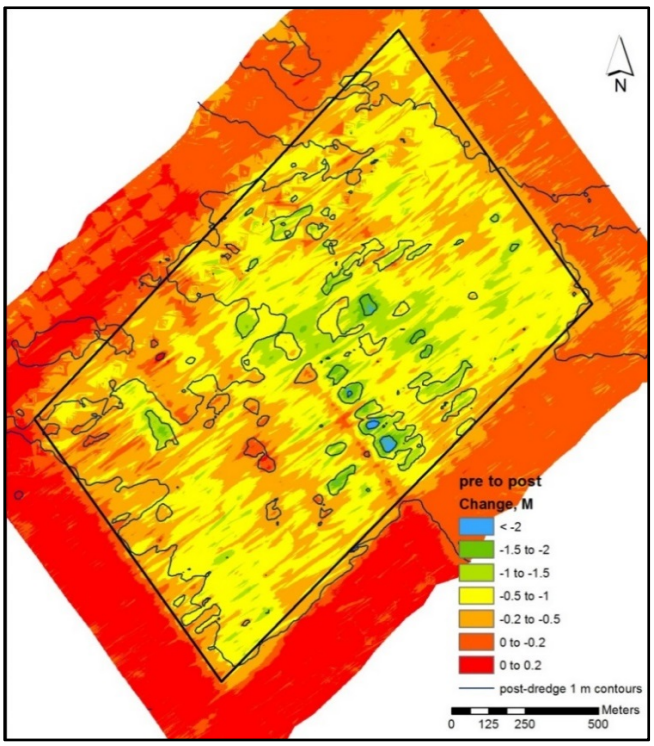

Figure V-1. Morphological change between the Cane South pre-dredge and post-dredge bathymetric surveys. The black rectangle identifies the dredged area.

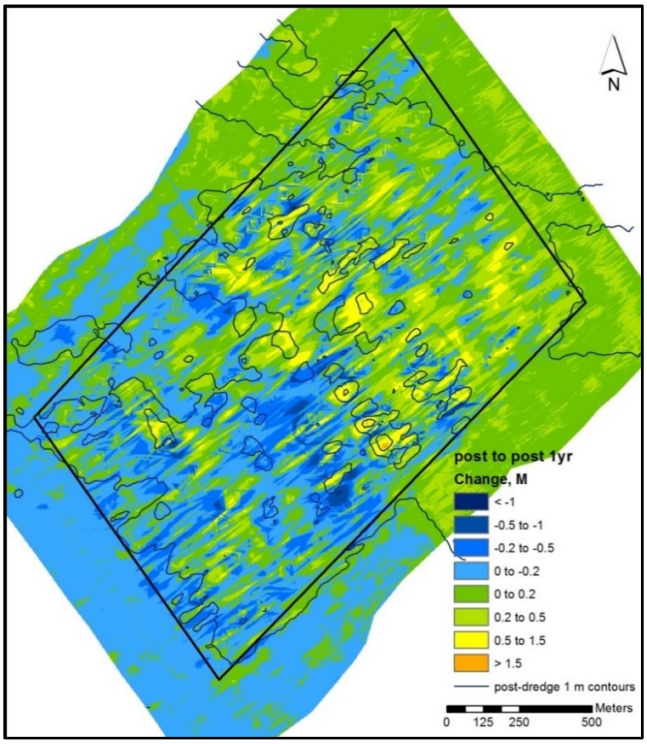

Figure V-2 Morphological change between the Cane South post-dredge and one year post-dredge bathymetric surveys. The black rectangle identifies the dredged area.

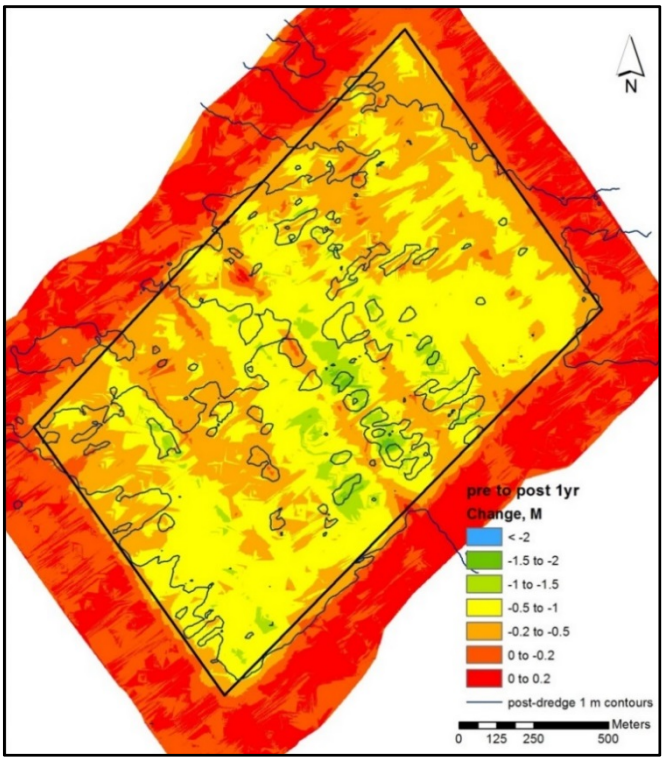

Figure V-3. Morphological change between the Cane South pre-dredge and one year post-dredge bathymetric surveys. The black rectangle identifies the dredged area.

Table V-1. Net volume changes and max erosion and accretion values within the dredge area for the measured data and the month-long model simulations multiplied by twelve. A negative value indicates erosion.

Model	**Net erosion (m^3)**	**Net deposition (m^3)**	**Net total (m^3)**	**Morphological change (m)**	
				Max erosion	**Max accretion**
Measured	-198,205	413,476	215,271	-1.31	2.04
NearCoM Soulsby-Van Rijn 1997	-150,676	161,970	11,294	-0.54	0.55
MIKE 21 Q3D	-21,393	16,185	-5,208	-0.03	0.04
MIKE 21 2D	-6,595	6,806	211	-0.01	0.03
CMS Lund-CIRP 2006	-289,701	28,730	-260,971	-0.19	0.28
CMS Van Rijn 1998	-14,468	11,208	-3,260	-0.02	0.03

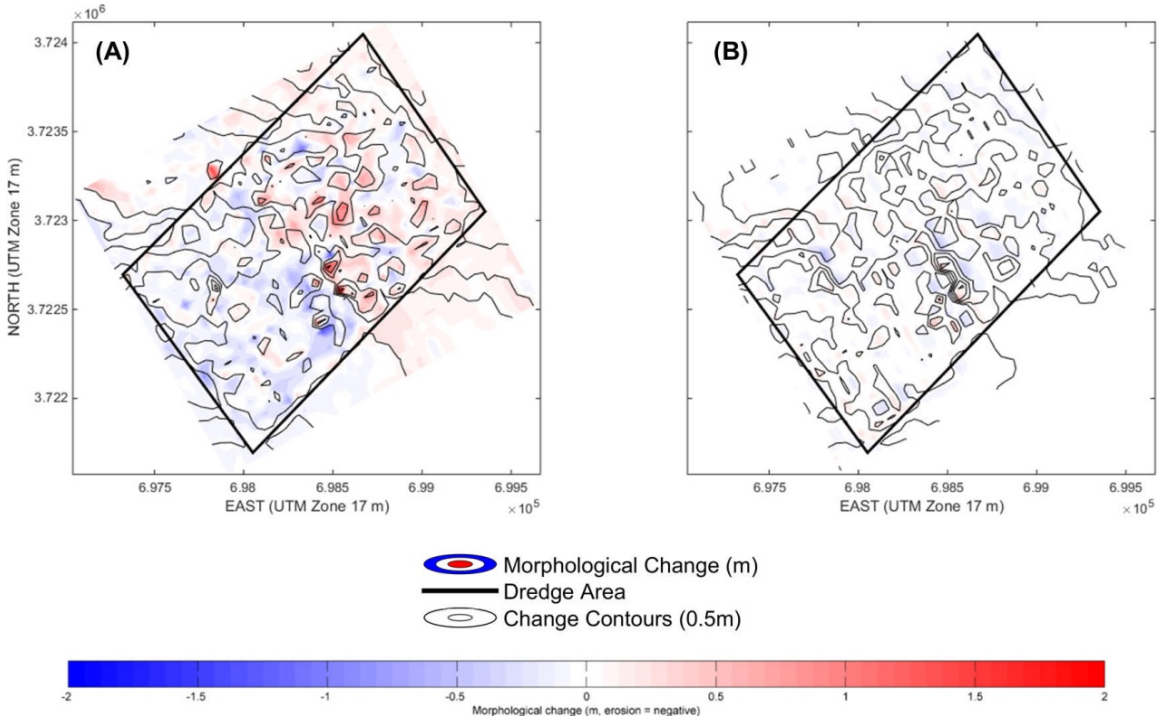

Figure V-4. Morphological change in meters from (A) the measured post to one year post dredge survey data and (B) the month-long NearCoM simulation using the Soulsby-Van Rijn 1997 formulation results multiplied by twelve.

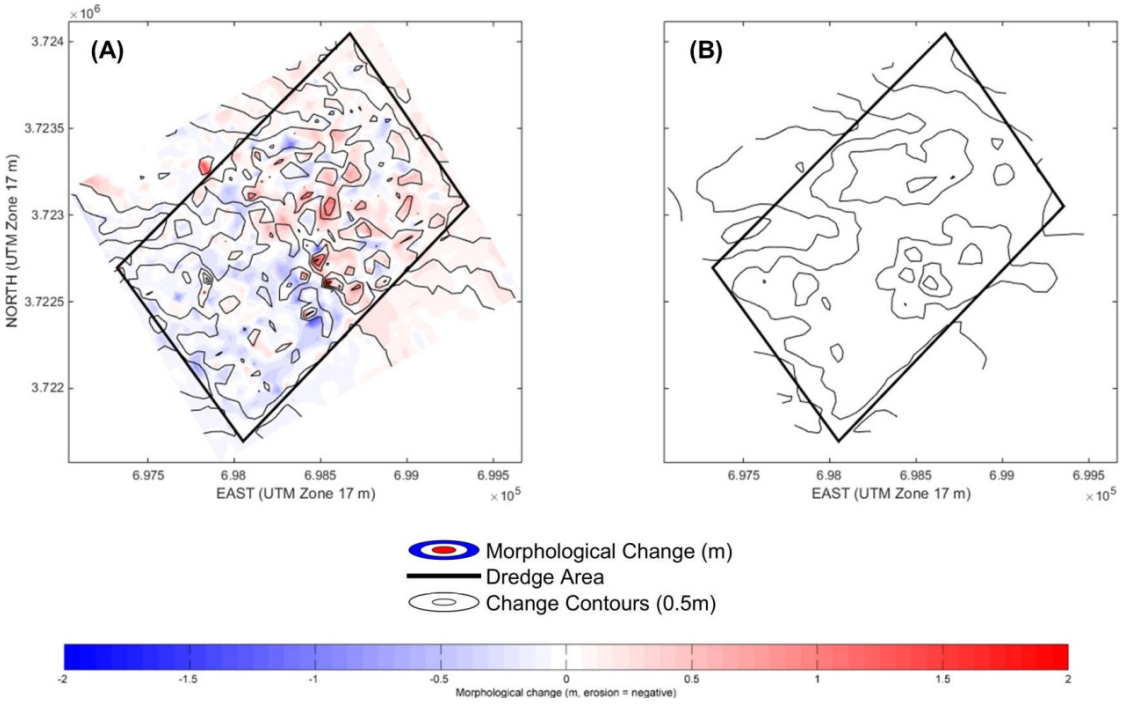

Figure V-5. Morphological change in meters from (A) the measured post to one year post dredge survey data and (B) the month-long MIKE 21 simulation using the Q3D approach results multiplied by twelve.

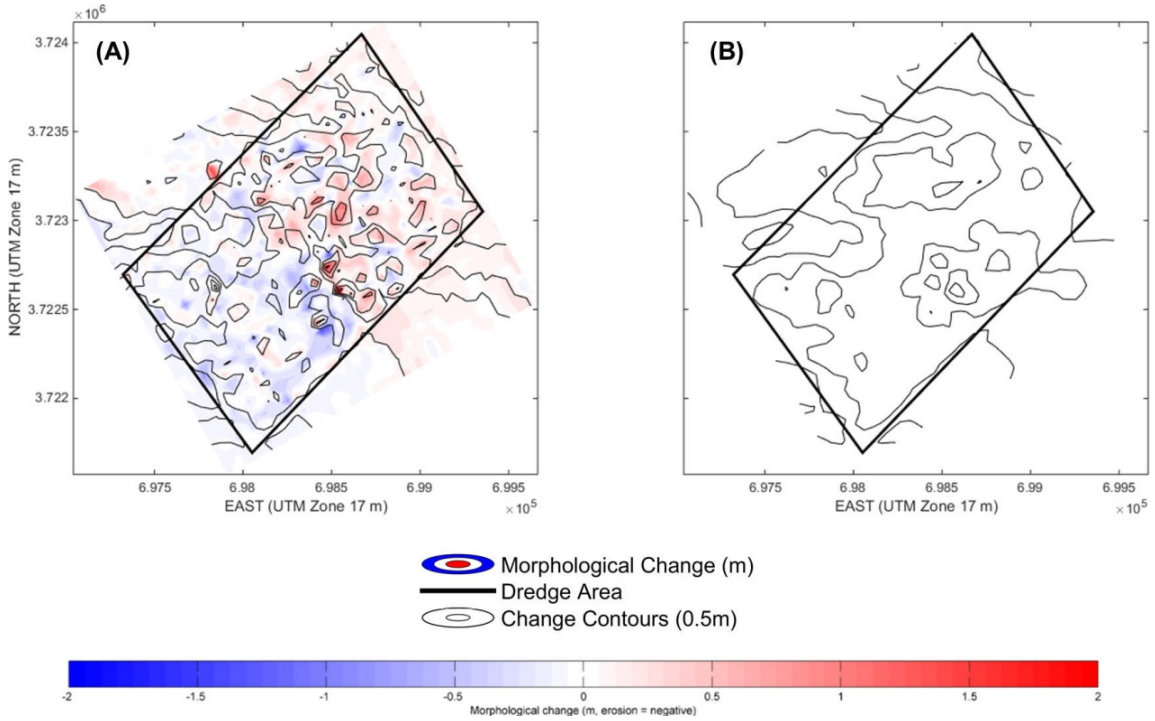

Figure V-6. Morphological change in meters from (A) the measured post to one year post dredge survey data and (B) the month-long MIKE 21 simulation using the 2D approach results multiplied by twelve.

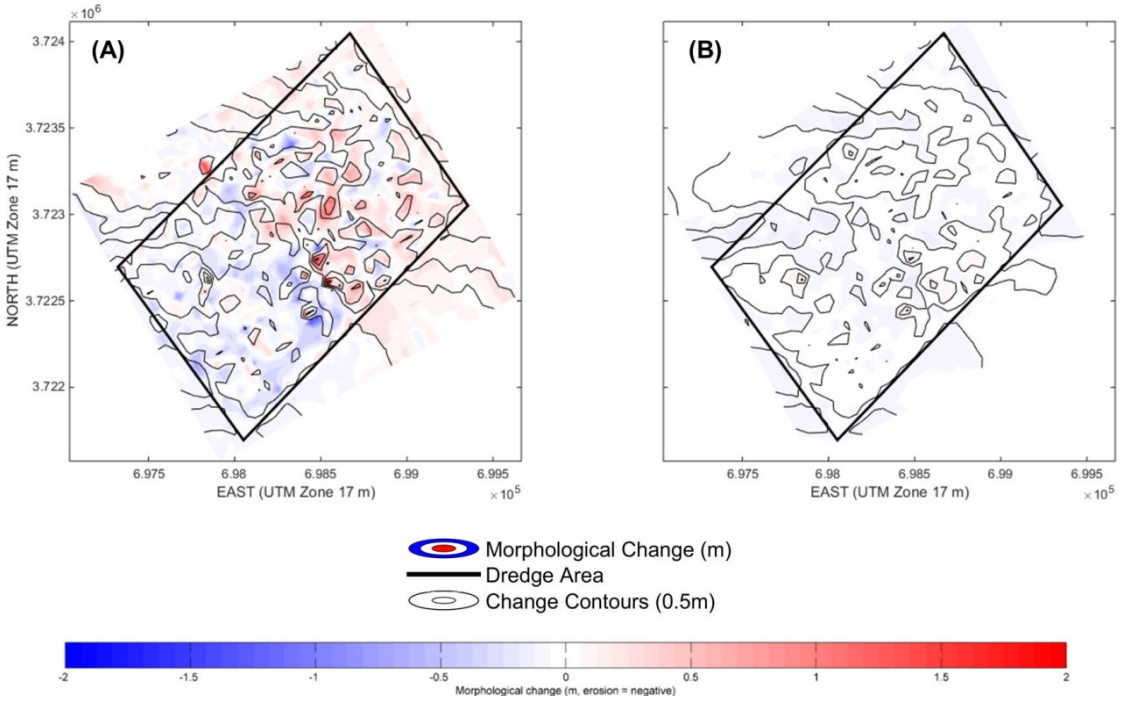

Figure V-7. Morphological change in meters from (A) the measured post to one year post dredge survey data and (B) the month-long CMS simulation using the Lund-CIRP 2006 formulation results multiplied by twelve.

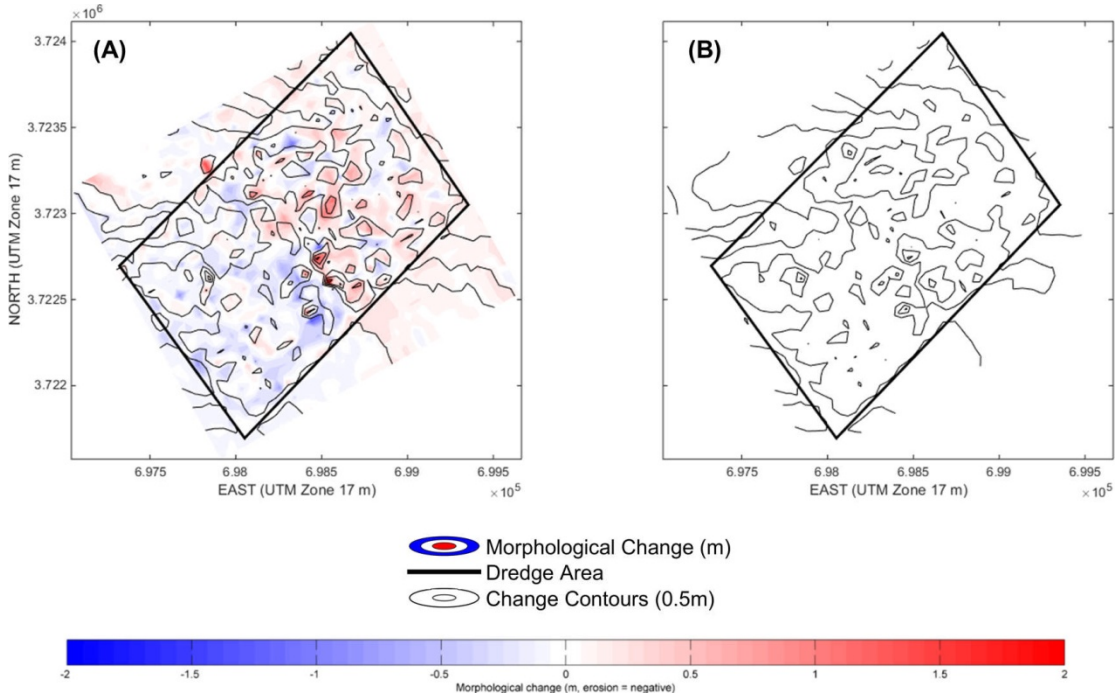

Figure V-8. Morphological change in meters from (A) the measured post to one year post dredge survey data and (B) the month-long CMS simulation using the Van Rijn 1998 formulation results multiplied by twelve.

V.B.1 NearCoM

The magnitude of change from the measured data was best represented by the NearCoM month-long simulation using the Soulsby-Van Rijn 1997 (Soulsby, 1997) formula with the measured data slightly greater in magnitude for certain areas. This NearCoM month-long simulation does a fair job predicting the overall patterns of erosion and accretion within the left half of the dredge area. However, this simulation did not predict the general deposition in the right (east) half of the borrow area. While it is not possible to definitively determine this short-coming in the model predictions, it appears that the measured accretion in this region may be sourced from the far-field sediments. The one area that the NearCoM model did predict well was the location that was excavated to the greatest extent during dredging (the lower half of the dredge area in the center) which then experienced accretion between the post- and one year post-dredging surveys. Overall, in comparing the net total change for all the models to the measured results the NearCoM model net total was the closest.

V.B.2 MIKE21

Both versions (2D and Q3D) of the MIKE 21 non-cohesive sediment transport model under-predicted the magnitude of morphological change compared to the measured data by more than an order of magnitude, with the Q3D approach giving slightly higher values than the 2D approach. From a qualitative point of view the 2D approach reproduced the observed evolution of the seabed (backfilling of dredged areas) better than the results from the Q3D simulation. The wave-related transport component in the Q3D transport model was apparently too large and significantly distorted the calculated morphological response of the post-dredge bathymetry,

making it impossible to recognize the main features of this response from the MIKE 21 model results. As a result, henceforth the MIKE 21 simulations were only run using the 2D approach.

While the results obtained from the 2D sediment transport approach more closely resemble the measured evolution of the post-dredge bathymetry from a qualitative perspective, the bed level changes calculated by the MIKE 21 model were found to be approximately one order of magnitude smaller than their measured counterpart, as previously mentioned. These results were likely due to the fact that the 2D sediment transport model in MIKE 21 was developed for nearshore/surfzone hydrodynamic and related sediment transport conditions, which are quite different from the conditions at the borrow area, which showed larger water depths, weaker currents and non-breaking waves. For example, the assumption in the sediment transport program (STP) that the wave-induced velocity uniformly penetrates the entire water column may not be satisfied at the site for some of the shorter period waves.

V.B.3 CMS

The CMS simulation using the Lund-CIRP formulation compared to the measured data showed bed elevation changes of the same general magnitude as illustrated by the net total bed change in Table V-1. However, from a qualitative perspective the Lund-CIRP simulation did a poor job reproducing the measured morphological change patterns. This simulation showed erosion occurring primarily throughout the dredge area instead of showing the right (east) and left (west) halves of the domain dominated by accretion and erosion, respectively. However, this simulation was able to predict the areas (not magnitude) of maximum accretion and erosion fairly well.

Quantitatively the simulation using the Van Rijn 1998 formula under-predicted the measured change by an order of magnitude and had similar values to the MIKE 21 simulations. Qualitatively, the Van Rijn formulation predicted significant accretion on the left edge of the dredge area which was found in the measured results. Additionally, the lower left quadrant of the dredge area showed accretion in the measured results but exhibited erosion with this formulation. The remainder of the dredge area's morphological change was able to be reproduced qualitatively. However, due to the Van Rijn formulation severely under-predicating the measured bed elevations by an order of magnitude the remainder of the CMS calibration simulations were run using the Lund-CIRP formula.

V.C. METHODS TO IMPROVE OVERALL COMPARISONS

V.C.1. Concerns with Bathymetric Data Sets

As previously mentioned there were high backscatter lineations in the post- and one year post-dredging bathymetric surveys which created sharp boundaries in elevation change. Part of these sharp boundary changes have the potential to be real as a result of the hopper dredging operations; however, it was not possible to definitively determine which changes were a results of the dredging scheme. Additionally, variable data coverage along survey transects between the three bathymetric surveys (Figure V-9) was concerning because numerous cross-lines (southwest-to-northeast orientated transects) of the post-dredging survey are missing and many of the lines were not completed for the one year post-dredging survey. Consistent data coverage

for the time series bathymetry data would have been beneficial to (1) enhance the elevation coverage that was measured following the excavation and (2) allow direct comparisons of the same transects for each survey. As a result, of the sharp boundaries in elevation change and the missing data the surveys were smoothed to improve the quality of data.

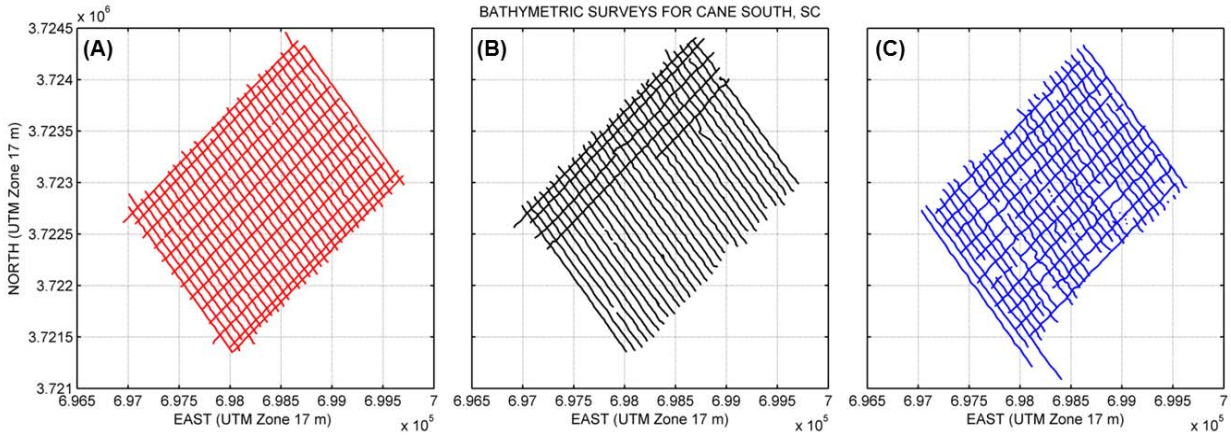

Figure V-9. Cane South bathymetric survey lines for the (A) pre-dredge (B) post-dredge and (C) one year post-dredge surveys.

V.C.2 Re-evaluating Borrow Area Bathymetric Data (Interpolation Schemes)

Evaluation of the triangulated (TIN) surfaces generated from bathymetry data collected for the post dredging surveys in the Cane South borrow area indicated that there were some irregular values and missing data in the datasets. As a result, a different interpolation method followed by a smoothing technique was used to create improved surface models for the post-dredge surveys. Triangulation was first used because it honors the original data points. The Delaunay method of triangulation used in ArcGIS creates triangles that are as equi-angular as possible where each value for a new node is as close as possible to a known data point. The main disadvantage of this method is that the surfaces generated are often not smooth and give a jagged appearance. This is caused by discontinuous slopes at the triangle edges and was observed in the post dredging surfaces produced for the study area. Additionally, triangulation can be unsuitable for extrapolation beyond the extent of the observed data points, which as previously stated numerous data points were missing from both post dredge surveys.

Therefore, a kriging interpolation method was then used to estimate surface values where no measurements were taken. The resulting surface, or grid, contains equally spaced data points. Kriging was used because it is a weighted average method of interpolation that assumes that the spatial variation in a dataset is the same at all locations. It produced an estimate of the underlying surface by a weighted average of the data, with weights declining as the distance increased between the point at which the surface is being estimated and the locations of the data points. Kriging is a smooth interpolation method and essentially filters the data points. The method does not intend to create a surface that duplicates reality, the point is to avoid creating errors by following the general spatial trends in the observed data points. The spatial variation was

expressed as a semi-variogram which controls the way that the kriging weights were assigned to data points during interpolation, and therefore controlled the quality of the results. The semi-variogram was estimated from the observed data values by selecting the statistical model that best fits the dataset. This process involved some judgment and required some "trial and error" computations. In this case, ordinary kriging using the spherical model in ArcGIS 3-D Analyst was chosen to generate appropriate surfaces for the irregular bathymetry data.

The post-dredging bathymetry surfaces were refined further using the aggregate tool in ArcGIS Spatial Analyst. The aggregation statistical method produced a reduced-resolution version of the surface where each output cell in the grid contains the average of the cells that neighbor that cell. The output value is calculated by determining the sum, minimum, maximum, mean, or median value of the cells from the input raster that fall within the output cell's specified spatial extent. For these datasets, the mean statistics option was used and produced output grids with 10 meter cells. This increased the cell size from the kriging grids so that the surfaces were smoothed but continued to provide a good representation of the underlying spatial pattern in the datasets.

The updated smoothed post- and one year post-dredging bed elevations are shown in Figure V-10 and V-11, respectively. Additionally, the morphological change plots using these smoothed datasets are shown in Figure V-12, V-13, and V-14. In these figures the sharp boundaries seen in the previous change plots have been smoothed in order to get a better representation of the overall morphological changes. The three morphological models' initial bathymetry was updated with the smoothed post-dredge dataset to be run on all simulations henceforth.

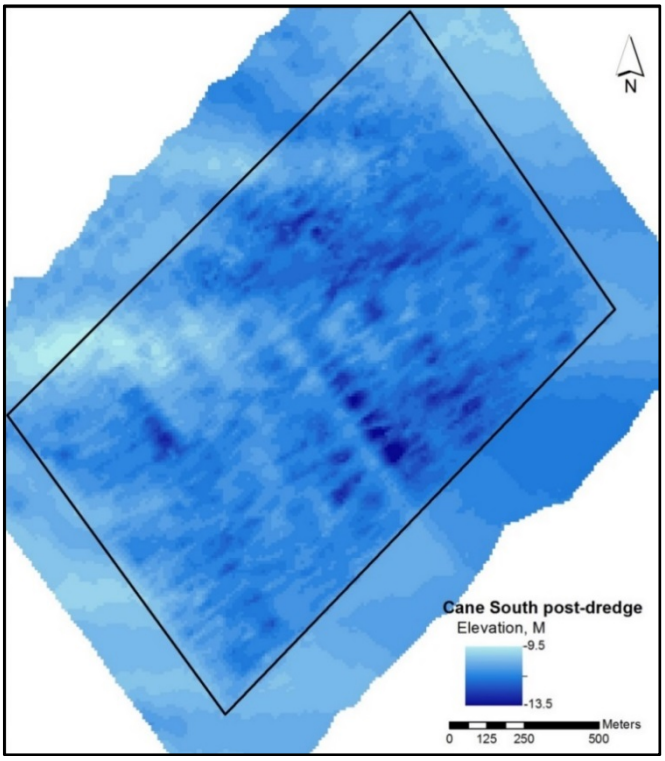

Figure V-10. Smoothed Cane South post-dredge bathymetry. The bed levels are in m NAVD88.

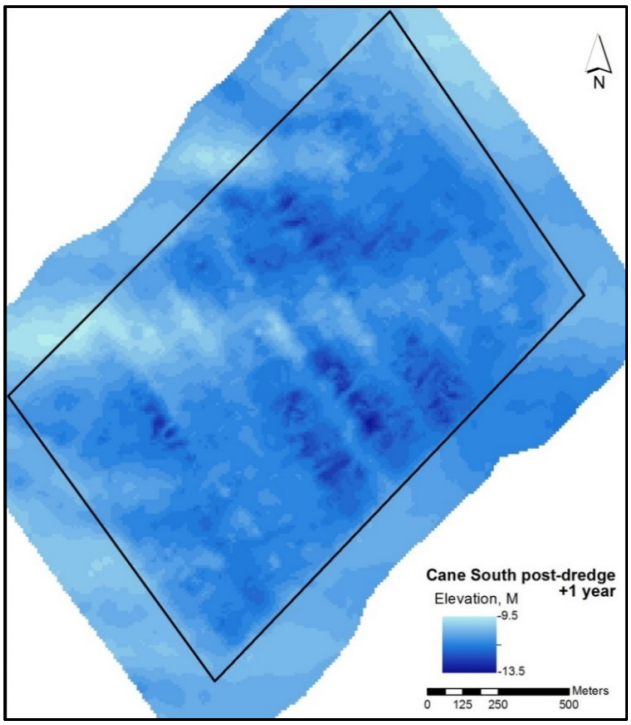

Figure V-11. Smoothed Cane South one year post-dredge bathymetry. The bed levels are in m NAVD88.

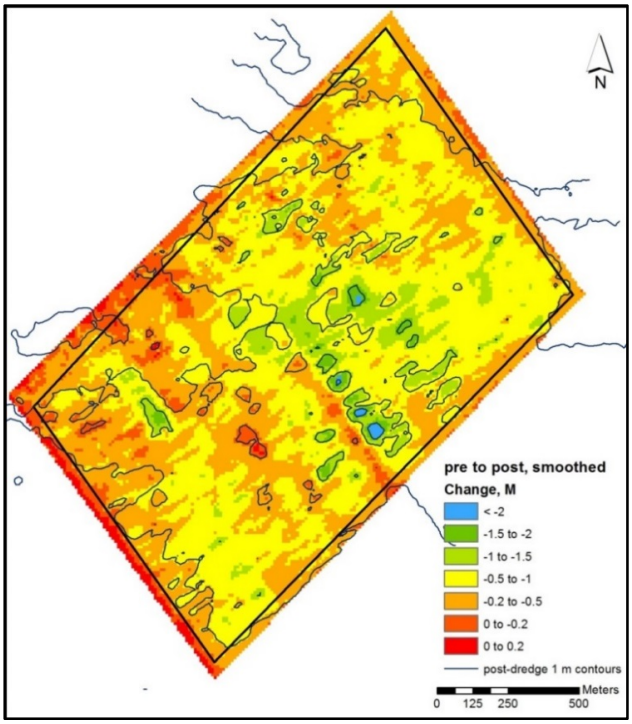

Figure V-12. Morphological change between the Cane South pre-dredge and the smoothed post-dredge bathymetric surveys. The black rectangle identifies the dredged area.

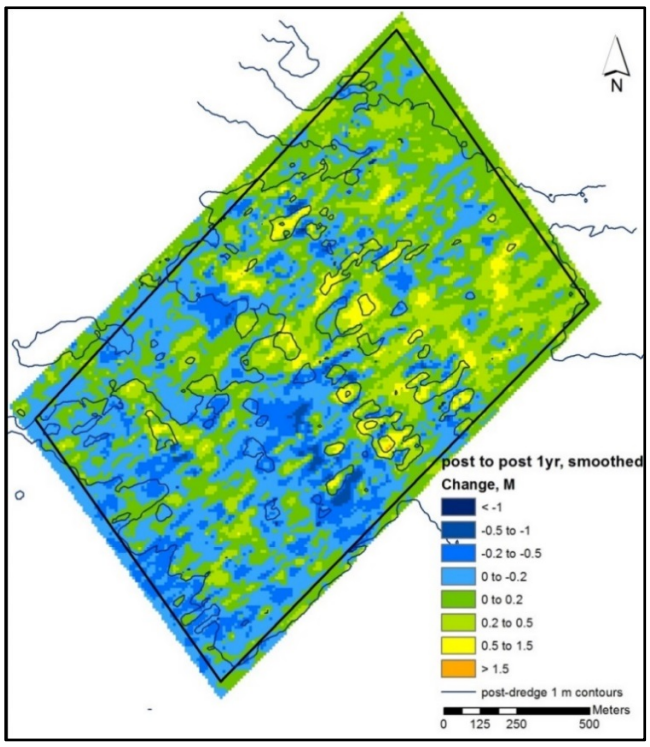

Figure V-13. Morphological change between the smoothed Cane South post-dredge and one year post-dredge bathymetric surveys. The black rectangle identifies the dredged area.

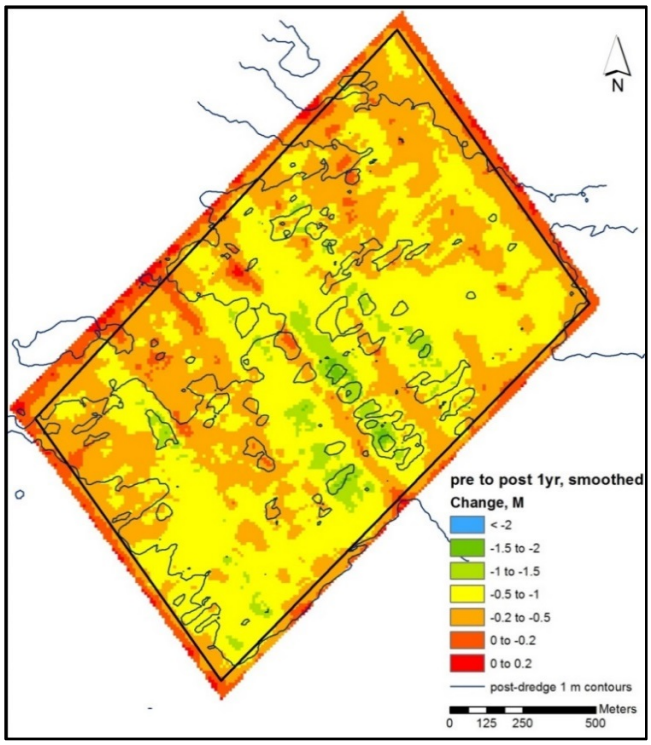

Figure V-14. Morphological change between the Cane South pre-dredge and the smoothed one year post-dredge bathymetric surveys. The black rectangle identifies the dredged area.

V.C.3 Model Grid Refinement

In addition to smoothing the post-dredging bathymetric datasets to enhance the validity of the models, the resolution model grids/meshes also was increased. The bathymetry plots and the morphological change plots show that the spatial elevation changes rapidly. To better resolve the long narrow troughs created by the hopper dredge excavation of Cane South, the resolution was increased from 50 m to 25 m. Comparison plots of the morphology change with the different grid spacing and the smoothed initial bathymetry are shown in Figure V-15, V-16, and V-17. The net morphological change and maximum changes values are displayed in Table V-2. From the increased grid spacing, the models were better able predict to the finer bed changes observed in the measured data. However, with this increase in resolution the computational time for each simulation increased more than five times. The NearCoM, MIKE 21 and CMS month-long simulations with 25 m grid resolution took approximately 52 hours using 32 processors, 65 hours using an 8 core processor PC, and 13 hours using an 8 core processor PC, respectively. Quantitatively and qualitatively the results from the smoothed initial bathymetry and 25 m grid spacing model simulations gave consistently better results than the non-smoothed initial bathymetry simulations with 50 m simulations which made the longer computational simulations advantageous. Furthermore, the increase in grid resolution would have taken significantly more computation time to complete the year-long simulation and further justified the use of the month-long simulation multiplied by twelve as a useful speed up factor.

Table V-2. Net volume changes and max erosion and accretion values within the dredge area for the measured data and the month-long model simulations multiplied by twelve using the smoothed bathymetry and 25 meter grid spacing. A negative value indicates erosion.

Model	Net erosion (m^3)	Net deposition (m^3)	Net total (m^3)	Morphological change (m)	
				Maximum erosion	Maximum accretion
Measured	-139,734	245,070	105,336	-0.94	1.37
NearCoM Soulsby-Van Rijn 1997	-86,892	92,980	6,088	-0.49	0.52
MIKE 21 2D	-4,979	5,953	974	-0.03	0.05
CMS Lund-CIRP 2006	-102,564	31,905	-70,659	-0.25	0.45

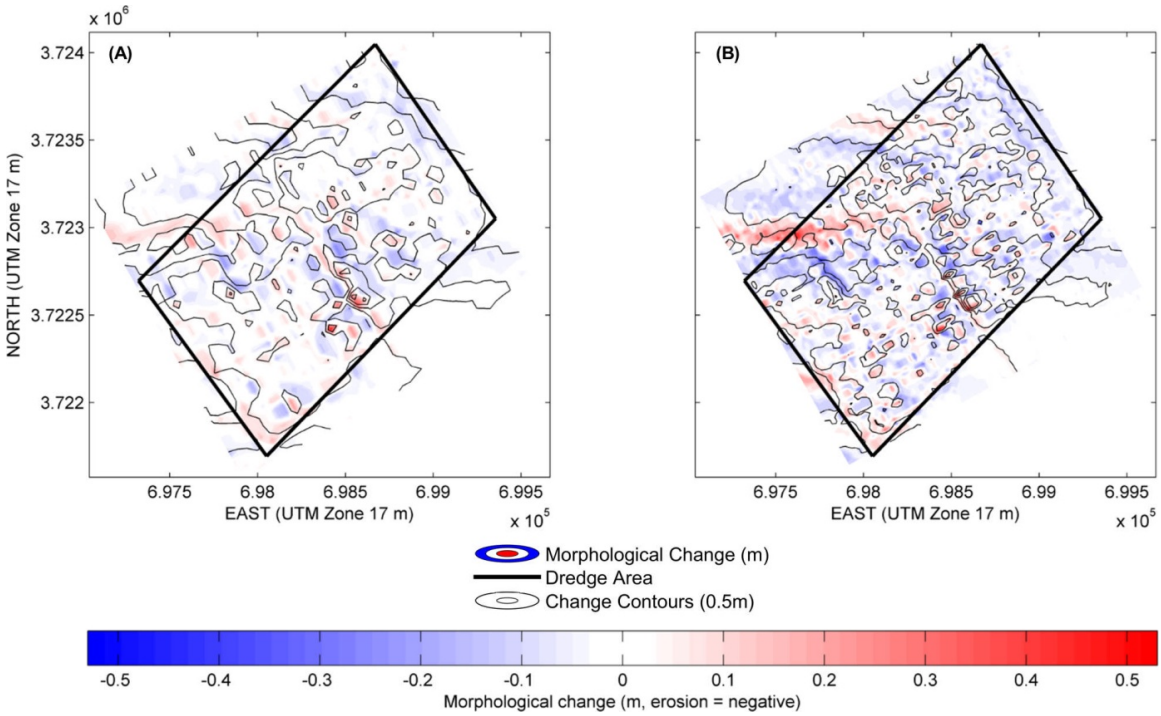

Figure V-15. Morphological change in meters from the NearCoM month-long simulation multiplied by twelve using the Soulsby-Van Rijn formula with the smoothed initial bathymetry and grid spacing of (A) 50 m and (B) 25 m.

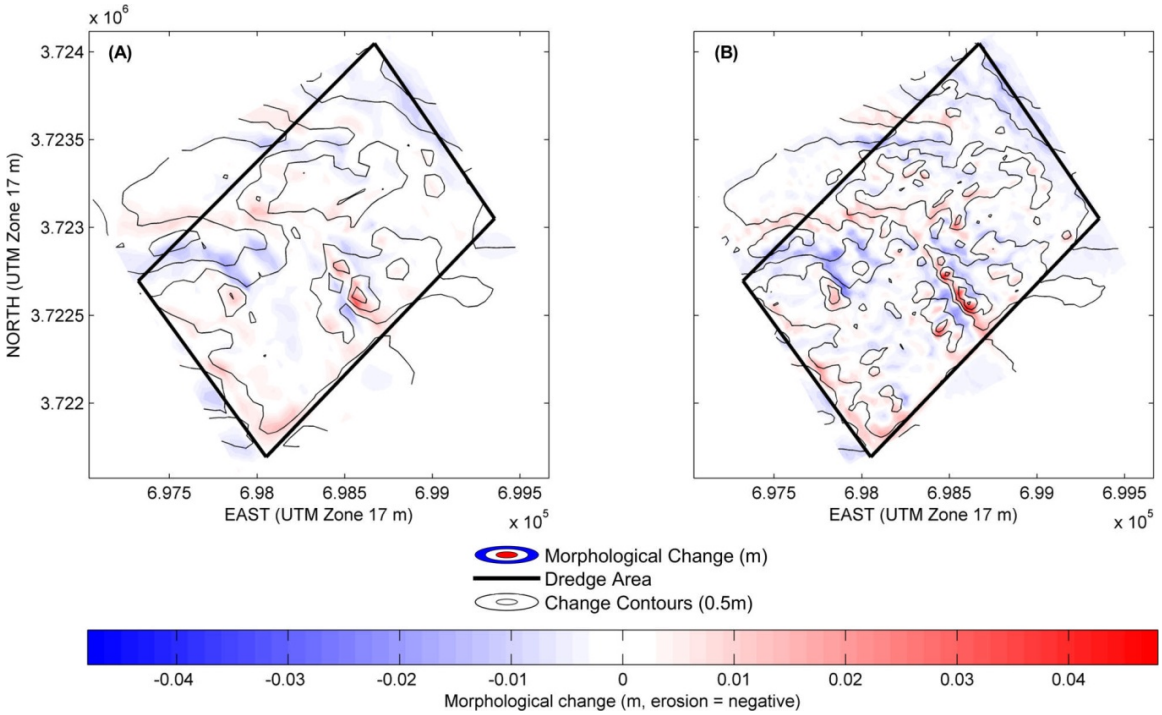

Figure V-16. Morphological change in meters from the MIKE 21 month-long simulation multiplied by twelve using the 2D approach with the smoothed initial bathymetry and grid spacing of (A) 50 m and (B) 25 m.

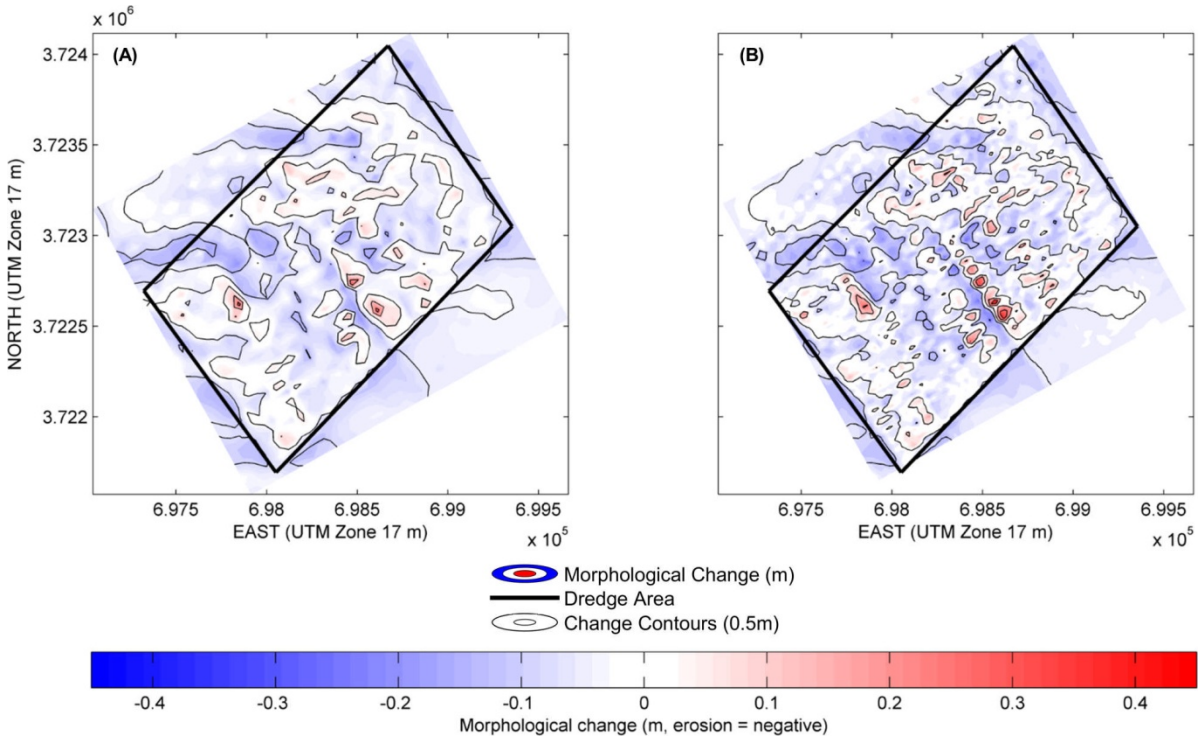

Figure V-17. Morphological change in meters from the CMS month-long simulation multiplied by twelve using the Lund-CIRP formula with the smoothed initial bathymetry and grid spacing of (A) 50 m and (B) 25 m.

V.C.4 Sediment Transport Formulations

As previously shown in Chapter IV, the tidal currents at the Cane South borrow area are generally small with the maximum magnitude less than 0.2 m/s in the computational domain. With these relatively weak tidal currents the current induced bottom stress rarely reached the threshold value able to mobilize the sediment at the dredge depth. As a result it was determined that the sediment transport at Cane South was strongly wave-dominated. Even though the three sediment transport models incorporated wave-induced sediment transport the model formulations favored current-dominated conditions, where waves can be responsible for mobilizing the sediment, but combined ambient wave-induced and tidal currents transport the suspended material. Additionally, the sediment transport due to wave asymmetry is neglected in the existing form of the three models. As previously referenced, the SANDPIT project used scaling factors beyond the typical variation of model parameters and altered the sediment transport formula to deal with the inabilities of the sediment transport formulas to match the observed transport. The only model that was easily able to alter the sediment transport and incorporate wave asymmetry was NearCoM due to its open source code. The scaling factors used for this application are discussed below.

At this point, the NearCoM simulations were all run using the Soulsby-Van Rijn 1997 sediment transport model. This formulation modeled the effect of waves on sediment transport as an enhancement to the current-induced transport. Additionally, the Soulsby-Van Rijn formula

calculated the transport in the direction of the tidal current as well as the direction of wave propagation and assumed the bed to be rippled. All of these assumptions made this transport model unsuited for the Cane South application, where the sediment transport was mainly related to the action of the waves. For these reasons it was decided to implement an alternative sediment transport formula, based on Van Rijn (1991), in NearCoM which was more suited for this application. The Van Rijn 1991 formula predicts the total time-averaged sediment transport rate by vector addition of the sediment transport rate due to the current, which has the same direction as the current, and that induced by the waves which is pointed in the direction of wave propagation, respectively. A more detailed explanation on how the current and wave induced sediment transport rates were calculated is discussed below. Furthermore, compared to other more recent sediment transport formulations by Van Rijn, the 1991 formula was advantageous because it predicted the sediment transport by means of a simple algebraic expression which did not require the numerical integration of additional partial differential equations at each time step, thus saving computational power and time.

For the Van Rijn 1991 the current induced sediment transport rate due was computed as sum of bedload and suspended load. The bedload was computed in terms of:

- a dimensionless bed shear stress parameter
- D_{50}
- the friction velocity (related to effective bed shear stress)
- the particle Reynolds number.

The dimensionless bed shear stress parameter depends on the critical bed shear stress and the effective bed shear stress. The effective bed shear stress takes into account the shear stress induced both by the current and the waves. In order to estimate the shear stress due to waves it was necessary to compute the wave friction factor, which depends on the wave-related bed roughness. The wave-related bed roughness was fixed equal to 3 times the ripple height in the ripple regime and equal to 30 times d_{90} in the sheet flow regime. The estimation of the bed regime (sheet flow or rippled bed) as well as the prediction of ripple height made use of the Soulsby & Whitehouse (1997) predictor. The suspended load rate due to the current alone was evaluated as the product of:

- the local water depth
- the depth-averaged velocity
- the reference concentration
- a constant which depends on the vertical distribution of the sediment concentration.

The wave-related contribution to the sediment transport was computed by a formula similar to that used for computing the current-related sediment transport. In this wave induced formula the friction velocity (related to effective bed shear stress) was substituted by the peak orbital velocity in addition to other wave-related quantities. The net wave transport was calculated by the difference in the average positive (in the direction of wave propagation) and negative wave induced sediment transport components. These components were calculated on the basis of

second order wave theory (Soulsby, 1997). For asymmetric waves, these wave components will be different magnitudes.

To evaluate the two NearCoM sediment transport formulas (Soulsby-Van Rjin 1997 and Van Rjin 1991, shown in Table V-3) the time averaged sediment transport volumes across the dashed boundaries shown in Figure V-18 were compared. The total Van Rijn 1991 current related sediment transport (obtained from summing the two Van Rijn 1991 current induced columns in Table V-3) is smaller than the total sediment transport predicted by Soulsby-Van Rijn 1997. However, the direction of transport is the same at each boundary for both the Van Rijn 1991 current induced sediment transport and the Soulsby-Van Rijn 1997 total sediment transport. On the contrary the wave induced sediment transport from the Van Rijn 1991 formula was in the opposite direction of the current transport and two to three orders of magnitude larger than current induced transport and the total transport from the Soulsby-Van Rijn 1997 formula. Therefore, it was concluded that the total sediment transport and bottom topography of the borrow area was strongly wave-dominated.

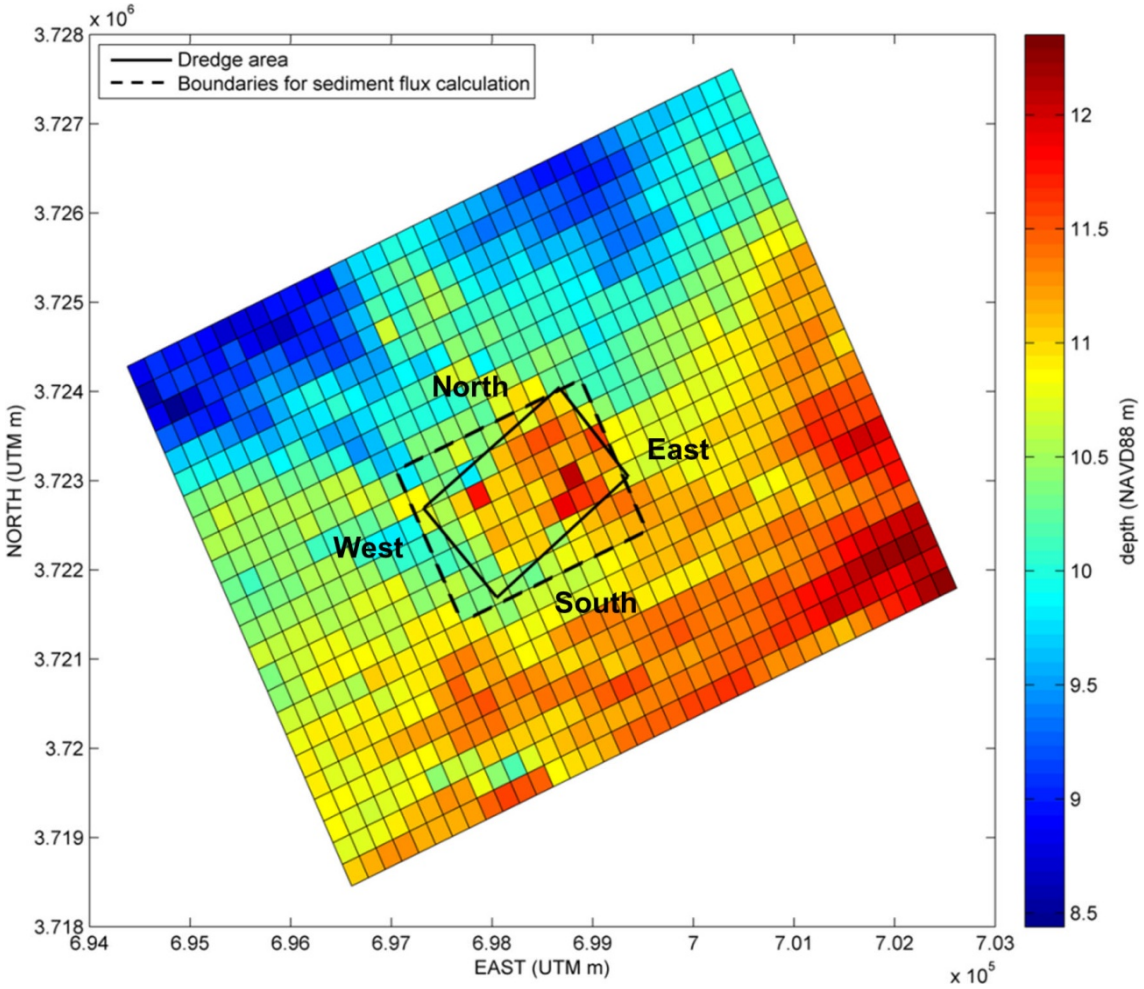

Figure V-18. Outline of the NearCoM grid and bathymetry for the Cane South application. The boundaries used to calculate the sediment flux are shown with the dashed line, while the dredge area is outline in solid line.

Table V-3. The sediment transport averaged fluxes from the month-long simulations at the Cane South borrow area at the four boundaries (dashed lines in Figure V-18) of the computational domain computed according to Soulsby-Van Rjin 1997 and Van Rjin 1991. Negative values mean outward flux.

Sediment transport formula		Soulsby-Van Rijn 1997	Van Rijn 1991			
Sediment transport ($m^3 \times 10^3$)		Total load	Current induced bed load	Current induced suspended load	Wave induced	Total load
Boundary	**North**	5.53	0.48	2.20	-99.98	-97.31
	East	-5.75	-0.60	-2.39	84.26	81.27
	South	-2.78	-0.39	-0.14	239.61	239.08
	West	3.66	0.56	0.54	-247.63	-246.54

The morphology change volumes from the measured data and NearCoM month-long simulations multiplied by twelve with 25 meter grid spacing using the Van Rijn 1991 sediment transport formula and the Soulsby-Van Rijn 1997 formula are listed in Table V-4. Additionally, the morphology change from the measured and these two NearCoM simulations were plotted in Figure V-19. Quantitatively, the NearCoM simulation using the Van Rijn 1991 formulation showed approximately triple the amount of net erosion and deposition and maximum values an order of magnitude more than the simulation using the Soulsby-Van Rijn 1997 formula. The net total volume from the Van Rijn 1991 formula showed erosion, which was the opposite of the measured data that showed deposition. This primarily results from the substantial increase in wave-induced transport associated with the Van Rijn 1991 formula. Figure V-20 shows an interpolated grid of erosion and deposition points within the dredge area for the measured data and the two NearCoM simulations. Morphological change less than 10 cm was excluded to account for bathymetric measurement errors. While the Van Rijn formulation shows net erosion, the Van Rijn 1991 simulation was able to better qualitatively duplicate the accretional and erosional patterns seen in the measured data plot in the right (east) and left (west) halves of the dredging area, respectively, than the Soulsby-Van Rijn 1997 simulation. Quantitatively, 56% of the points showed agreement with the measured data in the Van Rijn 1991 simulation as compared to 24% for the Soulsby-Van Rijn 1997 simulation.

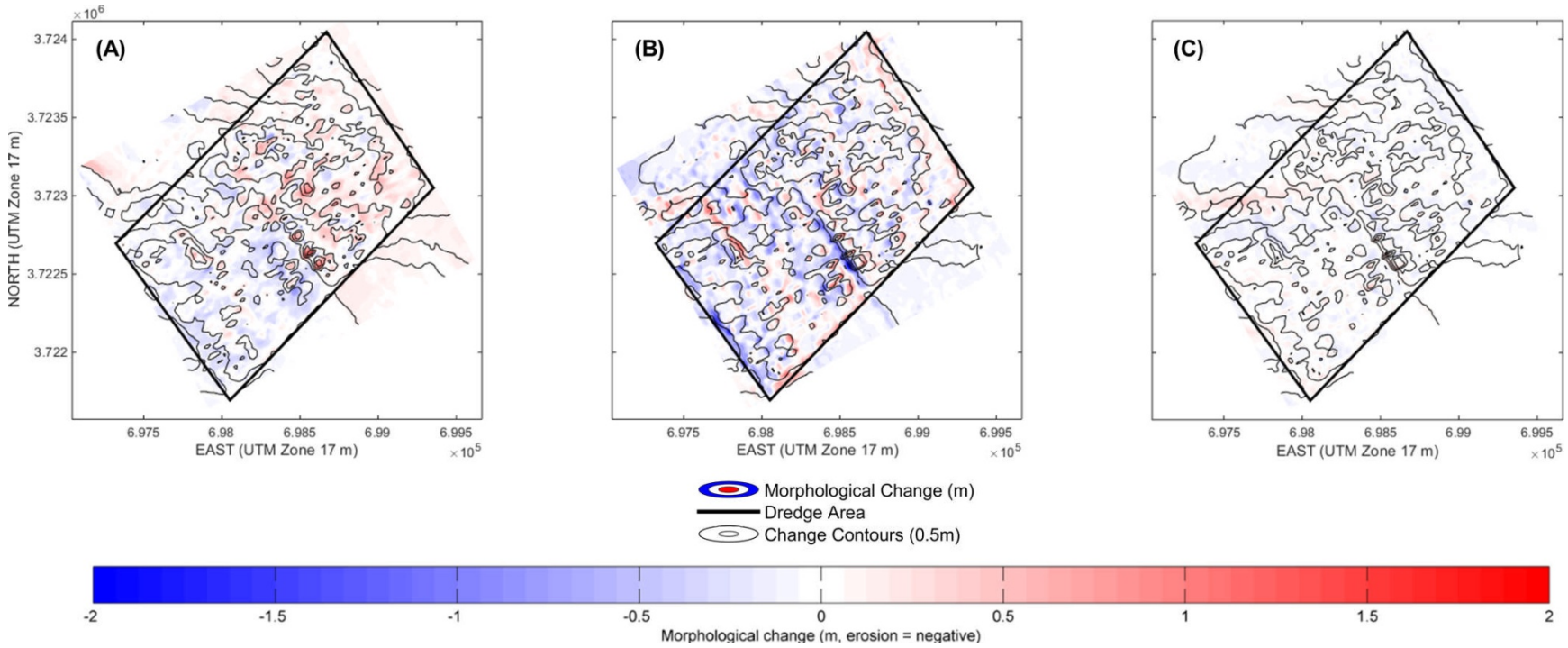

Figure V-19. Morphological change in meters from (A) the measured post to one year post dredge survey data, (B) the month-long NearCoM simulation using the Van Rijn 1991 formulation results multiplied by twelve and (C) the month-long NearCoM simulation using the Soulsby-Van Rijn 1997 formulation results multiplied by twelve.

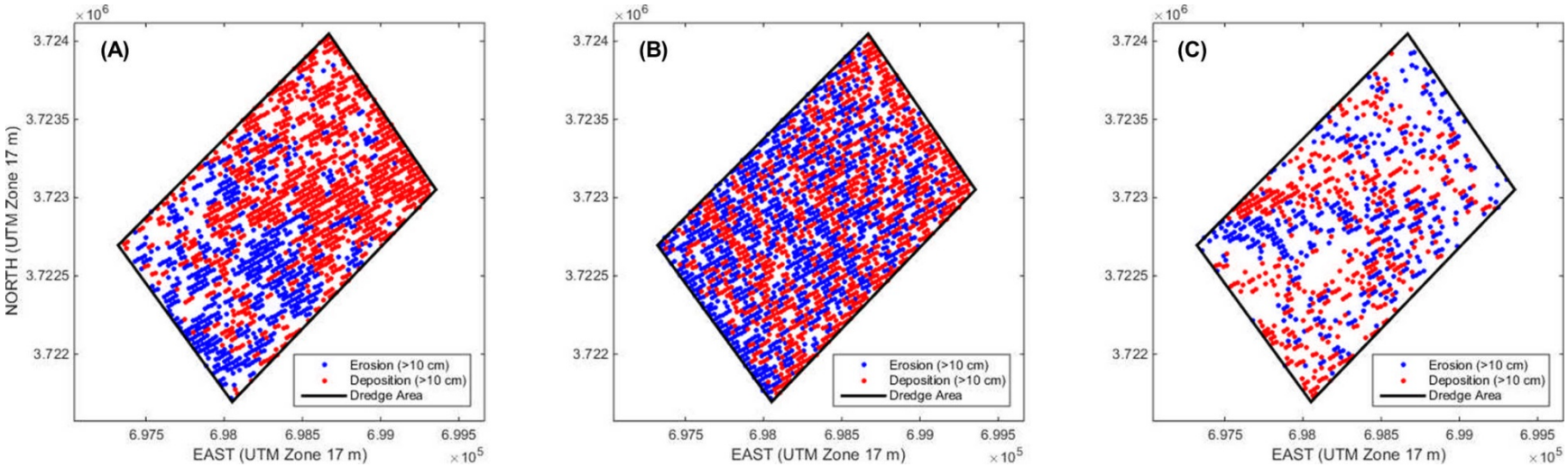

Figure V-20. Erosion and deposition patterns from (A) the measured post to one year post dredge survey data, (B) the month-long NearCoM simulation using the Van Rijn 1991 formulation results multiplied by twelve and (C) the month-long NearCoM simulation using the Soulsby-Van Rijn 1997 formulation results multiplied by twelve. Morphological change less than 10 cm was excluded to account for bathymetric measurement errors.

Table V-4. Net volume changes and max erosion and accretion values within the dredge area for the measured data and the month-long model simulations multiplied by twelve using the smoothed bathymetry and 25 meter grid spacing. A negative value indicates erosion.

Model	Net erosion (m^3)	Net deposition (m^3)	Net total (m^3)	Morphological change (m)	
				Maximum erosion	Maximum accretion
Measured	-139,734	245,070	105,336	-0.94	1.37
NearCoM Van Rijn 1991	-350,391	319,916	-30,475	-2.09	1.72
NearCoM Soulsby-Van Rijn 1997	-86,892	92,980	6,088	-0.49	0.52

V.C.5 Slope Factor

As an attempt to obtain closer quantitative results to the measured data from NearCoM using the Van Rijn 1991 formula, a slope factor was added to the formulation to incorporate the effect of the morphological slope on sediment transport. This slope factor assumed that the bed slope only affected the sediment transport occurring close to the bed. To add this factor both the current- and wave-induced components of the total transport formula were modified by additional terms that included the effect of the local slope of the bed formations, the quantity of sediment present, and a correction factor based on the Shields parameter. The addition of this slope factor caused a minimal change to the qualitative or quantitative results. The net volume changes from the measured data and the NearCoM simulation with and without the slope are listed in Table V-5. Quantitatively, this factor created slightly more erosion and deposition in the dredge area and a net total change that was approximately 2,000 m^3 less erosional than the simulation without the slope factor. As a result of the slight correction to the net total the slope factor was included to the NearCoM simulations hereafter.

Table V-5. Net volume changes and max erosion and accretion values within the dredge area for the measured data and the month-long model simulations multiplied by twelve using the smoothed bathymetry and 25 meter grid spacing with and without the slope factor. A negative value indicates erosion.

Model	Net erosion (m^3)	Net deposition (m^3)	Net total (m^3)	Morphological change (m)	
				Maximum erosion	Maximum accretion
Measured	-139,734	245,070	105,336	-0.94	1.37
NearCoM Van Rijn 1991 without slope	-350,391	319,916	-30,475	-2.09	1.72
NearCoM Van Rijn 1991 with slope	-351,915	322,756	-29,159	-2.09	1.71

V.C.6 Model Calibration Factor

Since the MIKE 21 and CMS sediment transport formulations could not be modified within the models to include the substantial influence of wave-induced transport associated with wave asymmetry, a scaling factor had to be used to better match the observed transport and morphological change magnitudes. The only available scaling factor that can be used in MIKE 21 to increase the amount of morphological change by the needed order of magnitude is a factor that simply multiplied the bed level changes calculated by MIKE 21 on the basis of gradients in the sediment transport field. A similar model calibration factor (MCF) was used for CMS.

While specifying a large calibration factor may destabilize the hydrodynamic solution by generation of internal waves during the update, the bed level changes calculated by the MIKE 21 sediment transport model are relatively small and calibration factors of up to 50 could be used without any negative impact on the stability of the solution. Numerous calibration factors were tested for MIKE 21 and CMS and based on qualitative and quantitative comparisons to the measured data it was determined that a MCF of 25 and 3 was most appropriate for the models, respectively. The morphological change results from these simulations are shown in the final model results, discussed below.

V.C.7 Online Correction Method

Modeling the natural morphological change on the inner continental shelf is challenging due to complex sediment transport processes driven by multi-scale hydrodynamics, including surface waves, tidal currents, and ocean circulation, as well as wind-induced currents during storms. As a result of these hydrodynamic processes occurring over varying time periods an additional difficulty is created for morphology modeling in dealing with time difference between processes that are always occurring, such as waves and tidal currents, compared to processes that randomly occur, such as a storm (Roelvink, 2006). Typically the bed changes from the processes that are constantly naturally occurring are minimal and occur over a long time period. As a result, the system can be treated as in a state of equilibrium or quasi-equilibrium. However, if an event, such as a storm or offshore sediment extraction, occurs the seabed will be taken out of equilibrium due to relatively rapid morphological changes. In numerical modeling, a model is highly sensitive to a system not being in equilibrium and typically will not run unless the seabed geometry, sediment characteristics, and hydrodynamic forcing are in an equilibrium or quasi-equilibrium state. As a result, typically when a numerical model is not in equilibrium the solution used is to spin up the model, which entails starting the model prior to the desired start time to ensure the system is in equilibrium at the start. To spin up the model is computationally demanding and as a result infeasible when trying to calibrate a model or run various morphological settings and hydrodynamic conditions.

With regards to the Cane South application and the idealized cases, discussed in Chapter VI, the purpose was to determine the ability of the three morphological models to duplicate the changes at the borrow area as a result of the dredging and to evaluate the model's response to a variety scenarios, respectively. Upon commencing the idealized cases simulation it was determined that the dredged borrow area caused the system to not be in equilibrium. As a result, a new computational efficient method was applied to replace having to spin up the model for the numerous scenarios. This method was called the Online Correction Method (OCM). This method

allows only the modifications as a result of the dredging to be extracted. The OCM is implemented by conducting two scenarios concurrently on two separate processors on a parallel computer. The first scenario, Model 1, is a simulation of the seabed without the excavation, while the second scenario, Model 2, is a simulation of the seabed with the dredging. The two model simulations have the same hydrodynamic boundary conditions (e.g. tidal current velocities, water surface elevation, and wave parameters), sediment characteristics and numerical parameters. For Model 1 it is assumed the bed is in equilibrium and that the seabed will not change under the given hydrodynamic conditions. The seabed evolution equation for Model 1 can be written as:

$$(1-s)\frac{\partial h}{\partial t} = -\nabla \cdot Q_1 + \mathrm{Err} = 0 \quad (1)$$

where Q_1 represents sediment transport rate calculated based on the given hydrodynamic conditions and the sediment transport formulation, h is seabed elevation, t is time, s is bed porosity. Err represents the error induced by the misfit between hydrodynamic conditions and initial bathymetry setting, which for Model 1 is balanced by the sediment transport rate making it so there is no change to the bed elevation.

For Model 2, the seabed evolution equation is

$$(1-s)\frac{\partial h}{\partial t} = -\nabla \cdot Q_2 + \mathrm{Err} \quad (2)$$

where Q_2 is the sediment transport rate based on the given hydrodynamic conditions, the sediment transport formula and the excavation geometry. It is assumed that Err is the same as in (1) and is not related to the excavation geometry. As a result, the seabed evolution for Model 2 can be rewritten as

$$(1-s)\frac{\partial h}{\partial t} = -\nabla \cdot (Q_2 - Q_1) \quad (3)$$

to calculate the seabed change due to the dredging.

V.C.7.a Numerical Implementation

A schematic diagram of the OCM is shown in Figure V-21. A parallel scheme was implemented using two computer processors to allow the concurrent execution of Model 1 and 2. Additionally, the Message Passing Interface (MPI) was applied to allow data (e.g. the time step and the sediment transport rates) to be transferred between the two processors. The time step used for Model 1 and 2 was determined by choosing the smaller of the two values calculated by the CFL condition. At each time step the seabed that was dredged was updated by the sediment

transport rate calculated by Model 1, Q_1, and Model 2, Q_2. The seabed that was not excavated was not updated.

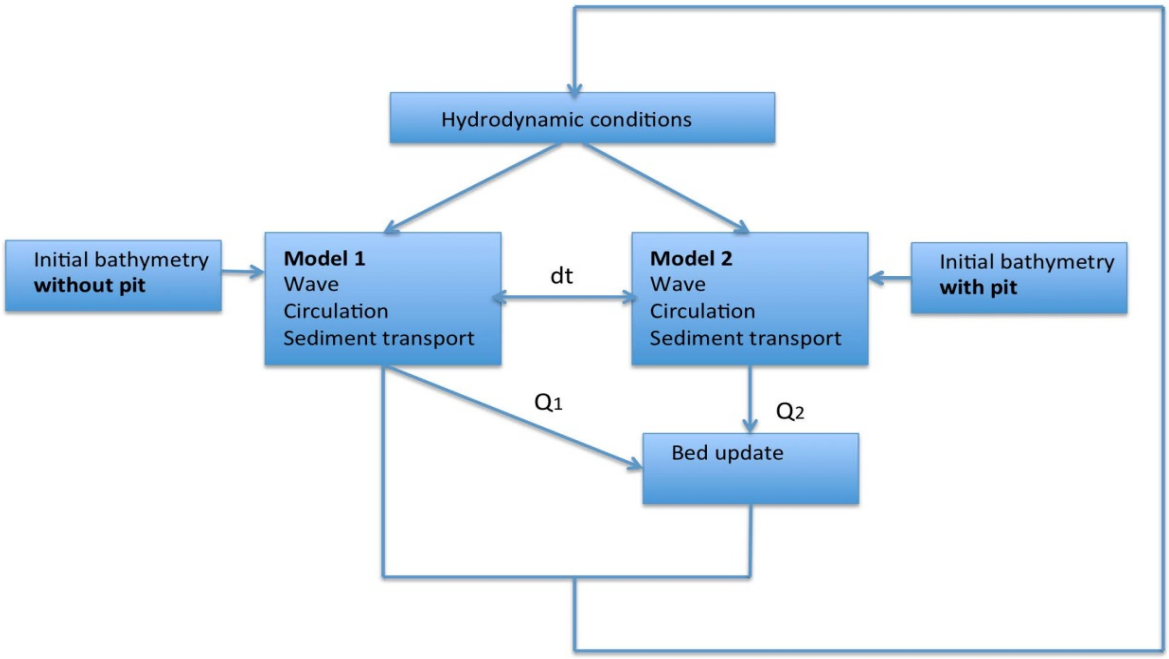

Figure V-21. Schematic diagram of the Online Correction Method. Q_1 and Q_2 are the sediment transport rates from Model 1 and 2, respectively. The time step is denoted as dt and is the same for both models.

V.C.7.b Idealized Case

To demonstrate the effectiveness of this method an idealized example was completed. For this example the domain considered is shown in Figure V-22. This figure shows the bathymetry and the ideal borrow area that was created based on the cross-shore profile measured at the offshore borrow area Cane South in South Carolina. The water depth at the borrow area was approximately 12 m and its shape was modeled roughly as a rectangular box with a length and width of 1,414 m and a depth of 1 m. Additionally, to model this domain without the borrow area the bathymetry without the borrow area was created and is shown in Figure V-23. The hydrodynamic forcing applied at the offshore boundary for this example was a constant wave condition. A tidal boundary condition was not applied to this example for simplicity. The wave forcing used a wave with a significant wave height of 2 m, a peak wave period of 10 s and a peak wave direction of normal incidence. From this wave condition a JONSWAP spectrum was created and applied to the entire eastern boundary and part of the southern and northern boundaries to avoid wave diffraction shadows at the lateral boundaries.

First, to demonstrate the problem caused by the system not being in equilibrium at the start of the simulation two simulations were carried out that used the original NearCoM code without the OCM. The first simulation used the bathymetry without the put, while the other simulation used the bathymetry with the borrow area. Both of these simulations were run for a year-long time period and the elevation changes from these simulations at the transect in Figure V-22 are shown

in Figure V-24. If the seabed was in equilibrium there would be minimal to no change in the profile without the borrow area. However, the results from the simulation without the borrow area show that the profile is not in equilibrium, where the seabed underwent significant erosion nearshore which continued seaward. The amount of erosion that occurred to the profile decreased with time as the profile reached equilibrium as the profile shape adjusted to the incoming wave field. The profiles with the borrow area, besides the noticeable bed change around the borrow area, showed a similar pattern of erosion as the simulation with the borrow area. Therefore, the profile adjustment to the equilibrium conditions may bias the morphodynamic modeling results within the "footprint" of the borrow area.

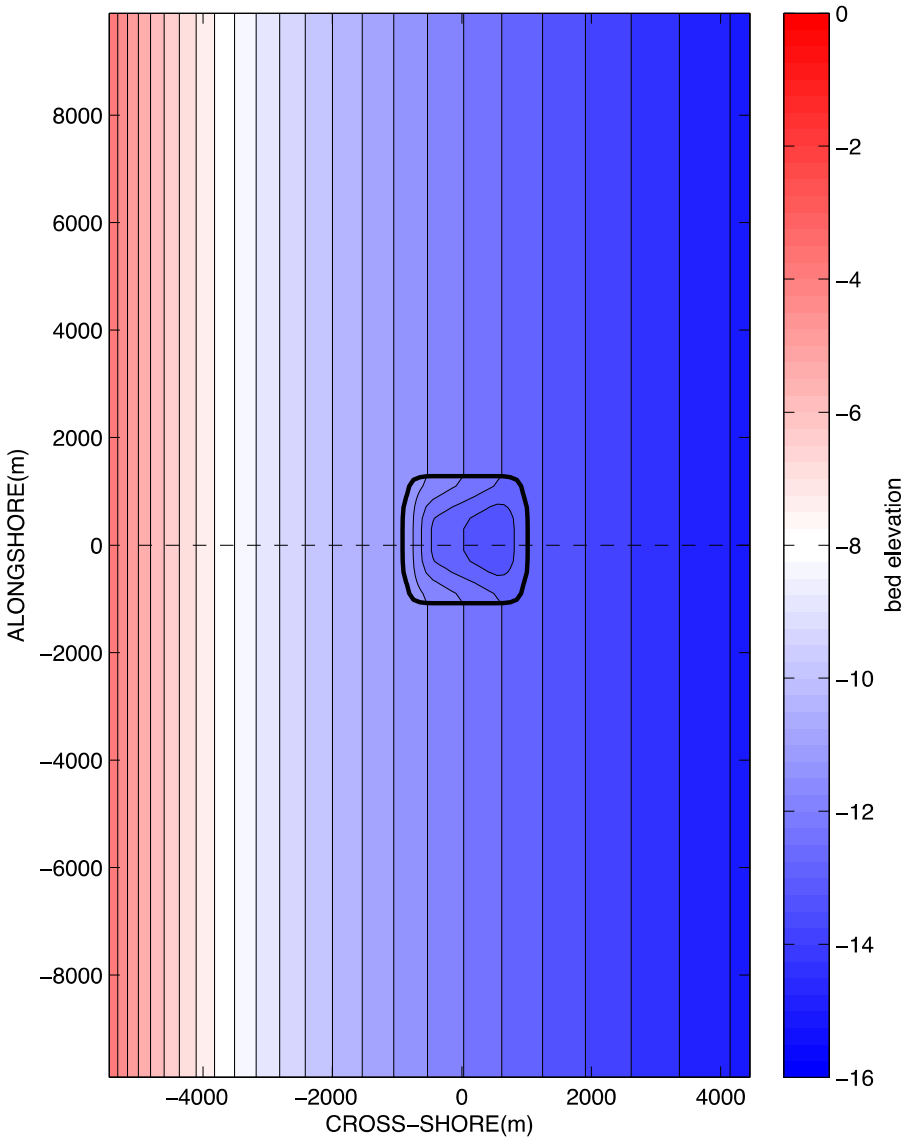

Figure V-22. Bathymetry with a borrow area. The dashed line is the transect used to show profile changes in Figure V-24.

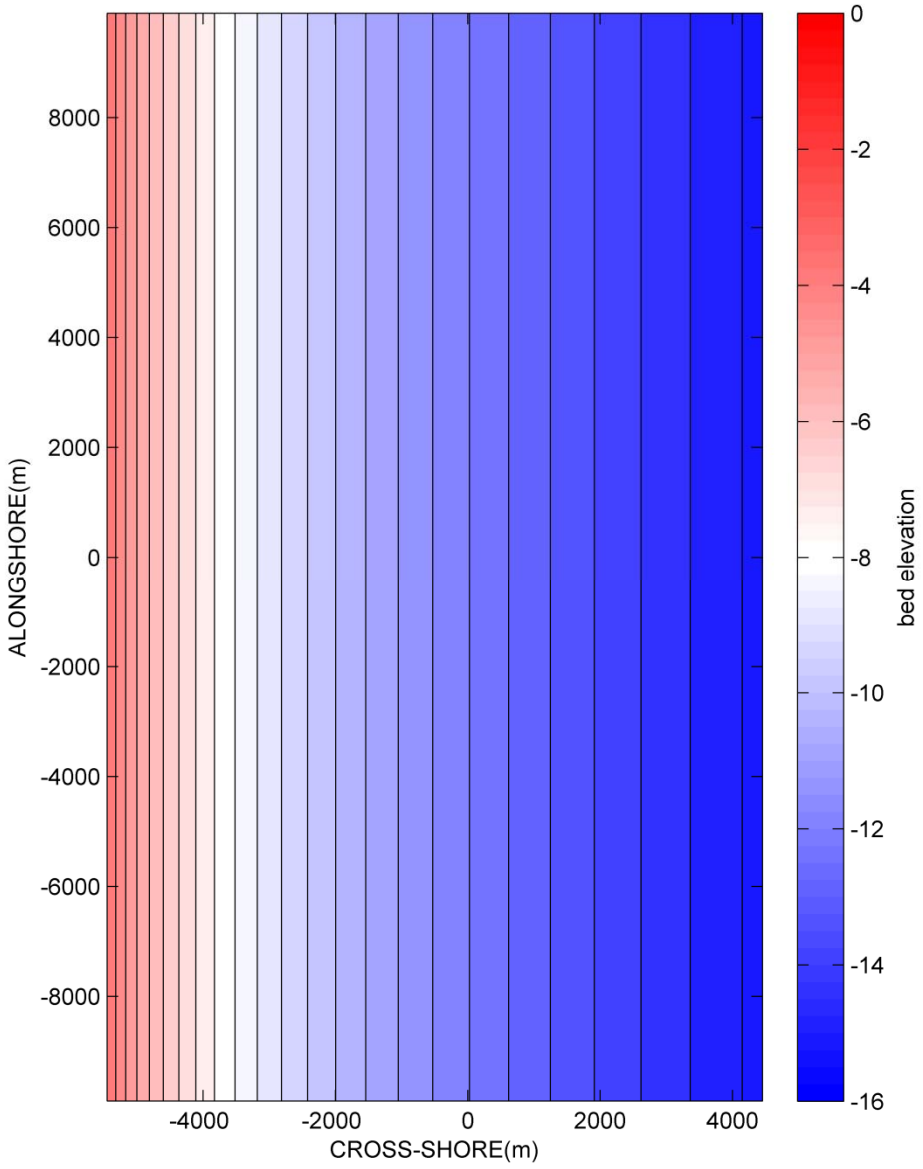

Figure V-23. Bathymetry without a borrow area.

The bed elevation change after six months is shown in Figure V-25 and V-26 for the simulation without and with the borrow area, respectively. The right panel of these two figures show the alongshore bed elevation changes at the 5 m contour. For both simulations the average bed change was approximately -1.55 m of erosion. For the simulation without the borrow area the bed change at the 5 m contour was approximately constant. However, for the simulation with the borrow area the bed change had more variability and ranged from approximately -1.6 m to -1.4 m of erosion, with the least erosion happening in the center of the domain. To demonstrate

the effect that only the borrow area had on the bed evolution and remove the bias caused by the profile trying to achieve equilibrium the bed change from the simulation without the borrow area had to be subtracted from the simulation with the borrow area results. This subtraction showed that borrow area caused approximately 0.1 m of accretion and -0.18 m of erosion along the alongshore 5 m contour.

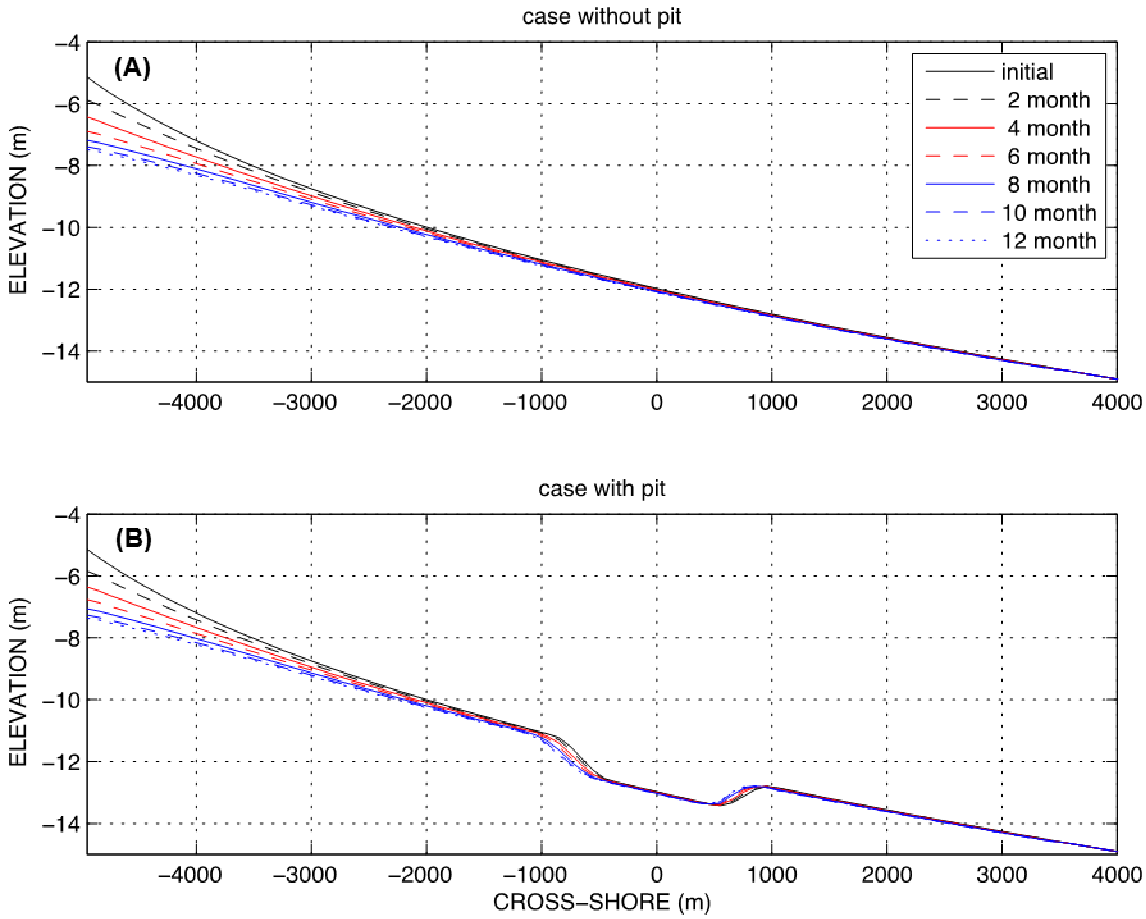

Figure V-24. Seabed profile changes over a year-long period for the simulation (A) without the borrow area and (B) with the borrow area.

The simulation with the borrow area was re-run; however, this time including the OCM. The results from this simulation after with the OCM are shown in Figure V-28. The bed change from this method due to the borrow area geometry showed a similar pattern and magnitude as the results shown in Figure V-27 which is the results from subtraction between the simulations with and without the borrow area not using the OCM. The original method predicts relatively larger variation of the bed change at the 5 m compared to the OCM. The over-prediction is caused by the general decrease of the water depth nearshore due to the bed profile adjustment in the original model allowing the hydrodynamic forcing to have a greater impact on bed creating more sediment transport.

The comparison between the result from the OCM and the original method indicated that the OCM was an effective method for predicting the morphodynamic impact of sandpit geometries, especially for the cases with complex hydrodynamic conditions. For any pre-described hydrodynamic conditions and seabed profile, the OCM does not need to spin up to get an equilibrium state before modeling a borrow area.

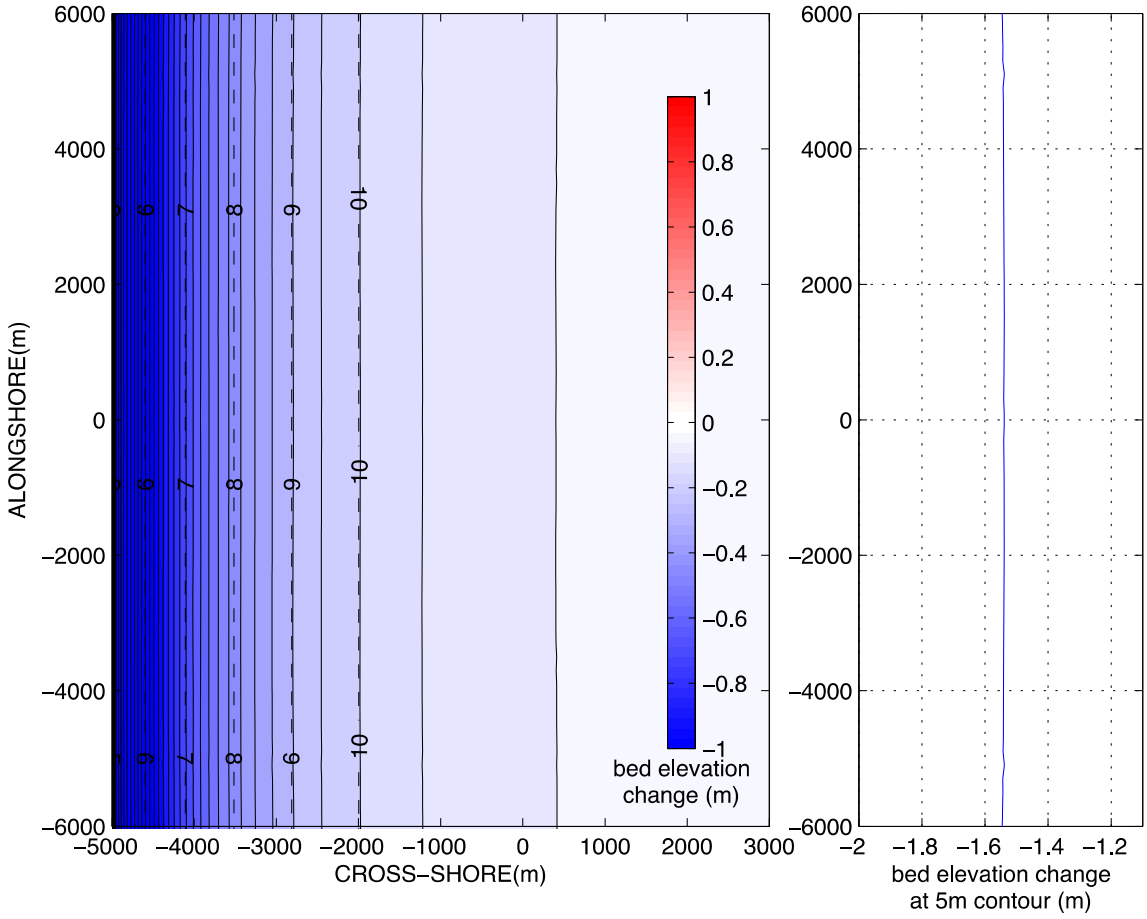

Figure V-25. The left panel shows the bed elevation change after 6 months from the simulation case without the borrow area. The dashed lines represent initial depth contours. The right panel shows the bed elevation change in meters at the 5 m contour.

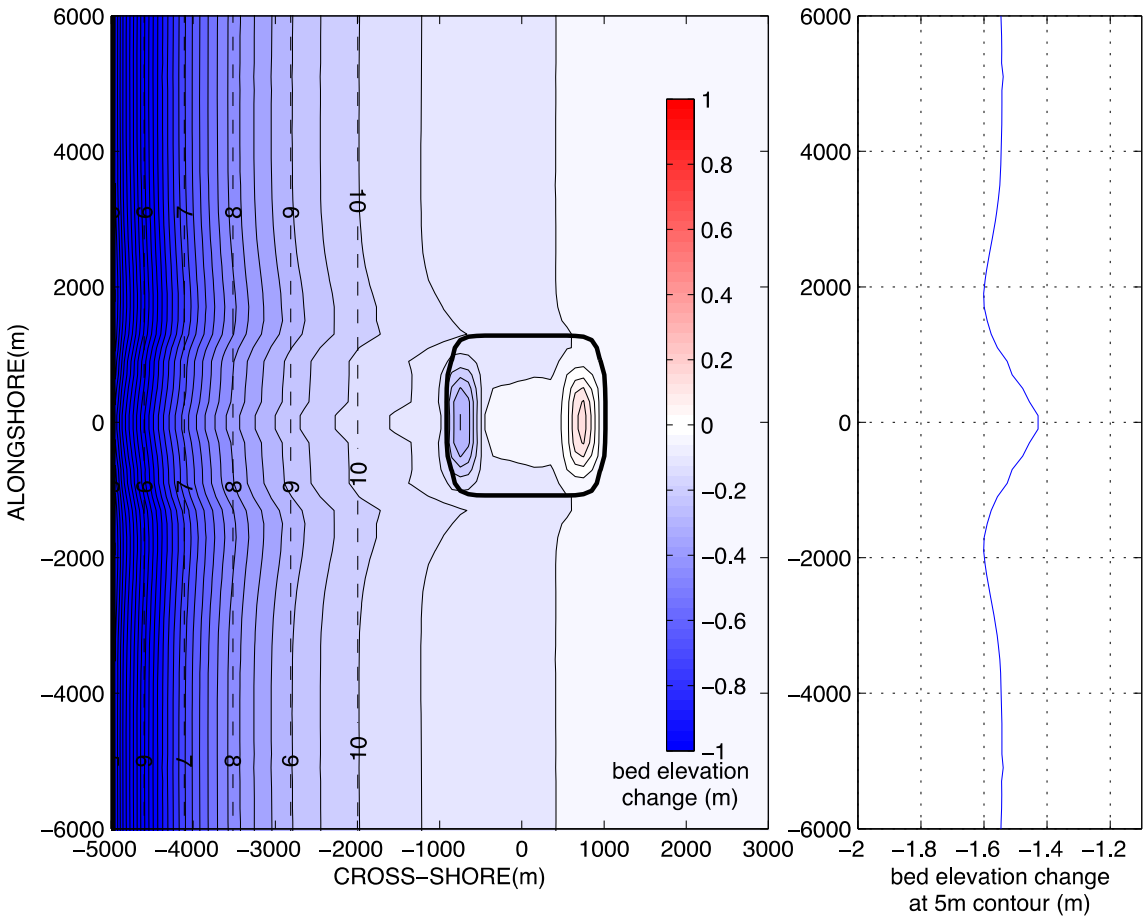

Figure V-26. The left panel shows the bed elevation change after 6 months from the simulation case with the borrow area. The dashed lines represent initial depth contours. The right panel shows the bed elevation change in meters at the 5 m contour.

V.C.7.c Cane South Application

As mentioned above, the OCM model is a reduced model which computes the morphological response to a single factor, e.g., the dredging of a borrow area. In other words, the morphological evolution is calculated based on the change of the hydrodynamics in the presence of the dredged borrow area. It is assumed that, in the absence of a borrow area, the morphodynamics and hydrodynamics are in an equilibrium state meaning that no morphological change will occur. Originally, the OCM was devised for idealized scenario cases, in which the initial hydrodynamics and morphodynamics associated with a given bathymetry profile were not in equilibrium. However, this method was also applied to the NearCoM application due to the inability of the simulations to accurately predict the net total accretion that was observed subsequent to site dredging. This method could only be applied to the NearCoM model due to its open source code.

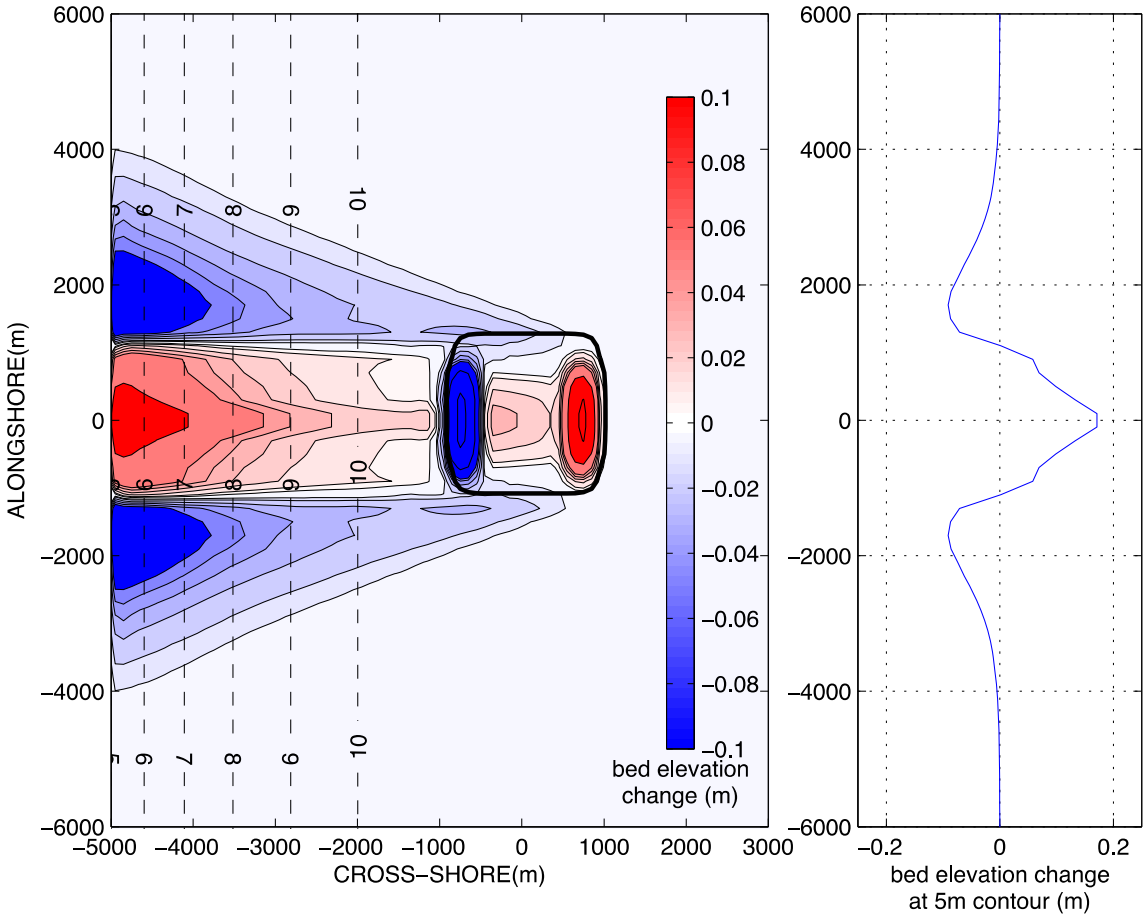

Figure V-27. The left panel shows the bed elevation change from subtracting the results from the simulation without the borrow area from the simulation with the borrow area. The dashed lines represent initial depth contours. The right panel shows the bed elevation change in meters at the 5 m contour.

Even though realistically in the field case the morphological evolution can be driven by many factors, the OCM model only takes into account the effect that the excavation had on the morphological change. The bed elevation change was calculated from the morphological differences from a reference situation, which is assumed to be in equilibrium. This approach was believed to be applicable due to the small sediment transport from the weak currents (< 0.2 m/s) and moderate wave heights. The bottom profile was essentially in equilibrium with the wave and current forcing. In the OCM NearCoM simulation two parallel processes were run, one that used the bathymetry from the pre-dredging bathymetric survey without a borrow area and the other process used the post-dredge bathymetry with a borrow area.

The results for the one-year NearCoM simulation using the OCM as well as the full model incorporating the Van Rijn 1991 formula and slope correction are shown in Figure V-29. The NearCoM model with the OCM predicted similar erosion and deposition patterns to the NearCoM model without the OCM. However, the OCM simulation predicted smaller morphological changes outside the dredge area compared to both the measured values and the

result from the NearCoM simulation without OCM. This finding was expected because of the reduction in the simulated morphological change outside of the borrow area. Table V-6 lists the net volume changes and max erosion and accretion values within the dredge area measured in the field and predicted by the model with and without the OCM. The comparison showed that the model without the OCM predicted generally larger erosion and deposition volumes than the simulation with the OCM because again it calculated the morphological changes based on the complete hydrodynamics rather than the change of hydrodynamics only due to the presence of the borrow area. Although the volume changes calculated from the OCM model are closer to the measured data than the simulation without the OCM, it cannot be definitively concluded that a model with the OCM will always predict the measured morphology changes better for a typical U.S. Atlantic OCS borrow area, especially if the ambient current and wave forcing is larger. However, in this Cane South application, the OCM method produced better quantitative results when compared to the measured data and was determined to be the most appropriate method of morphodynamic modeling in this case.

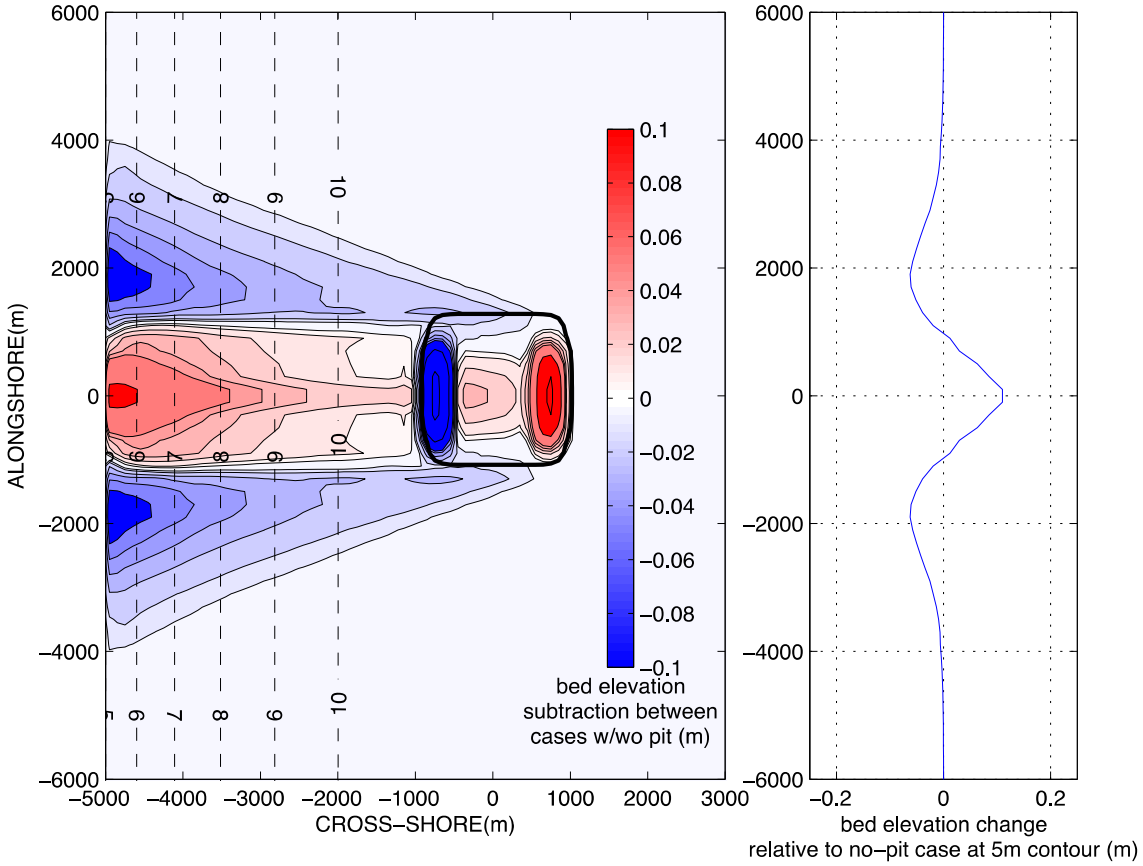

Figure V-28. The left panel shows the bed elevation change after 6 months from the simulation case with the borrow area using the OCM method. The dashed lines represent initial depth contours. The right panel shows the bed elevation change in meters at the 5 m contour.

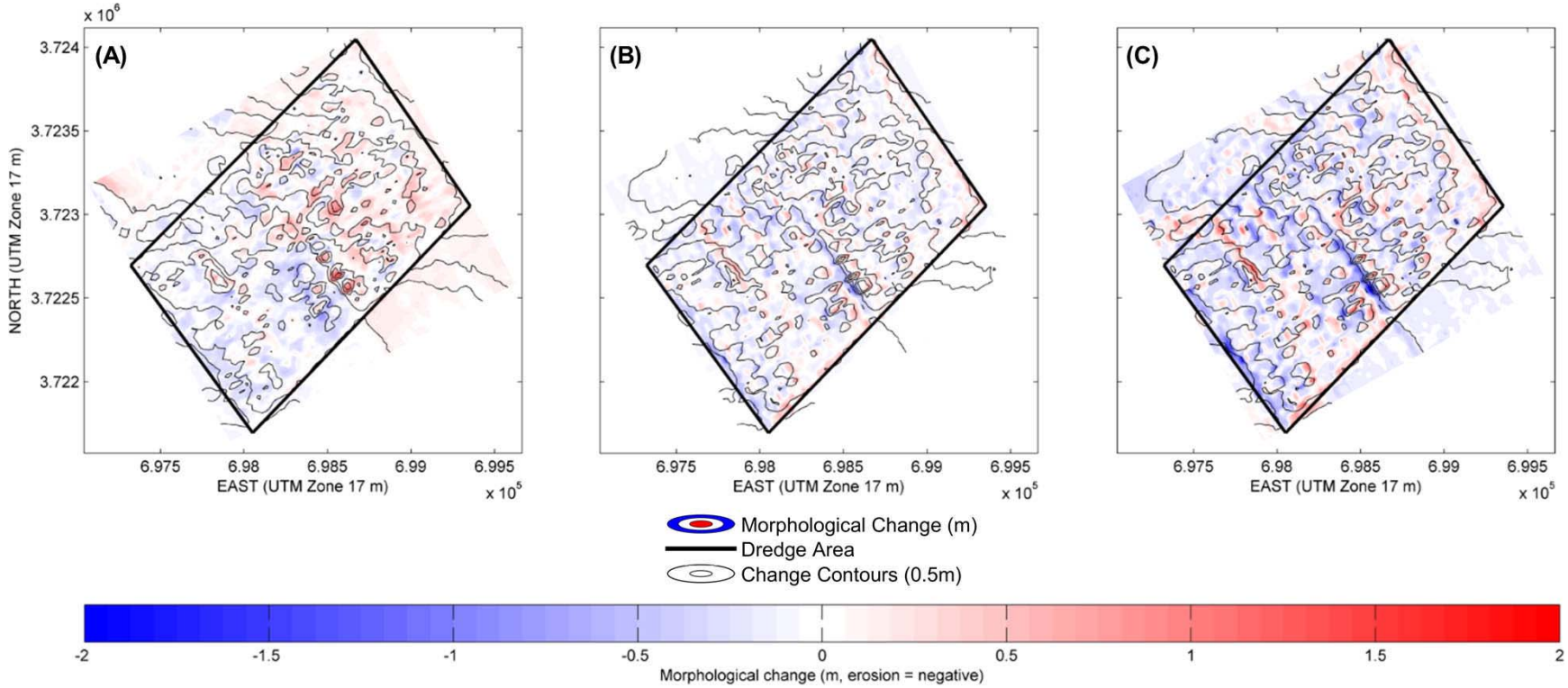

Figure V-29. Morphological change in meters from (A) the measured post to one year post dredge survey data, (B) the month-long NearCoM simulation using the Online Correction Method results multiplied by twelve and (C) the month-long NearCoM simulation using the original NearCoM model with the Van Rijn 1991 formula and the slope correction factor multiplied by twelve.

Table V-6. Net volume changes and max erosion and accretion values within the dredge area for the measured data and the month-long model simulations multiplied by twelve using the smoothed bathymetry, 25 meter grid spacing, and the slope factor with and without the Online Correction Method. A negative value indicates erosion.

Model	Net Erosion (m^3)	Net Deposition (m^3)	Net Total (m^3)	Morphological Change (m)	
				Max Erosion	Max Accretion
Measured	-139,734	245,070	105,336	-0.94	1.37
NearCoM Van Rijn 1991 with the OCM	-213,182	218,517	5,335	-1.16	0.93
NearCoM Van Rijn 1991	-351,915	322,756	-29,159	-2.09	1.71

V.D. FINAL MODEL RESULTS

Final model results were plotted to qualitatively compare the three models to the measured data, Figure V-30. Both the MIKE 21 and CMS model results are unable to reproduce the accretion seen on the eastern portion of the figure even with the refined grid spacing, smoothed bathymetry, and the model calibration factor. This accretion pattern was able to be duplicated by the NearCoM simulation. All three of the simulations were able to predict the accretion in the middle lower half of the dredge area where the most accretion occurred and the adjacent erosion to the left (west) of the accretion as seen on the measured plot. Additionally, all of the model results showed overall erosion in the right (east) half of the dredge area similar to the measured data. Overall, NearCoM was able to duplicate the measured morphological change the best due to its ability to predict the accretion in the right (east) half of the domain.

Quantitatively, the net erosion, accretion, and total volumes and the maximum erosion and accretion values for the measured data and the three model simulations are shown in Table V-7. The net total volume for NearCoM and MIKE 21 was accretional, similar to the measured results. However, both simulations under-predicted the amount of accretion, although NearCoM accretion rates were similar to measured values. Overall, the CMS simulation found the morphology change to be highly erosional, which was expected by the bed elevation change plot which showed primarily erosional. With the correction methods explained above the maximum erosion and accretion values for all of the models were of a similar magnitude to the measured values. For additional quantitative comparison the root mean squared error was calculated based on the measured and modeled morphological change for each of the bathymetric survey vertical lines within the dredge area, Figure V-31. The mean root mean squared error and mean BSS for each model is listed in Table V-8. The NearCoM model performed slightly better than the other two models with a mean root mean square error value of 0.22 meters. Utilizing the mean BSS, the NearCoM and MIKE 21 simulations yielded “fair” agreement with the measured dataset, while the CMS simulation produced “bad” agreement.

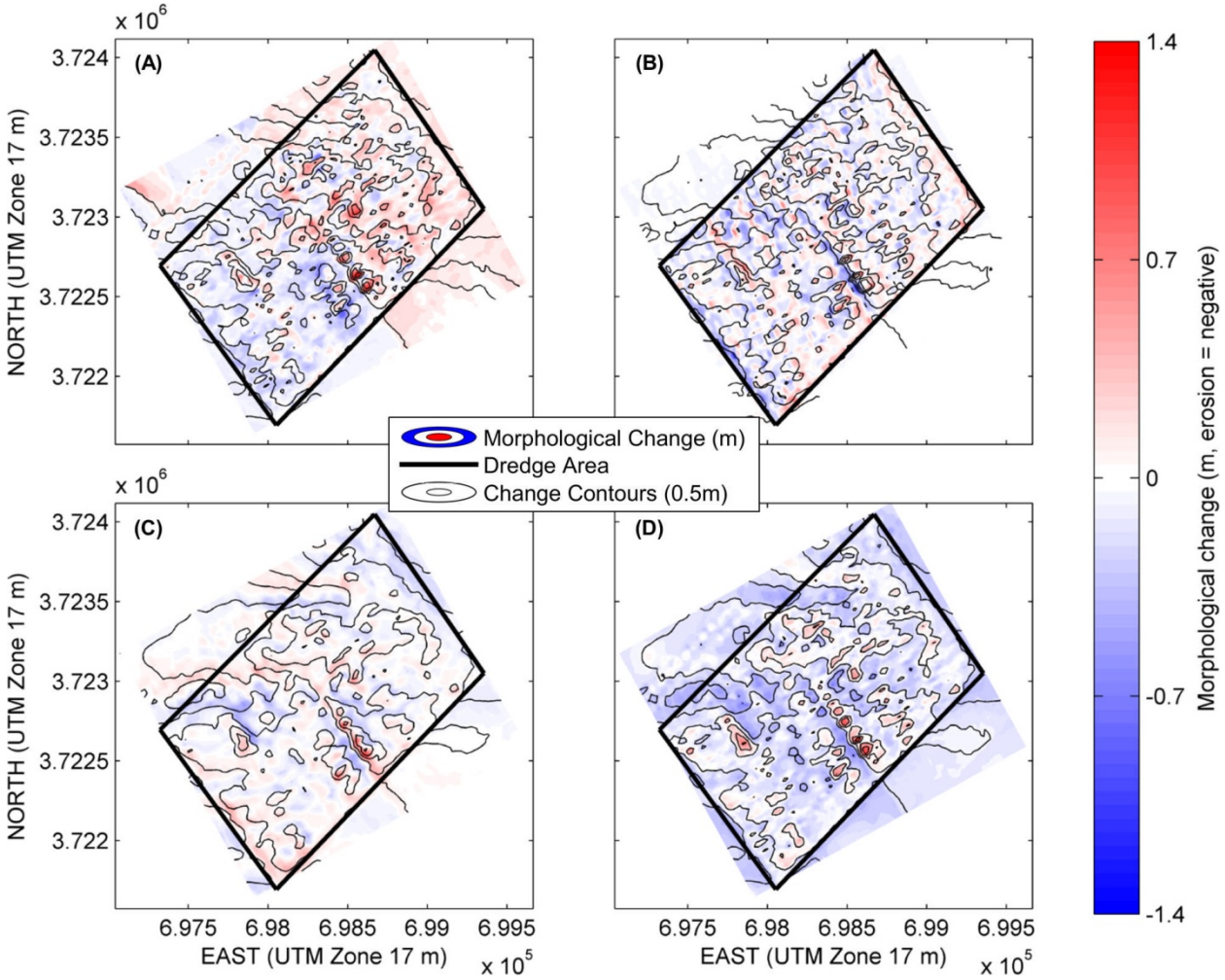

Figure V-30. Morphological change in meters from (A) the measured post to one year post dredge survey data, (B) the month-long NearCoM simulation using the Online Correction Method, (C) the month-long MIKE 21 simulation using a model calibration factor (MCF) of 25 and (D) the month CMS simulation using a MCF of 3. The model results were multiplied by twelve.

Table V-7. Net volume changes and max erosion and accretion values within the dredge area for the measured data and month model simulations multiplied by twelve using the correction methods described in Section V.C. A negative value indicates erosion.

Model	Net erosion (m^3)	Net deposition (m^3)	Net total (m^3)	Morphological change (m)	
				Maximum erosion	Maximum accretion
Measured	-139,734	245,070	105,336	-0.94	1.37
NearCoM Van Rijn 1991 with OCM	-213,182	218,517	5,335	-1.16	0.93
MIKE 21 2D MCF = 25	-121,172	146,130	24,958	-0.72	1.12
CMS Lund-CIRP 2006 MCF = 3	-304,700	93,342	-211,358	-0.74	1.32

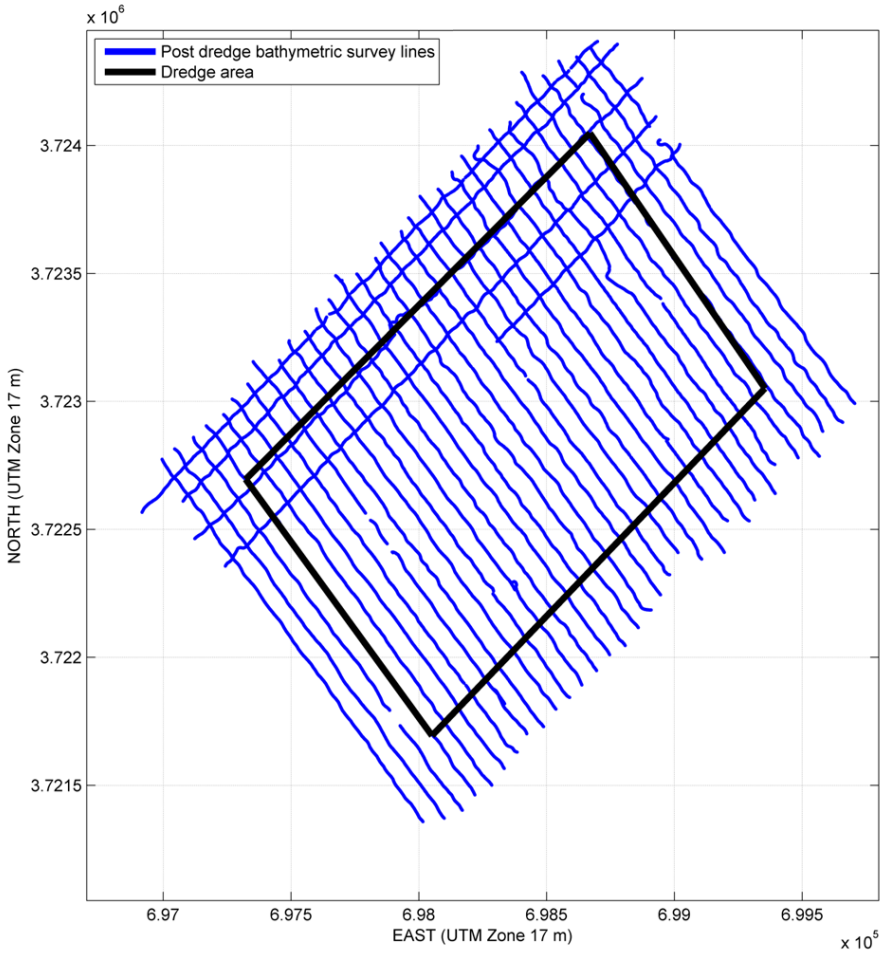

Figure V-31. Cane South bathymetric survey lines for the post-dredge surveys.

Table V-8. Mean root mean square error and mean BSS values for the 24 northwest-to-southeast survey lines within the dredge area for each model.

Model	Mean root mean square error for the survey transects (meters)	Mean Brier skill score (BSS) for the survey transects
NearCoM Van Rijn 1991 with the OCM	0.22	0.50
MIKE 21 2D MCF = 25	0.25	0.38
CMS Lund-CIRP 2006 MCF = 3	0.27	-0.51

VI. MODEL APPLICATION TO DEMONSTRATIVE GEOMETRIES

VI.A. MODEL SELECTION FOR DEMONSTRATIVE GEOMETRIES

Based upon the Cane South application NearCoM was selected to model the demonstrative geometries, where specific borrow area geometries were evaluated to determine model applicability under the expected range of geomorphic conditions. The primary reasons NearCoM was chosen over MIKE 21 and CMS was due to the ability of NearCoM to alter the sediment transport equations, not need a model "speed up" or calibration factor, and its ability to reproduce the morphological patterns seen in the measured data. Specifically, the NearCoM application was the only modeling package that was able to accurately simulate the observed accretion subsequent to dredging at the Cane South field site.

Typically sediment transport on U.S. Atlantic OCS is strongly wave-induced due to the offshore tidal regime and typical depths of offshore borrow areas; therefore, it was necessary to ensure that wave-dominated sediment transport was incorporated in the NearCoM model. As a result, the Van Rijn formula 1991 was implemented in NearCoM. This Van Rijn formula is based on flume and fields measurements of sediment concentration profiles in waves and currents and provides the net (wave-averaged) sediment flux for combined current and waves directly. When waves and current coexist, the total time-averaged sediment transport rate can be obtained by vector addition of the sediment transport rate due to current which points to the current direction and that induced by waves which points in the direction of wave propagation. In the Van Rijn 1991 formula, the current-related component is then divided into the bedload (i.e. the sediment flux taking place in contact with the bed) and suspended load, related to the presence of sediment concentration in a significant part of the water column. The simulations performed for the Cane South borrow area have shown that the current-related suspended load is one order of magnitude larger than the bedload. The wave-related transport accounts for the sediment transport taking place near the bed and it is directly related to the presence of waves. In the Cane South case, this wave contribution to the total sediment transport dominants, thus showing that most of the sediment flux is related to the presence of waves and takes place within three-to-five ripple heights from the bottom.

An additional relevant issue in morphological modeling is the ability to predict the bottom roughness (ripples), which is important because the amount of sediment to be picked up from the bed is highly dependent on the bottom roughness. In order to accurately predict bed conditions (flat, rippled or sheet flow), as well as ripple characteristics, the ripple predictor by Soulsby & Whitehouse (2005) was coded into the open source code NearCoM. From the Cane South application of the three morphological models, NearCoM was the only model that predicted the correct magnitude of bed change and erosion/deposition patterns compared to the measured data without the need of a model 'speed up' or calibration factor. As a result, NearCoM was selected as the candidate model to be used in testing various conditions representative of U.S. Atlantic OCS to evaluate the model response to a range of scenarios.

VI.B. BASELINE BORROW AREA

The scenario testing was performed starting from an "idealized" baseline case. Using the idealized case as a baseline, the geometry of the borrow area and the amplitude of the tidal currents were varied, to assess the influence of the different parameters. The baseline bottom geometry (i.e. approximate area and depth of excavation, as well as ambient water depth) was chosen and varied based upon the dimensions of typical U.S. Atlantic OCS borrow areas, specifically the geometry of the Cane South borrow area.

The external dimensions of the baseline case were 2,000 m in the alongshore direction and 1,000 m in the cross-shore direction. The baseline borrow area depth was 1 m which made the borrow area volume 2.0×10^6 m^3. The orientation of the baseline borrow area was aligned approximately with the South Carolina coastline and the centroid of the borrow area was 6,000 m offshore.

Initially the borrow area was shaped as a truncated inverted pyramid that had 1:3 side slopes. However, this geometry, which had 90° corners, produced unrealistic oscillations that resulted in an improbable outcome as shown by Figure VI-1. These unrealistic oscillations were induced by the discontinuous behavior of the bottom slope and by the limited spatial resolution. To increase the spatial resolution to resolve this discontinuity would have been computationally time consuming; therefore, the borrow area corners were rounded which addressed this problem. The final geometry of the baseline borrow area is shown in Figure VI-2. It should be noted that as a result of rounding the corners the average side slope of the borrow area was slightly less than 1:3.

Based on an assessment of the near- and far-field scenarios, it was decided that the borrow area should have a sloping bottom to make the simulations more realistic relative to typical field conditions. The near-field model domain focused on the borrow area and the region within ~1,000 meters of the borrow area edge. Far-field scenarios focused on more regional influence that extended more than 5,000 meters from the borrow area edge. The sloping bottom was determined by following the water depth (d) law:

$$d = 8x^{0.35} \qquad \text{Eq. 1}$$

where x is the distance from the shoreline (in kilometers). The beach profile was chosen on the basis of the cross-shore profile measured offshore from the Cane South borrow area. Figure VI-3 shows the bathymetry profile based on Eq. 1 and the measured cross-shore profile. The idealized bathymetry was assumed to be uniform in the alongshore direction. The borrow area was located in between the 11.5 m and 12.5 m contours and had at an approximate depth of 12 m. The sediment grain size and the hydrodynamic conditions (tidal currents, water surface elevations, and wave parameters) remained the same as Cane South's because of Cane South being a typical U.S. Atlantic OCS borrow area.

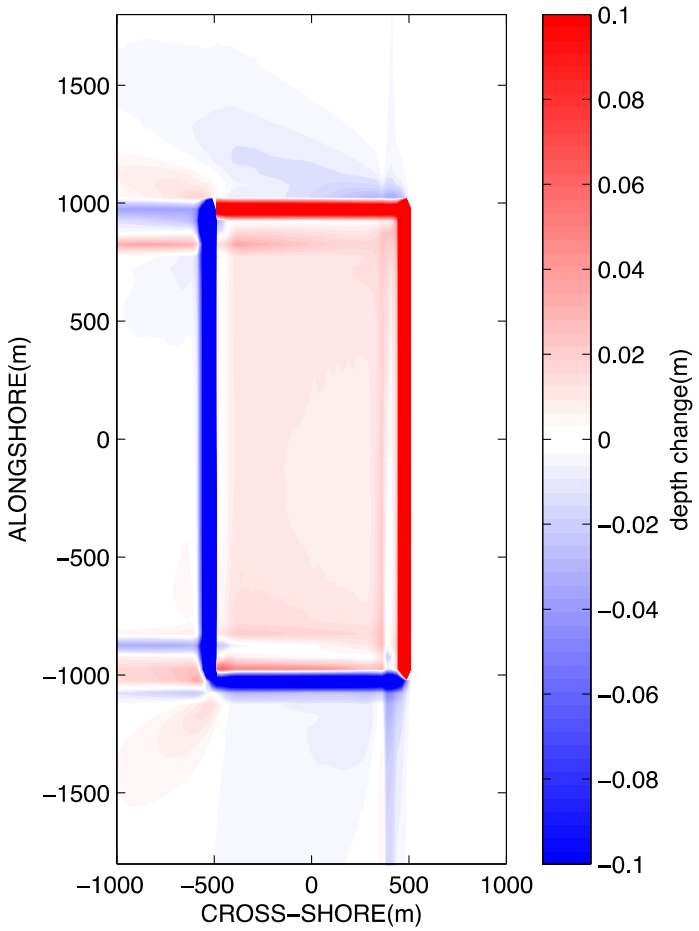

Figure VI-1. Unrealistic results from a preliminary run when the borrow area was shaped as a truncated inverted pyramid with sharp corners.

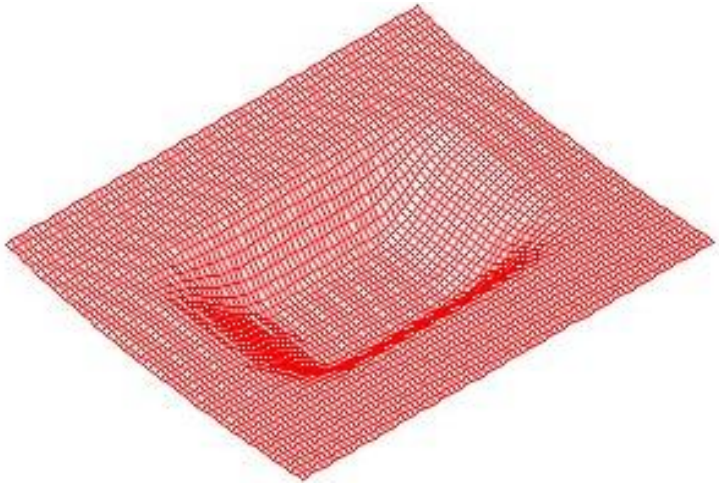

Figure VI-2. Sketch of the baseline borrow area with the rounded corners.

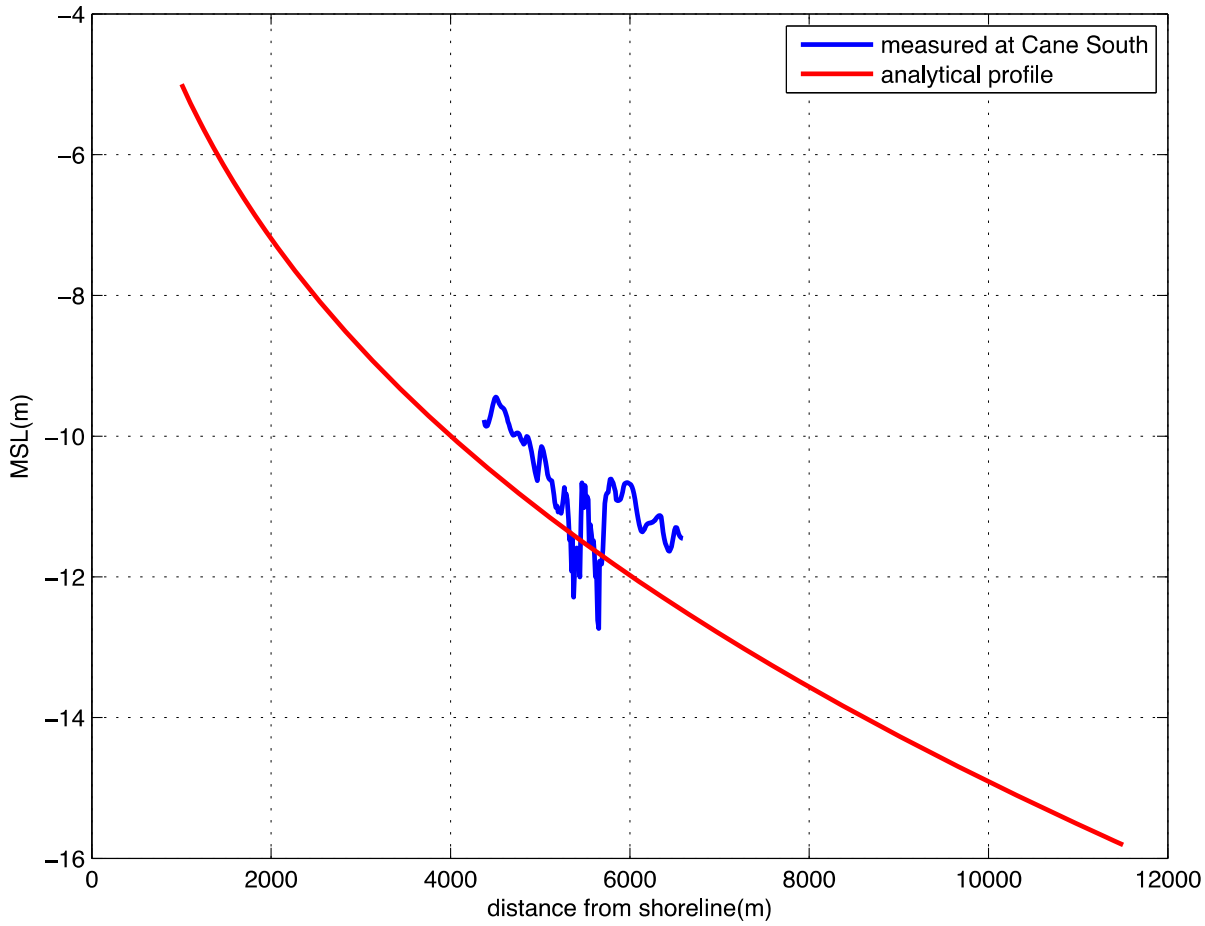

Figure VI-3. The analytical bathymetry profile (red) and measured profile at Cane South borrow area (blue).

Additionally, the influence of the baseline borrow area on the wave height and current speeds in the near-field domain are shown in Figures VI-4 and VI-5, respectively. With the addition of the borrow area, there was a decrease in wave height between the eastern edges of the borrow area to the western extent of the near-field domain. The depth-average flow velocity decreased throughout the majority of the domain with the addition of the borrow area. The area where there was an increase in velocity was at the inflow and outflow section of the borrow area which occurred due to the reduced flow resistance in the borrow area as a result of the increased water depth.

The morphological change from the baseline case is shown in Figure VI-6. As previously stated discussed, the sediment transport at the borrow area is strongly wave-dominant; therefore, the transport direction will coincide with the wave propagation direction. As a result, the borrow area migrated shoreward in Figure VI-6, as predicted based on the cross-shore directed waves

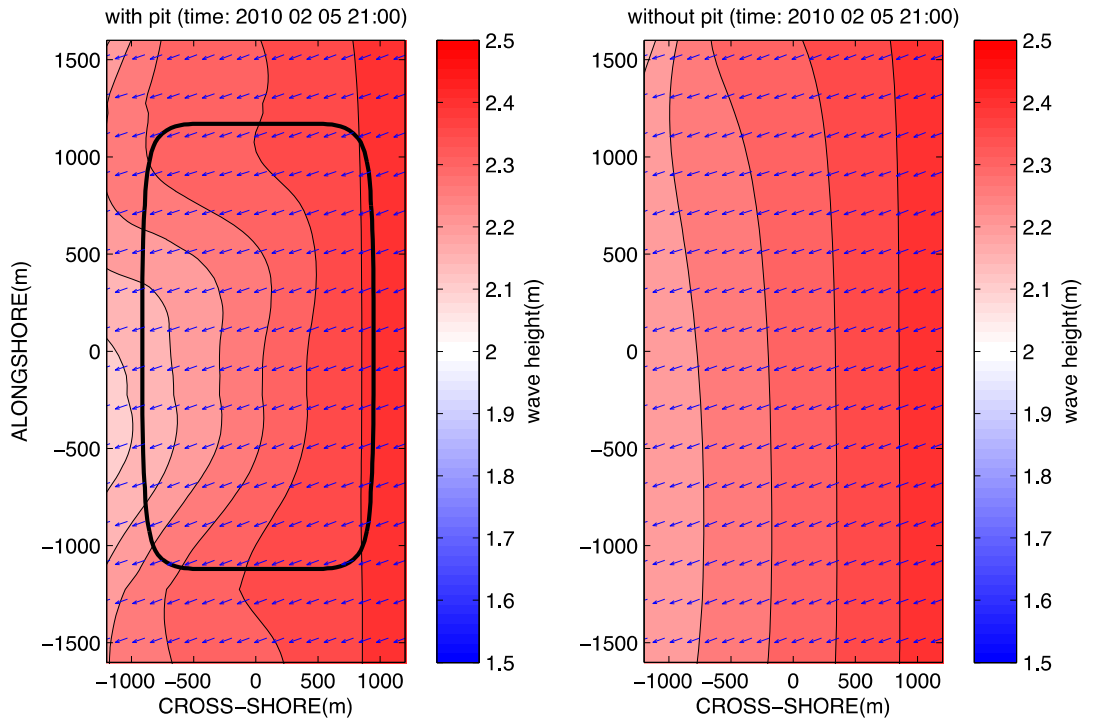

Figure VI-4. Influence of borrow area (black) on wave height (color) and wave direction (arrows).

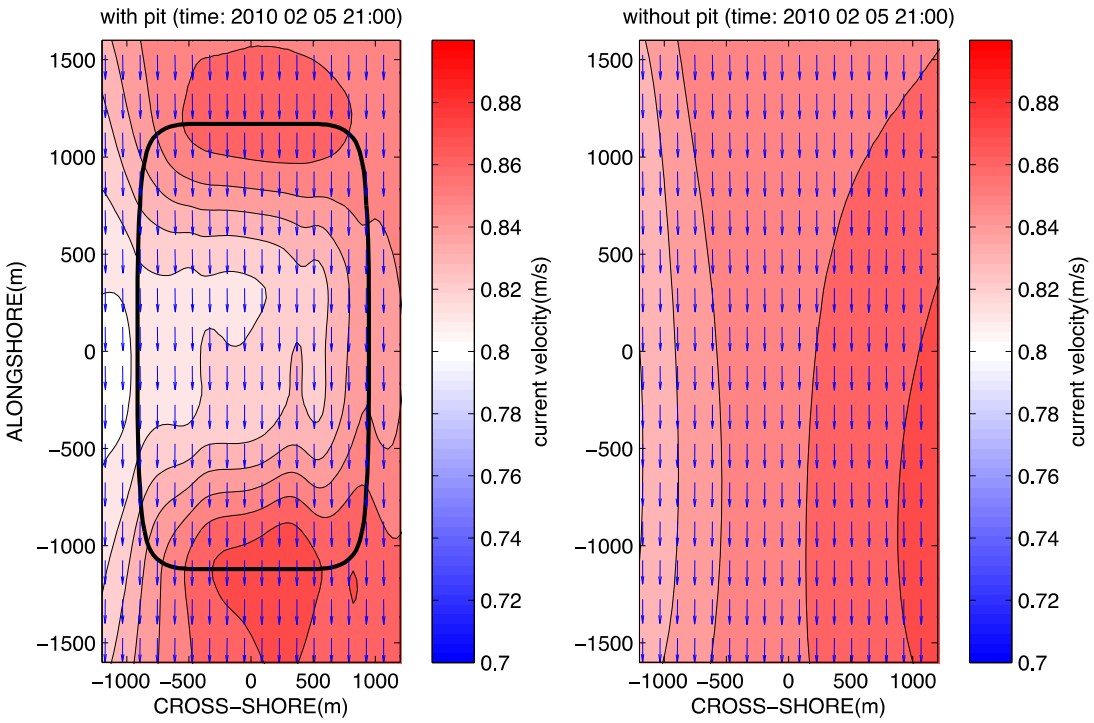

Figure VI-5. Influence of borrow area (black) on current speed.

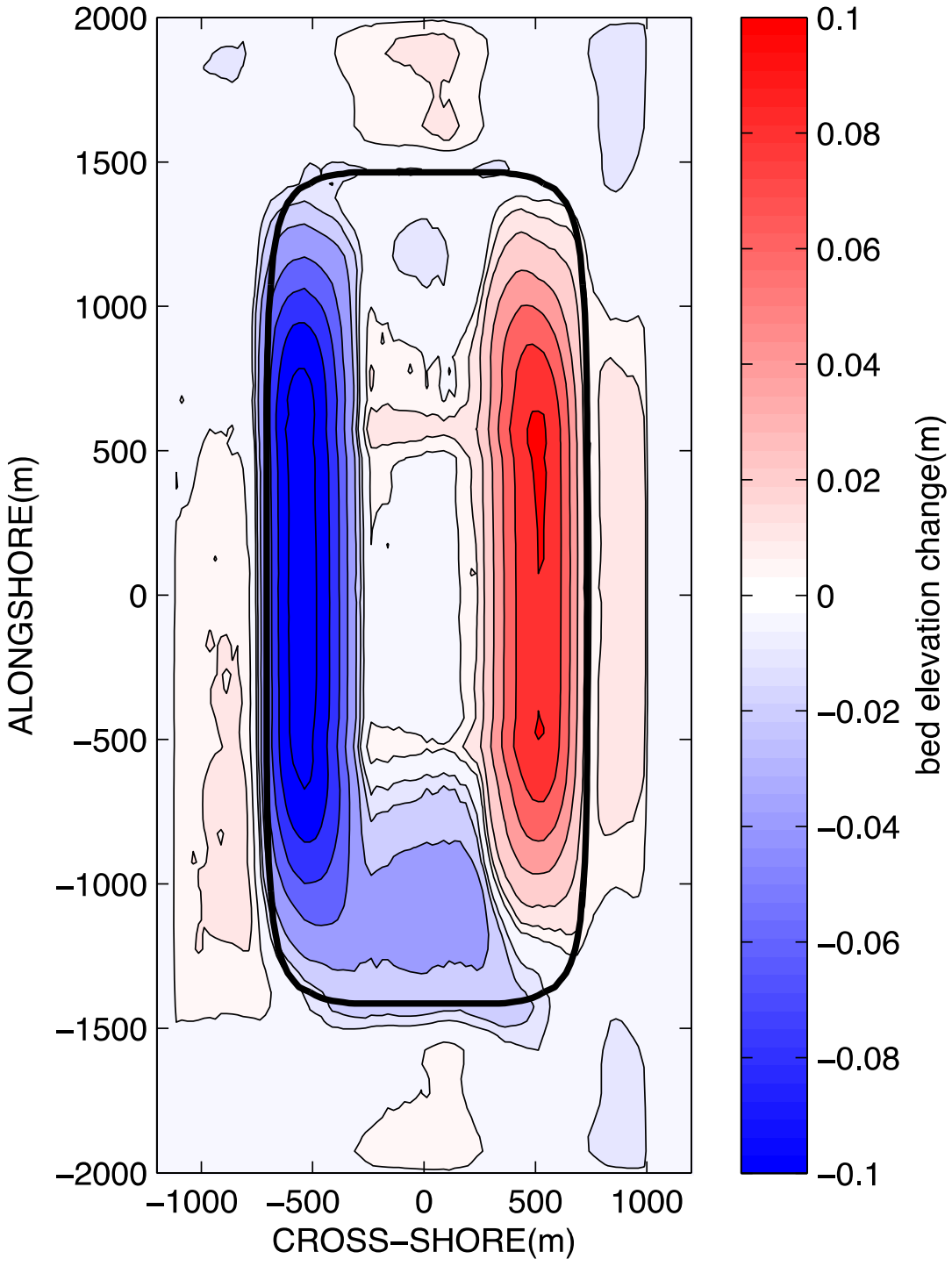

Figure VI-6. Erosion and deposition patterns of the baseline borrow area in the near-field region.

VI.C. NEAR-FIELD MORPHOLOGY, AMBIENT FLAT BED TEST CASES

Initially, scenarios were evaluated to assess the effect of borrow area aspect ratios and current speeds on a flat bed in the near-field region. The dimensions of the computational domain varied

depending on the borrow area aspect ratio. However, the number of grid points remained the same at one hundred points in each direction. In total, nine scenarios were evaluated for this set of scenarios by using three different borrow area aspect ratios and three different magnitudes of ambient tidal currents (ranging from 0.2 to 1.0 meters per second). The nine scenarios and their respective computational domain are listed in Table VI-1. It should be noted that by alternating the borrow area aspect ratio, the borrow area depth (1 m) and volume (2.0×10^6 m^3) remained constant for all scenarios.

The effect of the borrow area shape on the hydrodynamics was assessed by analyzing the variation in the wave height and in the current speed in the alongshore and cross-shore directions. In order to quantify the effect of the borrow area on wave height and on current speed, the wave height and current speed influence areas were computed. The wave height and current speed influence areas were defined as the area where the relative variation in wave height or current speed with respect to the case without the borrow area exceeded the assigned threshold, where the threshold values considered were 1% (0.01), 2%, 3% and 5%. The borrow area migration was determined based on the cross-shore and alongshore displacement of the borrow area centroid at the end of the simulation. To assess the morphodynamic evolution of the borrow area, the net volumes of erosion and accretion along with the maximum accretion and maximum erosion values were analyzed at the end of the simulation.

Table VI-1. Test scenarios and computational domain for the ambient flat bed near-field morphology.

Pit length alongshore (meter)	Pit length cross-shore (meter)	Computational domain in the alongshore direction (meter)	Computational domain in the cross-shore direction (meter)	Current speed (m/s)
2,000	1,000	5,000	2,500	0.20
2,000	1,000	5,000	2,500	0.50
2,000	1,000	5,000	2,500	1.00
4,000	500	10,000	2,500	0.20
4,000	500	10,000	2,500	0.50
4,000	500	10,000	2,500	1.00
1,414	1,414	8,000	4,000	0.20
1,414	1,414	8,000	4,000	0.50
1,414	1,414	8,000	4,000	1.00

VI.C.1. Borrow Area Aspect Ratio Scenarios

Overall, the aspect ratio significantly influenced the area where the relative variation of wave height was observed as shown in Figure VI-7, VI-8, VI-9, and VI-10. In Figure VI-7 through Figure VI-9 the 3%, 2% and 1% influence areas are shown. It should be noted that these three figures show the far-field computational domain in order to get the larger picture of wave influence area. It was observed that the influence of the borrow area on wave height was primarily confined to the southwest part of the computational domain. Figure VI-10 shows the 1%, 2%, 3% and 5% wave influence areas versus aspect ratio. This figure showed that 5% influence area was negligible while the 3%, 2% and 1% wave height influence areas increased as the aspect ratio was increased.

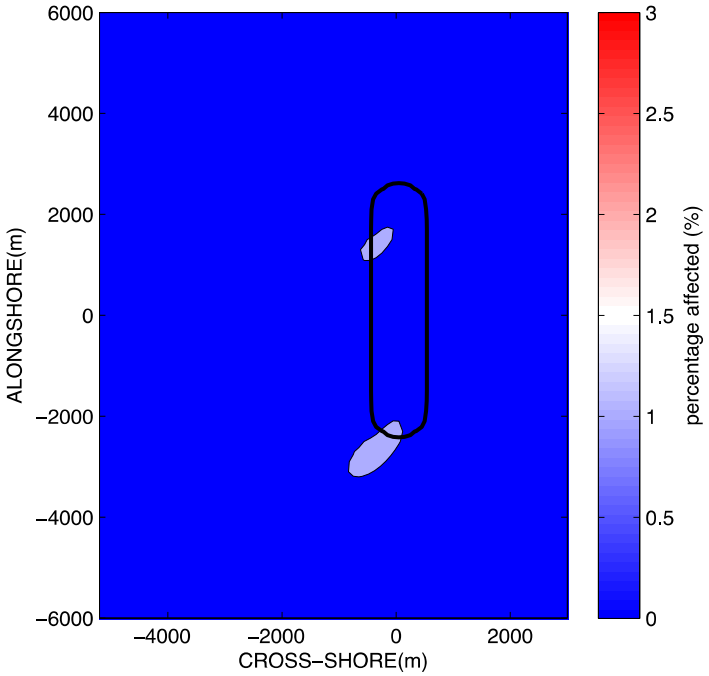

Figure VI-7. The relative variation of wave height during the maximum wave height (February 5, 2010 21:00) in the near-field region around the borrow area when the borrow area aspect ratio equaled 0.25. The red, light red and light blue areas indicate 3%, 2% and 1% influence, respectively. The tidal current speed remained constant at 0.2 m/s.

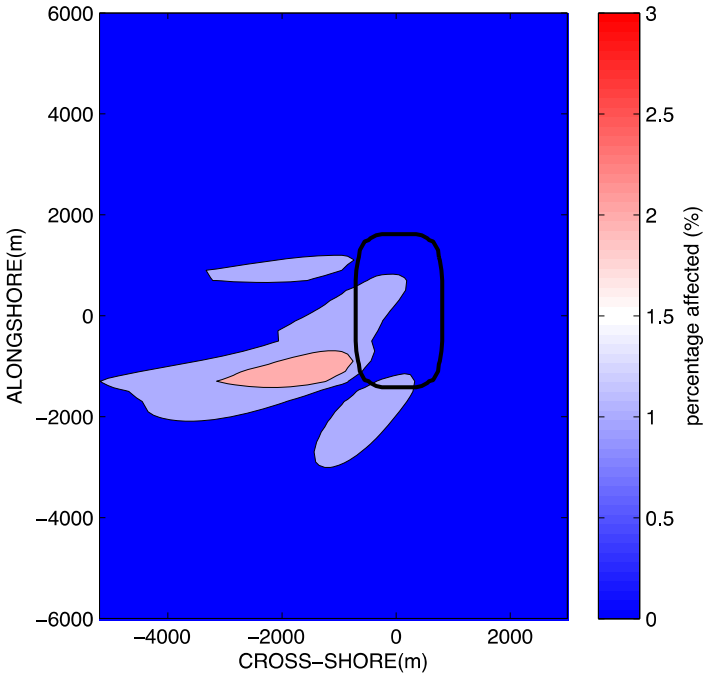

Figure VI-8. The relative variation of wave height during the maximum wave height (February 5, 2010 21:00) in the near-field region around the borrow area when the borrow area aspect ratio

equaled 0.5. The red, light red and light blue areas indicate 3%, 2% and 1% influence, respectively. The tidal current speed remained constant at 0.2 m/s.

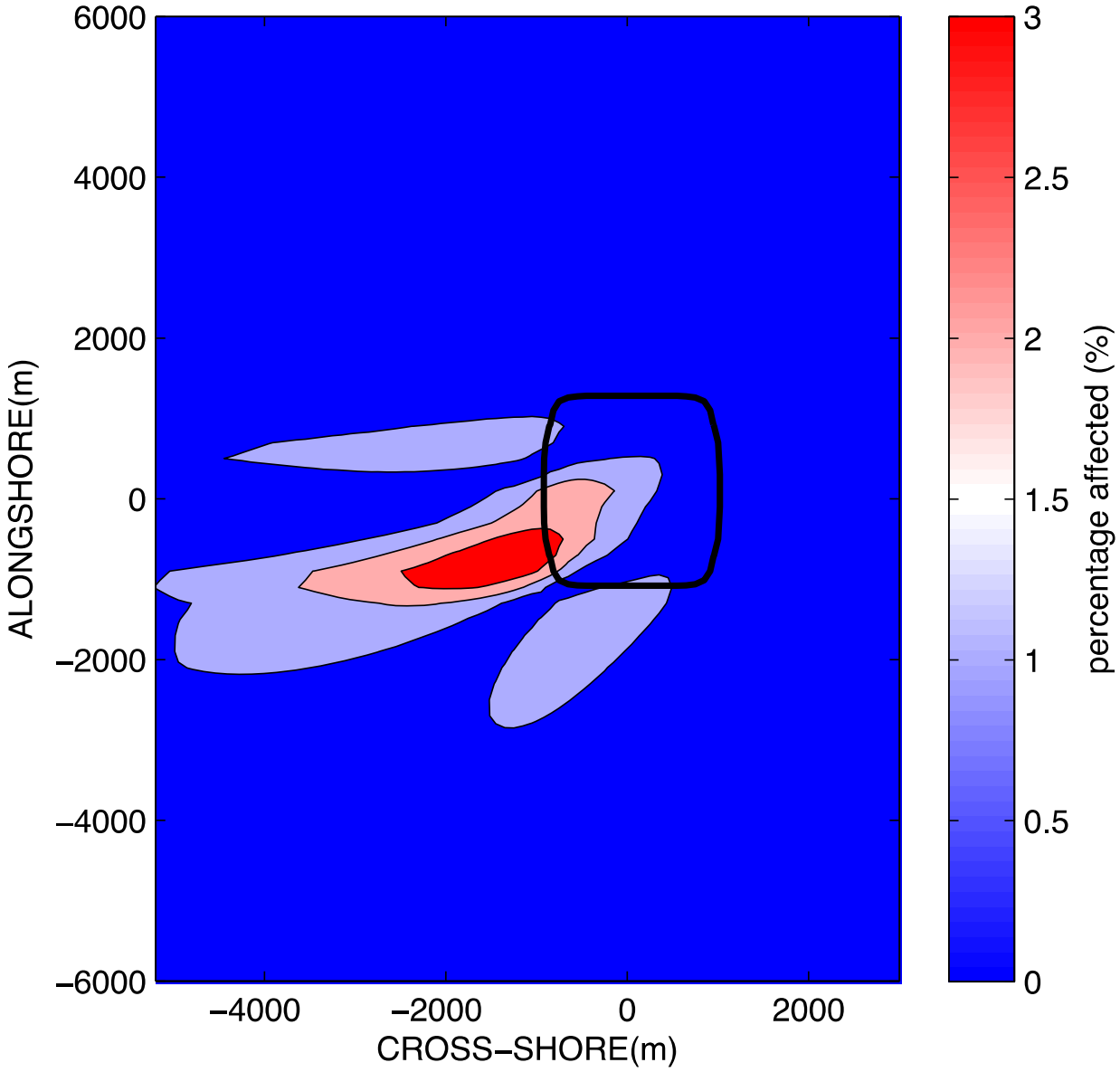

Figure VI-9. The relative variation of wave height during the maximum wave height (February 5, 2010 21:00) in the near-field region around the borrow area when the borrow area aspect ratio equaled 1.0. The red, light red and light blue areas indicate 3%, 2% and 1% influence, respectively. The tidal current speed remained constant at 0.2 m/s.

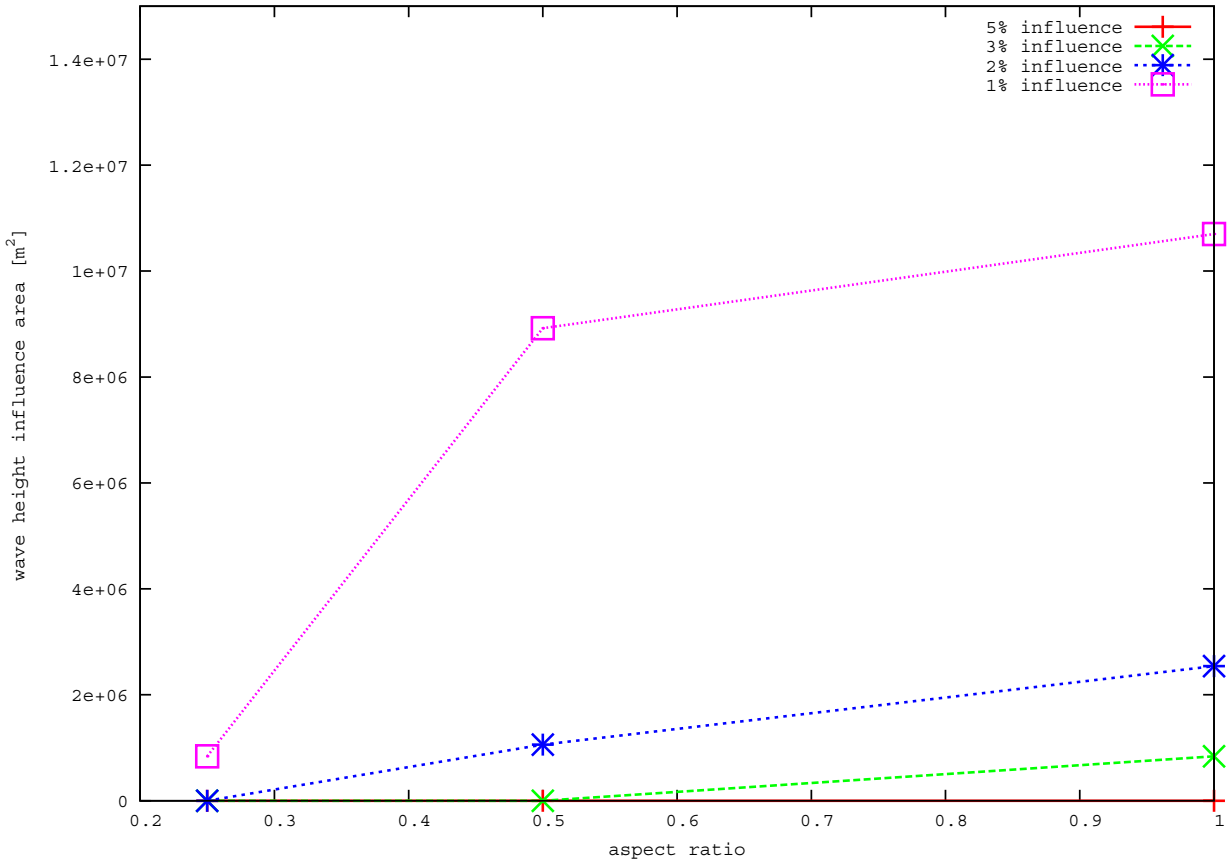

Figure VI-10. Wave height influence area (m^2) versus aspect ratio. Current speed is equal to 0.2 m/s.

The effect the borrow area aspect ratio had on the current speed is shown in Figures VI-11, VI-12, VI-13, and VI-14. This influence area extended more in the cross-shore direction than in the alongshore direction as shown in Figures VI-11, VI-12, and VI-13. Figure VI-14 shows the influence area of tidal current (m^2) versus aspect ratio at the time when tidal current reaches its maximum value of 1 m/s. From this figure it was concluded that the 3% and 2% current speed influence area increased as the borrow area aspect ratio increased while the 5% influence area remained zero.

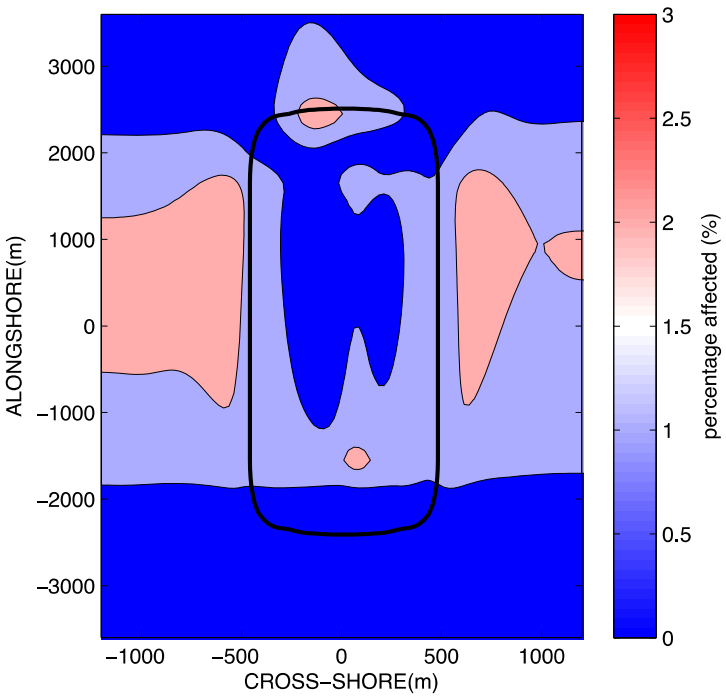

Figure VI-11. The relative variation of current speed during the maximum tidal current (02/05 21:00, 2010) in the near-field region around the borrow area when the borrow area aspect ratio of 0.25. The value of the maximum current is 1 m/s. The red, light red and light blue areas indicate 3%, 2% and 1% influence, respectively.

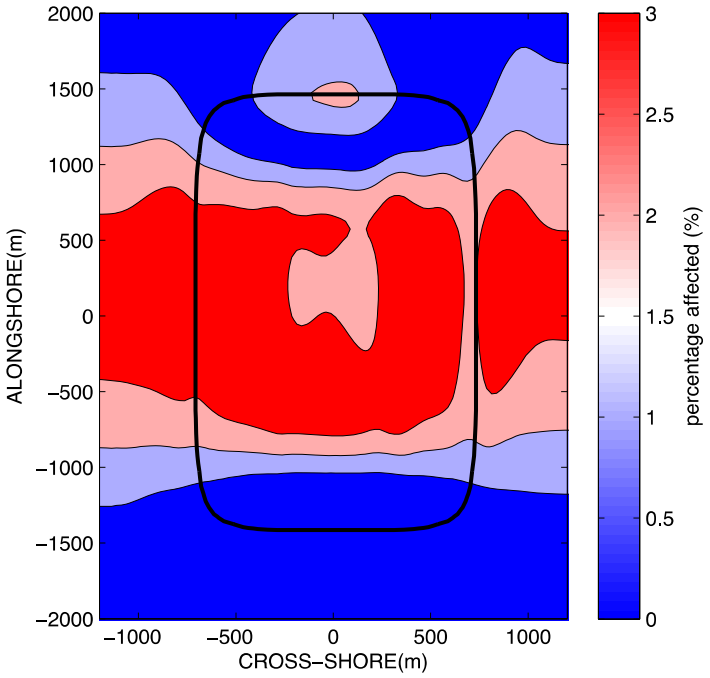

Figure VI-12. The relative variation of current speed during the maximum tidal current (02/05 21:00, 2010) in the near-field region around the borrow area when the borrow area aspect ratio

of 0.5. The value of the maximum current is 1 m/s. The red, light red and light blue areas indicate 3%, 2% and 1% influence, respectively.

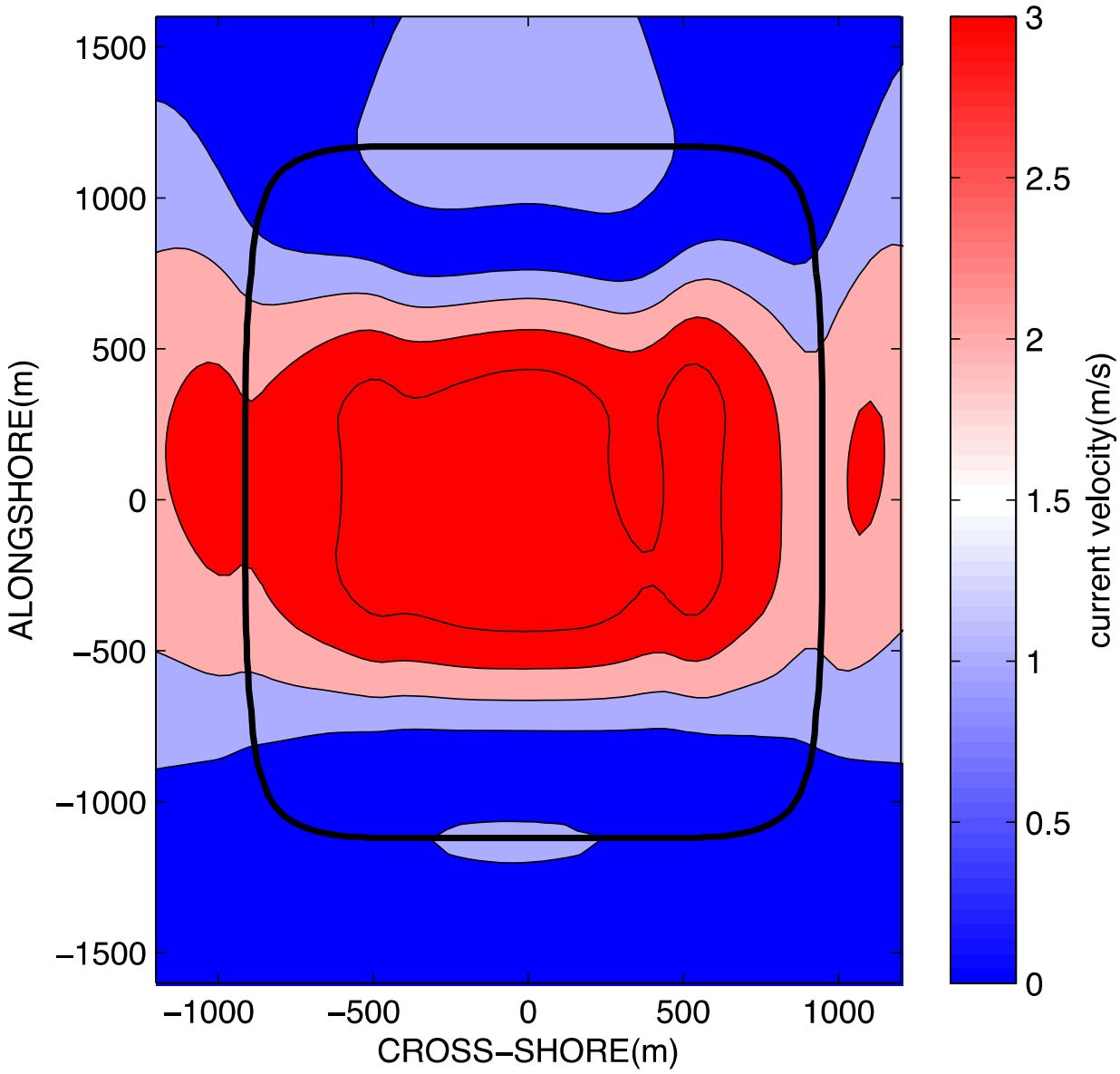

Figure VI-13. The relative variation of current speed during the maximum tidal current (02/05 21:00, 2010) in the near-field region around the borrow area when the borrow area aspect ratio of 1.0. The value of the maximum current is 1 m/s. The red, light red and light blue areas indicate 3%, 2% and 1% influence, respectively.

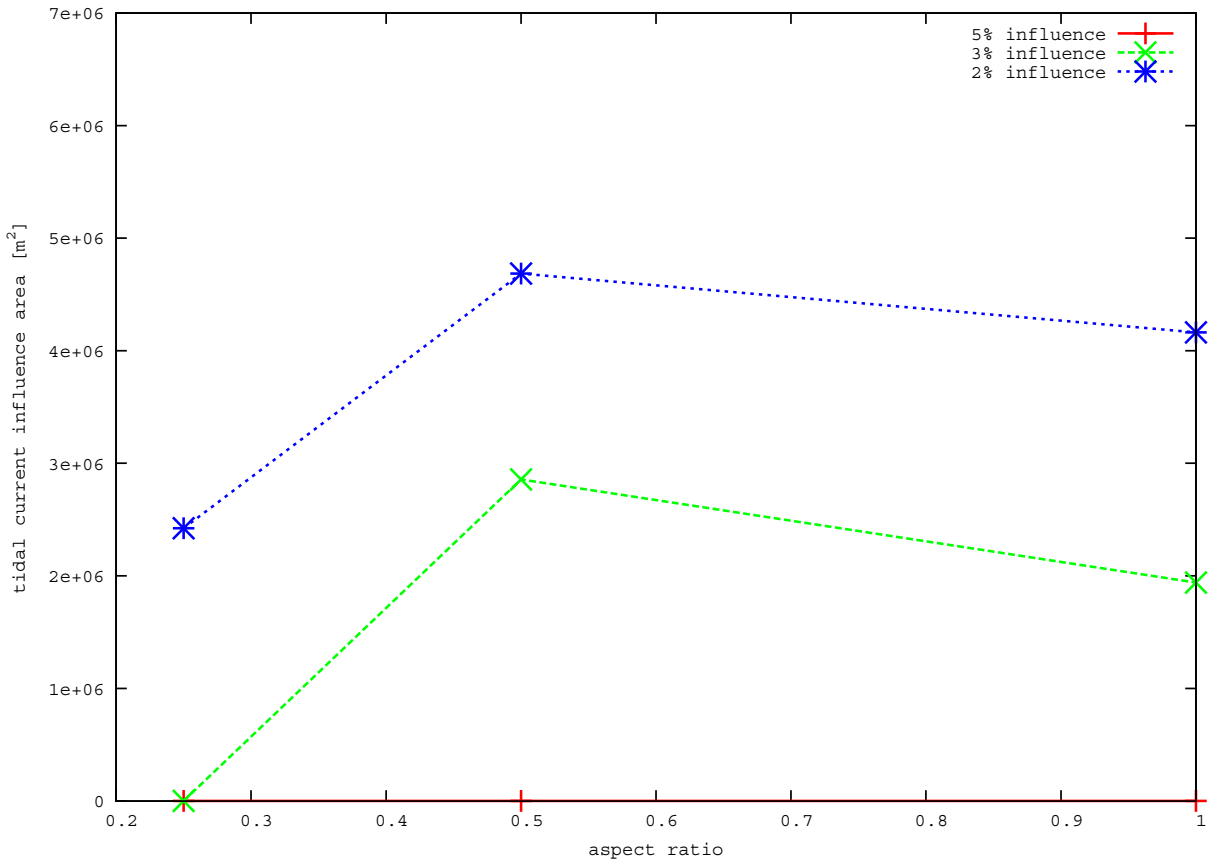

Figure VI-14. Influence area of tidal current (m^2) versus aspect ratio. Current speed is equal to 1 m/s.

The borrow area shape modified as time progressed in the simulation due to sediment transport. To determine the migration of the borrow area, the position of the borrow area centroid at the end of the simulation was analyzed, see Figures VI-15 and VI-16. In all the borrow area aspect ratio test cases considered, the borrow area centroid migrated onshore (Figure VI-15) and in the negative (southward) direction of the alongshore axis (Figure VI-16), resulting from the influence of predominant wave propagation. The cross-shore displacement of the borrow area was approximately three times larger than the alongshore displacement. The largest cross-shore displacement of borrow area centroid was measured when the current speed equaled 1 m/s and the borrow area had a 1:1 aspect ratio. The measured displacement in this case was 37.93 m, which corresponds to 2.7% of the cross-shore borrow area dimension. The minimum cross-shore displacement of borrow area centroid was observed with the current speed equaled 0.5 m/s and the borrow area aspect ratio was 1:1. The measured displacement for this case was 32.25 m.

Additionally, Figure VI-15 shows that the cross-shore migration of the various borrow areas varied based on the current speed. For the smaller current speeds (0.2 m/s and 0.5 m/s) the cross-shore displacement decreases as aspect ratio is increased. However, for the higher current speed (1 m/s) the cross-shore migration at first decreases as aspect ratio is increased from 0.25 to 0.5 and then significantly increases for the square borrow area (aspect ratio equal to 1).

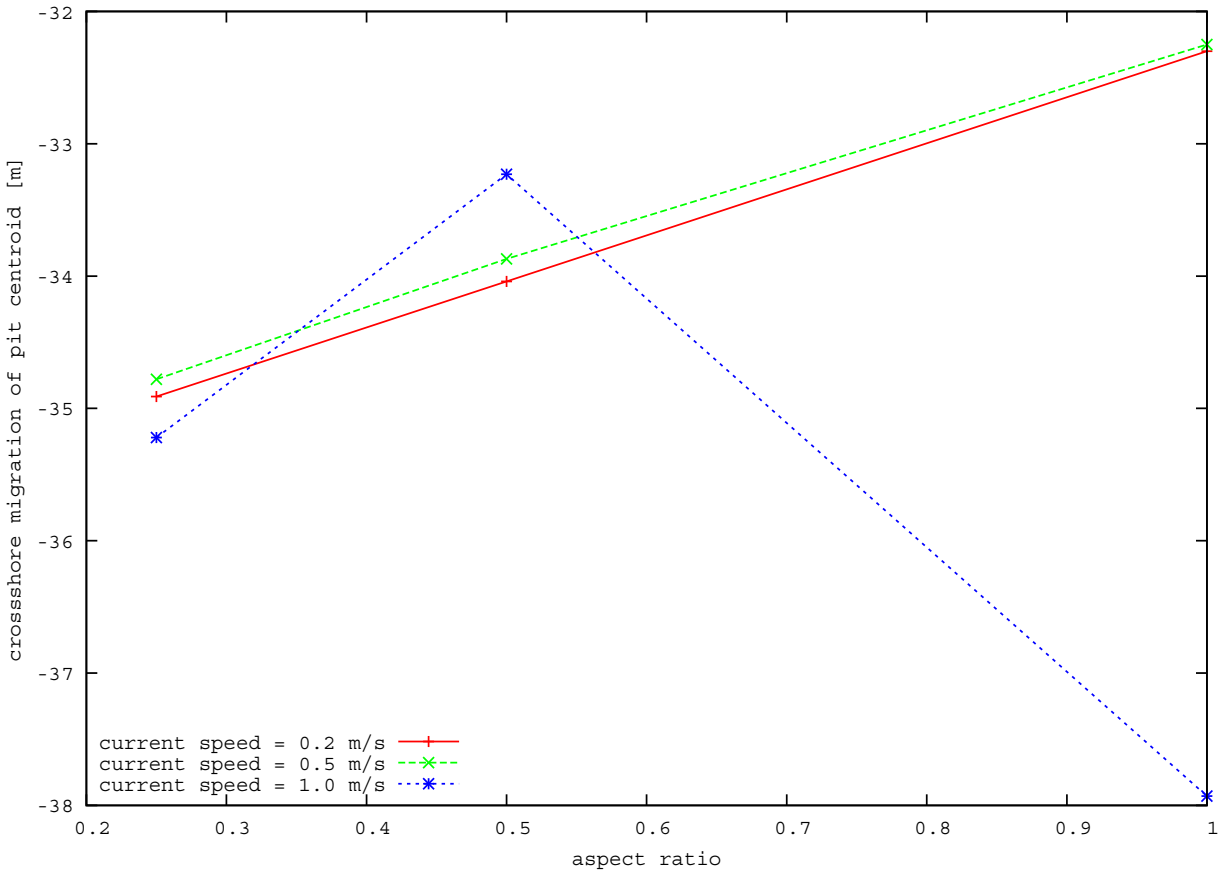

Figure VI-15. Cross-shore migration of borrow area centroid versus aspect ratio (distances in m from initial position of borrow area centroid; negative values mean shoreward direction).

The migration of the borrow area in the alongshore direction is due to nonlinear effects and to the interaction between the tidal current, parallel to the coast, and the waves. It should be noted that in the present scenarios, no residual current was present and therefore the net sediment transport in the direction parallel to the coast was caused by the interaction of tidal current and the waves. Figure VI-16 shows the largest alongshore displacement of borrow area centroid was equal to 10.82 m and was observed for the borrow area that had an aspect ratio of 0.25 and a 0.2 m/s tidal current. The minimum displacement of borrow area centroid was 6.82 m which occurred when the borrow area had a squared aspect ratio and tidal currents equaled to 1 m/s (Figure VI-16). Furthermore, Figure VI-16 showed that the alongshore displacement of borrow area centroid decreased as the aspect ratio was increased from 0.25 to 0.5 and then when the borrow area aspect ratio increased to 1.0 the difference in the displacement was only a minor decrease. The maximum increase of 2.57 m in alongshore migration occurred when the aspect ratio equaled 0.25 and the tidal current was 0.2 m/s.

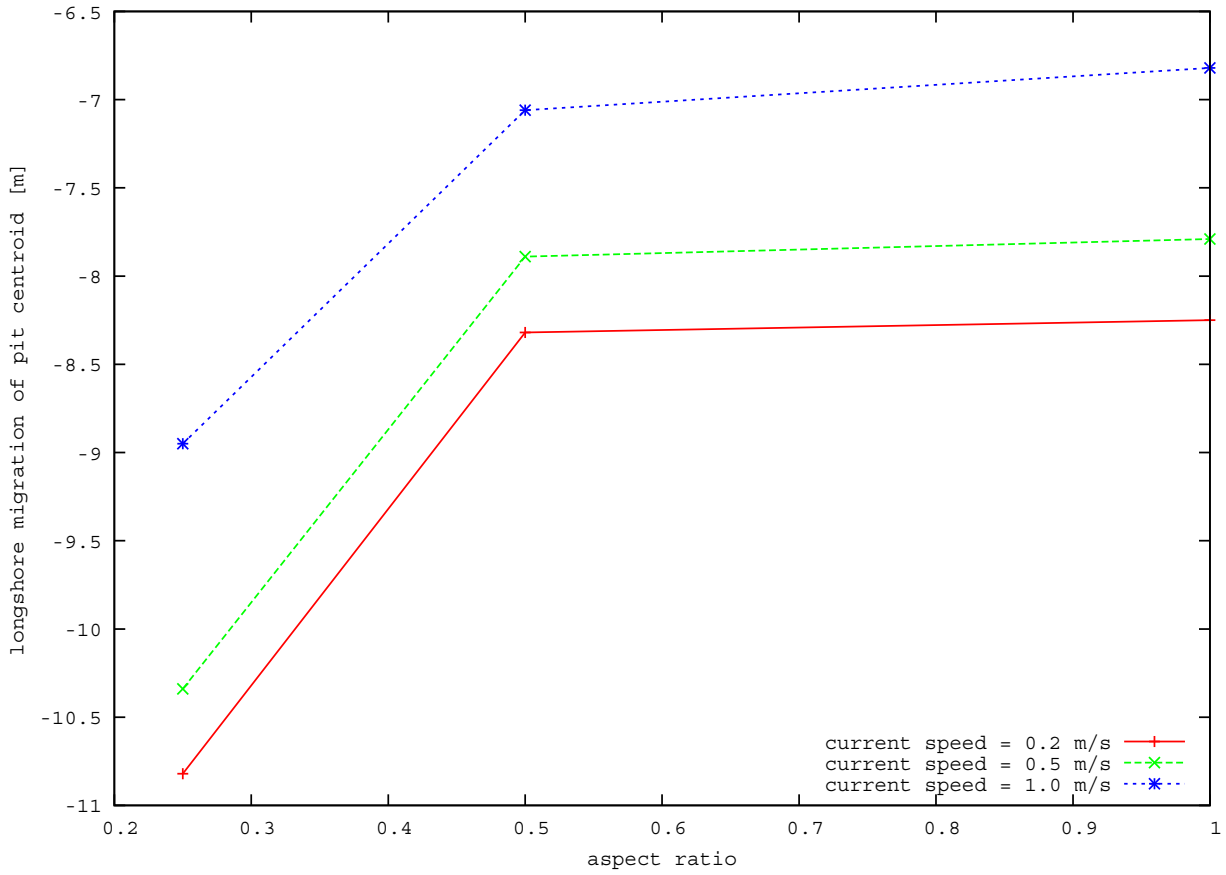

Figure VI-16. Alongshore migration of borrow area centroid versus aspect ratio (distances in m from initial position of borrow area centroid; negative values mean southward direction).

The results obtained for the deposition and erosion volumes inside the near-field area versus aspect ratio are shown in Figure VI-17 and VI-18. The largest volume of deposition and erosion were 135,993 m^3 and -141,021 m^3, respectively. Both of these volumes were obtained when the aspect ratio equaled 0.25. The tidal current speed was equal to 0.2 m/s and 1 m/s when the largest accretion and erosion occurred, respectively. Figure VI-17 showed that the deposited volumes decrease as the aspect ratio is increased. While Figure VI-18 showed that eroded volumes (negative values) decrease as the aspect ratio is increased.

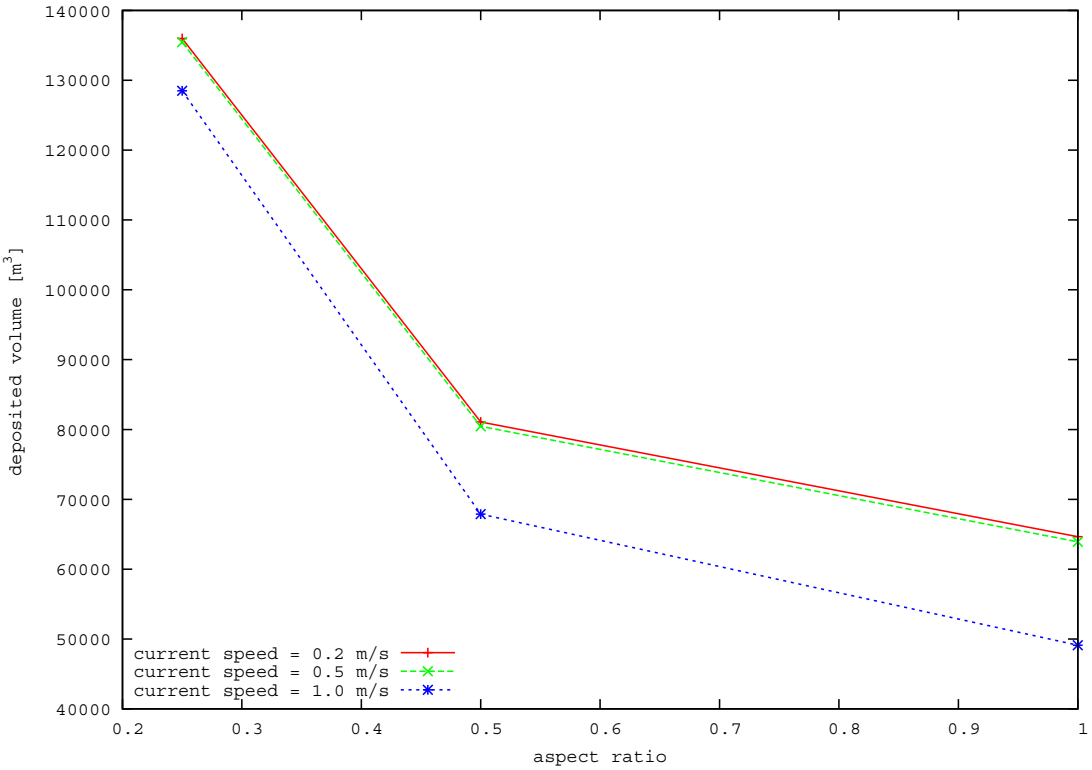

Figure VI-17. Total deposition (m^3) in the near-field area versus aspect ratio.

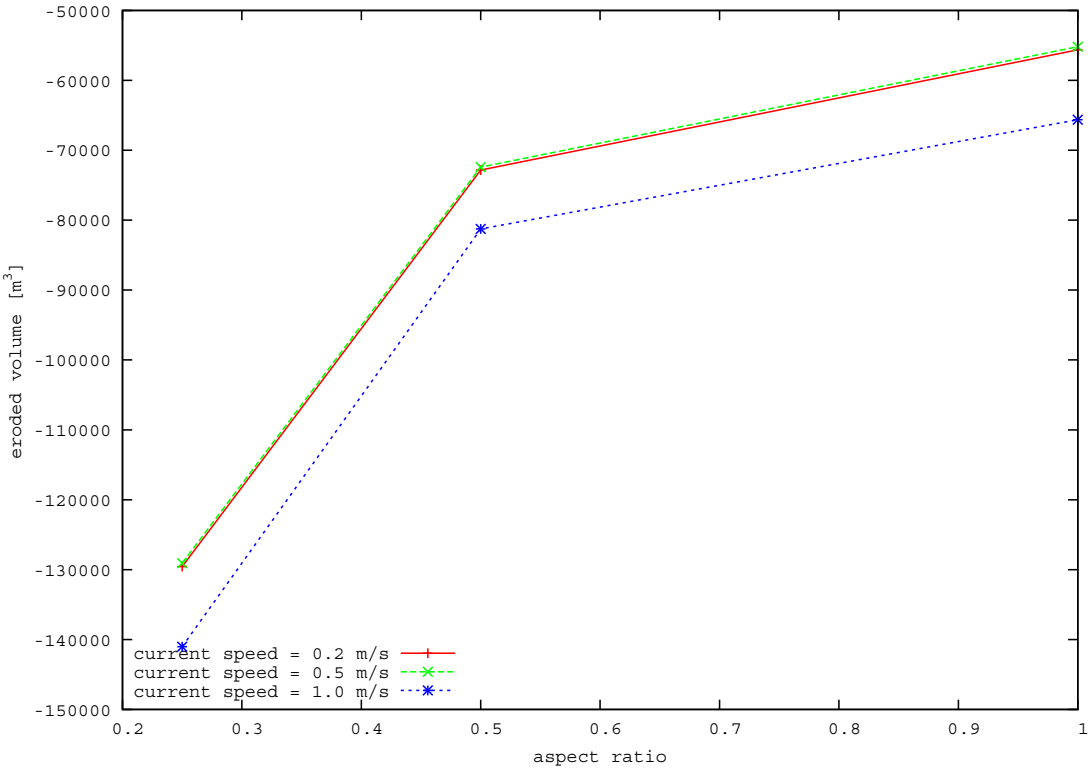

Figure VI-18. Total erosion (m^3, negative values) in the near-field area versus aspect ratio.

The net erosion/deposition inside the near-field area is shown in Figure VI-19. When the tidal current speed equaled 0.2 m/s or 0.5 m/s both deposition and erosion was modeled inside the near-field area; however, only erosion was measured when the current speed equaled 1 m/s. Furthermore, Figure VI-19 showed that for both deposition-dominated cases (tidal current speed equal to 0.2 m/s and 0.5 m/s) and for the erosion-dominated cases (tidal current speed equal to 1 m/s) the deposited or eroded volumes increase as aspect ratio is increased. The square borrow area was subject to the largest erosion/deposition.

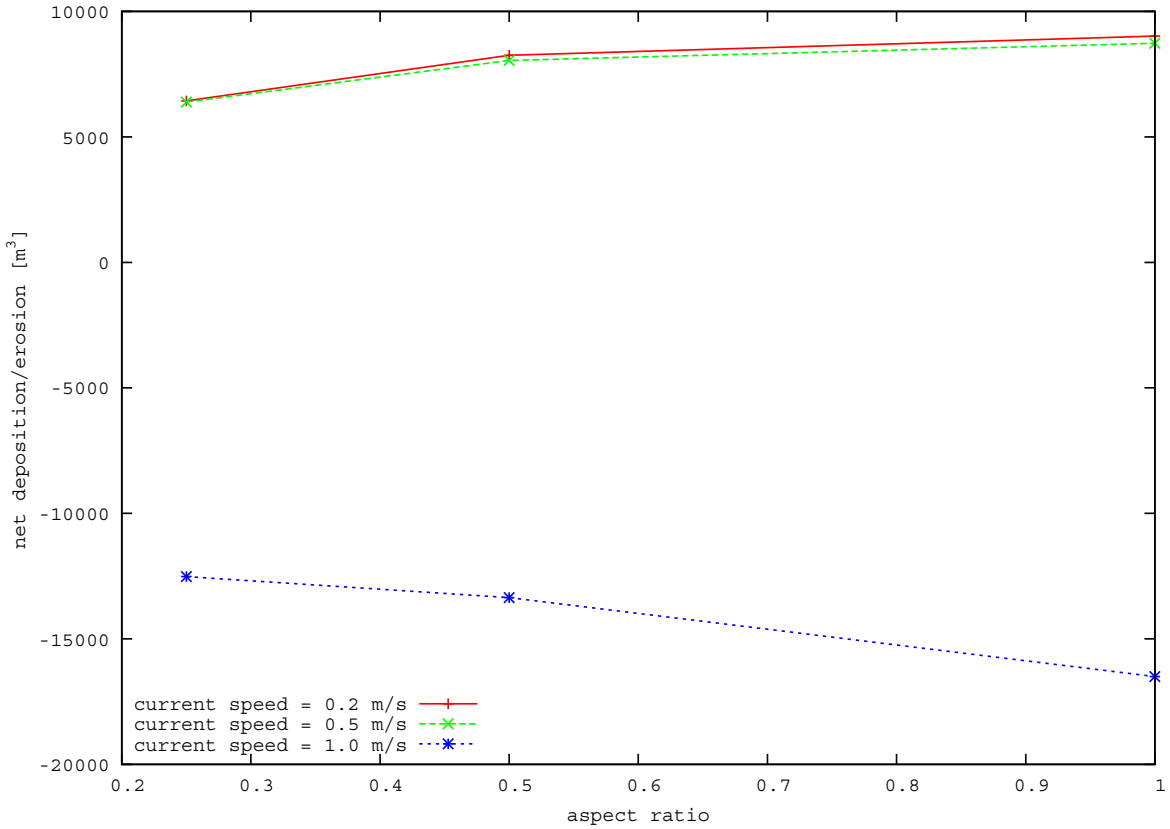

Figure VI-19. Net deposition (positive) erosion (negative) volumes (m^3) in the near-field area versus aspect ratio.

The maximum accretion and erosion measured inside the borrow area versus aspect ratio are shown in Figure VI-20 and VI-21, respectively. Both quantities attained small values and were approximately 10% of the initial borrow area depth. The maximum accretion and erosion observed occurred when the aspect ratio equaled 0.25 and the tidal current speed equaled 1 m/s. Figure VI-20 showed that the maximum accretion inside the borrow area decreased as the aspect ratio is increased. Figure VI-22 showed that the maximum erosion varied with aspect ratio. There was a different behavior depending on the value of the tidal current speed. In particular for the tidal current speed equaled to 1 m/s, the maximum erosion shows a minimum when the aspect ratio was equaled 0.5, while for the smaller values of current speed the maximum erosion increased as aspect ratio is increased.

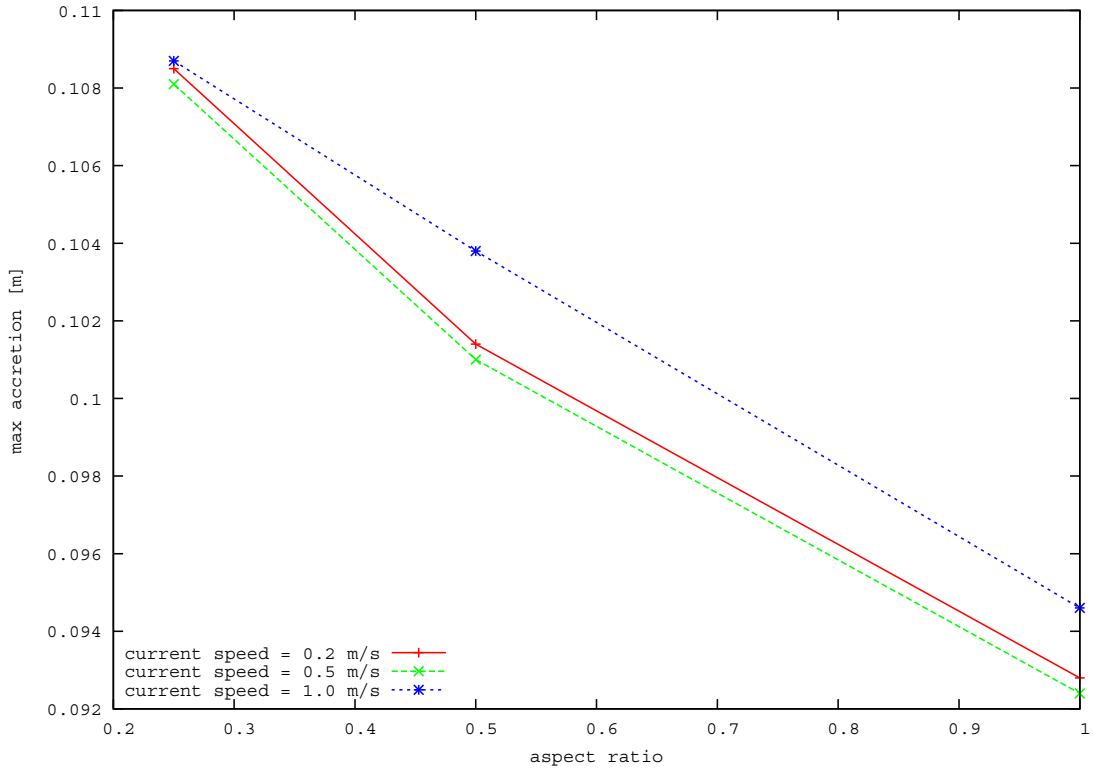

Figure VI-20. Maximum accretion (m) in the near-field area versus aspect ratio.

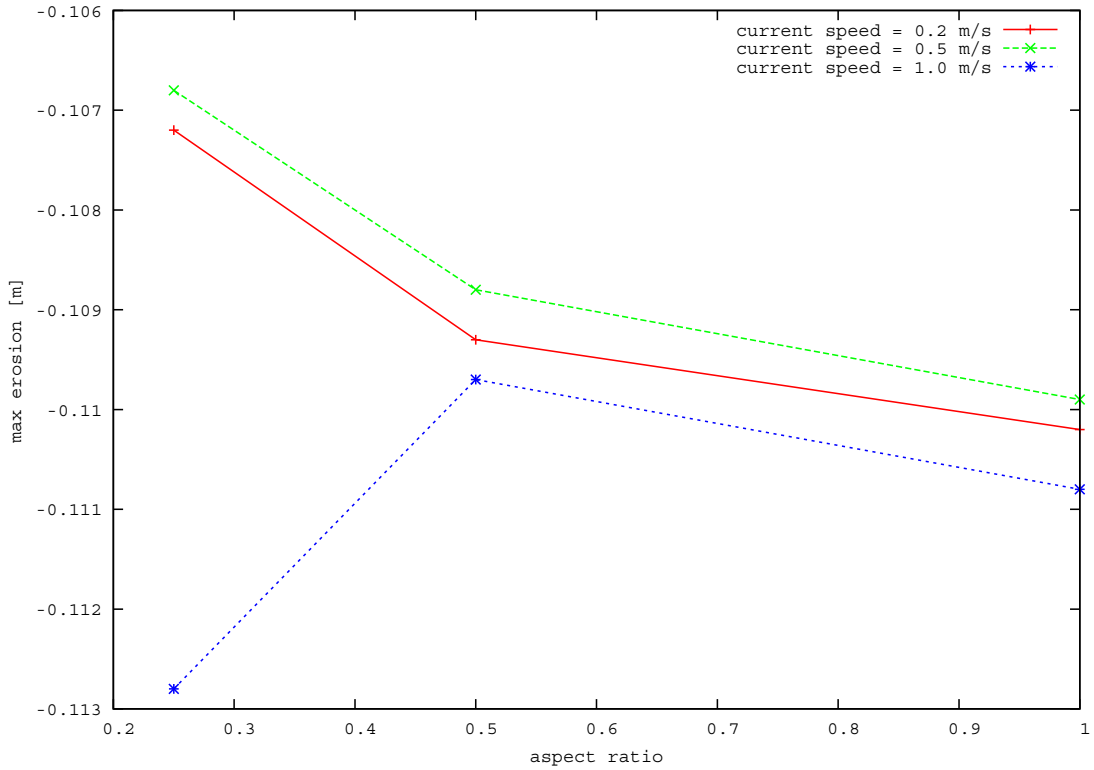

Figure VI-21. Maximum erosion (m^3) in the near-field area versus aspect ratio.

VI.C.2 Ambient Tidal Current Speed Scenarios

In a similar fashion to the aspect ratio scenarios, current speed scenarios also had a significant influence on morphological change. Three current speed scenarios were evaluated, where Figures VI-22 through VI-24 show the relative variation of wave height caused by the borrow area with an aspect ratio of 1 and varying current speeds of 0.2 m/s, 0.5m/s and 1.0m/s, respectively. The results were obtained on February 5, 2010 at 21:00 when both the maximum wave height and maximum current occurred. The figures show that the wave variation patterns are similar and that the 3% influence areas extended outside the computational domain. Figure VI-25 shows the influence area of wave height (m^2) versus the maximum current speed at the time when both the tidal current and wave height were at a maximum value for the cases with an aspect ratio of 1. It should be noted that the effect of the maximum current speed on wave height distribution is minimal. It should be mentioned that the calculations of the influence area may not be accurate due to the limited size of the computational domain versus the area affected, as the alteration to wave height extends beyond the boundaries of the model grid in the direction of wave propagation.

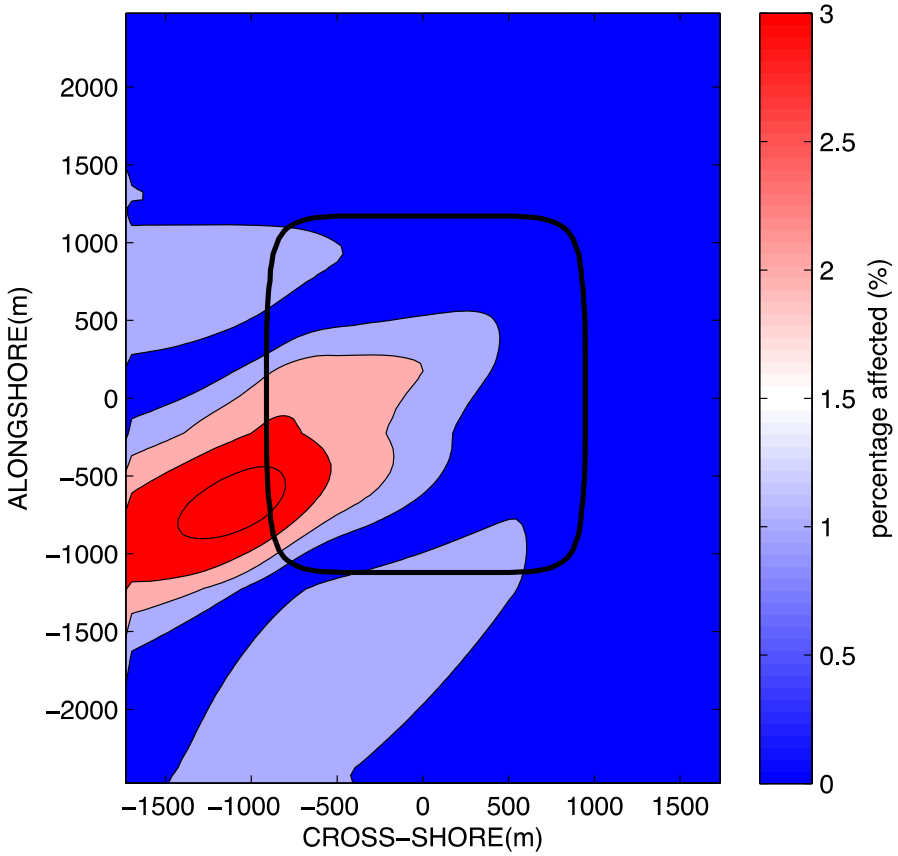

Figure VI-22. The relative variation of wave height during the maximum wave height (February 5, 2010 21:00) in the near-field region around the borrow area when the maximum current speed reached at 0.2 m/s. The red, light red and light blue areas indicate 3%, 2% and 1% influence, respectively. The aspect ratio remained constant at 1.

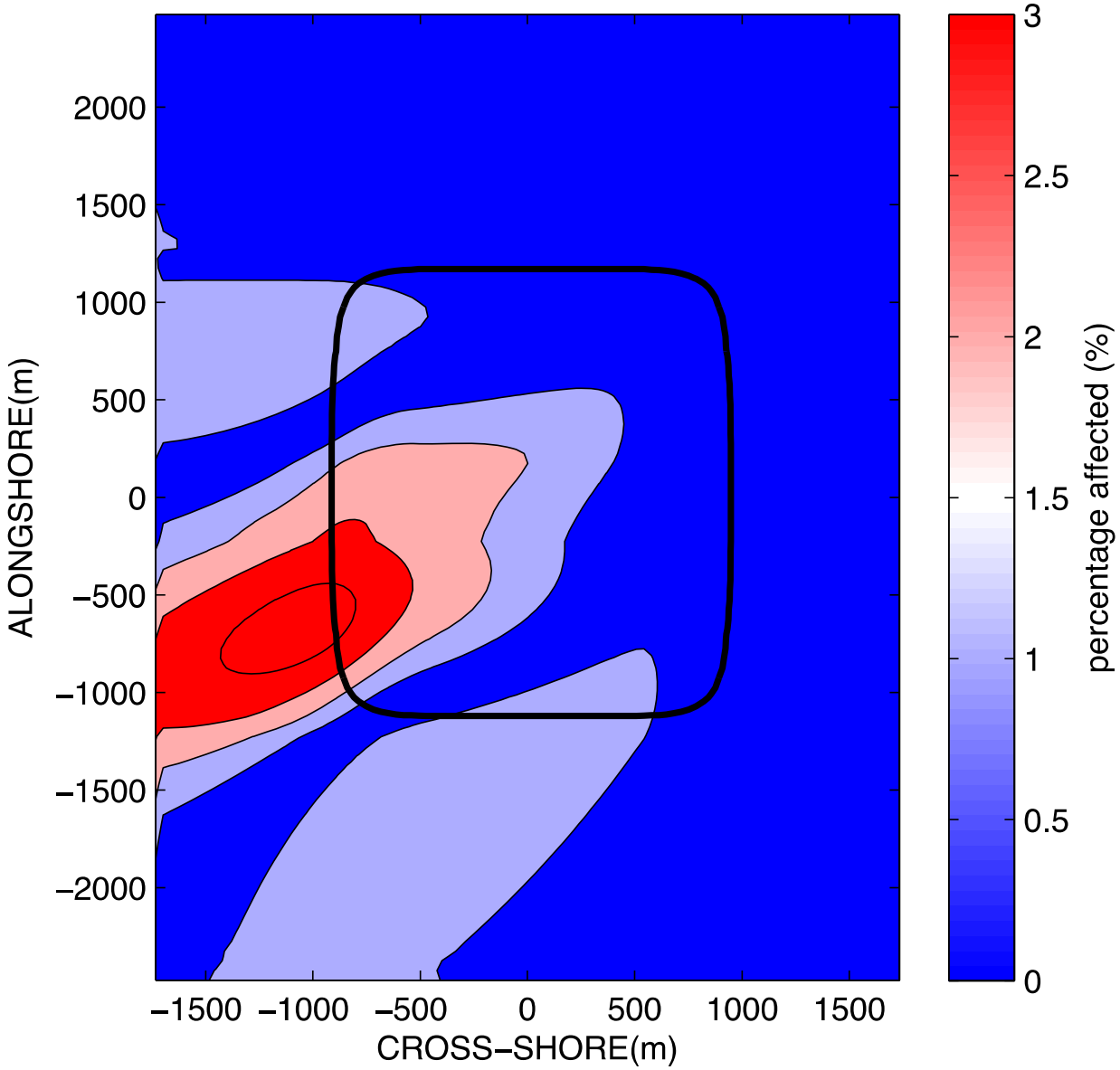

Figure VI-23. The relative variation of wave height during the maximum wave height (February 5, 2010 21:00) in the near-field region around the borrow area when the maximum current speed reached at 0.5 m/s. The red, light red and light blue areas indicate 3%, 2% and 1% influence, respectively. The aspect ratio remained constant at 1.

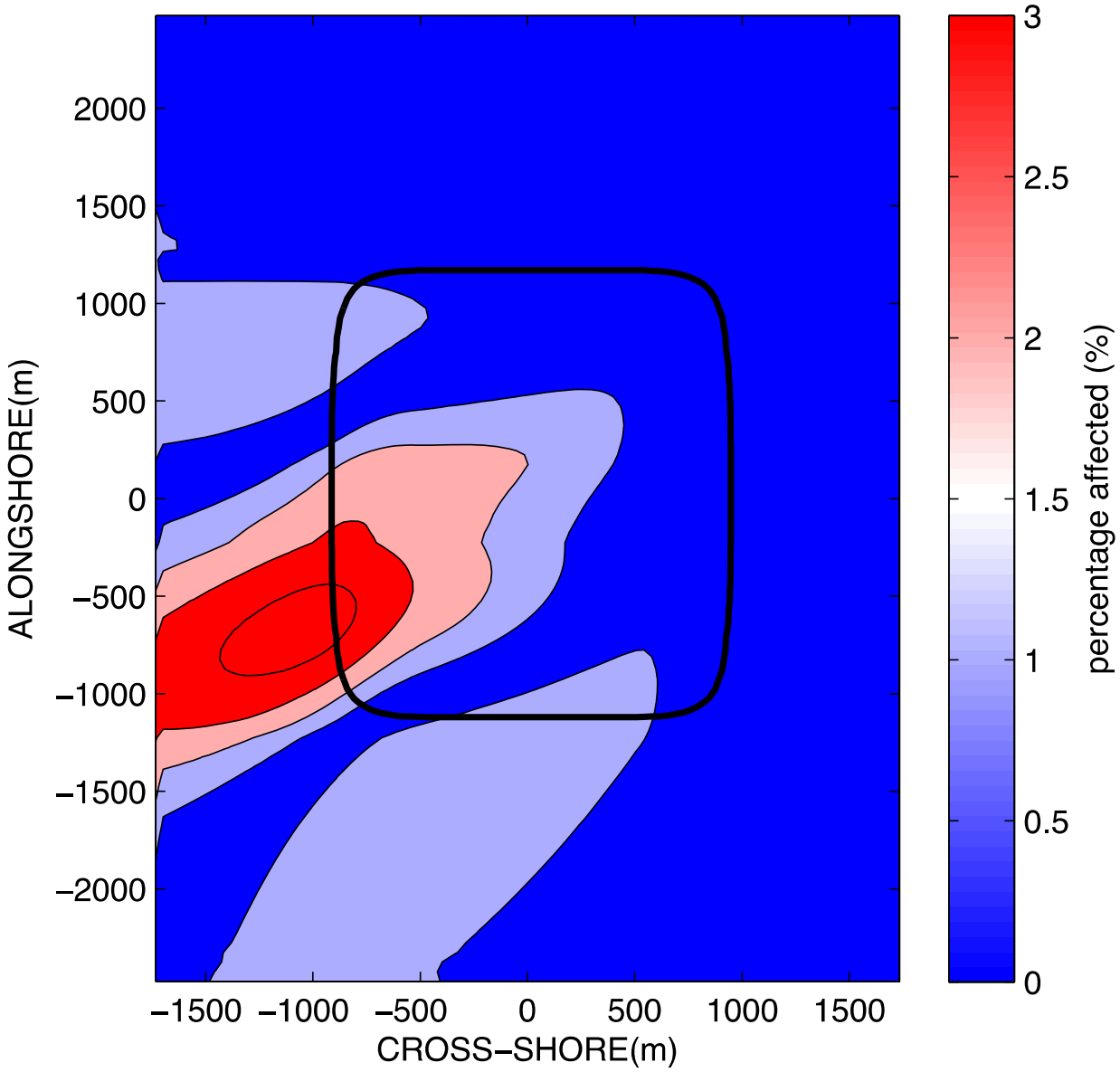

Figure VI-24. The relative variation of wave height during the maximum wave height (February 5, 2010 21:00) in the near-field region around the borrow area when the maximum current speed reached at 1.0 m/s. The red, light red and light blue areas indicate 3%, 2% and 1% influence, respectively. The aspect ratio remained constant at 1.

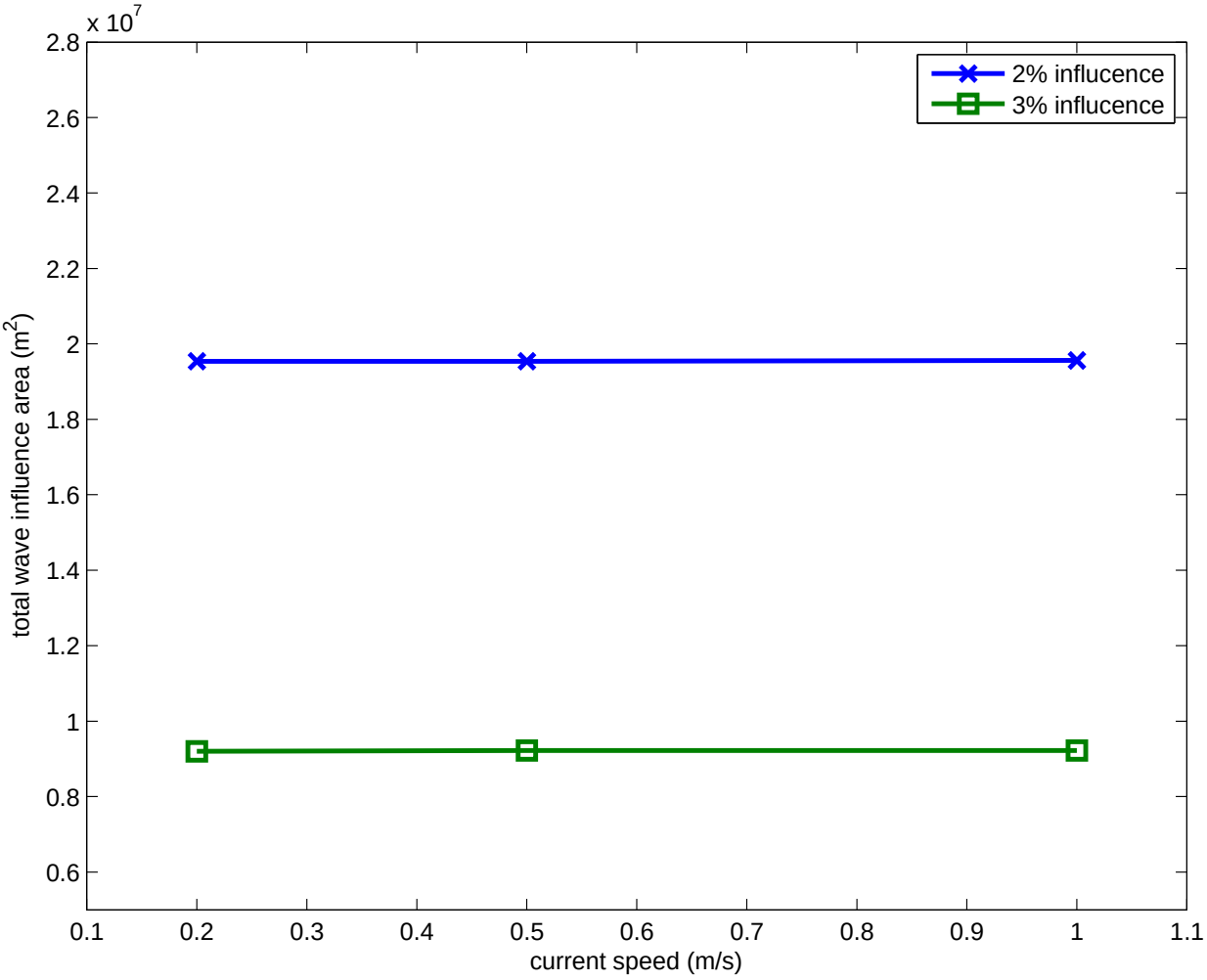

Figure VI-25. Wave height influence area (m^2) versus current speed. Aspect ratio remained constant at 1.

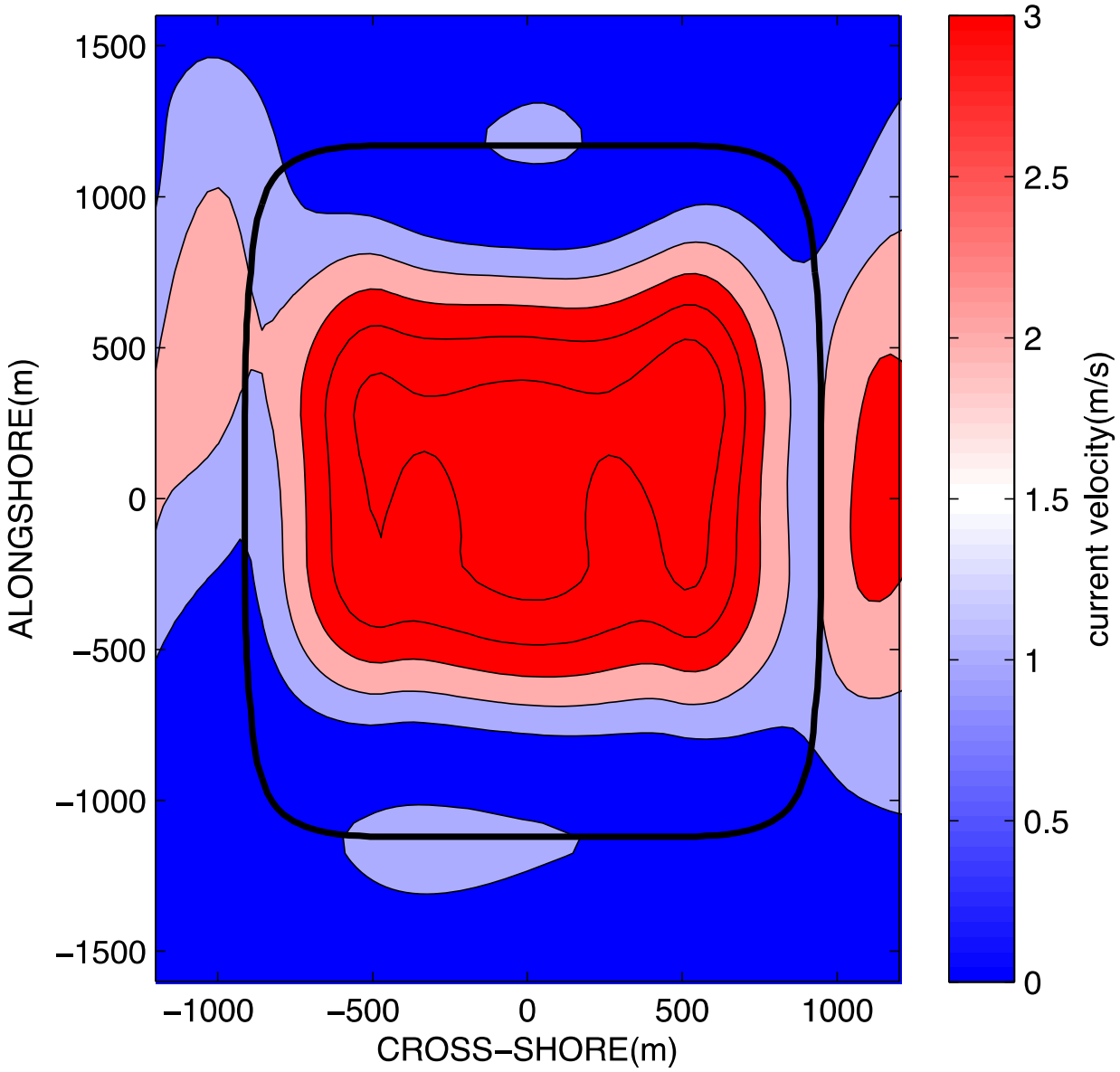

Figure VI-26. The relative variation of current speed during the maximum tidal current (02/05 21:00, 2010) in the near-field region around the borrow area when the maximum current speed equaled 0.2 m/s. The red, light red and light blue areas indicate 3%, 2% and 1% influence, respectively. The aspect ratio remained constant at 1.

Figures VI-26, VI-27, and VI-28 show the relative variation of current speed during the maximum tidal current (02/05/2010 21:00) in the three cases with the aspect ratio of 1 and the maximum current speed of 0.2 m/s, 0.5 m/s, and 1.0 m/s, respectively. The current variations due to the presence of borrow area were concentrated at the center of the borrow area in all cases. Figure VI-29 shows the tidal current influence area versus current speed, where alterations in current speed only slightly affected the area of total current influence. Moreover, the area of current influence actually decreases with increasing current speed. However, similar to the wave height influence described previously, the influence of currents also extends beyond the near-

field model domain. Therefore, definitive conclusions regarding area of influence relative to current speeds cannot be derived from Figure VI-29.

The cross-shore displacement of the borrow area centroid was again approximately three times larger than the alongshore displacement (Figures VI-30 and VI-31). The largest cross-shore displacement of the borrow area centroid was equal to 37.93 m south, corresponding to 2.7% of cross-shore borrow area dimension, and was observed for a current speed equal to 1 m/s and the square borrow area (aspect ratio equal to 1). The minimum cross-shore displacement of the borrow area centroid, 32.25 m south, was observed for a current speed equaled to 0.2 m/s and a square borrow area (aspect ratio equal to 1).

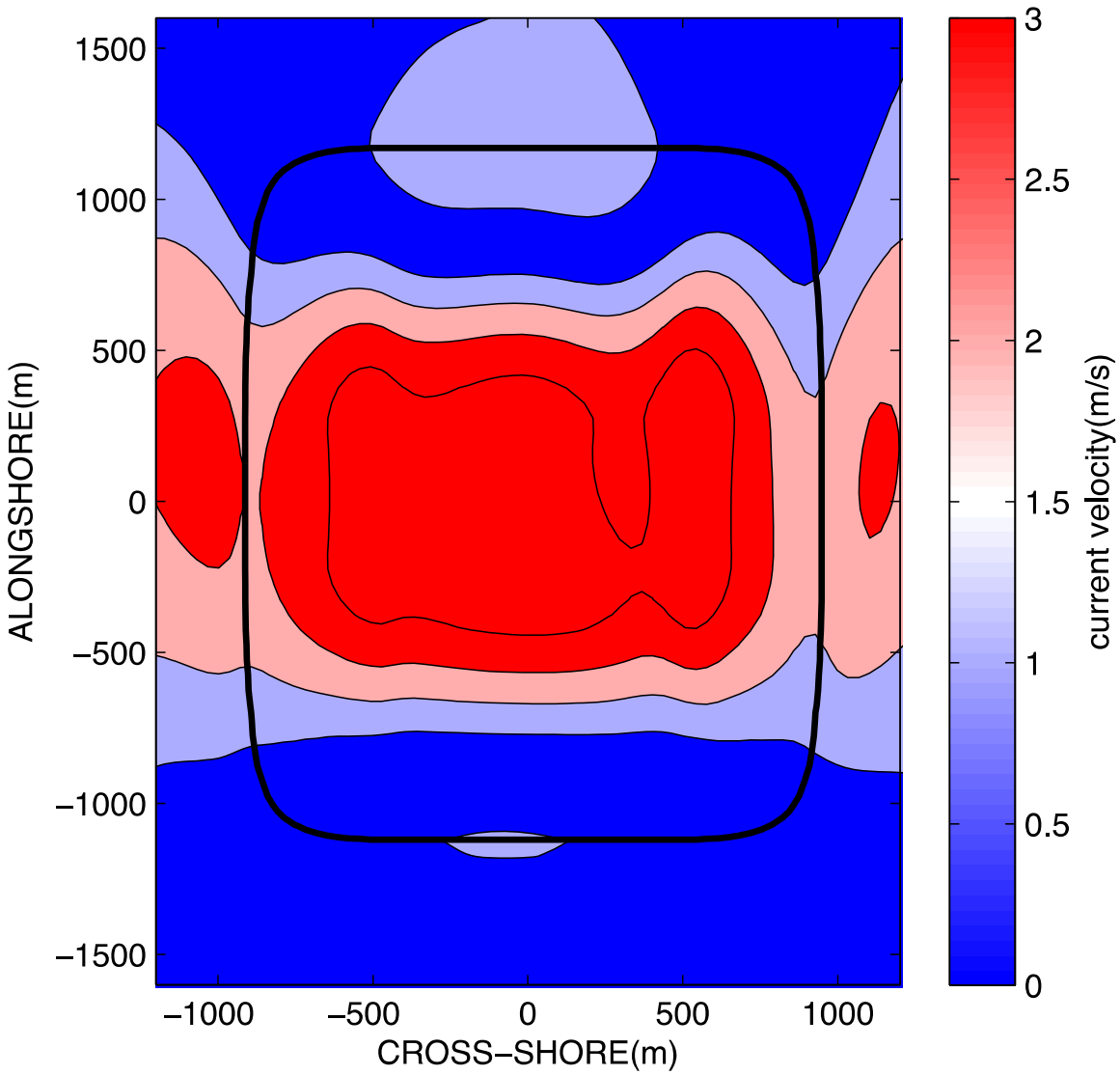

Figure VI-27. The relative variation of current speed during the maximum tidal current (02/05 21:00, 2010) in the near-field region around the borrow area when the maximum current speed equaled 0.5 m/s. The red, light red and light blue areas indicate 3%, 2% and 1% influence, respectively. The aspect ratio remained constant at 1.

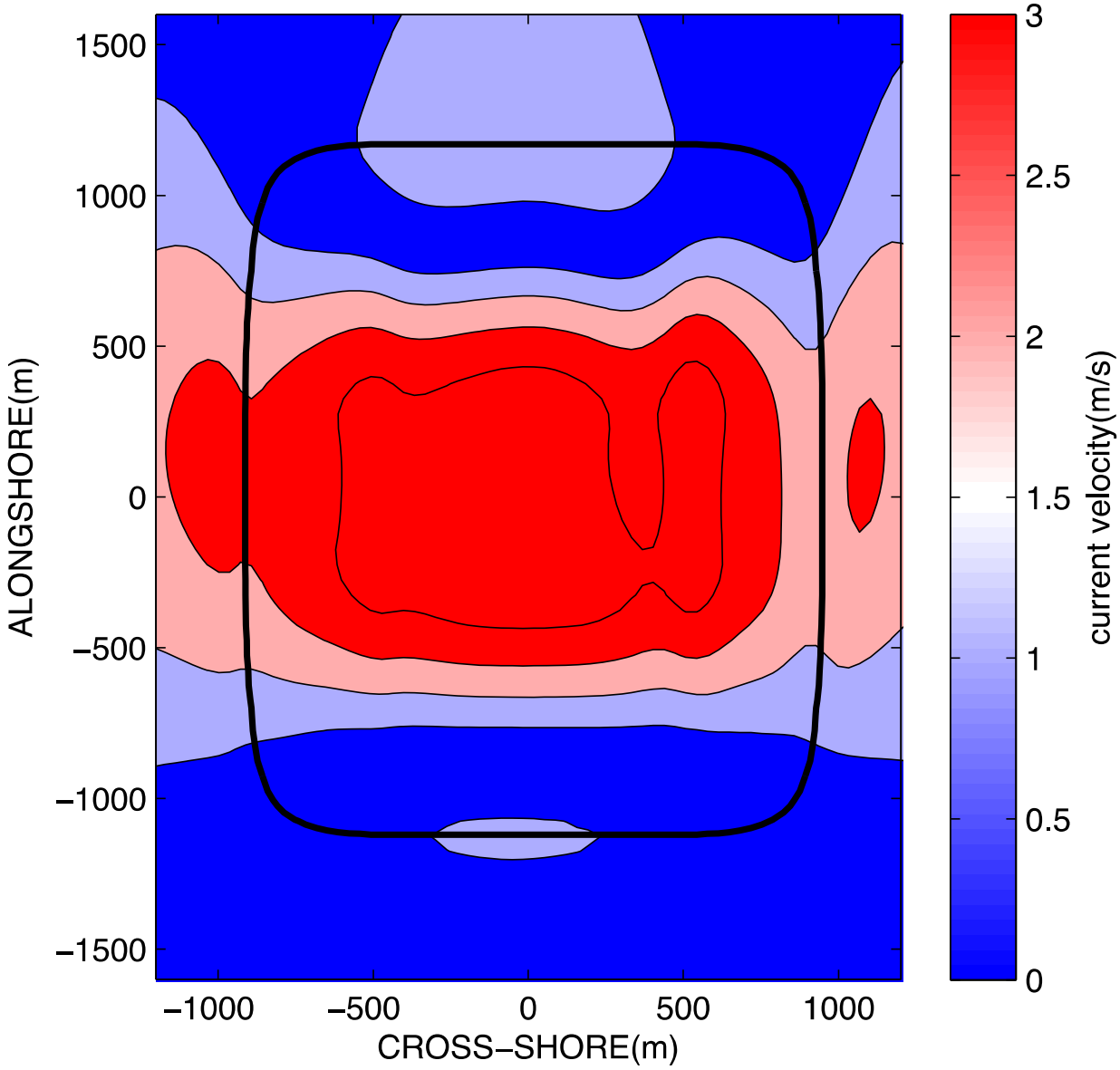

Figure VI-28. The relative variation of current speed during the maximum tidal current (02/05 21:00, 2010) in the near-field region around the borrow area when the maximum current speed equaled 1.0 m/s. The red, light red and light blue areas indicate 3%, 2% and 1% influence, respectively. The aspect ratio remained constant at 1.

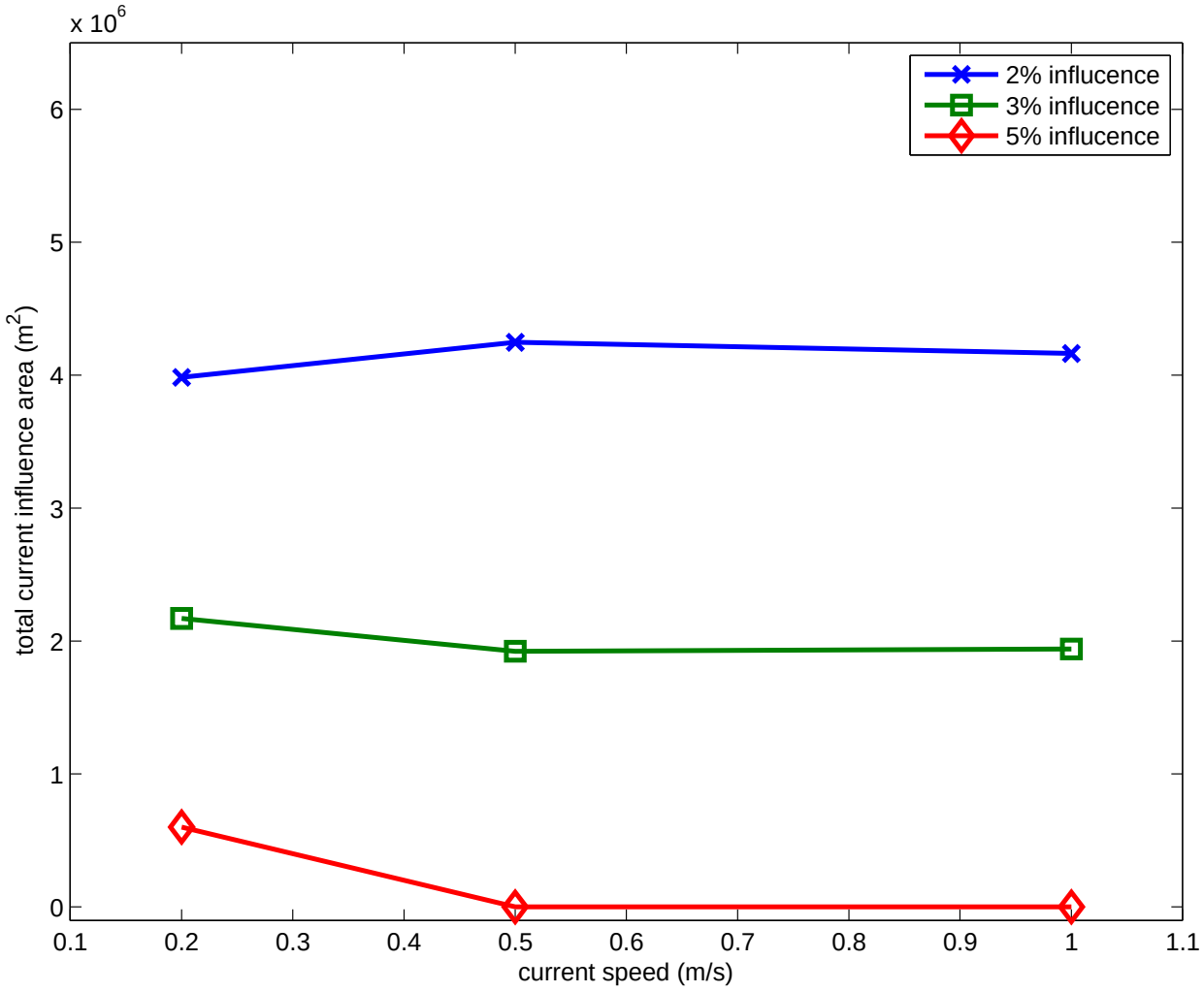

Figure VI-29. Influence area of tidal current (m^2) versus current speed. Aspect ratio remained constant at 1.

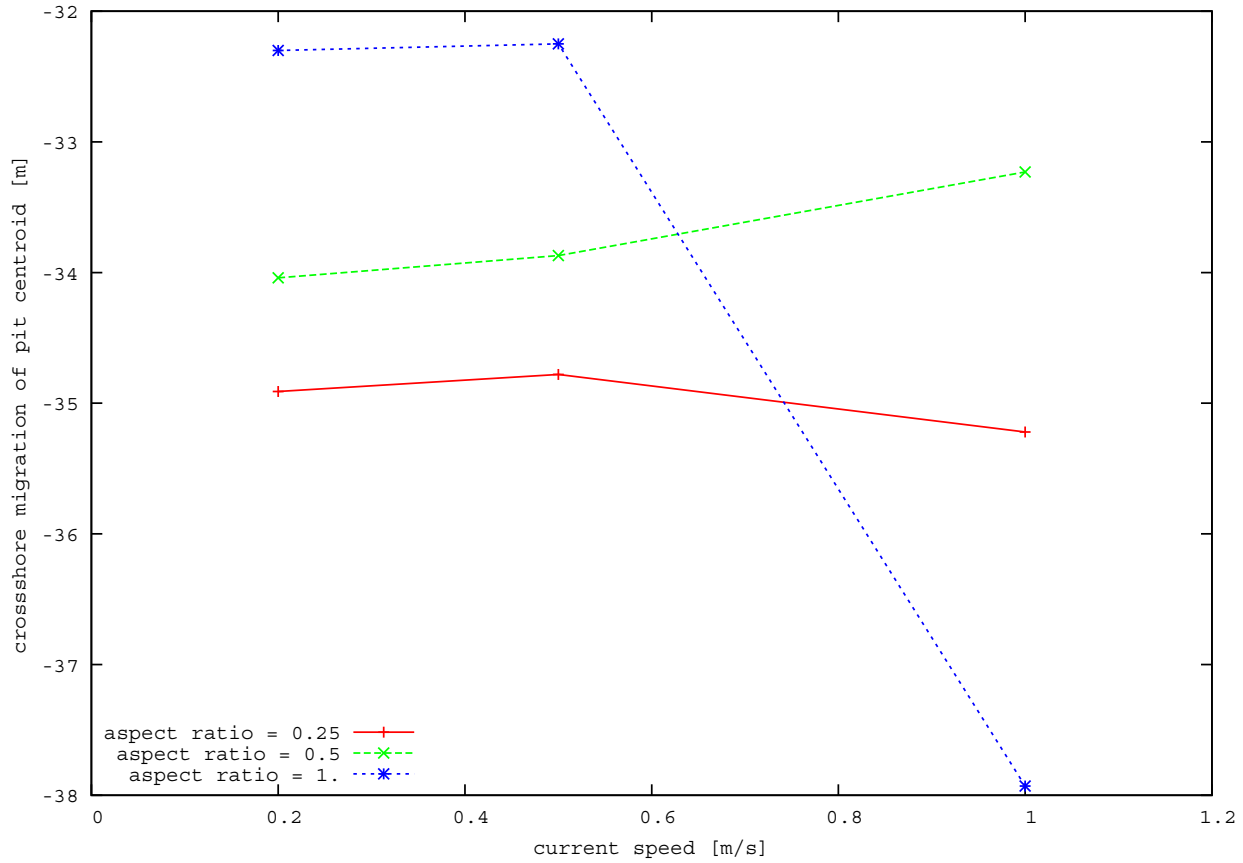

Figure VI-30. Cross-shore migration of borrow area centroid versus current speed (distances in m from initial position of borrow area centroid; negative values mean shoreward direction).

Figure VI-30 shows the variation of the cross-shore position of the borrow area centroid at the end of the simulation versus current speed. This figure showed that the variation of the cross-shore migration of the borrow area centroid depended on the borrow area aspect ratio as the current speed is increased from 0.2 m/s to 1 m/s. When the aspect ratio equaled 0.25 there was a very slight decrease when the current speed increased from 0.2 m/s to 0.5 m/s followed by a slight increase when the current speed increased to 1 m/s. A similar behavior occurred, but with more borrow area displacement cross-shore when the current speed was increased to 1 m/s and the aspect ratio was equal to 1. The baseline borrow area (aspect ratio equal to 0.5) showed a decrease in the cross-shore displacement of borrow area centroid as the current speed was increased.

Once the ambient current speeds reached 1 m/s, the influence of aspect ratio was difficult to discern. For lower current speeds (0.2 m/s and 0.5 m/s), the influence of currents indicated an inverse relationship with borrow area migration, where the higher current speed of 0.5 m/s showed less landward migration than the 0.2 m/s scenarios for all aspect ratios. This is indicative that the higher current velocities may offset some of the strongly wave-induced landward transport.

Figure VI-31 shows the alongshore displacement of the borrow area centroid versus the current speed. The largest alongshore displacement of borrow area centroid, equal to 10.82 m south, was measured for the borrow area with an aspect ratio of 0.25 and a tidal current of 0.2 m/s. The minimum displacement of the borrow area centroid, equal to 6.82 m south, was measured for the square borrow area with a current speed of 1 m/s. Figure VI-31 shows that displacement of the borrow area centroid in the alongshore direction decreases as the tidal current speed was increased. The maximum increase of the alongshore displacement as the current speed was varied was equal to 1.87 m for an aspect ratio equal of 0.25. Similar to the results regarding landward migration, there appears to be an inverse relationship between alongshore borrow area migration and current speed, likely due to the current velocity offsetting the wave-induced south-directed migration in this case.

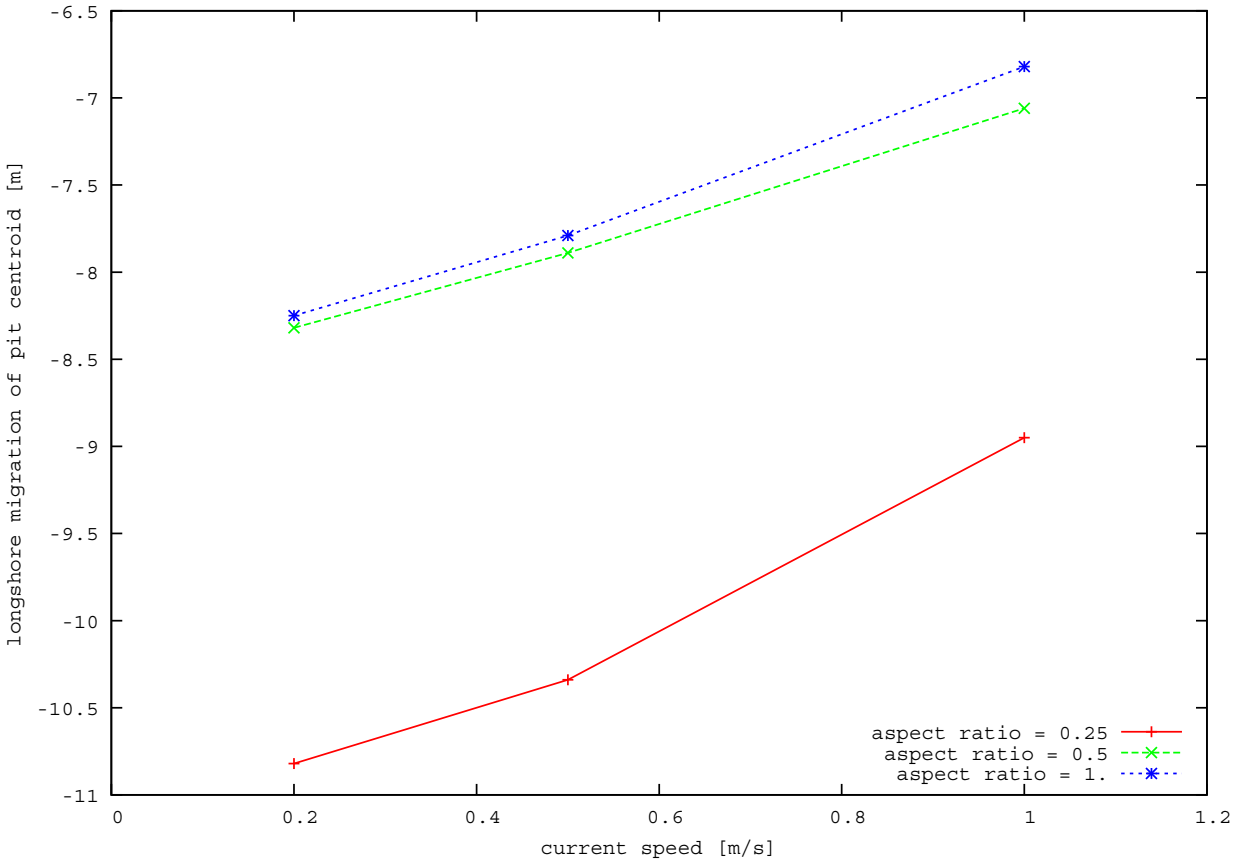

Figure VI-31. Alongshore migration of borrow area centroid versus current speed (distances in m from initial position of borrow area centroid; negative values mean southward direction).

The deposition and erosion volumes inside the near-field area versus current speed are shown in Figure VI-32 and VI-33, respectively. The largest volume of deposition and erosion were 135,993 m^3 and -141,021 m^3, respectively, and occurred when the aspect ratio equaled 0.25. When the tidal current speed was 0.2 m/s, the largest amount of deposition occurred, while when the current speed equal to 1 m/s the largest amount of erosion occurred. Figure VI-32 shows that deposited volumes decrease as the tidal current speed was increased. Figure VI-33 shows that the amount of erosion increased as the tidal current speed increased. In general, the amount of

erosion and deposition for the lower current speeds (0.2 m/s and 0.5 m/s) was equivalent fir a given aspect ratio, and there was significantly less deposition and more erosion for the 1.0 m/s current scenarios for all aspect ratios. This is shown in Figure VI-34 that illustrates the net erosion/deposition inside the near-field area versus current speed. When the current speed was equal to 0.2 m/s and 0.5 m/s the near-field area experienced moderate accretion; however, when the current speed was increased to 1.0 m/s, the near-field area experienced substantial erosion. Figure VI-34 also shows that square borrow area experienced the largest erosion, although all borrow area aspect ratios indicated similar results.

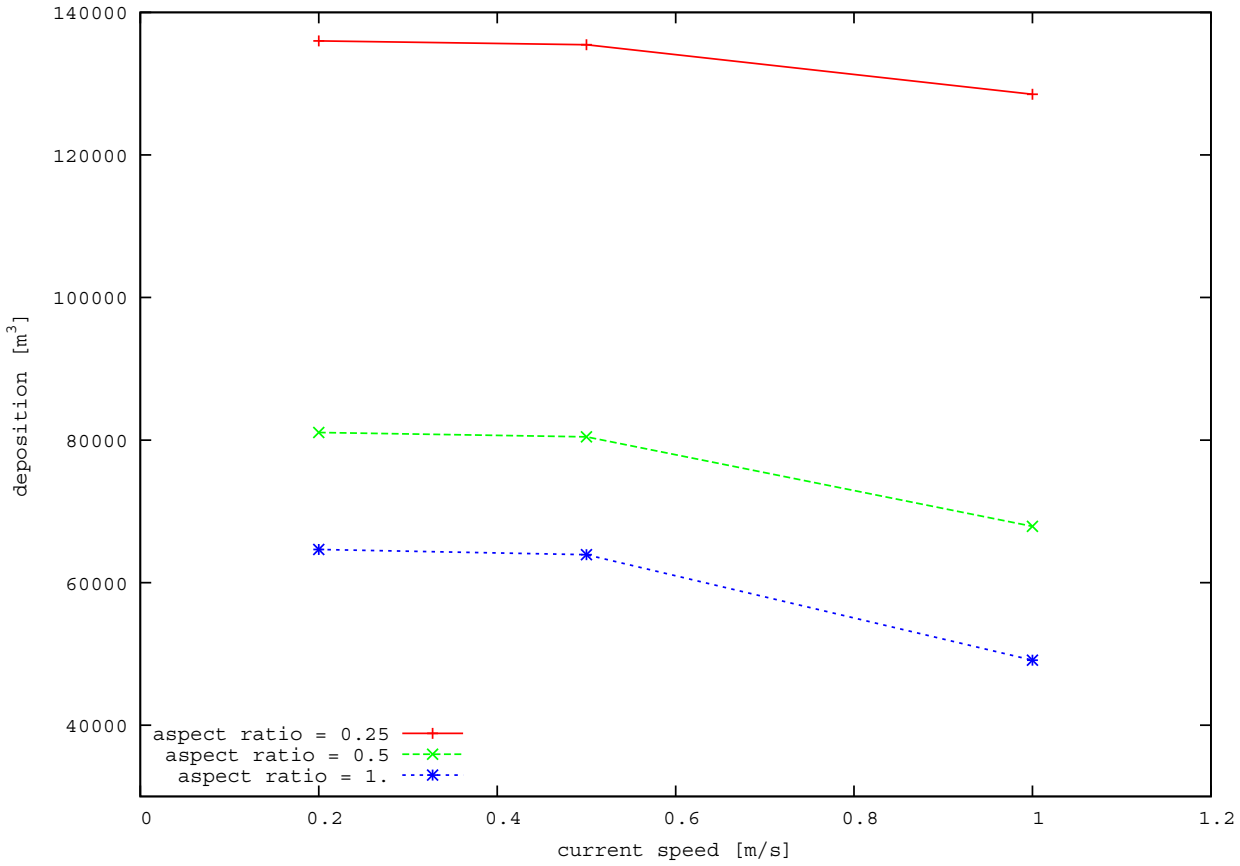

Figure VI-32. Total deposition (m^3) in the near-field area versus current speed.

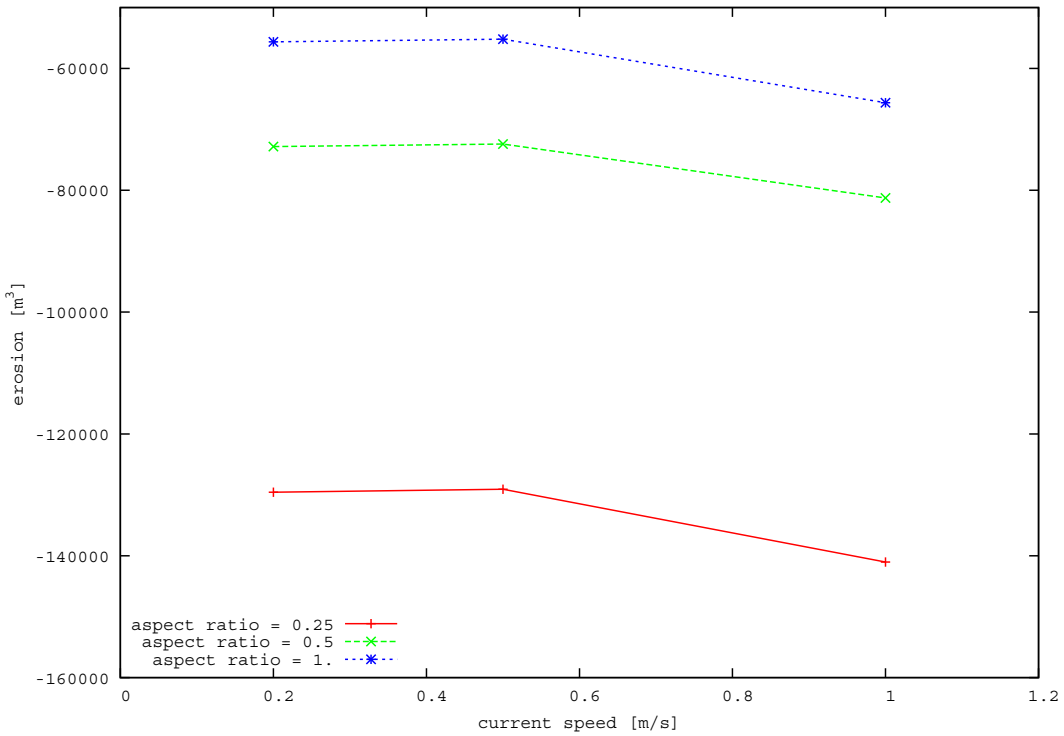

Figure VI-33. Total erosion (m^3, negative values) in the near-field area versus current speed.

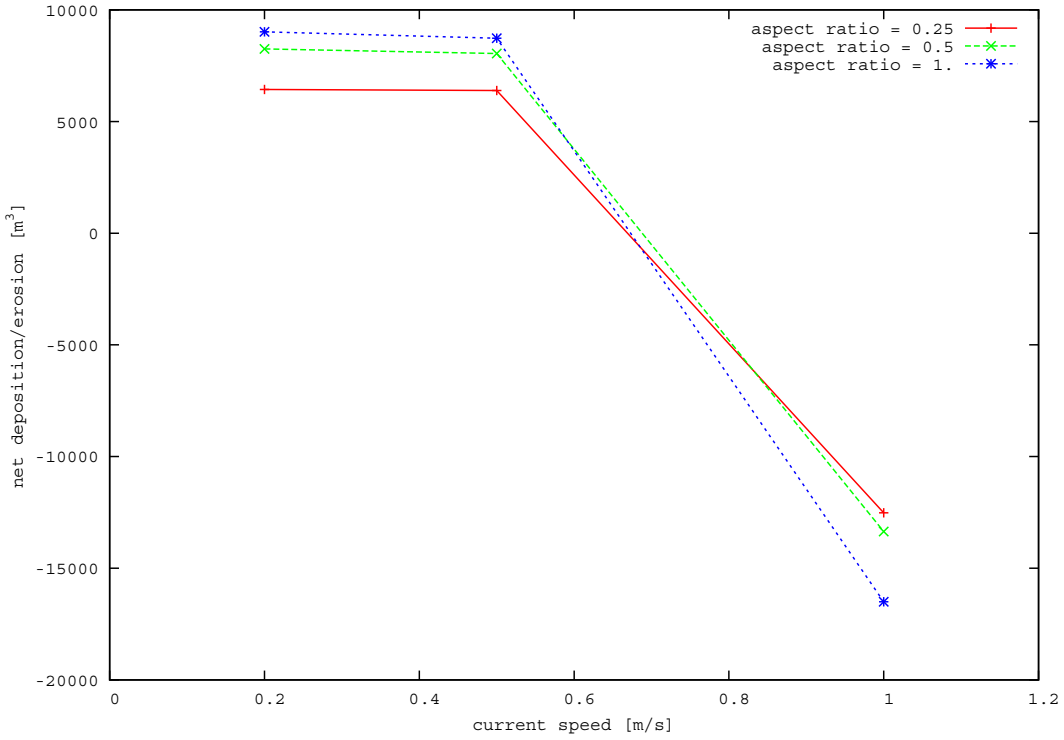

Figure VI-34. Net deposition (positive) erosion (negative) volumes (m^3) in the near-field area versus current speed.

Figures VI-35 and VI-36 show the maximum accretion and erosion values measured inside the borrow area versus current speed. Both maximum values were small and ranged around 10% of the initial borrow area depth. Figure VI-35 shows that the maximum accretion inside the borrow area increased very mildly as the tidal current speed was increased. Figure VI-36 shows that the largest maximum erosion occurred when the current speed was 1 m/s and the smallest maximum erosion occurred when the current speed was equal to 0.5 m/s.

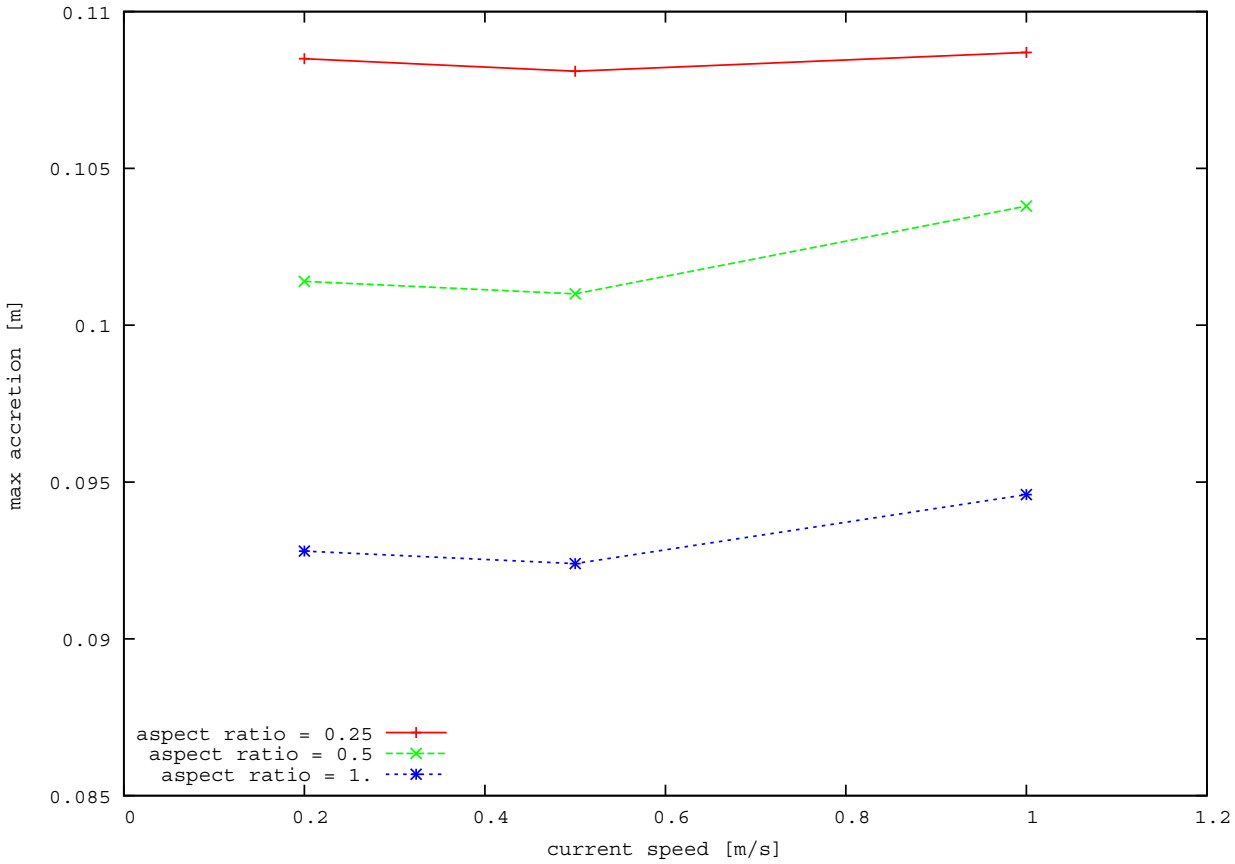

Figure VI-35. Maximum accretion (m) in the near-field area versus current speed.

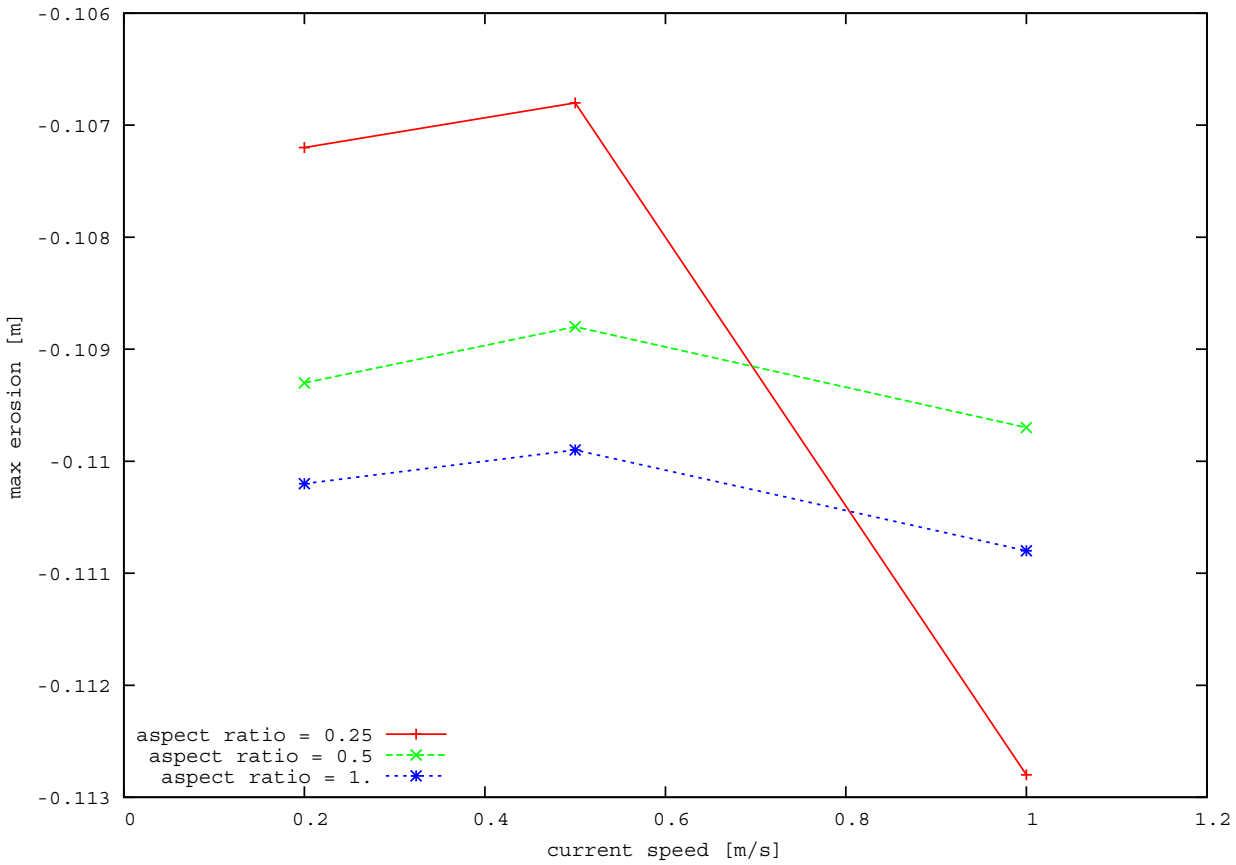

Figure VI-36. Maximum erosion (m^3) in the near-field area versus current speed.

VI.C.3. Conclusions for Near-field Flat Bed Scenarios

Utilizing the idealized bathymetry and dredged borrow area, a NearCoM model was developed to assess varying borrow area aspect ratios and current speeds on morphological change over a one-year period. The idealized case was based on the general characteristics of the Cane South borrow area off the coast of South Carolina. A total of nine test cases were evaluated, where three different borrow area aspect ratios (1, 0.5, and 0.25) and three different ambient tidal current speeds (0.2 m/s, 0.5 m/s, and 1.0 m/s) were considered. Based on the results of the nine test cases, the following conclusions have been made:

- The influence area of the borrow area both on wave height and on ambient tidal current increases as the aspect ratio of the borrow area is increased. Since the wave and current conditions are based on information derived from Cane South, where the borrow area aligns obliquely with the incoming wave field and ambient tidal currents, the larger aspect ratios cause a greater perturbation to both the background wave and current fields.
- At the end of the morphodynamic model simulations (1-year model run), the cross-shore displacement of the borrow area centroid is greater in the cross-shore direction than the alongshore direction in all cases. This indicates that the wave asymmetry component of sediment transport is dominant.

- The variation of the alongshore migration of the borrow area centroid is more sensitive to changes of the aspect ratio of the borrow area than of the tidal current speed.
- For the lowest values of the current speed considered (0.2 m/s and 0.5 m/s), the borrow areas tend to accrete (deposition prevails over erosion) and the net deposited volumes increase as the borrow area aspect ratio is increased. As described above, the larger perturbations to primarily the wave field by the higher aspect ratio borrow area shape, which is likely responsible for the larger accretion rates.
- For tidal current speed of 1 m/s, erosion in the borrow area prevails over deposition, and the eroded volumes increase as the current speed is increased. In this case, current speed is responsible for mobilizing sediment and can alter the overall wave-induced sediment transport that is 'typical' of U.S. Atlantic OCS borrow areas.
- The values of the maximum erosion and accretion depths measured inside the borrow area are only on the order of 10% of the borrow area depth over the 1-year simulation period. At water depths similar to 'typical' U.S. Atlantic OCS borrow areas, recovery of the borrow areas bathymetric conditions to the pre-dredging surface can take several years and perhaps more than a decade in sites dominated by wave-induced transport. However, this is highly dependent on frequency of storms.

In evaluating the obtained results and conclusions it should be kept in mind that they have been obtained for a limited number of scenario cases (three borrow areas with different aspect ratios and three different tidal current speeds) with fixed sediment characteristics and wave conditions (i.e. February 2010 at the Cane South site). To develop a more complete understanding relative to the influence of the different parameters and processes influencing sediment transport at 'typical' U.S. Atlantic OCS borrow areas, further investigations likely are necessary. Additional scenarios could include a more robust analysis of borrow site shapes including aspect ratio, total size, and borrow site excavation depth. It is anticipated that site-specific information would be utilized to further define appropriate borrow site geometries.

VI.D. FAR-FIELD MORPHOLOGY, AMBIENT FLAT BED TEST CASES

The NearCoM model was also used to investigate the far-field effects of the borrow area. The scenarios considered were the same as those considered in the near-field investigation, described in the previous section. However, the dimensions of the computational domain were larger than those used in the near-field investigation. The number of grid points remained the same as the near-field cases of 100 points in both the cross-shore and long-shore directions. The nine scenarios considered and their respective computational domains are listed in Table VI-2.

Table VI-2. Test scenarios and computational domain for the ambient flat bed far-field morphology.				
Pit length alongshore (meter)	**Pit length cross-shore (meter)**	**Computational domain in the alongshore direction (meter)**	**Computational domain in the cross-shore direction (meter)**	**Current speed (m/s)**
2,000	1,000	20,000	10,000	0.20
2,000	1,000	20,000	10,000	0.50
2,000	1,000	20,000	10,000	1.00
4,000	500	20,000	10,000	0.20
4,000	500	20,000	10,000	0.50
4,000	500	20,000	10,000	1.00
1,414	1,414	20,000	10,000	0.20
1,414	1,414	20,000	10,000	0.50
1,414	1,414	20,000	10,000	1.00

In order to assess the far-field effect of the borrow area and to avoid the near-shore region, where NearCoM might not give reliable results, due to the complex phenomena taking place in the surf region, it was decided to assess the far field effects of the borrow area by considering the region between the 5 m and 10 m contour, where results were evaluated at the 5m contour. In particular total deposition, total erosion and net volume change in the region between 5m and 10m contour were evaluated for all the scenarios tests. Moreover the maximum accretion and maximum erosion measured at the 5 m contour were determined.

VI.D.1. Borrow Area Aspect Ratio Scenarios

Similar to the near-field test cases, the far-field flat bed scenarios were evaluated to assess the effect of the borrow area aspect ratio. Figure VI-37 illustrates the deposited volumes in the computational domain between the 5 m and 10 m contour versus the aspect ratio. For all the current speeds considered, the maximum increase in deposition occurred as the aspect ratio increased from 0.25 to 1, which approximately equaled 15% of the average value and 1.4% of the initial borrow area volume. The maximum deposition occurred when the aspect ratio equaled 1 and the current speed was 1 m/s. The minimum deposition between the 5 m and 10 m contours occurred when the aspect ratio equaled 0.25 and the current speed equaled 0.2 m/s. From this figure it was concluded that the volume of deposition increased as aspect ratio increased. The curves for the different current speeds are similar to each other for all cases. The maximum difference between these curves occurred when the current speed was 1 m/s and 0.2 m/s, where this difference was equal to approximately 4% of the average deposition volume.

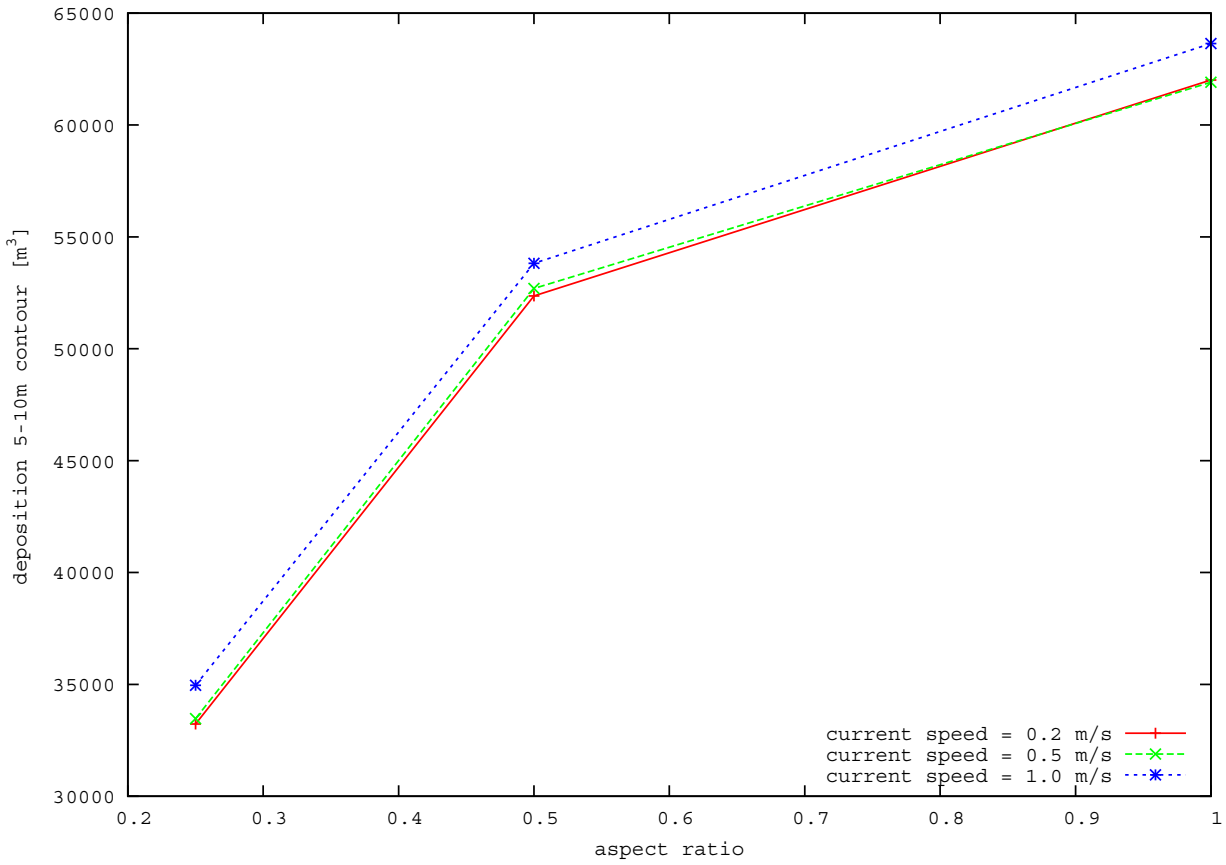

Figure VI-37. Total deposited volumes (m^3) between the 5 m and 10 m contours versus the borrow area aspect ratio.

Figure VI-38 shows the volume of erosion between the 5m and the 10 m contour versus the aspect ratio. Similarly to deposition plot, as the aspect ratio increased, the amount of erosion also increased. The maximum erosion occurred when the current speed was 1 m/s and totaled approximately 4% of the average erosion volume. For all of the test cases, the maximum increase of erosion occurred as the aspect ratio increased from 0.25 to 1. This increase equaled approximately 16% of the averaged erosion and approximately 1.5% of the initial borrow area volume.

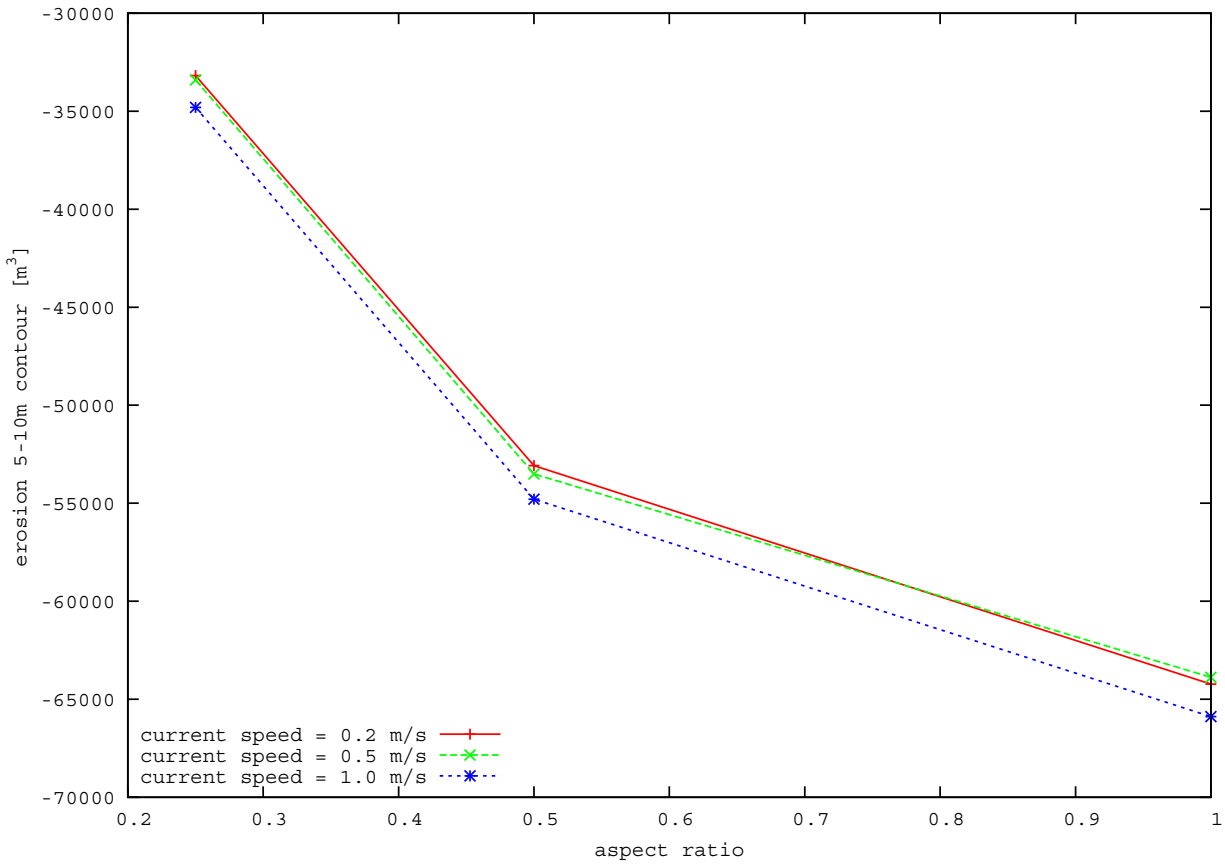

Figure VI-38. Total eroded (m^3) volumes between the 5 m and 10 m contours versus the borrow area aspect ratio.

Figure VI-39 shows the net volume (deposited = positive, eroded = negative) measured between the 5m and 10 m contour versus aspect ratio. For the borrow areas with an aspect ratio of 0.25, the net volume was slightly accretional, although the accretion volume was negligible. While for the borrow area with an aspect ratio of 0.5 and 1, the net volume was erosional. The most erosion occurred when the borrow area had an aspect ratio of 1.

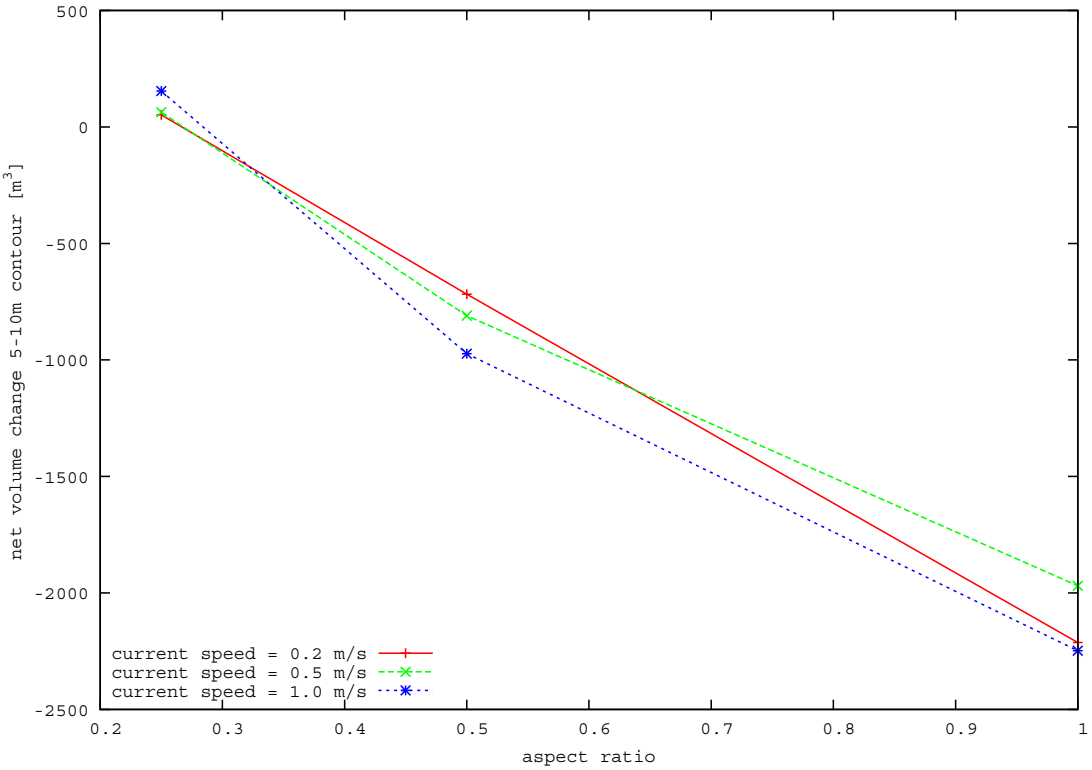

Figure VI-39. Net volume change (erosion = negative) (m^3) between the 5 m and 10 m contours versus the borrow area aspect ratio.

The bed elevation change at the 5 m contour at the end of the one-year model simulation showed areas of erosion and deposition (Figure VI-40). The amount of maximum erosion and deposition that occurred at the 5 m contour was insignificant (< 0.05 m). The largest deposition occurred in the southern half of the domain for all cases. The bed profile did not change significantly as the current speed was varied and therefore it is not shown. However, there were significant variations as aspect ratio was varied. Figure VI-40 shows that erosion and deposition areas were located next to each other and that the distance affected alongshore increased as the borrow area aspect ratio decreased. The amplitude of change increased as the aspect ratio is increased, indicative of more wave focusing for the larger aspect ratio borrow areas.

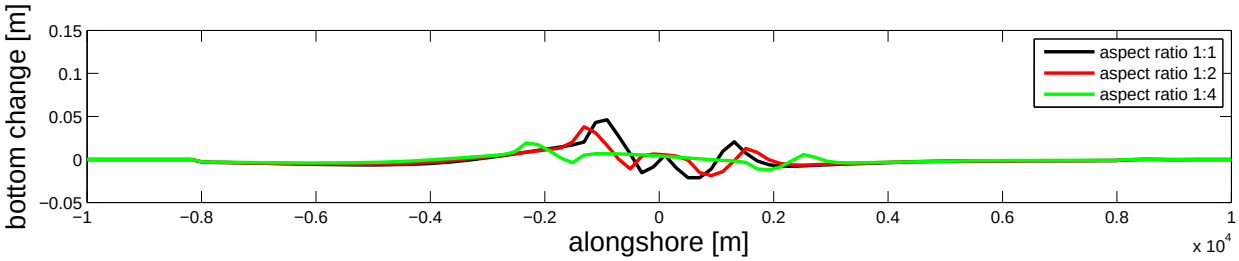

Figure VI-40. Variation in bottom elevation (positive = accretion) at the 5 m contour for three different values of the aspect ratio. The current speed remained constant at 0.2 m/s.

Figure VI-41 shows the maximum accretion value at the 5 m contour versus aspect ratio. The measured values were small with the maximum accretion being 4.6 cm, which corresponded to approximately 1% of the local depth. For all the considered current speeds the maximum accretion value increased as the aspect ratio of the borrow area increased. The largest variation was equal to approximately 20% of the averaged value.

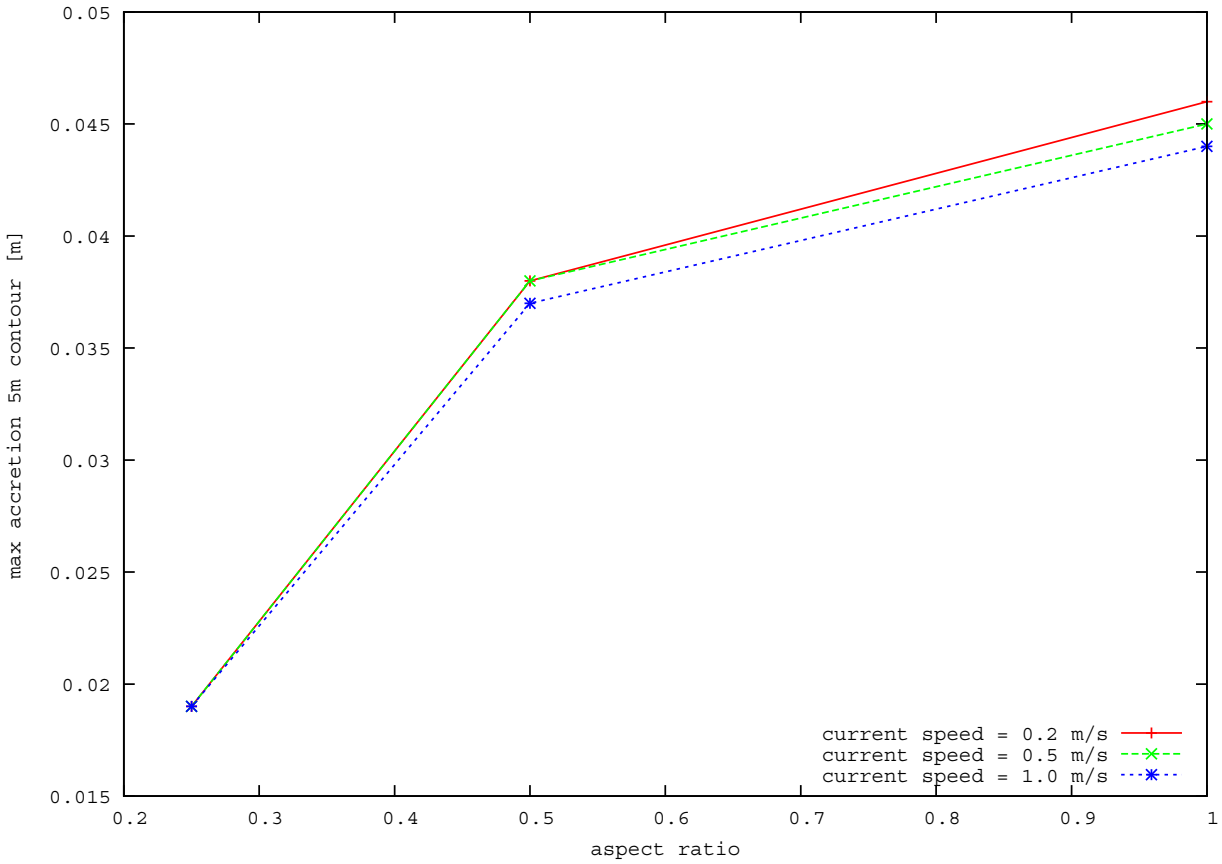

Figure VI-41. Maximum accretion (m) at the 5 m contour versus borrow area aspect ratio.

Figure VI-42 shows the maximum erosion values at the 5 m contour versus the borrow area aspect ratio. The measured maximum erosion values are smaller than the maximum deposition values. The largest measured erosion was equal to 2.5 cm, corresponding to 0.5% of the local depth. As the aspect ratio of the borrow area increased the maximum erosion at the 5 m contour increased by approximately 28% of the averaged value.

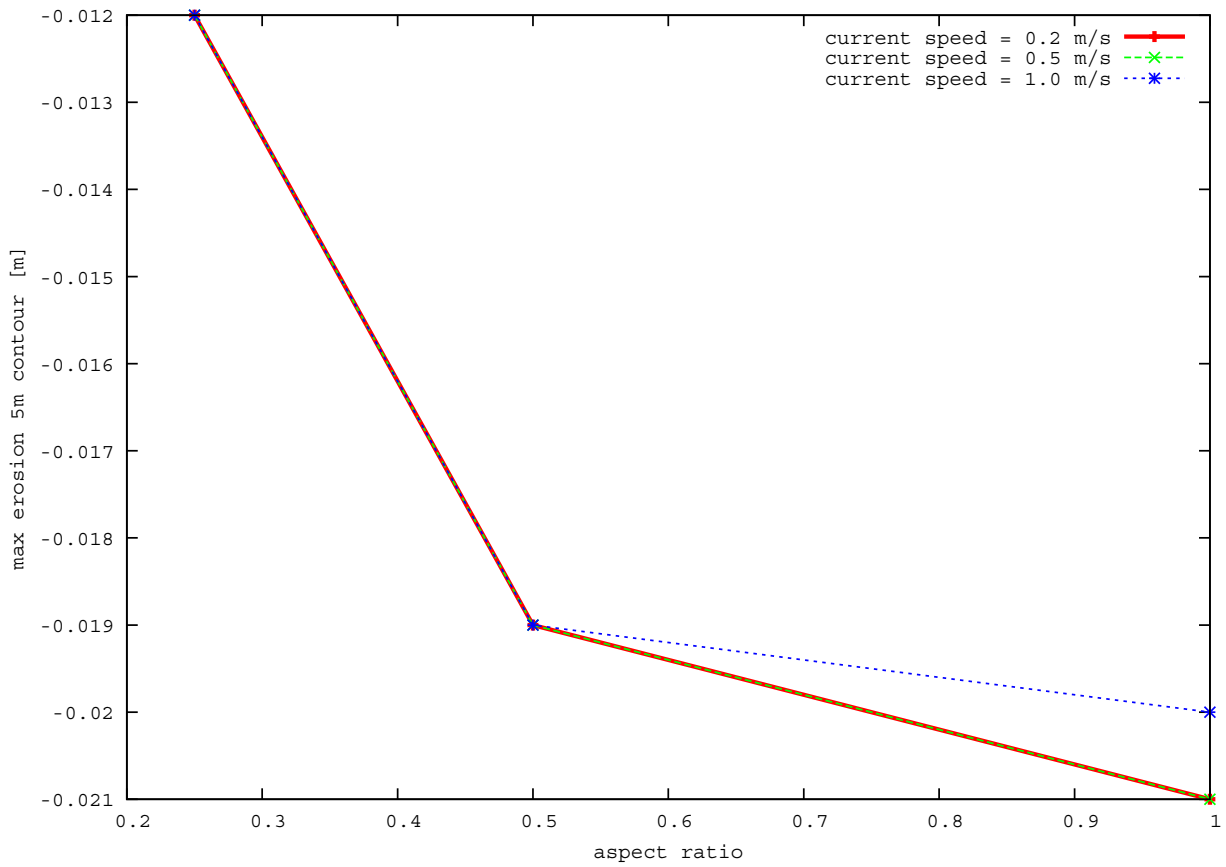

Figure VI-42. Maximum erosion (m) at the 5 m contour versus borrow area aspect ratio.

VI.D.2. Current Speed Scenarios

In addition to evaluating the influence of borrow area aspect ratio on modeled morphological change, the influence of current speed was evaluated for the full range of scenarios. Figure VI-43 shows the deposition that occurred between the 5 m and 10 m contour versus the tidal current speed. This figure shows that only minor variations were observed as the tidal current speed increased, where the largest variation, equal to approximately 1% of the average value, occurred when the aspect ratio was 0.25.

Figure VI-44 shows the erosion that occurred between the 5 m and 10 m contour versus the tidal current speed. Similar to the deposition volumes, the dependence of eroded volumes on current speed was negligible; the largest recorded variation was equal to approximately 1% of the average value, and again associated with the aspect ratio of 0.25.

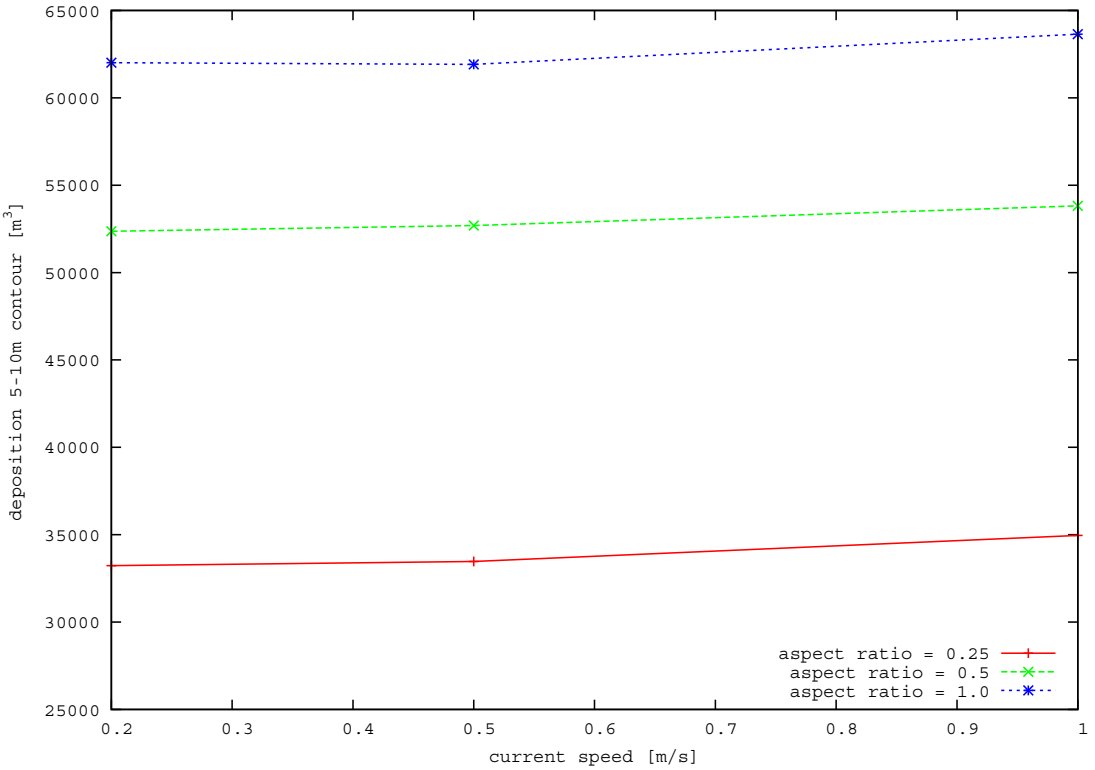

Figure VI-43. Total deposited volumes (m^3) between 5 m and 10 m contours versus current speed.

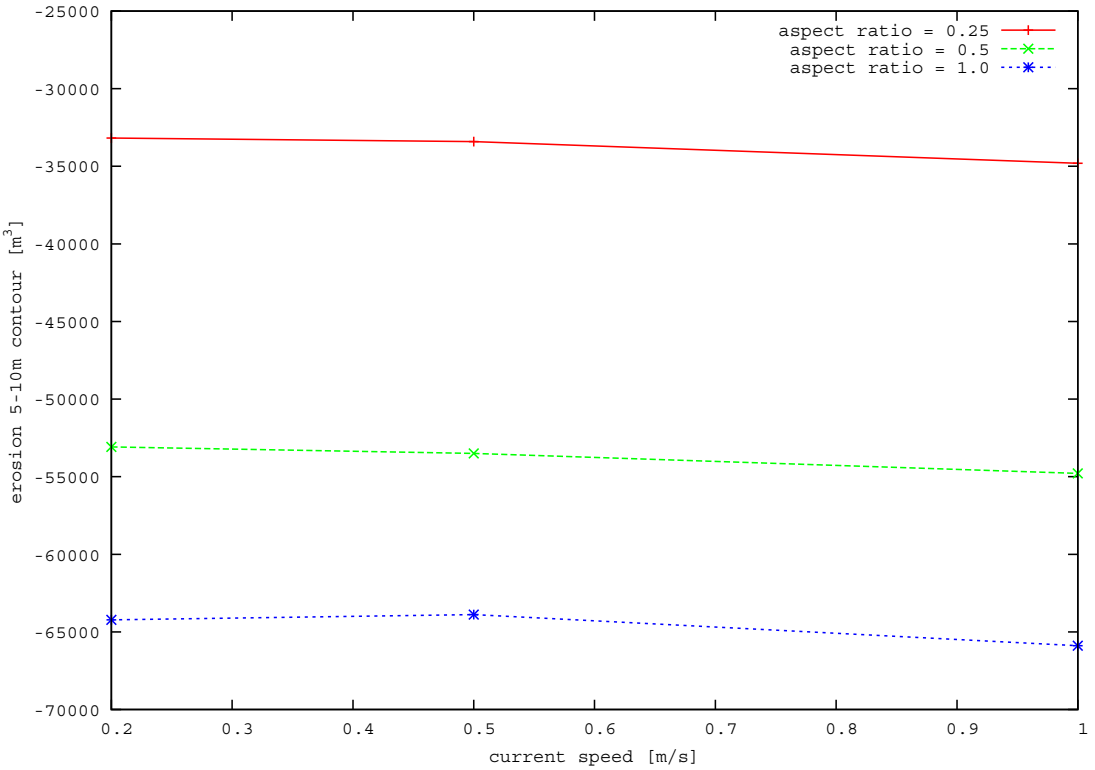

Figure VI-44. Total eroded volumes (m^3) between 5 m and 10 m contours versus current speed.

Figure VI-45 shows the net volumes (deposited=positive, eroded=negative) that occurred between the 5 m and 10 m contour as a function of current speed. The figure shows that for an aspect ratio of 0.25 a small amount of deposition occurred for the three current speeds. When the aspect ratio was increased to 0.5 or 1.0, the net volume was erosional. When the aspect ratio was 0.5, the amount of erosion increased slightly as the current speed increased. However, when the aspect ratio was equal to 1.0, the volume of erosion was at a minimum when the current speed was 0.5 m/s and a maximum when the current speed was 1.0 m/s.

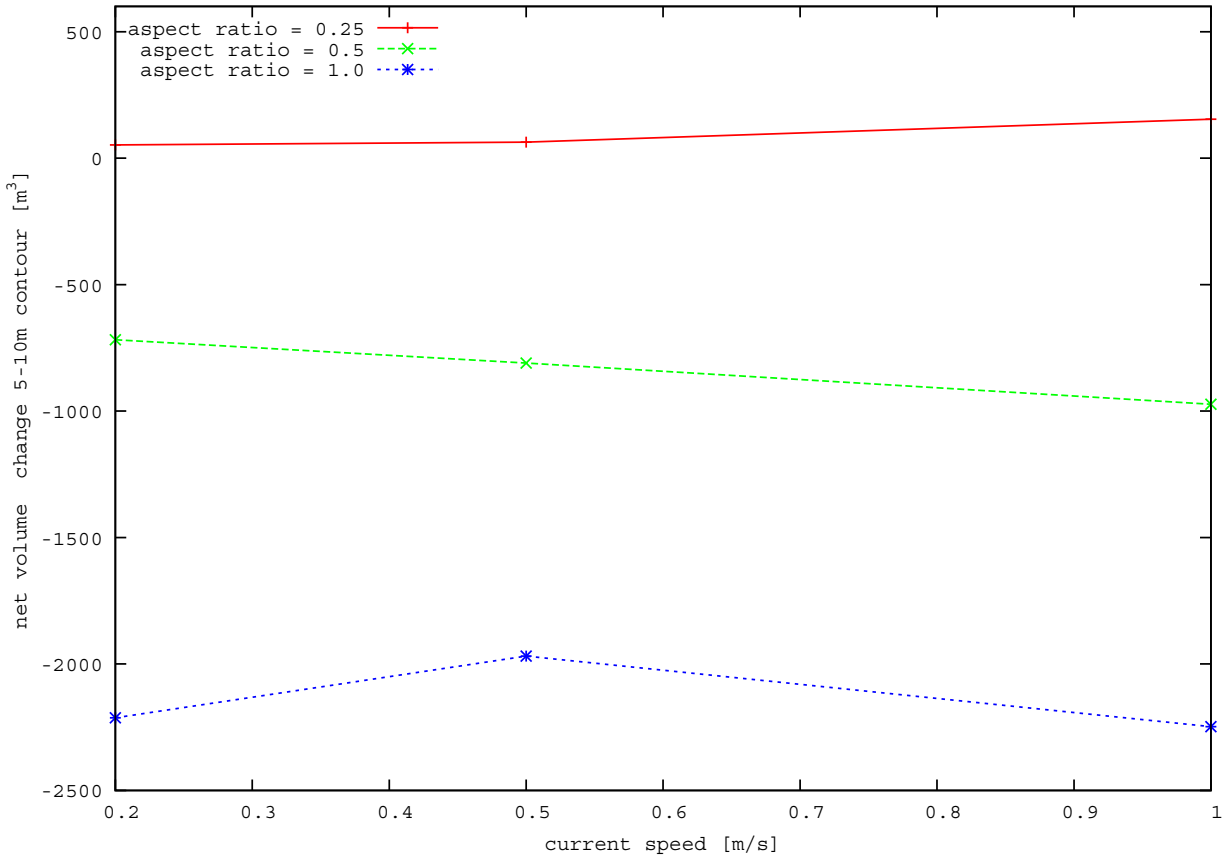

Figure VI-45. Net volume change (erosion = negative) (m^3) between 5m and 10 m contours versus current speed.

Figure VI-46 shows the maximum accretion at the 5 m contour versus the current speed. This figure shows that for the three borrow area aspect ratios, the recorded variations are minimal and at most approximately 1% of the average value. Figure VI-47 shows the maximum erosion at the 5 m contour versus the current speed. When the aspect ratio was equal to 0.25 and 0.5, no dependence on the tidal current speed was observed in the model results. For the aspect ratio of 1.0, a modest increase (approximately 0.5% of the average value) was observed as tidal current speed was increased from 0.5 m/s to 1 m/s.

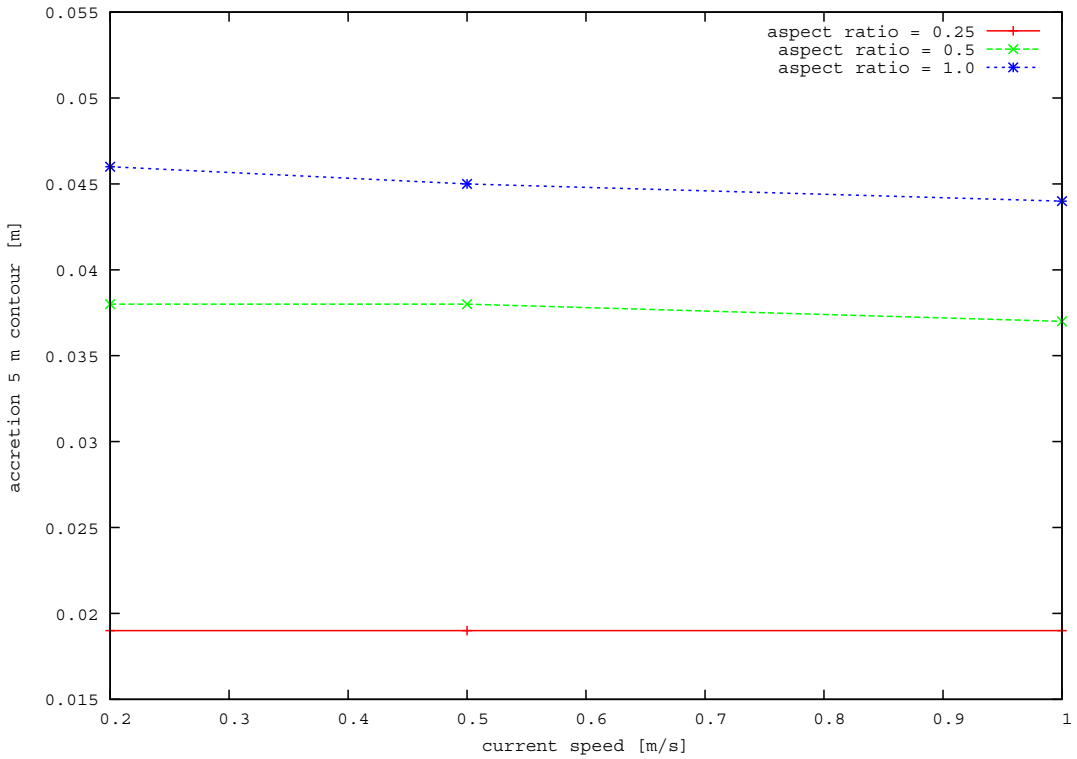

Figure VI-46. Maximum accretion (m) at the 5 m contour versus current speed.

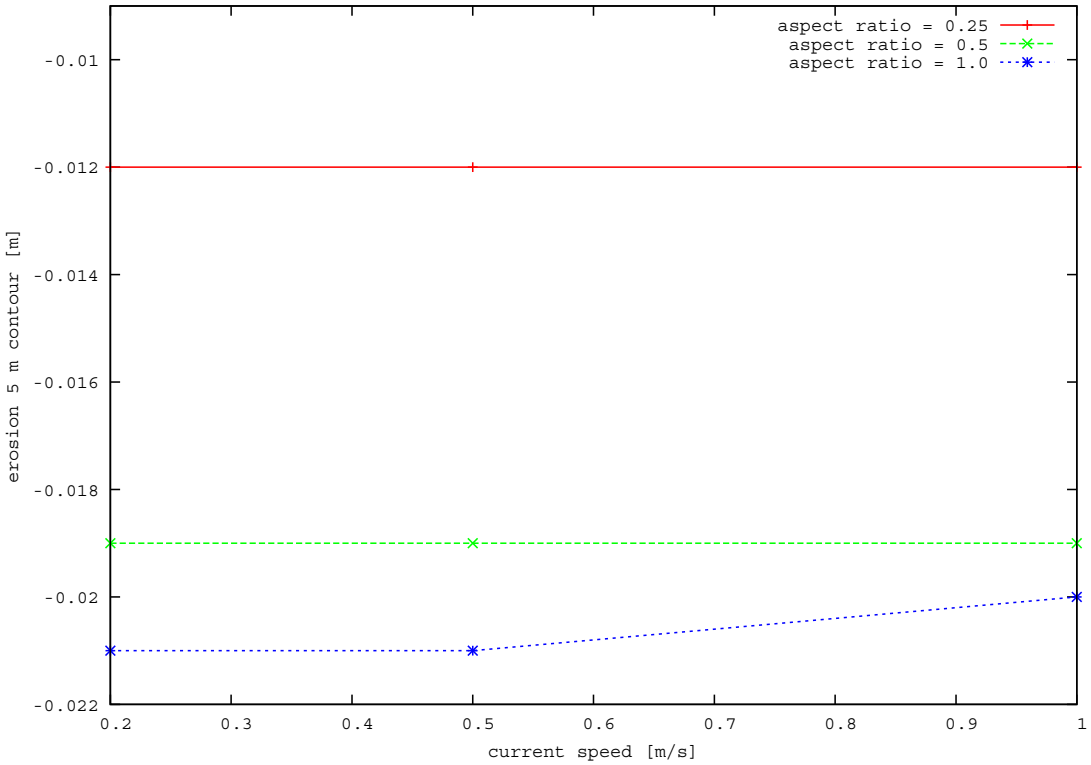

Figure VI-47. Maximum erosion (m) at the 5 m contour versus current speed.

VI.D.3. Conclusions for Far-field Flat Bed Scenarios

Utilizing the idealized bathymetry and dredged borrow area, a NearCoM far-field model was developed to assess varying borrow area aspect ratios and current speeds on morphological change over a one-year period. The idealized case was based on the general characteristics of the Cane South borrow area off the coast of South Carolina. A total of nine test cases were evaluated, where three different borrow area aspect ratios (1, 0.5, and 0.25) and three different ambient current speeds (0.2 m/s, 0.5 m/s, and 1.0 m/s) were considered. Based on the results of the nine test cases for the far-field flat bed model, the following conclusions have been made:

- Both the deposited and eroded volume between the 5 and 10 m contours showed a weak dependence on the tidal current speed. More significant variations of eroded/deposited volumes were recorded as the borrow area aspect ratio was varied.
- Only the borrow area with aspect ratio equal to 0.25 causes a net deposition between the 5 to 10 m contours, where the other two cases (aspect ratios of 0.5 and 1) caused net erosion.
- The maximum accretion and erosion both in between the 5 to 10 m contours and at the 5 m contour were very small. It should be noted that the far-field net volume change is approximately an order of magnitude less than the modeled near-field net volume change, described previously. This indicates that significant morphological change associated with borrow area dredging of this magnitude is limited in spatial extent.
- Both the maximum accretion and erosion at the 5 m contour showed a more significant dependence on borrow area aspect ratio than on tidal current strength. This influence appears to be dependent on wave refraction effects associated with the different aspect ratio borrow areas.

Similar to the near-field results, the far-field results and associated conclusions were derived from a limited number of scenario cases (three borrow areas with different aspect ratios and three different tidal current speeds) with fixed sediment characteristics and wave conditions (February 2010 at Cane South site). Specifically for the far-field results, the modeled sediment transport quantities are very small and the associated morphological change is generally negligible. To develop a more complete understanding relative to the influence of the different parameters and processes influencing sediment transport at 'typical' U.S. Atlantic OCS borrow areas, further investigations likely are necessary. However, it should be noted that the far-field influence of the borrow areas is significantly less than the near-field effect on morphological change.

VI.E. FAR-FIELD MORPHOLOGY, AMBIENT RIDGED BED TEST CASES

As an expansion of the far-field modeling effort, consideration was also given to investigating the effect of the borrow area on the far-field if the bottom was ridged. In general, the scale of the ridges was modeled after typical in the Long Bay, South Carolina region. A sloping bed with regular ridges with constant wavelength was considered. The baseline case, featuring a bed with ridges at an angle of 60 degrees with the coastline and with wavelength equal to 600 m, was selected by idealization of the bottom bathymetry at Cane South. The amplitude of ridges decreased linearly with water depth; the amplitude of the ridges was 2 m at 12 m depth and 0.83 m at 5 m depth. Both the sediment characteristics and wave forcing were

kept the same as those selected for the flat bed cases. The amplitude of the tidal current was fixed equal at 0.2 m/s.

Because of numerical efficiency, related to the new online correction method used to compute the borrow area effect in non-equilibrium conditions, it was chosen to consider a square borrow area, aligned with the shoreline with dimensions of 1414 m (measured at middle points of the slope) and an excavation depth of 1 m.

In order to investigate the effect of the ridge wavelength and the ridge orientation relative to that of the tidal current and of the borrow area, three tests cases were run as shown in Table VI-3 and their corresponding bathymetry are shown in Figures VI-48 to VI-50, respectively.

Table VI-3. Parameters for the ridged bed scenario testing.

Case	Ridge wavelength (m)	Angle between ridge and tidal current-dominant (degrees)
A	600	60
B	600	90
C	1,200	60

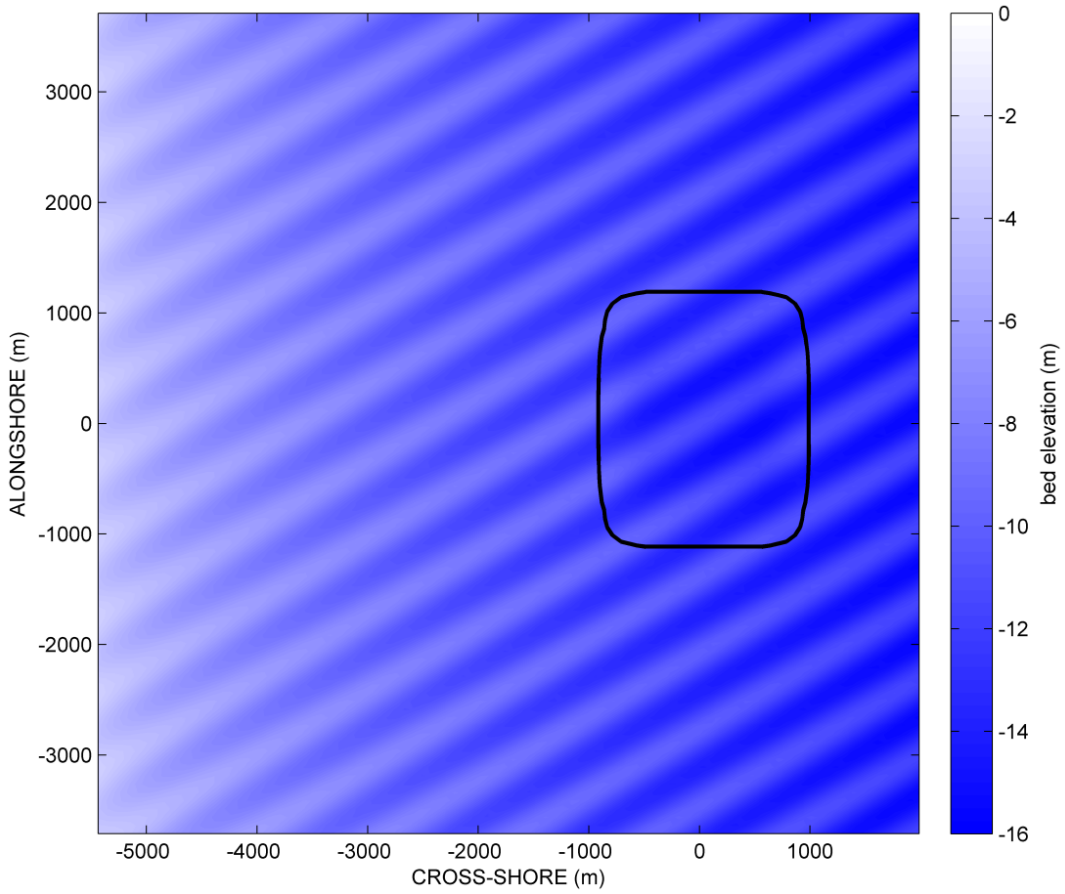

Figure VI-48. Case A geometry for ridged bed testing.

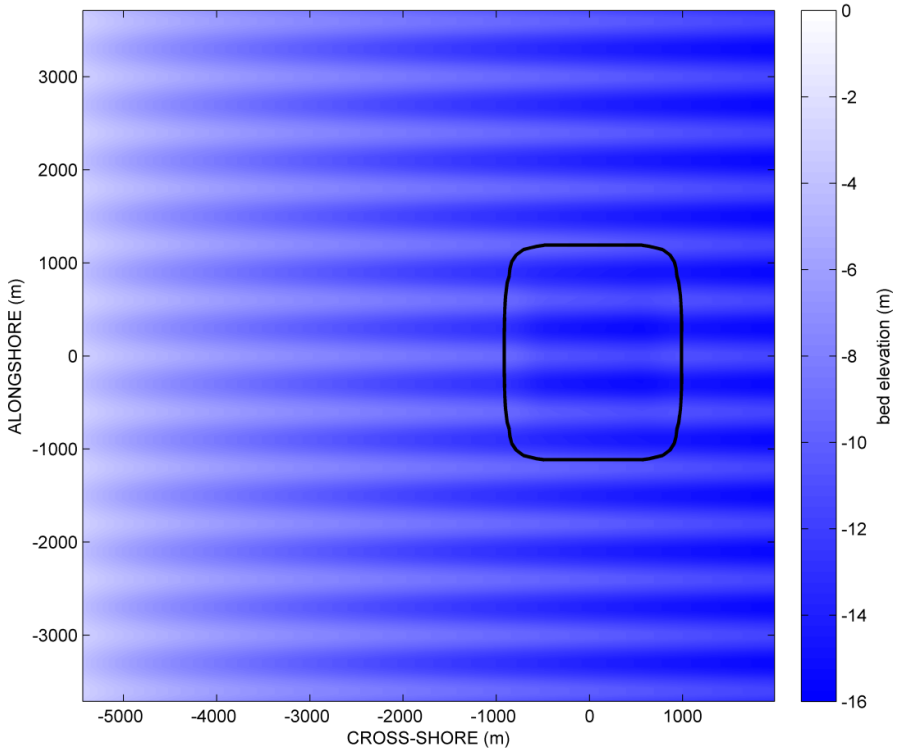

Figure VI-49. Case B geometry for ridged bed testing.

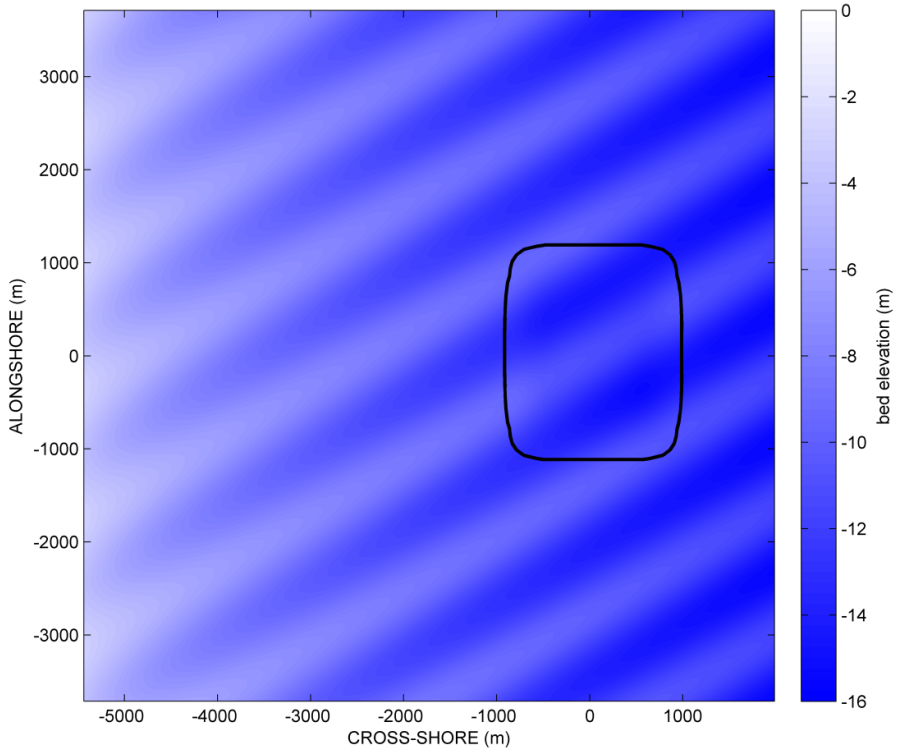

Figure VI-50. Case C geometry for ridged bed testing.

The baseline computational domain is 7,500 m both in the long-shore and cross-shore directions and the number of grid-points is 100 in each direction. Since previous far-field modeling indicated the influence of the borrow area excavation extended a significant distance (i.e. on the order of 5,000 meters) from the site, a second series of runs with a larger extension in the alongshore direction (15 km) and 200 grid-points in the alongshore direction was performed. This expanded grid ensured that lateral boundary conditions did not significantly affect the obtained results. Table VI-4 shows the deposited volumes between the 5 m and 10 m contours both for the small computational domain extending from -3,750 m to 3,750 m in the alongshore direction and for the larger computational domain, extending from -7.5 km to 7.5 km in the alongshore direction. The greatest difference between the calculated deposition volumes for the two domains was for case B. For case B the difference was approximately 50% of the average volume. The greatest difference between the calculated erosional volumes for the two domains was for case C. For case C the difference was approximately 40% of the average volume. Table VI-4 shows that the borrow area influence extended to a large alongshore distance and that selected dimensions for the computational domain are critical to the validity of the overall modeling effort. Table VI-5 shows that the alongshore extent of the computational domain had a slight influence on the maximum accretion and erosion values at the 5 m contour.

Table VI-4. Eroded and deposited volumes (m^3) measured from the 5 to 10 contour for the small (columns 2 and 3) and large computational domains (columns 4 and 5).

Case	Deposition (5 m – 10m contours) in the alongshore region of 7.5 km (m^3)	Deposition (5 m – 10 m contours) in the alongshore region of 15 km (m^3)	Erosion (5 m – 10 m contours) in the along shore region of 7.5 km (m^3)	Erosion (5 m – 10 m contours) in the along shore region of 15 km (m^3)
A	109,712	141,871	-118,891	-163,858
B	53,344	90,425	-87,581	-119,987
C	60,729	80,576	-58,015	-88,261

Table VI-5. Maximum accretion and erosion measured at the 5 m contour for the small and large computational domains.

Case	Max accretion at 5 m contour in the alongshore region of 7.5 km (m)	Max accretion at 5 m contour in the alongshore region of 15 km (m)	Max erosion at 5 m contour in the alongshore region of 7.5 km (m)	Max erosion at 5 m contour in the alongshore region of 15 km (m)
A	0.040	0.037	-0.064	-0.063
B	0.125	0.117	-0.062	-0.060
C	0.021	0.021	-0.019	-0.021

VI.E.1. Ridge Orientation Scenarios

As described above, the ridge bed scenarios were run by varying the orientation of the ridges. In Figure VI-51 and VI-52 the 3%, 2% and 1% wave height influence areas are shown for case A and case B. Table VI-6 gives the area of the influence areas (3%, 2% and 1%) for wave height. Table VI-6 showed that Case B (ridges at 90 degrees) showed smaller 3% and 2% wave height influence areas than Case A. However, the 1% influence area for case B was larger than case A.

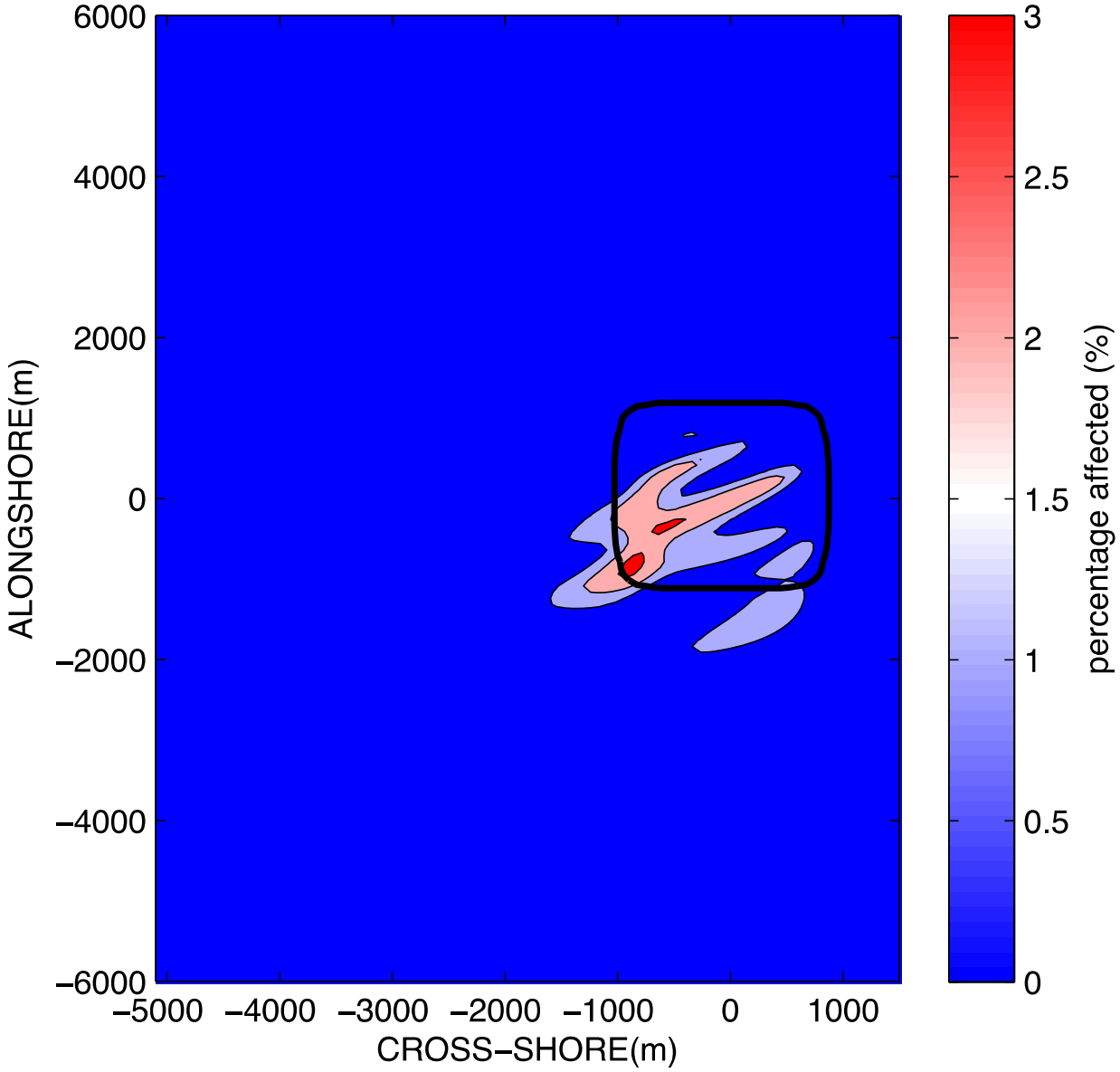

Figure VI-51. The relative variation of wave height during the maximum wave height (February 5, 2010 21:00) in the near-field region around the borrow area for case A. The red, light red, and light blue areas indicate 3%, 2% and 1% influence, respectively. The tidal current speed remained constant at 0.2 m/s.

Table VI-6. Wave height influence areas for the ridge orientation scenarios

Case	3% Influence (m^2)	2% Influence (m^2)	1% Influence (m^2)
A	78,750	860,625	2,621,250
B	28,125	804,375	4,488,750

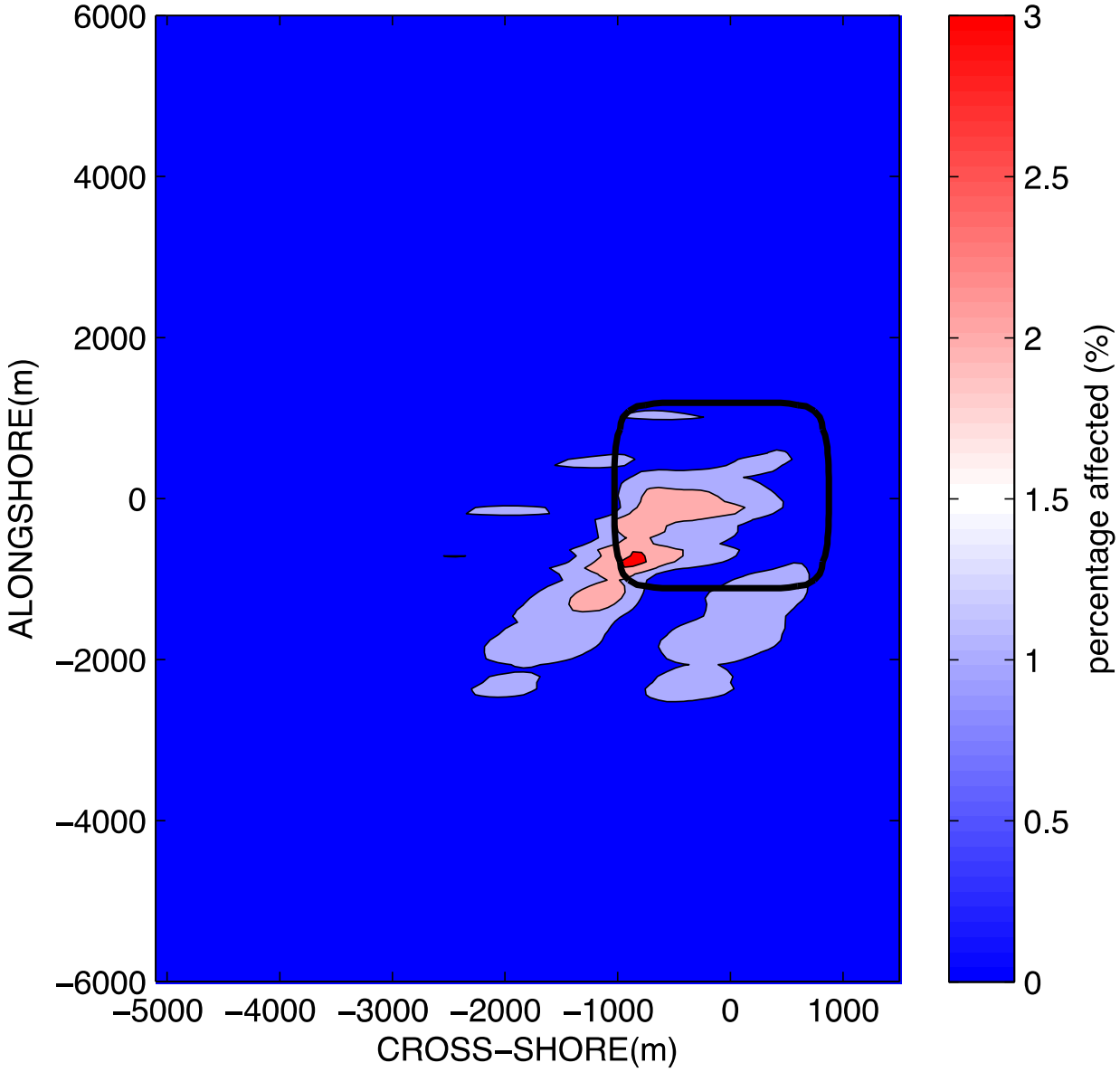

Figure VI-52. The relative variation of wave height during the maximum wave height (February 5, 2010 21:00) in the near-field region around the borrow area for (A) case A, (B) case B. The red, light red, and light blue areas indicate 3%, 2% and 1% influence, respectively. The tidal current speed remained constant at 0.2 m/s.

Figure VI-53 and VI-54 the 3%, 2% and 1% tidal current influence areas are shown for case A and case B. This figure showed that the 3% influence area was contained inside the borrow area while 2% and 1% influence areas extend outside the borrow area both in the offshore and shoreward directions. The 2% and 1% influence areas appeared to extend slightly more toward the north than toward the south. Table VI-7 gives the areas of the 5%, 3% and 2% influence areas for the tidal current. This table shows that the largest influence areas occurred for case A (ridges with 60° orientation). It should be noted that the variation of the extent of the influence areas decreases from 49% variation for 5% influence to 1% variation for 2% influence area.

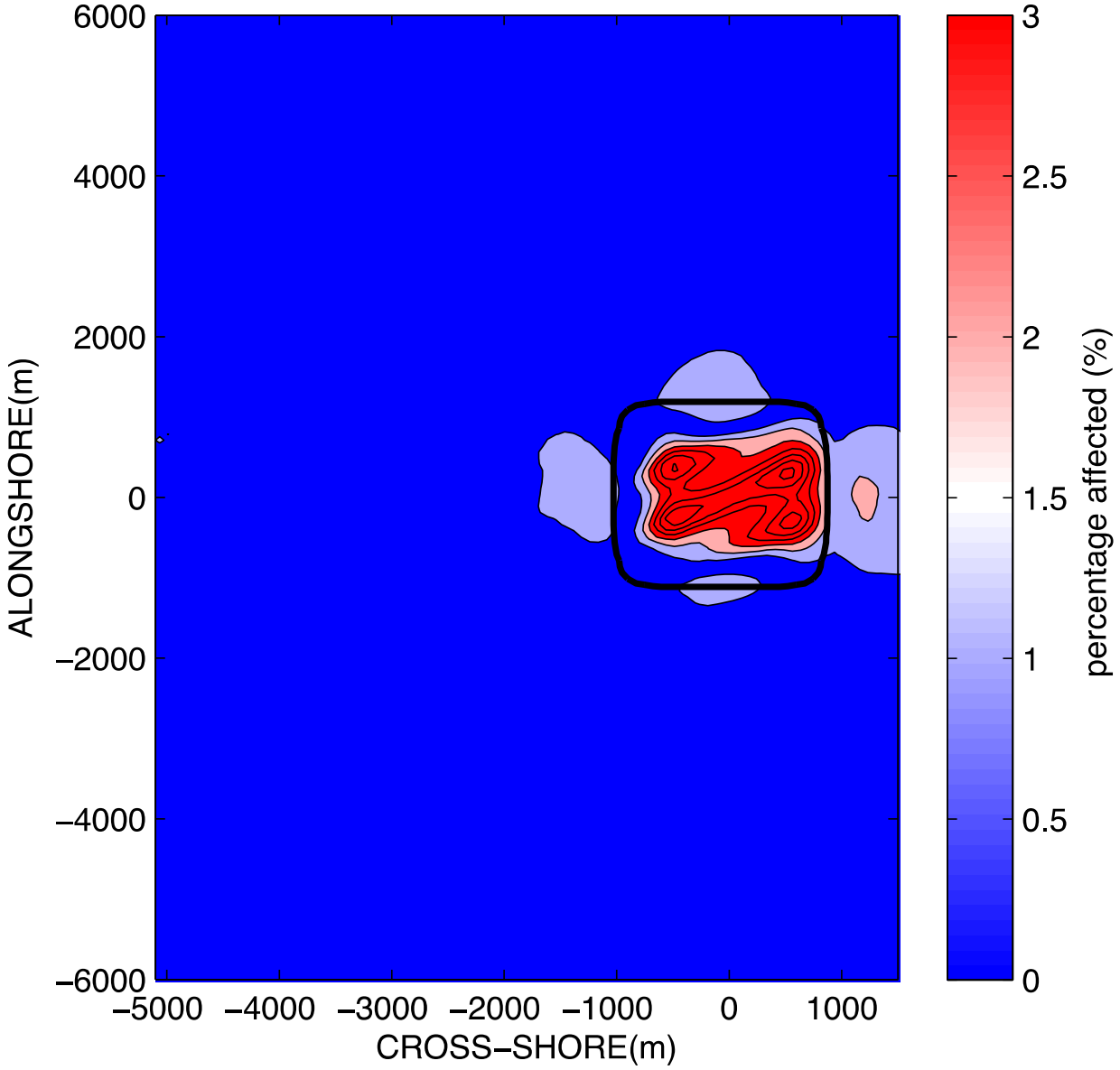

Figure VI-53. The relative variation of current speed during the maximum tidal current (02/05 21:00, 2010) in the region around the borrow area for case A. The red, light red, and light blue areas indicate 3%, 2% and 1% influence, respectively.

Table VI-7. Current speed influence areas for the ridge orientation scenarios (m^2).

Case	5% Influence (m^2)	3% Influence (m^2)	2% Influence (m^2)
A	579,375	1,693,125	2,255,625
B	348,750	1,631,250	2,233,125

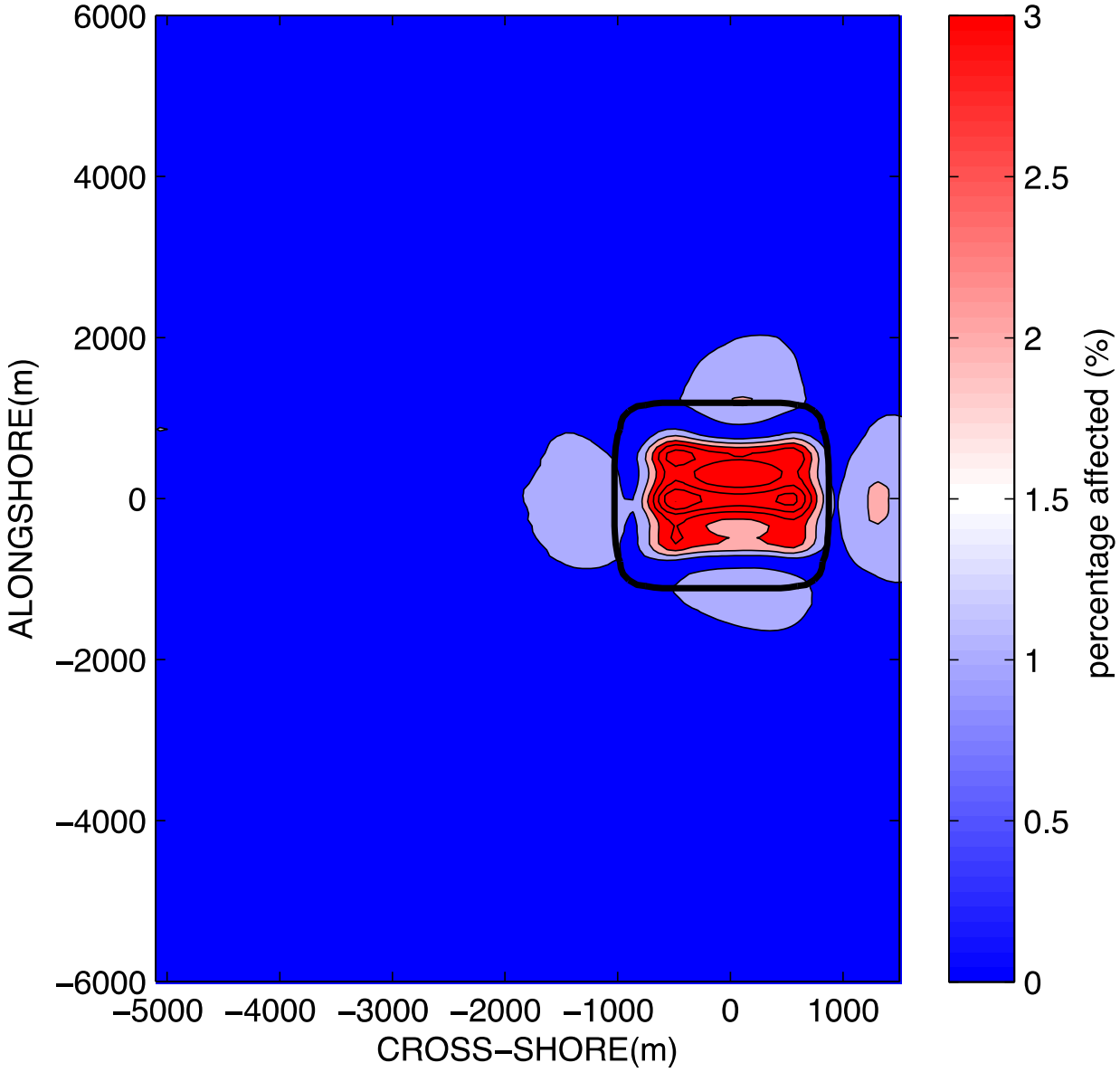

Figure VI-54. The relative variation of current speed during the maximum tidal current (02/05 21:00, 2010) in the region around the borrow area for (A) case A, (B) case B. The red, light red, and light blue areas indicate 3%, 2% and 1% influence, respectively.

Figures VI-55 and VI-56 show the bed elevation changes measured at the end of the simulated period (February 2010 multiplied by 12 to simulate one year), where areas of both minor erosion and deposition occurred. These figures showed that erosion areas tend to be located at the crest of the ridges while depositional areas tend to be located at the troughs. The amount of the deposition and erosion was largest inside the borrow area and then decreases as the distance from the borrow area increased. This is generally consistent with the conceptual driving forces governing sediment transport, where there is a natural tendency for aberrant features to become "smoothed". Moreover, the figures illustrate that the interaction of borrow

area geometry, ridge orientation and currents cause a periodic erosional/depositional pattern on ridges crests and troughs with a distinct wavelength. Figures VI-55 and VI-56 showed that for case A, the far-field region affected by the borrow area presence extended to the northern part (positive alongshore direction) of the domain while for case B (ridges at 90°) the far-field region affected by the borrow area presence extended to the southern part (negative alongshore direction) of the domain. Table VI-8 shows the erosional and depositional volumes between the 5m to 10 m contours for the two tests considered. Table VI-8 showed that the two tests were subject to net erosion. Moreover case B (90° orientation) was subjected to smaller erosion and deposition than case A (60° orientation).

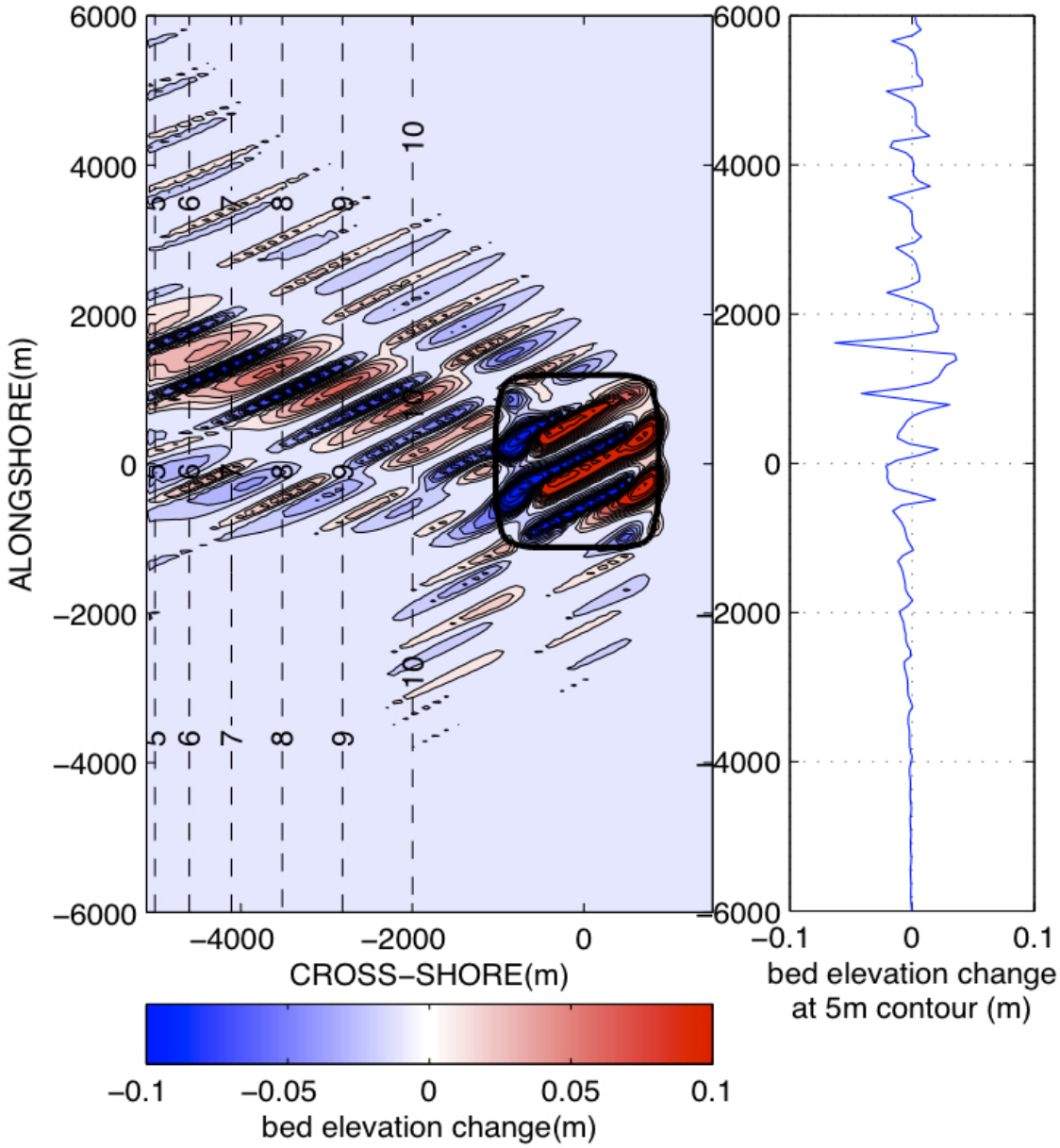

Figure VI-55. Depth change in Case A. Dashed lines: contours of depth before change, solid lines: contours of depth change, color: depth change.

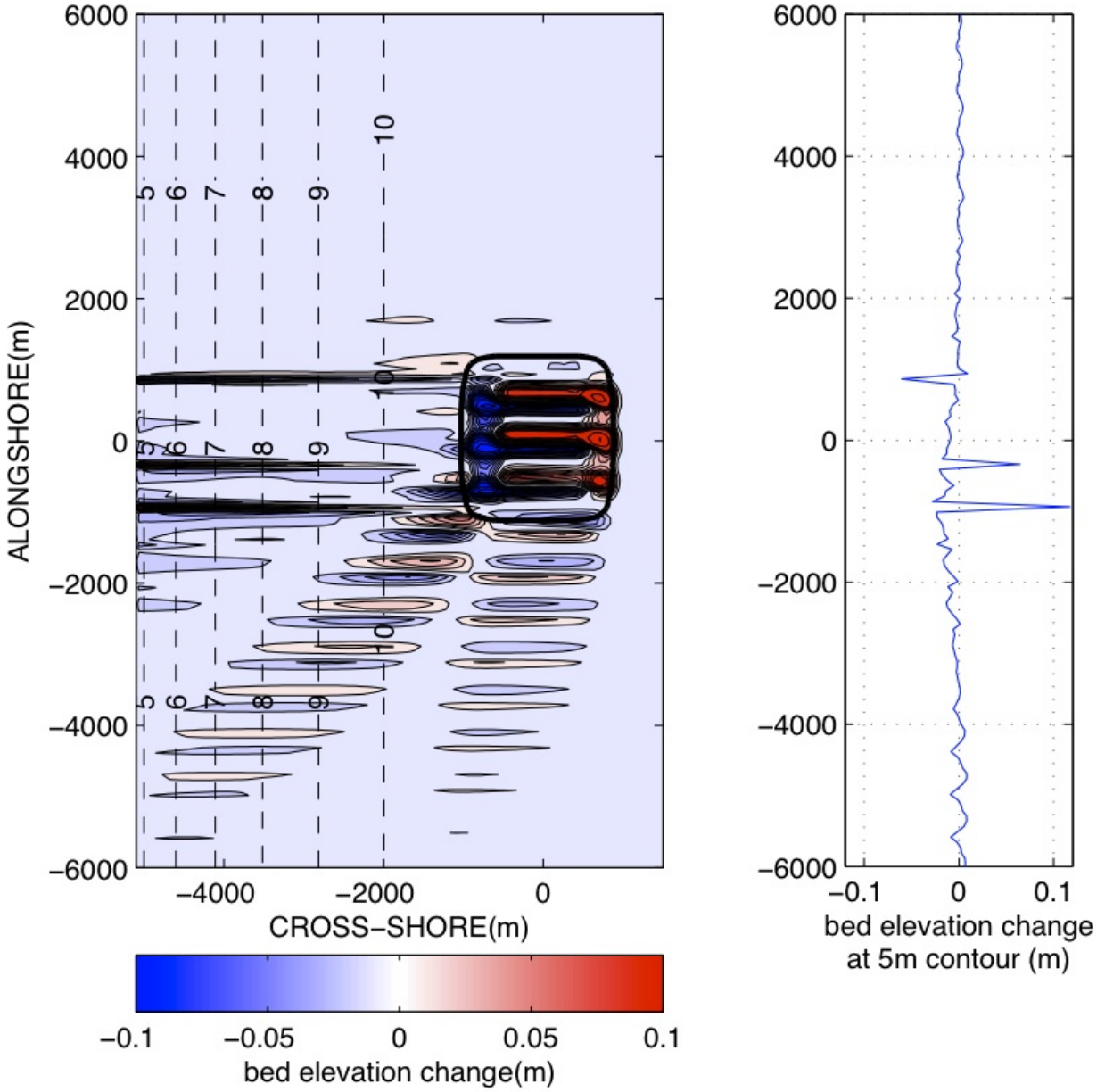

Figure VI-56. Depth change in Case B. Dashed lines: contours of depth before change, solid lines: contours of depth change, color: depth change

Table VI-8. Eroded, deposited and net volumes (m^3) measured from the 5 to 10 contour for the Ridge Orientation Scenarios.

Case	Deposition (5 m – 10 m contours) in the alongshore region of 15 km (m^3)	Erosion (5 m – 10 m contours) in the along shore region of 15 km (m^3)	Net erosion/deposition (5 m – 10 m contours) in the along shore region of 15 km (m^3)
A	141,871	-163,858	-21,99
B	90,425	-119,987	-29,56

Figure VI-57 shows the bed elevation change for the one-year simulation at the 5m contour. The figure showed small amplitude areas of erosion and deposition. The bed elevation changes for Case B were primarily confined to the negative alongshore direction (south). While the bed elevation changes at the 5 m contour for Case A was primarily confined to the positive alongshore direction (north).

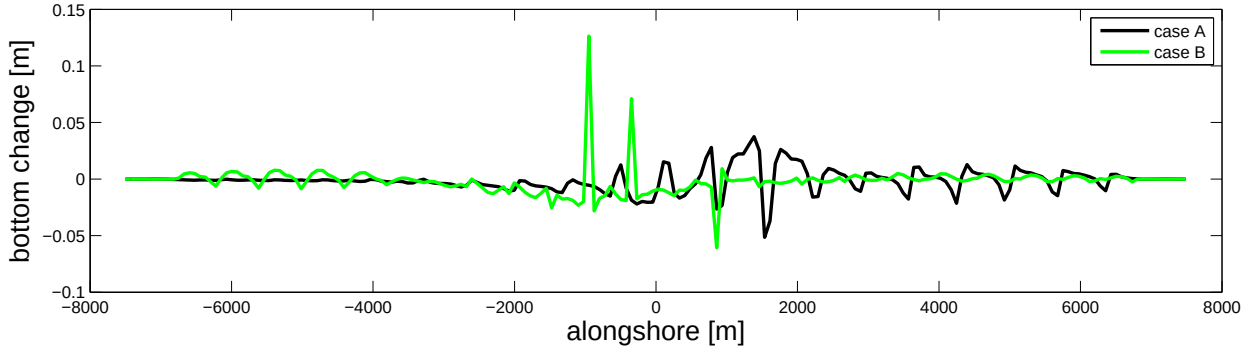

Figure VI-57. Variation (from the beginning to the end of the simulation) in bottom elevation (positive = accretion) at the 5m contour for Case A and Case B.

VI.E.2. Ridge Wavelength Scenarios

In addition to the ridge orientation, the influence of the ridge bed wavelength also was evaluated within the context of the modeled morphological change. In Figure VI-58 and VI-59 the 3%, 2% and 1% wave height influence areas are shown for case A and case C. This figure showed that the influence areas of case C extended more significantly in the south-west part of the domain. Table VI-9 gives the area of the influence areas (3%, 2% and 1%) for wave height. It was observed that Case C (ridges with longer wavelength) had larger wave influence areas than Case A.

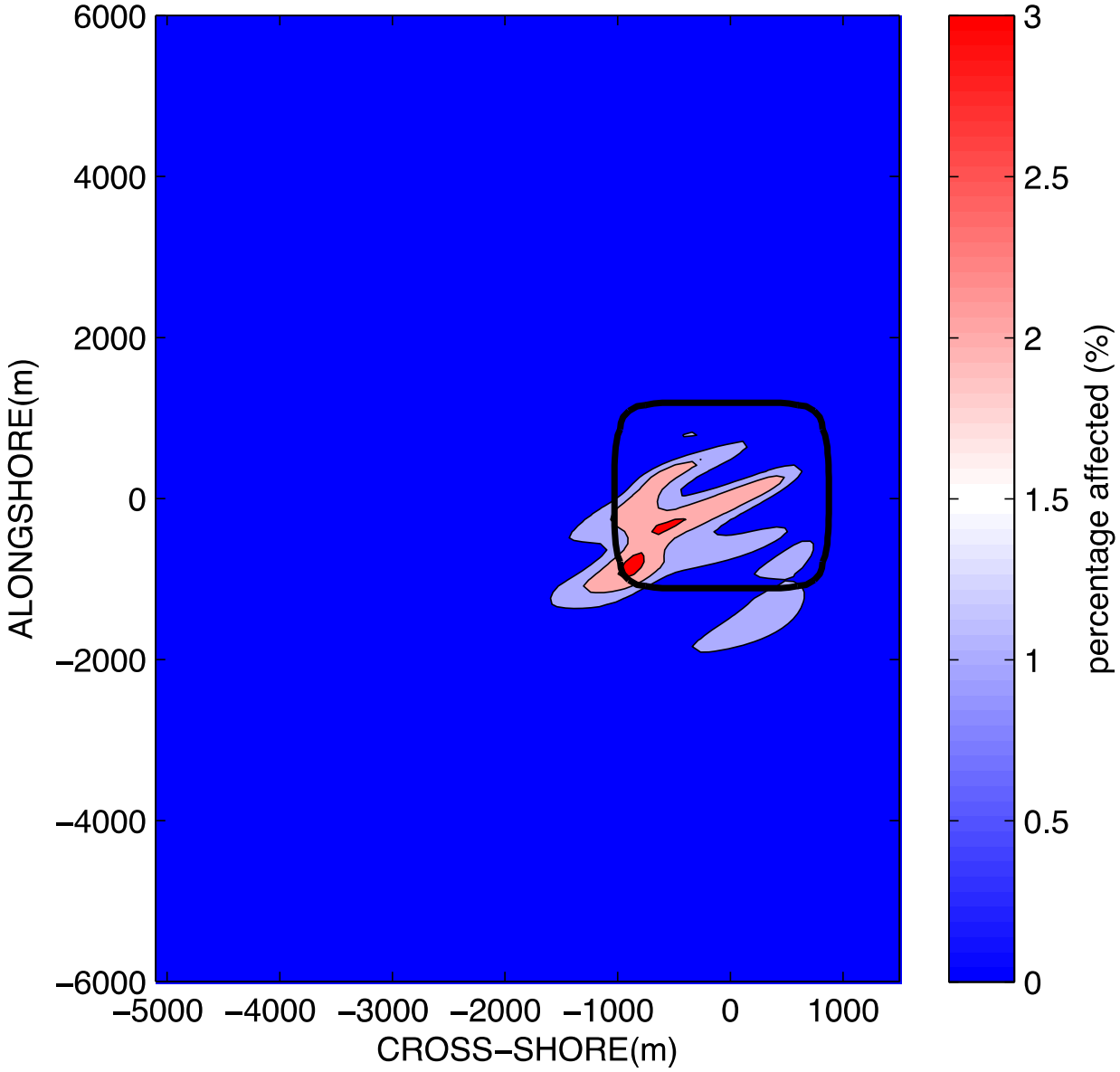

Figure VI-58. The relative variation of wave height during the maximum wave height (February 5, 2010 21:00) in the near-field region around the borrow area for case A. The red, light red, and light blue areas indicate 3%, 2% and 1% influence, respectively. The tidal current speed remained constant at 0.2 m/s.

Figure VI-60 and VI-61 shows the influence areas for the tidal current. The 3% influence area was contained inside the borrow area while 2% and 1% influence areas extended outside the borrow area both in the offshore and shoreward directions. The 2% and 1% influence areas appear to extend slightly more toward the north than toward the south. Table VI-10 shows the area of the extent of the influence areas for tidal current. It was observed that the Case A had larger 5% and 3% influence areas, while the 2% influence areas was basically the same for both cases. It should be noted that the relative difference of the influence areas measured in the two tests decreased from 16% for 5% influence area to a negligible value for the 2% influence area.

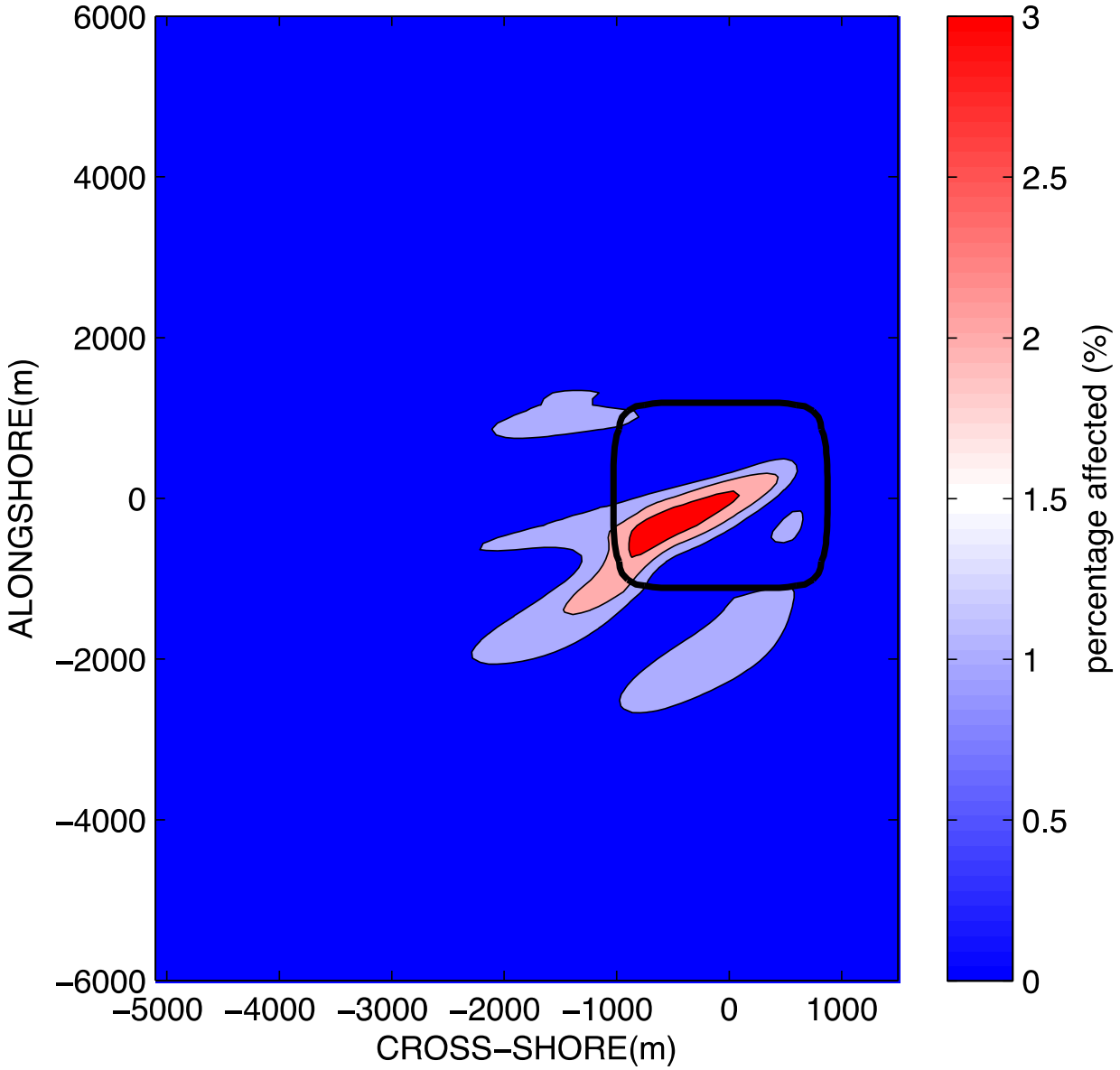

Figure VI-59. The relative variation of wave height during the maximum wave height (February 5, 2010 21:00) in the near-field region around the borrow area for (A) case A, (C) case C. The red, light red, and light blue areas indicate 3%, 2% and 1% influence, respectively. The tidal current speed remained constant at 0.2 m/s.

Table VI-9. Wave height influence areas (m^2) for the ridge wavelength scenarios.

Case	3% Influence (m^2)	2% Influence (m^2)	1% Influence (m^2)
A	78,750	860,625	2,621,250
C	309,375	995,625	4,190,625

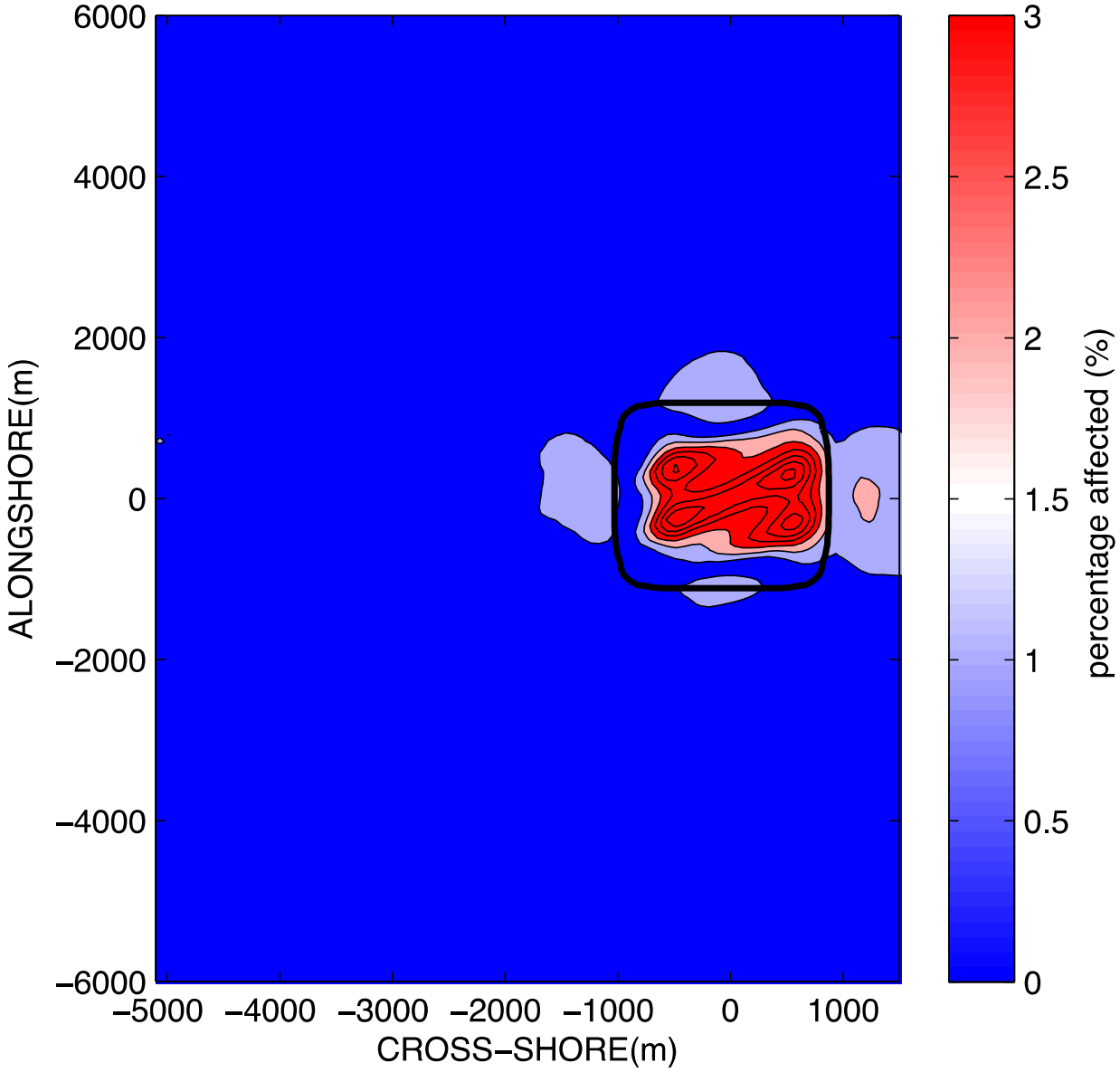

Figure VI-60. The relative variation of current speed during the maximum tidal current (02/05 21:00, 2010) in the region around the borrow area for case A. The red, light red, and light blue areas indicate 3%, 2% and 1% influence, respectively.

Figures VI-62 and VI-63 show the bed elevation changes measured at the end of the simulated period (February 2010 times 12 to simulate one year). Both modest erosion and deposition areas were observed in the overall model results. Similar to the assessment of ridged beds above, the erosion areas tended to be located on the crest of the ridges while depositional areas tended to be located in the troughs. The amount of deposition and erosion were the largest inside the borrow area and then decreased as the distance from the borrow area is increased. The results showed that the interaction of borrow area geometry, ridge orientation and currents cause a periodic erosional/depositional three-dimensional pattern on ridges crests and troughs with a distinct wavelength.

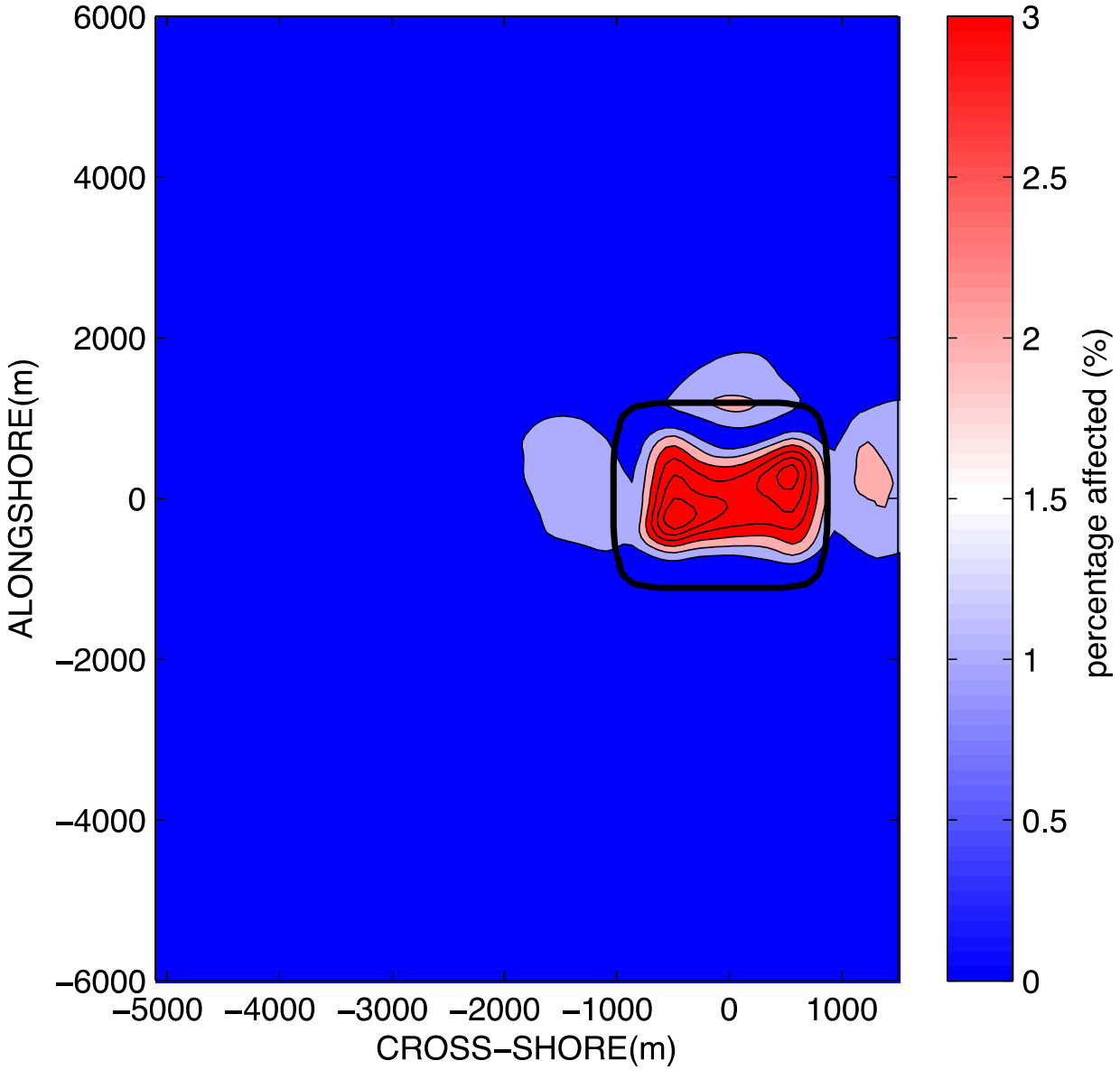

Figure VI-61. The relative variation of current speed during the maximum tidal current (02/05 21:00, 2010) in the region around the borrow area for (A) case A, (C) case C. The red, light red, and light blue areas indicate 3%, 2% and 1% influence, respectively.

Table VI-10. Current speed influence areas (m^2).

Case	5% Influence (m^2)	3% Influence (m^2)	2% Influence (m^2)
A	579,375	1,693,125	2,255,625
C	489,375	1,530,000	2,261,250

Table VI-11 shows erosion and deposition volumes between the 5 m and 10 m contours for the two tests considered. This table showed that case C (larger wavelength) was subject to smaller erosion and deposition than case A. In case C the deposition decreased with respect to

case A, by 55% of the average value, while the erosion for case C decreased with respect to case A by 60% of the averaged value. Table VI-11 showed that the two tests were subject to net erosion with case A experiencing more erosion; however the overall volumes are negligible relative to the size of the model domain.

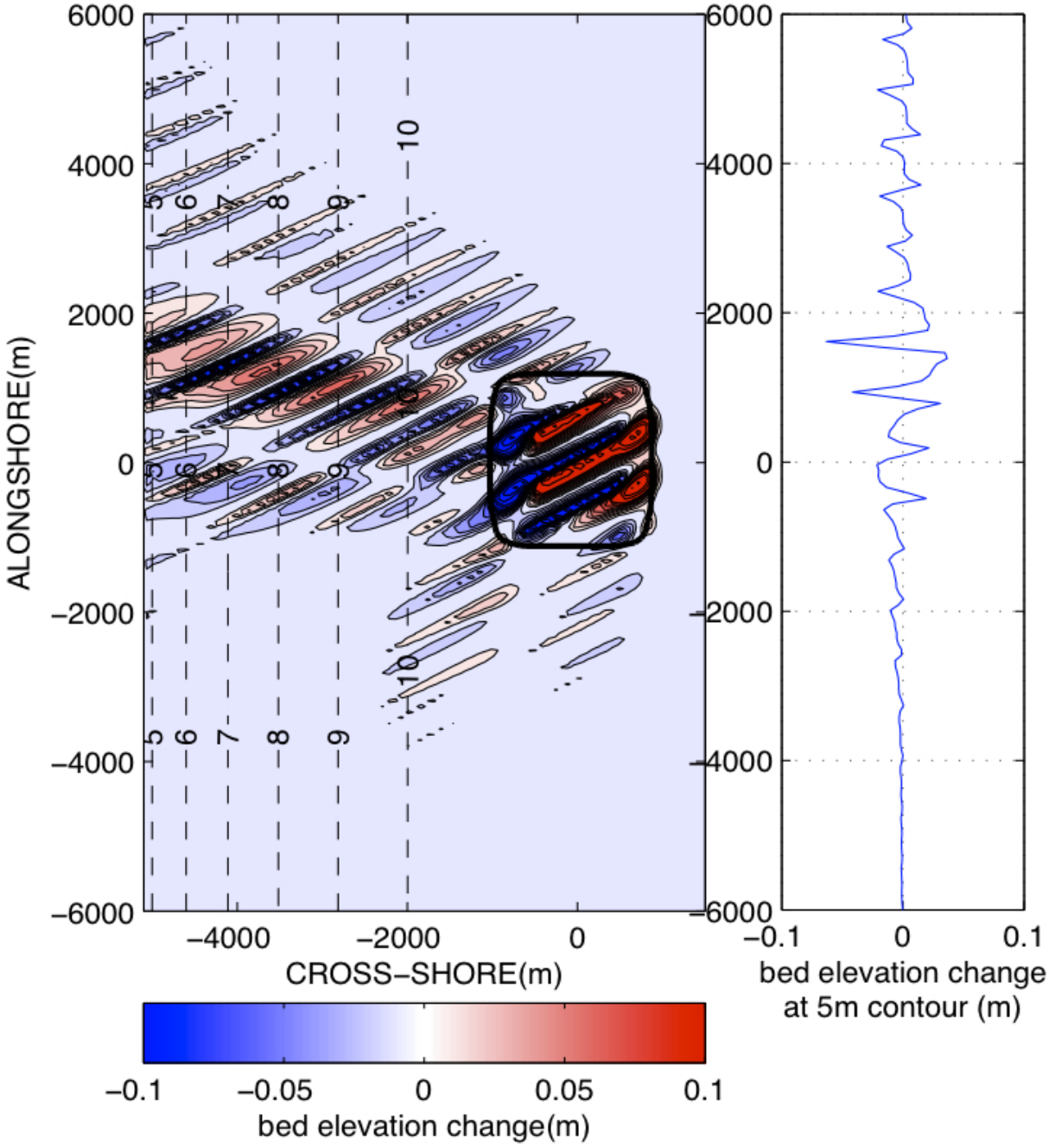

Figure VI-62. Depth change in Case A. Dashed lines: contours of depth before change, solid lines: contours of depth change, color: depth change.

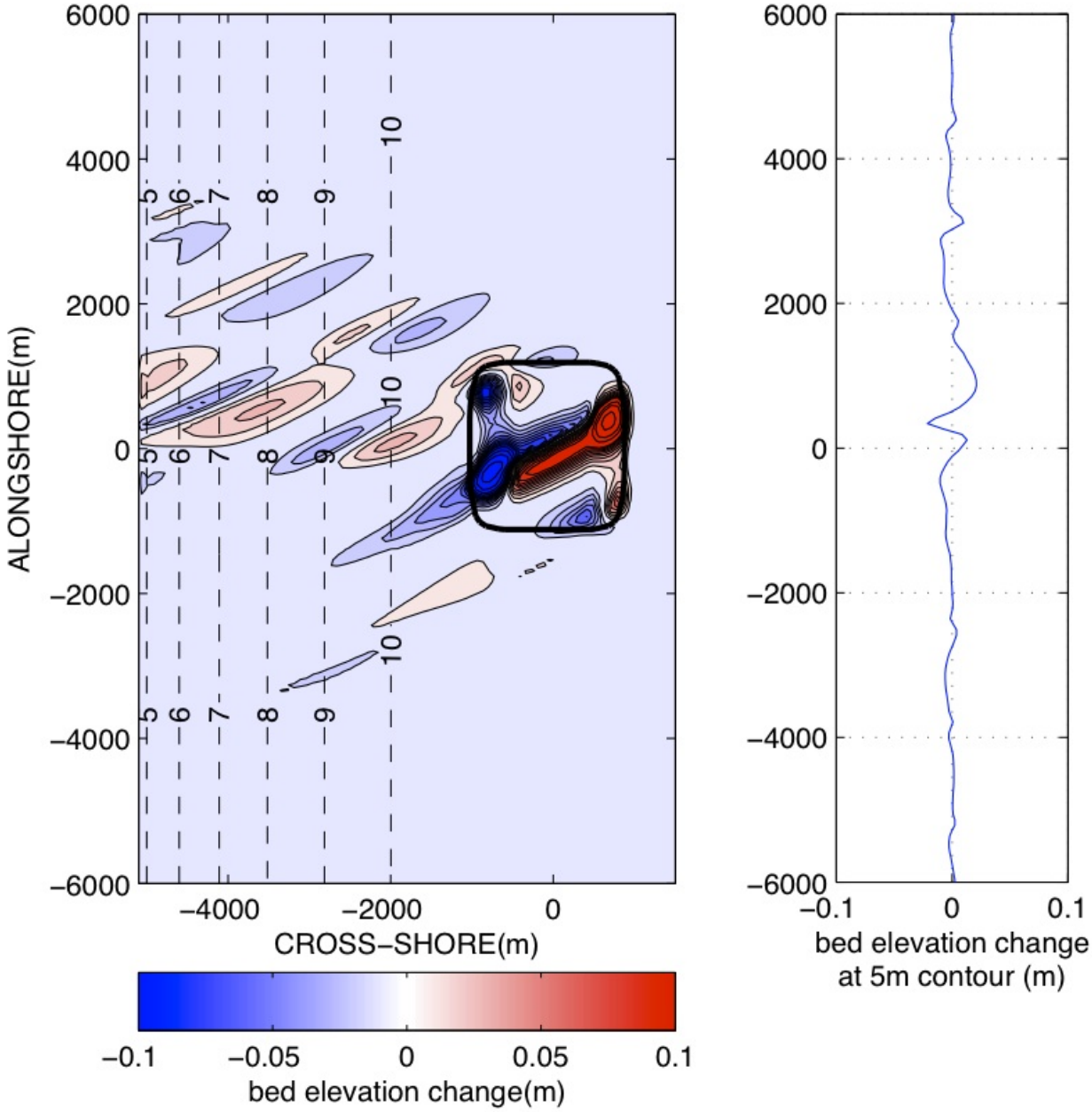

Figure VI-63. Depth change in Case C. Dashed lines: contours of depth before change, solid lines: contours of depth change, color: depth change

Table VI-11. Eroded, deposited and net volumes (m^3) measured from the 5 to 10 contour for the Ridge Wavelength Scenarios.

Case	Deposition (5 m – 10 m contours) in the alongshore region of 15 km (m^3)	Erosion (5 m – 10 m contours) in the along shore region of 15 km (m^3)	Net erosion/deposition (5 m – 10 m contours) in the along shore region of 15 km (m^3)
A	141,871	-163,858	-21,987
C	80,576	-88,261	-7,685

Figure VI-64 shows the change in bottom elevation at the 5 m contour at the end of the simulation for case A and case C. The variations were small and of similar magnitude to the flat bed cases described previously. The erosion and deposition zones, similarly to the non-ridged bed cases, are next to each other and extended mainly in the positive alongshore direction (north). The distance between successive depositional and erosional peaks appeared to be larger for case C, which is characterized by ridges with larger wavelength. In general, the variation appears directly linked to the ridge wave lengths.

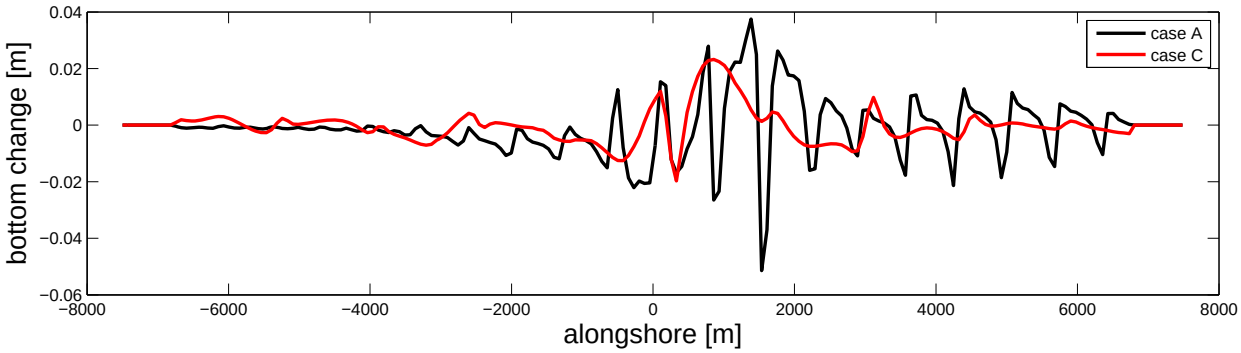

Figure VI-64. Variation (from the beginning to the end of the simulation) in bottom elevation (positive = accretion) at the 5m contour for Case A and Case C

VI.E.3. Concluding Remarks on Far-field Ridged Bed Investigation

Utilizing the idealized bathymetry and dredged borrow area, a NearCoM model was developed to assess the influence of borrow areas dredged on ridged-bed bathymetry, where morphological change over a one-year period was simulated. Similar to the non-ridged-bed simulations, the idealized case was based on the general characteristics of the Cane South borrow area of South Carolina. A total of three test cases were evaluated, as described in Table VI-3. Based on the results of these test cases, the following conclusions have been made:

- The borrow area influence potentially extends significant distances alongshore; therefore, ridged-bed simulations suggest that process-based numerical models should consider computational domains with a large alongshore extent to ensure that model boundary conditions do not influence results.
- The far-field region where the effect of the borrow area was observed in the model results extended to the north or to the south, which indicated a strong dependence on ridge orientation with respect to the shoreline. All the considered scenario cases have shown net erosion in the region from 5m to 10m contour. The erosional and depositional patterns, measured at the 5m contour, did not show a clear periodicity; however, there appeared to be a link between ridge wavelength and nearshore erosion/deposition patterns, where the lower ridge wavelength corresponded to a lower wavelength erosion/deposition pattern.

Given the limited number of test cases considered, present results can give only a very rough idea of the influence of ridge orientation and wavelength on the far-field region. In order to get a

more precise idea on the influence of the variation of the two considered parameters, more scenario tests should be run. To develop a more complete understanding of how different parameters and processes influence morphologic change, other parameters not included in the overall analysis could be considered for future evaluation (e.g. tidal current strength, residual current, wave climate, sediment characteristics, etc.).

VII. ASSESSMENT OF NEAR-FIELD IMPACTS DUE TO EXTRACTION AT SAND RIDGES

An assessment of potential near-field impacts associated with sand ridge fields was investigated utilizing non-linear process-based modeling techniques. This effort was a logical extension of the previous geometries evaluated, where length scales of both the sand ridge geometry and the size of a typical borrow area are assessed.

Sand ridge, swale, and shoal fields along the U.S. Atlantic coast exhibit a wide range of variability with regard to their geometry, location, orientation, sediment characteristics, etc. The mechanisms responsible for their generation and evolution, including geological and hydrodynamic controls (McKinney et al., 1974; Conkwright et al., 2000; Edwards et al., 2003; Hayes and Nairn, 2004; Finkl et al., 2006; Robinson, 2007; Robinson and McBride, 2008; USACE/MMS, 2009; Applied Coastal Research and Engineering et al., 2010; Dibjania and Nairn, 2010 and others), vary greatly from site to site. A comprehensive evaluation of the near- and far-field impacts due to extraction of sand from offshore ridges would need to address a wide range of ridge characteristics and associated ambient conditions, including hydrodynamic forcing. The effect of varying the pit aspect ratio, the position of the pit centroid relative to the bed morphology, and the pit orientation on the near-field evolution of the sand ridges is investigated. Due to the complex physical processes that govern sand ridge morphology, a nonlinear process-based model is required to properly assess sediment transport patterns and the associated morphodynamic evolution of a pit dredged in a field of sand ridges. Interaction of the local flow-field induced by a ridge of large amplitude (having a spatial scale of the order of kilometers) and dredged pit calls for a fully non-linear model to properly resolve all the spatial scales involved in the phenomenon. The adopted process-based model is NearCoM, an open-source model that can be used to predict the coastal hydrodynamics, sediment transport, and seabed morphology changes for given offshore wave conditions and tidal currents. The NearCoM model integrates wave, circulation, and morphology modules which can be selected from a group of candidate models with standardized interaction threads, inputs, and outputs.

In order to better address the influence of the dredging of a pit on the nearfield, the modeling approach incorporated the Concurrent Correction Method, named Online Correction Method in the previous part of the report, which is particularly suited to investigate the near-field effects. The Concurrent Correction Method (or CCM) is described in section V.C.7 of the report and in Shi et al. (2015). CCM can be implemented into any physics based numerical model used to predict the morphological evolution of the seabed. In this study, CCM is implemented within the NearCoM model that can incorporate different sediment transport formulas. At Cane South pit, which is used as a model site for the test conditions, the sediment transport is strongly wave-induced, due to the weak offshore tidal regime and the relatively shallow depths. Therefore, the Van Rijn formula (1991) is implemented in NearCoM in order to properly take into account the wave-dominated sediment transport. Furthermore, the contribution to sediment transport rate due to the bottom slope is added to the original formula.

The bottom roughness (ripples), which is significant because the amount of sediment picked up from the bed is highly dependent on the bottom roughness, is predicted through use of the ripple predictor developed by Soulsby and Whitehouse (2005).

VII.A. BASELINE CONDITIONS

The geometry of the baseline case was based on idealized morphodynamic characteristics of sand ridge fields along the Atlantic Continental shelf (e.g. Hayes and Nairn, 2004). Figure VII-1 shows the initial idealized ridge bathymetry prior to dredging of the borrow site. The sand ridges were represented by regular ridges with 5,000 m crest spacing on a sloping bed, where the crests were oriented at an angle of 60 degrees to the coastline. The amplitude of the ridges was 5 m at a water depth of 12 m, and the amplitude of the ridges decreased towards the coastline as the water depth decreased. Both the sediment characteristics and wave forcing were kept the same as those selected for the flat bed cases of Section VI. In addition, the tidal current with amplitude magnitude of 0.2 m/s was applied at the northern and southern boundaries of the domain, equivalent to the lowest ambient tidal current evaluated for Section VI. The dimensions of the computational domain were 15,000 m in the longshore direction and 11,250 m in the cross-shore direction with 200 and 150 grid-points, respectively. This idealized ridge bathymetry provided the basis for simulating near-field effects of positioning borrow areas on the ridge crest, ridge flank, and within the ridge trough for excavations of the same magnitude as evaluated in Section VI.

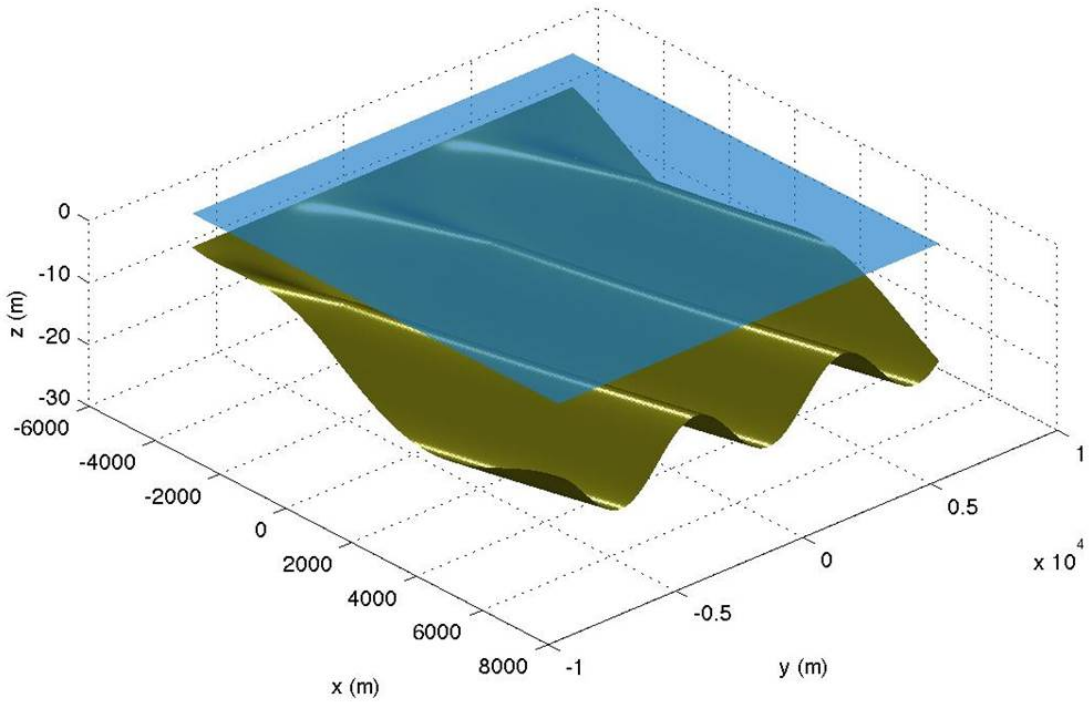

Figure VII-1. Initial bathymetry before dredging of the pit.

The geometry of the pit in the baseline case was designed based on the pit at Cane South (see Section VI). In the baseline case, a rectangular pit with dimensions of 2,000 m (alongshore) by 1,000 m (cross-shore) located on the ridge crest was considered (see Figure VII-2). This model domain extent was determined from initial model assessment runs indicating the relative influence of the proposed pit geometry on overall physical processes, including alterations to wave heights, tidal current patterns, and the associated morphological change. As described in Section VI, the pit was shaped as a truncated inverted pyramid with rounded corners and 1:3 side slopes. The pit was dredged at a depth of 12 m and a depth equal to 1 m below the local bed level.

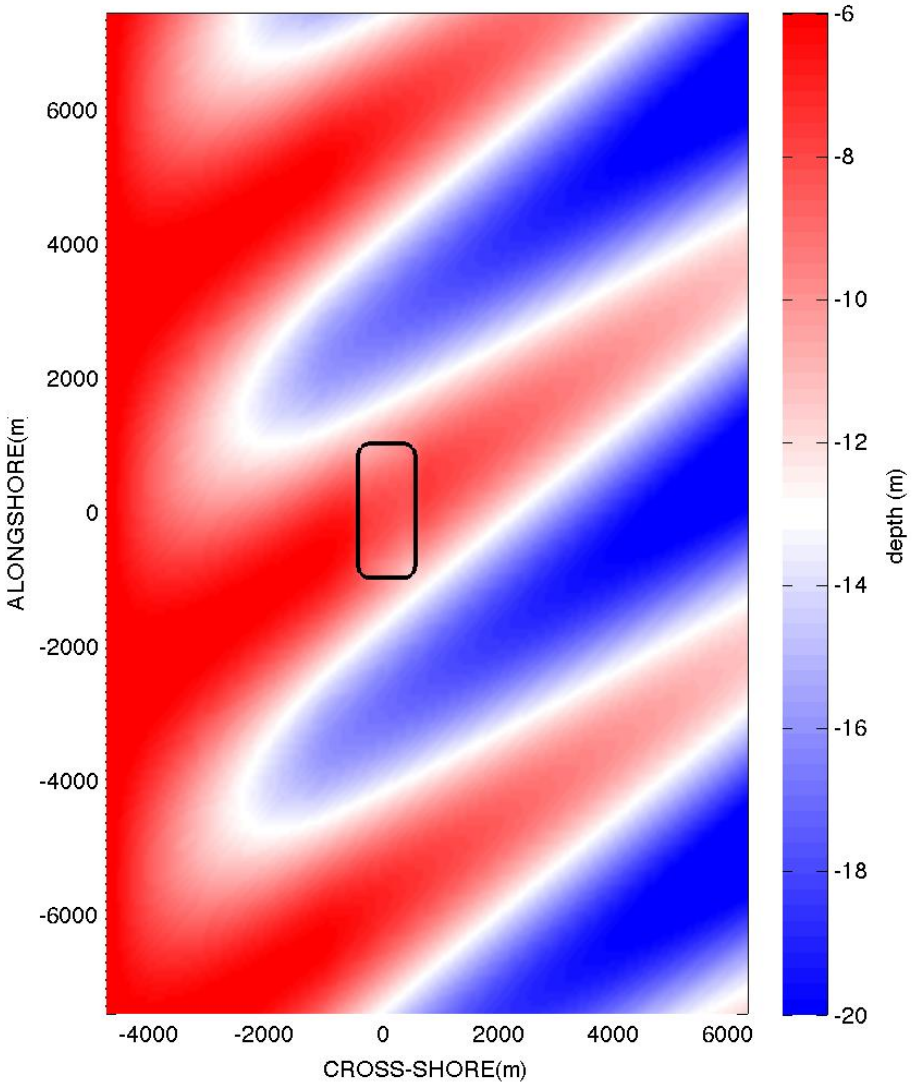

Figure VII-2. Initial bathymetry for the baseline case (Case A1).

Figure VII-3 and Figure VII-4 shows the relative variation of wave height and depth-averaged current speed, respectively) due to the dredging of the pit during the maximum wave height (02/05 21:00, 2010). The dredging of the pit caused an increase in wave height due to wave focusing effects in the north-west and southern regions adjacent to the pit area. In general, wave height decreased inside the pit area and in the near-field area west of the pit, due to wave focusing along the north and south edges of the pit. Figure VII-3 shows that the variations were greatest in the area of the ridge crest. The relative variations of wave height were due to the combined effects of depth variations and the focusing of wave rays. A relative increase in current speed upstream and downstream of the pit, by 3% and 5%, respectively, was observed. Inside the pit area, the current speed was reduced, particularly close to the east and west boundaries by 5% and 2%, respectively. Due to the localized reduction in bottom elevation of the ridge crest associated with the pit excavation, greater flow occurs in the areas both 'upstream' and 'downstream' of the excavated ridge. In general, removal of the ridge crest alters the asymmetric influence of the natural ridge crest on the ambient tidal current patterns. Similar to the variation of wave heights, the tidal current changed because of the depth variations and the convergence/divergence of the streamlines, i.e. the presence of the natural ridge caused a deflection in the tidal current, but excavation of the ridge crest reduces this effect. Additionally, reduction in the current speed and sediment transport across the pit can be anticipated, as the greater water column depth for similar flow would lead to localized net reduction in current speed and sediment transport potential. The reduction in tidal current speed in the far-field east and west of the excavated ridge area generally balances the increase in flow through the gap in the ridge crest.

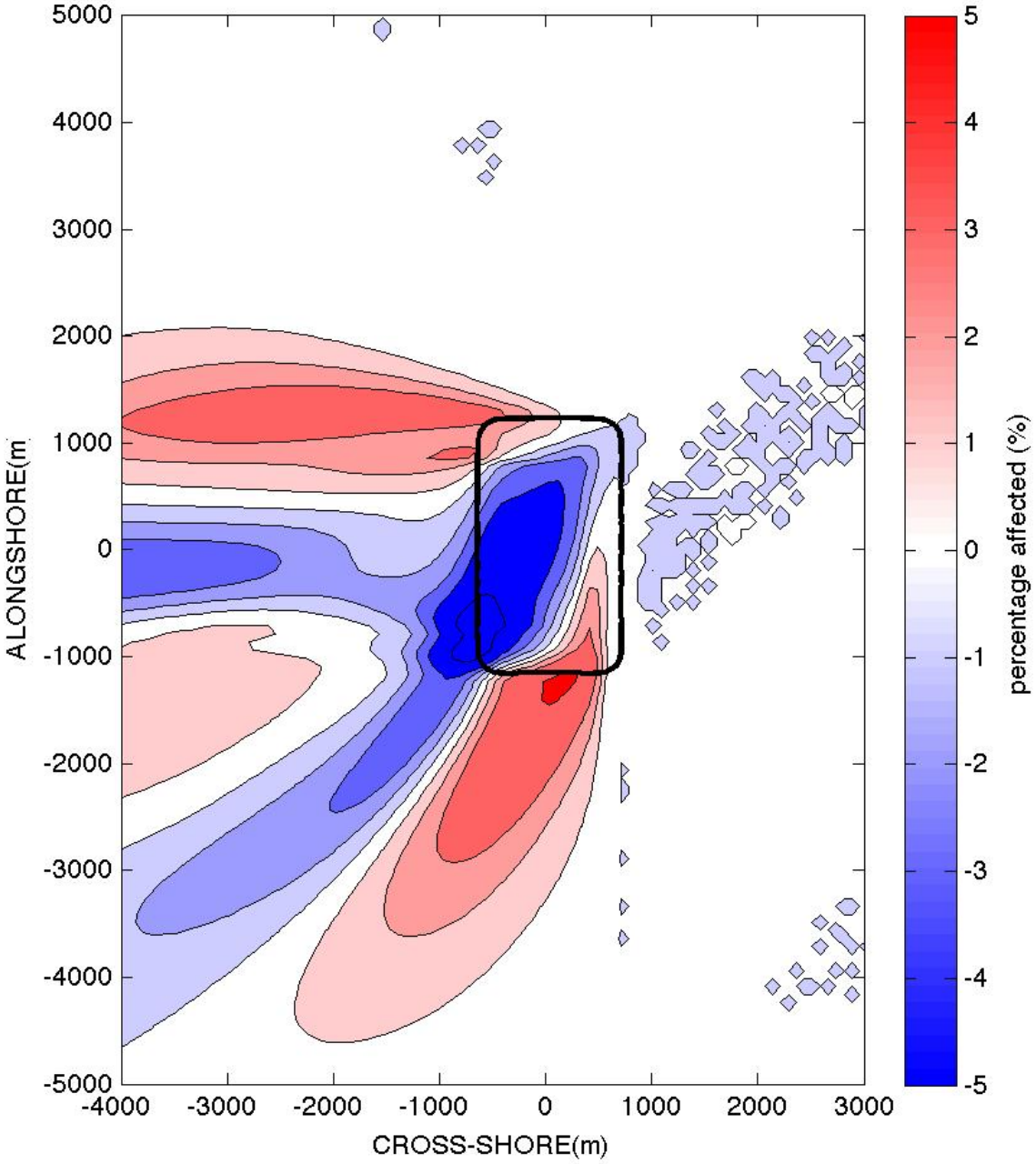

Figure VII-3. The relative variation of wave height during the maximum wave height (02/05 21:00, 2010) in the region around the pit with a pit aspect ratio of 0.5. The pit centroid is located on the ridge crest. Waves propagate from the eastern to the western domain boundaries (propagation from right-to left on the figure).

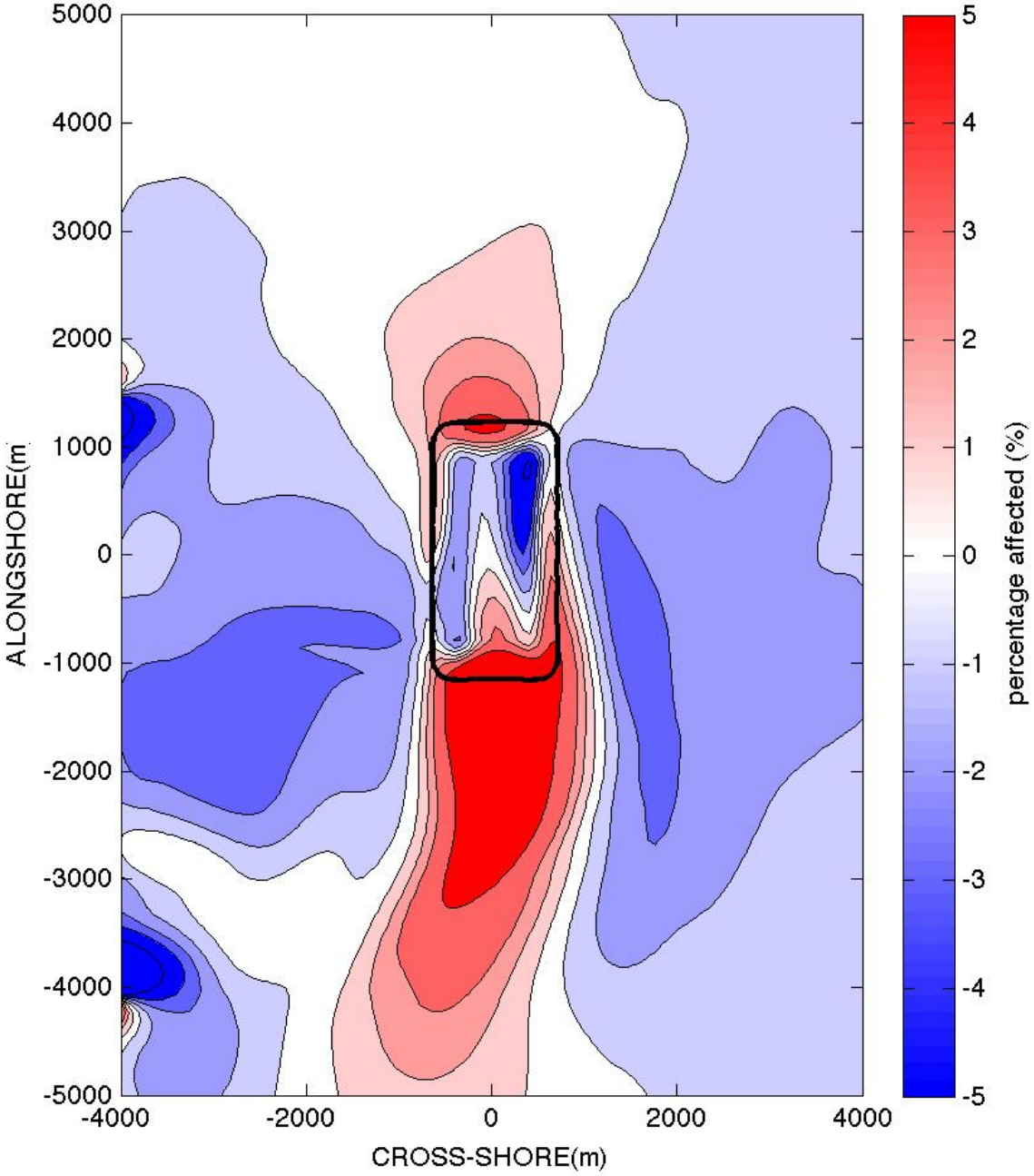

Figure VII-4. The relative variation of depth-averaged current speed during the maximum tidal current (02/05 21:00, 2010) in the region around the pit with a pit aspect ratio of 0.5. The pit centroid is located on the ridge crest. Tidal current with an amplitude of 0.2 m/s was applied at the northern and southern boundaries of the domain.

Figure VII-5 shows the depth variation 12 months after dredging of the pit. Sediment transport at the pit is strongly wave dominated, where the influence of changes to the ambient tidal currents does not appear to influence morphological change. Similar to the scenarios in Section VI, wind driven currents were not considered. In general, the ambient tidal currents are of insufficient magnitude to either mobilize the bottom sediments or to keep them in suspension once mobilized by wave action. Therefore, the transport direction principally coincided with the direction of wave propagation (from east to west). Sediment transport was also influenced by the presence of the ridges. Erosion and deposition areas illustrated patterns consistent with the migration of the pit in the south-west direction. Twelve months after dredging of the pit, the position of the pit centroid moved 587 m towards the west and 246 m towards the south. Table VII-1 shows that deposition inside the pit area was greater than erosion. However, in the entire computational domain, erosion was greater than deposition. Based on migration of the pit centroid and the computed bathymetric change shown in Figure VII-5, the model results suggest a net flux of sediment towards the shore. As the computational domain experienced slightly greater erosion than accretion (Table VII-1), it is likely that the influence of to the south and west of the borrow area extends beyond the computational domain in the general direction of the ridge crest orientation.

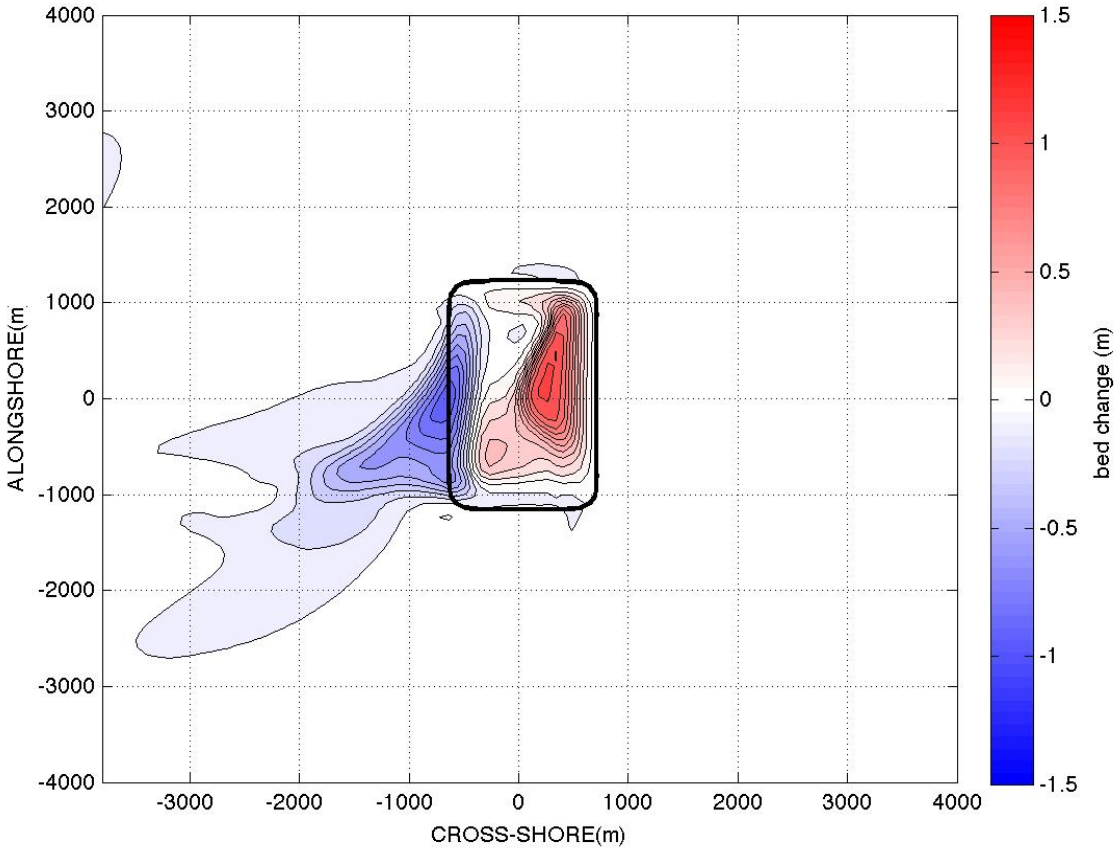

Figure VII-5. Erosion and deposition patterns of the baseline pit 12 months after dredging of the pit.

Table VII-1. Eroded and deposited volumes inside the area of the pit and in the entire computational area 12 months after dredging of the pit for the baseline case.				
Area	**Eroded volume (m^3)**	**Deposited volume (m^3)**	**Net volume (m^3)**	**Average Elevation Change (mm)**
Pit Area	2.52×10^5	8.31×10^5	5.79×10^5	175.4
Entire Computational Area	10.25×10^5	9.27×10^5	-0.98×10^5	-0.6

VII.B. CASES CONSIDERED

In order to investigate the effect of pit aspect ratio, pit centroid position, and pit orientation on hydrodynamic and morphodynamic processes, a total of seven cases were modeled (Table VII-2). The baseline case was represented as Case A1. The depth (equal to 1 m) and the dredged volume (2×10^6 m^3) of the pit were the same for all cases.

Table VII-2. Cases considered.			
Case	**Aspect ratio of the pit**	**Position of the pit with respect to the ridge**	**Orientation of the pit major axis with respect to the y-axis (long-shore)** **0° = pit is parallel to shore** **60° = pit is aligned with ridge**
A1 (baseline)	0.5	crest	0^o
A2	1	crest	0^o
B1	0.5	flank	0^o
B2	0.5	trough	0^o
C1	0.5	crest	60^o
D1	1	flank	0^o
D2	1	trough	0^o

VII.C. PIT ASPECT RATIO SCENARIO

In order to assess the effect of the pit aspect ratio on the hydrodynamic and morphodynamic processes, three series of runs were used: Cases A1 and A2 (pit centroid on the ridge crest), Cases B1 and D1 (pit centroid on the ridge flank), and Cases B2 and D2 (pit centroid on the ridge trough). Two pit aspect ratios were considered: a rectangular shaped pit with dimension of 2,000 m (longshore) by 1,000 m (cross-shore), resulting in an aspect ratio of 0.5, and a square pit

with an aspect ratio of 1.0 and dimensions of 1,414 m by 1,414 m. Schematics of the cases are shown in Figure VII-6 through VII-8.

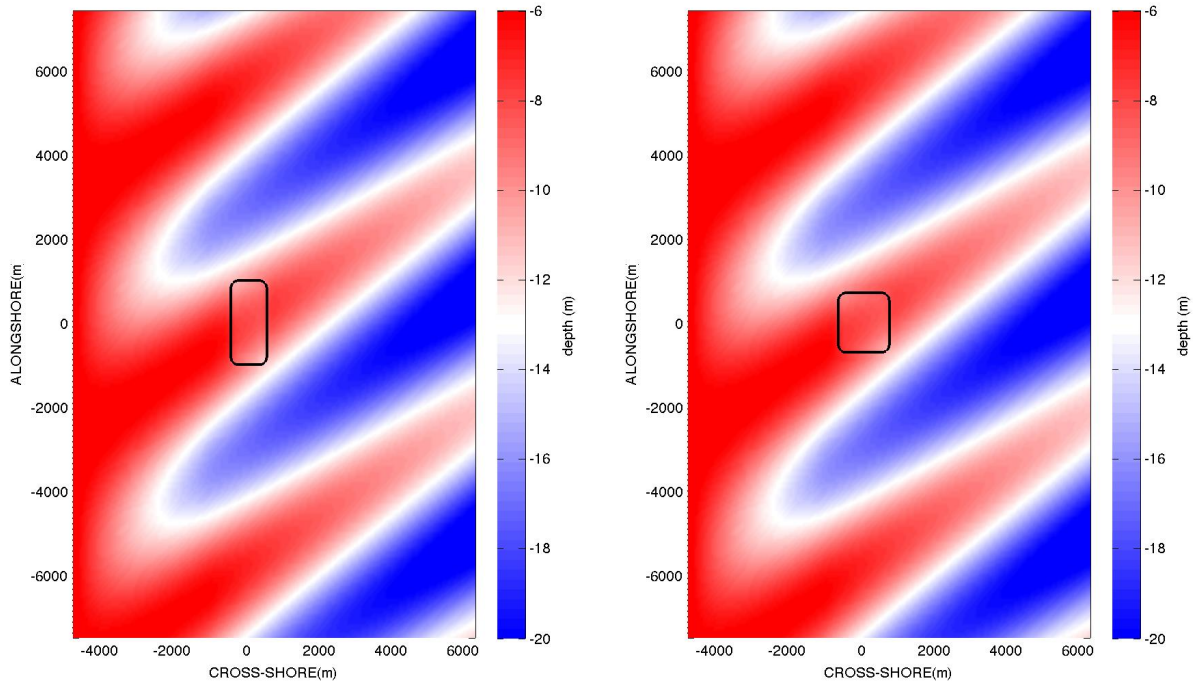

Figure VII-6. Initial bathymetry for Case A1 (left) and A2 (right). These cases were run to investigate the effect of pit aspect ratio of pits with centroids located on the ridge crest.

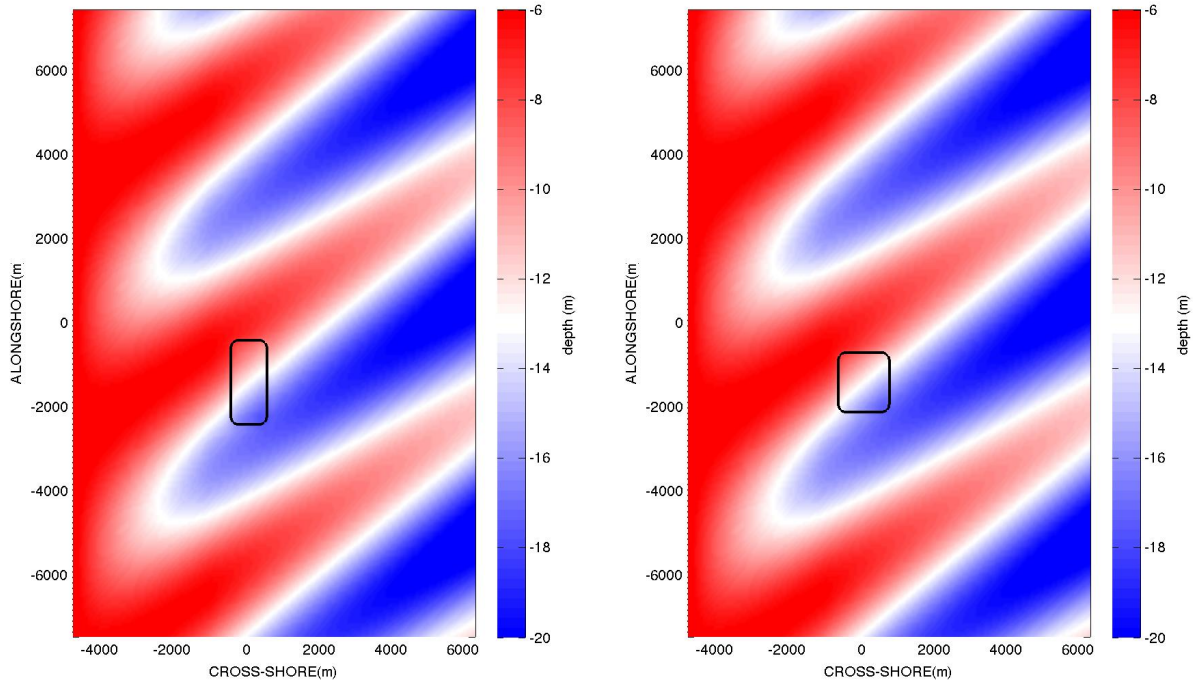

Figure VII-7. Initial bathymetry for Case B1 (left) and D1 (right). These cases were run to investigate the effect of pit aspect ratio of pits with centroids located on the ridge flank.

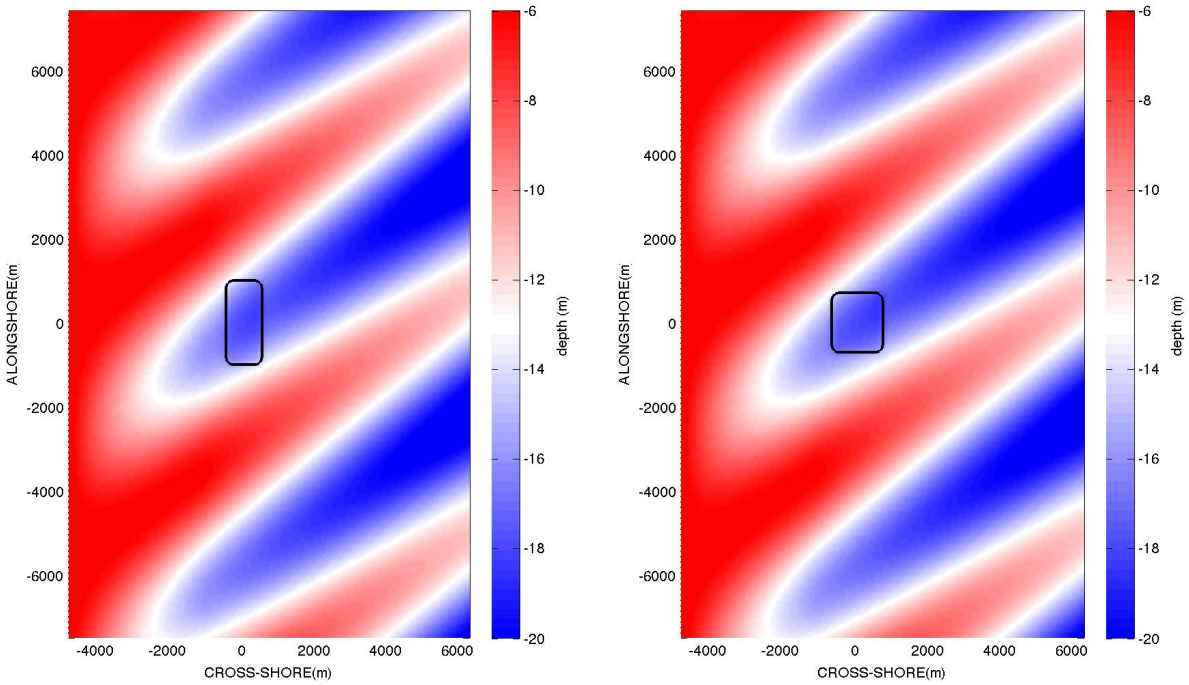

Figure VII-8. Initial bathymetry for Case B2 (left) and D2 (right). These cases were run to investigate the effect of pit aspect ratio of pits with centroids located on the ridge trough.

Figure VII-9 shows the relative variation of wave height during the period of maximum wave height modeled (02/05 21:00, 2010) in the region around the pits with pit aspect ratios of 0.5 and 1.0, respectively, where the pit centroids were located at the ridge crest for both cases. The 5% influence areas (where a relative variation of wave height larger than 5% is observed) were larger for the pit with an aspect ratio of 1.0 (i.e. the 'square' pit) because length of the pit was longer in the direction of wave propagation. The bathymetric alteration longer in the direction of wave propagation caused greater convergence of wave rays along the northern edge of the borrow pit, with a corresponding increase in wave heights along this edge and a coincident reduction of wave heights directly west of the pit.

Figures VII-10 and VII-11 show the areas of relative wave height variation when the pit centroid was located on the ridge flank and on the ridge trough, respectively. The 5% influence area vanished for both the square and the rectangular pits when the pit centroid was located on the ridge flank. The effect of pit aspect ratio on the wave height influence area is qualitatively similar to that observed for all pit centroid locations. The 5% influence area vanished, while the 3% influence area vanished only for the rectangular pit when the pit centroid is located within the ridge trough. As expected, the location of the pit on either the ridge flank or within the trough increases the water depth; therefore, a smaller relative variation in wave height can be expected with respect to the baseline case. In general, the alterations to wave height shown in

Figures VII-10 and VII-11 indicate that the borrow pit causes a ‘shadow’, resulting in a decrease in wave heights landward of the excavated pit.

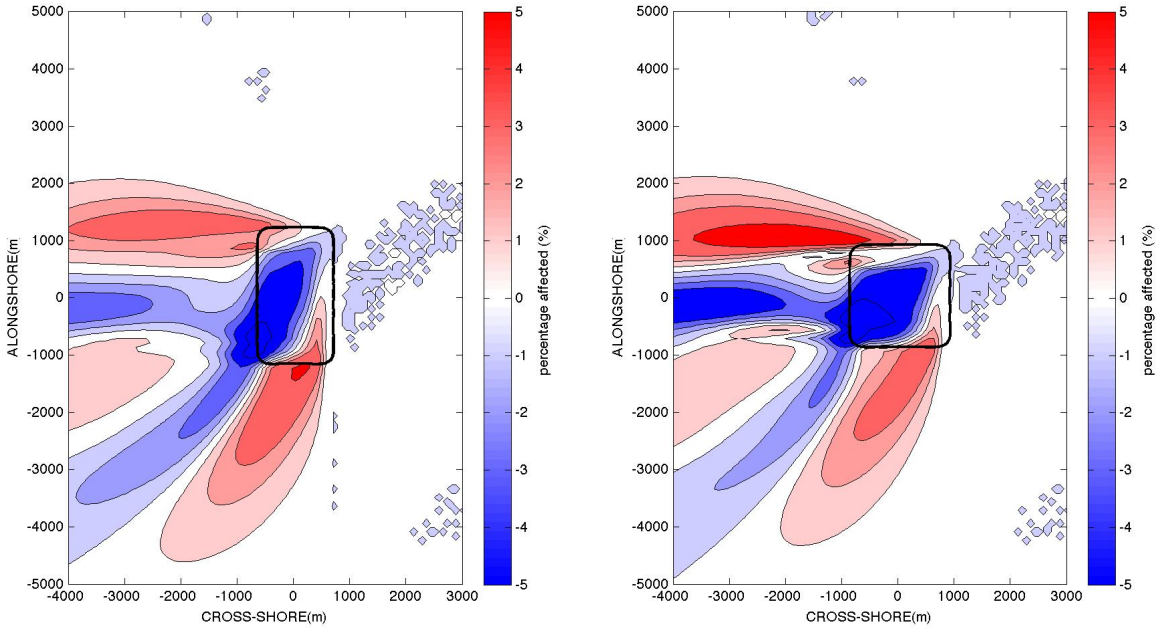

Figure VII-9. The relative variation of wave height during the maximum wave height (02/05 21:00, 2010) in the region around the pit. Case A1 (pit aspect ratio of 0.5) is shown on the left while Case A2 (pit aspect ratio of 1.0) is shown on the right. The pit centroid is located on the ridge crest in both cases.

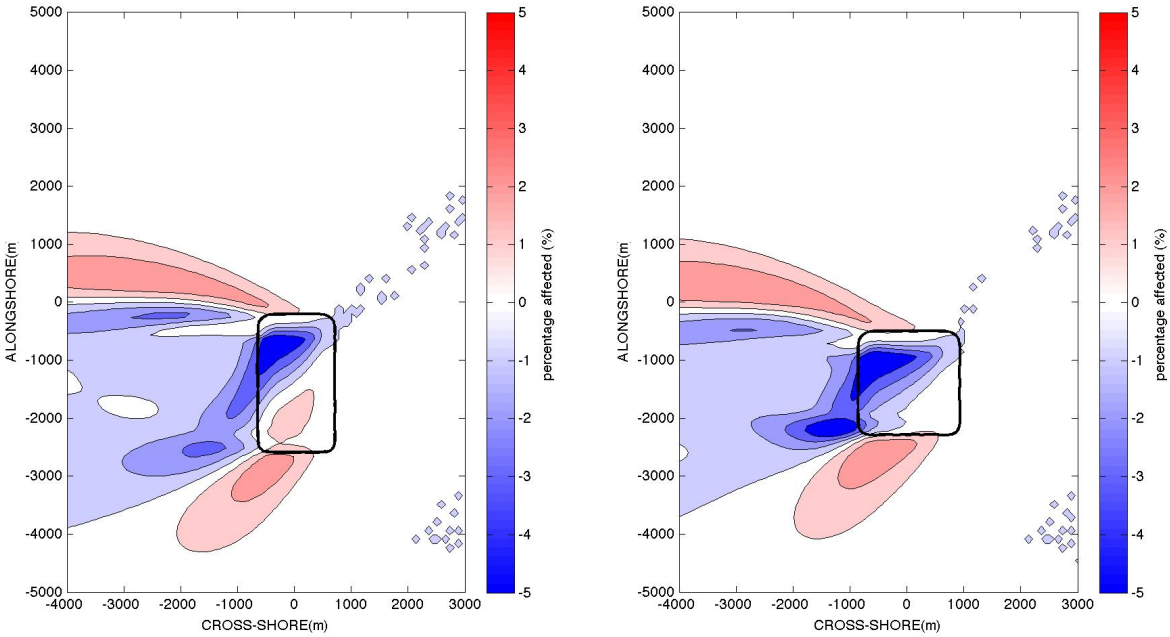

Figure VII-10. The relative variation of wave height during the maximum wave height (02/05 21:00, 2010) in the region around the pit. Case B1 (pit aspect ratio of 0.5) is shown on the left while Case D1 (pit aspect ratio of 1.0) is shown on the right. The pit centroid is located on the ridge flank in both cases.

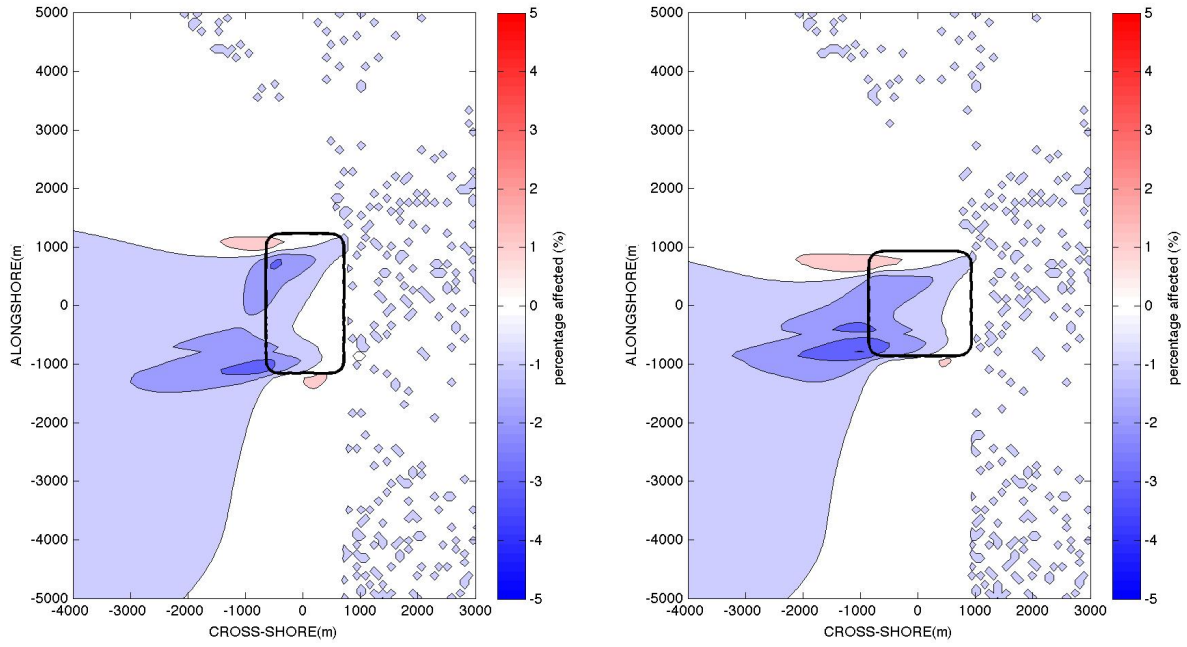

Figure VII-11. The relative variation of wave height during the maximum wave height (02/05 21:00, 2010) in the region around the pit. Case B2 (pit aspect ratio of 0.5) is shown on the left while Case D2 (pit aspect ratio of 1.0) is shown on the right. The pit centroid is located on the ridge trough in both cases.

Figures VII-12 through VII-14 show that the overall areas affected by wave height variations decrease when the pit centroid was relocated from the ridge crest to the flank and to the trough due to the increase in water depth. In addition, the influence areas increased as the pit aspect ratio was increased, even though the 5% influence area was nearly constant. To quantitatively compare the effect of pit aspect ratio on the influence area for different series, the parameter $\Delta^{hs}_{X\%}$ was defined as the difference between the X% influence area of the square pit (aspect ratio equal to 1.0) and the X% influence area of the rectangular pit (aspect ratio of 0.5), divided by the latter. In all cases considered above, $\Delta^{hs}_{5\%}$, $\Delta^{hs}_{3\%}$, and $\Delta^{hs}_{2\%}$ were positive, indicating that the square pit caused more variations of wave height than the rectangular pit. The value of $\Delta^{hs}_{1\%}$ nearly vanished, indicating that far from the pit, the details of pit geometry were not significant.

Figures VII-15, VII-16, and VII-17 show the effect of pit aspect ratio on the relative variation of the tidal current speed during the maximum tidal current (02/05 21:00, 2010) where the pit centroid was located at the ridge crest, flank, and trough, respectively. In all cases, it was observed that there was an increase of current speed upstream and downstream of the pit and a decrease inside the pit area. Also, the square pit (pit aspect ratio of 1.0) causes larger relative variations in current speed than the corresponding rectangular pit (pit aspect ratio of 0.5).

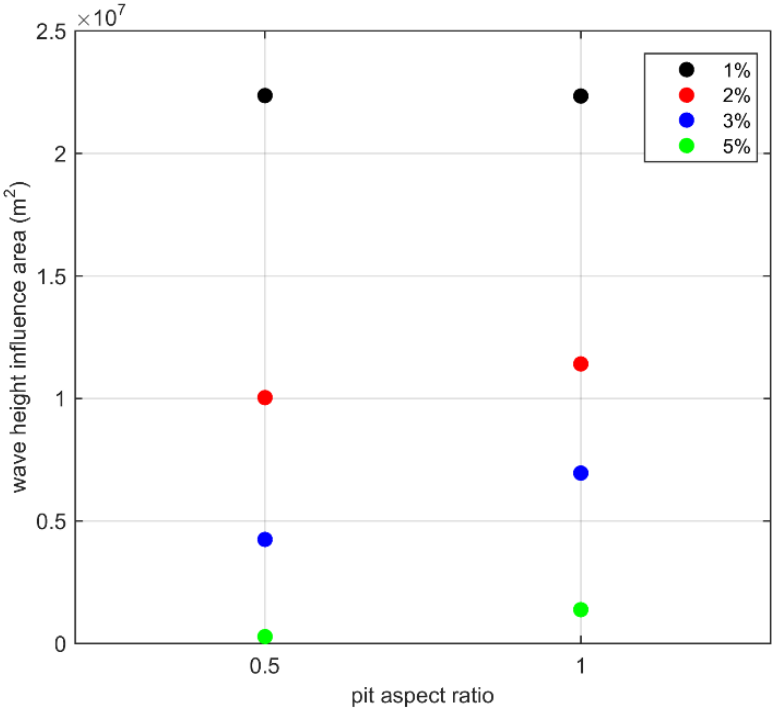

Figure VII-12. Influence area (m^2) of wave height with respect pit aspect ratio, where the pit centroid is located on the ridge crest.

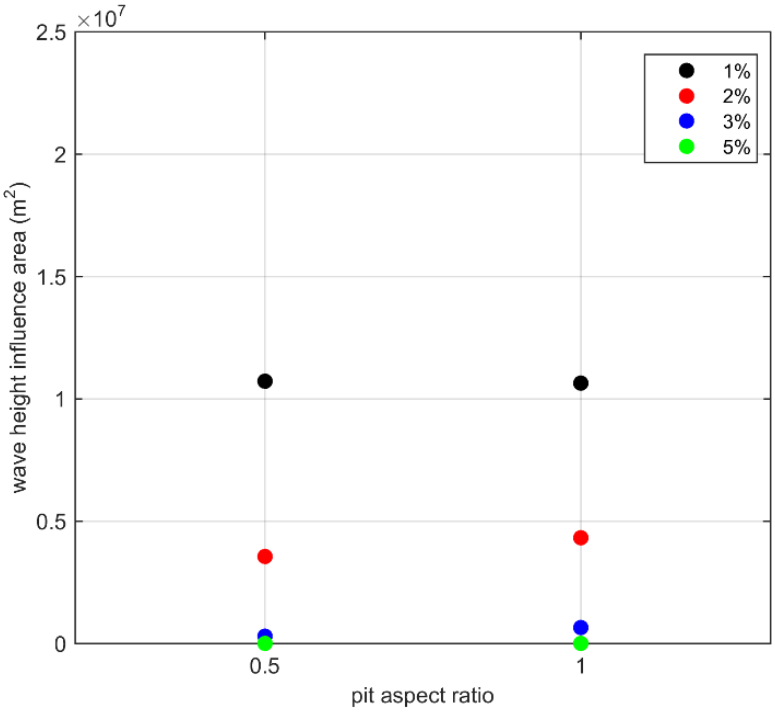

Figure VII-13. Influence area (m^2) of wave height with respect pit aspect ratio, where the pit centroid is located on the ridge flank.

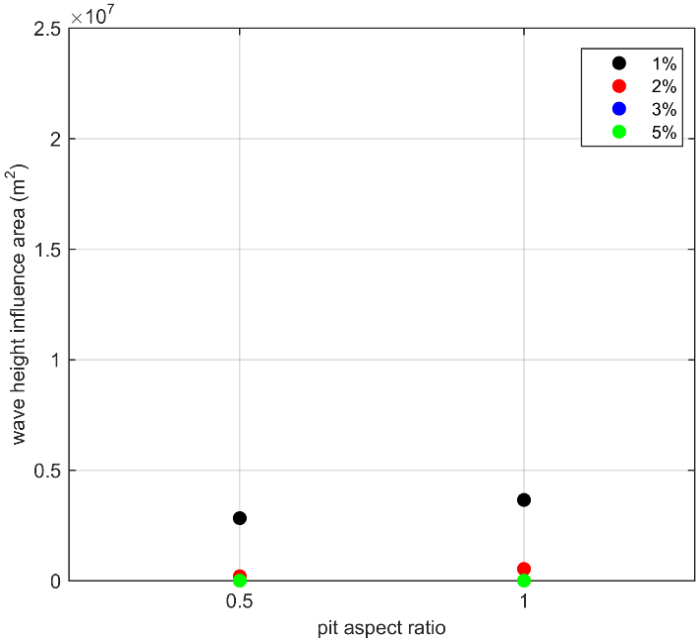

Figure VII-14. Influence area (m^2) of wave height with respect pit aspect ratio, where the pit centroid is located within the trough.

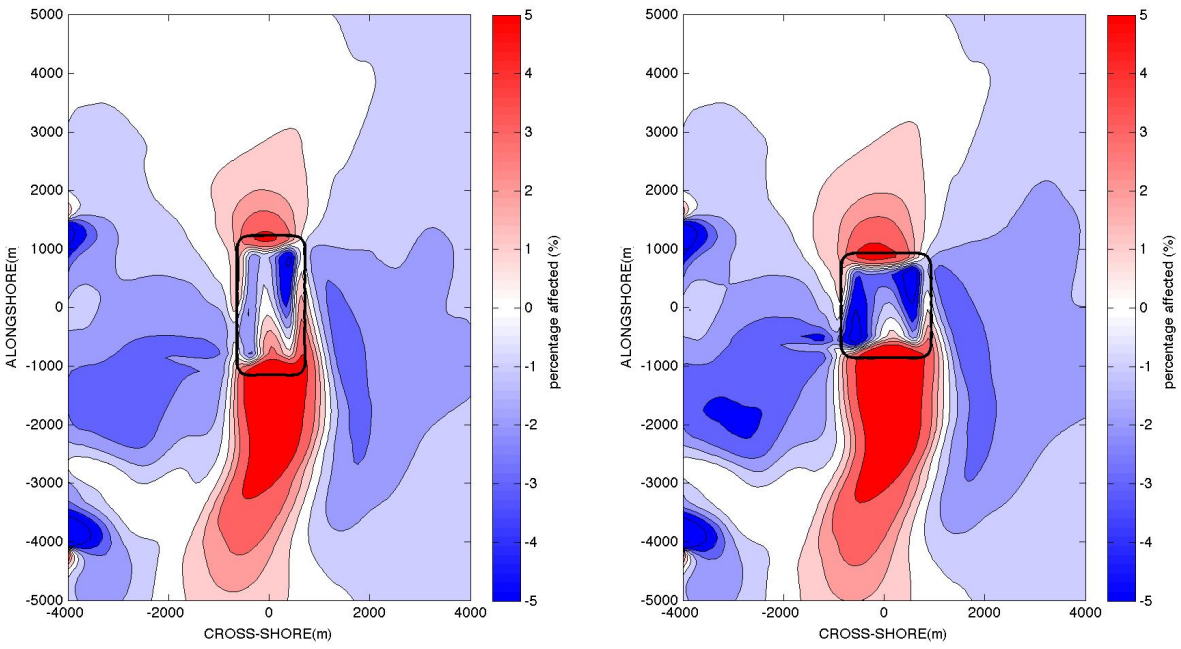

Figure VII-15. The relative variation of the tidal current in the region around the pit during the maximum tidal current (02/05 21:00, 2010). Case A1, with pit aspect ratio of 0.5, is shown on the left while Case A2, with pit aspect ratio of 1.0, is shown on the right. The pit centroid was located on the ridge crest in both cases.

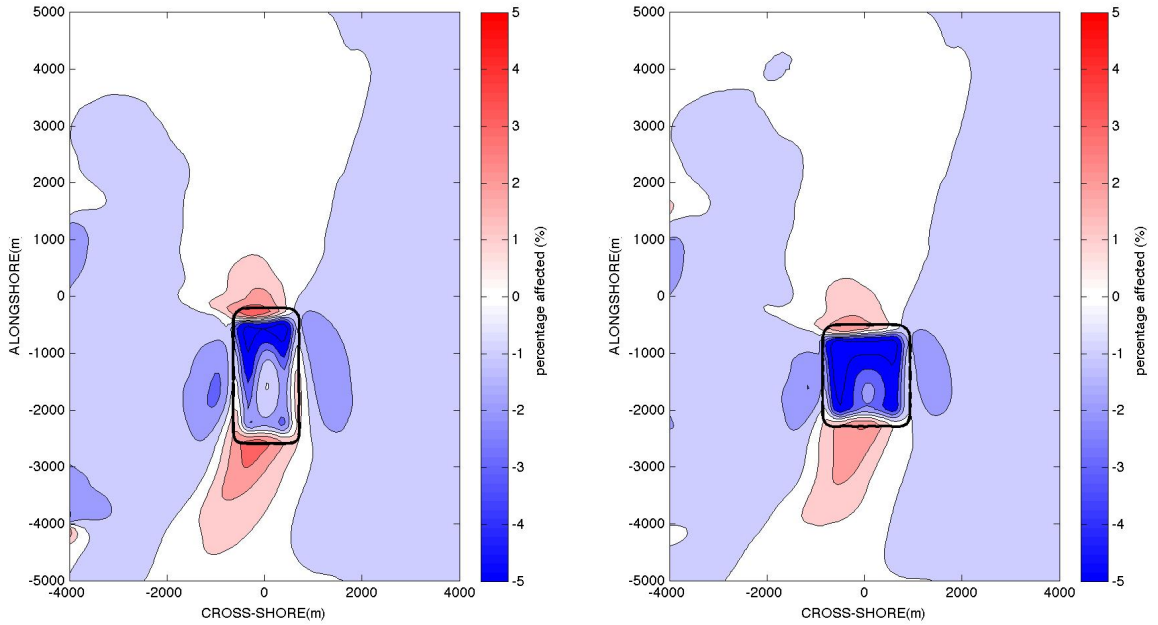

Figure VII-16. The relative variation of the tidal current in the region around the pit during the maximum tidal current (02/05 21:00, 2010). Case B1, with pit aspect ratio of 0.5, is shown on the left while Case D1, with pit aspect ratio of 1.0, is shown on the right. The pit centroid was located on the ridge flank in both cases.

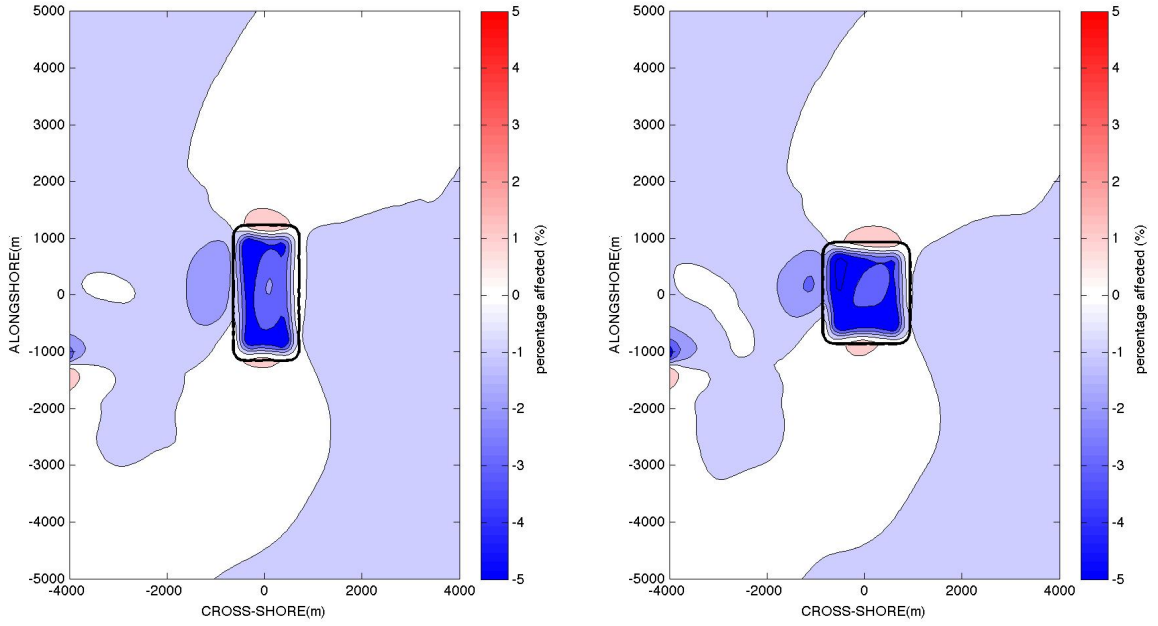

Figure VII-17. The relative variation of the tidal current in the region around the pit during the maximum tidal current (02/05 21:00, 2010). Case B2, with pit aspect ratio of 0.5, is shown on the

left while Case D2, with pit aspect ratio of 1.0, is shown on the right. The pit centroid was located on the ridge trough in both cases.

Considering the effect of pit aspect ratio on the tidal current influence area, see Figures VII-18 through VII-20, it was observed that the 5% and 3% influence areas increased as the pit aspect ratio was increased. Considering the values of $\Delta^{curr}_{X\%}$, which are similarly defined as $\Delta^{hs}_{X\%}$, it was observed that $\Delta^{curr}_{X\%}$ was generally positive, indicating that aspect ratio is important relative to impacts in the near-field. The only negative value of $\Delta^{curr}_{X\%}$ was obtained for the case where the pit centroid was located on the ridge flank for the 1% influence area ($\Delta^{curr}_{1\%} = -0.21$), indicating that the impact area of the square pit was smaller than that of the rectangular pit. The largest values of $\Delta^{curr}_{3\%}$ and $\Delta^{curr}_{5\%}$ were obtained when the pit centroid was located within the ridge trough, signifying that changing the pit aspect ratio when the pit centroid was located within the ridge trough has the largest relative influence on tidal currents.

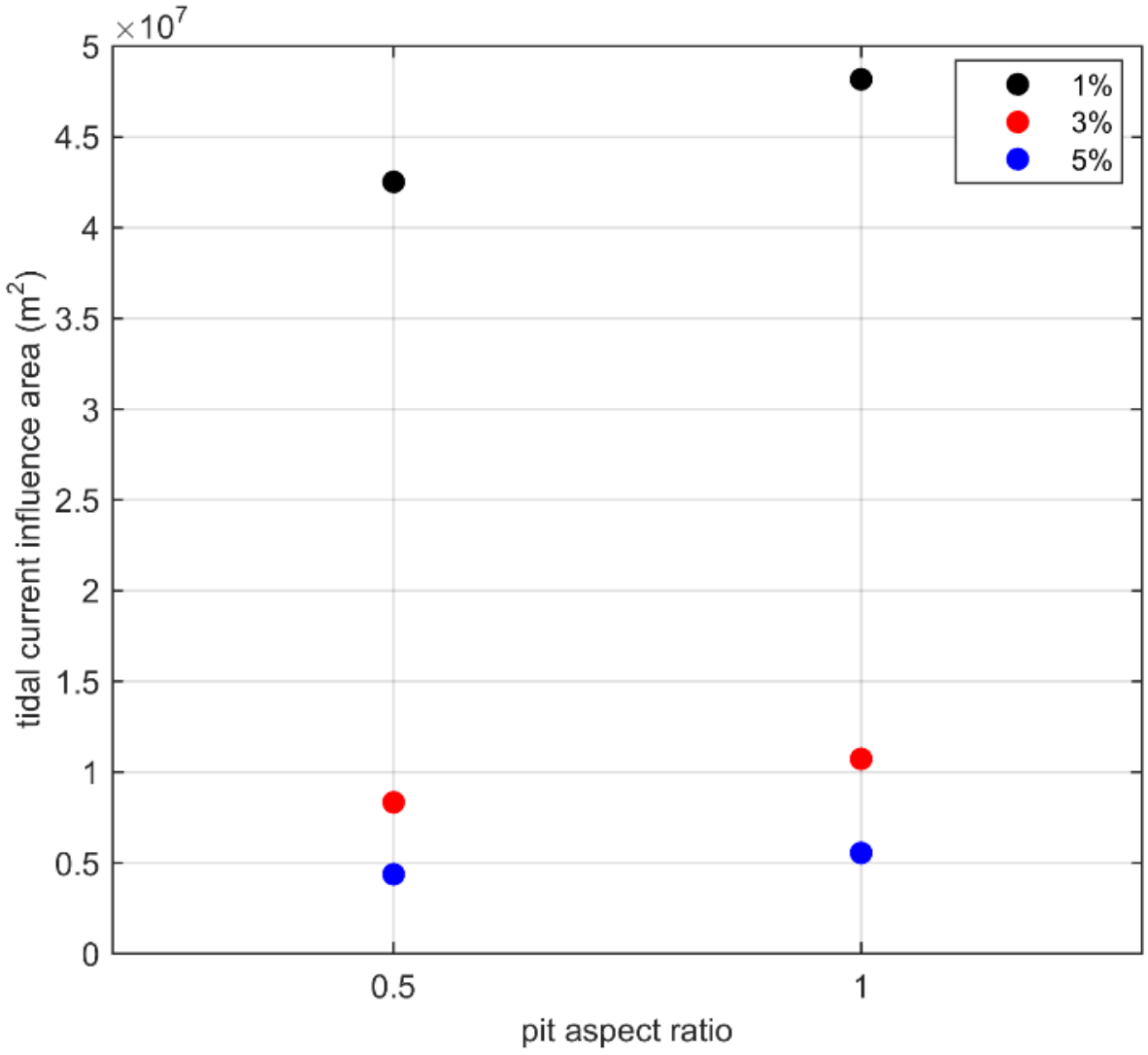

Figure VII-18. Influence area (m^2) of tidal current with respect to pit aspect ratio, where the pit centroid is located on the ridge crest.

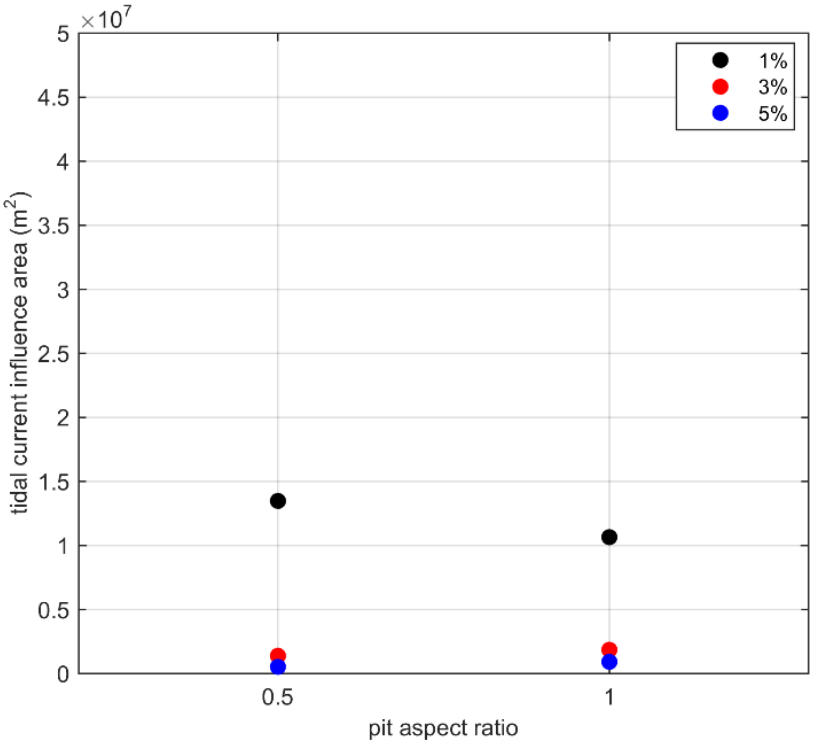

Figure VII-19. Influence area (m^2) of tidal current with respect to pit aspect ratio, where the pit centroid is located on the ridge flank.

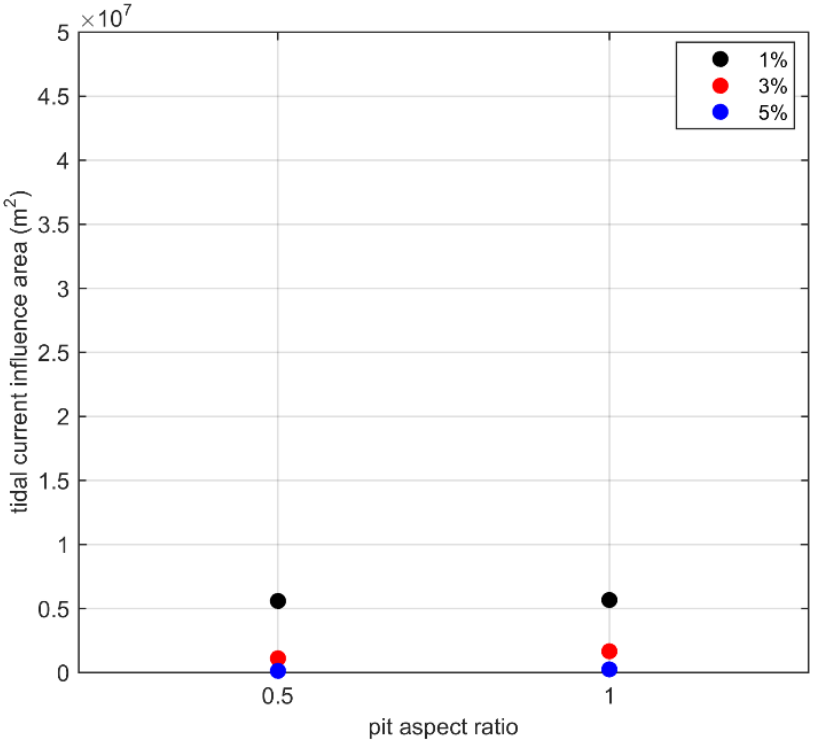

Figure VII-20. Influence area (m^2) of tidal current with respect to pit aspect ratio, where the pit centroid is located within the ridge trough.

Figures VII-21, VII-22, and VII-23 show the influence of the pit aspect ratio on the depth changes 12 months after dredging when the pit centroid is located on the ridge crest, flank, and trough, respectively. The sediment transport was strongly wave dominated, where the influence of the north-south ambient tidal current had a minimal effect on sediment transport patterns. When the pit centroid was located on the ridge crest, a depositional area formed inside the pit close to the east boundary both for the 0.5 and 1.0 aspect ratio pit. Erosion was observed in the western area of the pit and the adjacent area to the west. The presence of the ridge crest caused the most significant erosion and deposition to be aligned with the ridge crest. For the model simulations where the pit centroid was located on the ridge flank, the erosion and deposition areas were mainly located at the north-west region, close to the pit edge where the local water depth was shallowest, as shown in Figure VII-22. Erosion and deposition was minimal for the simulations where the pit centroid was located within the trough, as shown in Figure VII-23. No qualitative differences in the erosional and depositional patterns were observed with variation in pit aspect ratio.

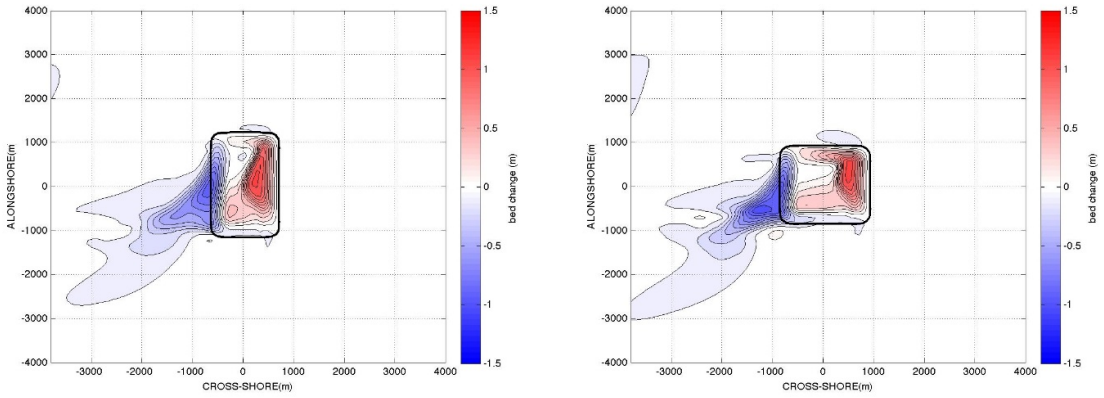

Figure VII-21. Depth change in Case A1 (pit aspect ratio of 0.5, left) and Case A2 (pit aspect ratio of 1.0, right) 12 months after dredging of the pit. Pit centroid is located on the ridge crest in both cases.

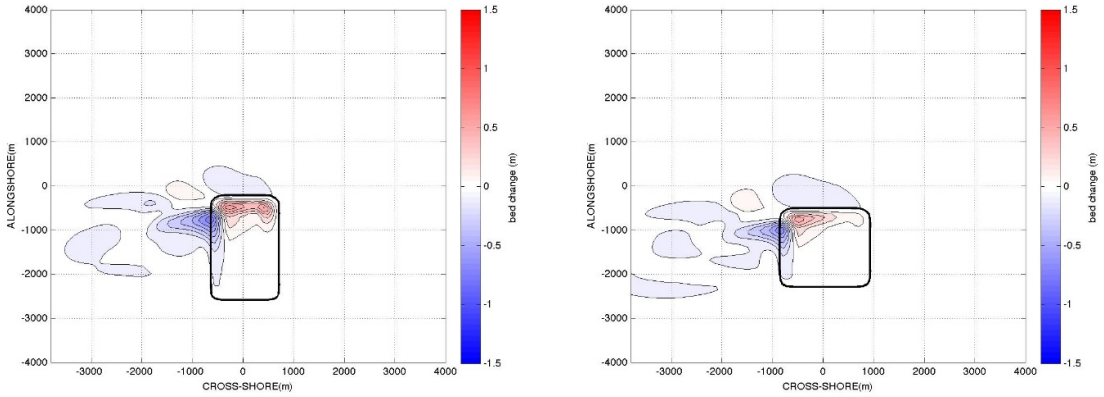

Figure VII-22. Depth change in Case B1 (pit aspect ratio of 0.5, left) and Case D1 (pit aspect ratio of 1.0, right) 12 months after dredging of the pit. Pit centroid is located on the ridge flank in both cases.

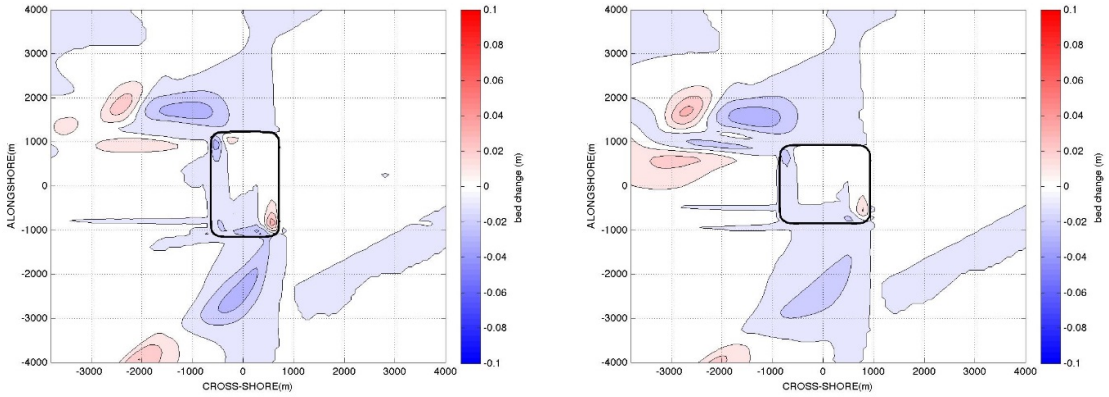

Figure VII-23. Depth change in Case B2 (pit aspect ratio of 0.5, left) and Case D2 (pit aspect ratio of 1.0, right) 12 months after dredging of the pit. Pit centroid is located on the ridge trough in both cases.

Figures VII-24 through VII-26 show the effect of pit aspect ratio on the deposited, eroded, and net volumes inside the pit area 12 months after dredging, respectively. Deposition, erosion, and net volumetric change were smaller when the pit centroid was located on the ridge trough than on the ridge crest or flank. The magnitude of erosion and deposition decreased as the pit aspect ratio increased. In order to compare the effect of the variation of pit aspect ratio on deposited and eroded volumes for pits with different centroid locations, the parameter Δ^e_{pit} (Δ^d_{pit}) was defined as the ratio between the difference between the eroded (deposited) volume in the square and rectangular pit and the eroded (deposited) value in the rectangular pit. The parameters Δ^e_{pit} and Δ^d_{pit} were negative for all the three pit centroid positions, as the magnitude of erosion and deposition decreased as the pit aspect ratio was increased.

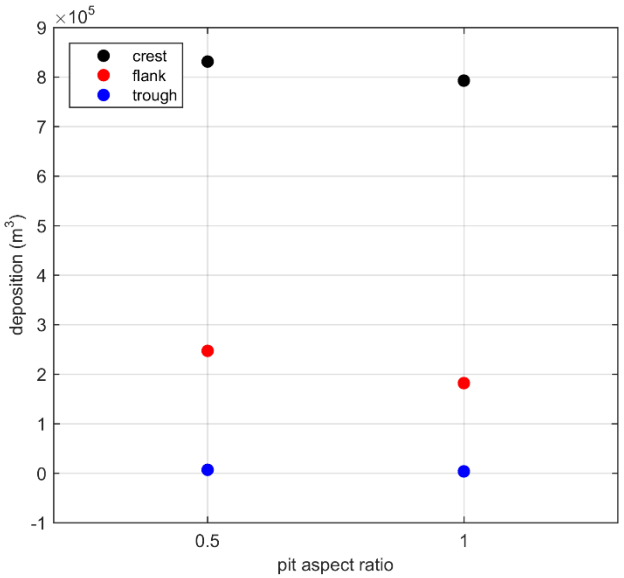

Figure VII-24. Deposition inside the pit area 12 months after dredging of the pit with respect to pit aspect ratio.

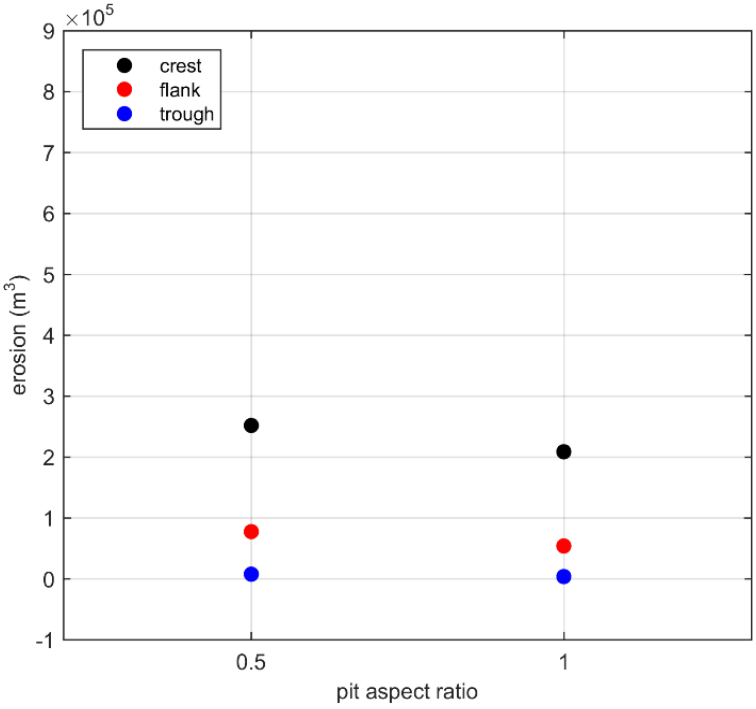

Figure VII-25. Erosion the pit area 12 months after dredging of the pit with respect to pit aspect ratio.

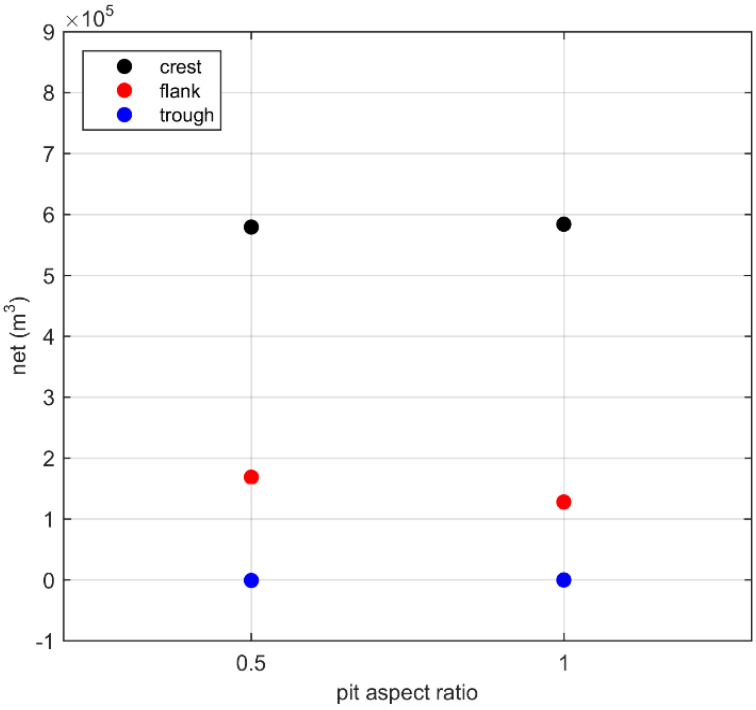

Figure VII-26. Net volumetric change (deposition minus erosion) inside the pit area 12 months after dredging of the pit with respect to pit aspect ratio.

From Table VII-3, Δ^{d}_{pit} had the largest proportional change between deposition for the different pit aspect ratios (0.39) when the pit centroid was located within the ridge trough; however, the total volumes of sediment deposition and erosion were two orders of magnitude lower compared to all other simulated cases. Therefore, use of the proportional changes to deposition associated with the pit centroid located within the trough and are not meaningful within the context of a comparative analysis with the other simulation cases.

The smallest proportional change between deposition fort the different aspect ratios, Δ^{d}_{pit}, (0.05) occurred when the pit centroid was located on the ridge crest. When the eroded volumes were considered, again the smallest value of Δ^{e}_{pit} (0.17) was encountered when the pit centroid was located on the ridge crest. These observations indicate that the change in pit aspect ratio has a smaller proportional change on deposited and eroded volumes when the pit centroid was located on the ridge crest. However, as shown in Table VII-3, the overall magnitude of deposited and eroded volumes is greatest for the cases where the pit centroid is located on the ridge crest.

Table VII-3. Erosion and deposition inside the pit area 12 months after dredging of the pit for all the cases considered for pit aspect ratio.

Case		**Pit Aspect Ratio**	**Eroded volume (m^3)**	**Deposited volume (m^3)**	**Net volume (m^3)**	**Average Elevation Change (mm)**
Crest	A1	0.5	2.52×10^5	8.31×10^5	5.79×10^5	175.4
	A2	1.0	2.09×10^5	7.93×10^5	5.84×10^5	188.1
Flank	B1	0.5	0.78×10^5	2.47×10^5	1.69×10^5	49.7
	D1	1.0	0.54×10^5	1.82×10^5	1.28×10^5	39.9
Trough	B2	0.5	0.08×10^5	0.07×10^5	-0.01×10^5	-0.1
	D2	1.0	0.04×10^5	0.04×10^5	0	0.1

Comparing the deposition and erosion inside the pit, listed in Table VII-3, and those in the entire computational area, listed in Table VII-4, it was observed that the largest value of the ratio of deposited (eroded) volumes inside the pit area and the volumes deposited (eroded) in the entire computational domain was found for the rectangular pit, suggesting that the rectangular pit has a larger morphodynamic influence than the square pit. This may be due to the greater length of the borrow pit boundary facing the incoming wave field, which results in more deposition within the pit. Furthermore, it was found that the largest value of the ratio (0.90 for deposited volumes and 0.25 for eroded volumes) was obtained for the rectangular pit located on the crest of the ridge.

Table VII-4. Erosion and deposition inside the entire computational domain 12 months after dredging of the pit for all the cases considered for pit aspect ratio.						
Case		**Pit Aspect Ratio**	**Eroded volume (m^3)**	**Deposited volume (m^3)**	**Net volume (m^3)**	**Average Elevation Change (mm)**
Crest	A1	0.5	10.25×10^5	9.27×10^5	-0.98×10^5	-0.6
	A2	1.0	10.70×10^5	9.47×10^5	-1.23×10^5	-0.8
Flank	B1	0.5	3.61×10^5	3.41×10^5	-0.2×10^5	-0.1
	D1	1.0	3.02×10^5	2.83×10^5	-0.19×10^5	-0.1
Trough	B2	0.5	0.79×10^5	0.97×10^5	0.18×10^5	0.1
	D2	1.0	0.75×10^5	1.02×10^5	0.27×10^5	0.2

In order to further characterize the effect of the pit aspect ratio on erosion and deposition in the near-field area outside the pit, the volumes deposited and eroded in two areas outside the pit, as shown in Figure VII-27 and herein named the *2X* and *4X* area, were computed. The *2X* and *4X* areas have horizontal dimensions equal to two and four times that of the pit area, respectively. While this approach required different dimensions based on borrow area aspect ratios, it preserved the influence of the aspect ratio on the surrounding sea bed.

The eroded and deposited volumes of the *2X* and *4X* areas are given in Table VII-5 and VII-6, respectively. From the values in Table VII-4, VII-5, and VII-6, it was observed that the volume deposited inside the *2X* and *4X* areas, excluding the contribution due to the initial borrow area, are smaller than the volume deposited inside the borrow area. On the other hand, the volume eroded inside the *2X* and *4X* areas, again excluding the contribution due to the initial borrow area, are larger than the volume eroded inside the borrow area. This finding was related to the migration of the borrow area centroid which causes erosion in areas outside the borrow area and deposition inside the initial borrow area footprint.

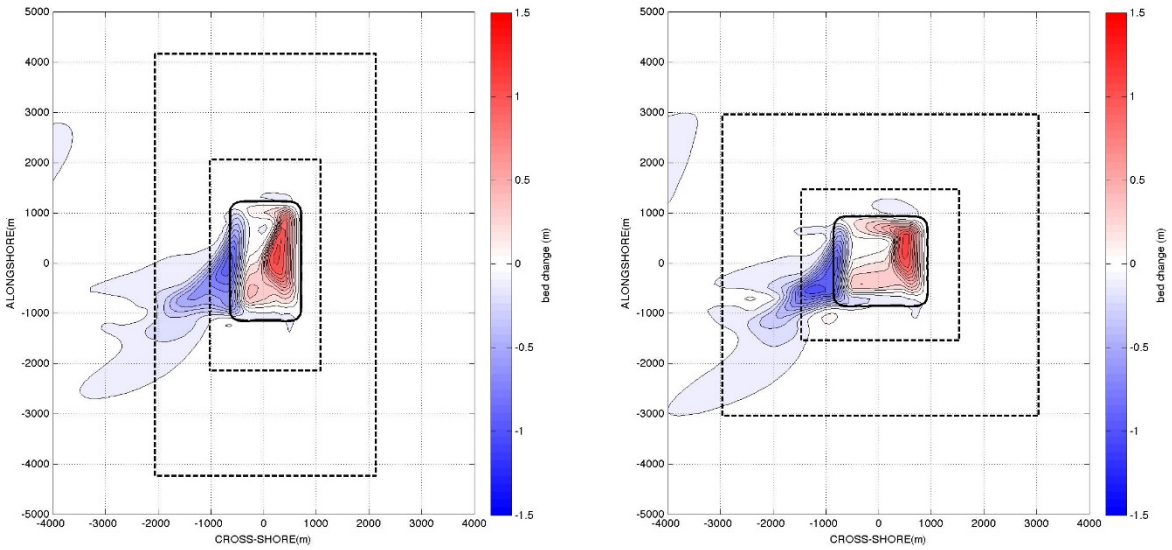

Figure VII-27. Areas *2X* and *4X* for the rectangular (left) and for the square pit (right).

Table VII-5. Eroded and deposited volumes inside the *2X* area 12 months after dredging of the borrow area for all the cases considered for borrow area aspect ratio.

Case		**Borrow Area Aspect Ratio**	**Eroded volume (m^3)**	**Deposited volume (m^3)**	**Net volume (m^3)**	**Average Elevation Change (mm)**
Crest	A1	0.5	5.24×10^5	8.57×10^5	3.33×10^5	35.8
	A2	1.0	6.36×10^5	8.4×10^5	2.04×10^5	21.6
Flank	B1	0.5	1.96×10^5	2.64×10^5	0.68×10^5	7.3
	D1	1.0	1.81×10^5	2.16×10^5	0.35×10^5	3.6
Trough	B2	0.5	0.3×10^5	0.08×10^5	-0.22×10^5	-2.3
	D2	1.0	0.16×10^5	0.06×10^5	-0.1×10^5	-1.0

Table VII-6. Eroded and deposited volumes inside the *4X* area 12 months after dredging of the borrow area for all the cases considered for borrow area aspect ratio.						
Case		**Borrow Area Aspect Ratio**	**Eroded volume (m^3)**	**Deposited volume (m^3)**	**Net volume (m^3)**	**Average Elevation Change (mm)**
Crest	A1	0.5	8.68×10^5	8.63×10^5	-0.05×10^5	-0.1
	A2	1.0	9.6×10^5	8.65×10^5	-0.95×10^5	-2.6
Flank	B1	0.5	2.94×10^5	3.13×10^5	0.19×10^5	0.5
	D1	1.0	2.45×10^5	2.68×10^5	0.23×10^5	0.6
Trough	B2	0.5	0.65×10^5	0.37×10^5	-0.28×10^5	-0.8
	D2	1.0	0.61×10^5	0.4×10^5	-0.21×10^5	-0.6

Figures VII-28 through VII-33 show the effect of pit aspect ratio on deposition, erosion, and net volumetric change inside the *2X* and *4X* areas, respectively, 12 months after dredging the pit. The largest influence of the pit aspect ratio was observed when the pit is located on the ridge crest, particularly with respect to erosion. If the pit is located either on the ridge flank or trough, eroded volumes decrease in the *2X* and *4X* areas. Little effect is observed for deposited volumes and based on the different shape of the *2X* and *4X* areas, the changes in deposition rates could be considered negligible..

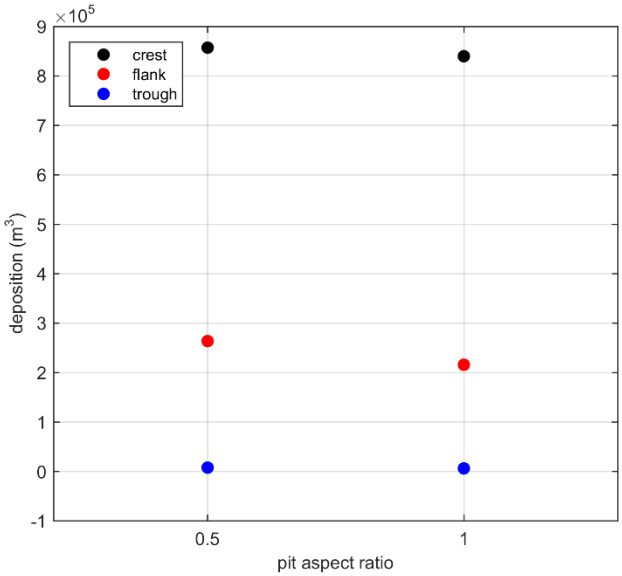

Figure VII-28. Deposition inside the *2X* area 12 months after dredging of the pit with respect to pit aspect ratio.

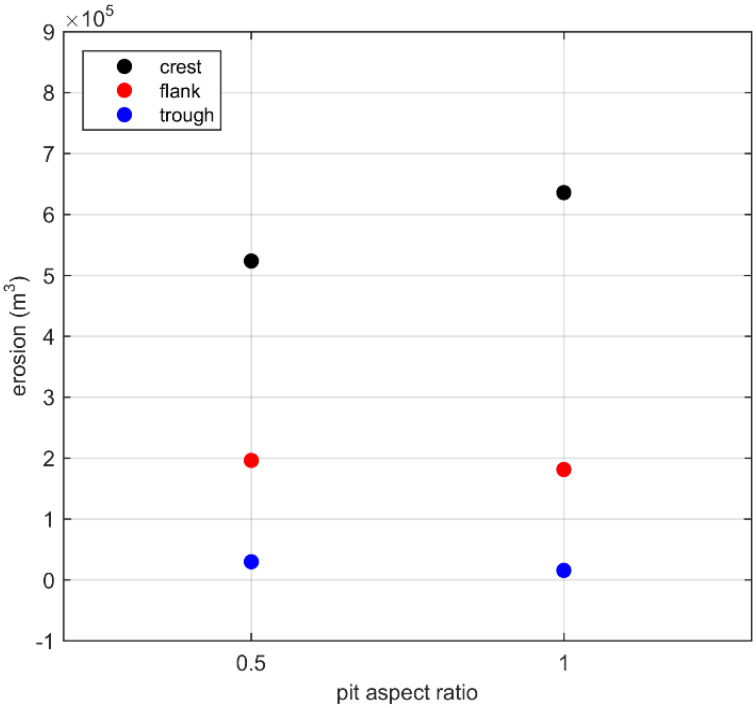

Figure VII-29. Erosion inside the *2X* area 12 months after dredging of the pit with respect to pit aspect ratio.

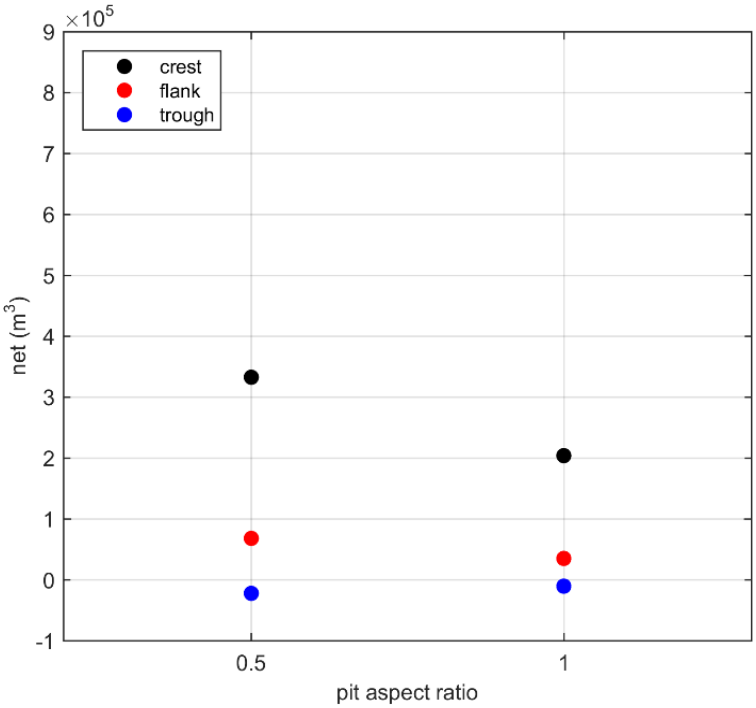

Figure VII-30. Net volumetric change inside the *2X* area 12 months after dredging of the pit with respect to pit aspect ratio.

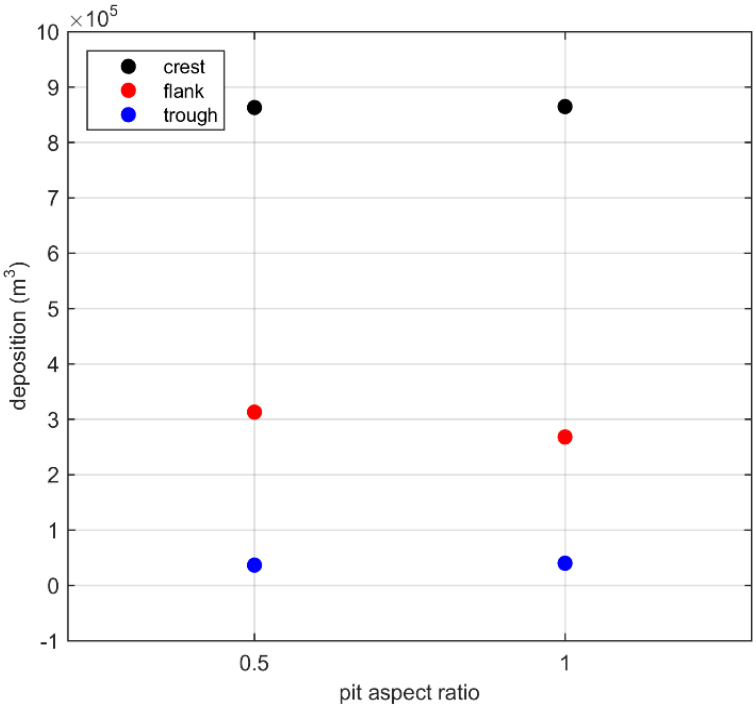

Figure VII-31. Deposition inside the *4X* area 12 months after dredging of the pit with respect to pit aspect ratio.

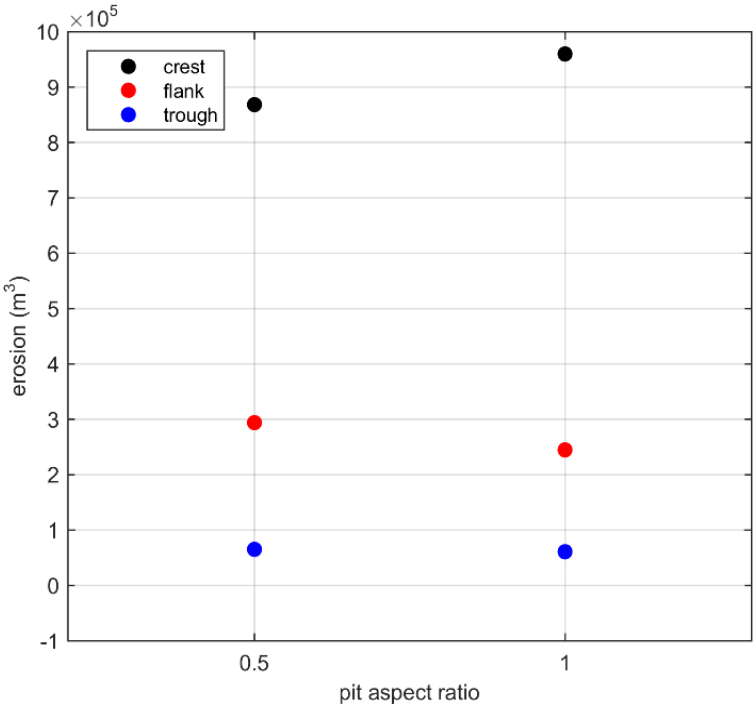

Figure VII-32. Erosion inside the *4X* area 12 months after dredging of the pit with respect to pit aspect ratio.

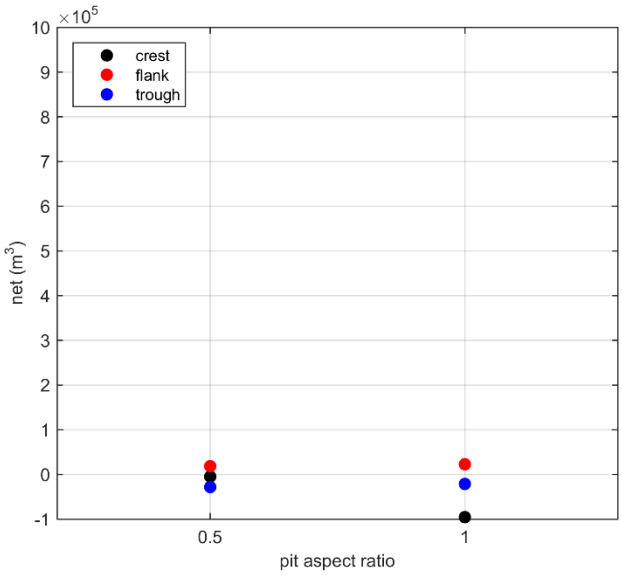

Figure VII-33. Net volumetric change inside the *4X* area 12 months after dredging of the pit with respect to pit aspect ratio.

Figure VII-34 shows the migration of the pit centroid in the cross-shore (x) and longshore (y) directions with respect to the pit aspect ratio. Where the pit centroid was located on the ridge flank, the displacement of the pit centroid decreased as the pit aspect ratio was increased from 0.5 to 1. When the pit centroid was located either on the ridge crest or trough, the displacement of the pit centroid increased as the pit aspect ratio of the pit was increased. In the case of the borrow pit located on the ridge crest, this increase in displacement correlates to a migration of the pit centroid in the direction of wave propagation.

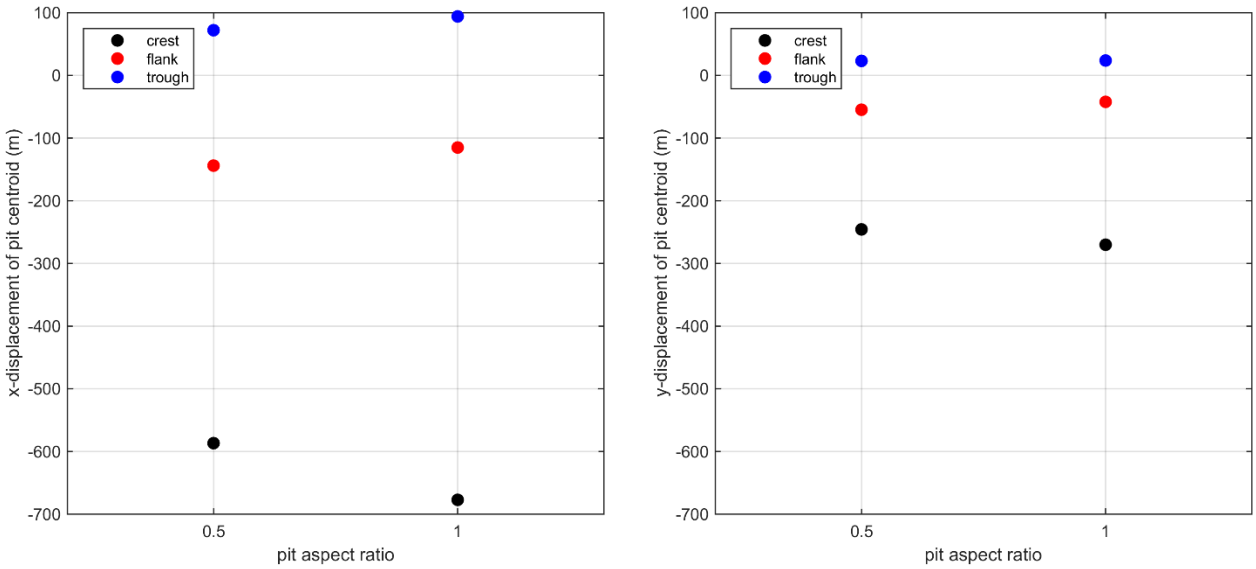

Figure VII-34. Displacement of pit centroid in the cross-shore (x) direction (left) and in the longshore (y) direction (right) with respect to pit aspect ratio.

VII.D. PIT CENTROID POSITION SCENARIO

In order to assess the effect of the pit centroid position, two series of scenarios are used. The first series includes Cases A1, B1, and B2, which considers a rectangular pit (pit aspect ratio of 0.5) located on the ridge crest, flank, and trough, respectively. The second series, includes Cases A2, D1 and D2, which consider a square pit (pit aspect ratio of 1.0) also located on the ridge crest, flank, and trough, respectively. Schematics of the considered cases are shown in Figure VII-35 and VII-36.

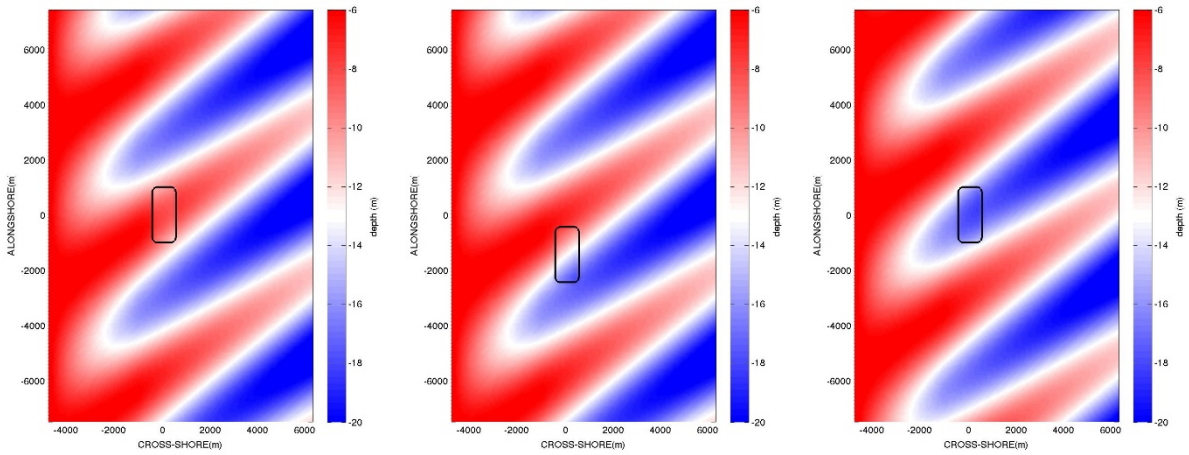

Figure VII-35. Initial bathymetry for Case A1 (left), B1 (middle), and B2 (right). These cases were developed to investigate the effect of pit centroid position on 0.5 aspect ratio pits.

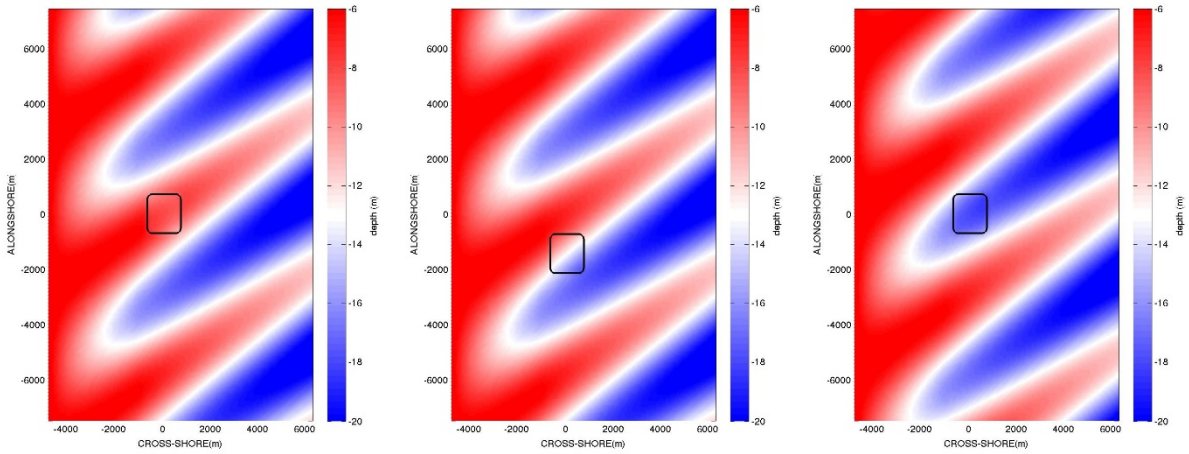

Figure VII-36. Initial bathymetry for Case A2 (left), D1 (middle), and D2 (right). These cases were developed to investigate the effect of pit centroid position on 1.0 aspect ratio pits.

Figure VII-37 shows the areas of relative variation of wave height caused by the rectangular pit (pit aspect ratio of 0.5) located on the ridge crest, flank, and trough. Variations of wave height were reduced as the pit centroid was moved to deeper depths (from ridge crest to trough).

As previously noted, this was due to the decrease in influence of the bottom geometry on wave dynamics as the water depth increases. Figure VII-38 shows the areas of relative variation of wave height caused by the square pit (pit aspect ratio of 1.0). A qualitative dependence on pit centroid position similar to that of the rectangular pit was observed.

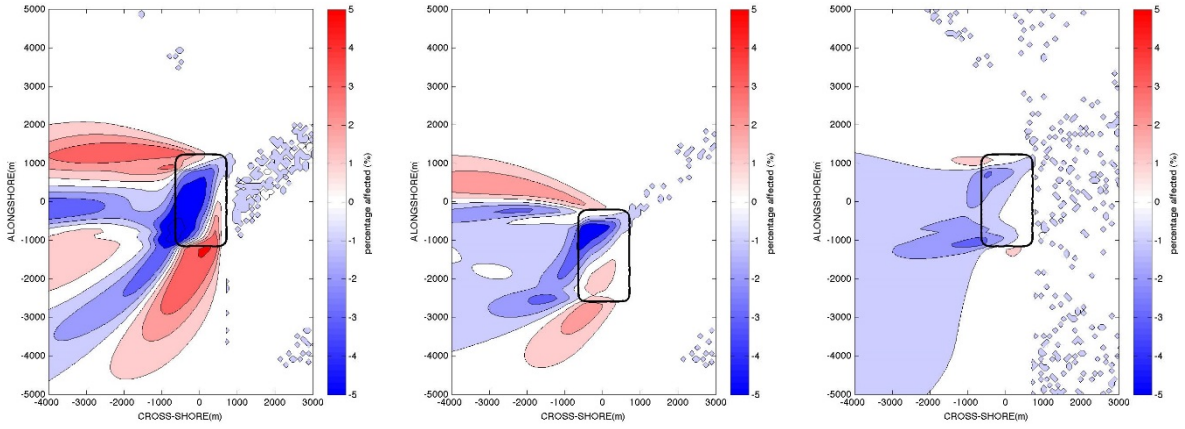

Figure VII-37. The relative variation of wave height during the maximum wave height (02/05 21:00, 2010) in the region around the pit. The pit centroid is located on the ridge crest (Case A1, left), flank (Case B1, middle), and trough (Case B2, right). The pit aspect ratio was 0.5 for all cases.

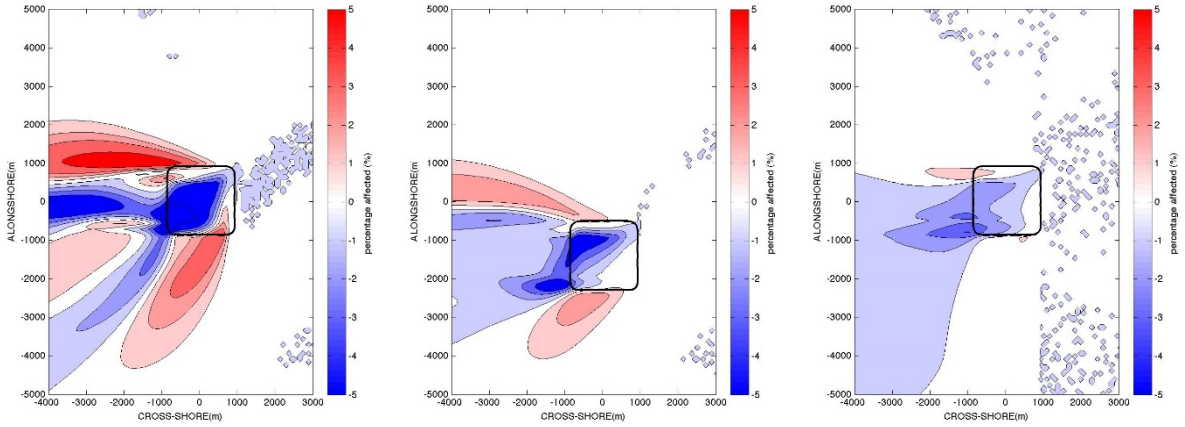

Figure VII-38. The relative variation of wave height during the maximum wave height (02/05 21:00, 2010) in the region around the pit. The pit centroid is located on the ridge crest (Case A2, left), flank (Case D1, middle), and trough (Case D2, right). The pit aspect ratio was 1.0 for all cases.

Figure VII-39 evaluates the effect of pit centroid position on the 1%, 2%, 3%, and 5% wave height influence areas. The 5% influence area vanished when the pit centroid was located on the ridge flank and trough, while the 3% influence area vanished for a rectangular pit located on the ridge trough only. As the pit centroid position was moved from the ridge trough to the crest, the local water depth decreased and the influence areas increased for both the rectangular and the

square pits. Again, this strong link between water depth and magnitude of sediment movement is indicative of the wave-dominant sediment transport associated with the modeled scenarios. It should be noted that the influence of water depth on both accretion and deposition was of similar magnitude.

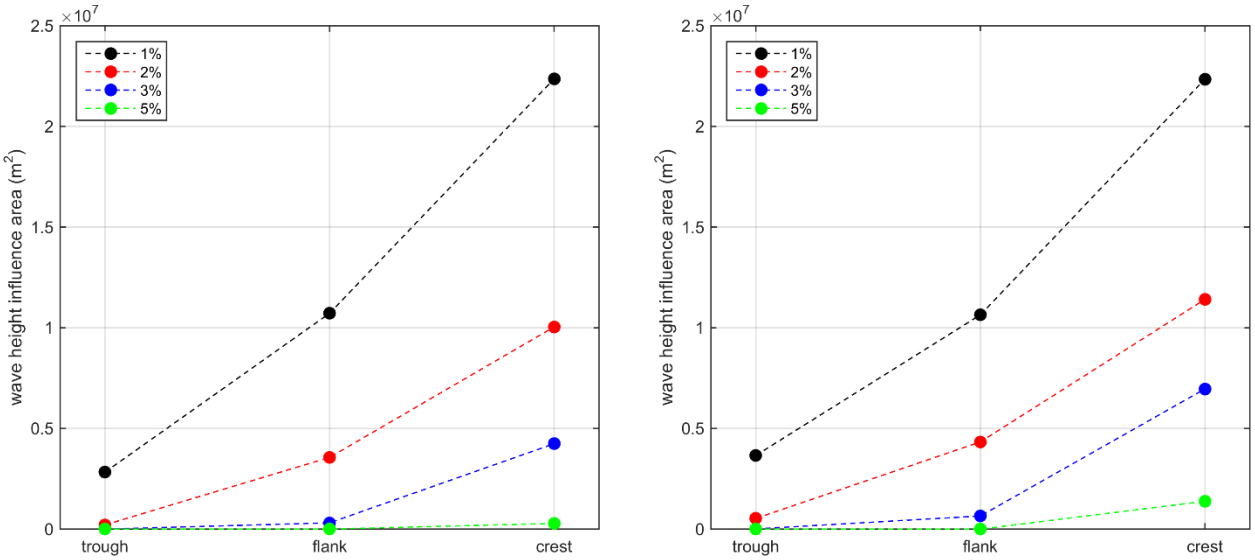

Figure VII-39. Influence area (m^2) of wave height versus pit centroid position. The pit aspect ratios are 0.5 (left) and 1.0 (right).

In order to quantify the rate of increase of the influence areas as the pit centroid position varied, the parameters $\Delta^{hs}_{X\%,FT}$ and $\Delta^{hs}_{X\%,CF}$ were introduced. Equation 1, below, define $\Delta^{hs}_{5\%,FT}$ and $\Delta^{hs}_{5\%,CF}$ and hold for similar relationships for the 3%, 2%, and 1% influence areas. In Equation 1, $IA5\%^{hs}_{trough}$ ($IA5\%^{hs}_{flank}$, $IA5\%^{hs}_{crest}$) indicates the 5% wave height influence area for a pit centroid located on the ridge trough (flank, crest).

$$\Delta^{h_s}_{5\%,FT} = \frac{IA5\%^{hs}_{flank} - IA5\%^{hs}_{trough}}{0.5\left(IA5\%^{hs}_{flank} + IA5\%^{hs}_{trough}\right)}$$
$$\Delta^{h_s}_{5\%,CF} = \frac{IA5\%^{hs}_{crest} - IA5\%^{hs}_{flank}}{0.5\left(IA5\%^{hs}_{crest} + IA5\%^{hs}_{flank}\right)} \qquad (1)$$

For a rectangular pit, the largest values of $\Delta^{hs}_{2\%}$ and $\Delta^{hs}_{1\%}$ were obtained comparing the pits with centroids located on the ridge flank and trough ($\Delta^{hs}_{2\%,FT} = 1.77$ and $\Delta^{hs}_{1\%,FT} = 1.16$). Similarly, if a square pit is considered, the largest values of $\Delta^{hs}_{3\%}$, $\Delta^{hs}_{2\%}$, and $\Delta^{hs}_{1\%}$ were obtained comparing pits with centroids located on the ridge flank and trough as well ($\Delta^{hs}_{3\%,FT} = 1.93$, $\Delta^{hs}_{2\%,FT} = 1.56$, and $\Delta^{hs}_{1\%,FT} = 0.98$).

Figures VII-40 and VII-41 show the effect of pit centroid position on the relative variation of the tidal current speed during the maximum tidal current (02/05 21:00, 2010). The area where an increase of the tidal current was observed decreased significantly as the pit location was moved

from the ridge crest to trough. Where the pit aspect is square, the area of tidal current variation increases inside the pit as the centroid of the pit was moved to smaller depths.

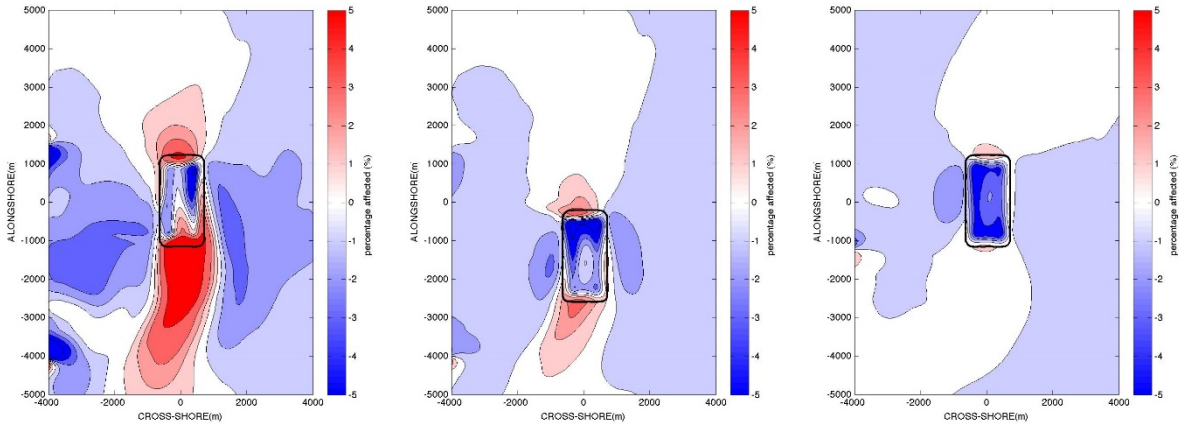

Figure VII-40. The relative variation of tidal current in the region around the pit during the maximum tidal current (02/05 21:00, 2010). The pit centroid is located on the ridge crest (Case A1, left), flank (Case B1, middle), and trough (Case B2, right). The pit aspect ratio for all cases was 0.5.

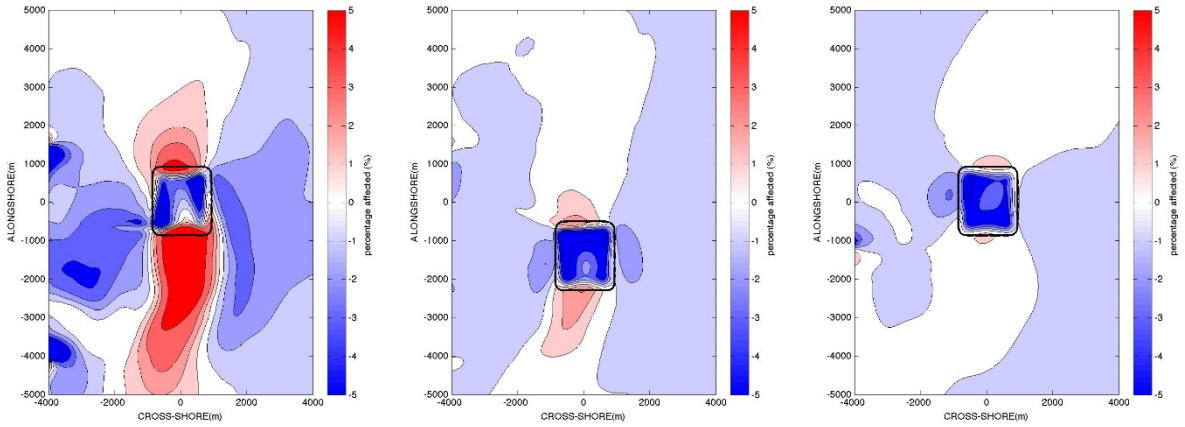

Figure VII-41. The relative variation of tidal current in the region around the pit during the maximum tidal current (02/05 21:00, 2010). The pit centroid is located on the ridge crest (Case A2, left), flank (Case D1, middle), and trough (Case D2, right). The pit aspect ratio for all cases was 1.0.

Figure VII-42 presents a quantitative evaluation of the effect of pit centroid position on the tidal current influence area. For both the rectangular and the square pits, the influence area increased as the pit moved to smaller depths (i.e. from the ridge trough to crest). The parameters $\Delta^{curr}{}_{1\%,FT}$, $\Delta^{curr}{}_{3\%,FT}$, $\Delta^{curr}{}_{5\%,FT}$, $\Delta^{curr}{}_{1\%,CF}$, $\Delta^{curr}{}_{3\%,CF}$, and $\Delta^{curr}{}_{5\%,CF}$ are defined similarly to the corresponding parameters for the wave height influence area. For the square and the rectangular pits, the $\Delta^{curr}{}_{,FT}$ parameter is smaller than the corresponding $\Delta^{curr}{}_{,CF}$, indicating that the larger

influence on the tidal current is encountered when the pit centroid is moved from the ridge flank to the crest.

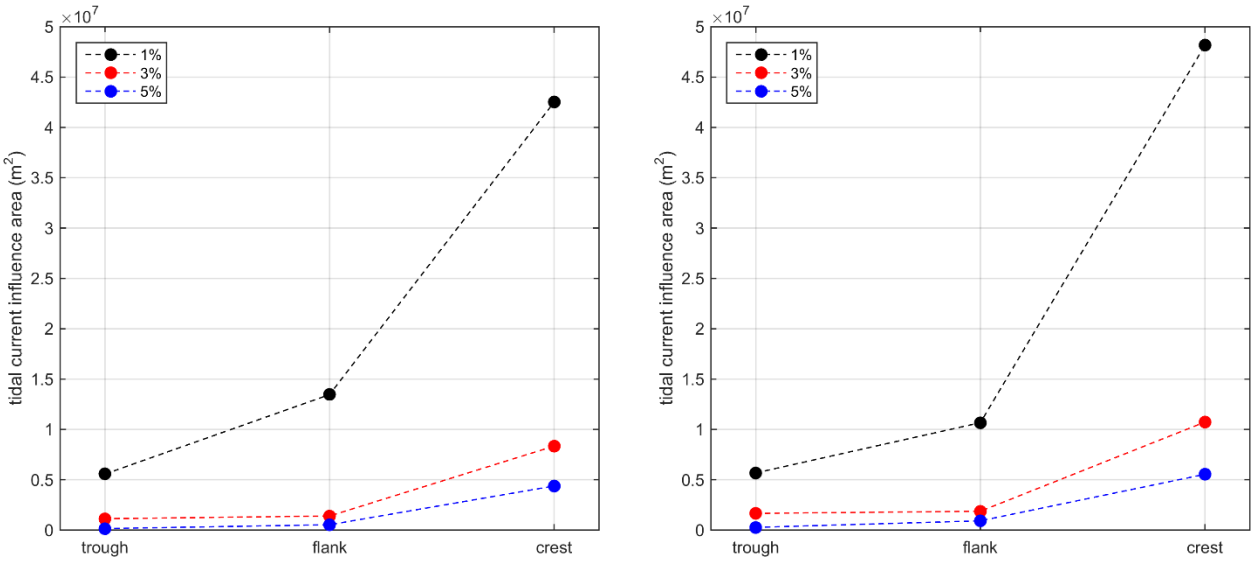

Figure VII-42. Influence area (m^2) of tidal current with respect to pit centroid position. The pit aspect ratios are 0.5 (left) and 1.0 (right).

Figures VII-43 and VII-44 show the influence of the pit centroid on the depth changes in the rectangular and square borrow areas 12 months after dredging, respectively. For both pit aspect ratios, the negative (depositional areas) and positive (erosional areas) depth changes are generally confined in the areas with shallower depths. This trend appeared for the cases where the pit centroid was located on the ridge flank, where the larger depth changes took place on the north side of the pit, which is closer to the ridge crest.

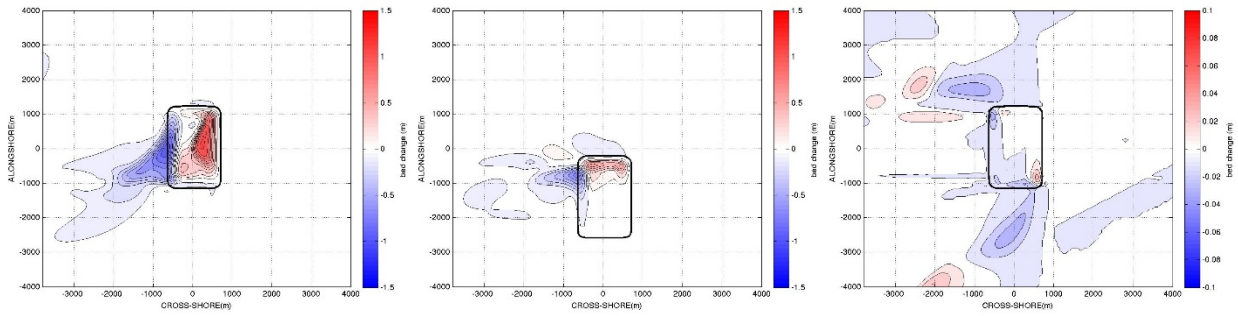

Figure VII-43. Depth change in Case A1 (pit centroid on ridge crest, left), B1 (pit centroid on ridge flank, middle), and B2 (pit centroid on ridge trough, right) 12 months after dredging of the pit. The pit aspect ratio for all cases was 0.5.

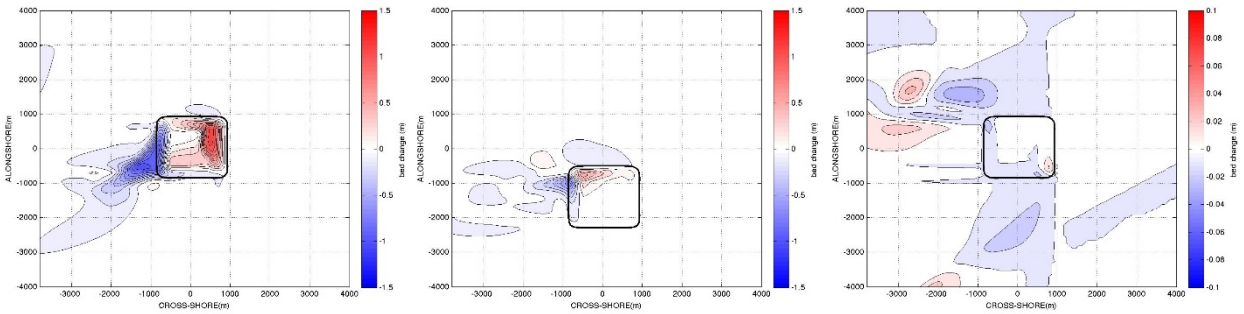

Figure VII-44. Depth change in Case A2 (pit centroid on ridge crest, left), D1 (pit centroid on ridge flank, middle), and D2 (pit centroid on ridge trough, right) 12 months after dredging of the pit. The pit aspect ratio for all cases was 1.0.

Comparing the volumes deposited inside the pit area in Table VII-7 and those in the entire computational domain in Table VII-8, deposition is dominant inside the pit area when the pit centroid was located on the ridge crest. In these model simulations where the pit centroid was located on the ridge crest, the deposition in the pit was 90% and 84% of the total deposition for a pit aspect ratio of 0.5 (Case A1) and 1.0 (Case A2), respectively. For the test cases where the borrow pit was located either on the ridge crest or flank (i.e. where water depths allowed consistent mobilization of sediment by wave action), deposition within the pit was dominated by migration of material from the offshore portion of the ridge migrating in a landward direction.

Table VII-8 shows that erosion in the entire computational domain exceeded deposition when the pit was located on the ridge crest and flank for both the rectangular and the square pits. This indicated that in test cases where the pit centroid was located either on the ridge crest and flank, a sediment flux out of the computational domain existed; however, the total net flux is relatively small relative to the scale of the model domain. From Figures VII-43 and VII-44, excavation of the borrow pit on either the ridge crest or ridge flank reduces the volume of material available to supply the ridge in the direction of wave propagation, resulting in an area of erosion extending to the west and southwest of the borrow pit.

For the two cases where the pit centroid was located within the trough (Case B2 and Case D2), Table VII-7 indicates either a slight erosion or no net change within the borrow pit. For the entire computational domain (summarized in Table VII-8), the net sediment flux is positive (depositional), with a maximum value of 0.27×10^5 m^3 for Case D2. This total volume of change represents less than 0.2 mm of bathymetric change averaged over the model domain over the one-year simulation. Due to the negligible scale of change, it has been determined that sediment flux associated with excavation of the borrow pit within the trough is inconsequential in relation to the natural processes governing (and inherent change) the cases where the borrow pit centroid was either located on the ridge crest or flank.

Table VII-7. Erosion and deposition inside the pit area 12 months after dredging for all the cases considered for the effect of pit centroid position.						
Case		**Pit Centroid Position**	**Eroded volume (m^3)**	**Deposited volume (m^3)**	**Net volume (m^3)**	**Average Elevation Change (mm)**
Pit Aspect Ratio 0.5	A1	Crest	2.52×10^5	8.31×10^5	5.79×10^5	175.4
	B1	Flank	0.78×10^5	2.47×10^5	1.69×10^5	49.7
	B2	Trough	0.08×10^5	0.07×10^5	-0.01×10^5	-0.1
Pit Aspect Ratio 1.0	A2	Crest	2.09×10^5	7.93×10^5	5.84×10^5	188.1
	D1	Flank	0.54×10^5	1.82×10^5	1.28×10^5	39.9
	D2	Trough	0.04×10^5	0.04×10^5	0	0.1

Table VII-8. Erosion and deposition inside the entire computational domain 12 months after dredging for all the cases considered for the effect of pit centroid position.						
Case		**Pit Centroid Position**	**Eroded volume (m^3)**	**Deposited volume (m^3)**	**Net volume (m^3)**	**Average Elevation Change (mm)**
Pit Aspect Ratio 0.5	A1	Crest	10.25×10^5	9.27×10^5	-0.98×10^5	-0.6
	B1	Flank	3.61×10^5	3.41×10^5	-0.2×10^5	-0.1
	B2	Trough	0.79×10^5	0.97×10^5	0.18×10^5	0.1
Pit Aspect Ratio 1.0	A2	Crest	10.70×10^5	9.47×10^5	-1.23×10^5	-0.8
	D1	Flank	3.02×10^5	2.83×10^5	-0.19×10^5	-0.1
	D2	Trough	0.75×10^5	1.02×10^5	0.27×10^5	0.2

Figures VII-45 through VII-47 show deposition, erosion, and net volumetric change inside the pit area 12 months after dredging of the pit, respectively. The volumetric change increased as the position of the pit changed from the ridge trough to crest, where the volumetric change associated with the pit centroid located within the trough was negligible relative to the other cases.

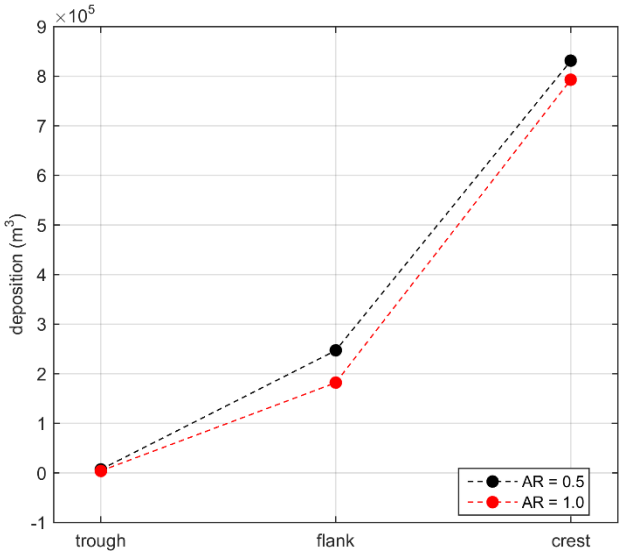

Figure VII-45. Deposition inside the pit area 12 months after dredging of the pit with respect to pit centroid position.

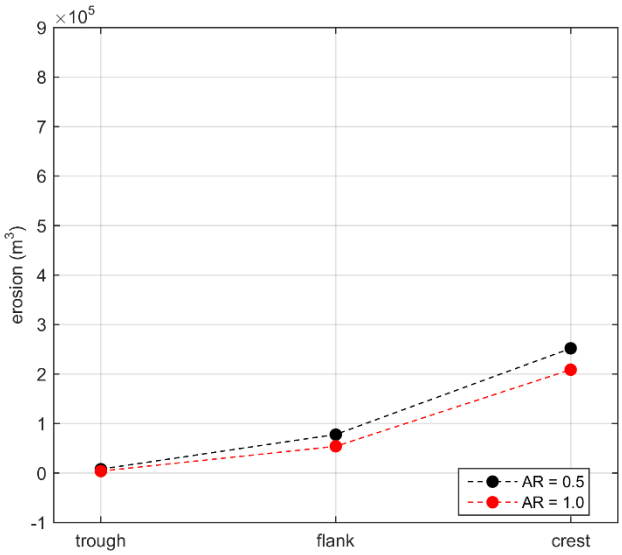

Figure VII-46. Erosion inside the pit area 12 months after dredging of the pit with respect to pit centroid position.

Figures VII-47 through VII-53 compare deposition, erosion, and net volumetric change inside the *2X* and *4X* areas, respectively, 12 months after the dredging. The dependence of the deposition and erosion volumetric change on pit centroid position was similar to that of the net volumetric change inside the pit area on pit centroid position. The dependence of the net volumes in the *4X* area on pit centroid position did not show any distinct trend, indicating generally that the influence of the borrow area on the surrounding seafloor is likely confined to an area within approximately 4X of the dredged borrow area. When the pit centroid was located on the ridge crest, the maximum erosion occurred between the *4X* and *2X* area for the rectangular pit (34% of the total eroded volumes) and between the *2X* and the pit area for the square pit (42% of the total eroded volume). The maximum erosion occurred between the *2X* and pit area; the

volume was equal to 33% and 42% of the total erosion for the rectangular and square pit, respectively, when the pit centroid was located on the ridge flank. When the pit centroid was located on the ridge trough, the maximum erosion was small relative to the test cases where the pit was located on either the ridge crest or ridge flank. For the ridge trough cases, the erosion measured between the *4X* and *2X* areas is equal to 45% and 61% of the total erosion for the rectangular and square pit, respectively.

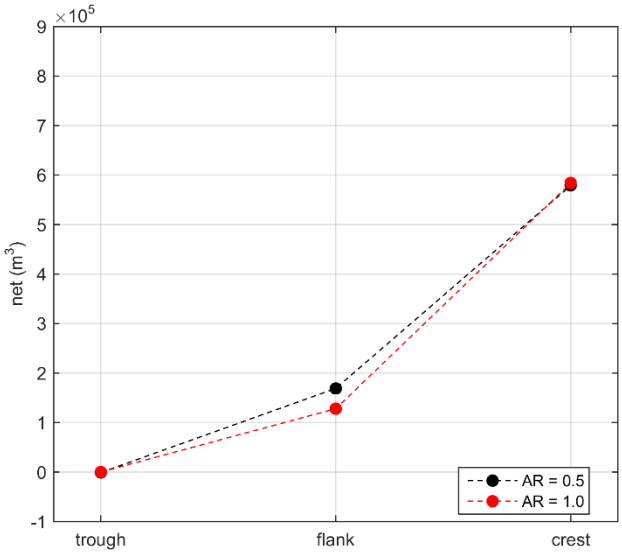

Figure VII-47. Net volumetric change (deposition minus erosion) inside the pit area 12 months after dredging of the pit with respect to pit centroid position.

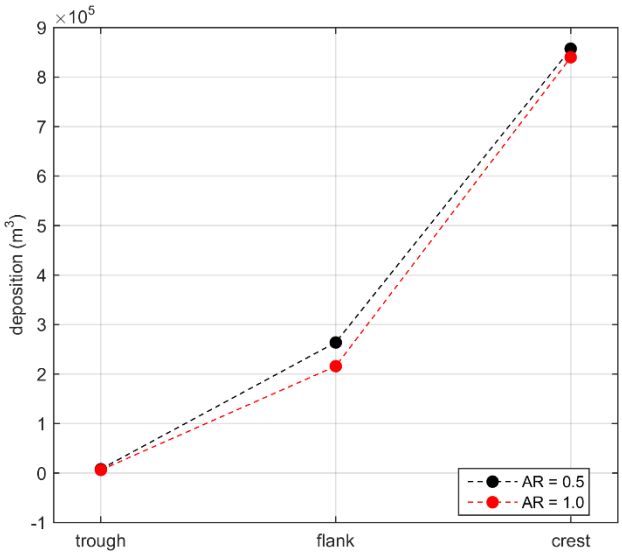

Figure VII-48. Deposition inside the *2X* area 12 months after dredging of the pit with respect to pit centroid position.

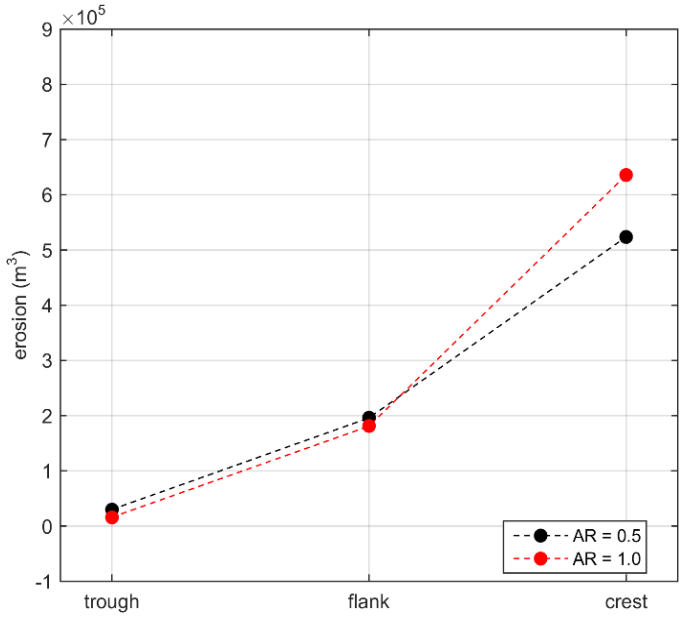

Figure VII-49. Erosion inside the *2X* area 12 months after dredging of the pit with respect to pit centroid position.

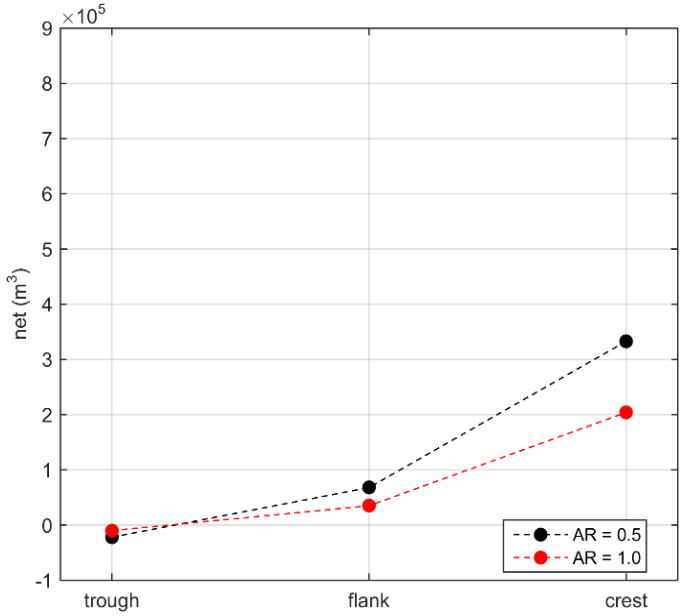

Figure VII-50. Net volumetric change (deposition minus erosion) inside the *2X* area 12 months after dredging of the pit with respect to pit centroid position.

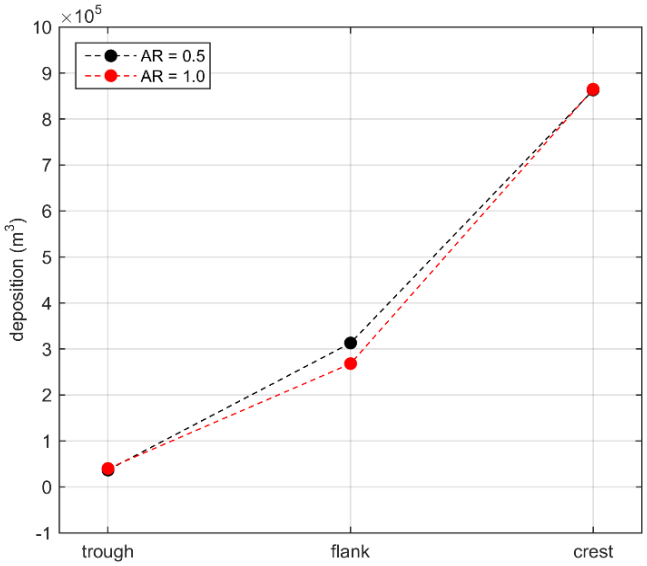

Figure VII-51. Deposition inside the *4X* area 12 months after dredging of the pit with respect to pit centroid position.

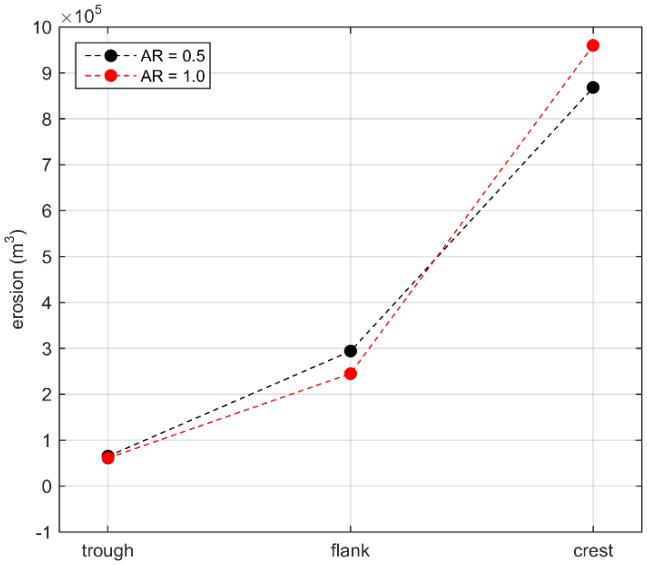

Figure VII-52. Erosion inside the *4X* area 12 months after dredging of the pit with respect to pit centroid position.

Figure VII-54 shows the migration of the pit centroid in the cross-shore (x) and longshore (y) direction with respect to the initial pit centroid position. The pit centroids of both the rectangular and the square pits migrate onshore and towards the south when the initial pit centroid was located on the ridge crest and flank, where onshore migration likely is primarily due to the influence of wave-induced transport caused by wave asymmetry and the slight southerly migration is due to the influence of south-directed ambient tidal currents utilized for all scenarios. When the initial pit centroid was located on the ridge trough, a slight migration in the offshore direction and towards the north was observed; however, this is likely due to the negligible sediment transport rates spread across the model domain and this result may not

accurately represent the physical processes governing pit migration for this case. As the initial pit centroid position varied from the ridge trough to crest, the displacement of the centroid increased.

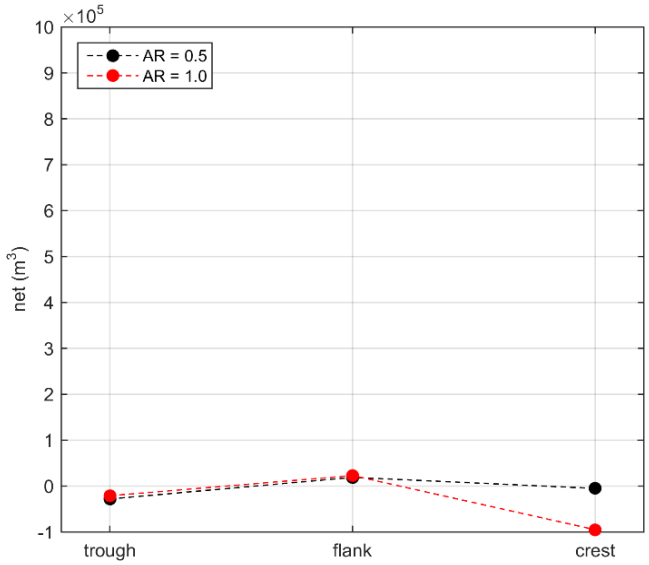

Figure VII-53. Net volumetric change (deposition minus erosion) inside the *4X* area 12 months after dredging of the pit with respect to pit centroid position.

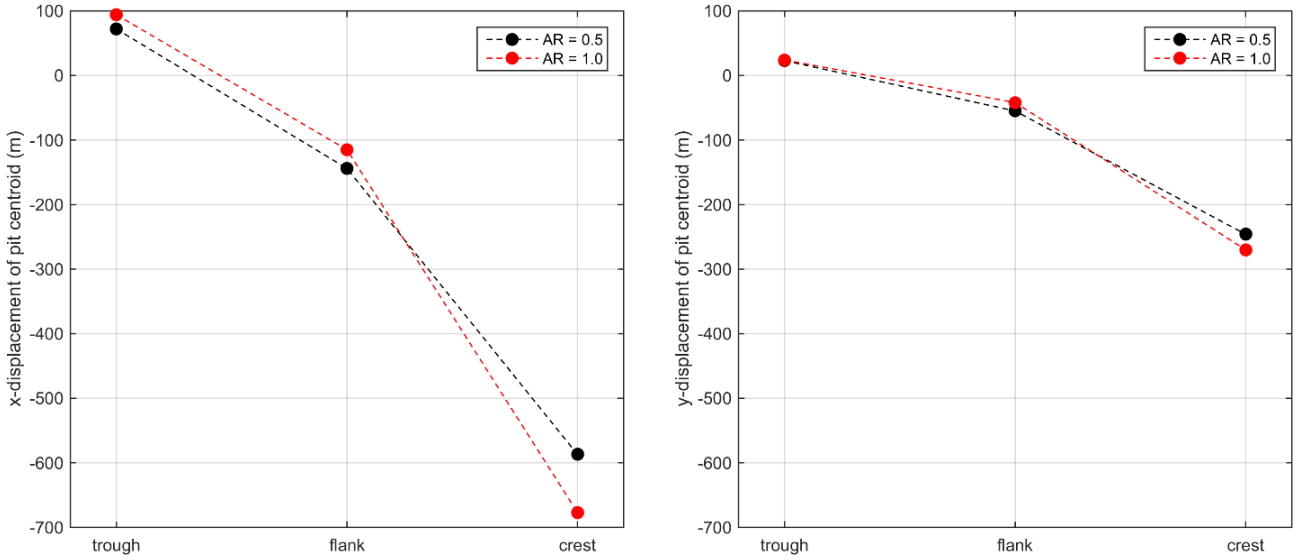

Figure VII-54. Displacement of pit centroid in the cross-shore (*x*) direction (left) and in the longshore (*y*) direction (right) with respect to initial pit centroid position.

VII.E. PIT ORIENTATION SCENARIO

To evaluate the effect of the pit orientation relative to the ridge crest, the Cases A1 and C1 were considered. Schematics of the cases considered are shown in Figure VII-55. Figure VII-56 shows the areas of relative wave height variation due to the rectangular pit with the major axis parallel to the coastline and with the major axis aligned with the ridge crest, i.e. rotated by 60^{o} clockwise with respect to the coastline.

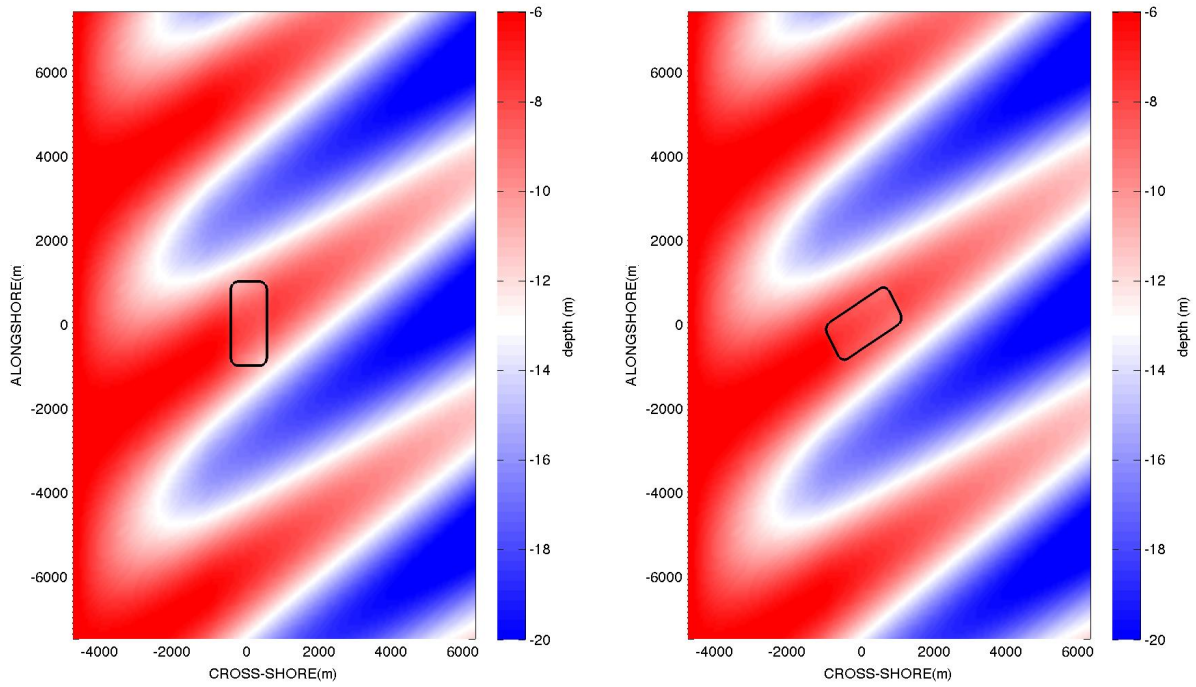

Figure VII-55. Initial bathymetry for Case A1 (left) and C1 (right). These cases were developed to investigate the effect of pit orientation.

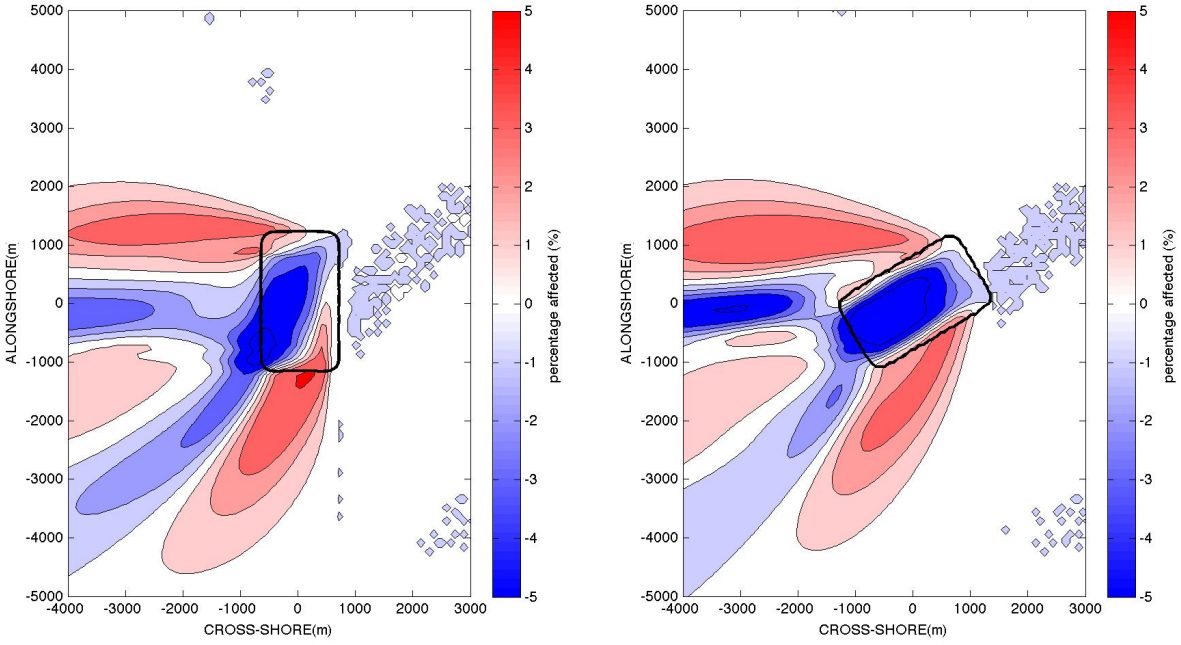

Figure VII-56. The relative variation of wave height during the maximum wave height (02/05 21:00, 2010) in the region around the pit. The major axis of the pit was parallel to the coastline (Case A1, left) and the major axis of the pit was aligned with the ridge crest (Case C1, right). The pit aspect ratio for both cases was 0.5.

The areas of significant wave height influence with respect to the pit orientation appear qualitatively similar. The quantitative evaluation of the effect of pit orientation on the influence areas (see Figure VII-57) showed that the 5%, 3%, and 2% influence areas increased when the pit was aligned with the ridge crest. The 1% wave height influence area is nearly equal for the baseline pit and for the rotated pit. Overall, it appears that the slight increase in wave height influence area for the pit oriented with the ridge crest (Case C1) is due to the greater length of the pit boundary facing the direction of wave propagation. This orientation allows greater focusing of wave energy, as observed in the increased wave heights northwest of the borrow pit, as well as the corresponding decrease in wave heights west of the pit, illustrated on the right plot in Figure VII-56.

Figures VII-58 and VII-59 show the effect of pit orientation on the relative variation of the tidal current speed during the maximum tidal current (02/05 21:00, 2010). Both the shape and the extents of the influence areas were affected by the pit orientation. Where the pit was rotated to align with the ridge crest, a larger area of reduced tidal current was observed within the pit area. Outside the pit area, a larger area of increased tidal current was also observed for the rotated pit. As expected, these results indicate that removal of the highest part of the ridge crest would have the most significant impact on the overall tidal current regime, due to in the stronger influence of the bottom geometry in shallower water.

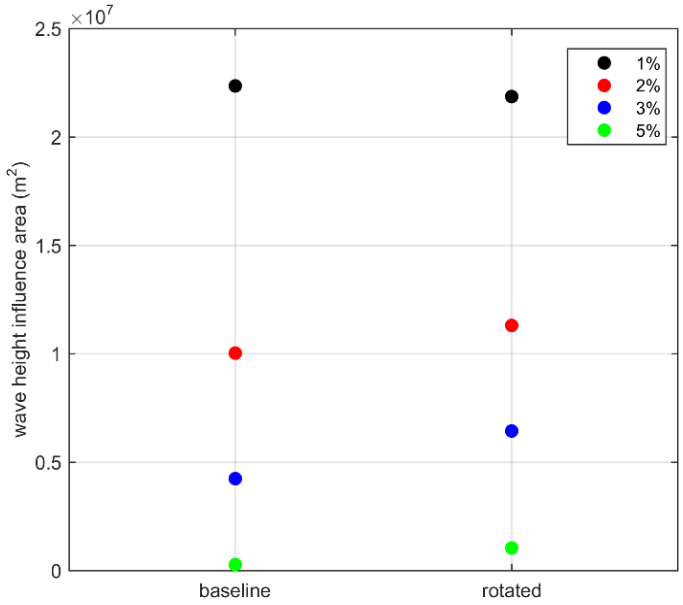

Figure VII-57. Influence area (m^2) of wave height with respect to pit orientation.

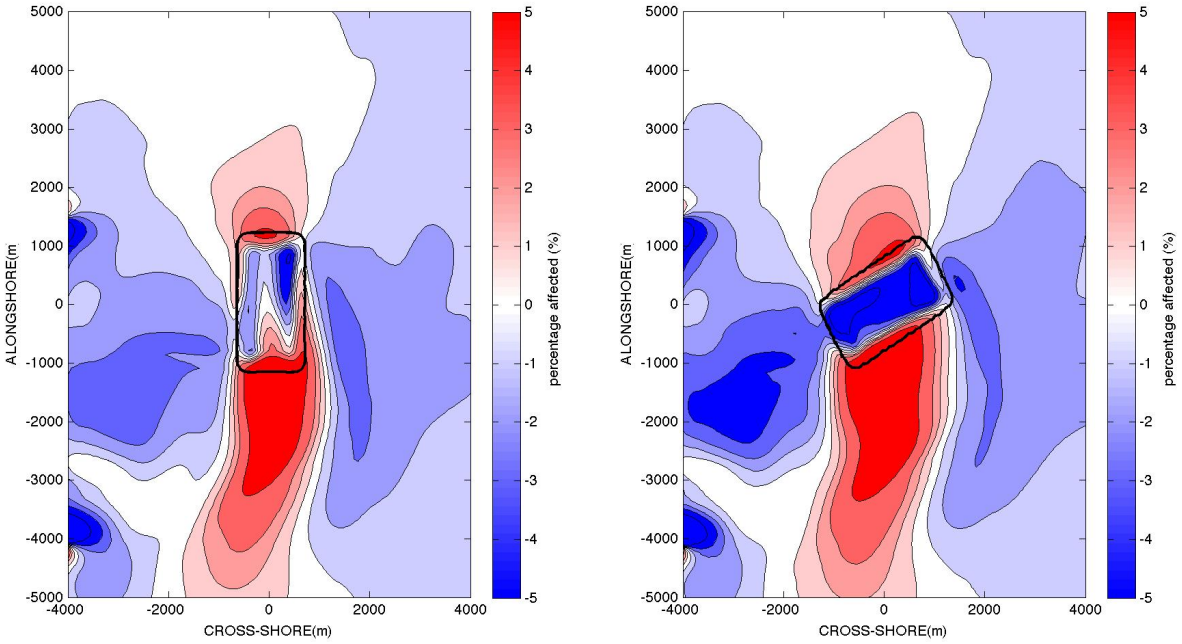

Figure VII-58. The relative variation of tidal current during the maximum tidal current (02/05 21:00, 2010) in the region around the pit. The major axis of the pit was parallel to the coastline (Case A1, left) and the major axis of the pit was aligned with the ridge crest (Case C1, right). The pit aspect ratio for both cases was 0.5.

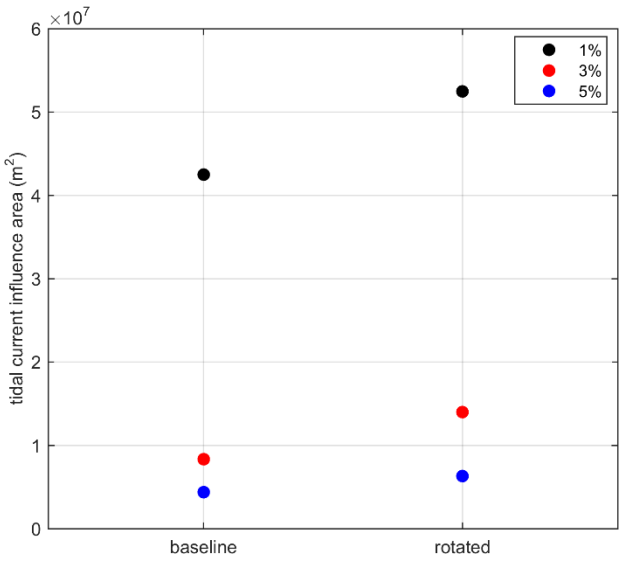

Figure VII-59. Influence area (m^2) of tidal current with respect to pit orientation.

Figure VII-60 shows the influence of pit orientation on the depth change 12 months after dredging. The rotated pit induced larger variations on the morphology inside the pit and in the near-field area. The depth change in the rotated pit corresponds to a larger displacement of the pit centroid towards the shore and in the along-shore direction towards the south. Table VII-9 shows that, with respect to the baseline case, the displacement of the pit centroid in the cross-shore (x) direction was increased by 178 m (shoreward), while the displacement in the longshore (y) direction was increased by 51 m (towards the south).

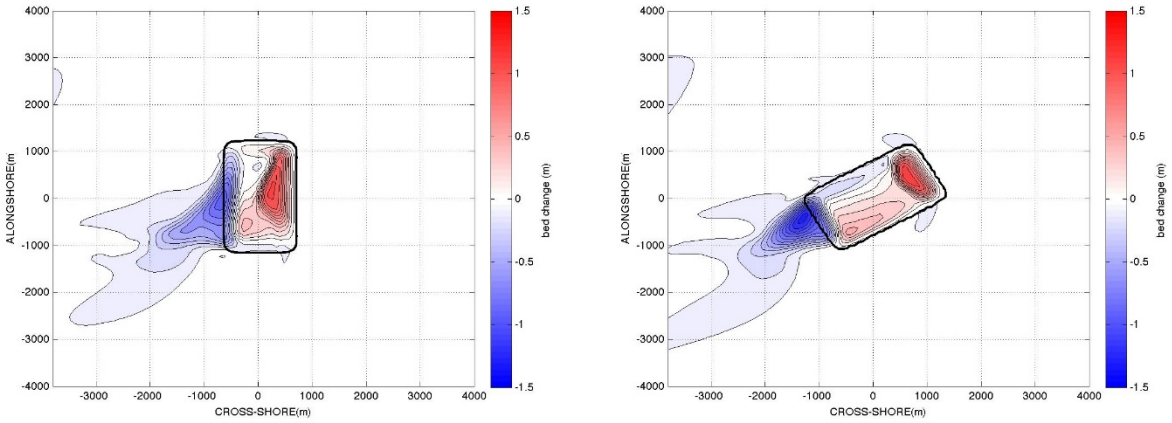

Figure VII-60. Depth change in Case A1 (major axis aligned with coastline, left) and Case C1 (major axis aligned with ridge crest, right) 12 months after the dredging of the pit. The pit aspect ratio for both cases was 0.5.

Table VII-9. Displacement in the cross-shore (*x*) and longshore (*y*) directions of the pit centroid for the cases considered for pit orientation.			
Case	**Orientation**	**Cross-shore displacement of pit centroid (m)**	**Long-shore displacement of pit centroid (m)**
A1	parallel with coastline	-587	-246
C1	aligned with ridge crest	-765	-297

Figures VII-61 through VII-63 and Table VII-10 show the deposition, erosion, and net volumetric change inside the pit, *2X* and *4X* areas 12 months after dredging. The rotation of the pit caused a decrease of deposition in all the cases considered, likely due to the smaller cross-sectional area of the pit orientated towards the dominant direction of the incoming wave field. With pit rotation, erosion decreased in the pit area but increases in the *2X* and *4X* areas. When the pit is rotated, Figure VII-63 show that the net volumetric change inside the pit area slightly increased while a slight decrease in the *2X* area was observed. The net volumetric change inside the *4X* area and the whole computational domain was negative and decreased with pit rotation (i.e. increased net erosion), as shown in Figure VII-63 and Table VII-11. Therefore, the rotation of the pit causes a larger flux of sediment along the length of the ridge crest and outside the model domain.

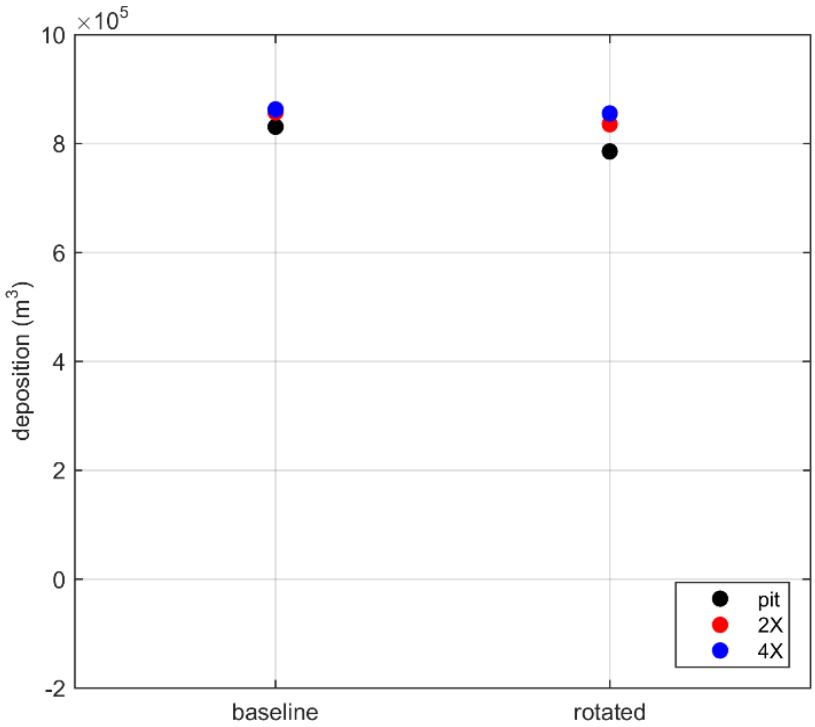

Figure VII-61. Deposition inside the pit area, *2X* area, and *4X* area after 12 months after dredging of the pit with respect to pit orientation.

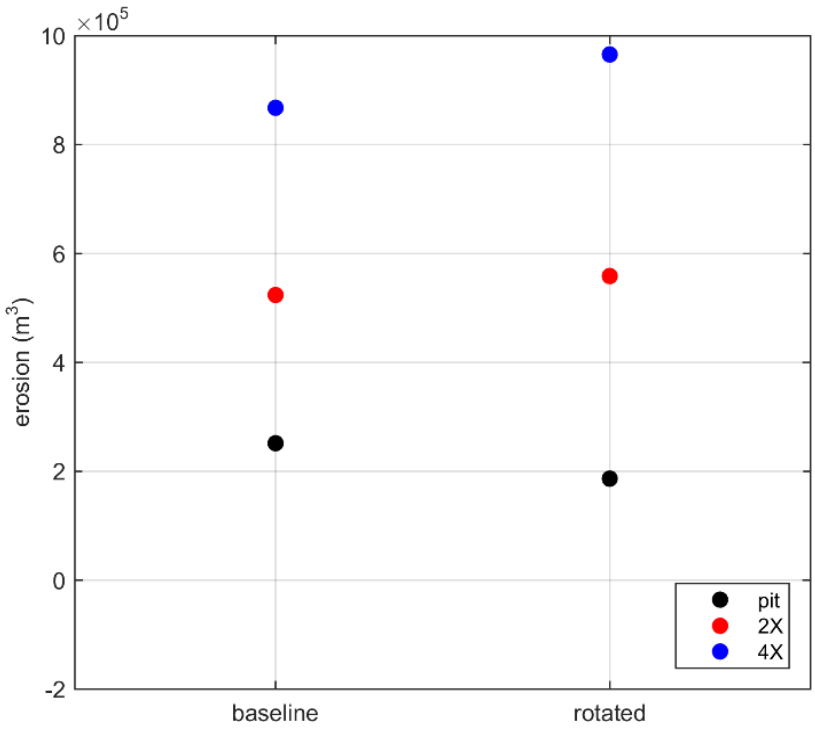

Figure VII-62. Erosion inside the pit area, *2X* area, and *4X* area after 12 months after dredging of the pit with respect to pit orientation.

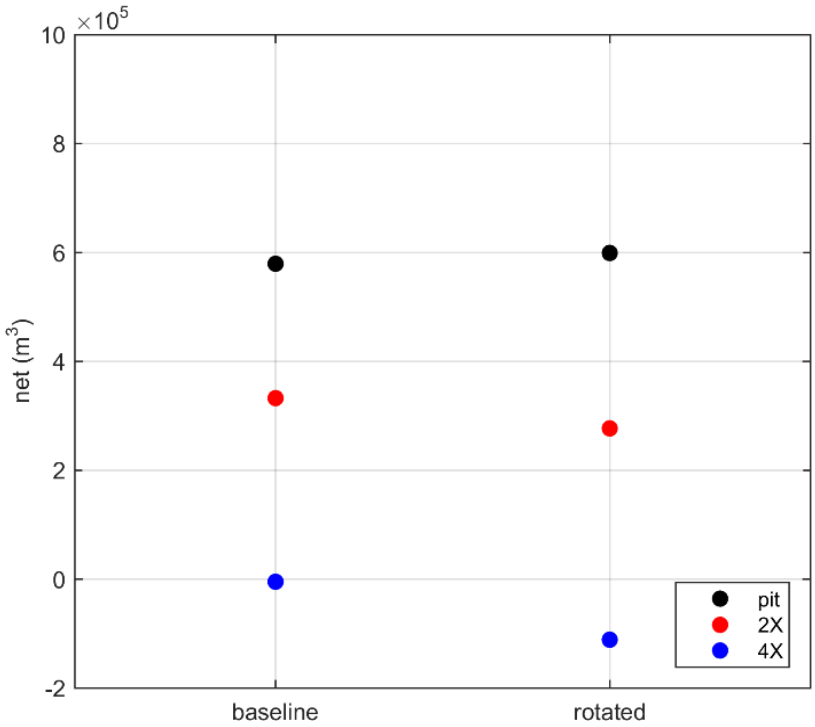

Figure VII-63. Net volumetric change (deposition minus erosion) inside the pit area, *2X* area, and *4X* area after 12 months after dredging of the pit with respect to pit orientation.

Table VII-10. Erosion and deposition inside the pit area 12 months after dredging of the pit for the cases considered for pit orientation.

Case	Pit Orientation	Eroded volume (m^3)	Deposited volume (m^3)	Net volume (m^3)	Average Elevation Change (mm)
A1	parallel with coastline	2.52×10^5	8.31×10^5	5.79×10^5	175.4
C1	aligned with ridge crest	1.87×10^5	7.86×10^5	5.99×10^5	170.4

Table VII-11. Erosion and deposition volumes inside the whole computational area 12 months after dredging of the pit for the cases considered for pit orientation.

Case	Pit Orientation	Eroded volume (m^3)	Deposited volume (m^3)	Net volume (m^3)	Average Elevation Change (mm)
A1	parallel with coastline	10.25×10^5	9.27×10^5	-0.98×10^5	-0.6
C1	aligned with ridge crest	10.81×10^5	9.45×10^5	-1.36×10^5	-0.9

VII.F. CONCLUDING REMARKS ON NEAR-FIELD RIDGED-BED INVESTIGATION

Seven model scenarios were run to investigate the influence of pit aspect ratio, pit centroid position, and pit orientation on the hydrodynamics and morphodynamics of the area inside the pit and in the near-field region. Similar to previous modeling scenarios, the borrow pit evaluated consisted of an excavation depth of 1 m and a total pit volume 2.0×10^6 m^3. Both rectangular and square pit geometries were evaluated. Scaling of the ridge field was based on typical ridge spacing found on the Atlantic Continental Shelf (e.g. Hayes and Nairn, 2004). To assess the influence of pit location within the ridge field, scenarios were evaluated with the pit centroid located at the ridge crest, flank, and within the trough. In addition, the scenarios also considered two different pit aspect ratios, as well as the influence of orienting the pit geometry with the orientation of the ridge field. For all cases, sediment transport at the pit is strongly wave dominated, where the influence of changes to the ambient tidal currents does not appear to influence morphological change. In general, the ambient tidal currents are of insufficient magnitude to either mobilize the bottom sediments or to keep them in suspension once mobilized by wave action.

The pit aspect ratio scenarios indicated that the square borrow area (i.e. a borrow area with an aspect ratio of 1.0) generally causes larger areas of variations in the hydrodynamics (wave height and tidal current) than a rectangular borrow area (aspect ratio of 0.5). Qualitatively, the depth change patterns both inside the pit area and in the near-field region for the square and the rectangular pits were similar. However, the volumes of deposition and erosion were smaller for the square pit. In general, it appears that the broader expanse of borrow area boundary exposed to the incoming wave field caused both more deposition within the pit, as well as more correlating erosion west of this region. This broader exposure causes an increase in the area

where wave-induced sediment transport is influenced by the borrow area, causing greater wave-induced deposition in the excavation footprint. Likewise, the broader exposure of the landward edge of the rectangular borrow area also serves to cause greater erosion, as the influence of the deeper excavation area tends to decrease wave-induced transport. Therefore, the overall morphologic change for the rectangular borrow area with its long axis oriented with the wave crests is greater than for a square borrow area of the same excavation volume.

The results of the morphodynamic evolution (a period of 12 months after dredging of the pit) show that the displacement of the pit centroid decreases as the pit aspect ratio was increased from 0.5 to 1.0 (rectangular to square pit), when the pit centroid was located on the ridge flank. When the pit centroid was located either on the ridge crest or trough, the displacement of the pit centroid increased as the pit aspect ratio was increased from 0.5 to 1.0. In the case of the borrow pit located on the ridge crest, this increase in displacement correlates to a migration of the pit centroid in the direction of wave propagation.

The pit centroid position affects the extents of the influence areas (area where the relative variation with respect to the case without the pit exceeded an assigned threshold) of both the wave height and the tidal current speed. Tidal current speed was reduced as the pit centroid was moved to larger depths, i.e. when its position was moved from the ridge crest to the trough. When the pit centroid was located at shallower depths, both the pit and the near-field area show large volumes of erosion and deposition, and larger variations in depth changes compared to the corresponding change for pits at larger depths. When the pit centroid was located at the ridge crest, the net volumetric change inside the pit and near-field areas was larger than those found when the pit centroid was located either in the ridge flanks or troughs. The displacement of the pit centroid 12 months after dredging increased both in the longshore and cross-shore direction when the initial pit centroid was located at shallower water depths. As the sediment transport regime within the ridge field is strongly dominated by waves, deposition and erosion along the crest of the ridge can be anticipated to have a higher magnitude than the deeper depths associated with the ridge flank or trough.

A pit with the major axis aligned with the ridge crest causes larger areas of variations in the significant wave height and current speed then the baseline pit (with major axis parallel to coastline). Overall, modeling demonstrated that the slight increase in the wave height influence areas observed when the pit is oriented with the ridge crest is due to the greater length of the pit boundary that is facing the direction of wave propagation. This orientation allows greater focusing of wave energy, as observed in the increased wave heights northwest of the borrow pit, as well as the corresponding decrease in wave heights west of the pit. The rotation of the pit caused a decrease in deposition in all the areas considered, likely due to the smaller cross-sectional area of the pit orientated towards the dominant direction of the incoming wave field. The net volumetric change inside the whole computational domain was negative and decreased with pit rotation (i.e. increased net erosion); therefore, the rotation of the pit causes a larger flux of sediment along the length of the ridge crest and outside the model domain.

In assessing the results, it should be noted that a limited number of scenario cases and fixed hydrodynamics and sediment characteristics were considered. To develop a more complete understanding of the influence of the different parameters and processes on the hydrodynamics

and sediment transport further investigations would be necessary. However, the scenarios developed provide an in-depth overview of how specific parameters related to pit aspect ratio, pit centroid position, and pit orientation influence the morphodynamics within the near-field of the borrow pit in ridged bathymetry.

VIII. CONCLUSIONS

The objective of this project was to test, tailor, and apply existing numerical morphological modeling tools and methods in order to provide robust and defensible predictions of morphological behavior in OCS sand borrow areas, as well as the associated near-field and far-field impacts. Although much progress has been made through previous studies (including those funded by BOEM within the U.S., as well as European efforts such as SANDPIT, SEDMOC, and others), the current state-of-the-art regarding morphological behavior or borrow pits remains limited. As a first step to address these known limitations, the project focused on evaluating several available numerical modeling tools as the basis for providing *practical* guidance regarding OCS sand extraction sought by BOEM. The primary questions which are of direct relevance to BOEM's mandate are:

- What are the infilling rates of extraction pits/areas after completion?
- What is the nature and magnitude of morphologic changes that occur on longer time scales (decades to centuries)?
- What are the optimum dimensions of the sand extraction areas with regard to minimizing near-field and far-field impacts?
- How do predictions of process-based modeling compare to observed morphologic change?
- Which model "sensitivity" parameters cause the largest changes in the predicted response in the near-field and far-field?
- What are the relative strengths and weakness in the predictive capabilities for various process-based modeling tools, including both established commercial packages and recently developed community models?
- What combination of model system(s), model options, and environmental forcing scenarios can be considered best practice for impact assessments supporting OCS sand extraction?

The review of past numerical modeling studies aimed at morphological evolution at borrow areas revealed that detailed understanding of sediment transport and the associated morphological change processes is limited, where general trends (e.g. direction of transport and overall areas of accretion/erosion) are often predictable; however, actual magnitudes for different modeling approaches can vary widely. General conclusions from previous evaluations of numerical morphologic change models have indicated the following:

- No single numerical modeling tool or set of tools yields consistent agreement with field and/or laboratory measurements for a broad range of geomorphic and oceanographic conditions
- Numerical modeling tools generally perform better in plan-bed (flat bottom) cases than cases involving rippled beds (i.e. sand waves)
- Numerical modeling tools generally perform better under conditions of larger waves and stronger bottom currents
- Based on the models evaluated to date, some field measurements are required to provide

reasonably accurate predictions of sediment transport processes

Although previous studies have indicated that the application of either research or practical models in an un-tuned manner may not yield useful results or predictions, modeling tools that are 'calibrated' with site-specific field data greatly reduce uncertainty. A key to the overall morphological modeling effort was to ensure that a characteristic site representative of borrow areas and dredging along the U.S. Atlantic inner shelf provided the basis for model calibration and testing.

A range of well-documented sites and projects were evaluated along the U.S. Atlantic inner shelf, including sites from Virginia to southern Florida (Figure VIII-1). Criteria for site selection included the availability of detailed recent bathymetric data, availability of detailed borrow site bathymetry and geotechnical data pre- and immediately post-dredging, and availability of local wave and hydrodynamic data to establish model boundary conditions and validate model results if possible.

The Long Bay, South Carolina borrow sites were found to be the only borrow areas to meet all of the above criteria and these sites were selected for further analysis utilizing the morphodynamic modeling tools. The regional hydrodynamic, wave, and sediment transport model (COAWST) was utilized by USGS for a Long Bay-specific assessment of localized sediment transport patterns. The more detailed model grid for this assessment did not include all borrow sites dredged offshore of the Myrtle Beach area. The only borrow site included within the USGS near-field grid was Cane South; therefore, this borrow site was selected for the detailed analysis described in this report.

Boundary conditions were derived using the Coupled Ocean Atmospheric-Wave-Sediment Transport Modeling System (COAWST). The atmospheric model (Advanced Weather Research and Forecasting Model - WRF) and wave model (Simulating Waves Nearshore – SWAN) components were implemented to provide the boundary conditions for the local morphological models. Due to the excessive time and computing resources required to simulate one full year with COAWST, one representative month, February 2010, was selected. This representative month was repeated to simulate one year of forcing.

Three different morphological models were tested; model results compared with pre- and post-one year dredging surveys from the Cane South borrow area. The models selected were Nearshore Community Model (NearCoM), MIKE 21 Coupled Model FM (MIKE 21), and Coastal Modeling System (CMS). Each of these model systems are:

- State-of-the art
- Extensively tested, validated, and quantified with regard to skill assessed in different applications and environments
- Widely accepted and used by the research community for their stated purpose as evidenced in peer-reviewed literature, and
- Well described in model documentation and user manuals.

Figure VIII-1. Sites evaluated for the morphological modeling including Sandbridge Shoals (Virginia), Long Bay (South Carolina), Canaveral Shoals (Florida), and Jupiter Island (Florida).

During the initial modeling process, several methods were adjusted to improve model skill. These corrections include refined model grid spacing, smoothed bathymetric surfaces for model

validation, and adjustment of the model calibration factor. The Online Correction Method (OCM), which calculates morphological changes given changes in hydrodynamics, was applied only to NearCoM due to its open source code. NearCoM and MIKE 21 models predicted net accretion in the borrow area similar to measured bathymetric change, whereas CMS predicted net erosion. Both NearCoM and MIKE 21 under-predicted the amount of accretion, but NearCoM had similar accretion rates to measured values. Because NearCoM was able to reproduce the morphological patterns seen in the measured data, it was selected as the preferred model for scenario testing.

Nine (9) scenarios were evaluated to assess the effect of borrow pit aspect ratio and varying tidal current speeds on a flat bed in the near-field region for a one-year period. Pit aspect ratios were varied from 0.25 to 1.0, and tidal current speeds were varied from 0.20 to 1.00 m/s. Modeled wave height and tidal current influence areas increased as the pit aspect ratio was increased. Displacement of the borrow area centroid was greater in the cross-shore than alongshore direction. Alongshore migration of the borrow area centroid was more sensitive to changes in the pit aspect ratio than the tidal current speed. Lower current speeds tend to cause net deposition, while higher speeds (1.00 m/s) tend to cause erosion. Maximum erosion and deposition values were observed to be on the order of 10% of the borrow area depth over the one-year simulation period. The same nine (9) scenarios were assessed for the far-field region where a larger computational domain was used. Erosional and depositional trends were more dependent on pit aspect ratio than tidal current speed in the area between the 5 to 10 m contours. A pit aspect ratio of 0.25 caused net deposition, while a pit aspect ratio of 0.5 and 1.0 (square pit) caused net erosion. It was determined that significant morphological change associated with borrow site dredging had a limited spatial extent, at least for excavations of the magnitude evaluated within this study.

The far-field region effects of ridged beds were evaluated in three (3) cases. The cases considered sloping beds with regular ridges at constant wavelengths of 600 to 1,200 m and orientation angles of 60º and 90º relative to the coastline. The scale of the ridges was modeled after bed forms observed in the Long Bay, South Carolina region. The influence of the borrow area extended significant distances alongshore (in some cases as much as 2,000 meters), and it was observed that ridge orientation influenced the extent of the borrow area effects (either to the north or south in the case of the Long Bay, South Carolina site simulated). Lower ridge wavelengths were found to correspond to lower wavelength erosion/deposition patterns.

Seven (7) additional cases were evaluated to investigate the influence of borrow area aspect ratio, borrow area centroid position, and borrow area orientation on the hydrodynamics and morphodynamics of the near-field region. It was observed that the square excavation (i.e. a borrow area with an aspect ratio of 1.0) generally causes larger areas of variations in the hydrodynamics (wave height and tidal current) than a rectangular excavation (aspect ratio of 0.5); however, depositional and erosional volumes were smaller for the square borrow area. It appears that the comparatively greater dimension of the rectangular borrow area boundary exposed to the incoming wave field led to reduced bottom boundary stress, ultimately leading to more deposition within the borrow area. The extents of the influence areas of both the wave height and the tidal current speed was reduced as the borrow area centroid was moved to greater depths, i.e. when its position was moved from the ridge crest to the trough. When the borrow

area centroid was located at shallower depths, both the borrow area and the near-field area show larger eroded and deposited volumes and larger variations of the depth changes compared to the corresponding quantities for borrow area with centroids at larger depths. A borrow area with the major axis aligned with the ridge crest causes larger areas of variations in the significant wave height and current speed then the baseline borrow area (major axis parallel to coastline). The net volumes inside the borrow area decreased when the borrow area is aligned parallel to the coastline, likely due to the smaller cross-sectional area of the borrow area orientated towards the dominant direction of the incoming wave field.

Based upon the results of the sensitivity analyses, as well as the inter-model comparison relative to measured bathymetric change at the selected borrow site, a range of demonstrative borrow area attributes (aspect ratio, centroid location, orientation), ambient tidal currents, and ambient seabed conditions (flat, ridged) for typical forcing were evaluated. As expected, model results were strongly dependent upon the process and input filtering decisions. However, some simplifying assumptions associated with filtering techniques are more critical than others for evaluating sediment transport pathways that influence morphological change associated with dredging shoals. Utilizing a combination of the results from the model sensitivity assessment and results from the evaluation of borrow area geometries, the report provides necessary input to effectively incorporate morphological modeling tools into the decision-making process for sand extraction within the U.S. Atlantic coast region. It should be noted that the assessment used a limited number of scenario cases and fixed hydrodynamics and sediment characteristics were considered and can only give an approximate idea of the near-field and far-field effects of dredging. To develop a more complete understanding of the influence of the different parameters and processes on the hydrodynamics and sediment transport further investigations would be necessary.

The following factors should be considered in morphodynamic modeling and are critical to effective model performance:

- Collection of site-specific data is critical to characterize both the wave climate and ambient tidal currents at a particular borrow area. For the generally wave-dominated sediment transport regime along much of the U.S. Atlantic coast, wave information, especially during storms, is important to characterize accurately for a particular borrow area.
- Large-scale hydrodynamic models can be utilized to provide boundary conditions for project-scale morphodynamic models, but it is important to ensure that the model simulation time period corresponds to (a) a relevant post-dredging period when bathymetry surveys are available at the beginning and the end, and (b) hydrodynamic and wave field data are available at the site or at least within the general vicinity of the borrow site excavation.
- Bathymetry data collected prior to dredging, immediately after dredging, and (likely) on an annual basis following the dredging event provides the necessary information to calibrate the model to *in situ* morphologic changes.
- In the case of Long Bay, South Carolina, bathymetry data collected using a single beam fathometer for all surveys became problematic because (a) bathymetry track lines were

not consistent and (b) full bathymetric coverage was not achieved for every survey. To evaluate bathymetric change accurately, it is critical to ensure that single-beam survey coverage is performed in a consistent and complete manner. Multi-beam bathymetric surveys with complete borrow area coverage would alleviate concerns related to line spacing.

- Based on model simulations, it appears that bathymetry surveys that extend to an area approximately twice the size of the borrow site (i.e. the overall survey area would be two times the excavation area and mimic the shape of the borrow area) incorporates a majority of the potential bathymetric change. Outside of this area, it appears that bathymetric change would be limited to several centimeters in overall depth change.
- It was possible to 'tune' each of the morphodynamic models assessed to simulate general trends of erosion and deposition; however, this requires that model calibration be performed for each specific site. A priori calibration of the models would be required prior to dredging to provide meaningful site-specific information that could be utilized to predict post-dredging morphologic change.
- Simulated bed elevation changes in the borrow area are small (of the order of 10% of the pit depth over the 1-year simulation period). At water depths similar to 'typical' U.S. Atlantic coast borrow areas, recovery of the borrow areas bathymetric conditions to the pre-dredging surface may take several years and perhaps more than a decade in sites dominated by wave-induced transport. However, this is highly dependent on frequency of storms and sediment transport rates.
- The influence area of the borrow area both on wave height and on tidal current increases as the aspect ratio of the pit increases. Since the wave and current conditions are based on information derived from Cane South (Long Bay, South Carolina), where the borrow area aligns obliquely with the incoming wave field and ambient tidal currents, the larger aspect ratios cause a greater perturbation to both the background wave and current fields.
- For flat bed scenarios, maximum accretion and erosion at the 5 m contour was more dependent on borrow pit aspect ratio than tidal current magnitude. This difference in influence appears to be related to wave refraction effects associated with the different aspect ratio borrow areas.
- For ridged bed scenarios, the borrow area influence extended significant distances alongshore (up to 2,000 meters) ; therefore, process-based numerical models should consider computational domains with a large alongshore extent to ensure that model boundary conditions do not influence results.
- For the ridged bed far-field scenarios, it appears that the comparatively greater dimension of the rectangular borrow area boundary exposed to the incoming wave field caused both more deposition within the borrow area, as well as more correlating erosion landward of this region. In general, borrow areas oriented with the longer dimension aligned parallel with the predominant incoming wave crests will infill more readily for wave-dominated sites. In addition, wave-induced sediment transport is highly dependent on water depth and shallower borrow areas located at the shoal crest (versus shoal flank or trough) will exhibit higher sediment transport rates (i.e. increased erosion and deposition potential).

IX. REFERENCES

Basco, D.R., 1999. "Methodology and Criteria to Assess the Impact of Sand Volume Removed in Federal Waters on the Nearshore Wave Climate," Final Report (MMS OCS Study 99-0046) Mineral Management Service, Department of Interior, October 1999.

Booij, N., Holthuijsen, L.H., Doorn, N., Kieftenburg, A.T.M.M., 1997. Diffraction in a spectral wave model. Proc. 3rd Intl. Symposium Ocean Wave Measurement and Analysis WAVES 97. ASCE, New York, pp. 243– 255.

Booij, N., Ris, R.C., Holthuijsen, L.H., 1999. A third-generation wave model for coastal regions, Part I, model description and validation. J. Geophys. Res. 104 (C4), 7649– 7666.

Byrnes, M.R., R.M. Hammer, B.A. Vittor, J.S. Ramsey, D.B. Snyder, J.D. Wood, K.F. Bosma, T.D. Thibaut, N.W. Phillips, 2000. Environmental Survey of Potential Sand Resource Sites: Offshore New Jersey. U.S. Department of the Interior, Minerals Management Service, International Activities and Marine Minerals Division (INTERMAR), Herndon, VA. OCS Report MMS 2000-052, Volume I: Main Text 380 pp. + Volume II: Appendices 291 pp.

Byrnes, M.R., R.M. Hammer, B.A. Vittor, J.S. Ramsey, D.B. Snyder, K.F. Bosma, J.D. Wood, T.D. Thibaut, and N.W. Phillips, 1999. Environmental Study of Identified Sand Resource Areas Offshore Alabama: Volume I: Main Text, Volume II: Appendices. U.S. Department of the Interior, Minerals Management Service, International Activities and Marine Minerals Division (INTERMAR), Herndon, VA. OCS Report MMS 99-0052, 326 pp. + 132 pp. appendices.

Byrnes, M.R., R.M. Hammer, B.A. Vittor, S.W. Kelley, D.B. Snyder, J.M. Cote, J.S. Ramsey, T.D. Thibaut, N.W. Phillips, and J.D. Wood, 2003. Collection of Environmental Data within Sand Resource Areas Offshore North Carolina and the Environmental Implications of Sand Removal for Coastal and Beach Restoration. U.S. Department of the Interior, Minerals Management Service, Leasing Division, Sand and Gravel Unit, Herndon, VA. OCS Report MMS 2000-056, Volume I: Main Text, 256 pp. + Volume II: Appendices, 69 pp.

Camenen, B., and Larson, M. 2005. A general formula for non-cohesive bed load sediment transport. Estuarine, Coastal and Shelf Science, 63, 249–260.

Camenen, B., and Larson, M. 2007. A unified sediment transport formulation for coastal inlet application. Technical report ERDC/CHL CR-07-1, US Army Engineer Research and Development Center, Vicksburg, MS.

Camenen, B., and Larson, M. 2008. A general formula for non-cohesive suspended sediment transport. Journal of Coastal Research, 24 (3), 615–627.

Chen, J., Shi, F., Hsu, T.-J., and Kirby, J. T., in revision, "NearCoM-TVD - a quasi-3D nearshore circulation and sediment transport model", Coastal Engineering.

CSA International, Inc., Applied Coastal Research and Engineering, Inc., Barry A. Vittor & Associates, Inc., C.F. Bean, L.L.C., and Florida Institute of Technology, 2009.

Analysis of Potential Biological and Physical Impacts of Dredging on Offshore Ridge and Shoal Features, U.S. Department of the Interior, Minerals Management Service, OCS Study MMS 2010-010. 160 pp. + appendices.

Davies A.G., Van Rijn L.C., Damgaard J.S., van de Graaff J. and J.S. Ribberink, 2002. Intercomparison of research and practical sand transport models. Coastal Engineering, 46, 1-23.

de Swart, HE., Calvete, D. Non-linear response of shoreface-connected sand ridges to interventions. OCEAN DYNAMICS (2003) 53, pp. 270-277 doi: 10.1007/s10236-003-0044-9

Deigaard, R., 1993. A note on the three-dimensional shear stress distribution in the surf zone. Coastal Eng. 20, 47–59.

Deigaard, R., Fredsøe, J., Hedegaard, I.B., 1986a. Suspended sediment in the surf zone. J. Waterw., Port, Coastal Ocean Eng., ASCE 112 (1), 115– 128.

Deigaard, R., Fredsøe, J., Hedegaard, I.B., 1986b. Mathematical model for littoral drift. J. Waterw., Port, Coastal Ocean Eng., ASCE 112 (3), 351–369.

Denny, J.F., W.E. Baldwin, W.C. Schwab, P.T. Gayes, R. Morton and N.W. Driscoll (2007) "Morphology and Texture of Modern Sediments on the Inner Shelf of South Carolina's Long Bay from Little River Inlet to Winyah Bay" USGS Open File Report, 2005-1345.

Denny, Jane F., William C. Schwab, Wayne E. Baldwin, Walter A. Barnhardt, Paul T. Gayes, Robert A. Morton, John C. Warner, Neal W. Driscoll, George Voulgaris, Holocene sediment distribution on the inner continental shelf of northeastern South Carolina: Implications for the regional sediment budget and long-term shoreline response, Continental Shelf Research, Volume 56, 15 March 2013, Pages 56-70, ISSN 0278-4343, http://dx.doi.org/10.1016/j.csr.2013.02.004.

DHI, 2009: LITTREN User Guide, DHI Water and Environment.

Dibajnia, M. and R.B. Nairn, 2010. Investigation of Dredging Guidelines to Maintain and Protect the Geomorphic Integrity of Offshore Ridge Shoal Regimes, U.S. Dept. of Interior, Mineral Management Service, XXX OSC Region, YYYY. OCS Study MMS 2010-XXX. 150 pp. + appendices.

Dibajnia, M., and Watanabe, A., 1992. "Sheet flow under nonlinear waves and currents." Proc. 23rd Int. Conf. on Coastal Eng., ASCE. pp. 2015-2028.

Drucker, B.S.; Waske, W., and Byrnes, M.R., 2004: The U.S. Minerals Management Service's Outer Continental Shelf Sand and Gravel Program: Environmental Studies to Evaluate the Effects of Offshore Dredging Operations in Federal Waters. J. Coastal Research, 20(1), 1-5.

Elfrink, B., Brøker, I., Deigaard, R., Asp Hansen, E., Justesen, P., 1996. Modelling of 3D sediment transport in the surf zone. Proceedings of the 25th Intl. Conference on Coastal Eng., ASCE, Orlando, FL, USA, pp. 3805– 3817.

Elfrink, B., Rakha, K.A., Deigaard, R., Brøker, I., 1999. Effect of near-bed velocity skewness on cross shore sediment transport. Proc. Coastal Sediments '99, Hauppage, Long Island, NY, vol. 1, pp. 33– 47.

Engelund, F., Fredsøe, J., 1976. A sediment transport model for straight alluvial channels. Nordic Hydrology 7, 293-306.

Fewings, M., S. Lentz, P. Howd, K Hathaway (2013) "Nearshore Velocity Patterns and Tidal Sloshing at the Chesapeake Bay Outflow Plume".

Fredsøe, J., 1984. Turbulent boundary layer in wave-current motion. J. Hydraul. Eng., ASCE 110 (8), 1103–1120.

Fredsøe, J., Andersen, O.H., Silberg, S., 1985. Distribution of suspended sediment in large waves. J.Waterway, Port, Coastal Ocean Eng., ASCE 111 (6), 1041– 1059.

Giordana, A.C., Drucker, B., and Bassim, K. (1999): Guidelines for Obtaining Minerals Other than Oil, Gas, & Sulphur on the Outer Continental Shelf. Herndon, Virginia: U.S. Department of the Interior, Minerals Management Service, OCS Report MMS 99-0070, 19p.

Haidvogel, D. B., Arango, H., Budgell, W. P., Cornuelle, B. D., Curchitser, E., Di Lorenzo, E., ... & Wilkin, J., 2008. Ocean forecasting in terrain-following coordinates: Formulation and skill assessment of the Regional Ocean Modeling System. Journal of Computational Physics, 227(7), 3595-3624.

Hayes, M.O. and Nairn, R.B., 2004. Natural Maintenance of Sand Ridges and Linear Shoals on the U.S. Gulf and Atlantic Continental Shelves and the Potential Impacts of Dredging, J. Coastal Research, 20 1 138–148 West Palm Beach, Florida Winter 2004.

Holthuijsen, L.H., Booij, N. and Herbers, T.H.T. (1989): A prediction model for stationary, short crested waves in shallow waters with ambient currents. Coastal Eng. 13, 23-54.

Hommes, S., Hulscher, S.J.M.H., and Stolk, A. (2007): Parallel modeling approach to assess morphological impacts to offshore sand extraction, J. Coastal Res., 23 (6), 1565-1579.

Kelley, S.W. and J.S. Ramsey, 2006. Shoreline Hotspot Development Due to Sand Mining Offshore Jupiter Island, Florida. Proceedings of the 30th International Conference on Coastal Engineering, San Diego, California.

Kelley, S.W., J.S. Ramsey, M.R. Byrnes (2001). Numerical Modeling Evaluation of the Cumulative Physical Effects of Offshore Sand Dredging for Beach Nourishment. U.S. Department of the Interior, Minerals Management Service, International Activities and Marine Minerals Division (INTERMAR), Herndon, VA. OCS Report MMS 2001-098, 95 pp. + 106 pp. appendices

Kelley, S.W., Ramsey, J.S. and Byrnes, M.R., 2004. Evaluating Shoreline Response to Offshore Sand Mining for Beach Nourishment, J. Coastal Research, 20 1 89–100 West Palm Beach, Florida Winter 2004.

Kelley, S.W., Ramsey, J.S., and Byrnes, M.R., 2001. Numerical Modeling Evaluation of the Cumulative Physical Effects of Offshore Sand Dredging for Beach Nourishment. U.S. Department of the Interior, Minerals Management Service, International Activities and

Marine Minerals Division (INTERMAR), Herndon, VA. OCS Report MMS 2001-098, 95 pp. 1 106p. appendices.

Kobayashi, N., Payo, A., & Schmied, L., 2008. Cross-shore suspended sand and bed load transport on beaches. Journal of Geophysical Research: Oceans (1978–2012), 113(C7).

Komen, G.J., Cavaleri, L., Doneland, M., Hasselmann, K., Hasselmann, S. and Janssen, P.A.E.M. (1994): Dynamics and modeling of ocean waves. Cambridge University Press. UK, 560 pp.

Lin, L., Demirbilek, Z., and Mase, H., 2011. Recent capabilities of CMS-Wave: A coastal wave model for inlets and navigation projects. Journal of Coastal Research, Special Issue 59, 7-14.

Lin, L., Demirbilek, Z., Mase, H., Zheng, J., and Yamada, F. 2008. CMS-Wave: a nearshore spectral wave processes model for coastal inlets and navigation projects. Tech. Report ERDC/CHL TR-08-13. Vicksburg, MS: U.S. Army Engineer Research and Development Center.

Maa, J. P.Y. (1995) "Investigation of Isolated Sand Shoals on the Inner Continental Shelf of Virginia Relative to the Potential for Aggregate Mining" Report submitted to the Minerals Management Service, pp. 54.

Mase, H., 2001. "Multi-directional random wave transformation model based on energy balance equation," Coastal Engineering Journal 43(4), 317-337.
Massey, C. (2013) "ERDC's Coastal Storm Modeling Program" Presentation at the 26th Annual National Conference on Beach Preservation Technology http://fsbpa.com/2013TechPresentations/Chris_Massey.pdf

Michel, J., 2004. Regional Management Strategies for Federal Offshore Borrow Areas, U.S. East and Gulf of Mexico Coasts, J. Coastal Research, 20(1), 149-154.

Misra, S.K., Driscoll, A.M., Kirby, J.T., Cornett, A., Lomonoco, P., Sayao, O. and M. Yavary, 2008. Surface Gravity Wave Interactions with Deep-draft Navigation Channels – Physical and Numerical Case Studies, Proceedings of ICCE 2008.

Putrevu, U., & Svendsen, I. A., 1999. Three-dimensional dispersion of momentum in wave-induced nearshore currents. European Journal of Mechanics-B/Fluids, 18(3), 409-427.

Ribberink, J.S., 2004. Migration and infill of trenches in the marine environment: an analytical engineering model. SANDPIT report, University of Twente, The Netherlands.

Roelvink, J.A., 2006. Coastal morphodynamic evolution techniques. Coastal Engineering, 53(2), 277-287.

Roos, P.C., Hulscher, S.J.M.H., 2007. Nonlinear modeling of tidal sandbanks: wavelength evolution and sand extraction. In: McKee Smith, J. (Ed.), Proc. of the 30th Int. Conference on Coastal Engineering (ICCE2006). ASCE, San Diego, US, pp. 2761–2771.

Roos, P.C., Hulscher, S.J.M.H., and de Vriend, H., 2008. Modelling the morphodynamic impact of offshore sandpit geometries, Coastal Engineering, 55, 704-715.

Rosati, J.D., and N.C. Kraus, 1991. Practical Considerations in Longshore Transport Calculations. CETN II-24, U.S. Army Engineer Waterways Experiment Station, Coastal and Hydraulics Laboratory, Vicksburg, MS, 6 pp.

Shchepetkin, A. F., & McWilliams, J. C., 2005. The regional oceanic modeling system (ROMS): a split-explicit, free-surface, topography-following-coordinate oceanic model. Ocean Modelling, 9(4), 347-404.

Shchepetkin, A. F., & McWilliams, J. C., 2009. Correction and commentary for "Ocean forecasting in terrain-following coordinates: Formulation and skill assessment of the regional ocean modeling system" by Haidvogel et al., J. Comp. Phys. 227, pp. 3595–3624. Journal of Computational Physics, 228(24), 8985-9000.

Shi, F., Kirby, J. T., Hsu, T.-J., and Chen J.-L., 2013, "NearCoM-TVD, documentation and users' manual", Research Report, CACR 13-06, University of Delaware, Newark, Delaware.

Shi, F., Kirby, J.T. and Hanes, D.M. (2010): Is the erosional hotspot at Ocean Beach, San Francisco, caused by wave focusing? - From modeling point of view, AGU Ocean Sciences Meeting, Portland, February, 2010.

Shi, F., Kirby, J.T., Hanes, D. (2007): An efficient mode-splitting method for a curvilinear nearshore circulation model, Coastal Engineering, 54, 811-824.

Shore Protection Manual. 1984. 4th ed., 2 Vols. U.S. Army Engr. Waterways Expt. Station, Coastal Engrg. Res. Center, U.S. Govt. Printing Office, Washington, DC.

Skamarock, W. C., Klemp, J. B., Dudhia, J., Gill, D. O., Barker, D. M., Wang, W., & Powers, J. G., 2005. A description of the advanced research WRF version 2 (No. NCAR/TN-468+ STR). National Center for Atmospheric Research Boulder Co Mesoscale and Microscale Meteorology Div.

Soulsby, R. and Whitehouse, R. (1997). "Threshold of sediment motion in coastal environment," Proc. Pacific Coasts and Ports '97 Conf', University of Canterbury, Christchurch, New Zealand, 149-154.

Soulsby, R.L., 1997. Dynamics of Marine Sands. Thomas Telford, London, 249pp.

Sullivan, Charlene, John C. Warner, Marinna A. Martini, George Voulgaris, Paul A. Work, Kevin A. Haas, and Daniel Hanes (2006) "South Carolina Coastal Erosion Study Data Report for Observations October 2003 - April 2004" U.S. Geological Survey Open-File Report 2005-1429. http://woodshole.er.usgs.gov/pubs/of2005-1429/start.html

Taylor, L.A., B.W. Eakins, R.R. Warnken, K.S. Carignan, G.F. Sharman, D.C. Schoolcraft, and P.W. Sloss (2008) "Digital Elevation Models of Myrtle Beach, South Carolina: Procedures, Data Sources and Analysis". NOAA Technical Memorandum NESDIS-NGDC-1, National Geophysical Data Center, Boulder Colorado.

U.S. Army Corps of Engineers (1998) "Environmental Assessment: Canaveral Shoals Borrow area II", USACE Jacksonville District, Planning Division. pp. 56.

U.S. Army Corps of Engineers (2009) "Final Environmental Assessment: Sandbridge Beach Erosion Control and Hurricane Protection Project, Virginia Beach, Virginia", USACE

Norfolk District, Planning Division in Cooperation with the Mineral Management Service. pp. 260.

U.S. Army Corps of Engineers, Jacksonville District (2009) "Plans for the Construction of Beach Renourishment 2009 South Reach"

van der Wegen, M., and J. A. Roelvink, 2008. Long-term morphodynamic evolution of a tidal embayment using a two-dimensional, process-based model, J. Geophys. Res., 113, C03016, doi: 10.1029/2006JC003983.

van der Wegen, M., Z. B. Wang, H. H. G. Savenije, and J. A. Roelvink, 2008. Long-term morphodynamic evolution and energy dissipation in a coastal plain, tidal embayment, J. Geophys. Res., 113, F03001, doi: 10.1029/2007JF000898.

Van Rijn, L. C., 1991. Sediment transport in combined waves and currents. In Proceedings of Euromech (Vol. 262, pp. 3-15).

Van Rijn, L.C. 1998. Principles of Coastal Morphology. AquaPublications, Amsterdam, The Netherlands.

Van Rijn, L.C. 2007a. Unified View of Sediment Transport by Currents and Waves. I: Initiation of Motion, Bed Roughness, and Bed-load Transport. Journal of Hydraulic Engineering, 133(6), 649-667.

Van Rijn, L.C. 2007b. Unified View of Sediment Transport by Currents and Waves. II: Suspended Transport, Journal of Hydraulic Engineering, 133(6), 668-689.

Van Rijn, L.C. and Tan, G.L., 1985. SUTRENCH-model: Two-dimensional vertical mathematical model for sedimentation in dredges channels and trenches by currents and waves. Technical report. The Hague: Delft Hydraulics Laboratory.

Walstra, D-J.R., van Rijn, L.C., and de Boer, G., 2002. Morphology of pits, channels and trenches, Part III: Investigation of the longshore and cross-shore impact of various pit designs, WL|Delft Hydraulics, Z3223.30.

Warner, J. C., B. Armstrong, C. S. Sylvester, G. Voulgaris, T. Nelson, W.C. Schwab, and J. F. Denny (2012), Storm-induced inner-continental shelf circulation and sediment transport: Long Bay, South Carolina, Cont. Shelf Res., 42, 51–63, doi:10.1016/j.csr.2012.05.001.

Warner, J.C., Armstrong, B., He, R., and Zambon, J.B., 2010. Development of a Coupled Ocean-Atmosphere-Wave-Sediment Transport (COAWST) modeling system: Ocean Modeling, v. 35, no. 3, p. 230-244.

Warner, J.C., Sherwood, C.R., Signell, R.P., Harris, C.K., and Arango, H.G., 2008. Development of a three-dimensional, regional, coupled wave, current, and sediment transport model, Computer and Geosciences, 34, 1284-1306.

Watanabe, A. 1987. 3-dimensional numerical model of beach evolution. Proceedings Coastal Sediments '87, 802-817.

Young, I.R. (1999): Wind generated ocean waves. Elsevier Ocean Engineering Book Series, Volume 2, Editors R. Bhattacharyya and M.E. McCormick, Elsevier.

Zyserman, J.A., Fredsøe, J., 1994. Data analysis of bed concentration of suspended sediment. Journal of Hydraulic Engineering, ASCE 120(9), 1021-1042.

APPENDIX A – WAVE ROSE PLOTS

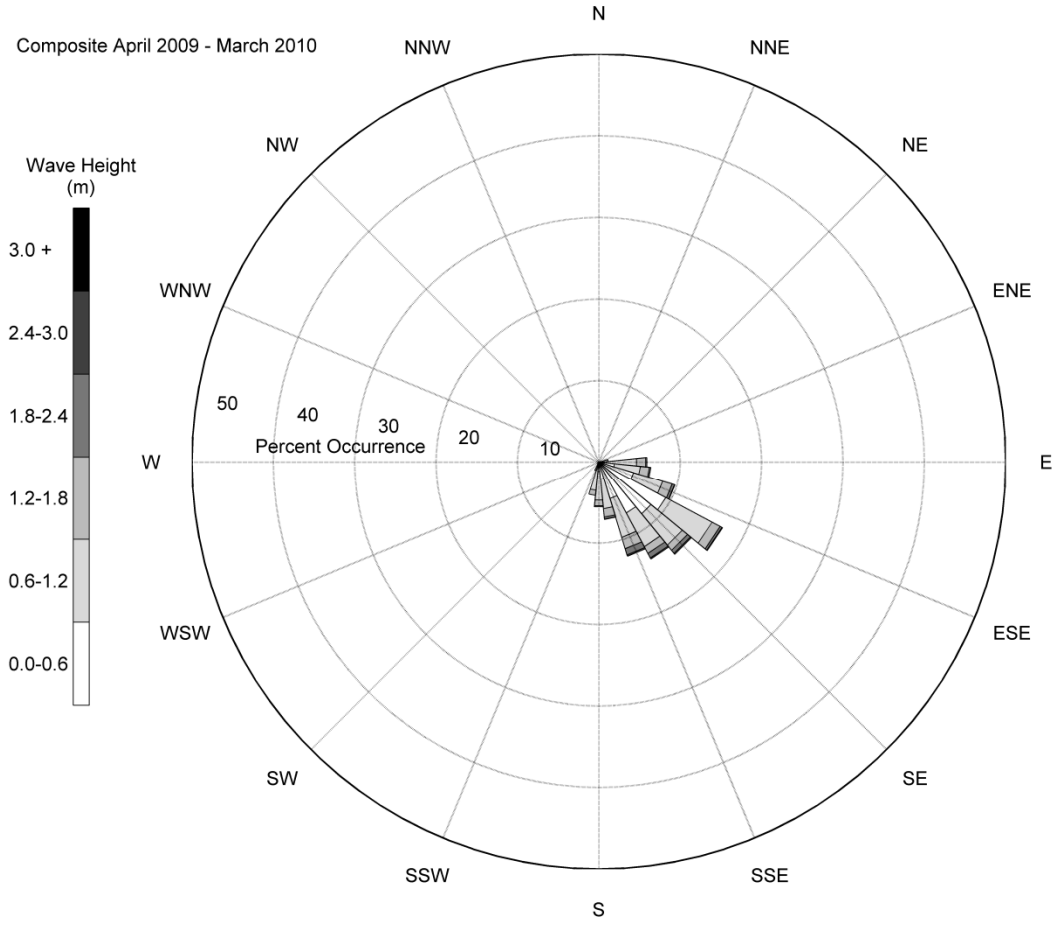

Figure A-1. Wave rose for April 2009 to March 2010 at Cane South, where waves from NDBC Buoy #41013 (Frying Pan Shoal, NC) were refracted to the Cane South borrow area. Wave directions are in meteorological convention.

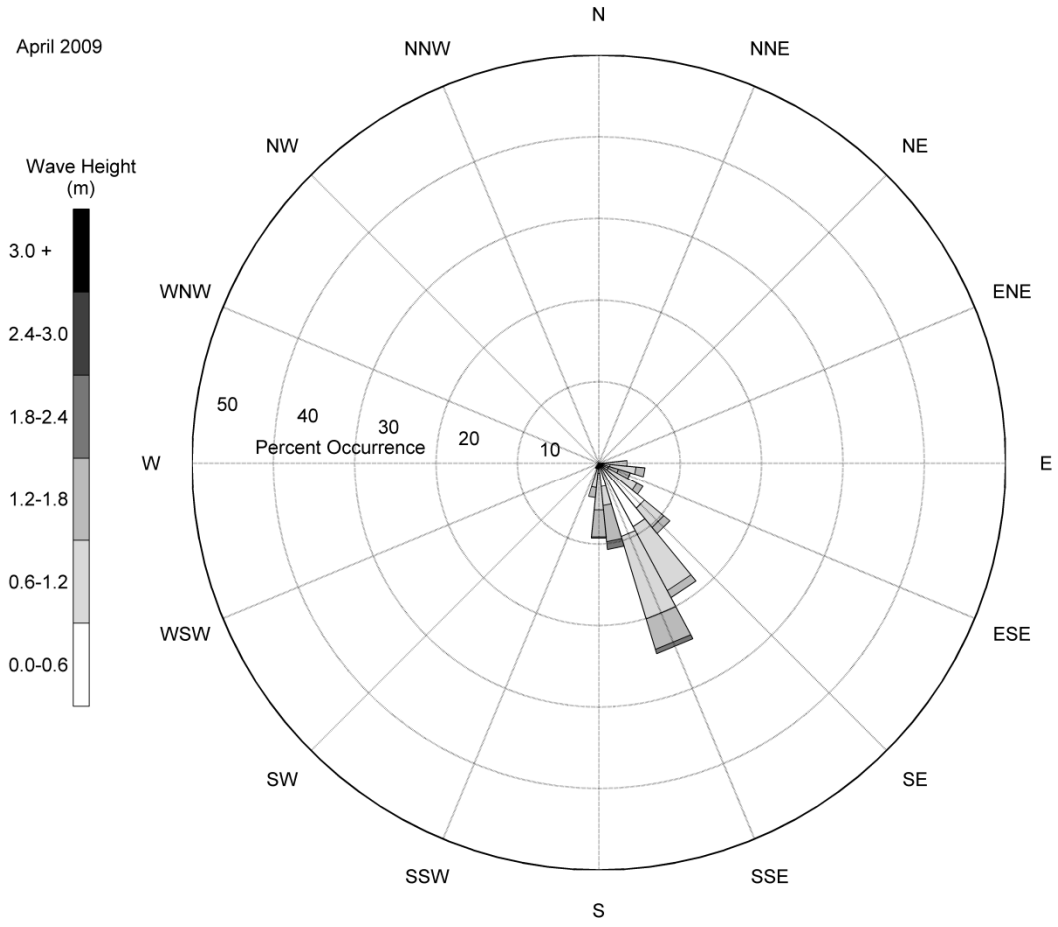

Figure A-2. Wave rose for April 2009 at Cane South, where waves from NDBC Buoy #41013 (Frying Pan Shoal, NC) were refracted to the Cane South borrow area. Wave directions are in meteorological convention.

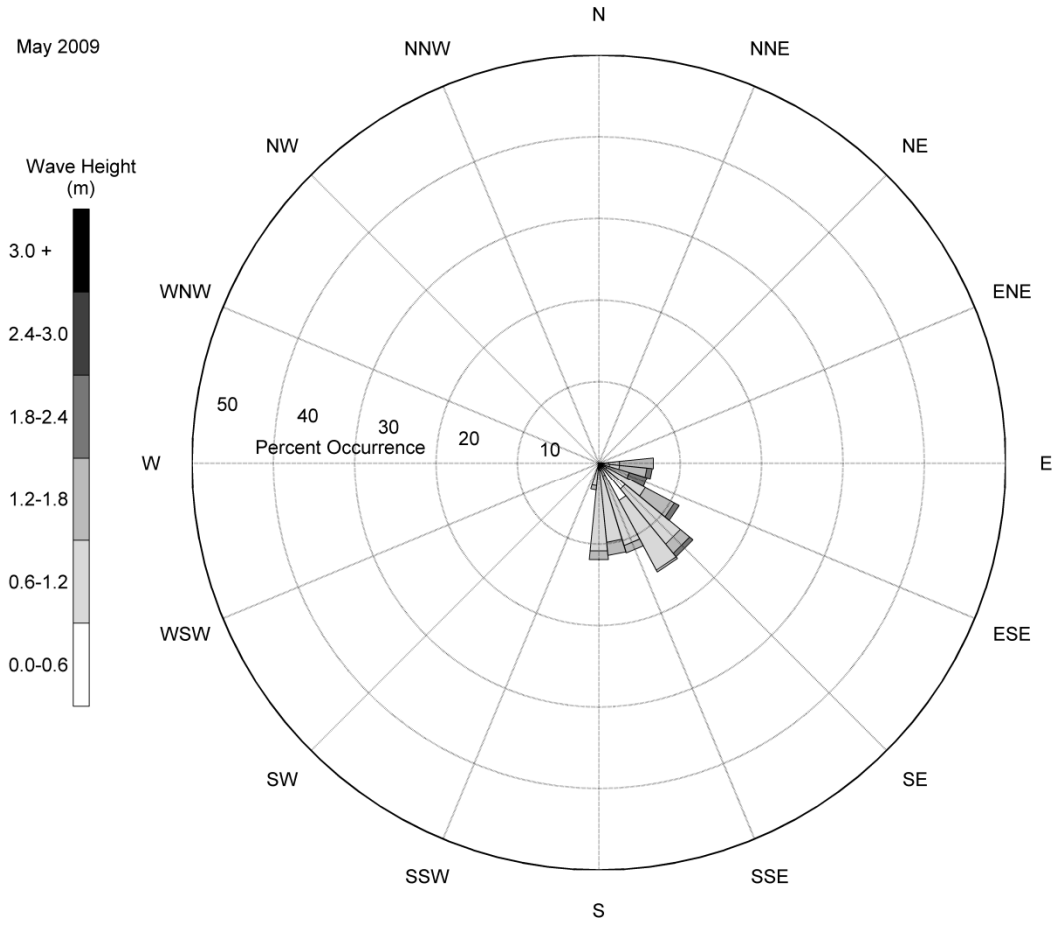

Figure A-3. Wave rose for May 2009 at Cane South, where waves from NDBC Buoy #41013 (Frying Pan Shoal, NC) were refracted to the Cane South borrow area. Wave directions are in meteorological convention.

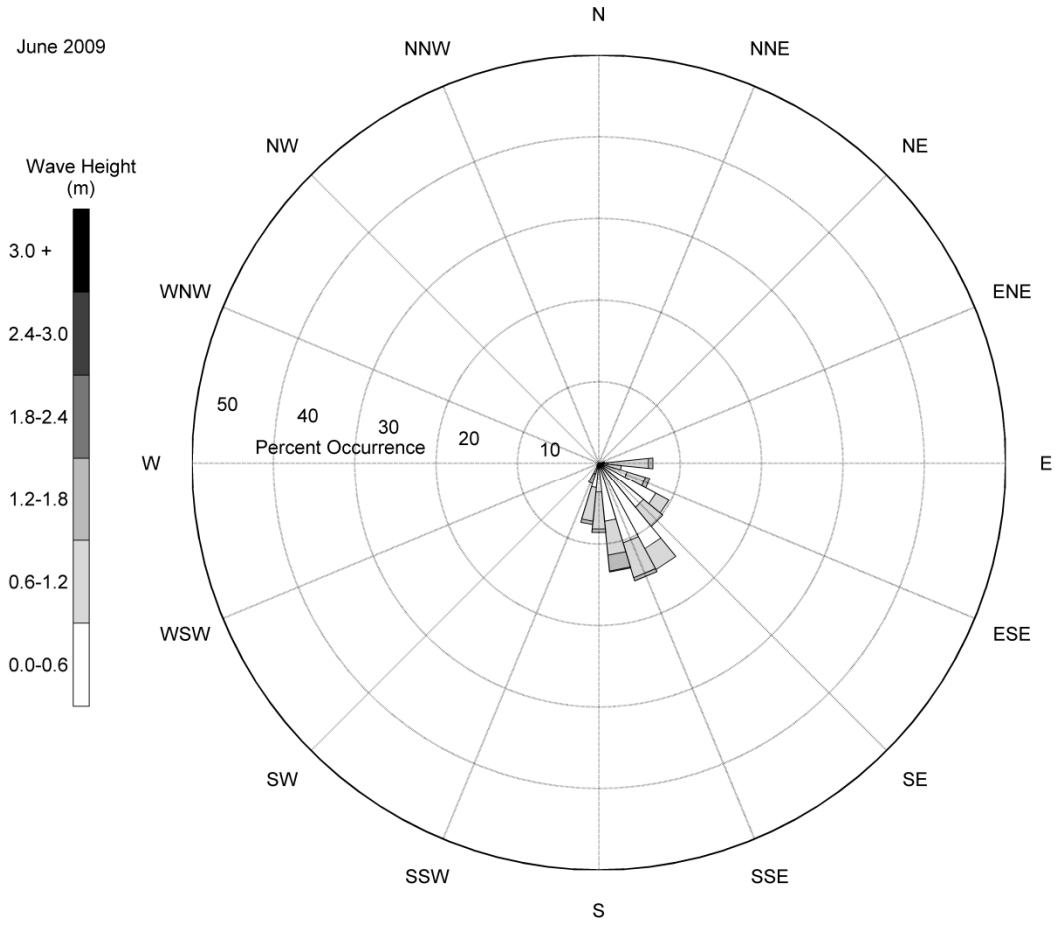

Figure A-4. Wave rose for June 2009 at Cane South, where waves from NDBC Buoy #41013 (Frying Pan Shoal, NC) were refracted to the Cane South borrow area. Wave directions are in meteorological convention.

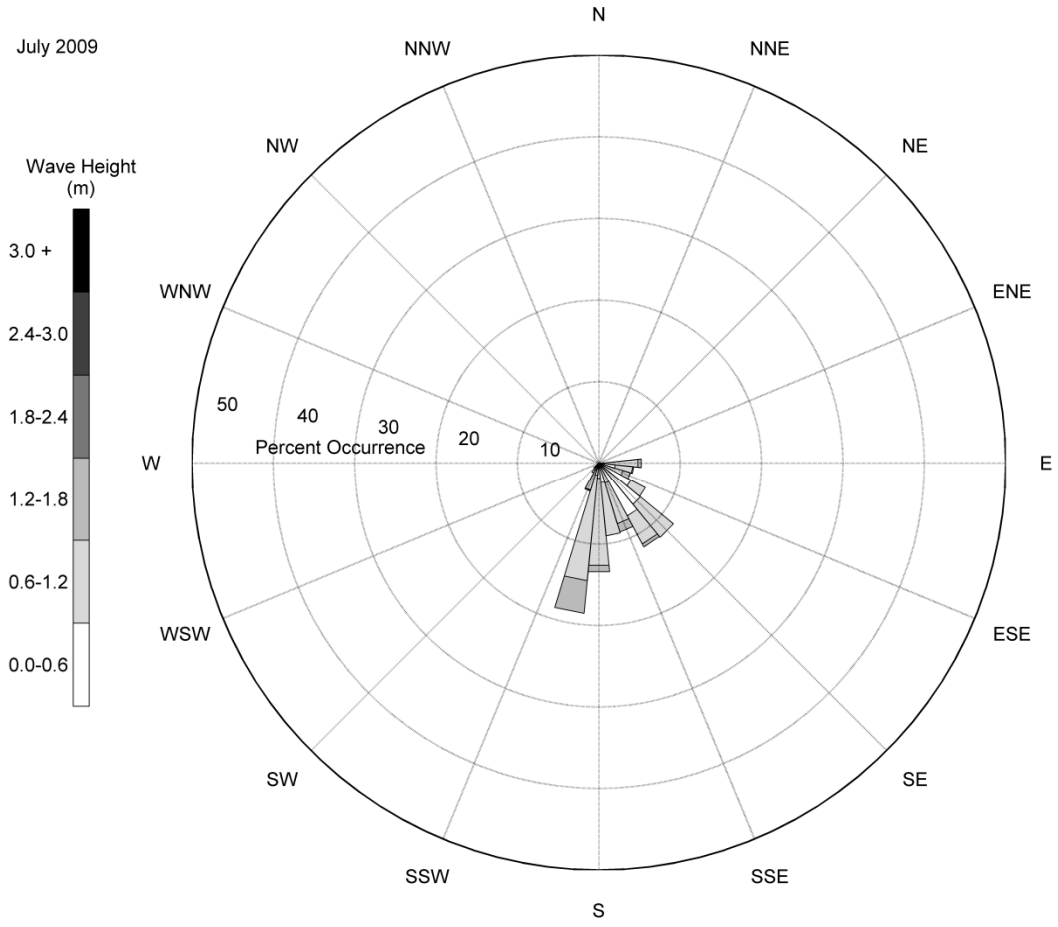

Figure A-5. Wave rose for July 2009 at Cane South, where waves from NDBC Buoy #41013 (Frying Pan Shoal, NC) were refracted to the Cane South borrow area. Wave directions are in meteorological convention.

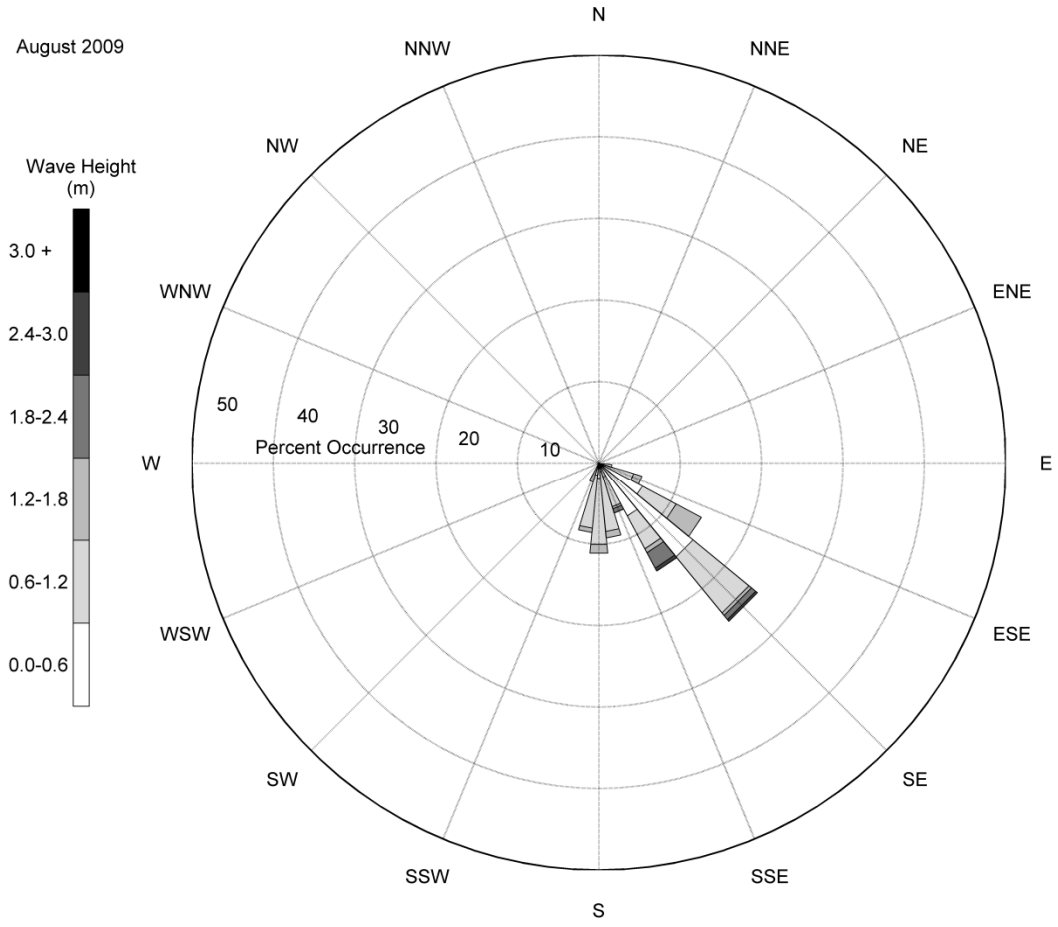

Figure A-6. Wave rose for August 2009 at Cane South, where waves from NDBC Buoy #41013 (Frying Pan Shoal, NC) were refracted to the Cane South borrow area. Wave directions are in meteorological convention.

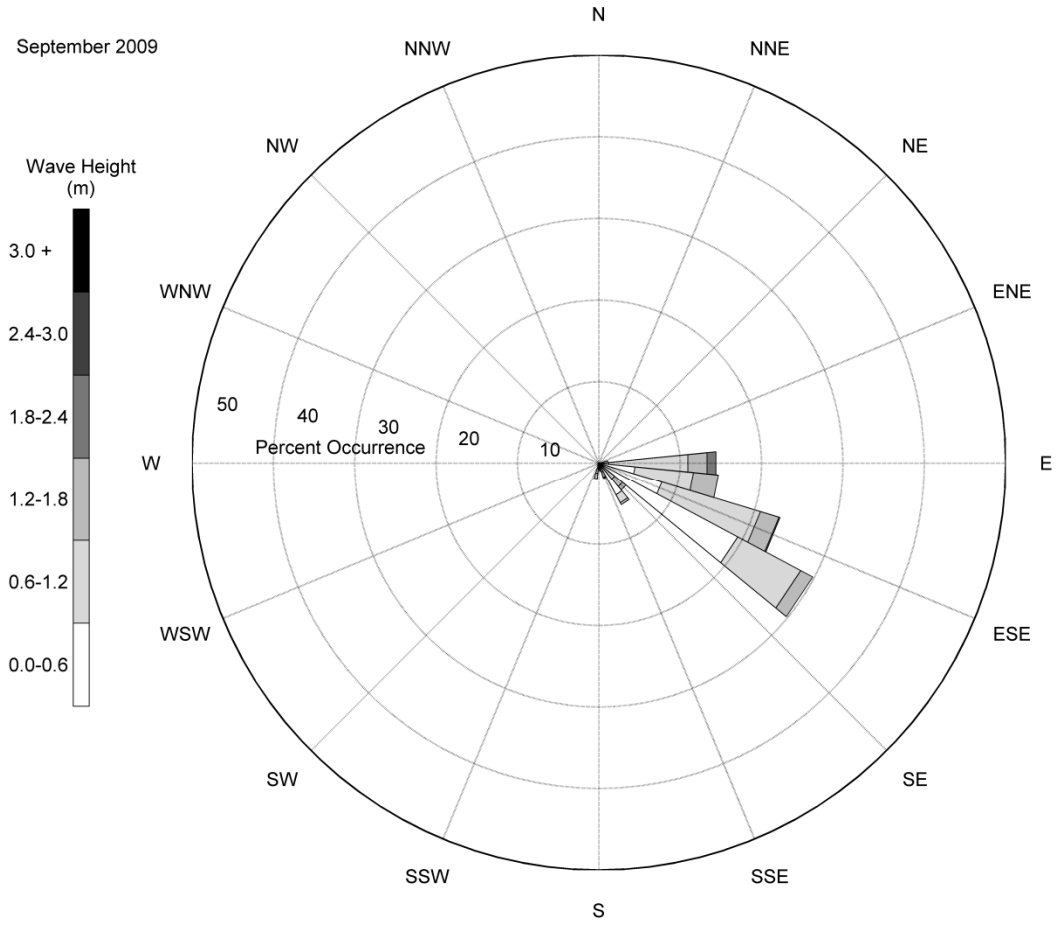

Figure A-7. Wave rose for September 2009 at Cane South, where waves from NDBC Buoy #41013 (Frying Pan Shoal, NC) were refracted to the Cane South borrow area. Wave directions are in meteorological convention.

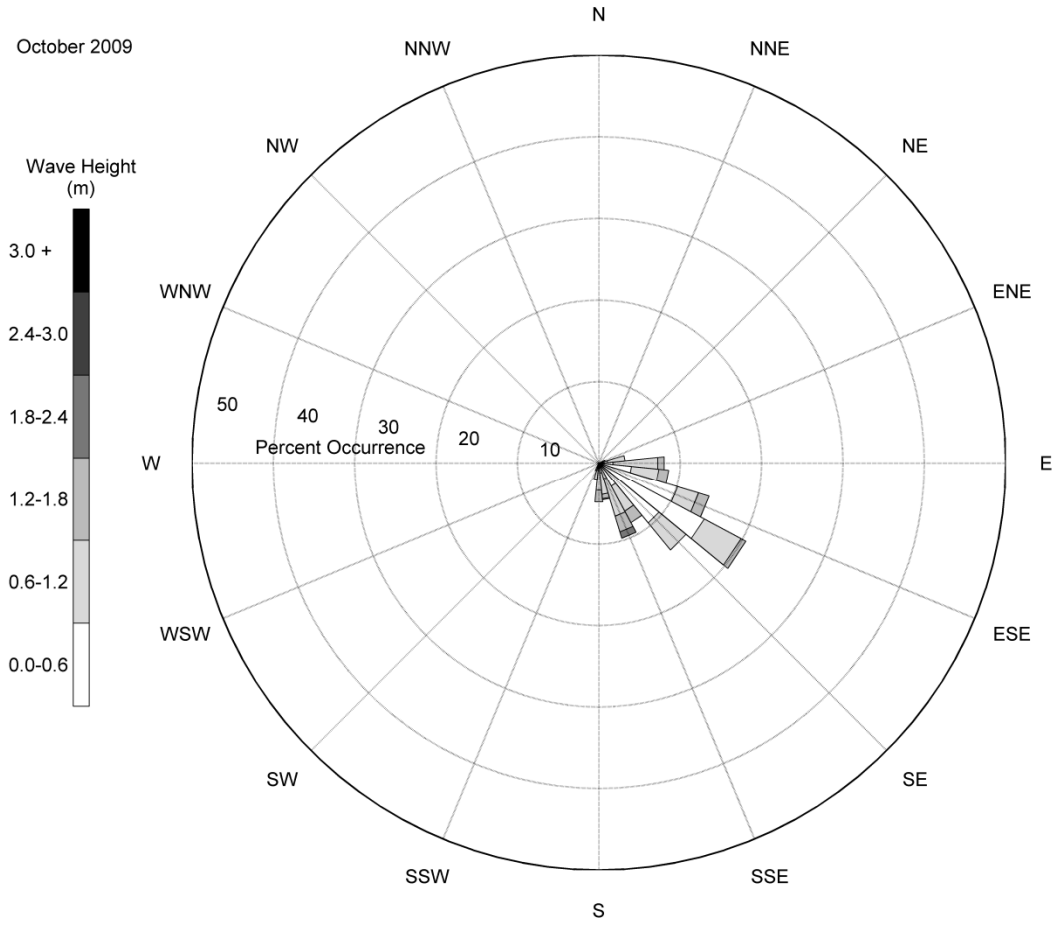

Figure A-8. Wave rose for October 2009 at Cane South, where waves from NDBC Buoy #41013 (Frying Pan Shoal, NC) were refracted to the Cane South borrow area. Wave directions are in meteorological convention.

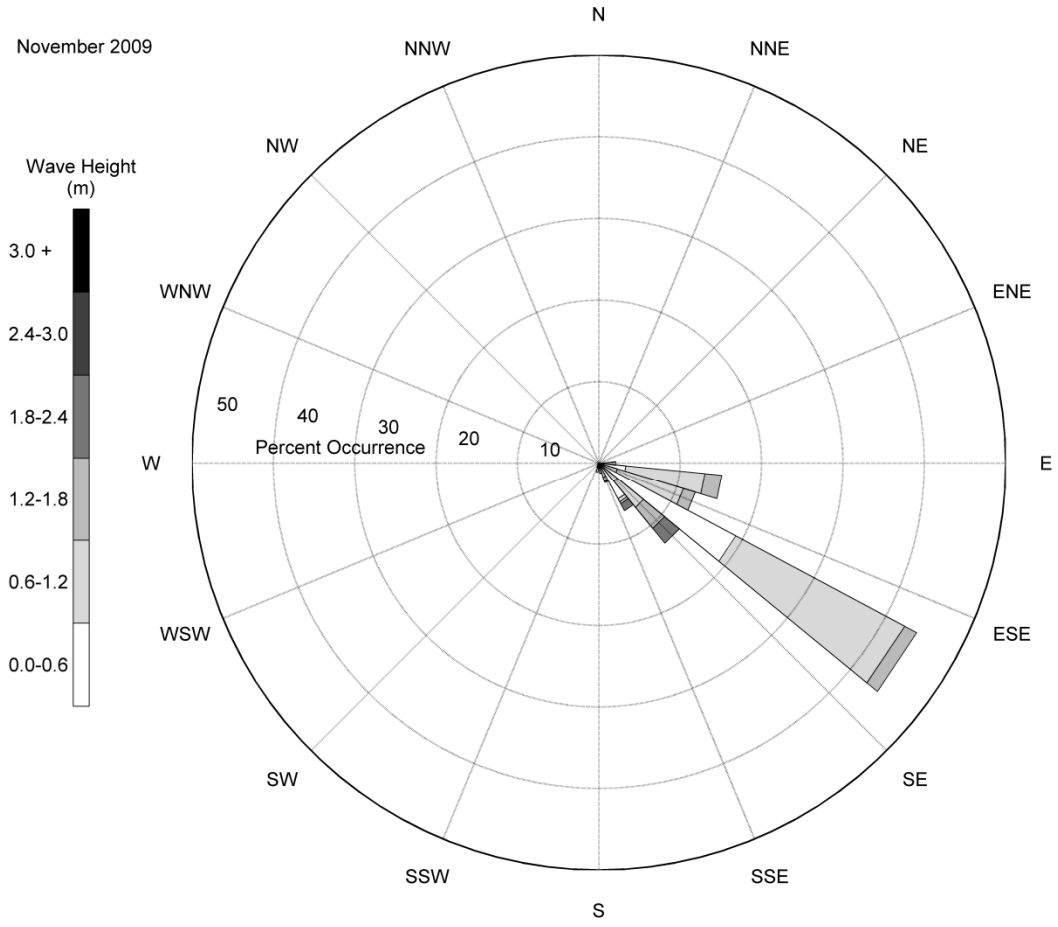

Figure A-9. Wave rose for November 2009 at Cane South, where waves from NDBC Buoy #41013 (Frying Pan Shoal, NC) were refracted to the Cane South borrow area. Wave directions are in meteorological convention.

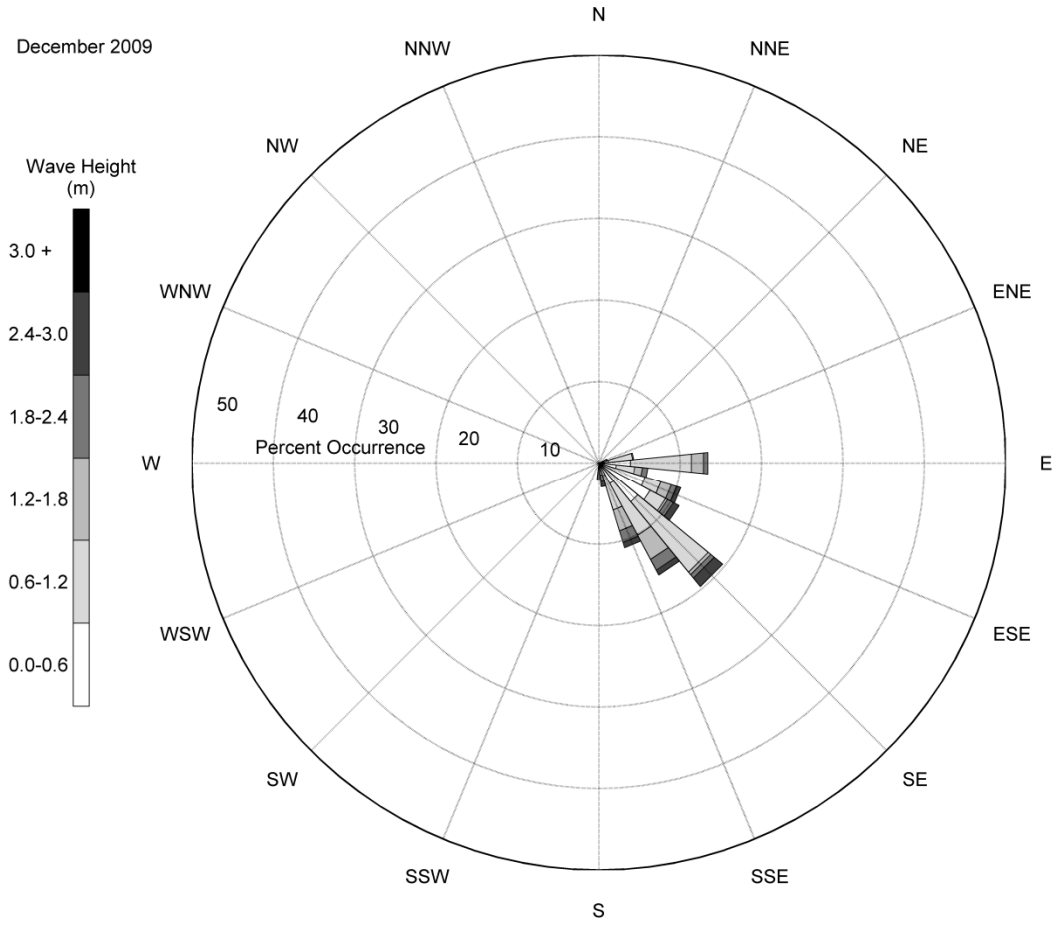

Figure A-10. Wave rose for December 2009 at Cane South, where waves from NDBC Buoy #41013 (Frying Pan Shoal, NC) were refracted to the Cane South borrow area. Wave directions are in meteorological convention.

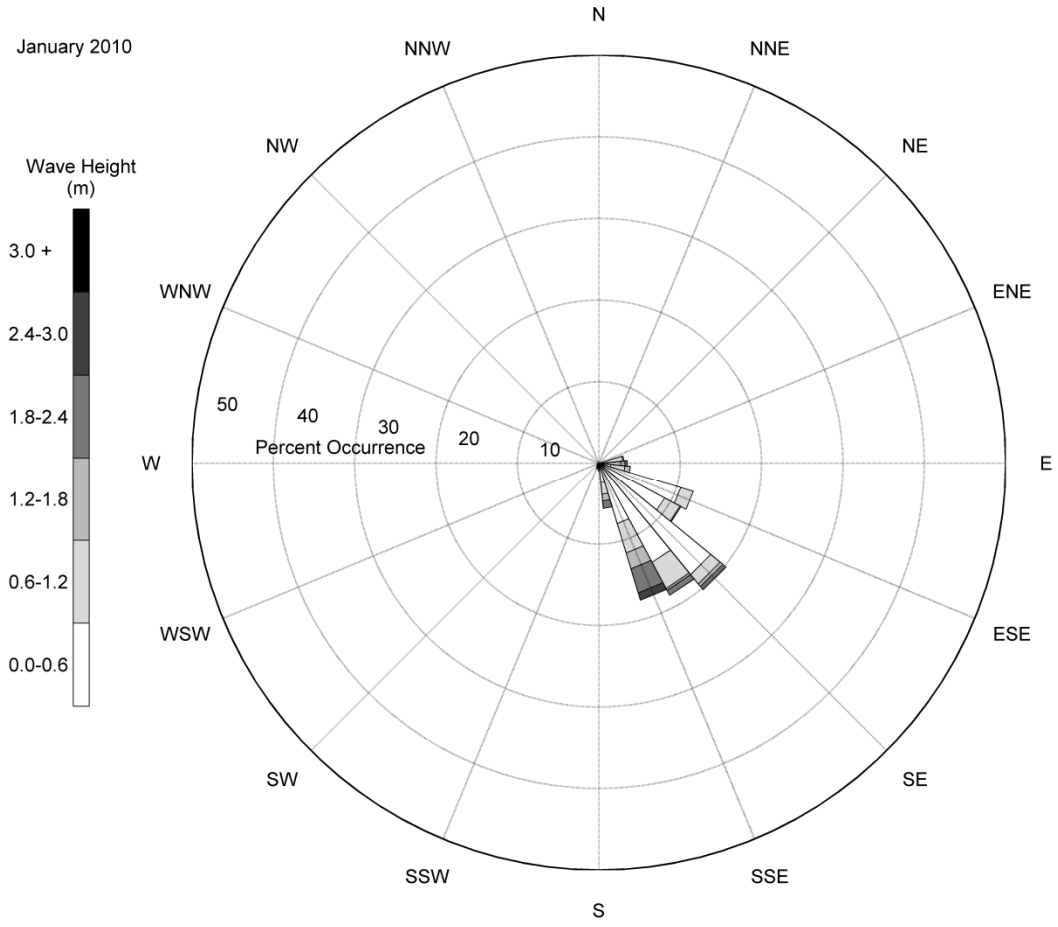

Figure A-11. Wave rose for January 2010 at Cane South, where waves from NDBC Buoy #41013 (Frying Pan Shoal, NC) were refracted to the Cane South borrow area. Wave directions are in meteorological convention.

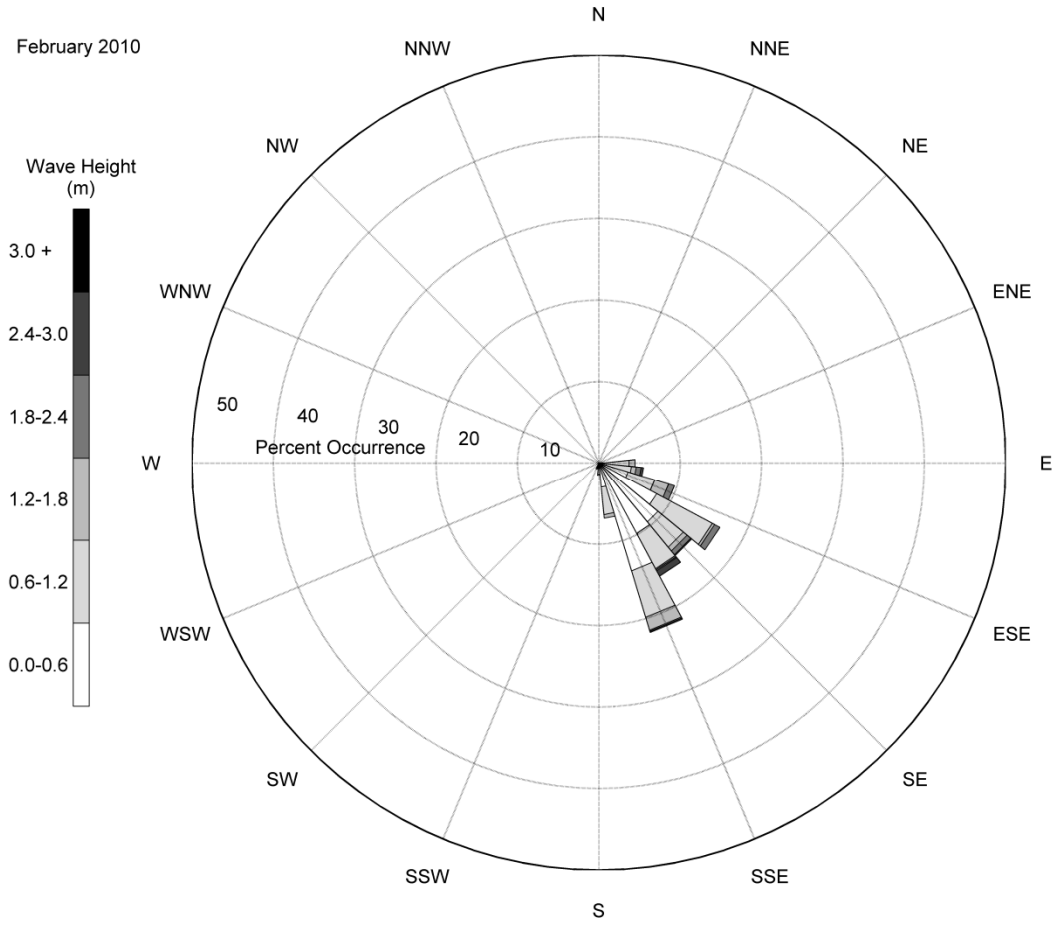

Figure A-12. Wave rose for February 2010 at Cane South, where waves from NDBC Buoy #41013 (Frying Pan Shoal, NC) were refracted to the Cane South borrow area. Wave directions are in meteorological convention.

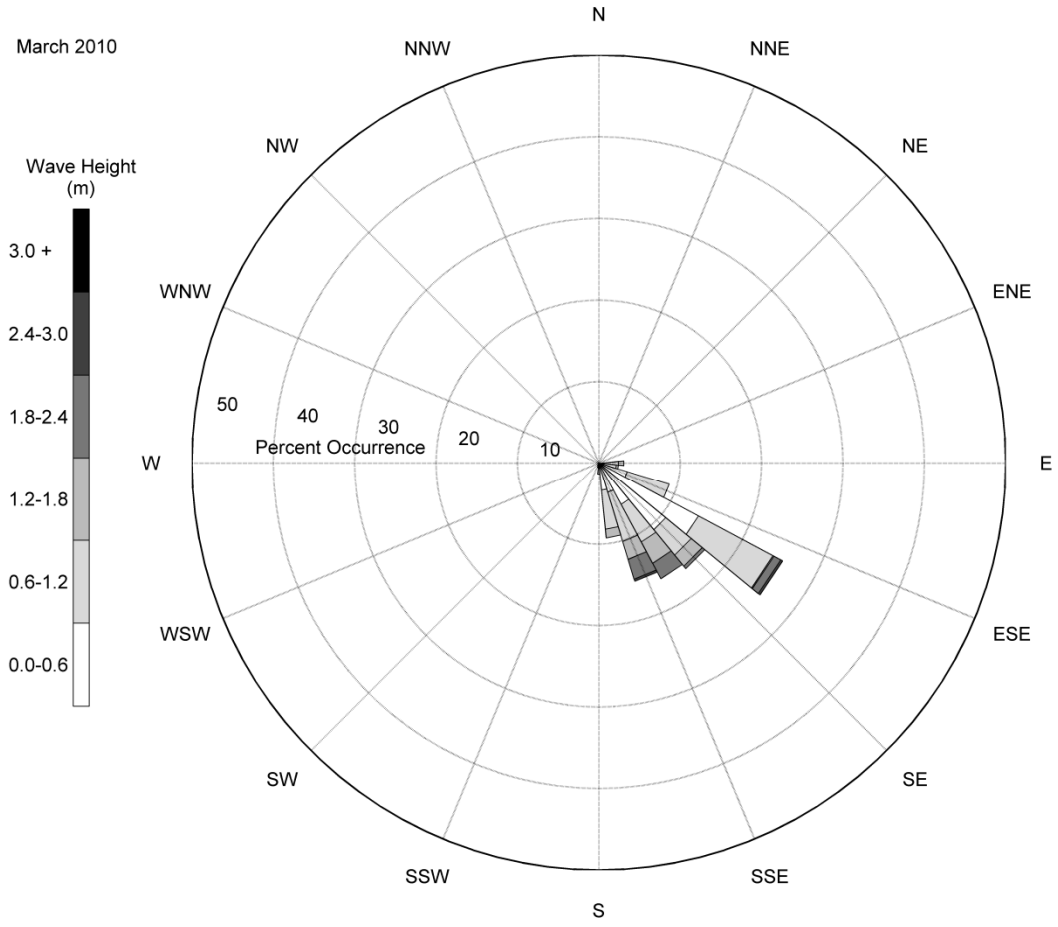

Figure A-13. Wave rose for March 2010 at Cane South, where waves from NDBC Buoy #41013 (Frying Pan Shoal, NC) were refracted to the Cane South borrow area. Wave directions are in meteorological convention.

The Department of the Interior Mission

As the Nation's principal conservation agency, the Department of the Interior has responsibility for most of our nationally owned public lands and natural resources. This includes fostering sound use of our land and water resources; protecting our fish, wildlife, and biological diversity; preserving the environmental and cultural values of our national parks and historical places; and providing for the enjoyment of life through outdoor recreation. The Department assesses our energy and mineral resources and works to ensure that their development is in the best interests of all our people by encouraging stewardship and citizen participation in their care. The Department also has a major responsibility for American Indian reservation communities and for people who live in island territories under US administration.

The Bureau of Ocean Energy Management

BOEM
Bureau of Ocean Energy Management

As a bureau of the Department of the Interior, the Bureau of Ocean Energy (BOEM) primary responsibilities are to manage the mineral resources located on the Nation's Outer Continental Shelf (OCS) in an environmentally sound and safe manner.

The BOEM Environmental Studies Program

The mission of the Environmental Studies Program (ESP) is to provide the information needed to predict, assess, and manage impacts from offshore energy and marine mineral exploration, development, and production activities on human, marine, and coastal environments.